Krishna Mohan Singh
Sushanta Dutta
Sudhakar Subudhi
Nikhil Kumar Singh *Editors*

Fluid Mechanics and Fluid Power, Volume 3

Select Proceedings of FMFP 2022

🖎 Springer

Lecture Notes in Mechanical Engineering

Krishna Mohan Singh · Sushanta Dutta ·
Sudhakar Subudhi · Nikhil Kumar Singh

Editors

Fluid Mechanics and Fluid Power, Volume 3

Select Proceedings of FMFP 2022

Editors
Krishna Mohan Singh
Department of Mechanical and Industrial
Engineering
Indian Institute of Technology Roorkee
Roorkee, Uttarakhand, India

Sushanta Dutta
Department of Mechanical and Industrial
Engineering
Indian Institute of Technology Roorkee
Roorkee, Uttarakhand, India

Sudhakar Subudhi
Department of Mechanical and Industrial
Engineering
Indian Institute of Technology Roorkee
Roorkee, Uttarakhand, India

Nikhil Kumar Singh
Department of Mechanical and Industrial
Engineering
Indian Institute of Technology Roorkee
Roorkee, Uttarakhand, India

Paper in this product is recyclable.

Contents

About the Editors

Prof. Krishna Mohan Singh is Professor in the Department of Mechanical and Industrial Engineering at Indian Institute of Technology (IIT) Roorkee. His research interests include the areas of computational mechanics, development of novel parallel algorithms, meshfree methods, shape and topology optimization, fluid dynamics, DNS/LES of turbulent flows, CAE, computer-aided analysis and design of thermo-fluid and multi-physics systems, computational fluid dynamics, modeling and simulation of flow and heat transfer in turbomachines, transport and energy systems.

Prof. Sushanta Dutta is Professor in the Department of Mechanical and Industrial Engineering at Indian Institute of Technology (IIT) Roorkee. His research interests are in the areas of experimental fluid mechanics, experimental heat transfer, optical measurement techniques, active and passive control of flow field, wake dynamics, turbulence study, Schlieren, HWA, PIV, LCT, PSP, microfluidics and heat transfer augmentation using phase change material.

Prof. Sudhakar Subudhi is Professor in the Department of Mechanical and Industrial Engineering at Indian Institute of Technology (IIT) Roorkee. His research interests are in the area of experimental heat transfer and fluid mechanics, heat transfer enhancement of natural and forced convection in water/nanofluids, natural ventilation and unconventional energy systems.

Dr. Nikhil Kumar Singh is Assistant Professor in the Department of Mechanical and Industrial Engineering at Indian Institute of Technology (IIT) Roorkee. His broad research interests include direct numerical simulations of two-phase flows and phase change, computational fluid dynamics and heat transfer, numerical methods and turbulent flows.

CFD Analysis for the Study of Automotive Underhood Aerodynamics and Thermal Management

Rutuja J. Tambekar and Ashwinkumar S. Dhoble

1 Introduction

1.1 *Automotive Aerodynamics*

The subject aerodynamics deals with the study of relative flow of fluid over the vehicle or some other entity of interest like train, buildings, aircraft, etc. A solid body will experience a net force, F, when it is placed in a flowing viscous fluid. This net force, F, is resolved into the drag force, F_D, defined as the force component acting in the flow direction, and the lift force, F_L, which is the component of the force perpendicular to the flow direction. The drag coefficient C_D and the lift coefficient C_L are calculated as

$$C_D = \frac{F_D}{\frac{1}{2}\rho U^2 A}, \tag{1}$$

$$C_L = \frac{F_L}{\frac{1}{2}\rho U^2 A}. \tag{2}$$

Automotive aerodynamics is defined as the study of flow of air, around and through a vehicle during its operating conditions with the main objective of reducing the drag. Because of drag there are added forces which resists the vehicle movement and hence upsurge in consumption of fuel. Due to growing environmental issues and the fuel prices reaching its peak, the primary factor now is cutting down on vehicle fuel use. Optimization of drag and lift specifically emphasizes on the critical zones of the fluid flow for attachment or reattachment after separation from the vehicle body

R. J. Tambekar (✉) · A. S. Dhoble
Department of Mechanical Engineering, Visvesvaraya National Institute of Technology, Nagpur 440010, India

[1]. Generally, reduction in drag and lift is done using add on devices, like spoilers, underbody diffusers, air dams, wings, side skirts, etc.

1.2 Underhood Aerodynamics

In their work on aerodynamics of cooling systems, Renn and Gilhaus studied that various underhood components which would act as hindrances such as the fans, engine and its accessories, radiator together called underhood aerodynamics add up to 10% of the total vehicular drag [2].

The interaction between external aerodynamics and the cooling air is termed as interference. Thus additional drag results because of this underhood interference. This drag arises from the cooling air which mainly depends on the car shape and its cooling configuration. Apparently, for cars with low-drag aerodynamics, cooling drag should be kept to a minimum [3].

1.3 Aero-Thermal Research, EVs and Battery Cooling

Aerodynamic thermal (aero-thermal) management is very much reliant on air flow around the components that needs cooling [1], and this traditionally focuses on under hood cooling. The air flow penetrating the underhood is useful for cooling the components but simultaneously it increases drag. In recent years, electric vehicle (EV) and hybrid electric vehicle (HEV) technology is emerging; however, there are still some challenges in battery pack cooling and require innovative solutions. The battery packs in EVs and HEVs have particular cooling requirements, which includes uniform cooling within a preferred range that is still hard to attain. Therefore, there are various research theories which focuses on various cooling methods like using liquid cooling, phase-change material, and air cooling by both natural and forced convection [4–6].

1.4 Boundary Layer Theory

When the fluid flows over a solid surface, due to no-slip condition fluid particles will get stick to the surface. If the surface is stationary, then bottom fluid layer will have zero velocity. Bottom layer will try to retard the movement of adjacent layer. This process continues and a velocity gradient is developed in a fluid. A thin region over a surface in which this velocity gradient is significant is called hydrodynamic boundary layer. If velocity of flow along the direction of flow decreases, then pressure increases and pressure gradient is positive, thus resulting in boundary layer separation. Similarly, if there exists a temperature difference between the fluid flowing over

the surface and the surface, bottom layer will reach the thermal equilibrium with the surface and there is a thin zone in which temperature gradient is significant which is called as thermal boundary layer.

2 Literature Review and Objective

2.1 Automotive Aerodynamics

Some previous studies on automotive aerodynamics highlight on enhancing outward appearance of the car body, like advantages of rounded edges or closed openings for drag reduction purpose. [7] Also further studies on extra aerodynamic components like air dams, diffusers, and spoilers as thoroughly studied by Katz [8, 9]. Also there are studies that considered the interaction between underhood and exterior of airflow, such as one that lowers the temperature by 20% and improves cooling flow through the radiator by optimizing the external airflow using ducts and air dams [10]. Also, Saab et al. [11] proposed that decreasing the front grille opening size decreases both cooling and overall drag.

2.2 Underhood Aerodynamics

The additional drag caused due to interference under the hood should be minimized. Barnard [12] used a modified Ahmed model that consist of internal ducting to undertake numerous unique experimental studies into cooling drag. Kuthada and Wiedemann [13] used numerical and experimental methods to examine the reasons of cooling air drag on a vehicle. As was to be predicted, the front of the car saw the most drag because the hood abruptly redirects airflow there. In a study on the impact of engine bay packaging density and layout on a vehicle's exterior aerodynamics, Christoffersen [14] discovered that directing cooling airflow out of the rearmost area of the front wheel housings could reduce overall drag. According to Baeder, the engine compartment and grill's directed cooling air flow may increase pressure at the grill while reducing the vehicle's aerodynamic drag [3]. A general guide for design for the optimal geometry and dimensions of an automotive underhood diffuser for the purpose of higher downforce and lower drag when taking into account an Ahmed body was mentioned in a study by Jowsey and Passmore [15].

2.3 Electric Vehicle and Battery Cooling

Generally, batteries are subjected to localized temperatures and hence may result in damage. To maintain the uniform temperature is the main objective. For the purpose of guiding the air to the battery at the proper temperature, active cooling works by bringing fresh cooling air from outside the car through a supporting air heating or cooling system first [16]. For the case of liquid cooling, though the heat transfer rate is higher when compared with air cooling but it is associated with more power to pump the cooling liquid thus affecting the mass flow rate. For air cooling forced convection method, using fans is generally used. Also focus is on channelling the air flow using ducts. For a battery pack with multiple cooling passageways, six distinct tapered shape air manifold inlet and outlet designs were numerically evaluated by Park [4]. By externally cooling the battery pack using air flow under the hood, energy required in forced convection can be saved. Khasow, R. and Agelin-Chaab, M. conducted experimental and numerical study to analyse underhood aerodynamics and cooling using underbody diffuser. Chevrolet Aveo5 test vehicle was used at different yaw angles with eddy viscosity-based SST turbulence model [1].

Thus, the overall gap is the linkage between aerodynamics and the thermal aspect specifically in the underhood of a vehicle and how the aerodynamic drag reducing add on device or modification like diffuser can be used for underhood cooling.

2.4 Objectives

- To perform numerical simulation to study automotive aerodynamics with the main aim to reduce overall drag.
- To analyse the velocity and temperature profiles at the underhood of a car affixed with heat source, i.e. a hot plate. This general case of hot plate is further extended to a specific case to study how underhood components like battery pack can be cooled.
- To study the use of diffuser for drag reduction as well as for underhood cooling specifically for battery cooling.

3 Materials and Methods

3.1 Numerical Simulation

The fluid flow is represented in differential form by the Navier–Stokes equations. The steady-state Navier–Stokes equations are as mentioned below.

$$\nabla.V = 0 \,[\text{continuity}], \tag{3}$$

$$(V.\nabla)V = -\frac{1}{\rho}\nabla p + v\nabla^2 V \text{ [momentum]},\tag{4}$$

$$0 = -V.\nabla s + \frac{Q}{T}\left[\text{Energy}\right].\tag{5}$$

The flow in this study is predominantly turbulent. Navier–Stokes equations cannot be solved directly as for turbulent flows there is no exact solution for these equations. Computational Fluid Dynamics (CFD) uses numerical methods to get the approximate solutions of the Navier–Stokes equations. Reynolds-Averaged Navier–Stokes Equations (RANS) are used here as this study involves turbulent flow. The Reynolds-Averaged Energy equation is also solved because the temperature field is also involved. The k-ω SST model in ANSYS Fluent is used for this study.

3.2 Geometry and Mesh Generation

The three-dimensional car model was developed in Creo 4.0 for the simple Honda car with a heat source, i.e. a hot plate affixed at the under hood of it and then with the diffuser. The computational flow domain's dimensions are obtained in relation to L, where L is the length of the car. The inlet flow section is located at 2.4 L upstream of the model front, while the outlet flow section is at 6.6 L downstream from the rear of the car model [17] as shown in Fig. 1. In second case, the heat source is further approximated as HEV battery pack. The battery pack is built into the angled surface of a drag and downforce diffuser design as given by Jowsey and Passmore [15], and it is compared with the scenario in which diffuser is not used. The angle for this diffuser was set to 14.5°. The named selections given are inlet, outlet and walls for the enclosure, and the entire car surface and hot plate are termed as "car" and "hotplate", respectively.

Unstructured tetrahedral mesh was generated for the geometry and finer mesh was used near the car surface in critical areas as shown in Fig. 2.

3.3 Grid Independence

The grid independence test was studied as given in Table 1. From Table 1 it can be observed that, after mesh 3 further increase in the mesh size will not have a remarkable effect on the results, so mesh 3 is used for all numerical computations.
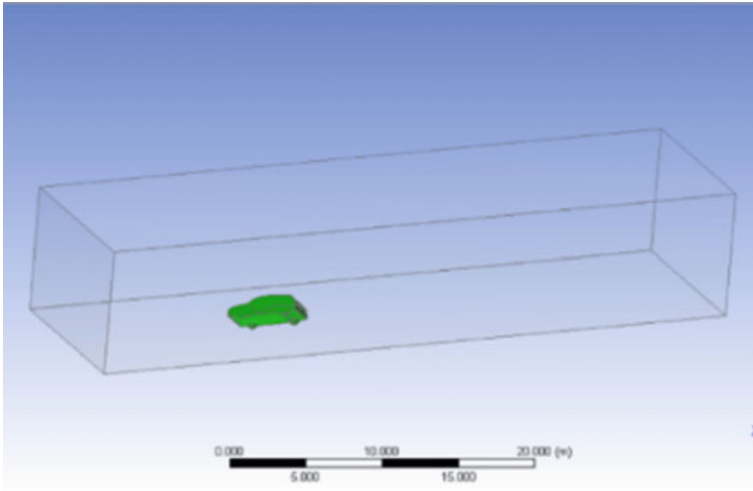
Fig. 1 Vehicle model inside computational domain
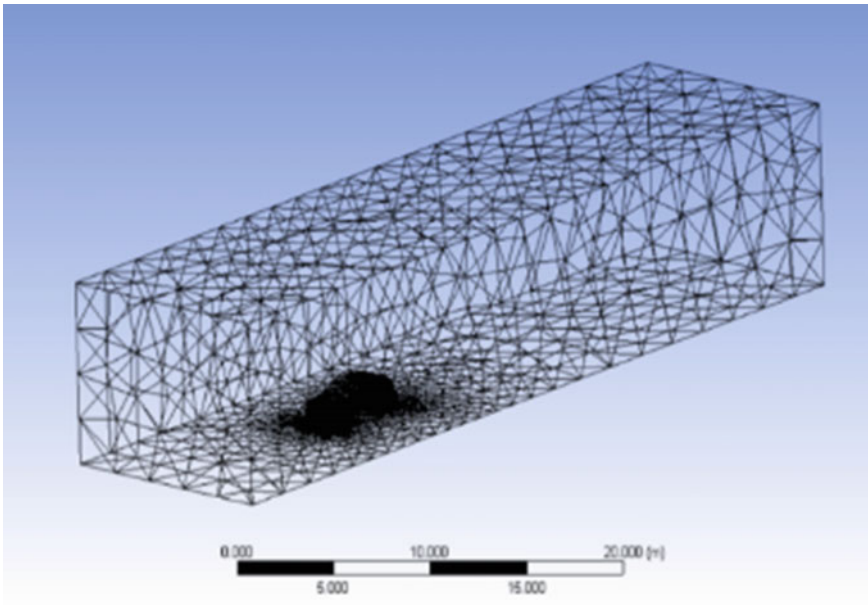
Fig. 2 Entire mesh domain

Table 1 Grid independence results

Mesh size (no. of elements)	C_D
Mesh 1—650,000	0.326
Mesh 2—830,000	0.317
Mesh 3—920,000	0.301
Mesh 4—1,000,000	0.301

3.4 Boundary Conditions

The floor and all the surfaces of the car model are subjected to the no-slip boundary condition. To consider the highway condition, the inlet velocity is specified as 100 km/h, such that air cooling would be efficient because of higher speed and higher convective rate of heat transfer. The turbulent intensity was set to 1% [17]. A constant average temperature was the applied boundary condition to the hotplate. At the domain outlet, zero relative pressure was stated as the outflow condition. For the underbody battery pack cooling case, 245 W/m^2 heat flux was specified from the battery pack surface as suggested by Park [4]. Both the ambient temperature and the inlet air temperature were assumed to be 300 K.

4 Results and Discussion

4.1 Velocity Results

The air flow strikes the front portion of the car, stops, and then splits to go over and under it. Because of various obstructions in the under hood path, the flow is slower under the vehicle as compared to over it. In the rear part, there is a wake because of air separation. In practical case, the underhood heating sources are radiator, engine, and auxiliary components such as turbo, starter motor and pump and batteries in case of EVs and HEVs. As the cooling of battery packs in EV and HEV vehicles involves many challenges, external air cooling can be used like in hotplate case. Also, the battery capacity is reduced because of the damage caused by overcharging of individual cell due to different charging rate. For prevention of these high temperature zones, it is important to maintain the batteries at a uniform and consistent temperature. Thus instead of using other forced convection cooling methods like fans, diffuser is used. This results in potential energy saving.

This section analyses the local velocity variations via the diffuser and the impact it has on the battery pack surface temperature. The goal is to determine if an increase in velocity and convective heat transfer at the diffuser's inlet can compensate for a decrease in convective heat transfer at the diffuser's exit caused by a decrease in velocity [1].

Figure 3 depicts the velocity contours at the mid-plane of the car for both diffuser and without diffuser scenario. The wake region can be identified in both the cases at the rear of the car with certain differences in both the situation.

Figure 4 depicts the enlarged view of the flow patterns at the vehicle's rear part at the mid-plane, respectively. As the front geometries for both cases are same, the velocity contours in front are same. For rear of the vehicle, variation is seen as the dead air volume, or the region of little or no velocity, is bigger for the diffuser example. Since it is a drag and downforce optimized design of the diffuser, it means that there is a high pressure region at the rear of the car to balance the stagnation point at the front, lowering pressure drag. Again, the flow is not completely detached from the battery pack.

The flow nearer to battery pack is slower, as estimated since the flow continues downstream to the rear part of the vehicle. At the diffuser throat, a larger portion of the air is faster when compared with the case of no diffuser. Another advantage is that the diffuser helps in controlling of vortices formation in the wake in the rear

Fig. 3 Contours of velocity at car mid-plane (**a**) without diffuser (**b**) with diffuser

(a)

(b)
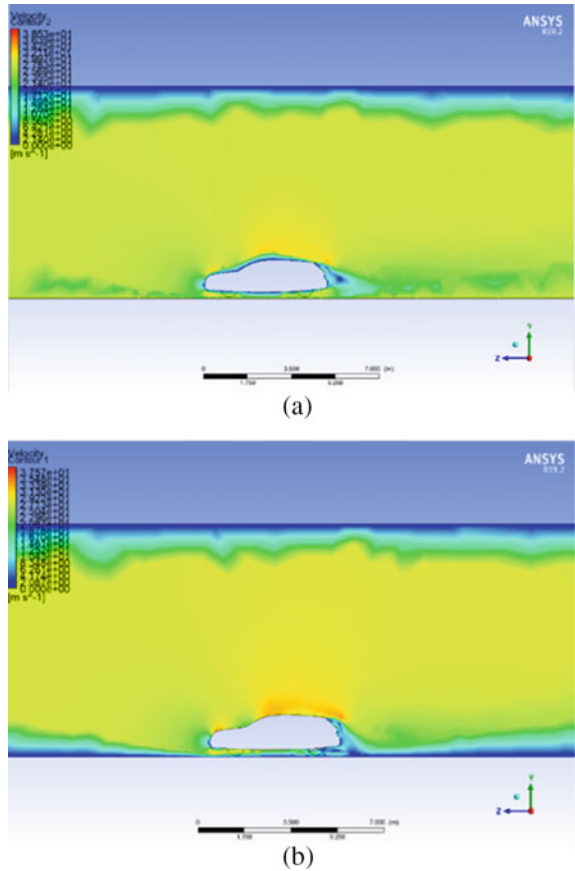
Fig. 4 Contours of velocity at mid-plane at the rear of the car (**a**) without diffuser (**b**) with diffuser

(a)

(b)
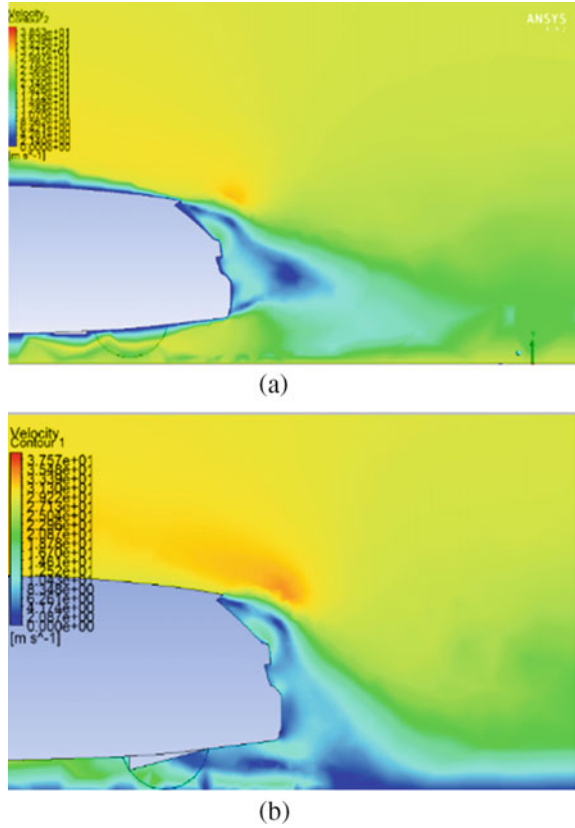
bumper section. The decrease in vortices raises the pressure behind the car in the diffuser scenario and reduces drag as predicted from the drag-optimized design of diffuser.

4.2 Thermal Results

Figure 5 shows zoomed in view of the contours of temperature from the side profile of the car for a generalized hotplate case. Figure 5 depicts the way the heat convection takes place away in the direction perpendicular (vertically in Fig. 5) to the surface of the hotplate. As the air moves downstream down the hotplate, the temperature differential is reduced as the heat convects away in a boundary layer under the influence of air velocity and air heating.

To illustrate the heat convection away from the hotplate, Fig. 6a–c shows the temperature isosurfaces for three different temperatures of 300.125, 301, 303 K [18]. The heat that is convected away moves in the same direction of the flow. From
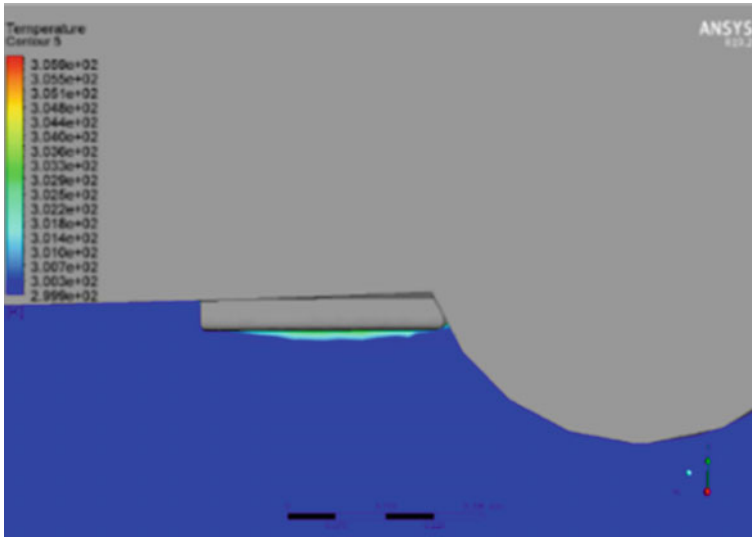
Fig. 5 Zoomed in view of the temperature profile around the hot plate from the vehicle side profile

the contours it can be understood that as the temperature increases heat flow gets trapped. Also for a particular case, the more temperature would be near the heat source and cold air diffuses further.

Figure 7 depicts the temperature contours for the battery pack. In both the cases hot spots are present, mainly because of the asymmetrical underbody which affects the flow. For the first case, i.e. the no diffuser one, there is the presence of hot spots mainly in two areas near the leading edge and in the middle of trailing edge. However, for the second case, the one which includes diffuser, the hot spots exist roughly in the middle of the rear trailing edge. Another observation is that due to diffuser there is a delay in the appearance of hotspot and there is shift further downstream. Though there is minor increase in the maximum value of the temperature in the battery pack, the leading edge of the pack is cooled by the increase in velocity at the diffuser throat.

Figures 8, 9 and 10 indicate isosurface plot at temperatures values of 300.125 K, 301 K and 303 K, respectively [18]. Figure 8(a) indicates how recirculation directly off the trailing edge cause the heat to somewhat become trapped behind the battery pack; on the other hand in the diffuser case of Fig. 8b, there is faster heat dissipation because of build in design of the battery pack with the diffuser which removes the zone of recirculation. Also it shows the relatively quick movement of heat from the diffuser inlet.

Figure 9 indicates isosurfaces at temperature of 301 K. In the diffuser scenario, more air at this given temperature is found near the battery, particularly downstream and close to the battery pack's back, where there appear to be greater pockets of 301 K air. As a result, hot air is rapidly removed from the diffuser's leading edge, as indicated by the isosurface further downstream in the diffuser one compared to the
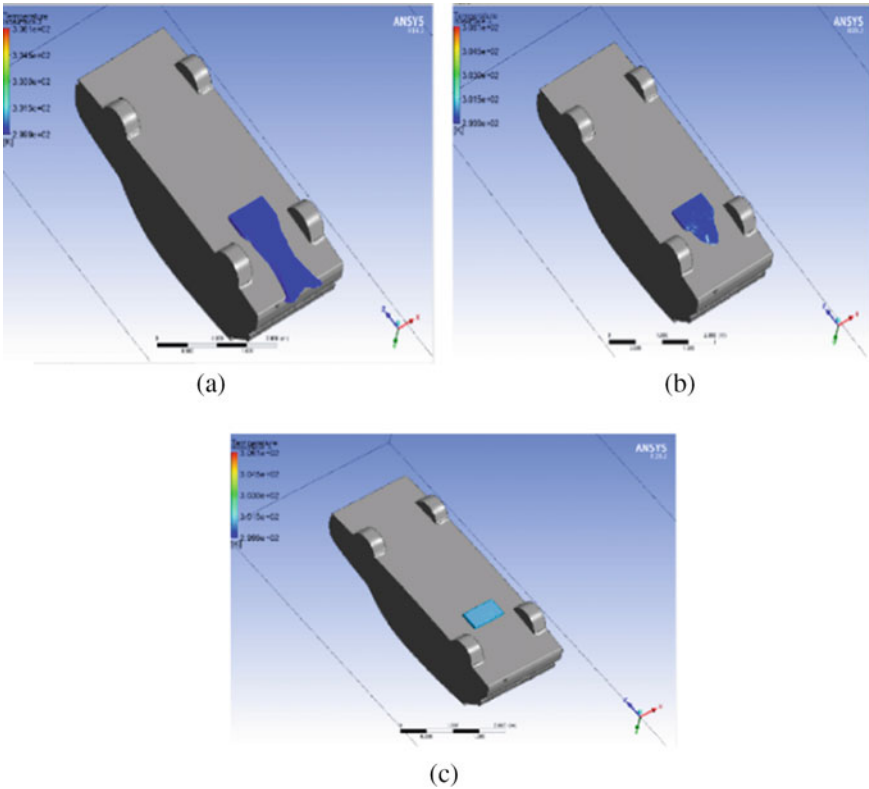
Fig. 6 Temperature isosurface **(a)** 300.125, **(b)** 301 **(c)** 303 K

without diffuser scenario. Figure 10 shows temperature isosurfaces at 303 K with a comparatively smaller isosurface.

4.3 Validation

Table 2 depicts the C_D values from the numerical simulation carried out in the previous studies with comparative analysis of with and without diffuser. The results from the present work including velocity and temperature contours and temperature isosurfaces are in good agreement with the literature. Also for the battery pack simulation, the maximum surface temperature obtained is 305.6 K which is close to 306 K from the study by Khasow and Agelin-Chaab [18].

Fig. 7 Contours of temperature for the battery pack surface **(a)** without diffuser **(b)** with diffuser
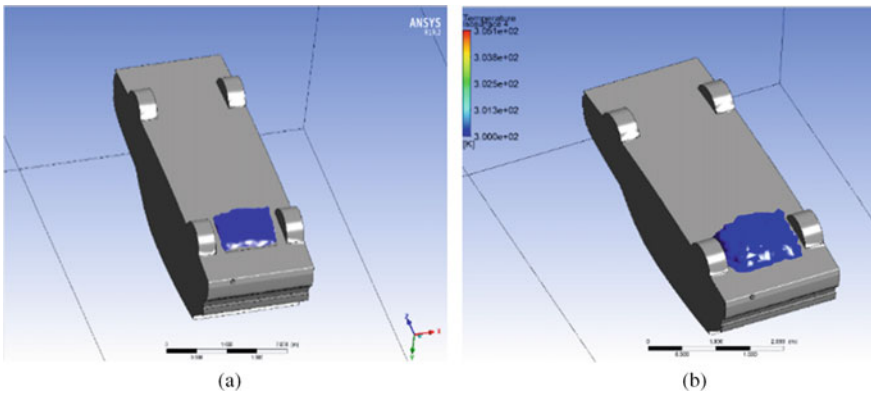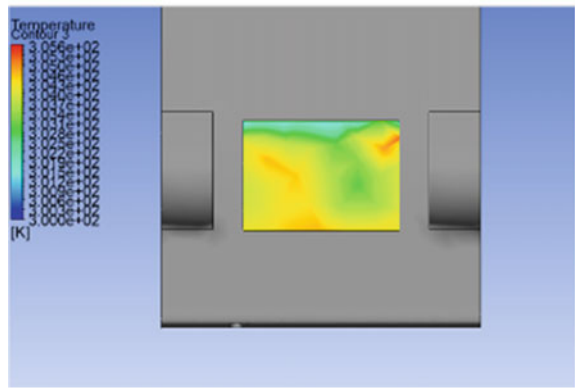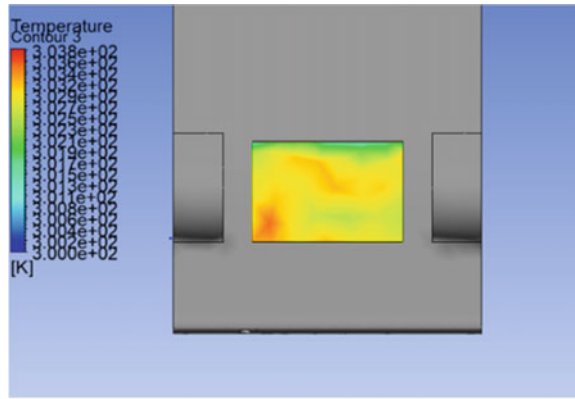
Fig. 8 Temperature isosurface for the battery pack at 300.125 K **(a)** without diffuser **(b)** with diffuser
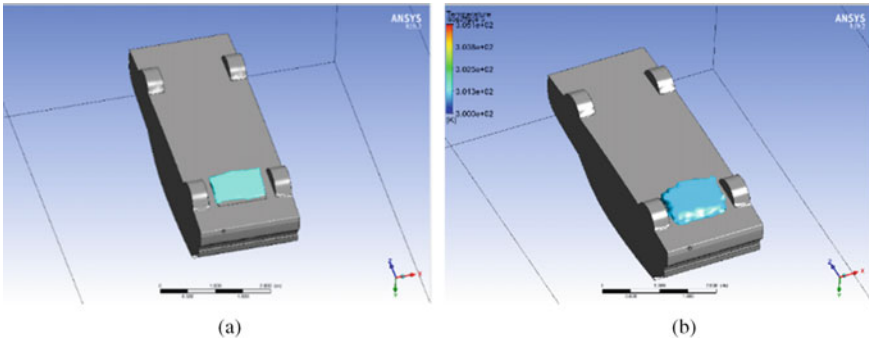
Fig. 9 Temperature isosurface for the battery pack at 301 K **(a)** without diffuser **(b)** with diffuser
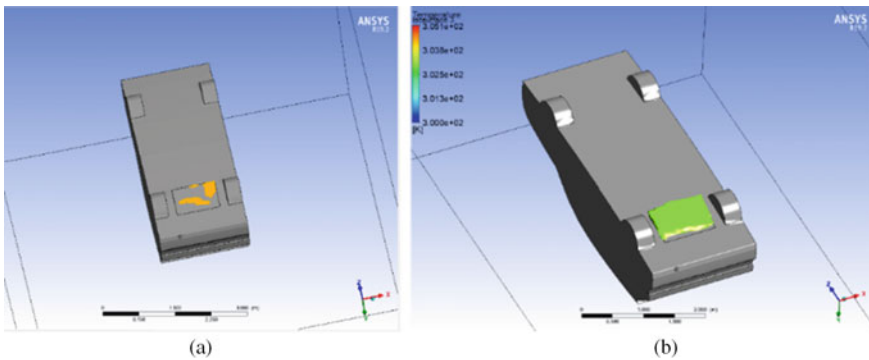
Fig. 10 Temperature isosurface for the battery pack at 303 K **(a)** without diffuser **(b)** with diffuser

Table 2 Comparison of drag coefficient with literature data

Literature review	C_D (No diffuser)	C_D (diffuser)
Kang [20]	0.2838	0.2721
Ajith Balaa [19]	0.3015	0.2895
Present work	0.3012	0.2887

5 Conclusion

To summarize, the results shows that the underhood rear diffuser has significant impact on the velocity and temperature distribution of the underhood geometry specifically the inbuilt battery surface. Due to diffuser, there is more consistent temperature distribution and thus smaller hotspots than without it. Thus, the battery damage can be avoided that may occur because of number of cells getting affected by temperature localization. Also when compared with the no diffuser situation, the

temperature upstream of the battery pack surface is decreased and that of down-stream increased. This can further be improved by working on the modification in the diffuser design. Thus this can be considered as one of the method for underhood cooling without using source like fan and thus saving energy as well.

Nomenclature

A	Frontal area of rotor [m^2]
U	Free stream velocity [m/s]
C_D	Drag coefficient
C_L	Lift coefficient
ρ	Density of air [kg/m^3]
F_D	Drag force [N]
F_L	Lift force [N]
ν	Kinematic viscosity [m^2/s]
p	Pressure [Pa]
V	Velocity vector
Q	Heat transferred [W]
T	Temperature [K]

References

1. Khasow R (2014) Aerodynamic and thermal analysis of a heat source at the underside of a passenger vehicle. Master of Applied Science Thesis, University of Ontario Institute of Technology
2. Renn V, Gilhaus A (1986) Aerodynamics of vehicle cooling systems. J Wind Eng Ind Aerodyn 22:339–346
3. Baeder D, Indinger T, Adams N, Unterlechner P (2012) Aerodynamic investigation of vehicle cooling-drag. In: SAE technical paper, no. 2012-01-0170. https://doi.org/10.4271/2012-01-0170
4. Park H (2013) A design of air flow configuration for cooling lithium ion battery in hybrid electric vehicles. J Power Sour 239:30–36
5. Pesaran AA (2001) Battery thermal management in EVs and HEVs: issues and solutions. National Renewable Energy Laboratory
6. Pesaran AA (2002) Battery thermal models for hybrid vehicle simulations. J Power Sour 110:377–382
7. Cooper KR (1993) Bluff body aerodynamics as applied to road vehicles. J Wind Eng Ind Aerodyn 49(1–3):1–22
8. Katz J (1995a) Airfoils and wings. In: Katz J (ed) Race car aerodynamics: designing for speed. Bentley Publishers, Cambridge, MA, USA
9. Katz J (1995b) Aerodynamics of the complete vehicle. In: Katz J (ed) Race car aerodynamics: designing for speed. Bentley Publishers, Cambridge, MA, USA
10. Costa E (2003) CFD approach on underhood thermal management of passenger cars and truck. In: SAE technical papers, 2003-02-3577

11. Saab S, Hetet J-F, Maiboom A, Charbonnelle F (2013) Impact of the underhood opening area on the drag coefficient and the thermal performance of a vehicle. In: SAE technical paper, no. 2013-01-0869. https://doi.org/10.4271/2013-01-0869
12. Barnard RH (2000) Theoretical and experimental investigation of aerodynamic drag due to automotive cooling systems. J Automob Eng 214(8):919–927
13. Kuthada T, Wiedemann J (2008) Investigations in a cooling air flow system under the influence of road simulation. In: SAE technical papers, 2008-01-0796
14. Christoffersen L, Löfdahl L, Jönson A (2010) Interference between engine bay flow and external aerodynamics of road vehicles. In: SAE technical paper, no. 2010-01-0288. https://doi.org/10.4271/2010-01-0288
15. Jowsey L, Passmore M (2010) Experimental study of multiple-channel automotive underbody diffusers. Proc Inst Mech Eng 224:865–879
16. Rao Z, Wang S (2011) A review of power battery thermal energy management. Renew Sustain Energy Rev
17. Lan KT, Srinivasan K (2009) Influences of free stream conditions on vehicle thermal management—an analytical study. In: SAE technical papers, 2009-01-1152
18. Khasow R, Agelin-Chaab M (2015) Automotive underbody diffuser for battery thermal management. Int J Process Syst Eng 3(1/2/3):110–125
19. Ajith Balaa S, Aravind S, Kowshik Santhakumar N, Saravana Kumar S (2021) Drag reduction in the sedan car by implementing diffuser to improve the fuel efficiency. https://doi.org/10.1007/978-981-15-9809-8_49
20. Kang SO, Jun SO, Park HI, Song KS, Kee JD, Kim KH, Lee DH (2012) Actively translating a rear diffuser device for the aerodynamic drag reduction of a passenger car. Int J Automot Technol 13(4):583–592. https://doi.org/10.1007/s12239-012-0056-x

Numerical Study of Nozzle Exhaust Plume Impingement on Flat Plate Under Low Pressure Environment

Anant Singhal, Deepak K. Agarwal, T. John Tharakan, and S. Sunil Kumar

1 Introduction

Thrusters are used in spacecraft for various purposes ranging from attitude control to orbit raising. Hot gas exhaust plume from these thrusters expand widely into the vacuum of space and often impinge on the spacecraft structure. The plume impingement on the spacecraft produces disturbing torques and heat fluxes that are undesirable. Besides, multiple thrusters are employed in the lunar lander and manned mission spacecraft where the interaction of plumes from these thrusters generate a complex flow field and impinge on the spacecraft components. This impingement results in high heat fluxes on the components that need to be protected using an appropriate multi-layer thermal protection system. However, the design of such thermal protection systems require estimation of the heat fluxes generated due to plume impingement. In view of this, it is essential to study the plume expansion into low pressure ambient and estimate the plume impingement parameters such as pressure and heat flux on the surface.

2 Literature Review and Objective

The structure of highly under-expanded jets was investigated by Adamson and Nicholls [1] and Latvala [2]. It was determined that the dimensions of exhaust plumes in quiescent atmosphere scale as the inverse square root of the ambient pressure. The issues associated with plume impingement on spacecraft surfaces were discussed by Vick et al. [3]. An early description of plume impingement forces was given by

A. Singhal (✉) · D. K. Agarwal · T. John Tharakan · S. Sunil Kumar
Liquid Propulsion Systems Centre, ISRO, Trivandrum, Kerala 695547, India
e-mail: anantsinghal@lpsc.gov.in

Boettcher and Legge [4]. A survey on plume flow and impingement in space technology has been given by Dettleff [5]. The emphasis was on chemical and cold gas plume model development, and on force and heat transfer determination. Piesik et al. [6] performed an experimental study of nozzle plume impingement on a flat plate located at various angles and distances. The impingement pressure and temperature were measured on the plate. Heating rates were determined from the temperature rise rate. It was found that the impingement pressure and heat flux decreases as the plate is moved away from the plate. The local impingement heat flux was found to be drastically reduced for plates canted away from the nozzle.

Woronowicz et al. [7] derived an analytical solution for one-dimensional unsteady free jet expansion in to a vacuum. The widely used cosine law or the Boynton/Simons plume model [8, 9] provides an approximate far field density distribution which takes a form of a cosine function. Based on these, Cai et al. [10] presented a set of gas kinetic solutions to the problem of unsteady collisionless round plume development. Gimelshein et al. [11] carried out DSMC simulations to investigate the interaction of a jet from a 3000-N-class thruster positioned on the side of small rocket with a rarified atmosphere at 80 km and 100 km. Chemical reactions between freestream and plumes were included. The results presented for the flow field and surface mass flux demonstrated possible contamination of an on-board radiance sensor located on the cylindrical part of the rocket for different freestream and plume conditions.

Usually, for thrusters firing in vacuum, the flow inside the nozzle is in continuum regime, whereas the plume lies in the rarefied regime. In view of this, a hybrid approach with the combination of Navier–Stokes solvers and DSMC has been reported by various researchers. Lumpkin [12] has carried out study of plume expansion and impingement using the hybrid approach. Numerical simulations and experimental works on vacuum plume and its effects have been reported by He et al. [13]. They carried out experiments in a supersonic low density wind tunnel and simulated the same using DSMC and Navier–Stokes combined approach to verify PWS (plume workstation) software. Bermúdez et al. [14] have reported the simulations of plume impingement effects on the Cygnus spacecraft using the hybrid approach. Vashchenkov et al. [15] have used hybrid approach to study of the mechanisms of the flow turn around the nozzle lip and the back flow origination.

The present work is aimed to conduct a CFD modelling of the nozzle plume expansion into low pressure environment and estimate the pressure and heat fluxes due to plume impingement on a flat surface. The study is carried out for the experimental conditions reported in [6]. Initially, CFD modelling is carried out with no-slip boundary, and the obtained results are compared with the reported experimental data. Subsequently, a temperature jump boundary is incorporated at the plate in the CFD model and the effect of the partial slip condition on the plume impingement heat flux are brought out. The details of the modelling and its results are presented in this paper.

3   Governing Equations

The governing equations of continuity, momentum and energy are as follows:

$$\frac{\partial \rho}{\partial t} + \nabla \cdot (\rho \vec{v}) = 0, \tag{1}$$

$$\frac{\partial (\rho \vec{v})}{\partial t} + \nabla \cdot (\rho \vec{v} \vec{v}) = -\nabla p + \nabla \cdot \left(\overline{\overline{\tau}} \right) + \rho \vec{g} + \vec{F} \tag{2}$$

where p is the static pressure, $\rho \vec{g}$ is the gravitational body force, and $\overline{\overline{\tau}}$ is the stress tensor given as

$$\overline{\overline{\tau}} = \mu \left[(\nabla \vec{v} + \nabla \vec{v}^T) - \frac{2}{3} \nabla \cdot \vec{v} I \right], \tag{3}$$

$$\frac{\partial (\rho E)}{\partial t} + \nabla \cdot (\vec{v}(\rho E + p)) = \nabla \cdot \left(k_{\text{eff}} \nabla T - \sum_j h_j \vec{J_j} + \left(\overline{\overline{\tau_{eff}}} \cdot \vec{v} \right) \right), \tag{4}$$

where $\overline{\overline{\tau_{\text{eff}}}}$ is the effective stress tensor and $\vec{J_j}$ is the diffusion flux of species j.

The SST k-ω model was used to include the effects of turbulence. The transport equations solved for k and ω are as follows:

$$\frac{\partial}{\partial t} (\rho k) + \frac{\partial}{\partial x_i} (\rho k u_i) = \frac{\partial}{\partial x_j} \left[\Gamma_k \frac{\partial k}{\partial x_j} \right] + \overline{G}_k - Y_k, \tag{5}$$

$$\frac{\partial}{\partial t} (\rho \omega) + \frac{\partial}{\partial x_i} (\rho \omega u_i) = \frac{\partial}{\partial x_j} \left[\Gamma_\omega \frac{\partial \omega}{\partial x_j} \right] + G_\omega - Y_\omega + D_\omega. \tag{6}$$

4   Solution Approach

4.1   Numerical Model

Steady state 3D simulations are carried out using the commercial CFD code ANSYS FLUENT, which is based on the cell centred finite volume approach. A density-based coupled solver was used to solve the governing equations. The nonlinear governing equations were solved iteratively until the solution was converged [16]. The algorithm solves the system of momentum, continuity and energy equations in a closely coupled manner. Second-order discretization schemes were used for better accuracy.

The simulation was considered to be converged when the globally scaled residuals decreased to 10^{-4} for all the equations except the energy equation for which the criteria used was 10^{-5}. Additional criteria set for convergence were the stabilization

of various parameters of interest, viz. maximum heat flux, average heat flux, and the maximum pressure on the plate. The mass and energy flux imbalances for the domain were less than 0.5%.

4.2 Computational Domain and Boundary Conditions

Figure 1 shows the computational domain used for the study. A conical nozzle of 34.85 mm exit radius (R_e) and area ratio (ε) $= 10$ is used in the simulations. The plate on which the plume impinges is $1.83 \times 1.83 \times 0.0254$ m. The domain is 2.8 m in height and width and 3.1 m along the nozzle axis. In the current work, simulations were carried out for three conditions given in Table 1.

Similar domains are also used for cases 2 and 3. The domain is meshed with hexahedral elements. Finer elements are created in the nozzle and in the plume region to capture the gradients accurately. Boundary layers are generated on the plate with the first cell distance of 0.2 mm that results in wall $y+ < 1$. The minimum mesh orthogonality is 0.2, and maximum skewness is 0.79.

Fig. 1 Computational domain for nozzle $\varepsilon = 10$, $\delta = 0°$ and $h = 3R_e$
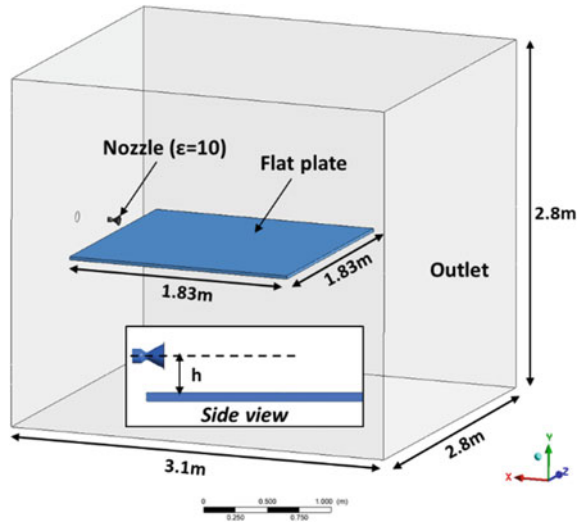
Table 1 Cases modelled in the current work

Case	Nozzle area ratio (ε)	Angle of plate with nozzle axis (δ)	Distance of plate from nozzle axis (h)
1	10	0°	$3R_e$
2			$5R_e$
3			$7R_e$

Table 2 Boundary conditions specified in the analysis

Boundary	Total pressure, MPa	Total temperature, K	Static pressure, MPa
Nozzle inlet	0.621	3112.6	–
Domain outlet	–	–	6.8×10^{-6}

Table 2 gives the boundary conditions used in the present simulations. Pressure, temperature at the nozzle inlet and pressure at the domain outlet, shown in Fig. 1, are specified as boundary conditions for the steady state analysis. All other surfaces of the vacuum chamber are specified as walls. The values of the boundary conditions are given in Table 2. It is reported in [6] that the fuel used was 50% UDMH, 50% N_2H_4 and the oxidizer used was N_2O_4. These fuel and oxidizer were used at a mixture ratio of 2. Therefore, mixture of the combustion products of the above fuel and oxidizer was used as the working fluid in the present analysis.

4.3 Grid Independence Study

Simulations were carried out for three grid sizes, viz. 11 lakhs, 49 lakhs and 64 lakhs for the case $\varepsilon = 10$, $\delta = 0°$ and $h = 3R_e$. The variation of Mach number along the centreline passing through the nozzle axis is shown in Fig. 2 for the three grids. It can be seen that the difference in results with 49 lakhs and 64 lakhs grid size is insignificant. Thus, all simulations reported in this work are carried out using the grid size of 49 lakhs.

Fig. 2 Mach number variation along nozzle axis for three grid sizes ($\varepsilon = 10$, $\delta = 0°$ and $h = 3R_e$)
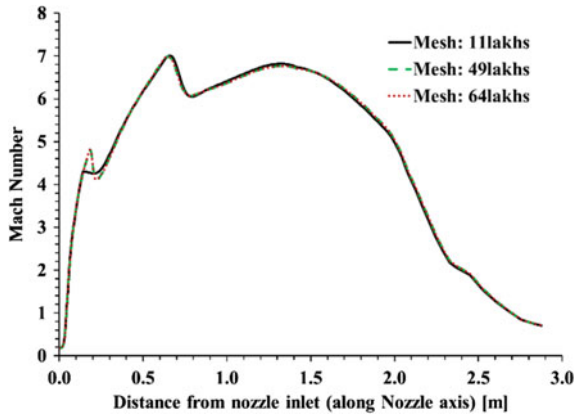
5   Results and Discussion

Figure 3 shows the contours of Mach number on a symmetric cut-plane passing through the nozzle and the plate for $h = 3R_e$. It is seen that the under-expanded plume further expands into the ambient as it flows out of the nozzle. However, the plate at the bottom restricts the plume expansion and a compression shock is formed. The plume on the top side expands until it encounters the chamber wall. The plume then reflects from the wall and flows out of the chamber.

Considering that the present work pertains to the CFD simulation of plume expansion into low pressure environment, the distribution of Knudsen number was computed to identify the regions where the flow field is in continuum regime. The classification of flow regimes based on Knudsen number is shown in Table 3 [17]. The error in the Navier–Stokes result becomes significant in regions, where $0.1 <$ Kn < 0.2 [18].

Figure 4 shows the distribution of Knudsen number (Kn) clipped to 0.1 on the cut-plane and the plate. It is seen that the regions near the nozzle exit and at the plume impingement location are within Knudsen number of 0.1.

Figure 5 shows the variation of Knudsen number along the plate centreline. It is seen that the Knudsen number < 0.01 in the region between $X/R_e = 1.3–9$. Thus, the assumption of continuum is valid in these regions. However, the region beyond $X/$

Fig. 3 Contours of Mach number on a symmetry plane for $\varepsilon = 10$, $\delta = 0°$ and $h = 3R_e$
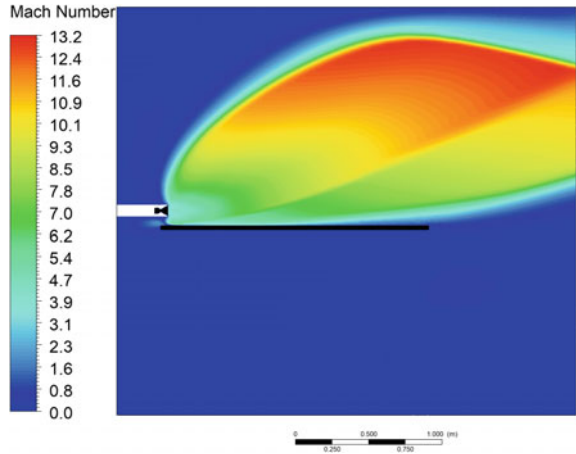
Table 3 Classification of flow regimes based on Knudsen number [Anderson]

Knudsen number	Flow regime
Kn < 0.01	Continuum
0.01 < Kn < 0.2	Transitional
Kn > 0.2	Free molecular

Fig. 4 Contours of Knudsen number on symmetry plane and plate for $\varepsilon = 10$, $\delta = 0°$ and $h = 3R_e$
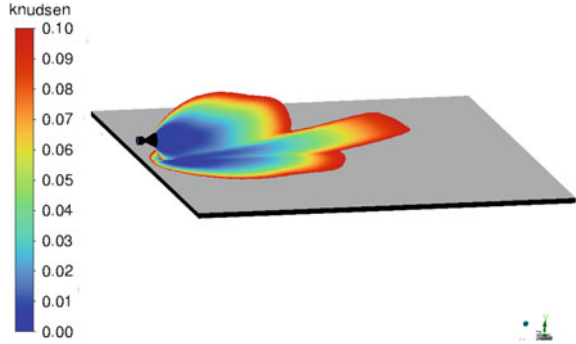
Fig. 5 Knudsen number variation on the plate centreline for $\varepsilon = 10$, $\delta = 0°$ and $h = 3R_e$
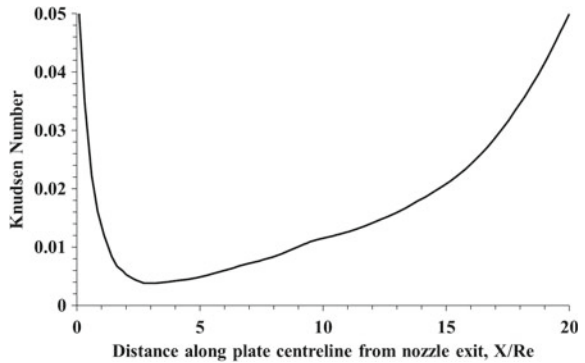
$R_e = 9$, where Knudsen number is in the range of 0.01–0.2, lies in the transitional regime.

The pressure distribution due to plume impingement on the plate kept at a distance of $3R_e$ is shown in Fig. 6. The pressure is maximum at the location, where the plume impinges on the plate due to momentum transfer from the high velocity plume. Subsequently, the pressure decays in both downstream and radial directions as seen in Fig. 6.

The distribution of heat flux on the plate kept at a distance of $3R_e$ is shown in Fig. 7. It is seen that the heat flux distribution on the plate is similar to the pressure distribution shown in Fig. 6. The heat flux is maximum at the plume impingement point on the plate and then decreases in the radial and downstream directions. The heat flux is maximum at the impingement location due to the conversion of plume kinetic energy to thermal energy.

Figure 8 shows the pressure variation along the plate centreline obtained from the present numerical model and its comparison with the measured data [6] for $h = 3R_e$ condition. The maximum pressure estimated from CFD is 2304.4 Pa compared to the experimental value of 2343.4 Pa. Thus, the difference between the maximum pressures between numerical and experimental data is 1.6%. It is seen that the location of the maximum pressure obtained numerically compares well with the experimental

Fig. 6 Pressure distribution
on flat plate for $\varepsilon = 10$, $\delta =$
$0°$ and $h = 3R_e$ (view normal
to the plate)
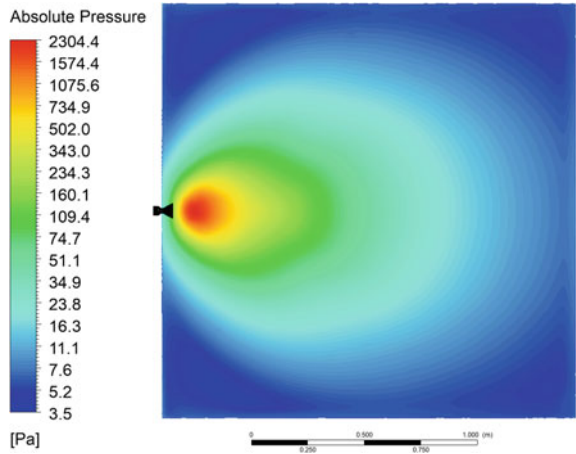
Fig. 7 Heat flux distribution
on flat plate for $\varepsilon = 10$, $\delta =$
$0°$ and $h = 3R_e$ (view normal
to the plate)
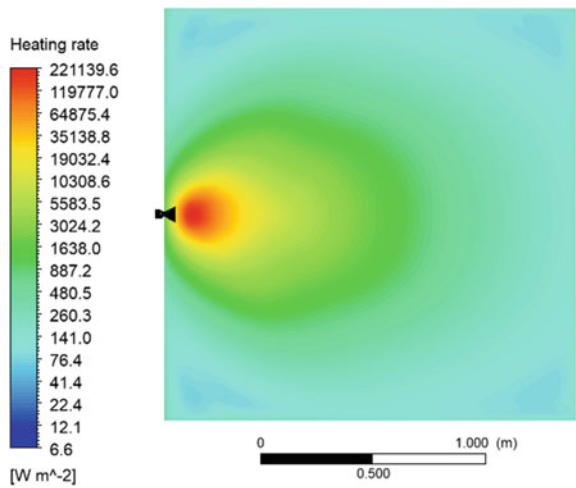
data. However, downstream of the impingement point simulated pressure is over-
estimated compared to the experimental value. It is to be noted that flow field changes
from continuum to transitional regime from $X/R_e = 9$ onwards. This may be the
reason of mismatch observed in computed pressure values compared to experimental
values.

The comparison of pressure variation along the plate centreline for the three
standoff distances is shown in Fig. 9. The maximum pressure decreases with increase
in the plate standoff distance from the nozzle. It is also seen that the location of the
maximum pressure shifts downstream with increase in the standoff distance.

The variation of heat flux on the plate centreline is shown in Fig. 10 for the three
cases simulated in the present work. The comparison with the reported measured

Fig. 8 Comparison of pressure on plate centreline between CFD and test data
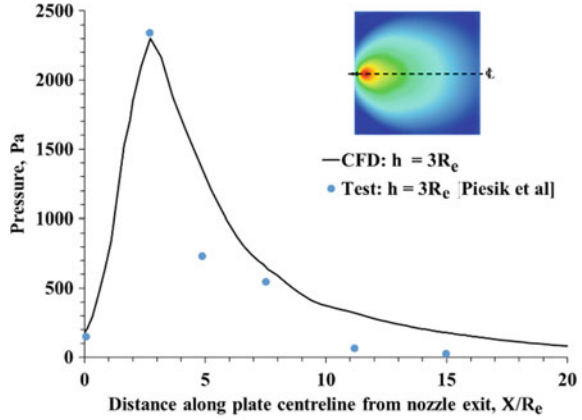
Fig. 9 Pressure distribution along the plate centreline for the three cases simulated
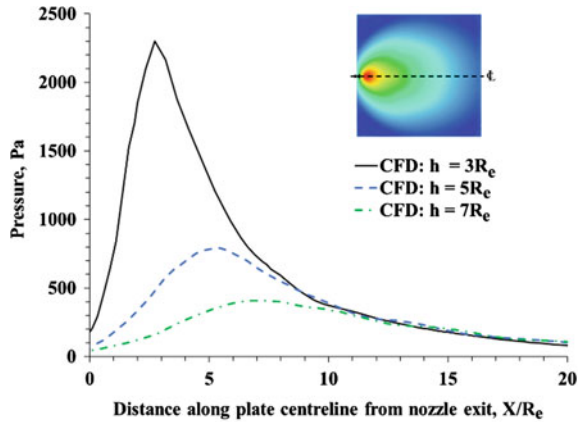
data [6] is also shown in Fig. 10. It is seen that the locations of the maximum heat flux estimated from current numerical study compare well with the measured value for all the three cases. The maximum heat flux is over-predicted for $h = 3R_e$ by 6.2% and under-predicted for $h = 5R_e$ and $7R_e$ by 11.9% and 2.9%, respectively. It is also seen that the numerical model consistently under-predicts the heat flux beyond $X/R_e = 6$, 9 and 12, respectively for $h/R_e = 3$, 5 and 7. Maximum under-prediction of 30.2% is obtained for $h/R_e = 3$. This under-prediction may be due to the effects of non-continuum in the regions away from the impingement point as shown in Figs. 4 and 5.

It is seen from Fig. 10 that the maximum heat flux decreases as the distance of plate from the nozzle increases. The location of the maximum heat flux also shifts downstream for increasing plate distance. It is to be noticed from Fig. 10 that downstream of $X/R_e = 7$, the heat flux for the case of $h = 3R_e$ is lower compared to the other two cases. This is because the flow downstream of impingement is turned

Fig. 10 Comparison of heat
flux on plate centreline
between CFD and test data
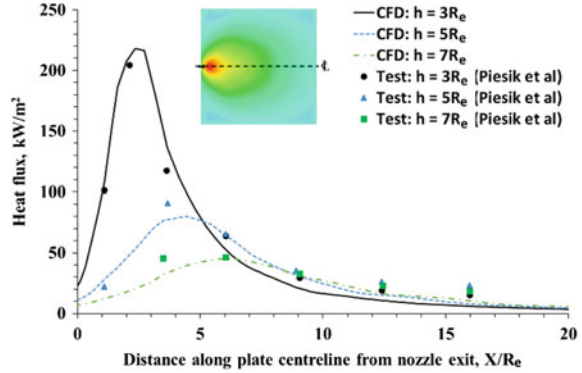
away from the plate due to the compression shock for $h/R_e = 3$ as shown in Fig. 11a.
However, as shown in Fig. 11b, c, the hot plume flows along the plate downstream
of the impingement point for $h/R_e = 5$ and 7.

As mentioned above and seen in Fig. 10, the heat flux estimated from CFD is
under-predicted in the transitional regime. In view of this observation, a partial slip
with temperature jump at the plate was subsequently incorporated in the model to
improve the heat flux estimation in the region having transitional regime. The heat
flux at the plate centerline estimated with temperature jump is shown in Fig. 12. The
heat flux estimated with no-slip condition and test data are also plotted in Fig. 12 for
comparison. It is seen that the heat flux estimated with temperature jump condition
at the plate compares better with the test data.

6 Conclusions

CFD studies were carried out to simulate the expansion of rocket nozzle plume in low
pressure ambient and impingement on a flat plate to validate the numerical model.
The simulations were carried out for flat plate located at standoff distances of h/R_e
= 3, 5 and 7 from the nozzle corresponding to the experimental conditions reported
in literature. The pressure and heat flux on the plate due to plume impingement
were determined and compared with the reported test data. It is found that the flow
maintains continuum in the vicinity of the nozzle exit and at the plume impact
location on the plate. The CFD model is able to capture the flow dynamics of the
plume impingement and predicted the peak pressure and heat flux within 1.6 and
11.9% of the measured data. The difference in the CFD prediction and the test data
was found to be higher in regions where the flow transitions from the continuum to
free molecular regime. Incorporating the temperature jump condition was found to
improve the heat flux estimations in the transition zone.

Fig. 11 Mach contours overlaid with velocity vectors on a cut-plane
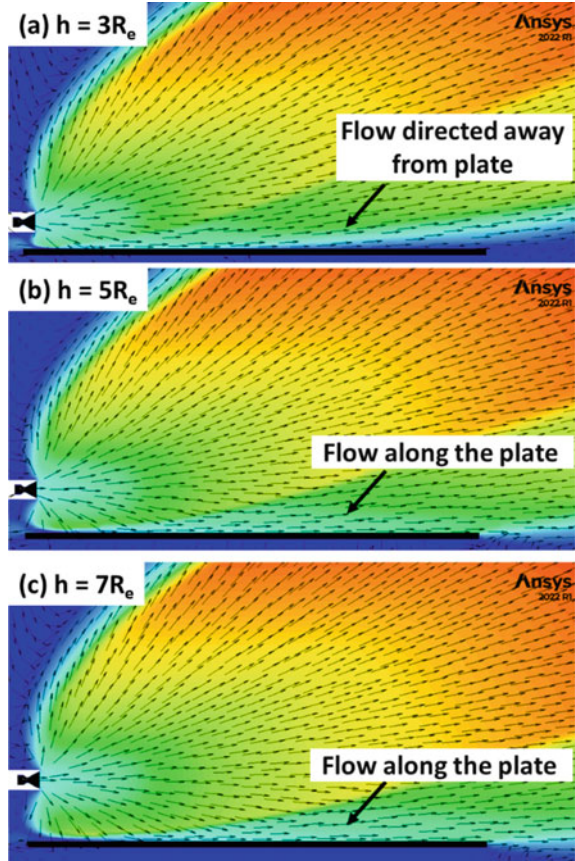
Fig. 12 Heat flux along plate centreline with no-slip and temperature jump condition at plate for $\varepsilon = 10$, $\delta = 0°$ and $h = 3R_e$
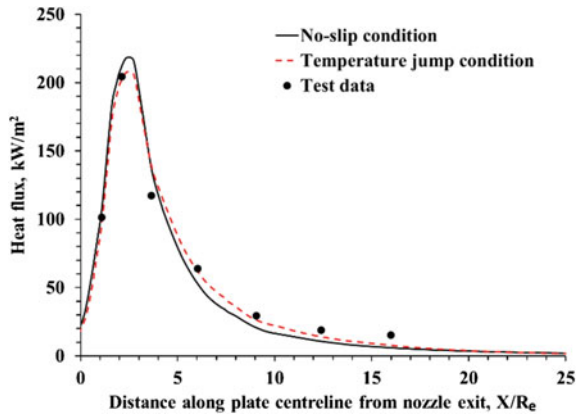
Nomenclature

E	Total energy [J]
g	Gravitational acceleration [m/s^2]
h	Distance of plate from nozzle axis [m]
p	Pressure [MPa]
R	Radius [m]
Kn	Kundsen number
t	Time [s]
v	Velocity [m/s]
ρ	Density [kg/m^3]
ω	Specific dissipation rate [s^{-1}]
ε	Nozzle area ratio
k	Turbulent kinetic energy [J/kg]
δ	Angle of plate with nozzle axis (°)

Subscripts

e	Nozzle exit

References

1. Latvala E (1959) Spreading of rocket exhaust jets at high altitudes. ASTIA document no. AD-215866, AEDC-TR-59.11, June 1959
2. Adamson TC, Nicholls JA. On the structure of jets from highly underexpanded nozzles into still air
3. Vick AR, Cubbage JM, Andrews EH (1966) Rocket exhaust plume problems and some recent related research. In: The fluid dynamic aspects of space flight, AGAR Dooraph 87, vol II. Gordon and Breach Science Publishers
4. Legge H, Boettcher RD (1985) Modelling control thruster plume flow and impingement. In: Belotserkovskii OM, Kogan MN, Kutateladze SS, Rebrov AK (eds) Rarefied gas dynamics. Springer, Boston, MA
5. Dettleff G (1991) Plume flow and plume impingement in space technology. Prog Aerosp Sci 28:1–71
6. Piesik ET, Koppang RR, Simkin DJ (1966) Rocket exhaust impingement on a flat plate at high vacuum. J Spacecraft Rockets 3(11):1650–1657
7. Woronowicz M. Initial molecular flow observations on bipolar planetary nebulae gaskinetics. AIAA Paper 599
8. Boynton FP (1968) Exhaust plumes from nozzles with wall boundary layers. J Spacecr Rocket 5:1143–1147
9. Simons GA (1972) Effect of nozzle boundary layers on rocket exhaust plumes. AIAA J 10:1534–1535
10. Cai C, Sun Q, Vanderwyst A (2013) Analytical exact solutions for unsteady collisionless plume flows in a vacuum. Acta Astronaut 91:218–227

11. Gimelshein S, Alexeenko A, Levin D (2002) Modeling of the interaction of a side jet with a rarefied atmosphere. J Spacecr Rocket 39:168–176
12. Lumpkin FE (1995) A CFD/DSMC analysis of plumes and plume impingement during Shuttle/Mir docking. In: AIAA, thermophysics conference, 30th, San Diego, CA
13. He B, Zhang J, Cai G (2013) Research on vacuum plume and its effects. Chin J Aeronaut 26:27–36
14. Bermúdez LM, Barnhart KJ, Brunner CW (2018) Modeling, simulation, and validation of plume impingement effects on the Cygnus spacecraft. J Spacecr Rocket 55(2):427–436
15. Vashchenkov P, Kudryavtsev A, Khotyanovsky D, Ivanov M (2005) DSMC and Navier-Stokes study of back flow for nozzle plumes expanding into vacuum. Technical report, DTIC document 2005
16. ANSYS Inc. (2022) ANSYS fluent theory guide 22
17. Anderson JD (2006) Hypersonics and high temperature gas dynamics, 2nd edn. AIAA
18. Bird GA (1992) Molecular gas dynamics and the direct simulation of gas flows. Clarendon Press, Oxford

Effect of Confinement in Coaxial Swirling Jets: Numerical Study

R. Santhosh, Arun Pattanshetti, and Shivansh Chaturvedi

1 Introduction

There are many industrial applications where swirl is added to the jet flows to improve performance. Most commonly, swirl is used in combustion chambers to increase the mixing between the fuel and air reactants. In addition, swirl is employed in gas turbine engines, diesel engines, industrial furnaces, etc. The benefit of employing swirl in these applications arises due to its ability to create a central toroidal recirculation zone (CTRZ). These swirls-induced recirculation structures facilitate the effective mixing of hot combustion products with active chemical radicals and incoming reactants leading to flame stability, complete combustion, and consequently resulting in lower emissions [1].

Coaxial swirling jets are used in many applications, such as industrial furnaces, combustion chambers, cooling systems, and fluid mixing. The present authors recently reported a numerical-cum-experimental study on recirculation structures in unconfined coaxial swirling condition [2]. The present work aims to present the effect of confinement on these recirculation structures.

R. Santhosh and Arun Pattanshetti—Contributed equally.

R. Santhosh (✉) · S. Chaturvedi
Department of Mechanical Engineering, IIT (BHU) Varanasi, Varanasi, Uttar Pradesh 221005, India
e-mail: rsanthosh.mec@iitbhu.ac.in

A. Pattanshetti
Department of Mechanical, Materials and Aerospace Engineering, IIT Dharwad, Dharwad 580011, India

2   Literature Review and Objective

This section presents a brief literature survey associated with coaxial swirling jets in unconfined and confined conditions. Both experimental and numerical works are considered. Dahm et al. [3] investigated the vortex structures and dynamics of their interactions for incompressible fluid in the near region of a round coaxial jet issuing into the ambient fluid. They concluded that a wide variety of near-field vortex patterns can arise, with different interaction dynamics, which depend on both the velocity ratio and the absolute velocity of the two coaxial streams.

Cheen et al. [4] studied the recirculation zones in the confined and unconfined conditions of the annular swirling jet flows by varying Reynolds number (Re $\cong$ 60–60,000) and swirl number in the range $S = 0 - 0.6$. They classified the recirculation zones into seven categories based on the value of Re and S. . Based on the observations, they concluded that the behaviors of these seven categories were the same in confined and unconfined configurations except for one regime (attachment regime). Next, Cai et al. [5] investigated the effect of confinement on the swirl cup installed in several square sections. Data on mean axial velocity and Reynolds stress components was obtained using 2D LDV. Their results concluded that a smaller confinement ratio has a more significant effect on the flow field. Whereas for large confinements, the effect is similar to unconfined conditions. Fu el al. [6] investigated the effect of confinement on the swirl flow field associated to counter-rotating radial inlet swirl. 2D LDV was employed to obtain the flow field's mean axial and turbulent quantities. They observed that the size of the recirculation zone in the confined condition was twice that of in unconfined conditions. Also, their results showed that confinement reduces turbulence near the swirler exit and as the flow moves downstream, higher turbulence was observed near the wall for the flow in the confined configuration as compared to near the centerline axis for unconfined flow. One of the present authors, Santhosh et al. [2] carried out the investigation on RZs in a coaxial swirling jet in the isothermal conditions as the flow parameters such as geometric swirl number (S_G), modified Rossby number (Ro_m) were varied. A transition in recirculation structures in the narrow band of geometric swirl number $S_G = 2.14 - 2.88$ was reported based on the change in the global topology of the recirculation structures.

Next, we report some past numerical studies pertaining to coaxial swirling jets. Kobayashi et al. [7] employed three different models, viz. standard $k - \varepsilon$, RSM and RNG $k - \varepsilon$ to simulate swirl flow in a straight pipe. The comparison between computed and experimental data showed that RNG $k - \varepsilon$ successfully captured the complex flow field. Nejad et al. [8] studied the swirling and non-swirling jets in confined conditions for swirl numbers of $S = 0.3$ and 0.5. 2D LDV was employed to measure the flow field. The standard $k - \varepsilon$ model was employed to simulate the flow field. They concluded that Reynolds stresses and turbulent triple product have been shown to have a 25 times higher value in swirling flows compared to non-swirling flows. Also, they stated that standard $k - \varepsilon$ model, which was used to predict the flow field, was found to be inadequate. Stuparu et al. [9] numerically studied turbulent flow inside a combustion chamber by employing three turbulent models. Their results

showed that the presence of RZ behind the bluff body positively impacts the mixing process inside the annular combustion chamber. In Parra et al. [10], the influence of swirl number on the mixing of two confined coaxial jets is studied. To simulate the flow field, RNG $k - \varepsilon$ model was employed. Their results showed that the presence of inner recirculation zone played an important role in the enhancement of heat and mass transfer in 3D confined coaxial burner. Jawarneh et al. [11] examined the effect of swirl number on the strongly swirling jet in the confined condition. RSM model was used to capture the turbulent flow field. They concluded that vortex core size contract with swirl number.

The main aim of the present study is to investigate the effect of confinement on the recirculation structures observed in a confined swirling jet. The present authors recently reported the numerical simulation results of the RZs in an unconfined configuration [12]. The present work is aimed as a continuation of efforts in the direction of studying coaxial swirling jets which find extensive industrial application.

3 Numerical Approach

3.1 Numerical Geometry and Mesh

A schematic view of the numerical geometry employed to simulate coaxial swirl flow in confined conditions and different 3D mesh parts of the geometry are depicted in Fig. 1a, b, respectively. The geometry created in 'SOLID WORKS' replicates the experimental setup described in [12]. It majorly consists of three parts. First, a central pipe of diameter $d_c = 6$ mm and length $l = 550$ mm that stands 2 mm out of the burner exit plane. Second, a coannular pipe that consists of a straight pipe ($d_a = 80$ mm) followed by a convergent section ($d_{\text{entrance}} = 80$ mm and $d_{\text{rear}} = 44$ mm). Third, a tangential swirl generator at the end of the convergent section. This swirl generator is employed to impart swirl momentum to the axially flowing coannular stream by directing air from eight swirl ports drilled at an angle 30° to the outward radial vector placed on the periphery of the swirl generator. Working fluid, which is air, is supplied to the inlets of the central pipe, coannular pipe, and swirl ports individually. A computational domain of length 300 mm (Fig. 1b) representative of the combustion chamber is employed to numerically capture the flow exiting out of the burner. The combustion chamber of two different diameters, viz. 80 mm and 100 mm, representing confinement ratios (CR) 1.81 and 2.7 respectively are employed in the present work to study the effect of confinement on the flow field. Here, the CR is defined as the ratio of the diameter of the combustion chamber to the coannular pipe diameter. The numerical domain is discretized by employing the ICEM CFD tool shown in Fig. 1b. The hexahedral cell is used to discretize the domain since it generates lower numerical dissipation [13] compared to the tetrahedral cell. The mesh characteristics of the different components of the numerical geometry are provided in Fig. 1c. Three mesh sizes, i.e., 1.8, 3.8, and 8.2 M are employed

to perform a grid independence study. To generate these three grid sizes, the grid refinement factor of (r) of 1.3 is maintained as per Celik [13]. Boundary conditions corresponding to PVB type RZ (provided in Table 1) are used to perform a grid independence study. Based on the axial velocity variation along the radial direction predicted using the three different mesh resolutions, the results do not vary much on increasing the number of cells from 3.8 to 8.2 M (results are not shown here for brevity). Thus, a mesh with 3.8 M is chosen as the optimum mesh.

3.2 Governing Equations

The unsteady, incompressible 3D turbulent flow field is analyzed by solving continuity, the transport equation for k, ω, and Navier–Stokes equations. These equations are reported in the past literature [11, 15]; thus, they are not shown here for brevity.

3.3 Numerical Method

The numerical simulations have been performed using ANSYS Fluent 19.2 (research license). The pressure–velocity coupling is obtained using the SIMPLE algorithm. SST $k - \omega$ turbulent model is employed to simulate the flow states in the present work. The suitability of this model in simulating the confined coannular swirling jet along with its validation is shown elsewhere [14]. The second-order upwind scheme is used to discretize the transport equation of momentum, turbulent kinetic energy, and specific rate of dissipation. Convergence is assumed when the residual values are 10^{-3} for continuity equation and 10^{-4} for momentum, turbulent kinetic energy, and specific rate of dissipation. The temporal discretization is first order implicit. Simulations are carried out in the unsteady state (URANS). A time step size of 0.001 s is employed with 30 iterations for each time step. The simulations are carried out to obtain flow field of 1 s (as 1000 time steps).

3.4 Test Cases/Boundary Conditions

The mass flow rate-type inlet boundary condition is used to simulate two types of RZs (flow cases) given in Table 1. The mass flow rate in the central jet for these flow cases, i.e., PVB and CTRZ is shown. The mass flow rates through the coannular and swirl generator (eight swirl ports combined) are maintained at 2.8×10^{-3} kg/s and 1.25×10^{-3} kg/s respectively for both the cases.

The geometric swirl number (S_G) is defined as [16]
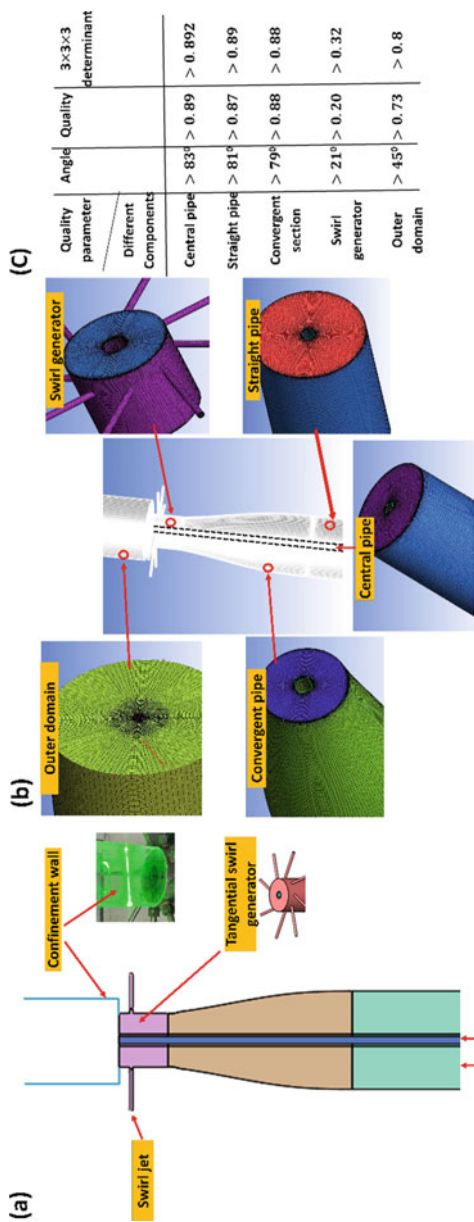
Fig. 1 Details of the confined coaxial burner and computational mesh

Table 1 Details of the boundary conditions employed in the present study

Flow case	Mass flow rate (kg/s) in central pipe	Geometric swirl number (S_G)	Modified Rossby number ($Ro_m = \frac{\Delta U_y}{U_\theta}$)
PVB	2.8×10^{-4}	2.14	3.15
CTRZ	3.73×10^{-5}	2.88	0.02

$$S_G = \frac{\pi r_o Do}{2A_t} \left(\frac{M_\theta}{M_\theta + M_A} \right)^2, \tag{1}$$

where M_θ is mass flow rate of the fluid in tangential direction, M_A is total mass flow rate of fluid in the axial direction (both central and coannular combined), and A_t is total area of the tangential ports. Modified Rossby number (Ro_m) is defined as [17]

$$Ro_m = \frac{\Delta U_y}{U_\theta}, \tag{2}$$

where U_θ is the characteristic tangential velocity and $\Delta U_y = |(U_c - U_a)|$ is the axial velocity deficit between the central jet (U_c) and coannular jet (U_a) measured using the volume flow rate.

4   Results and Discussion

This section presents the effect of confinement on two different types of recirculation zones (RZs), i.e., *pre-vortex breakdown* (PVB) and *central toroidal recirculation zone* (CTRZ) observed in the coaxial swirling jets in one of the authors' previous work [2]. They are, however, described here briefly for completeness. The ***PVB*** flow field (Fig. 2a) represents the first occurrence of recirculation in a coaxial swirling jet observed at $\boldsymbol{S_G} = 2.14$ (corresponding to $\boldsymbol{Ro_m} = 3.15$). The flow is characterized by a strong central jet in the central region and two pairs of counter-rotating eddies, ($L1$, $L2$ and $R1$, $R2$) on either side of the central jet. In PVB, three shear layers are observed, namely ISL 1 (between central jet and inner rotating eddy, $L1/R1$), ISL 2 (between coannular jet and outer rotating eddy $L2/R2$), and OSL (between coannular jet and quiescent ambient/confinement) (Fig. 2a). The $\boldsymbol{Ro_m} > 1$ for PVB implies that the radial pressure gradient developed due to the velocity difference between central and co-flow jet dominates over the radial pressure gradient developed due to imparted swirling motion [2].

The second type of RZ, i.e., CTRZ (Fig. 2d), is observed as the flow rate through the central jet is decreased from that of PVB's setting while keeping the flow through the coannular jet and swirl generator same. The S_G for CTRZ is 2.88. The $Ro_m \cong 0$ as the central jet flow rate is set such that $\Delta U_y \cong 0$. The flow field of CTRZ, when compared to the PVB, consists of only two shear layers: ISL 2 (between coannular
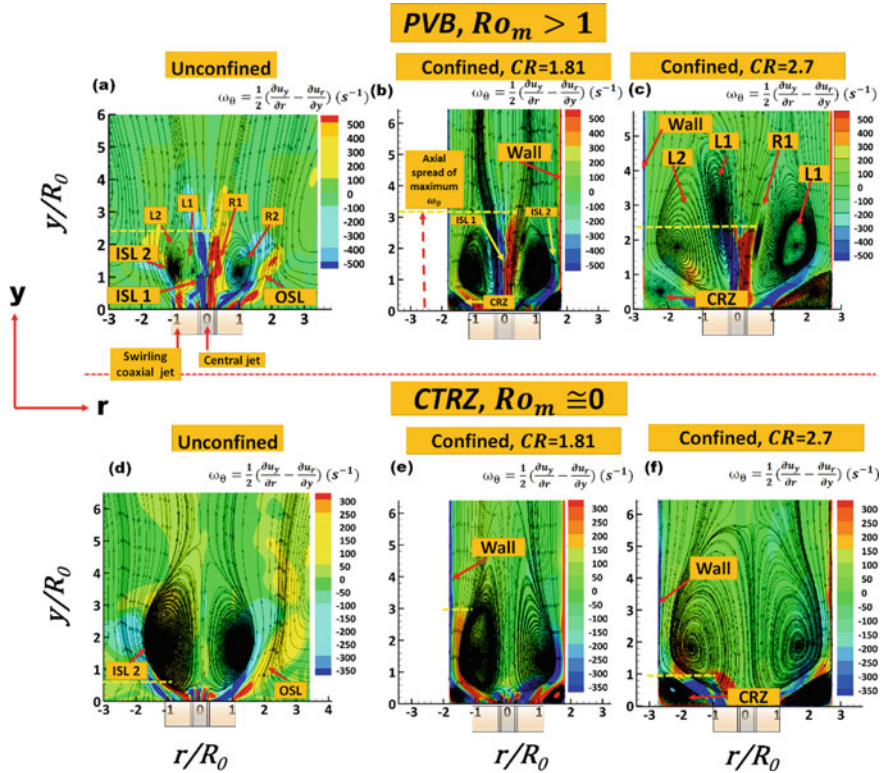
Fig. 2 Time-mean streamline plot superimposed on contour plot of time-averaged vorticity contours for PVB (**a–c**) and CTRZ (**d–f**)

jet and central recirculation zone) and OSL (between coannular jet and quiescent ambient/confinement). The $Ro_m \cong 0$ ($\Delta U_y \cong U_\theta$) for CTRZ indicates successful penetration of swirl momentum (that is imparted tangentially at the ISL 2) toward the central jet resulting in a flow field governed by the radial pressure gradient due to swirl influence as compared to radial pressure gradient due to entrainment effect [2].

Next, two different confinement configurations with $CR = 1.81$ and 2.7 are considered for *PVB* (Fig. 2b, c) and CTRZ (Fig. 2e, f) to describe the confinement effects on both the RZ. These figures represent time-mean streamline plot superimposed on the time-mean azimuthal vorticity (ω_θ) in the mid-longitudinal plane. y/R_0 and r/R_0 represent the axial and radial coordinates normalized by burner radius R_0. The most prominent observation pertaining to effect of confinement in both PVB and CTRZ is the enlargement of RZ. In addition, formation of an additional set of RZs known as corner recirculation zone (CRZ) between the wall and the central RZ is also evident. These observations are in line with previous studies [18, 19]. The greater enlargement of RZs for $CR = 2.7$ as compared to $CR = 1.81$ may be

attributed to availability of larger area for the RZs to spread radially outwards in former as compared to the latter. However, $CR = 1.81$ imparts a strong wall-effect which is evidenced in the enrichment of ω_θ till a greater streamwise extent in ISL 1 of PVB (marked with 'yellow' dashed line in Fig. 2b) as compared to unconfined configuration (Fig. 2a) and $CR = 2.7$ (Fig. 2c). For CTRZ, such enrichment is found in ISL 2 (Fig. 2e). In a way, the wall-effect fades away as the CR is increased from 1.81 to 2.7 which is intuitive. The $CR = 2.7$ is more closer to unconfined case with respect to distribution of ω_θ is concerned across the flow field.

The greater confinement effect at $CR = 1.81$ for both PVB and CTRZ results in a greater mixing/churning of fluid particles in regions where ω_θ enrichment is observed. This is witnessed by observing time-mean contour plots of Reynolds stress $(\overline{u'_y u'_r})$ and turbulent kinetic energy $(\overline{u'^2_y} + \overline{u'^2_r})$ shown in Figs. 3 and 4 respectively. As compared to unconfined case (Fig. 3a), the quantity $(\overline{u'_y u'_r})$ in PVB at CR = 1.81 (Fig. 3b) is observed to be more diffused in ISL 1 and in the region between ISL 2 and OSL implying greater churning of fluid particles. Also, higher turbulent kinetic energy in PVB at CR = 1.81 (Fig. 4b) is observed to be diffused until greater streamwise distance from the burner exit as compared to unconfined case (Fig. 4a). The region between the wall and the central RZ is also observed to depict greater TKE. This effect is greatly evident in the case of CTRZ (compare Fig. 4e with Fig. 4c) so much so that the maxima of $(\overline{u'^2_y} + \overline{u'^2_r})$ in CTRZ CR = 1.81 is witnessed between the wall and central RZ (Fig. 4e). The CR = 2.7 case, on the other hand, is different from CR = 1.81 cases. The magnitude, streamwise and transverse spread of both $(\overline{u'_y u'_r})$ and $(\overline{u'^2_y} + \overline{u'^2_r})$ is comparable for unconfined case for both PVB (Fig. 3c with Fig. 3a and Fig. 4c with Fig. 4a) and CTRZ (compare Fig. 3f with Fig. 3a compare Fig. 4f with Fig. 4a). This leads one to conclude that the CR = 2.7 is closer to unconfined case when fluid dynamical quantities such as $(\overline{u'_y u'_r})$ and $(\overline{u'^2_y} + \overline{u'^2_r})$ are considered. Thus, although the CR = 2.7 results in enlargement of RZ the wall/confinement effect measured in terms of enhancement of key fluid-dynamic and turbulent quantities as compared to unconfined case is observed to be greater for CR = 1.8 case for both $Ro_m > 1$ case (PVB) and $Ro_m \cong 0$ case (CTRZ) in the coaxial swirling jet in the $S_G = 2.14$–2.88 range.

5 Conclusions

The unsteady Reynolds-averaged Navier–Stokes (URANS) numerical simulations were carried out to study the effect of two confinement ratios (CR = 1.81 and 2.7) on two different recirculation zones (RZ) with modified Rossby number $Ro_m > 1$ case and $Ro_m \cong 0$ witnessed in coaxial swirling flow jet. The former is called as pre-vortex breakdown (PVB) and central toroidal recirculation zone (CTRZ). SST $k - \omega$ model was the turbulent model employed for simulations. The similarities observed between both flow cases (in terms of effect of confinement) are as follows:
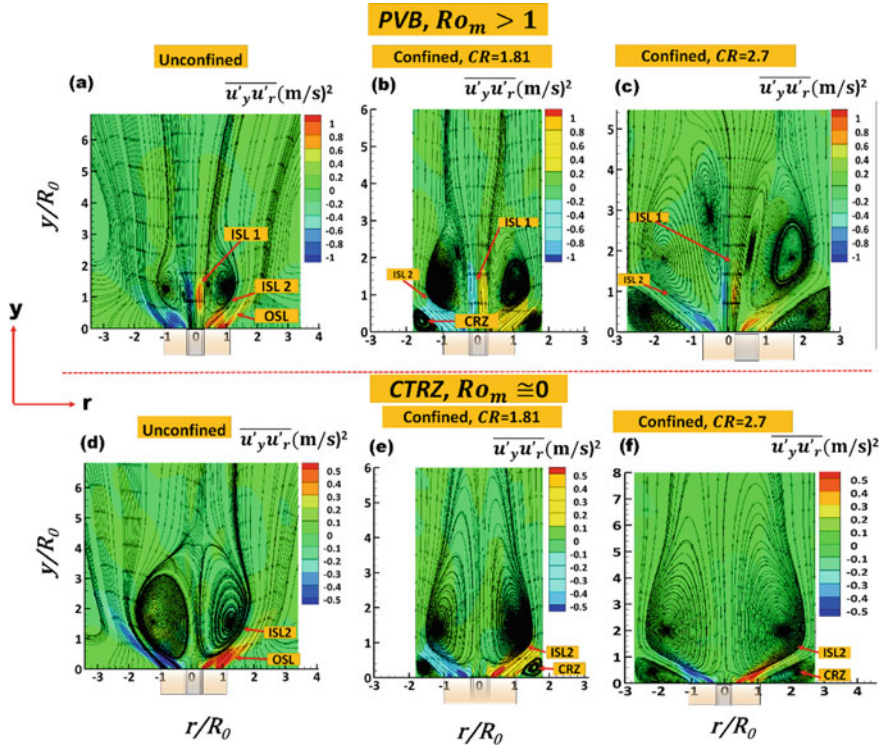
Fig. 3 Time-mean streamline plot superimposed on time-averaged Reynolds stress for PVB (**a–c**) and CTRZ (**d–f**)

- As compared to dimensions of the RZs (both PVB and CTRZ) in unconfined condition the size of the reticulation zones increased in the confined conditions.
- The enlargement of RZs for CR = 2.7 is greater than CR = 1.81.
- However, the wall/confinement effect is primarily witnessed in CR = 1.81 case evidenced by the enrichment/enhancement of vorticity, Reynolds stress and turbulent kinetic energy as compared to unconfined case.
- The time-mean vorticity, Reynolds stress, and turbulent kinetic energy for CR = 2.7 were very close to the unconfined case.

The key difference between the two flow states (in terms of confinement effect) observed were:

- While the enrichment/enhancement of vorticity and turbulent kinetic energy in $Ro_m \cong 0$ case was observed in the region between the wall and the central RZ, for the $Ro_m > 1$ case (PVB) this was observed in the region between the wall and the central RZ as well as between the central jet and the central RZ.
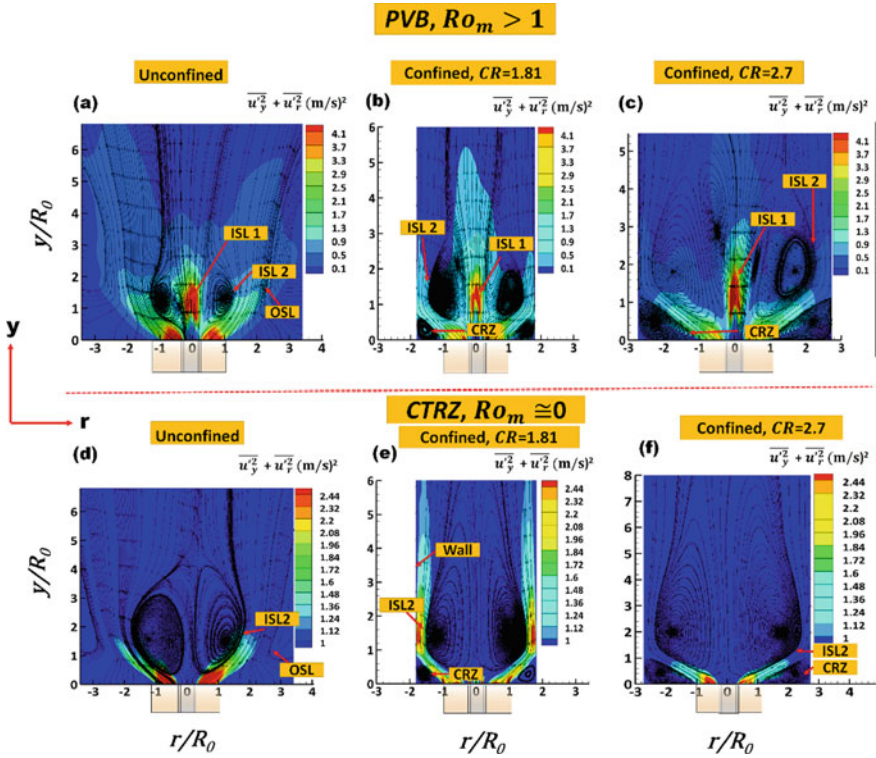
Fig. 4 Time-mean streamline plot superimposed on contour plot of time-averaged turbulent kinetic energy contours for PVB (**a**–**c**) and CTRZ (**d**–**f**)

Nomenclature

CRZ	Corner recirculation zone
CTRZ	Central toroidal recirculation zone
ISL 1	Inner shear layer
ISL 2	Intermediate shear layer
OSL	Outer shear layer
PVB	Pre-vortex breakdown
Re	Reynolds number
Ro_m	Modified Rossby number
S	Swirl number
S_G	Geometric swirl number
U_y	Axial velocity component
U_θ	Tangential velocity component
U_0	Weighted area-averaged bulk velocity

References

1. Gupta AK, Lilley DG, Syred N (1984) Swirl flows. Abacus Press, United Kingdom
2. Santhosh R, Miglani A, Basu S (2013) Transition and acoustic response of recirculation structures in an unconfined co-axial isothermal swirling flow. Phys Fluids 25(8)
3. Frieler CE, Tryggvason G (1992) Vortex structure and dynamics in the near field of a coaxial jet. J Fluid Mech 241(32):371–402
4. Sheen HJ, Chen WJ, Jeng SY (1996) Recirculation zones of unconfined and confined annular swirling jets. AIAA J 34(3):572–579
5. Hsiao G, Mongia H. Swirl cup modelling part 2: inlet conditions. In: 41st aerospace sciences meeting and exhibit
6. Fu Y, Cai AJ, Jend SM. Characteristics of the swirling flow generated by a counter rotating swirler. In: 43rd AIAA/ASME/SAE/ASEE joint propulsion conference & exhibit
7. Kobayashi T, Yoda M (1987) Modified K-ε model for turbulent swirling flow in a straight pipe. JSME Int J 30(259):66–71
8. Favaloro S, Nejad A, Ahmed S, Miller AT, Vanka S. An experimental and computational axisymmetric dump combustor investigation of isothermal swirling flow in an. In: 27th aerospace sciences meeting
9. Stuparu A, Holotescu S (2011) Numerical simulation of the 3D unsteady turbulent flow in a combustion chamber. Central Euro J Eng 1(2):189–194
10. Parra T, Perez R, Rodriguez MA, Castro F, Szasz RZ, Gutkowski A (2015) Numerical simulation of swirling flows—heat transfer enhancement. J Fluid Flow Heat Mass Transf 2
11. Jawarneh AM, Vatistas GH (2006) Reynolds stress model in the prediction of confined turbulent swirling flows. J Fluids Eng 128(6):1377–1382
12. Pattanshetti A, Santhosh R, Attar N (2022) Experimental and numerical investigation of recirculation structures in isothermal swirling coaxial jet. J Fluids Eng 144(10)
13. Celik IB, Ghia U, Roache PJ (2008) Freitas, procedure for estimation and reporting of uncertainty due to discretization in CFD applications. J Fluids Eng 130(7)
14. Santhosh R, Pattanashetti A, Chaturvedi S. Effect of confinement on recirculation structures in confined coaxial swirling jet. Review
15. Lien FS, Leschziner MA (1994) Assessment of turbulence-transport models including non-linear RNG Eddy-Viscosity formulation and second-moment closure for flow over a backward-facing step. Comput Fluids 23(8):983–1004
16. Feikema D, Chen RH, Driscoll JF (1990) Enhancement of flame blowout limits by the use of swirl. Combust Flame 80(2):183–195
17. Giannadakis A, Perrakis K, Panidis T (2008) A swirling jet under the influence of a coaxial flow. Exp Thermal Fluid Sci 32(8):1548–1563
18. Syred N, Dahman DR (1978) Effect of high levels of confinement upon the aerodynamics of swirl burners. J Energy 2(1):8–15
19. Syred N, Beér JM (1974) Combustion in swirling flows: a review. Combust Flame 23(2):143–201

Influence of Cryogenic Temperature on Degradation of Step-Graded Scaffold: A CFD Study

Khemraj Deshmukh and Arindam Bit

1 Introduction

Porous scaffolds are most frequently used in tissue engineering (TE) to determine biomaterial properties, cell functionality and drug delivery studies. The biomaterial-based high porous scaffold can pass different bio factors such as protein, cells and other growth factors. In tissue engineering applications, two types of scaffolds are used: uniform and non-uniform porous scaffolds. The porous scaffold is used frequently because of its simplicity and less computational deficiency during the evaluation [1]. In vivo tissue or organs have different layers, each with different functionality. In other words, in vivo tissue and organs are functionally graded. Also, for successful tissue and organ regeneration, the scaffold should also have graded functionality [2].

In the current scenario, natural and synthetic materials are used as a biomaterial for scaffold fabrication. Each type of material has their own advantages and disadvantages. Natural biomaterials provide higher cellular viability but suffer from poor mechanical properties. Similarly, synthetic biomaterial shows the opposite behaviour from natural material. Silicon-based polydimethylsiloxane (PDMS) lies in the category of synthetic material [3]. Higher cell-subtract interaction force to use PDMS as scaffold biomaterial [4]. Cell adhesion on the substrate surface is pivotal in measuring cell viability, proliferation, and differentiation. The chemical and mechanical properties of PDMS highly influence the adhesion properties of cells [5].

With the need for fast demand for organ transplants and rapid recovery of diseases, it is necessary to preserve biological substances. Cryopreservation is a technique to store natural and fabricated biological substances at an ultra-low temperature, where biological activity stops. In most of the studies, the temperature of range 233–177

K. Deshmukh · A. Bit (✉)
Department of Biomedical Engineering, National Institute of Technology, Raipur, India
e-mail: arinbit.bme@nitrr.ac.in

°K was used during cryopreservation [6–8]. At a shallow temperature, the preserved substances suffered from ice formation, which had been eliminated by cryoprotectant agents called CPA [9]. Bahari et al. [10] had found that cellular viability was affected by the cooling rate. Hunt et al. [11] proposed all the technical considerations which improve cellular viability. The fast cooling rate of cryopreservation suffered from intracellular ice formation, whereas slow cooling suffered from an osmotic effect [12]. However, the selection of an appropriate cooling rate was also a challenging task.

2 Literature Review and Objective

Dynamic changes in temperature during cryopreservation produce stress on a scaffold. Uniform heating was capable of reducing this stress. Thermal conductivity and specific heat of the scaffold were responsible for generating the stress, displacement and deformation on it [13]. Cryogenic temperature influences the mechanical properties of the scaffold. In most of the studies, the authors reported the impact of the cryogenic temperature on biological phenomena such as cell migration, differentiation. Limited articles had reported the effect of low temperature on the mechanical properties of scaffolds. Sun et al. [14] had evaluated the strain tensor of the hydrogel at room temperature and 240 °K. It was found that the stretchability of the PHEAA hydrogel and PHEAA/SF hydrogel had decreased significantly compared to that at room temperature. It [15] was observed the impact of ultra-low temperature on the vascular scaffold, and no variation was found in surface smoothness before and after cryopreservation. Arai et al. [16] had reported the vascular scaffold's tensile strength was significantly enhanced after cryopreservation. The tensile strength and Young modulus value were identical, with and without cryopreservation [17]. Carrillo et al. [18] had reported that the freezing point could be influenced by CPA concentration which was estimated by the numerical and asymptotic methods.

The current study evaluated the mechanical properties of PDMS material-based scaffold for both uniform and graded porosity. Various sets of scaffold conditions and structures were formulated based on pore size, distance and cooling rate. Each scaffold's conditions was evaluated for a cooling rate of -1, -2 and -5 °K/min in the presence of water. A transient study for each condition of the scaffold was carried out in COMSOL Multiphysics. Heat transfer in solid and fluid and solid mechanics modules were used to evaluate the different scaffolds for thermal and mechanical parameters such as temperature, stress, deformation gradient, strain tensor and displacement gradient under cryogenic conditions.

3 Materials and Methods

Figure 1 shows the 2D schematic of the proposed work. The 5 × 5 mm PDMS porous scaffold was placed in the water-filled container. The following inbuilt properties of PDMS material were considered: coefficient of thermal expansion: $9e-4$ K^{-1}, heat capacity at constant pressure: 1460 J/(kg * K), density: 970 kg/m^3, thermal conductivity: 0.16 W/(m * K), young modulus: 750 kPa, Poisson ratio: 0.49. From Fig. 1, the first half of the scaffold (2.2 × 5 mm) was covered with a uniform porosity (pore size: 0.05 mm, pore distance: 0.5 mm), and the second half of the scaffold covered the step-graded porosity. The following conditions defined the step-graded scaffolds; condition 1 (C1): hole distance (h) was made constant equal to 0.5 mm and hole diameter (ϕ_h) was variable, and its range was 0.05–0.2 mm, condition 2 (C2): hole distance (h) was made variable, and its range was 0.5–1 mm and hole diameter (ϕ_h) was constant (0.05 mm), condition 3 (C3): both hole distance and diameter were variable, and its range was 0.5–1 mm, 0.05–0.15 mm, respectively.

The cryogenic temperature was achieved by applying the temperature (300–230 °K) to the three surfaces of the outer chamber/container. The upper surface of the chamber was used as thermal insulation. For each condition, the temperature reaches from 300 to 230 °K at the cooling rate of -1, -2 and -5 °K/min as given in Table 1. Fourteen minutes and thirty-five minutes of the transient study had been performed for -5 °K/min and -2 °K/min, respectively. Similarly, seventy min of the transient study had been performed for -1 °K/min.

The heat transfer in single direction through a particular media is described by the Fourier's law of heat transfer [19], as given in Eq. 1

$$Q_{\text{Transfer}} = KA\frac{dT}{dx},\tag{1}$$

where K indicates thermal conductivity, A indicates heat transfer area, and $\frac{dT}{dx}$ is the temperature gradient. Thouh temperature influences the value of thermal conductivity, the average value of temperature produces a constant thermal conductivity. The temperature gradient was negative for heat transfer in positive of x-direction, so in normal cases a negative sign was used in Eq. 1 to make temperature gradient

Fig. 1 2D schematic of proposed model (length is not as per scale): **a** 2.5 mm, **b** 2.5 mm, **c** 5 mm, **d** 15 mm, **e** 25 mm
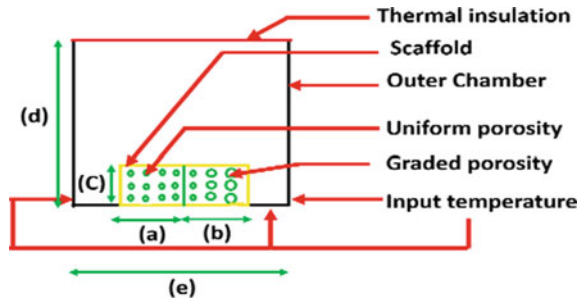
Table 1 Formation of structures based on different conditions and cooling rates

Condition	Parameter	Cooling rate (K/min)	Structure
C1	Hole distance (h): variable Hole diameter (ϕ_h) = constant	− 1	S1
		− 2	S2
		− 5	S3
C2	Hole distance (h): constant Hole diameter (ϕ_h) = variable	− 1	S4
		− 2	S5
		− 5	S6
C3	Hole distance (h): variable Hole diameter (ϕ_h) = variable	− 1	S7
		− 2	S8
		− 5	S9

positive. But in this study, the temperature gradient or heat transfer were in negative of x-direction; hence, the equation was not altered. The general relationship of total heat transfer to a 2D structure is expressed by the vector form, as shown in Eq. (2)

$$\overrightarrow{Q_n} = Q_x.\vec{l} \times Q_y.\vec{m},\tag{2}$$

where $\vec{l}$ and $\vec{m}$ are unit vectors and Q_x, Q_y are amount of heat transfer in X and Y directions, respectively. Q_x and Q_y are measured by the Fourier law of heat transfer, as shown in Eq. (3).

$$Q_x = KA_x\frac{\mathrm{d}T}{\mathrm{d}x} \quad \text{and} \quad Q_y = KA_{yx}\frac{\mathrm{d}T}{\mathrm{d}x}.\tag{3}$$

During the simulation, all the materials were considered as isotropic, so that there was uniform heat transfer in both X and Y directions. A fully coupled option was enabled in COMSOL Multiphysics to establish a possible correlation between solid mechanics and heat transfer in solid and fluid physics. The MUMPS-based direct linear solver was used to solve the proposed model.

The four points, a_1 to a_4, had been identified in conditions 1 and three points, a_1 to a_3, have been identified in conditions 2 and 3 on the wall of the hole, as shown in Fig. 2. The coordinates of all points were C1: $a_1(12.94, 2.5)$, $a_2(13.39, 2.5)$, $a_3(13.84, 2.5)$, $a_4(14.29, 2.5)$, C2: $a_1(12.94, 2.5)$, $a_2(13.45, 2.5)$, $a_3(14.45, 0)$ and C3: $a_1(12.94, 2.5)$, $a_2(13.39, 2.5)$, $a_3(14.35, 2.5)$.

At each point, five mechanical parameters temperature, stress, deformation gradient, strain tensor and displacement gradient were evaluated.
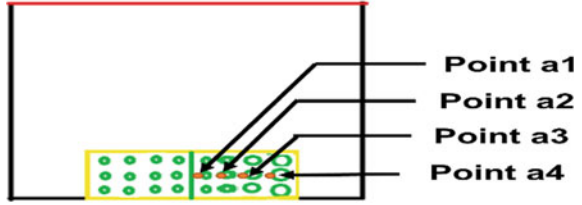
3.1 Grid Convergence Index (GCI)

Grid convergence index was also conducted for the proposed study to show how computational solver was independent from the grid. The grid convergence test was applied for the structure S11. Structure S9 was meshed at three different mesh size. GCI was measured in the form of percentage. In each point, the magnitude of temperature was different for same element size, but the difference in temperature magnitude for different element size at the similar points was equal. So that GCI percentage was also similar for different points. Equation 4 was used to calculate the order of convergence, where $f1, f2$ and $f3$ are the temperature values at point a_2 as given in Table 2.

$$p = \ln \frac{(f_3 - f_2)}{(f_2 - f_1)} / \ln(r). \tag{4}$$

From Eq. 4, the value of p was evaluated and refinement ratio 'r' was calculated from grid spacing. Richardson extrapolation method was used to obtain the GCI value [20]. GCI was estimated from the Eq. (5) as given in Table 3.

$$\text{GCI} = \frac{F_s |e|}{(r^p - 1)} \times 100\%. \tag{5}$$

Table 2 Meshing elements and temperature value at point a_2

S. No.	Element size	No of elements	Temperature (K)
1	Extremely fine	150,143	243.04151745838016
2	Finer	51,385	242.70939685754087
3	Coarser	45,755	242.55945367603263

Table 3 Order of accuracy and grid convergence index for temperature variable

Variable	r	p	F_s	GCI_{12} (%)	GCI_{23} (%)
Temperature	2.02	1.12	1.25	0.06	0.14

It was observed that GCI for extremely fine grid (GCI_{12}) is relatively low if compared to the coarser grid (GCI_{23}) for the temperature parameter. These observations demonstrate that the numerical simulation dependency on the cell size was found minimum with decrease in grid size.

4 Results and Discussion

4.1 Result

It had been observed that the maximum magnitude variation occurs at a point a_1 (located near the centre of the scaffold) and a_4 (near the outer side wall of the scaffold) in the condition 1for all parameters as well as cooling rate. Similarly for the conditions 2 and 3, the maximum magnitude variation was observed between point a_1 and a_3.

Table 4 shows the temperature distribution of different structures for different conditions. The temperature magnitude was decreased as move from point a_1 to a_4 and point a_1 to a_3 for condition 1 and conditions 2 and 3, respectively. The minimum temperature 233.34 °K was observed at a point a_4 in condition 1 for cooling rate − 1 °K/min. The change in temperature distribution among the ROI leads to the probable phenomena of deformation of ROI under systemic cooling rate. Hence, the deformation gradient was computed to estimate the rate of deformation. From Table 4, it was also observed that the magnitude of deformation gradient was maximum at point near the centre of scaffold (a_1) as compared to point located the wall (a_4 or a_3) for entire cooling rate. The maximum deformation gradient (0.97302) was obtained at a point a_1 in condition 3 for a cooling rate − 5 °K/min. It was anticipated that stress may be a fundamental factor for producing variation in deformation gradient. These assumption leads to observe the stress at ROI. Table 4 shows that the maximum stress 40,029.31 N/m^2 was generated in condition 3 for cooling rate − 2 °K/min at point a_3. Similarly, the stress 13,637.26 N/m^2 was observed at point a_1 in condition 3 for the cooling rate − 5 °K/min. As it is observed that the stress was developed within the scaffold varies with different condition and cooling rate at the study.

The contour plot of strain tensor and displacement gradient was shown in Fig. 3. It was observed that the magnitude (shown in Fig. 3) of contour plot for both parameters were identical for each others for individual condition and cooling rate. The maximum and minimum value of both parameters was 7×10^{-3} and $- 8.2 \times 10^{-3}$, respectively. Maximum displacement and strain tensor were generated at those area of scaffold, where temperature was higher (upper portion of Fig. 3a–i) except in condition 2 (Fig. 3d) for cooling rate − 1 °K/min. Figure 3 clearly shows that these two parameters were dependent on cooling rate. Strain tensor and displacement gradient were observed maximum for cooling rate − 5 °K/min as compared to other two cooling rates.

Table 4 Magnitude of temperature, deformation gradient and stress parameter at ROI for different conditions and cooling rate

Conditions and cooling rate	Temperature (K)		Deformation Gradient (1)		Stress (N/m^2)	
	Points		Points		Points	
	a_1	a_4	a_1	a_4	a_1	a_4
C1, − 1	233.34	233.23	0.96	0.96	17,669.77	17,820.89
C1, − 2	236.23	236.00	0.96	0.98	16,379.80	16,655.48
C1, − 5	243.05	242.52	0.97	0.97	13,692.87	14,241.22
	a_1	a_3	a_1	a_3	a_1	a_3
C2, − 1	233.44	233.28	0.97	0.96	17,629.16	17,843.4
C2, − 2	236.53	236.23	0.97	0.96	16,342.20	16,733.91
C2, − 5	242.89	242.12	9.73E − 01	9.71E − 01	13,692.87	14,082.66
	a_1	a_3	a_1	a_3	a_1	a_3
C3, − 1	233.35	233.21	9.65E − 01	9.65E − 01	17,654.04	17,833.38
C3, − 2	236.21	235.93	0.97	0.96	39,247.28	40,029.31
C3, − 5	243.91	236.89	0.97	0.97	13,637.26	14,281.41
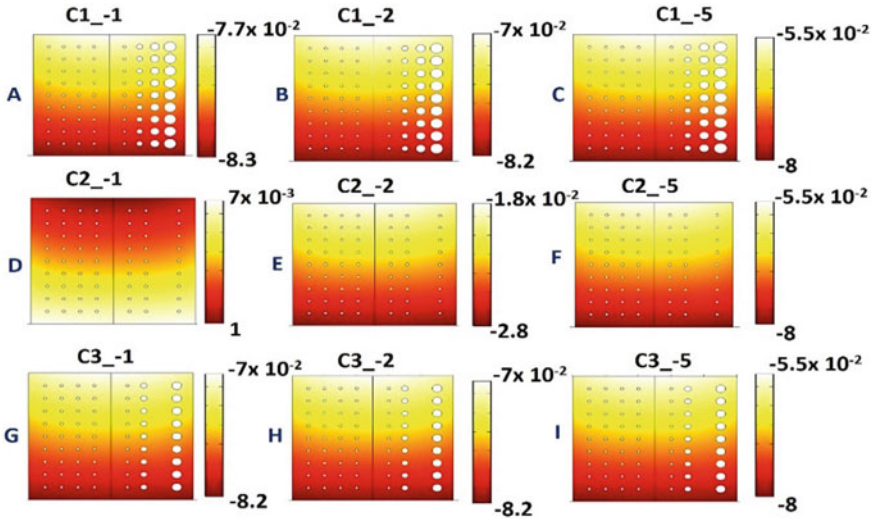
Fig. 3 Contour plot of strain tensor and displacement gradient for all conditions and cooling rates

4.2 Discussion

The mechanical properties of scaffold were influenced by the fabrication material, designing procedure and architecture. Present work showed the heat transfer at cooling rate of − 5, − 2 and − 1 °K/min rate within the different condition of

scaffolds in presence of water. The present study observed the effect of cryogenic temperature on different mechanical properties such as deformation gradient, stress, strain tensor and displacement gradient.

In the present study, the heat was transfer to the both solid and fluid phase. In was anticipated that heat was transfer between them. The heat transfer between them had been represented by Eq. (6). The subscript s and f used in equation was used for solid and fluid, respectively.

$$m_s C_s \frac{dT_s}{dt} = Q_{fs}, \tag{6}$$

where $m_s C_s \frac{dT_s}{dt}$ is mass and heat capacity of the solid scaffold. We know that $Q_{fs} = Q_{uu} + Q_{qs} + Q_{du}$. So Eq. (6) can be rearranged as

$$m_s C_s \frac{dT_s}{dt} = Q_{uu} + Q_{qs} + Q_{du}, \tag{6a}$$

where Q_{uu}, Q_{qs} and Q_{du} represent the undisturbed-unsteady, quasi-steady and diffusive unsteady contributions to the overall heat transfer due to inter-phase coupling.

Deformation gradient (DG) indicates how rapidly deformation occurs with respect to time or heat treatment. It was concluded that deformation gradient was linearly proportional to the temperature. At low temperature, the atomic interaction between two atoms was maximum which leads the reduction of deformation per unit time [21]. Also, stress is one of the major factors to evaluate the degradation of material at cryogenic temperature. Variation in deformation gradient leads to evaluate the dynamicity in stress. Table 4 indicates that the thermal stress was influenced by the cooling rate in each condition [12]. The minimum distance between the holes enhances the magnitude of stress in condition 1 for cooling rate $-$ 1 °K/min. Cryogenic temperature acts as thermal force for generation of stress. Low temperature increases the bonding energy between inter molecules which attenuate both the ionization energy as well as entropy energy. Attenuation of both energies lead to the reduction of stress [22]. Strain tensor is a physical quantity which shows how much deformation occurred at a particular point. Low variation of temperature between two ROI points (given in Table 4) was responsible for negligible variation in strain tensor magnitude. It can be concluded that due to very low temperature variation, inter atomic distance was not altered and it remained at stable state so that deformation of material was negligible. Minimum deformation gave the small changes of strain tensor response. The molecules of PDMS material cannot slip and slide on a microscopic level so that bond between the molecules cannot break and reform at very low temperature. These phenomena lead to minimize strain tensor (relative change) as well as displacement gradient in the same ratio.

5   Conclusions

The current work illustrates the cryogenic temperature effect on PDMS scaffold to evaluate scaffold degradation. Eleven types of structures were designed by changing the hole diameter, hole distance and rate of cooling. Six different parameters associated with scaffold degradation had been observed in the presence of water. It was observed that the rate of cooling heavily influenced degradation parameters. Results indicate that the temperature obtained from different cooling rates attenuates the deformation gradient value. It was observed that strain was decreasing, followed by increasing fashion at the boundary of the scaffold. It was also found that strain tensor value was slightly higher at the point near the scaffold's boundary. Collision of atoms was prohibited at a low temperature which reduces the magnitude of displacement gradient for the entire structure. Finally, it had been concluded that other than the bio-chemical properties, evaluation of the mechanical property of the scaffold helps to predict the degradation behaviour of the scaffold.

References

1. Esmaeili S, Shahali M, Kordjamshidi A, Torkpoor Z, Namdari F, Samandari SS, Ghadiri Nejad M, Khandan A (2019) An artificial blood vessel fabricated by 3D printing for pharmaceutical application. Nanomed J 6(3):183–194
2. Leong KF, Chua SC, Sudarmadji N, Yeong WY (2008) Engineering functionally graded tissue engineering scaffolds. J Mech Behav Biomed Mater 1(2):140–152
3. Jammalamadaka U, Tappa K (2018) Recent advances in biomaterials for 3D printing and tissue engineering. J Functional Biomater 9(1):22
4. Gao Y, Hou M, Yang R, Zhang L, Xu Z, Kang Y, Xue P (2019) Highly porous silk fibroin scaffold packed in PEGDA/sucrose microneedles for controllable transdermal drug delivery. Biomacromol 20(3):1334–1345
5. Hashemzadeh H, Allahverdi A, Sedghi M, Vaezi Z, Tohidi Moghadam T, Rothbauer M, Fischer MB, Ertl P, Naderi-Manesh H (2020) PDMS nano-modified scaffolds for improvement of stem cells proliferation and differentiation in microfluidic platform. Nanomaterials 10(4):668
6. Antebi B, Asher AM, Rodriguez LA, Moore RK, Mohammadipoor A, Cancio LC (2019) Cryopreserved mesenchymal stem cells regain functional potency following a 24-h acclimation period. J Transl Med 17(1):1–13
7. Bahsoun S, Coopman K, Akam EC (2019) The impact of cryopreservation on bone marrow-derived mesenchymal stem cells: a systematic review. J Transl Med 17(1):1–29
8. Linville RM, DeStefano JG, Nerenberg RF, Grifno GN, Ye R, Gallagher E, Searson PC (2020) Long-term cryopreservation preserves blood–brain barrier phenotype of iPSC-derived brain microvascular endothelial cells and three-dimensional microvessels. Mol Pharm 17(9):3425–3434
9. Jesus AR, Meneses L, Duarte ARC, Paiva A (2021) Natural deep eutectic systems, an emerging class of cryoprotectant agents. Cryobiology 101:95–104
10. Bahari L, Bein A, Yashunsky V, Braslavsky I (2018) Directional freezing for the cryopreservation of adherent mammalian cells on a substrate. PLoS ONE 13(2):e0192265
11. Hunt CJ (2019) Technical considerations in the freezing, low-temperature storage and thawing of stem cells for cellular therapies. Transfusion Med Hemother 46(3):134–150
12. Jang TH, Park SC, Yang JH, Kim JY, Seok JH, Park US, Choi CW, Lee SR, Han J (2017) Cryopreservation and its clinical applications. Integr Med Res 6(1):12–18

13. Gurruchaga H, Del Burgo LS, Hernandez RM, Orive G, Selden C, Fuller B, Ciriza J, Pedraz JL (2018) Advances in the slow freezing cryopreservation of microencapsulated cells. J Control Release 281:119–138
14. Sun X, He S, Yao M, Wu X, Zhang H, Yao F, Li J (2021) Fully-physically crosslinked silk fibroin/poly (hydroxyethyl acrylamide) hydrogel with high transparency and adhesive properties for wireless sensing and low-temperature strain sensing. J Mater Chem C 9(6):1880–1887
15. Costa PF, Dias AF, Reis RL, Gomes ME (2012) Cryopreservation of cell/scaffold tissue-engineered constructs. Tissue Eng Part C Methods 18(11):852–858
16. Arai K, Murata D, Takao S, Verissiomo AR, Nakayama K (2020) Cryopreservation method for spheroids and fabrication of scaffold-free tubular constructs. PLoS ONE 15(4):e0230428
17. Theodoridis K, Müller J, Ramm R, Findeisen K, Andree B, Korossis S, Haverich A, Hilfiker A (2016) Effects of combined cryopreservation and decellularization on the biomechanical, structural and biochemical properties of porcine pulmonary heart valves. Acta Biomater 43:71–77
18. Carrillo JA, Fornasier M, Rosado J, Toscani G (2010) Downloaded 03/24/14 to 150.203.210.155. Redistribution subject to SIAM license or copyright; see http://www.siam.org/journals/ojsa.php. Copyright © by SIAM. Unauthorized reproduction of this article is prohibited, 42(1), 218–236
19. Hahn DW, Özisik MN (2012) Heat conduction. John Wiley & Sons
20. Bit A, Chattopadhyay H (2014) Numerical investigations of pulsatile flow in stenosed artery. Acta Bioeng Biomech 16(4)
21. Reis JMLD (2012) Effect of temperature on the mechanical properties of polymer mortars. Mater Res 15:645–649
22. Rödel M, Baumann K, Groll J, Gbureck U (2018) Simultaneous structuring and mineralization of silk fibroin scaffolds. J Tissue Eng 9:2041731418788509

Improved MLPG Method for Potential Flow Problem

Rituraj Singh and Roman Trobec

1 Introduction

Many meshless methods have been developed to resolve the problem of re-meshing in conventional numerical methods such as FEM and FDM. The meshless local Petrov–Galerkin (MLPG) method seems to be the most successful meshless method among them [1]. It is based on a local weak form, and numerical integration is done over small local domains. A background mesh is generated locally rather than globally which makes the numerical integration relatively easier than by the global weak form-based meshless methods. The meshless shape functions in the MLPG method can be generated by meshless shape function generation schemes such as moving least squares (MLS), radial basis function (RBF), and several other approaches. The MLS scheme is mostly used due to its accuracy; however, it has some drawbacks such as the absence of Kronecker delta property (KDP) is computationally expensive, uses complicated polynomials, and could be instable for particular arrangements of nodal points. There is a motivation to further develop the MLPG method as two major problems remain: high computational cost and difficulty in the imposition of essential boundary conditions.

R. Singh (✉)
Department of Mechanical Engineering, National Institute of Technology Jamshedpur, Jamshedpur 831014, India
e-mail: rituraj.7am@gmail.com

R. Trobec
Department of Communication System, Jozef Stefan Institute, 1000 Ljubljana, Slovenia

2 Literature Review and Objective

Many researchers have reported a slightly improved versions of the MLS scheme which overcome the drawbacks of the original MLS scheme. They have tested these MLS variants in element free Galerkin (EFG) method, global boundary node method (GBNM), and some other meshless methods [2]. To enable the KDP, modified weight functions in the MLS scheme have been proposed [3], which closely satisfy the KDP. Another variant, namely interpolating MLS (IMLS) scheme has been proposed in [4, 5], where a singular weight function is used in the IMLS scheme. It exactly satisfies the KDP, however, on the computational nodes, the value of the singular weight function becomes infinite, and thus, the shape functions cannot be calculated. The IMLS is successful only if the evaluation points do not coincide with the computational nodes. This problem is removed in the improved version of IMLS, named the improved interpolation moving least squares (IIMLS) scheme [6]. In IMLS and IIMLS variants, the inverse of a moment matrix has to be calculated in the procedure of computation of shape functions, which makes the scheme computationally expensive. Another variant of the MLS scheme, which is based on the orthogonal weight function (OMLS), has been proposed in [6]. In this scheme, the moment matrix becomes a diagonal matrix that eliminates the calculation for inversion of moment matrix, which saves a substantial part of computational time.

The objective of this paper is to develop the MLPG method based on the above listed improved versions of MLS scheme and test their performance for the potential flow problem. The tested MLPG methods based on the four improved versions of MLS, i.e. MLS_k (MLS with the modified weight function), IIMLS, OMLS, and OMLS_k (OMLS with modified weight function) are named here: MLPG_k, IIMLPG, OMLPG, and OMLPG_k, respectively. In the next section, the MLPG formulation for the Laplace equation, which governs the potential flow, is introduced followed by numerical results, discussion, and conclusion.

3 Materials and Methods

In this section, we first present the procedure of MLS and OMLS approaches followed by the formulation of the MLPG method for the Laplace equation. Detailed information on the procedure of shape function generation by the above listed MLS schemes has been discussed in [2].

3.1 MLS Approximation

The MLS approximation for unknown variable $\mathbf{u}(\mathbf{x})$ at an evaluation point $\mathbf{x}$ can be written as

$$u^h(\mathbf{x}) = \sum_{j=1}^{m} p_j(\mathbf{x})a_j(\mathbf{x}) = \mathbf{p}^T(\mathbf{x})\mathbf{a}(\mathbf{x}), \tag{1}$$

where $\mathbf{p}^T(\mathbf{x})$ is a row vector containing m basis functions and $a_j(x)$ are unknown coefficients. The elements of the vector $\mathbf{p}^T(\mathbf{x})$ in 2D can be written as

$$\mathbf{p}^T(\mathbf{x}) = \left[1, x_1, x_2, x_1^2, x_1x_2, x_2^2\right]. \tag{2}$$

There are six basis functions ($m = 6$) in 2D. Similarly, the vector can be written for 1D and 3D [2]. The coefficient vector $\mathbf{a}(\mathbf{x})$ is derived by minimising a weighted residual using l_2 norm

$$\sum_{i=1}^{ns} w(\mathbf{x}, \mathbf{x}_i)\left[u^h(\mathbf{x}, \mathbf{x}_i) - u(\mathbf{x}_i)\right]^2 = \sum_{i=1}^{ns} w(\mathbf{x}, \mathbf{x}_i)\left[\mathbf{p}^T(\mathbf{x}_i)\mathbf{a}(\mathbf{x}) - u(\mathbf{x}_i)\right]^2, \tag{3}$$

where $w(\mathbf{x}, \mathbf{x}_i)$ is a weight function

$$w(\mathbf{x}, \mathbf{x}_i) = \begin{cases} 1 - 6d^2 + 8d^3 - 3d^4 & \text{if } 0 \le d \le 1 \\ 0 & \text{if } d > 1 \end{cases}. \tag{4}$$

$d = \|\mathbf{x} - \mathbf{x}_i\|/r_w$ and r_w is the radius of the support domain in which the weight function is nonzero. There are n_s number of nodes in the support domain, and $u(\mathbf{x}_i)$ is the nodal parameter of the field variable at the discretization node $\mathbf{x}_i$.

The m linear equations are obtained by differentiating Eq. (3) with respect to coefficient vector $\mathbf{a}(\mathbf{x})$ and equating it to zero

$$\sum_{i=1}^{ns} w(\mathbf{x}, \mathbf{x}_i)\left[\left[\mathbf{p}^T(\mathbf{x}_i)\mathbf{a}(\mathbf{x}) - u(\mathbf{x}_i)\right]\right]\mathbf{p}(\mathbf{x}_i) = 0, \tag{5}$$

which can be written in matrix form as

$$\mathbf{A}(\mathbf{x})_{m \times m}\mathbf{a}(\mathbf{x})_{m \times 1} = \mathbf{B}(\mathbf{x})_{m \times ns}\mathbf{u}_{ns \times 1}, \tag{6}$$

where

$$\mathbf{A}(\mathbf{x}) = \sum_{i=1}^{ns} w(\mathbf{x}, \mathbf{x}_i)\mathbf{p}(\mathbf{x}_i)\mathbf{p}^T(\mathbf{x}_i) \tag{7}$$

is defined as the moment matrix, and

$$\mathbf{a}(\mathbf{x}) = [a_1(\mathbf{x}), a_2(\mathbf{x}), \ldots .a_m(\mathbf{x})]^T$$

$$\mathbf{B}(\mathbf{x}) = \sum_{i=1}^{ns} w(\mathbf{x}, \mathbf{x}_i)\mathbf{p}(\mathbf{x}_i),$$

$$\mathbf{u} = [\overline{u}_1, \overline{u}_2, \ldots, \overline{u}_{ns}]^T, \tag{8}$$

where $\overline{u}_i$ is the value of the field variable at the discretization point $\mathbf{x}_i$. The coefficient vector $\mathbf{a}(\mathbf{x})$ is obtained from Eq. (6) and inserted in Eq. (1) to obtain the final MLS approximation

$$u^h(\mathbf{x}) = \mathbf{p}^T(\mathbf{x})\mathbf{A}^{-1}(\mathbf{x})\mathbf{B}(\mathbf{x})\mathbf{u}. \tag{9}$$

Denoting $\mathbf{p}^T\mathbf{A}^{-1}\mathbf{B}$ by ϕ, we obtain the vector of n_s MLS shape functions. Using a vector notation, the partial derivatives of ϕ can be obtained as

$$\phi_{,x} = \mathbf{p}_{,x}^T\left(\mathbf{A}^{-1}\mathbf{B}\right) + \mathbf{p}^T\left(A_{,x}^{-1}\mathbf{B} + A^{-1}\mathbf{B}_{,x}\right),$$

where

$$\mathbf{A}_{,x}^{-1} = -\mathbf{A}^{-1}\mathbf{A}_{,x}\mathbf{A}^{-1}.$$

To enable KDP, the modified weight function used in [2] can be used in MLS.

$$w(\mathbf{x}, \mathbf{x}_i) = \frac{\tilde{w}(\mathbf{x}, \mathbf{x}_i)}{\sum_{k=1}^{ns} \tilde{w}(\mathbf{x}, \mathbf{x}_k)}, \tag{10}$$

where

$$\tilde{w}(\mathbf{x}, \mathbf{x}_i) = \begin{cases} \frac{(d^2+\varepsilon^2)^{-2}-(1+\varepsilon)^{-2}}{\varepsilon^{-2}-(1+\varepsilon)^{-2}} & \text{if } 0 \leq d \leq 1 \\ 0 & \text{if } d \geq 1 \end{cases}. \tag{11}$$

ε is a small constant, e.g. 10^{-5} [2]. The modified weight function makes the MLS approximation very close to having the KDP.

3.2   OMLS Approximation

The weighted orthogonal basis functions were proposed in the MLS approximation [5], which makes the moment matrix a diagonal matrix. Let, f and g be functions of **x.** The inner product $(f \cdot g)$ is defined as

$$(f \cdot g)_{\mathbf{x}} = \sum_{k=1}^{ns} w(\mathbf{x}, \mathbf{x}_k) f(\mathbf{x}_k)g(\mathbf{x}_k), \tag{12}$$

where $w(\mathbf{x}, \mathbf{x}_i)$ is a weight function. The weighted orthogonal basis function is defined as

$$\tilde{p}_i(\mathbf{x}) = p_i(\mathbf{x}) - \sum_{k=1}^{i-1} \frac{(p_i, \tilde{p}_k)}{(\tilde{p}_k, \tilde{p}_k)} \tilde{p}_k, i = 2, 3 \ldots .m, \qquad (13)$$

where $\tilde{p}_i(\mathbf{x})$ is the new, orthogonal basis function of the OMLS scheme and $p_i(\mathbf{x})$ is the monomial basis function of MLS from Eq. (2). In the present paper, the notations are same as in the MLS procedure, except for $\tilde{p}$. For example, the first and second elements of the weighted orthogonal basis function ($\tilde{p}_i(\mathbf{x})$) are given as

$$\tilde{p}_1(\mathbf{x}) = 1$$
$$\tilde{p}_2(\mathbf{x}) = x_1 - \frac{(p_2, \tilde{p}_1)}{(\tilde{p}_1, \tilde{p}_1)} p_1$$
$$= x_1 - \sum_{k=1}^{ns} w(\mathbf{x}, \mathbf{x}_k)(x_{1k}) / \sum_{k=1}^{ns} w(\mathbf{x}, \mathbf{x}_k). \qquad (14)$$

In the same way, other weighted orthogonal basis functions for the OMLS can be obtained. The approach for obtaining the OMLS shape functions is the same as in the MLS. The only difference is the diagonal moment matrix ($\mathbf{A}$), which can be written as.

$$\mathbf{A}(\mathbf{x}) = \begin{bmatrix} (\tilde{p}_1 \cdot \tilde{p}_1) & 0 & \ldots & 0 \\ 0 & (\tilde{p}_2 \cdot \tilde{p}_2) & \ldots & 0 \\ \vdots & \vdots & \ddots & \vdots \\ 0 & 0 & \ldots & (\tilde{p}_m \cdot \tilde{p}_m) \end{bmatrix}. \qquad (15)$$

To enable the KDP in the OMLS (OMLS_k), a modified weight function of Eq. (10) can be used.

We further use shifted and scaled polynomials to improve the conditioning of the moment matrix. Its details can be found in [2].

3.3 MLPG Formulation

The Laplace equation governs the potential flow. The global domain and boundary are represented as Ω and Γ, respectively.

$$\nabla^2 u = 0 \quad \text{in } \Omega$$
$$u(\mathbf{x}) = \overline{u}(\mathbf{x}) \quad \text{for } \mathbf{x} \in \Gamma_e$$
$$\partial u(\mathbf{x}) / \partial n = \overline{q}(\mathbf{x}) \quad \text{for } \mathbf{x} \in \Gamma_n, \qquad (16)$$

u is the potential function, $\overline{u}$ is the specified value of potential function on the global Essential boundary Γ_e, $\overline{q}$ is the specified value on the global Natural boundary Γ_n, where $\Gamma_e \cup \Gamma_n = \Gamma$. The weighted residual statement for the above equation can be written as

$$\int_{\Omega_Q} \nabla^2 u v \mathrm{d}\Omega = 0, \tag{17}$$

where Ω_Q is a local quadrature domain and v is the test function. The above equation can be written in the weak form by applying the divergence theorem to reduce the continuity requirement. The equation in the vector notation can be written as

$$\int_{\Gamma_Q} u_{,x} n_x v \mathrm{d}\Gamma - \int_{\Omega_Q} u_{,x} v_{,x} \mathrm{d}\Omega = 0, \tag{18}$$

where Γ_Q denotes the boundary of Ω_Q. We use vector notation, subscript, x denotes derivative with respect to the spatial coordinate. In the first term, the weak MLPG form can be written for three possible types of Γ_Q

$$\int_{\Gamma_{Qe}} u_{,x} n_x v \, \mathrm{d}\Gamma + \int_{\Gamma_{Qn}} u_{,x} n_x v \mathrm{d}\Gamma + \int_{\Gamma_{Qin}} u_{,x} n_x v \, \mathrm{d}\Gamma - \int_{\Omega_Q} u_{,x} v_{,x} \mathrm{d}\Omega = 0, \tag{19}$$

where Γ_{Qe} is a part of Γ_Q that intersects Γ_e, Γ_{Qn} is a part of the local domain boundary that intersects Γ_n, and Γ_{Qin} is a part of the local domain boundary that does not intersect Γ. The test function in the MLPG method is chosen so that it vanishes at Γ_{Qin}, then the line integral term for Γ_{Qin} from Eq. (19) becomes zero. A discretization of the MLPG form leads to the system of algebraic equations given by

$$\boldsymbol{Ku} = \boldsymbol{F}, \tag{20}$$

where $\boldsymbol{K}$ is the global system matrix (traditionally named the stiffness matrix), $\boldsymbol{u}$ is the vector of unknown field variable, and $\boldsymbol{F}$ is the force vector. The elements of the matrix $\boldsymbol{K}$ and the vector $\boldsymbol{F}$ are as follows:

$$K_{ij} = \begin{cases} \phi_j(\mathbf{x}_i) & \mathbf{x}_i \in \Gamma_e \\ \int_{\Gamma_{Qe}} \phi_{j,x}(\mathbf{x}) n_x v(x, \mathbf{x}_i) \mathrm{d}\Gamma - \int_{\Omega_Q} \phi_{j,x}(\mathbf{x}) v_{,x}(\mathbf{x}, \mathbf{x}_i) \mathrm{d}\Omega & \mathbf{x}_i \notin \Gamma \end{cases}, \tag{21}$$

$$F_i = \begin{cases} \overline{u}(\mathbf{x}_i) & \mathbf{x}_i \in \Gamma_e \\ -\int_{\Gamma_{Qn}} \overline{q} v(\mathbf{x}, \mathbf{x}_i) \mathrm{d}\Gamma & \mathbf{x}_i \notin \Gamma \end{cases}. \tag{22}$$

The indices i and j represent computational node number and number of nodes in the support domain of the node i, respectively. In the MLPG method based on MLS and OMLS, the direct interpolation method is used to impose essential boundary condition, and in the MLPG method based on IIMLS, MLS_k and OMLS_k, the EBC can be directly imposed, in the same way as in the FEM.

Test Function

The MLPG test function is a quadratic function proposed in [7]

$$v(\mathbf{x}, \mathbf{x}_i) = \begin{cases} \left(1 - \left(\frac{x_1 - x_{1i}}{a_Q(\mathbf{x}_i)/2}\right)\right)^2 \cdot \left(1 - \left(\frac{x_2 - x_{2i}}{a_Q(\mathbf{x}_i)/2}\right)\right)^2 & \text{if } (x_1, x_2) \in \Omega_{Qi} \\ 0 & \text{if } (x_1, x_2) \notin \Omega_{Qi}, \end{cases} \tag{23}$$

where $a_Q(\mathbf{x}_i) = \beta_Q r_s(\mathbf{x}_i)$, $a_Q(\mathbf{x}_i)$ is the edge of the local quadrature domain, β_Q is the proportionality parameter, and $r_s(\mathbf{x}_i)$ is the radius of the support domain of point $\mathbf{x}_i$.

4 Results and Discussion

Four improved MLPG methods have been developed, namely, MLPG_k, IIMLPG, OMLPG, and OMLPG_k based on MLS scheme with modified weight function (MLS_k), improved interpolating MLS (IIMLS), MLS based on orthogonal basis function (OMLS) and OMLS with modified weight function (OMLS_k), respectively. Their performance is analysed and compared with the original MLPG method, based on a standard MLS scheme, regarding accuracy level, convergence behaviour, and computational speed for the potential flow problem. The MLPG computer code is developed on the C/C++ platform. The Laplace equation has been solved on two-dimensional non-rectangular domain with both EBC and Natural boundary conditions as shown in Fig. 1.

Results of the MLPG code have been verified with the exact analytical solution of the problem which is

$$u = x_2\left[1.0 - 1.0/\left\{(x_2)^2 - (x_1 - L)^2\right\}\right], \tag{24}$$

where u is the potential function, L is the length of the domain, x_1 and x_2 are spatial coordinates. Two error norms have been used in the current work, absolute l_1 norm is defined as

$$\text{Err}\_l_1 = \left|u_i - u_i^e\right|, \tag{25}$$

where u_i and u_i^e are approximate and exact values at the evaluation point i, respectively, and l_2 norm is defined as
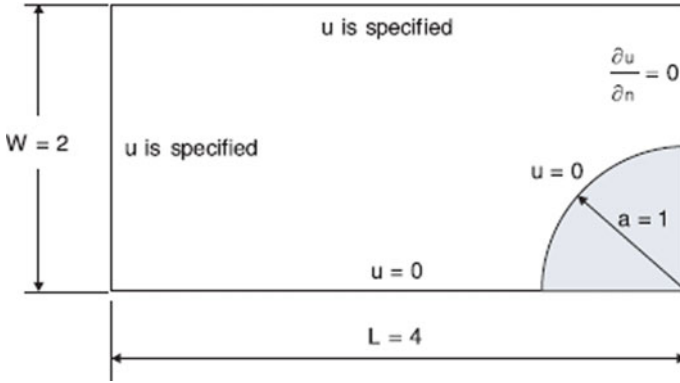
Fig. 1 Schematic diagram of the 2D non-rectangular domain with boundary conditions [8]

$$\text{Rerr}\_l_2 = 100 \times \sqrt{\sum_{i=1}^{N}\left(u_i - u_i^e\right)^2} \Big/ \sqrt{\sum_{i=1}^{N}\left(u_i^e\right)^2}, \qquad (26)$$

where N is the number of discretization nodes.

Often, there are two types of grid, discretisation grid, and evaluation grid. The MLPG solution is obtained on discretised grid points and further re-evaluated on evaluation grid points. In Fig. 2, the distribution of 30 discretised and 114 evaluation grid points in the domain are shown.

Tests have been performed for different sets of parameters such as the different number of nodes in the support domain n_s, different sizes of the local support domain by varying the proportionality parameter and the different number of Gaussian points in the local integration domain. The quadratic basis has been chosen in the MLS variants as it appears to be an optimum. Results obtained with optimised parameters are shown here, i.e. 3×3 Gaussian points in the local integration domain, proportionality
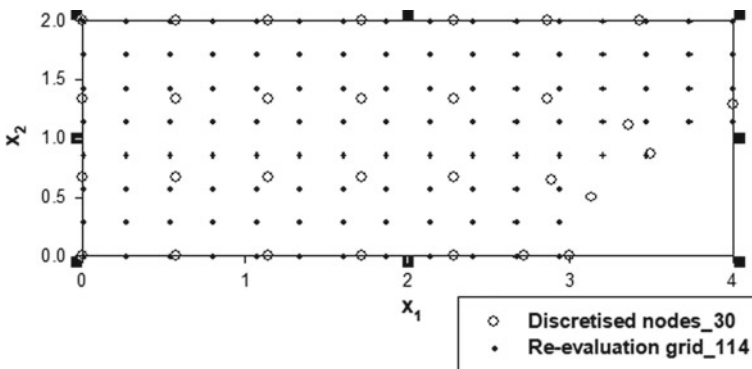
Fig. 2 Schematic diagram of the 2D non-rectangular domain with boundary conditions [2]

parameter $\beta_Q = 0.7$ and $n_s = 13$. First, the MLPG solution is obtained on the discretised grid, and then it is re-evaluated on the evaluation grid. Numerical experiments have been performed for different sizes of grids.

In Fig. 3, a comparison of analytical solution (top) with numerical MLPG solution (bottom) for 168 discretised and 717 evaluation points respectively is shown. Contour plots of constant potential lines are shown in the domain. Satisfactory result is found even for the coarser grid. The solution contour plots of other MLPG variants are visually similar to the MLPG method; thus, they are not shown.

The computational efficiency, of all the selected MLS variants in the MLPG method, relative to the original MLS, has been tested (Fig. 4). The IIMLS method is the most computationally expensive due to its complicated shape function generation procedure. The OMLS method is the fastest and almost 10% more efficient as the original MLS method. As it does not possess KDP, the use of the modified weight function in the OMLS enables KDP, and based on it, the OMLS_k method is
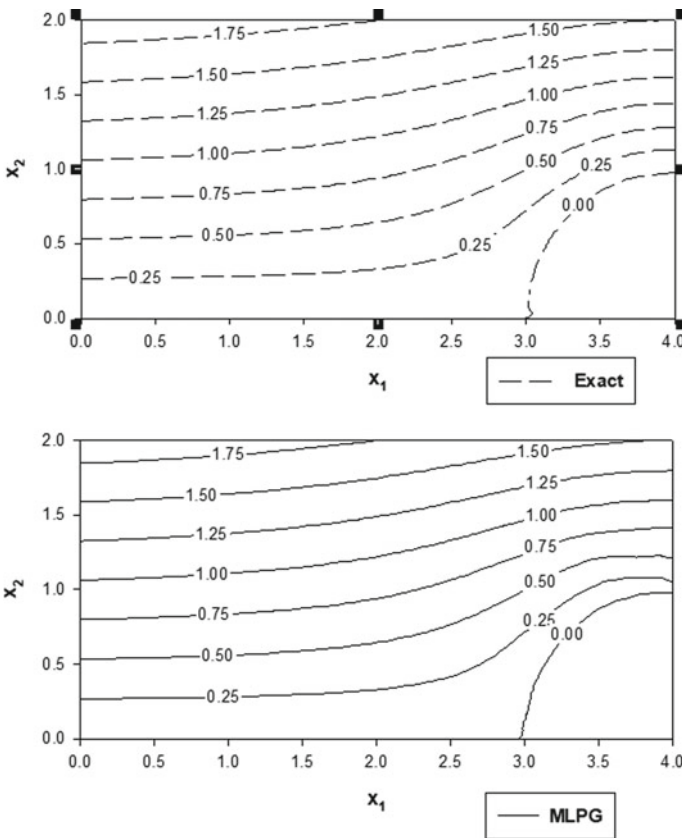
Fig. 3 Comparison of analytical solution (top) with numerical MLPG solution (bottom)
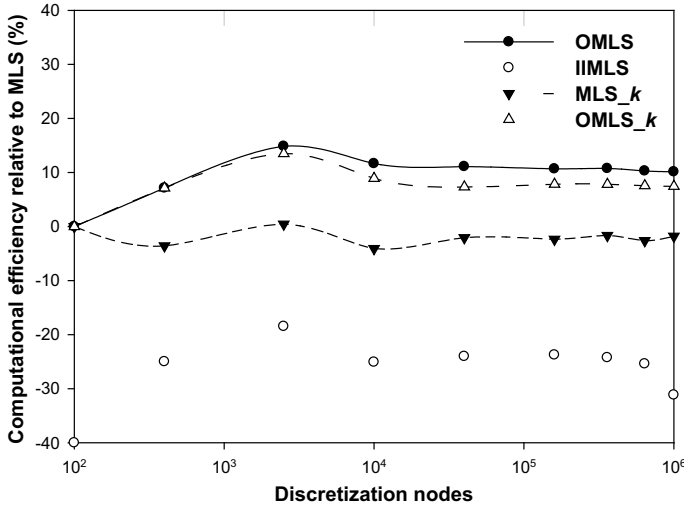
Fig. 4 Computational efficiency of MLPG with different MLS variants relative to MLS [2]

approximately 8% more efficient than the original MLS method. There is the little trade-off between possessing KDP and computational efficiency.

The results of MLPG and OMLPG are identical, and similarly, the results of MLPG_k and OMLPG_k are identical. The OMLPG_k seems to be optimum, and thus, we show only its convergence with the original MLPG method in Fig. 5; however, the IIMLPG method exhibits similar convergence behaviour. The x-axis shows the number of discretised grid points, and the y-axis shows the error. The convergence behaviour of both methods based on the l_2 norm (top) and l_1 norm (bottom) is shown in Fig. 5. Slight waviness in convergence can be seen, nevertheless, good and almost similar convergence behaviour and good accuracy level are found.

The accuracy level and convergence behaviour of all the selected methods are found almost similar and satisfactory. The IIMLPG possesses KDP; however, it is more computationally expensive than MLPG and MLPG_k. The OMLPG is almost 10% faster than the MLPG method; however, it does not possess KDP. The use of modified weight function in the OMLPG method enables KDP at the cost slight decrease in computational speed. Hence, OMLPG_k seems to be the optimum method which resolves both the problems, imposition of essential boundary conditions and moderate computational speed.
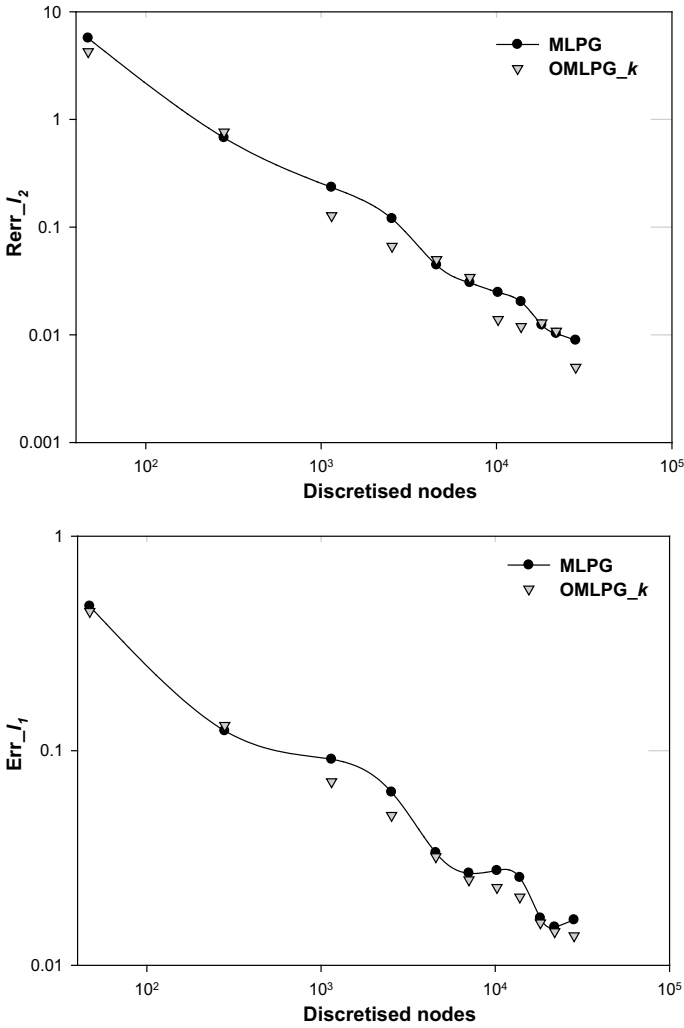
Fig. 5 Convergence of MLPG and OMLPG_*k* methods based on l_2 norm (top) and l_1 norm (bottom)

5 Conclusions

Four improved MLPG methods have been developed, i.e. MLPG_*k*, IIMLPG, OMLPG, and OMLPG_*k* based on MLS scheme with modified weight function (MLS_*k*), improved interpolating MLS (IIMLS), MLS based on orthogonal basis function (OMLS) and OMLS with modified weight function (OMLS_*k*), respectively. Their performance is analysed and compared with the original MLPG method based on accuracy level, convergence behaviour, and computational speed for potential flow problem. The accuracy level and convergence behaviour of all the selected

methods are found almost similar and satisfactory. The IIMLPG possesses KDP; however, it is more computationally expensive than MLPG and MLPG_*k*. The OMLPG is almost 10% faster than the MLPG method; however, it does not possess KDP. The use of the modified weight function in the OMLPG method enables KDP at the cost of slight decrease in the computational speed. Hence, OMLPG_*k* seems to be the optimum method which resolves both the problems, imposition of essential boundary condition and increase of computational speed.

Nomenclature

α_Q	Edge of the local quadrature domain
β_Q	Proportionality parameter
ϕ	Shape function
Γ	Global boundary
Γ_e	Global boundary on which essential boundary condition is applied
Γ_n	Global boundary on which natural boundary condition is applied
Ω_Q	Local quadrature domain
ν	Test function
n_s	Number of nodes in support domain
r_s	Radius of support domain
m	Basis function
u	Potential function
x	Spatial coordinate
KDP	Kronecker delta property
IIMLS	Improved interpolating moving least squares
MLS	Moving least squares
MLPG	Mehsless local Petrov Galerkin
OMLS	Moving least squares with orthogonal basis function

References

1. Sladek J, Stanak P, Han ZD, Sladek V, Atluri SN (2013) Applications of the MLPG method in engineering & sciences: a review. Comput Model Eng Sci 92(5):423–475
2. Singh R, Trobec R (2022) Engineering analysis with boundary elements analysis of the MLS variants in the meshless local Petrov-Galerkin method for a solution to the 2D Laplace equation. Eng Anal Bound Elem 135:115–131
3. Most T, Bucher C (2005) A moving least squares weighting function for the elementfree Galerkin method which almost fulfills essential boundary conditions. Struct Eng Mech 21:315–332

4. Netuzhylov H (2008) Enforcement of boundary conditions in meshfree methods using interpolating moving least squares. Eng Anal Bound Elem 32(6):512–516
5. Ren HP, Cheng YM, Zhang W (2009) An improved boundary element-free method (IBEFM) for two-dimensional potential problems. Chinese Phys B 18(10):4065–4073
6. Wang JF, Sun FX, Cheng YM (2012) An improved interpolating element-free Galerkin method with a nonsingular weight function for two-dimensional potential problems. Chinese Phys B 21(9):090204
7. Sterk M, Trobec R (2008) Meshless solution of a diffusion equation with parameter optimization and error analysis. Eng Anal Bound Elem 32(7):567–577
8. Zhu T, Zhang JD, Atluri SN (1998) A local boundary integral equation (LBIE) method in computational mechanics, and ameshless discretization approach. Comput Mech 21(3):223–235

Conjugate Heat Transfer Simulations Using Characteristic-Based Off-Lattice Boltzmann Method

Kuldeep Tolia and Kameswararao Anupindi

1 Introduction

Conjugate heat transfer is a result of coupled thermal dynamics between fluid and solid and is present in a wide range of engineering and natural phenomena, including blade cooling inside jet engines, electronic circuit cooling, thermal insulation of heat pipes, microfluidic devices as well as boiling water inside a cooking vessel [1, 2]. Two physical requirements must be met to describe the conjugate heat transfer condition at the interface of a multi-component system: (i) temperature continuity and (ii) normal heat flux continuity, which assure that the conservation of energy principle is satisfied.

The lattice Boltzmann method (LBM) is a promising computational tool for tackling fluid dynamics problems and a dependable alternative to conventional computational fluid dynamics tools. However, with LBM, the conjugate heat transfer research is relatively recent. The intrinsic nature of LBM allows for predicting the conjugate heat transfer effects automatically, where the conjugate interface is placed midway between the two lattice nodes. This method is called the "half-lattice division scheme" proposed by Wang et al. [3]. But it is only valid for steady-state flows, as it does not account for the variation of heat capacitance. Later, Meng et al. [4] introduced a conjugate scheme that modeled thermal inertia, used grid points on the interface, and was not constrained to steady-state conditions. Various source term formulations were proposed for the LBM conjugate models [5, 6]. Karani and Huber [6] mathematically compared the differences between the advection–diffusion equation and the conservation of energy equation and modified the advection–diffusion equation to resemble the energy equation by including a source term.

The objective of the present study is to introduce a conjugate source model in the characteristic-based off-lattice Boltzmann method (OLBM) framework and test its

K. Tolia · K. Anupindi (✉)
Department of Mechanical Engineering, IIT Madras, Chennai 600036, India
e-mail: kanupindi@iitm.ac.in

validity with a case of natural convection in a square cavity with wall conduction effects. The rest of the paper is presented in the following way: In Sect. 2, the details for the present OLBM and the conjugate source model are described. In Sect. 3.1, the current method is validated with the three test problems. Section 3.2 discusses the effects of wall conduction on the natural convection phenomenon inside a square enclosure. Finally, the conclusions of this work are discussed in Sect. 4.

2   Methodology

The discrete velocity Boltzmann equation (DBVE) can be derived from the Boltzmann equation by discretizing the velocity space into finite discrete velocities and approximating the collision term using the single-relaxation time (SRT) Bhatnagar-Gross-Krook (BGK) collision operator [7] and is given as

$$\frac{\partial f_k}{\partial t} + \boldsymbol{e}_k \cdot \nabla f_k(\boldsymbol{x}, t) = \frac{1}{\tau}\big[f_k^{\text{eq}}(\boldsymbol{x}, t) - f_k(\boldsymbol{x}, t)\big], \tag{1}$$

where the subscript k denotes the discrete velocity direction. In the present study, a double distribution function approach is adopted, where the density distribution function and the thermal distribution function account for the evolution of fluid-flow and thermal characteristics, respectively.

2.1   Numerical Details

A D2Q9 discrete lattice model is used for both distribution functions. The discrete equations for density and thermal distribution functions are given as

$$\frac{\partial f_k}{\partial t} + \boldsymbol{e}_k \cdot \nabla f_k = -\frac{f_k - f_k^{\text{eq}}}{\tau_v} + F_k, \tag{2}$$

$$\frac{\partial g_k}{\partial t} + \boldsymbol{e}_k \cdot \nabla g_k = -\frac{g_k - g_k^{\text{eq}}}{\tau_g} + G_k. \tag{3}$$

The equilibrium density and thermal distribution functions are computed as follows:

$$f_k^{\text{eq}} = \rho \omega_k \left[1 + \frac{\boldsymbol{e}_k \cdot \boldsymbol{u}}{c_s^2} + \frac{(\boldsymbol{e}_k \cdot \boldsymbol{u})^2}{2c_s^4} - \frac{\boldsymbol{u} \cdot \boldsymbol{u}}{2c_s^2}\right],$$

$$g_k^{\text{eq}} = T \omega_k \left[1 + \frac{\boldsymbol{e}_k \cdot \boldsymbol{u}}{c_s^2}\right], \tag{4}$$

where c_s is the lattice speed of sound. The weighting factor, ω_k, and the discrete velocity vector, $\boldsymbol{e}_k$, for the D2Q9 discrete lattice model are not presented for brevity and can be found in Mohamad [7]. The macroscopic flow variables are recovered by taking the moments of distribution functions and are defined as

$$\rho(\boldsymbol{x}, t) = \sum_{k=0}^{8} f_k, \, \rho \boldsymbol{u}(\boldsymbol{x}, t) = \sum_{k=0}^{8} f_k \boldsymbol{e}_k + \frac{\Delta t}{2} \boldsymbol{F}_{\text{ext}}, \tag{5}$$

$$T(\boldsymbol{x}, t) = \sum_{k=0}^{8} g_k + \frac{\Delta t}{2} G_{\text{conj}}. \tag{6}$$

Using the Chapman-Enskog expansion, a relationship is established between the macro- and meso-scales [7]. The kinematic viscosity of the fluid and the thermal diffusivity of fluid/solid are related to the respective relaxation times as

$$\tau_v = \frac{\nu}{c_s^2}, \, \tau_g = \frac{\alpha}{c_s^2}. \tag{7}$$

In the present work, a characteristic-based OLBM proposed by Bardow et al. [8] extended to a finite-difference method, which can handle generalized non-uniform and curvilinear grids, is used. The DVBE was discretized using a second-order accurate Lax-Wendroff scheme. The spatial derivatives of distribution functions are computed using a central difference scheme. The Crank-Nicolson time-stepping scheme was used to advance in time. The distribution function at the boundaries is calculated from the equilibrium and the non-equilibrium parts and is given as $f_k = f_k^{\text{eq}} + f_k^{\text{neq}}$, where the f_k^{eq} can be computed using Eq. 4. The non-equilibrium part of the density distribution function, f_k^{neq}, at the boundaries is computed as $\frac{\partial^2 f_k^{\text{neq}}}{\partial n^2} = 0$, where n is the local wall-normal direction. Similarly, g_k and g_k^{neq} can be computed at the boundaries. Polasanapalli and Anupindi [9] thoroughly explained the numerics and boundary condition treatment for the OLBM. The force term in Eq. 2 is introduced into the DVBE by utilizing the forcing method proposed by Guo et al. [10] and is given as

$$F_k = \omega_k \left[\frac{\boldsymbol{e}_k - \boldsymbol{u}}{c_s^2} + \left(\frac{\boldsymbol{e}_k \cdot \boldsymbol{u}}{c_s^4} \right) \boldsymbol{e}_k \right] \cdot \boldsymbol{F}_{\text{ext}}. \tag{8}$$

2.2 Conjugate Treatment Model

In the present study, a source term model proposed by Karani and Huber [6] is used to study conjugate heat transfer using OLBM. According to Karani and Huber [6], solving the conservative form of the advection–diffusion equation with a source

term corresponds to solving the conservative form of the energy equation. Thus, the effects of the spatial variation of the thermophysical properties that appear at any multi-component system's interface can be considered using a source term. Without additional interface treatment for the distribution function correction, it will automatically offer a proper temperature distribution based on the heat flux for both transient and steady circumstances. The present method assumes that the interface is midway between the two neighboring lattice nodes.

The product of the gradient of $1/\rho c$, where c is the material's specific heat capacity, and the total heat flux constitutes the conjugate source term formulation. Thus, the final source term applied to the multi-component system's interface for conjugate heat transfer is

$$G_{\text{conj}} = \nabla\left(\frac{1}{\rho c}\right) \cdot \boldsymbol{q}, \quad \boldsymbol{q} = -\lambda \nabla T + \rho c \boldsymbol{u} T, \tag{9}$$

where λ is the thermal conductivity of the material. The gradient of $1/\rho c$, in the jth direction, at any lattice node i is computed using a one-sided finite difference approximation and is given as follows:

$$\frac{\partial}{\partial x_j}\left(\frac{1}{\rho c}\right)_i = \frac{\frac{1}{(\rho c)_i} - \frac{1}{(\rho c)_{\text{avg}}}}{\left(\frac{\Delta x_j}{2}\right)},$$

$$(\rho c)_{\text{avg}} = \frac{(\rho c)_i + (\rho c)_{i+1}}{2}, \tag{10}$$

where $(\rho c)_{\text{avg}}$ is the average value of heat capacitance between the lattice points i and $i+1$ with the grid spacing of Δx_j. From Eq. 10, it is clear that the source term model will only be active at the lattice nodes that are neighboring the interface, where there is a change in the thermophysical properties. At any other lattice node, G_{conj} will be zero. Finally, this conjugate force term can be incorporated as a source term for thermal distribution function in Eq. 3 as $G_k = \omega_k G_{\text{conj}}$.

3   Results and Discussion

3.1   Validation

In this section, the present method is validated with three test cases. The aim is to investigate the current method's ability to predict the effects of conjugate heat transfer for various steady and transient flow conditions. The first and second test cases study the convection–diffusion phenomenon in a horizontal channel with a stratified flow parallel to the two-layered fluid interface under steady and transient

conditions, respectively. The final test case studies the effect of heat conduction in a solid for a square cavity with natural convection.

3.1.1 Steady-State Conjugate Heat Transfer in a Stratified Channel

Consider a horizontal channel filled with two immiscible fluids with distinct thermophysical properties, flowing uniformly at a constant speed U in the direction parallel to the interface as shown in Fig. 1. The domain size selected is $H = 1, L = 1$. The periodic boundary condition is applied to the vertical boundaries. The Dirichlet boundary condition is imposed at the top and bottom walls with a sinusoidal temperature variation and is given as

$$T(x, y = 0, H) = \cos\left(\frac{2\pi x}{L}\right). \tag{11}$$

The steady-state temperature distribution under these circumstances has an analytical solution provided by Li et al. [11]. The non-dimensional parameters governing the problem are the Peclet number, $Pe = UH/\alpha_1 = 20$, the thermal diffusivity ratio, $\kappa = \alpha_2/\alpha_1$, and the heat capacitance ratio, $\sigma = (\rho c)_2/(\rho c)_1$. The subscript here denotes the thermophysical property of a respective domain. A 100×101 grid is deployed to perform the simulation for the given problem. Figure 2 compares the analytical solution with the numerical results at various locations along the x-direction for the case $\kappa = 10, \sigma = 1$. Excellent agreement between the numerical results and the analytical solution is observed. The present method is also effective for cases with higher heat capacitance ratios, i.e., $\sigma = 5, 10$ with $\kappa = 10$.

Fig. 1 Schematic of conjugate heat transfer in a stratified horizontal channel flow
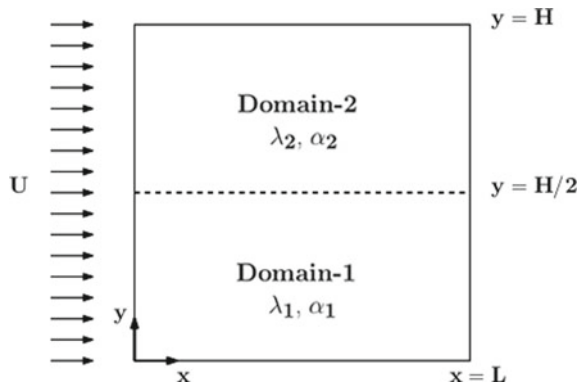
Fig. 2 Comparison of the present results and analytical solution [11] for temperature distribution for the case $\kappa = 10, \sigma = 1$. Solid lines are for present results, and symbols represent the analytical solution
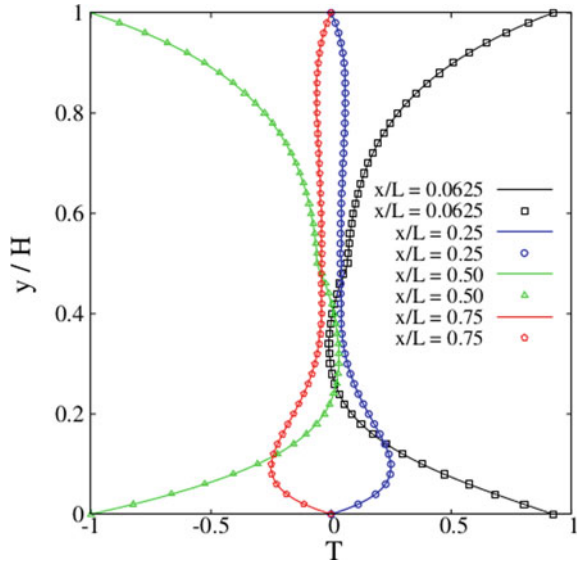
3.1.2 Transient Conjugate Heat Transfer in a Stratified Channel

This is an extension of the test problem from Sect. 3.1.1 to transient analysis. Consider the schematic as shown in Fig. 1. The Dirichlet boundary condition imposed at the top and bottom walls is now prescribed with a combination of sinusoidal and temporally varying temperature distributions and is given as follows:

$$T(x, y = 0, H, t) = \cos\left(\frac{2\pi x}{L} + \frac{2\pi t}{\Gamma}\right), \tag{12}$$

where Γ is the time period and is non-dimensionalized as the Stokes number, St $= \sqrt{H^2/(\Gamma\alpha_1)}$. The analytical solution for the given problem is provided by Li et al. [11]. In the present work, we have assumed Pe $= 20$, $St = 1$, $\kappa = 10$, $\sigma = 1, 10$. The domain is initialized using the analytical solution for $t = 0$ with a grid resolution of 100×101. Figure 3 compares the analytical solution with the present numerical results at various locations along the x-direction and at an instant of $t^* = 0.2$, where $t^* = t/\Gamma$. The present method thus gives accurate results in both steady and transient conditions.

3.1.3 Conjugate Heat Transfer for Natural Convection in a Square Enclosure with one Conducting Solid Vertical Wall

The present method is verified and studied for natural convection inside a square enclosure along with a finite-thickness vertical wall to include the physics of

solid wall heat conduction. The domain setup considered for the present work is adopted from Kaminski and Prakash [12] and is shown in Fig. 4. The vertical walls are imposed with the Dirichlet boundary condition, i.e., $T(x = 0, y) = T_c$, $T(x = L + w, y) = T_h$, where w is the solid wall thickness, $T_h > T_c$, and the horizontal walls are insulated. All the walls are prescribed with the no-slip boundary condition ($u = 0, v = 0$). Four dimensionless parameters govern this problem: the solid wall to fluid thermal conductivity ratio $\xi = \lambda_{solid}/\lambda_{fluid}$, the dimensionless solid wall thickness ratio w/L, the Prandtl number Pr, and the Grashof number Gr. The Pr and Gr are set to 0.7 and 10^5, respectively, for all simulations corresponding to the laminar flow regime. Table 1 presents the grid independence and the time step size independence studies for the case Gr $= 10^5$, $w/L = 0.2$, and $\xi = 5$. Thus, a fine and uniform grid of 243×240 with $\Delta t = 1 \times 10^{-4}$ s is used for all simulations. The present solver is developed in FORTRAN with MPI for distributed memory parallelization and has a parallel multi-block frame that decomposes the domain in both the x and y directions. The following parameters were chosen for the verification of the present method: $w/L = 0, 0.2$, and $\xi = 1$. Figure 5 shows the temperature distribution at the fluid–solid interface. For this problem, the average Nusselt number can be calculated as

$$\text{Nu}_{avg} = \frac{\overline{\text{Nu}}_{x=0} + \overline{\text{Nu}}_{x=L+w}}{2}, \tag{13}$$

$$\overline{\text{Nu}}_{x=L+w} = -L \frac{\int_0^L \frac{\partial T}{\partial x}\big|_{x=0,L+w} \mathrm{d}y}{\Delta T \int_0^L \mathrm{d}y}, \tag{14}$$

Table 1 Grid and time step size independence study for $Gr = 10^5$, $w/L = 0.2$, $\xi = 5$

Grid	123×120	243×240	495×480
Nu_{avg}	3.441	3.437	3.426
Δt (Grid: 243×240)	5×10^{-4}	2.5×10^{-4}	1×10^{-4}
Nu_{avg}	3.437	3.432	3.423

Table 2 Average Nusselt number for $Gr = 10^5$

–	ξ	w/L	Nu_{avg}	Error (%)
Case-1	–	0.0	4.082	0.049
Reference [12]	–	0.0	4.080	–
Case-2	1.0	0.20	2.091	0.529
Reference [12]	1.0	0.20	2.080	–
Case-3	5.0	0.12	3.663	–
Case-4	5.0	0.20	3.423	–

Fig. 4 Schematic of conjugate natural convection inside a square cavity with one conducting vertical wall
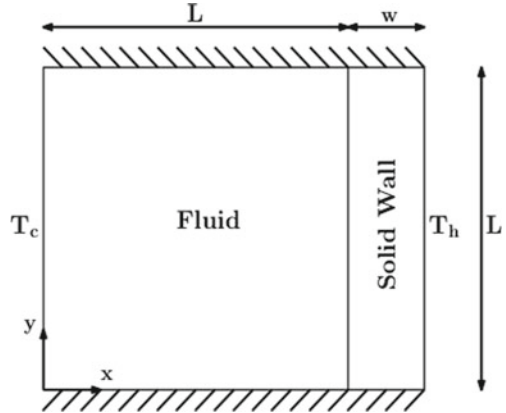
where $\Delta T = T_h - T_c$. Table 2 compares the average Nusselt number alongside their corresponding errors. In Table 2, case-1, case-2, case-3, case-4 denote the results obtained from the present simulations, and the reference indicates the results of Kaminski and Prakash [12]. The obtained results are in good agreement with the reference data reported by Kaminski and Prakash [12].

3.2 Effect of Solid Wall Thickness

The effects of solid wall thickness on the heat transfer and flow-thermal patterns are studied with different values of $w/L = 0.12, 0.2$ for $\xi = 5$. Under the isothermal

Fig. 5 Variation of temperature at the fluid–solid interface
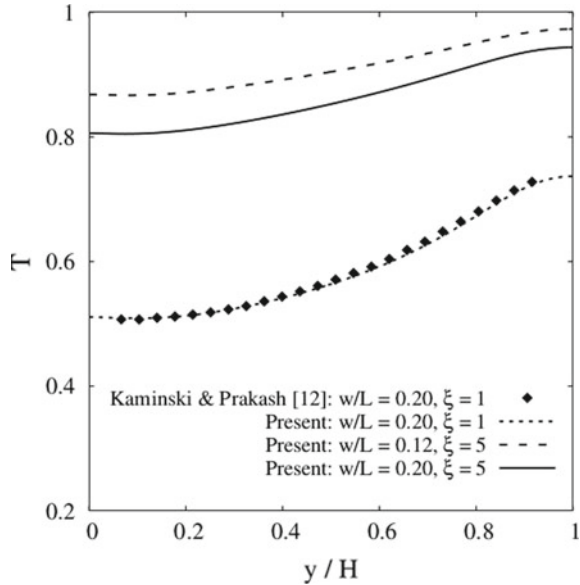
boundary conditions, i.e., $w/L = 0.0$, an anticlockwise and a symmetric flow circulation pattern is observed, as shown in Fig. 6. The addition of a solid wall introduces temperature gradients, which result in an asymmetric flow circulation pattern as shown in the streamlines plots of Figs. 7 and 8. The asymmetry of the flow pattern is also a direct consequence of the non-uniform temperature profile obtained at the fluid–solid interface as observed in Fig. 5. From Fig. 5, it can be seen that with an increase in the w/L ratio, the interface temperature drops. As a result, there will be a smaller temperature potential driving the flow, i.e., $T_i - T_c$, where T_i is the interface temperature instead of $T_h - T_c$. This phenomenon can be observed from the isotherms plots of Figs. 7 and 8. Thus, with an increase in the wall thickness, T_i decreases, which results in a lower effective Grashof number, which explains the reduction in the average Nusselt number, Nu_{avg}, as given in Table 2. Also, as the w/L ratio increases, the flow inside the cavity will become more imbalanced and asymmetric.

From Fig. 5, it can be seen that the interface temperature is higher near the top wall of the square cavity. This results from fluid advecting the heat from the solid wall as it rises by anticlockwise circular motion. Also, the colder fluid from the left wall will strike the fluid–solid interface's bottom region and thus making it colder. This temperature variation can also be noted from the isotherms plots of Figs. 7 and 8. The effect of thermal conductivity ratio is studied with two values of $\xi = 1$ and 5 for a given $w/L = 0.2$ ratio. From Fig. 5, a significant temperature drop at the interface can be observed when the ξ value is reduced from 5 to 1. This, in turn, tells that there is a lesser driving temperature potential available for case-2 ($\xi = 1$), which results in a drop of about 39% in the average Nusselt number compared with

Fig. 6 Isotherms and
streamlines contours for
natural convection at
$Gr = 10^5$, $w/L = 0$
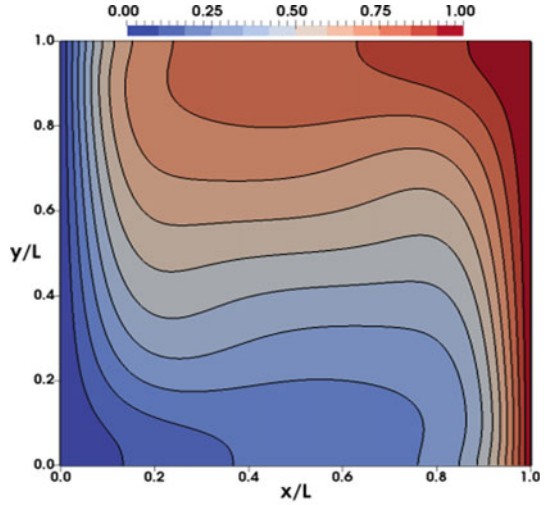
(a) Isotherms
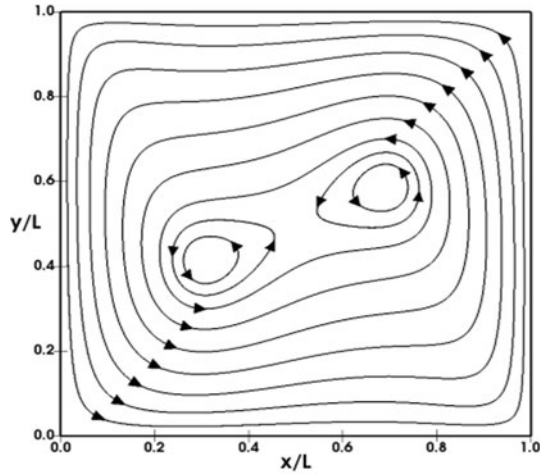
(b) Streamlines

case-4 ($\xi = 5$). As the value of ξ decreases, the non-uniformity in the interface
temperature distribution increases, indicating that the convection phenomenon is
more dominant than the conduction in the solid wall. For lower ξ values, an initial
interface temperature drop is observed near the bottom region of the cavity (around
$y \approx 0$), which can be inferred as a local event due to the presence of the cavity corner.
On the other hand, for large values of ξ, the interface temperature distribution will
be more uniform and try to attain the T_h boundary value. With an ideal solid wall
having $\xi \to \infty$, the interface temperature will also approach T_h, irrespective of the
w/L value.

Fig. 7 Isotherms and
streamlines contours for
natural convection at
$Gr = 10^5, \xi = 5$,
$w/L = 0.12$
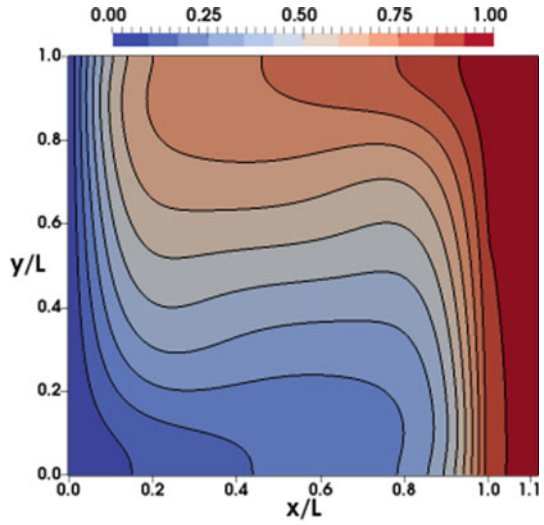
(a) Isotherms
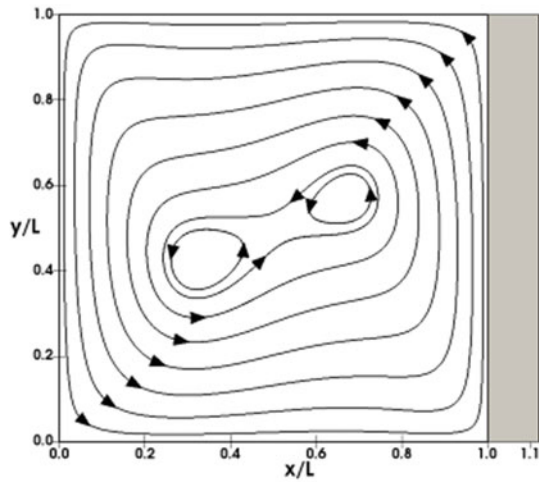
(b) Streamlines

4 Conclusions

The present paper implements a conjugate heat transfer source term model in the
characteristic-based off-lattice Boltzmann method framework. The proposed numer-
ical method has been successfully tested for different steady and transient flow condi-
tions. Natural convection in a square cavity is studied for combinations of ξ and w/L
ratios at $Pr = 0.7$, $Gr = 10^5$ and compared with the isothermal boundary condi-
tion case. The introduction of a solid wall has resulted in non-uniform temperature

Fig. 8 Isotherms and
streamlines contours for
natural convection at
$Gr = 10^5, \xi = 5, w/L = 0.2$
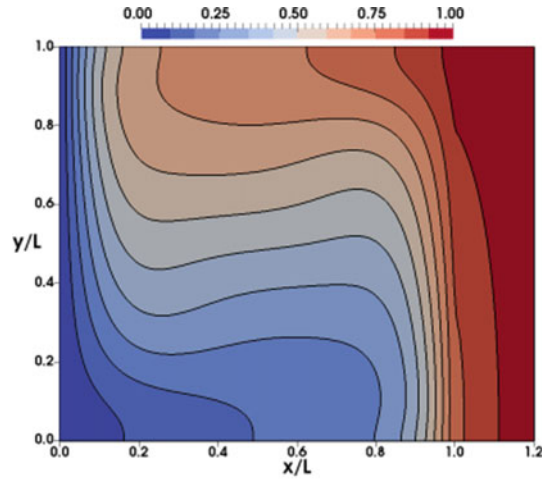
(a) Isotherms
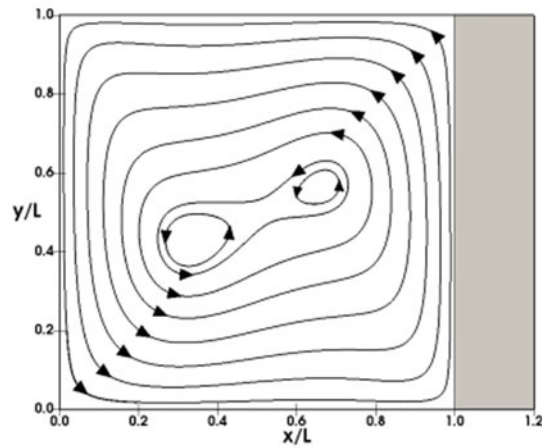
(b) Streamlines

distribution at the fluid–solid interface, which has made the flow circulation pattern asymmetric. For large w/L values and small ξ values, the Nu_{avg} was smaller than its maximum value of 4.082 observed in the isothermal boundary condition case. The proposed method accurately predicted the conjugate heat transfer effects without additional treatment at the fluid–solid interface. This work can now be extended to a 3D cubic enclosure with more than one conducting wall. Further studies must be done for higher Grashof numbers where the flow regime is unsteady and turbulent.

Nomenclature

c	Specific heat capacity
c_s	Lattice speed of sound
$\boldsymbol{e}_k$	Discrete velocity vector
$\boldsymbol{F}_{\text{ext}}$	External force term for fluid-flow
F_k	Source term for density distribution function
f_k	Density distribution function
f_k^{eq}	Equilibrium density distribution function
f_k^{neq}	Non-equilibrium density distribution function
G_{conj}	Conjugate force term
G_k	Source term for thermal distribution function
Gr	Grashof number
g_k	Thermal distribution function
g_k^{eq}	Equilibrium thermal distribution function
g_k^{neq}	Non-equilibrium thermal distribution function
Nu_{avg}	Average Nusselt number
Pe	Peclet number
Pr	Prandtl number
$\boldsymbol{q}$	Heat flux vector
St	Stokes number
T	Temperature
t	Time
$\boldsymbol{u}$	Velocity vector
w/L	Dimensionless solid wall thickness ratio
$\boldsymbol{x}$	Location vector
α	Thermal diffusivity
Γ	Time period
κ	Thermal diffusivity ratio
λ	Thermal conductivity
ν	Kinematic viscosity
ξ	Solid wall to fluid thermal conductivity ratio
ρ	Density
σ	Heat capacitance ratio
τ	Relaxation time
τ_g	Relaxation time for thermal distribution function
τ_v	Relaxation time for density distribution function
ω_k	Weighting factor

References

1. Le G, Oulaid O, Zhang J (2015) Counter-extrapolation method for conjugate interfaces in computational heat and mass transfer. Phys Rev E 91(3):033306
2. Pareschi G, Frapolli N, Chikatamarla SS, Karlin IV (2016) Conjugate heat transfer with the entropic lattice Boltzmann method. Phys Rev E 94(1):013305
3. Wang J, Wang M, Li Z (2007) A lattice Boltzmann algorithm for fluid–solid conjugate heat transfer. Int J Therm Sci 46(3):228–234
4. Meng F, Wang M, Li Z (2008) Lattice Boltzmann simulations of conjugate heat transfer in high-frequency oscillating flows. Int J Heat Fluid Flow 29(4):1203–1210
5. Chai Z, Zhao TS (2013) Lattice Boltzmann model for the convection-diffusion equation. Phys Rev E 87(6):063309
6. Karani H, Huber C (2015) Lattice Boltzmann formulation for conjugate heat transfer in heterogeneous media. Phys Rev E 91(2):023304
7. Mohamad AA (2011) Lattice Boltzmann method. Springer, London
8. Bardow A, Karlin IV, Gusev AA (2006) General characteristic-based algorithm for off-lattice Boltzmann simulations. Europhys Lett 75(3):434
9. Polasanapalli SR, Anupindi K (2022) Large-eddy simulation of turbulent natural convection in a cylindrical cavity using an off-lattice Boltzmann method. Phys Fluids 34(3):035125
10. Guo Z, Zheng C, Shi B (2002) Discrete lattice effects on the forcing term in the lattice Boltzmann method. Phys Rev E 65(4):046308
11. Li L, Chen C, Mei R, Klausner JF (2014) Conjugate heat and mass transfer in the lattice Boltzmann equation method. Phys Rev E 89(4):043308
12. Kaminski DA, Prakash C (1986) Conjugate natural convection in a square enclosure: effect of conduction in one of the vertical walls. Int J Heat Mass Transf 29(12):1979–1988

Sensitivity Mapping of TBL Wall-Pressure Spectra with CFD Turbulence Models for Wind Tunnel Test Result Prediction

Biplab Ranjan Adhikary, Ananya Majumdar, Subhadeep Sarkar, and Partha Bhattacharya

1 Introduction

Turbulent boundary layer (TBL) wall-pressure fluctuation is one of the key parameters for vibro-acoustic response prediction of TBL-excited flexible panels, mostly in aircraft, automobile, and marine industries. There are several semi-empirical single-point wall-pressure spectrum models [1–6] available and widely used for practical purposes. However, these models are essentially dependent on the feeding of the experimental data. Now, as the experiments are quite expensive, time- and resource-consuming, there are intense searches for alternate methods to the experimentations. With the increasing computing capacity, CFD simulations have emerged to fill the gap. Although direct numerical simulation (DNS) and large eddy simulation (LES) are proven to be robust and more accurate, considering the computation cost RANS techniques [7] is most commonly used for industrial purposes nowadays.

However, all the RANS models do not provide a similar level of accuracy for predicting TBL parameters. Their accuracy changes from case to case. A change in y^+ values or even a change in the solver alters the accuracy. Moreover, only the universal velocity plot $\left(y^+ \text{ vs } U^+\right)$ cannot be the determining factor for the prediction of the wall-pressure fluctuations. On the other hand, due to the differences in the method of their development, wall-spectrum models are differently sensitive to the TBL parameters. Therefore, extensive research work is required to (a) identify the best spectrum model to predict wind tunnel results, (b) quantify the accuracy of different solvers, CFD models, and y^+ values in comparison with the experimental results, (c) proper sensitivity mapping of the spectrum models with used CFD utilities.

B. R. Adhikary (✉) · A. Majumdar · P. Bhattacharya
Department of Civil Engineering, Jadavpur University, Kolkata 700032, India
e-mail: bradhikary.civil.rs@jadavpuruniversity.in

S. Sarkar
Department of Civil Engineering, IIEST Shibpur, Howrah 711103, India

The present study will definitely serve as comprehensive documentation for future researchers in the said domain.

2 Literature Review and Objective

In one of the latest works, Thomson and Rocha [8] compared different wind tunnel and in-flight test results with available semi-empirical spectrum models for zero pressure gradient cases. They have found Goody [1] and Smol'yakov [2] models to be the best predictor of the wind tunnel test results. Leneveu et al. [9] performed both wind tunnel test and CFD simulation using OpenFOAM solver. Dominique et al. [10] used an artificial neural network (ANN) that is trained with existing experimental and CFD results and predicts better spectrum formulation, especially for the adverse pressure gradients.

However, an attempt to map the best predicting spectrum models for wind tunnel test data with the in-house simulated CFD models with possible variants is not in existence. Therefore, in the present work, a careful study is carried out involving (a) identification of the best predicting single-point wall-pressure spectrum model concerning wind tunnel experiment, (b) quantification of accuracy of OpenFOAM and Fluent (V14.5) solvers, different CFD-RANS models with varying y^+ values, and (c) mapping the sensitivity of the spectrum models with varied CFD simulation and utility.

3 Methodology

First, wall-pressure spectra are calculated using several semi-empirical models with experimental TBL parameters. Out of them, Goody and Smol'yakov models are found to be the best predictor of the wind tunnel test results (Fig. 1), which is in good agreement with the findings of Thomson and Rocha [8]. Therefore, mathematical descriptions of TBL pressure spectra proposed by Goody [1] and Smol'yakov [2] are provided in the following equations.

Goody Model

$$\Phi_P = \frac{3(\omega\tau_\omega)^2\left(\frac{\delta}{U}\right)^3}{\left(\left(\frac{\omega\delta}{U}\right)^{0.75} + 0.5\right)^{3.7} + \left(1.1R_T^{-0.57}\frac{\omega\delta}{U}\right)^7}, \tag{1}$$

where

$$R_T = 0.11\left(\frac{U_e\theta}{\nu}\right)^{3/4}. \tag{2}$$

Fig. 1 Comparison of wall-spectrum models with Goody-Simpson experiment [10]. Ref. 4×10^{-10} Pa^2
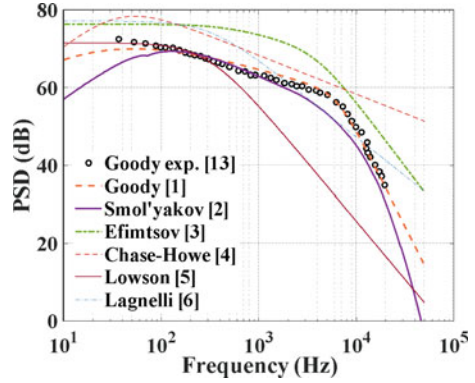
Smol'yakov Model

$$\Phi_P = \frac{1.49}{u_\tau^2} 10^{-5} \tau_\omega^2 \nu \mathrm{Re}_\theta^{2.74} \underline{f}^2 \left(1 - 0.117 \mathrm{Re}_\theta^{0.44} \underline{f}^{\frac{1}{2}}\right) \tag{3}$$

for $\underline{f} > \underline{f}_0$

$$= \frac{2.75 \tau_\omega^2 \nu}{u_\tau^2 \underline{f}^{-1.11}} \left(1 - 0.82 e^{-0.51\left(\frac{f}{f_0} - 1\right)}\right) \tag{4}$$

for $\underline{f}_0 < \underline{f} < 0.2$

$$= \frac{\tau_\omega^2 \nu [38.9 e^{-8.35\underline{f}} + 18.6 e^{-3.58\underline{f}} + 0.31 e^{-2.14\underline{f}}}{1 - 0.82 e^{-0.51\left(\frac{f}{f_0} - 1\right)}} \tag{5}$$

for $\underline{f} > 0.2$ where

$$\underline{f} = \frac{2\pi f \nu}{U_\tau^2}; \underline{f}_0 = 49.35 \mathrm{Re}_\theta^{-0.88}. \tag{6}$$

Other spectrum models used in this work are detailed in [3–6].

Next, a flat plate TBL wind tunnel experiment conducted by Leneveu et al. [9] is simulated using *four* RANS turbulence models [7]:

(i) Standard $k - \omega$ (ii) $k - \omega$ SST.
(iii) $k - \epsilon$ (iv) Realizable $k - \epsilon$

Mesh sensitivity studies for the flat plate boundary layer case [9] are first performed separately for OpenFOAM and Fluent solvers for different RANS models. Next, these two solvers are employed to simulate the flow field and extract the TBL parameters in alignment with the experiment at two different locations (point 1:

1495 mm and point 2: 1595 mm downstream of the domain inlet) and two different wind speeds (30 and 50 m/s). Then, different CFD models with different y^+ values are compared with experimental results both at the component level ($U_\tau, \delta, \delta^*, \theta$) and pressure spectrum level (Φ_P). Finally, sensitivity mapping is performed between a particular spectrum model and a particular CFD setup and presented.

4 Results and Discussion

This section contains *three* subsections:

(4.1) Comparison of single-point wall-pressure spectrum models with wind tunnel experimental PSD result.
(4.2) Mesh sensitivity study of CFD models.
(4.3) Accuracy analysis of different solvers, RANS models, and y^+ values. Sensitivity mapping.

4.1 Comparison of Spectrum Models with Wind Tunnel PSD

Several semi-empirical spectrum models are compared with PSD values from wind tunnel experiments conducted by Goody and Simpson [10] and presented in Fig. 1. The experimental spectrum is single-sided, for a two-dimensional ZPG flow [8]. They used naturally developed turbulent boundary layers to study wall-pressure fluctuations.

4.2 CFD: Mesh Sensitivity Study

Three types of meshing with uniform rectangular cells are studied for both Open-FOAM and Fluent solvers and presented in Table 1. The representative cell length (h) is calculated as $h = \frac{1}{N} \sum_{\text{cell}} A_p^{1/2}$, where N is the number of cells and A_p is the area of each cell.

The present meshing satisfies the recommendations of Celik et al. [11] that the representative cell lengths should be at least 30% different for each mesh. The mesh sensitivity study is performed by referencing the friction velocity value obtained

Table 1 Three different 2D meshes

Mesh	Number of cells	Representative cell length (h) [m]
Coarse	60,000	0.0029
Medium	120,000	0.0021
Fine	240,000	0.0015

Fig. 2 Mesh sensitivity study; point 1; OpenFOAM
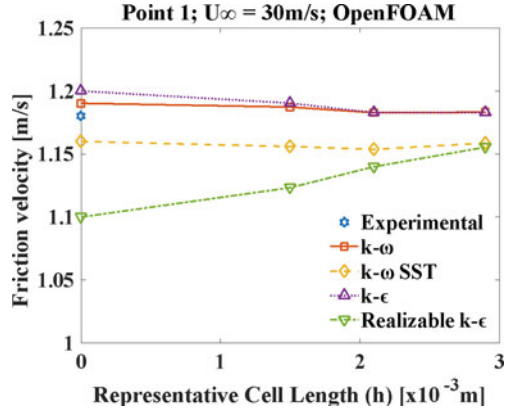
Fig. 3 Mesh sensitivity study; point 1; Ansys Fluent
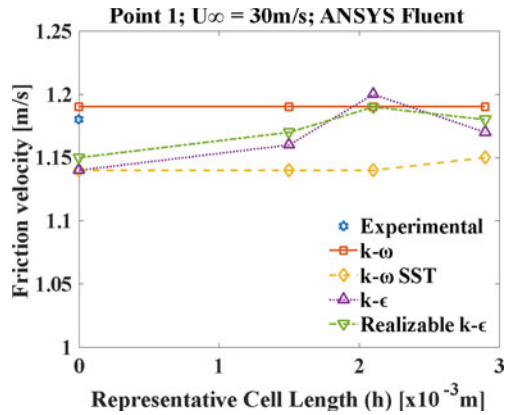
from the experiment conducted by Leneveu et al. [9] and presented in Figs. 2, 3, 4 and 5.

The most ideal mesh is having an infinite number of cells, corresponding to a representative cell length (RCL) (h) of *zero*. On designating fine, medium, and coarse mesh as 1, 2, and 3, respectively, friction velocity at $h = 0$ can be expressed as

$$U_{\tau 0} = \frac{r_{21}^p U_{\tau 1} - U_{\tau 2}}{r_{21}^p - 1}, \qquad (7)$$

where refinement ratio, $r_{21} = \frac{h_2}{h_1}$, and p is the order of convergence. The order of convergence p is estimated using the method proposed by Celik et al. [11] as it is a more general approach suitable for both monotonic and oscillatory convergence. In the beginning, differences in calculated friction velocities are determined for the fine mesh-medium mesh (ϵ_{21}), and the medium mesh-coarse mesh (ϵ_{32}) as

Fig. 4 Mesh sensitivity
study; point 2; OpenFOAM
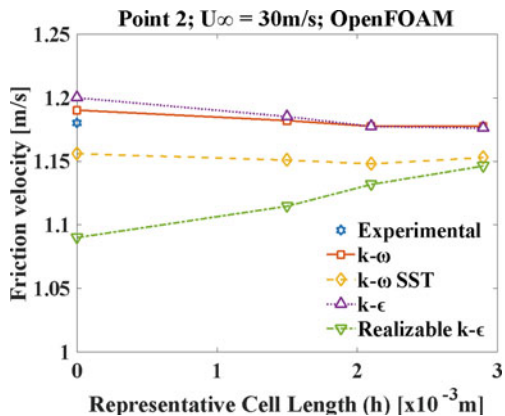
Fig. 5 Mesh sensitivity
study; point 2; Ansys Fluent
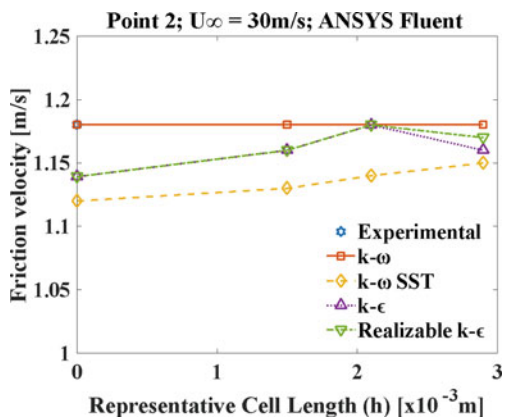
$$\epsilon_{21} = U_{\tau 2} - U_{\tau 1}; \epsilon_{32} = U_{\tau 3} - U_{\tau 2}. \tag{8}$$

Next, their ratio is calculated to find $s = \text{sign}\left(\frac{\epsilon_{32}}{\epsilon_{21}}\right)$.
The final form of the implicit nonlinear equation is

$$\frac{1}{\ln(r_{21})}\left|\ln\left|\frac{\epsilon_{32}}{\epsilon_{31}}\right| + \ln\left(\frac{r_{21}^p - s}{r_{32}^p - s}\right)\right| - p = 0. \tag{9}$$

This equation is solved using the Newton–Raphson iteration technique in MS
Excel.

In the present mesh sensitivity study, *three* types of errors are estimated for
each case, namely relative error (e_{21}), extrapolated relative error $\left(e_{21}^{\text{ext}}\right)$, and Grid
Convergence Index (GCI_{21}).

$$e_{21} = \left| \frac{U_{\tau 2} - U_{\tau 1}}{U_{\tau 1}} \right|; \quad e_{21}^{\text{ext}} = \left| \frac{U_{\tau 1} - U_{\tau 0}}{U_{\tau 0}} \right|; \quad \text{GCI}_{21} = \left| \frac{e_{21}}{r_{21}^p - 1} \right|. \tag{10}$$

Only *four* of them are presented in Tables 2, 3, 4 and 5 as representative results. Detailed studies are presented in Figs. 2, 3, 4 and 5.

As observed from the mesh sensitivity studies, it is found that the 'medium' mesh is sufficient for the subsequent studies, and thus the accuracy analysis of different CFD variants is conducted with this meshing. Different solvers (OpenFOAM, Fluent), turbulence models ($k - \omega$, $k - \omega$ SST, $k - \epsilon$ and Realizable $k - \epsilon$), and y^+ values (1, 30, and 100) are examined with the experimental values (U_τ, δ, δ^*, θ) obtained [8].

Table 2 Point 1; $k - \omega$ SST; OpenFOAM; $U_\infty = 30$ m/s

RCL (h) [m]	U_τ [m/s]	$U_\tau \text{ext} r$ [m/s]	e_{21} [%]	e_{21}^{ext} [%]	GCI$_{21}$ [%]
0.0015	1.156	1.159	0.19	0.29	0.36
0.0021	1.154				
0.0029	1.159				

Table 3 Point 1; $k - \omega$ SST; Fluent; $U_\infty = 30$ m/s

RCL (h) [m]	U_τ [m/s]	$U_\tau \text{ext} r$ [m/s]	e_{21} [%]	e_{21}^{ext} [%]	GCI$_{21}$ [%]
0.0015	1.140	1.140	0.00	0.00	0.00
0.0021	1.140				
0.0029	1.150				

Table 4 Point 2; $k - \omega$ SST; OpenFOAM; $U_\infty = 30$ m/s

RCL (h) [m]	U_τ [m/s]	$U_\tau \text{ext} r$ [m/s]	e_{21} [%]	e_{21}^{ext} [%]	GCI$_{21}$ [%]
0.0015	1.151	1.156	0.22	0.48	0.60
0.0021	1.148				
0.0029	1.153				

Table 5 Point 2; $k - \omega$ SST; Fluent; $U_\infty = 30$ m/s

RCL (h) [m]	U_τ [m/s]	$U_\tau \text{ext} r$ [m/s]	e_{21} [%]	e_{21}^{ext} [%]	GCI$_{21}$ [%]
0.0015	1.130	1.120	0.88	0.93	1.15
0.0021	1.140				
0.0029	1.150				

4.3   CFD Simulation; Part 1: Clustering and Convergence

The mathematical formulation of the RANS models can be found in reference [7]. Here, the formulation for the normalized wall distance and the numerical technique used to estimate δ^* and θ from the CFD-obtained velocity profiles.

Normalized wall distance:

$$y^+ = \frac{y_p U_\tau}{\nu}, \tag{11}$$

where y_p is the distance of the centroid of the first cell adjacent to the wall.

Displacement thickness (δ^*) and momentum thickness:

$$\delta^* = \sum_{i=2}^{N-1} \left(1 - \frac{u_i}{U_0}\right)\left(\frac{y_{i+1} - y_{i-1}}{2}\right), \tag{12}$$

$$\theta = \sum_{i=2}^{N-1} \frac{u_i}{U_0}\left(1 - \frac{u_i}{U_0}\right)\left(\frac{y_{i+1} - y_{i-1}}{2}\right). \tag{13}$$

To simulate TBL parameters properly, clustering near-wall is performed. For different y^+ values, the first cell height ($2\, y_p$) is initially calculated as per Eq. 12 and is presented in Tables 6 and 7. Bias Factor (BF) is the ratio of last cell height to the first cell height. Convergence is shown for realizable k-ε model with y^+ 30 in Fig. 6. Figures 7 and 8 depict universal velocity plots.

Table 6 y^+ calculation for $U_\infty = 30$ m/s

y^+	U_τ [m/s]	ν [10^{-5} m^2/s]	$2\, y_p$ [10^{-5} m]	BF
1	1.18	1.46	2.47	284.3
30			74.5	2.6
100			247	1

Table 7 y^+ calculation for $U_\infty = 50$ m/s.

y^+	U_τ [m/s]	ν [10^{-5} m^2/s]	$2\, y_p$ [10^{-5} m]	BF
1	1.89	1.46	1.55	496.29
30			46.5	5.64
100			155	1
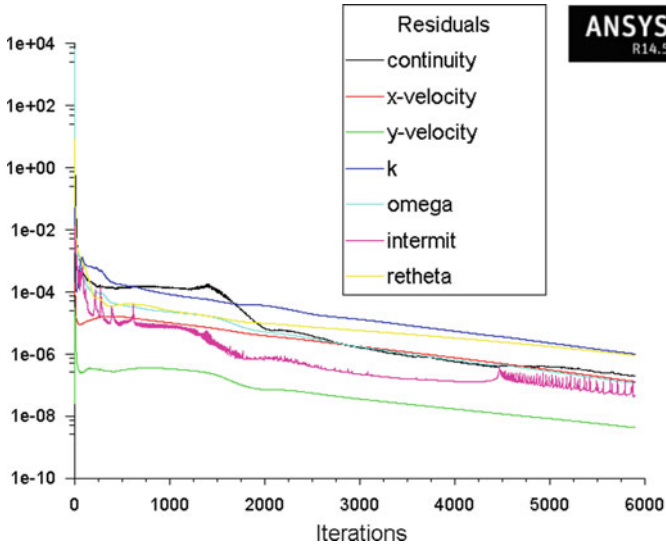
Fig. 6 Convergence; $U_\infty = 30$ m/s; $y^+ = 30$; Ansys Fluent
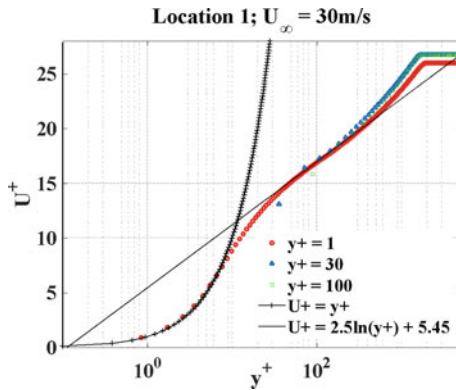
Fig. 7 Universal velocity plot; location 1; Ansys Fluent

4.4 CFD Simulation; Part 2: Component Error Analysis

Here, the accuracy of the turbulence models with various y^+ is analyzed in terms of estimating TBL components and presented in Figs. 9, 10, 11 and 12 with the following indices:
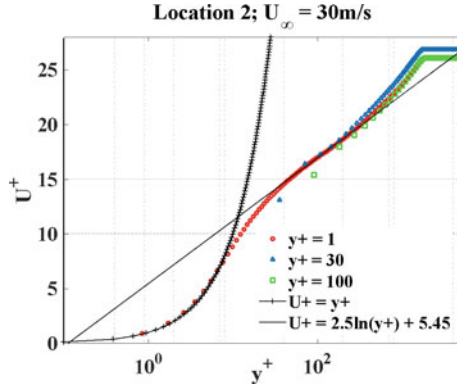
Fig. 8 Universal velocity plot; location 2; Ansys Fluent
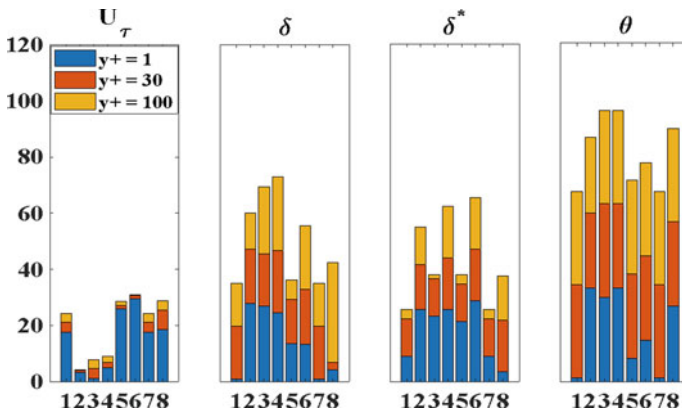
Fig. 9 Component error (%); $U_\infty = 30$ m/s; point 1

Index	Meaning	Index	Meaning
1	$k - \omega$ (fluent)	2	$k - \omega$ (OpenFOAM)
3	$k - \epsilon$ (fluent)	4	$k - \epsilon$ (OpenFOAM)
5	$k - \omega$ SST (fluent)	6	$k - \omega$ SST (OpenFOAM)
7	Realizable $k - \epsilon$ (fluent)	8	Realizable $k - \epsilon$ (OpenFOAM)
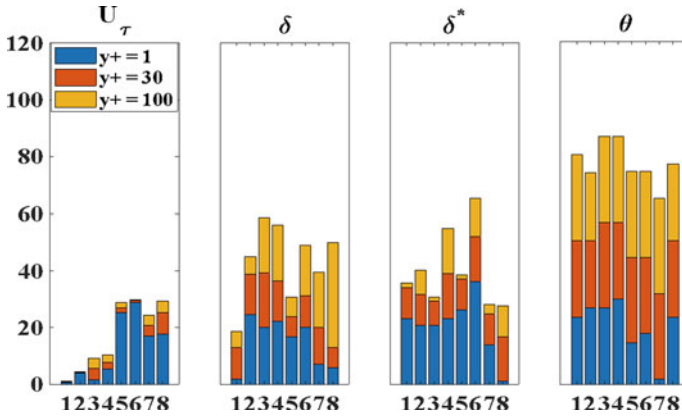
Fig. 10 Component error (%); $U_\infty = 30$ m/s; point 2
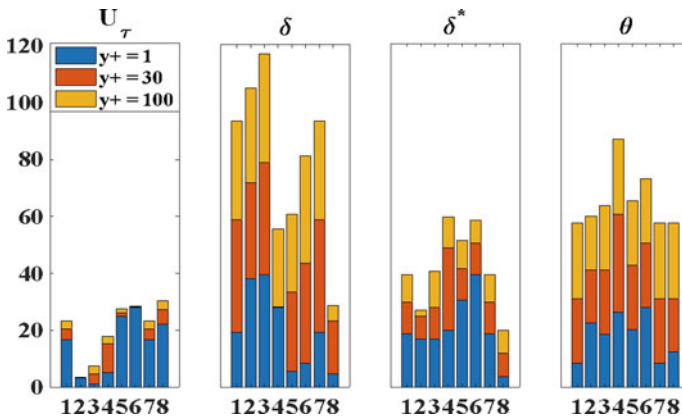
Fig. 11 Component error (%); $U_\infty = 50$ m/s; point 1

4.5 CFD Simulation; Part 3: $\underline{p}^2$ Error Analysis

Here, at first, the single-sided wall-pressure spectra (Φ_p) are calculated using Goody and Smol'yakov models for the CFD-obtained TBL parameters. Next, one can sum the spectrum over its collapsing frequency (50 kHz for the present case) as per Eq. 14 and estimate the mean square of pressure fluctuations $(\overline{p}^2)$ and compare them with the experimental $\overline{p}^2$ values.

$$\overline{p}^2 = \int\limits_{0}^{\infty} \Phi_p(f)\mathrm{d}f. \tag{14}$$
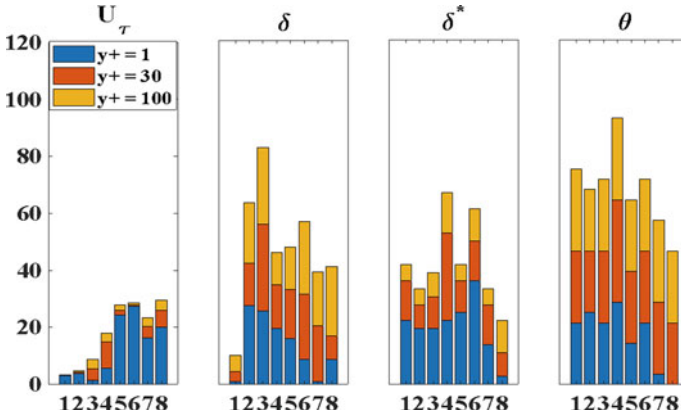
Fig. 12 Component error (%); $U_\infty = 50$ m/s; point 2

This is a practical approach as it accounts for the global energy over the entire frequency range and not the local pressure PSD values.

TBL pressure PSD using the Goody model can be estimated using Fluent solver ($k - \omega$ turbulence model with y^+ 100) even with close to 0% error. OpenFOAM is able to predict the same with a reasonable 4.99% error, but for a lower speed. With the increase in flow velocity, the accuracy of both the Fluent and OpenFOAM solvers is observed to be decreasing (Table 8).

In the case of Smol'yakov model with a higher flow speed both the Fluent and OpenFOAM solvers achieve better accuracy. With higher flow speed the $y^+ = 30$ and $y^+ = 100$ are found to be consistently better predictors (Table 9). Here also,

Table 8 Error analysis of $\overline{p}^2$ in %; Goody model; point 1

Model	y^+	30 m/s		50 m/s	
		OpenFOAM	Fluent	OpenFOAM	Fluent
$k - \omega$	1	− 23.59	**1.69**	− 28.42	**4.43**
	30	**− 5.61**	**0.75**	**− 15.15**	**− 2.58**
	100	**− 4.99**	**0.16**	**− 15.62**	**− 3.48**
$k - \omega$ SST	1	− 27.05	− 16.27	− 29.3	− 22.71
	30	− 16.28	− 21.03	47.69	− 29.4
	100	− 19.05	− 20.98	− 20.52	− 27.01
$k - \epsilon$	1	192.95	161.92	159.64	138.37
	30	− 4.52	− 11.66	− 15.93	− 16.51
	100	− 9.28	− 9.34	− 18.32	− 17.05
Realizable $k - \epsilon$	1	100.04	91.00	118.06	70.66
	30	− 25.84	− 21.03	− 25.38	− 29.75
	100	**− 3.49**	− 18.77	− 10.58	− 25.34

Table 9 Error analysis of $\overline{p}^2$ in %; Smol'yakov model; point 1

Model	y^+	30 m/s		50 m/s	
		OpenFOAM	Fluent	OpenFOAM	Fluent
$k - \omega$	1	− 26.08	**− 9.76**	− 19.67	**5.26**
	30	**− 8.86**	− 10.51	− 7.02	**− 6.73**
	100	− 11.89	− 12.23	**− 7.02**	**− 6.73**
$k - \omega$ SST	1	− 31.13	− 17.66	− 27.82	− 10.87
	30	− 19.20	− 26.08	25.53	− 21.40
	100	− 23.45	− 26.08	− 19.45	− 17.90
$k - \epsilon$	1	195.61	156.71	187.59	155.46
	30	− 10.51	− 16.38	− 8.67	− 12.45
	100	− 15.14	− 20.75	− 10.57	− 14.30
Realizable $k - \epsilon$	1	74.59	89.39	129.77	90.91
	30	− 34.66	− 26.08	− 25.11	− 21.40
	100	− 26.08	− 26.08	− 21.18	− 19.45

$k - \omega$ model turns out to be with better accuracy than the other models. In Tables 8 and 9 bolds indicate best possible accuracy out of all the tested combinations.

5 Conclusions

The conclusions of the present research work are as follows:

(a) Wind tunnel experimental results for ZPG flat plate TBL cases are best predicted by Goody and Smol'yakov single-point pressure spectrum models.
(b) All the comments on CFD turbulence models are restricted to flat plate cases with a velocity range of 30–50 m/s, typical for wind tunnel experiments.
(c) Goody and Smol'yakov models are mapped with the specific CFD-RANS model utilities that one can adopt in the future. The mapping is done through TBL parameters, which alters the sensitivity of any model. As the TBL parameters are coupled in the semi-empirical equations, it is only possible to predict the final error in $\overline{p}^2$ with extensive CFD analysis.
(d) Even with significant errors in component (TBL parameters) level, one can expect a very good accuracy in the final overall prediction in the wall-pressure fluctuations.

Model/solver	y^+	Error (%)				
		U_τ	δ	δ^*	θ	$\overline{p}^2$
$k - \omega$ fluent	30	$- 0.68$	$- 2.67$	$- 0.99$	$- 33.1$	0.16
$k - \omega$ OpenFOAM	30	0.23	$- 12.83$	$- 13.4$	$- 26.8$	3.48

(e) In general, 30 and 100 are found to be the most suited value for y^+ in terms of p^2 prediction accuracy.

(f) $k - \epsilon$ family of models cannot be relied upon, especially $y^+ = 1$ MUST be avoided, even though the $y^+ = 1$ exhibits the best-normalized velocity prediction in universal y^+ vs U^+ plots.

Nomenclature

Φ_p Wall-pressure PSD [Pa^2/Hz]
$\underline{p}^2$ Mean square pressure [Pa^2]
$\overline{U_\tau}$ Friction velocity [m^2/s]
δ Boundary layer thickness [m]
δ^* Displacement thickness [m]
θ Momentum thickness [m]
ρ Density of air [kg/m^3]
y^+ Normalized wall-normal distance
U^+ Normalized velocity
ω Radial frequency [Rad/s]
f Cyclic frequency [Hz]

References

1. Goody M (2004) Empirical spectral model of surface pressure fluctuations. AIAA J 42(9):1788–1794
2. Smol'yakov A (2000) Calculation of the spectra of pseudo-sound wall pressure fluctuations in turbulent boundary layers. Acoust Phys 46:342–347
3. Efimtsov BM (1984) Similarity criteria for the spectra of wall pressure fluctuations in a turbulent boundary layer. Akusticheskii Zhurnal 30:58–61
4. Howe MS (1998) Acoustics of fluid-structure interactions. Cambridge University Press, Cambridge, UK
5. Lowson M (1968) Prediction of boundary layer pressure fluctuations. Wyle Laboratories. Wright-Patterson Air Force Base
6. Lagnelli A, Wolfe H (1993) Prediction of fluctuating pressure in attached and separated turbulent boundary-layer flow. J Aircraft 30(6):962–970
7. ANSYS Inc. (2015) ANSYS fluent theory guide 12.0

8. Thomson N, Rocha J (2021) Comparison of semi-empirical single point wall pressure spectrum models with experimental data, fluids
9. Leneveu R, Rissmann M, Alonso Pinar A (2019) Validation with experimental data of a heterogeneous turbulent wall pressure fluctuation model in a FEM structural context, aeroacoustics conferences. In: 25th AIAA/CEAS aeroacoustics conference, 20–23 May 2019, Delft, The Netherlands
10. Goody MC, Simpson L (2000) Surface pressure fluctuations beneath two and three dimensional turbulent boundary layers. AIAA J 38
11. Celik IB, Ghia U, Roache PJ, Freitas CJ (2008) Procedure for estimation and reporting of uncertainty due to discretization in CFD applications. J Fluids Eng Trans ASME

Numerical Predictions of Two-Phase Natural Circulation Loop Transients Using DFM- and HEM-Based Models

K. N. V. Adinarayana, P. Mangarjuna Rao, and Seik Mansoor Ali

1 Introduction

The concept of two-phase natural circulation loops (NCL) finds numerous conventional and non-conventional industrial applications due to its passive nature, less cost, and fewer moving parts. The natural circulation loop is a vertical system consisting of a cooler and heater, and the flow generates due to hydrostatic pressure difference due to differential heating. The dynamics of these systems are quite complex due to their regenerative feedback. These instabilities are undesirable as they can affect heat transfer, mechanical vibration, boiling crisis, etc. The dynamics of two-phase NCLs depend on many factors such as power, diameter, loop height, etc.

Several theoretical and experimental studies on two-phase NCL are reported in the literature. Both transient and steady state behavior of the loops has been studied. Numerically, various modeling methods are used in two-phase NCLs modeling; Homogeneous Equilibrium Mixture Model (HEM), Drift Flux Model (DFM), and Two Fluid Model (TFM). Most studies on two-phase NCLs in literature are based on the HEM approach. HEM treats both phases as a mixture with the same velocity and temperature at each cross section. In the recent past, various two-phase NCL studies based on HEM have been reported [1]. However, such good mixing conditions are possible only in a bubbly flow regime.

K. N. V. Adinarayana · P. M. Rao (✉)
Homi Bhabha National Institute (HBNI), Training School Complex, Anushaktinagar, Mumbai 400094, India
e-mail: pmr@igcar.gov.in

K. N. V. Adinarayana · S. M. Ali
Atomic Energy Regulatory Board (AERB), Safety Research Institute, Kalpakkam, Tamil Nadu, India

P. M. Rao
Indira Gandhi Centre for Atomic Research (IGCAR), Kalpakkam, Tamil Nadu, India

However, in two-phase flow, there is always a velocity difference between vapor and liquid that varies with the flow regime. Bennett et al. [2] are the first to generate flow regime maps for two-phase flow. Further, Mishima and Ishii [3] developed a flow regime map for the air–water system. Taitel et al. [4] have theoretically studied two-phase flow regimes. The DFM model is comparatively more complex than HEM and can take the phase velocity differences in drift velocities. Zuber and Findlay [5] are the first to develop DFM-based two-phase model. Subsequently, different correlations for drift velocity and distribution parameters based on flow regimes are numerically studied by Hibiki and Ishii [6]. In the literature, very few studies are reported comparing DFM and HEM models. Rao et al. [7] have studied the steady state behavior of two-phase NCLs using both the HEM and DFM models. Dewangan and Das [1] have studied two-phase flashing at a steady state using these models. Most of the reported studies are conducted under steady state conditions. Therefore, the dynamics of two-phase NCL are investigated in the present study using DFM and HEM models.

In this connection, the authors have already developed a HEM-based two-phase NCL model in their previous studies [8]. The present paper develops a two-phase NCL model based on DFM, further enhancing the HEM model. The governing differential equations are solved using the finite volume method (FVM). Flashing phenomena, fluid and wall conduction, heat loss to ambient, etc., are considered in the model. Instead of using Boussinesq approximation for density variation, a more accurate water-steam properties program is adopted. The fluid properties such as density, viscosity, etc., are calculated based on local pressure and temperature using a water-steam properties program [9]. The models are validated against experimental NCL loops available in the literature. The validated DFM and HEM models are used to investigate the start-up transients of two-phase NCL, single-phase, transition, and two-phase flow. The flow patterns for the two-phase NCLs have been identified based on flow regime maps. Subsequently, a comparison of predictions from HEM and DFM is also carried out. The effects of input power, diameter, and loop height on two-phase NCLs are investigated and discussed to determine these variables' influence. Finally, the details of the models and outcomes from this study are presented and discussed.

2 DFM and HEM Models

The two-phase NCL models are developed based on DFM and HEM with the following assumptions.

- The flow is one-dimensional, and the fluid properties only vary in the axial direction.
- Wall conduction and axial conduction of the fluid are considered.

- Heat transfer (gain/loss) at any location along the loop is considered.
- Heat generation in the working fluid due to the frictional dissipation effect is neglected.

2.1 Governing Equations

The governing equations are written for a non-uniform diameter loop and assuming the coordinate 's' run along the loop. The mass, momentum, and energy equations based on the DFM model are given in Eqs. (1), (2), and (3) [10]. The governing equations for HEM are given in our previous works [8] and are not reproduced here.

$$\frac{\partial \rho_m}{\partial t} + \frac{\partial}{\partial s}(\rho_m u_m) = 0, \tag{1}$$

$$\frac{\partial(\rho_m u_m)}{\partial t} + \frac{\partial}{\partial s}(\rho_m u_m u_m) + \frac{\partial}{\partial s}\left[\frac{(\rho_f - \rho_g)\rho_g \rho_f}{\rho_m(\rho_m - \rho_g)}\overline{V}_{gj}^2\right]$$
$$= -\frac{\partial P_m}{\partial s} - \rho_m g \sin\theta - \frac{f_m}{2d_{in}}(\rho_m u_m^2) - \frac{K}{2L_s}(\rho_m u_m^2), \tag{2}$$

$$\frac{\partial(\rho_m h_m)}{\partial t} + \frac{\partial}{\partial s}(\rho_m h_m u_m) + \frac{\partial}{\partial s}\left[\frac{(\rho_f - \rho_m)\rho_g \rho_f}{\rho_m(\rho_f - \rho_g)}\Delta h_{fg}\overline{V}_{gj}\right] =$$
$$\frac{\xi_{in}\overline{h}_{in}(T_w - T_f)}{A_{in}} + \frac{1}{A_{in}}\frac{\partial}{\partial s}\left(A_{in}k_{f,e}\frac{\partial T_f}{\partial s}\right). \tag{3}$$

In the above equations, the two-phase mixture friction factor (f_m) is estimated by multiplying the single-phase friction factor with a two-phase friction multiplier (Eq. 4). The single-phase friction factor is calculated based on flow type (laminar, turbulent, and transition).

$$\phi_{Lo}^2 = \left[\frac{x_m \mu_f}{\mu_g} + (1 - x_m)\right]^{-b}\left[\frac{(1 - x_m)v_f + x_m v_g}{v_f}\right]. \tag{4}$$

The average drift velocity (Eq. 5) constitutive relations for various flow regimes are taken from Hibiki and Ishii [6]. The relations for drift velocities and distribution parameter are shown in Eqs. (6) and (7).

$$\overline{V}_{gj} = V_{gj} + (C_o - 1)j, \tag{5}$$

$$V_{gj} = \sqrt{2}\left[\frac{(\rho_f - \rho_g)}{\rho_f^2}g\sigma\right]^{\frac{1}{4}}(1 - \alpha_g)^{1.75}, \tag{6}$$

$$C_o = \varphi\left[1 + \left(\frac{1}{\varphi} - 1\right)^a\right] \quad a = \left[\frac{\rho_g}{\rho_f}\right]^{0.1} \quad \phi = \left[1 + \frac{\rho_g}{\rho_f}\left(\frac{1-x}{x}\right)\right]^{-1}. \quad (7)$$

The other relations for mixture density, total superficial velocity, and quality of the steam are given in Eqs. (8), (9), and (10), respectively.

$$\rho_m = \alpha_g \rho_g + (1 - \alpha_g)\rho_f, \quad (8)$$

$$j = \left[\frac{Gx}{\rho_g} + \frac{G(1-x)}{\rho_f}\right], \quad (9)$$

$$x_m = \left(\frac{h_m - h_f}{h_{fg}}\right). \quad (10)$$

The energy equation for the pipe wall is given in Eq. 11.

$$\frac{\partial}{\partial t}\left(\rho_w C_{p,w} T_w\right) - \frac{1}{A_w}\frac{\partial}{\partial s}\left(k_w A_w \frac{\partial T_w}{\partial s}\right)$$

$$= \begin{cases} \dfrac{\xi_o \dot{q}''}{A_w} - \dfrac{\xi_{in}\overline{h}_{in}(T_w - T_m)}{A_w} & \text{(Source)} \\[2ex] \dfrac{\xi_{in}\overline{h}_{in}(T_m - T_w)}{A_w} - \dfrac{\xi_o \overline{h}_\infty(T_w - T_\infty)}{A_w} & \text{(Pipes)}. \\[2ex] \dfrac{\xi_{in}\overline{h}_{in}(T_m - T_w)}{A_w} - \dfrac{\xi_o \overline{h}_{si}(T_w - T_{si})}{A_w} & \text{(Sink)} \end{cases} \quad (11)$$

The governing equations are discretized using the finite volume method (FVM) based on a staggered grid [8]. The time derivatives are discretized using an explicit scheme. An up-wind scheme is adopted for spatial derivatives.

2.2   Solution Procedure

The discretized governing equations are numerically solved simultaneously using an explicit time marching procedure. The solution method is implemented in the Fortran program. The enthalpy distributions are initially estimated using energy equations in each time step. The working fluid properties such as density, viscosity, temperature, and specific heat are evaluated using water-steam property tables. The steam quality is estimated based on local pressure and enthalpy conditions. Pressure drops due to skin friction in the loop are calculated based on the flow conditions. The friction multiplier is estimated using local quality and local saturation conditions. The drift velocity is estimated based on the available correlations (Eqs. 5–7). The mass flow rate in the loop is calculated using the discretized continuity and momentum equation.

Both time step and grid independence studies are conducted. A grid of 5 mm and a time step of 0.5×10^{-3} s have been chosen for the current study. A check for the courant number criteria is done at each time step. The transients are continued till a steady state solution is obtained.

3 Results and Discussions

The developed DFM and HEM models are employed to predict the flow behavior of three different experimental loops [11–13]. The transient two-phase flow regimes for one of the loops are predicted using available flow regime maps. Subsequently, the models are employed to predict the start-up transient of two-phase NCLs, and the relative difference between DFM and HEM is highlighted. Further, both models are employed to predict the influence of essential parameters on the dynamics of two-phase flow NCLs.

3.1 DFM and HEM Predictions Against the CIRCUS Experimental Facility

CIRCUS-IV is a thermal–hydraulic experimental facility for two-phase natural circulation loops [11]. It is located at the Delft University of Technology in the Netherlands. The total height of the facility is 4.95 m. The developed numerical models (i.e., DFM and HEM) are employed to predict the experimental flow transients of this facility. The heater input power and loop pressures are 2.5 kW and 100 kPa, respectively. The obtained mass flow rate transients are compared in Fig. 1. As shown in this figure, the trend predicted by both the models is nearly similar to experimental data. Further, the maximum flow rate spikes due to flashing are slightly higher for HEM than for DFM. However, DFM predicted the time of occurrence of flow spikes better than HEM, as shown in Fig. 1. The statistical analysis using relative root mean square (Eq. 12) against experimental data showed that DFM predictions (RRMS = 0.92) are better than HEM (RRMS = 1.05). The applicability of these models is further investigated by conducting a study on the flow regimes.

$$\text{RRMS} = \sqrt{\frac{\sum_{i=1}^{N} \left(\frac{\text{Exp}_i - \text{Model}_i}{\text{Exp}_i} \right)^2}{N}}. \tag{12}$$

Fig. 1 DFM and HEM predictions against CIRCUS
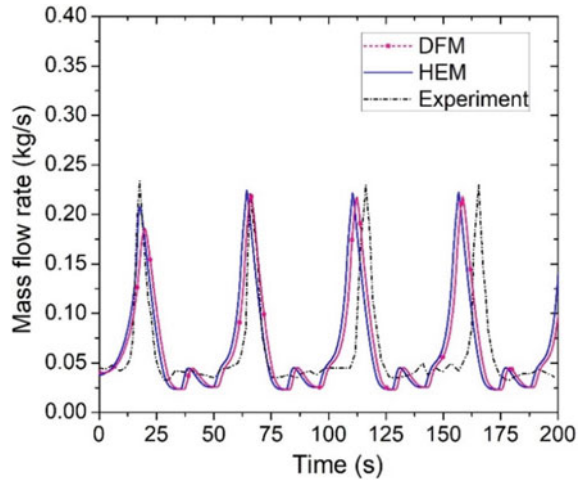
3.1.1 Flow Regimes in the Two-Phase Natural Circulation Loop

The two-phase flow regimes of the above facility (based on the flow conditions at the top of the riser) are predicted using three flow regime maps; Bennett [2], Mishima and Ishii [3], and Taitel [4]. The above flow regime maps are studied to confirm and identify the flow regime. Among these, the result of the Taitel maps is shown in Fig. 2. As shown in Fig. 2, the superficial velocities of liquid and vapor are considered ordinates in this map. This study revealed that most of the two-phase flow is in a bubbly regime. However, during the transient, the flow can be bubbly or slug. In slug flow, the assumption of a homogeneous model is not justified as there is no uniform mixing like bubbly flow. In such cases, a DFM model that can take the velocity difference between the phases may yield a better result. This could be the reason for better agreement of DFM results compared to HEM in CIRCUS experimental data.

3.2 Predictions Against HPNCL and PMCS Facilities

A high-pressure natural circulation loop (HPNCL) is a thermal–hydraulic facility with a total height of 3.34 m [12]. In this facility, the influence of pressure on two-phase flow has been studied experimentally. DFM and HEM models are used to predict the experimental data of this facility, and the results are plotted in Fig. 3, which shows the steady flow rate of HPNCL with loop pressure. This figure shows that the flow rate initially increases and decreases gradually with an increase in pressure. This can be attributed to the competing nature of fluid frictional pressure drop and gravity dominance. As shown, both DFM and HEM models are able to predict the flow and variation trend w.r.t. loop pressure. However, it is observed that the trend predicted by the DFM is closer to experimental data than HEM. In the
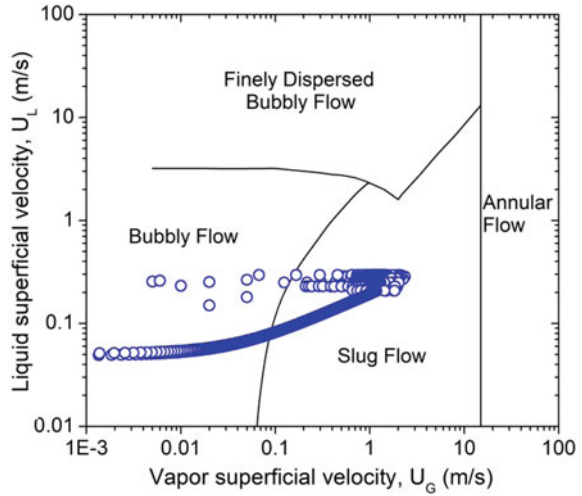
dominant gravity regime, the DFM flow predictions are higher than HEM, and in friction dominant, it is reverse. The average RRMS values for DFM and HEM are 0.08 and 0.09, respectively.

PMCS is a Passive Moderator Cooling System facility that works based on the flashing phenomenon [13]. The total height of the facility is 8.5 m. In this facility, the influence of flashing is studied at 1 atm pressure by raising the input heater power in steps of 20 kW. The mass flow transients are predicted using DFM and HEM models and compared against experimental data (Fig. 4). As shown in this figure, both models can predict the flashing phenomena quite well. It is also observed that as the heater input increases, the predictions by DFM are closer to experimental data than HEM

Fig. 3 DFM and HEM predictions against HPNCL
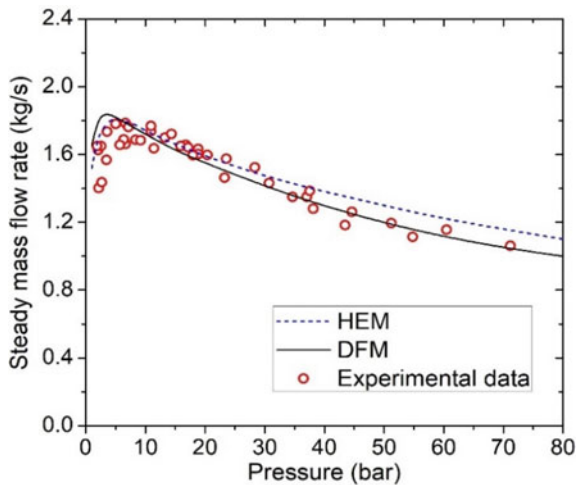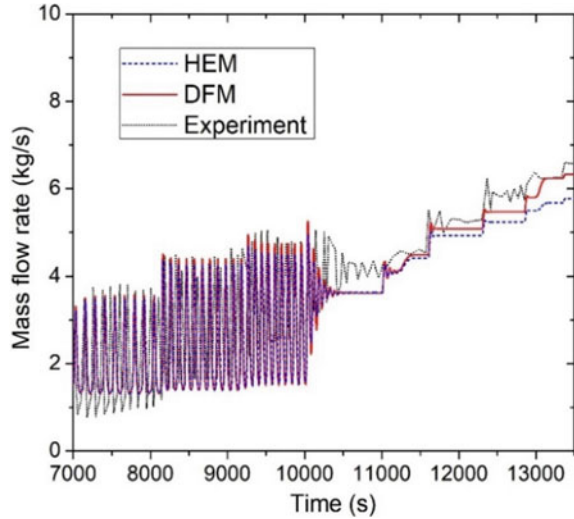
predictions. This observation suggested that DFM can predict better at higher power
than HEM. The RRMS value of DFM and HEM are 0.15 and 0.1, respectively. These
statistical comparisons indicated that DFM predictions are comparatively better than
HEM w.r.t. experimental data.

3.3 Start-Up Transients of Two-Phase NCLs

The start-up transients of two-phase NCLs are predicted using validated DFM and
HEM models. The loop configuration chosen is HPNCL [12], with a total height
of 3.64 m. The loop is at atmospheric pressure with water as a working fluid. The
heater input and initial temperatures are 30 kW and 310 K, respectively. The obtained
start-up transients using DFM and HEM models are depicted in Fig. 5. This figure
shows that both models could predict two-phase start-up transients; single-phase to
two-phase, via oscillatory transition region. As shown in the single-phase region,
both models predicted the same trend. However, the predictions are not the same
in the transition and two-phase regions. The relative deviations of DFM predictions
concerning HEM in single, transition, and two-phase regions are 0.0%, 3.6%, and
6.1%, respectively. In the transition region, 3.6% represents the average value over
the entire transition region. However, the maximum and minimum relative change
in the transition region is observed to range from (–) 20 to (+) 20%. Moreover,
depending on the two-phase flow region (gravity dominant, friction dominant, and
compensation regions), DFM may over-predict or under-predict compared to HEM
(as presented in Sect. 3.2).

Fig. 5 Start-up transients using DFM and HEM models
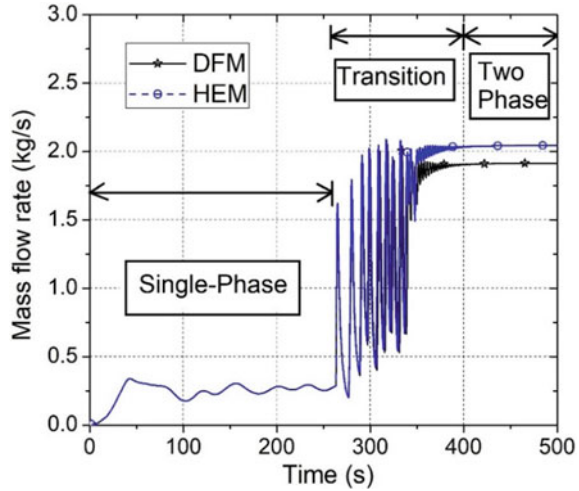
3.4 Parametric Studies Using DFM and HEM Models

The effect of a few key parameters, i.e., input power, loop diameter, and NCL height, on the start-up transients of HPNCL [12] is investigated by employing DFM and HEM models. The predictions are presented below.

3.4.1 NCL Height

The effect of NCL height is investigated for three different heights of 3.64, 3.34, and 3.04 m. The obtained flow rates are depicted in Fig. 6. In these simulations, the total volume of the loop is kept constant while changing the loop height. DFM and HEM models show that the flow rate is proportional to NCL height. The influence of loop height is observed to be higher in two-phase compared to single-phase. It is observed that the relative predictions by DFM can be higher or lower than HEM with a change in height. For 3.64 m, the DFM predictions are lower than HEM; this can be attributed to the dominant gravity region. Interestingly, for 3.04 m, DFM predictions are higher than HEM; this can be due to a change in governing dominant region from gravity to friction dominant. The relative change in steady flow rate predictions between DFM and HEM models with respect to HEM ranges from around (–) 6.34 to (+) 6.05%.

3.4.2 Loop Diameter

The loop diameter is another crucial parameter that influences the dynamics of NCLs. The predictions by DFM and HEM models for different diameters of 5.3, 4.9, and

Fig. 6 Influence of NCL height
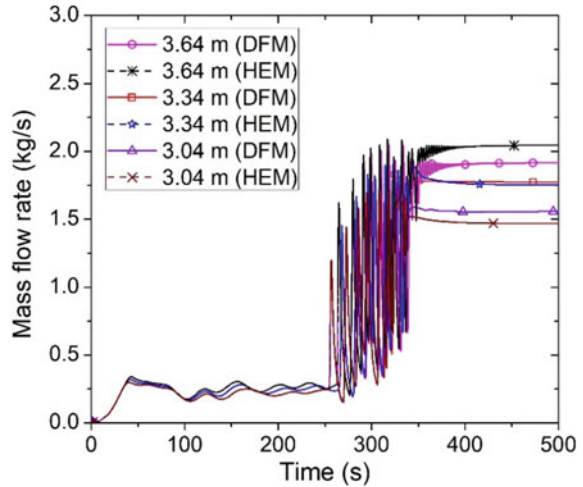
4.5 cm are plotted in Fig. 7. The flow is proportional to the loop diameter, and both models predict the same. The effect of diameter is higher in two-phase compared to single-phase. For 4.9 and 4.5 cm, the predictions of DFM are higher than HEM. Whereas for 5.3 cm, HEM is over predicting compared to DFM; this can be due to the presence of friction dominant region. The relative change in the steady flow rate of DFM with respect to HEM is observed to range from (–) 6.31 to (+) 15.51% at steady state conditions.

Fig. 7 Influence of loop diameter
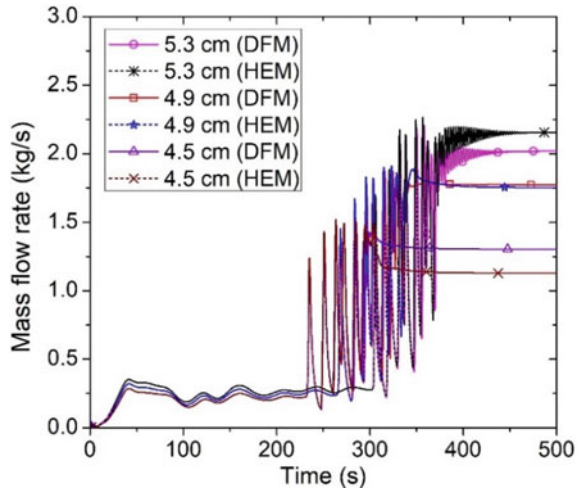
Fig. 8 Influence of input power
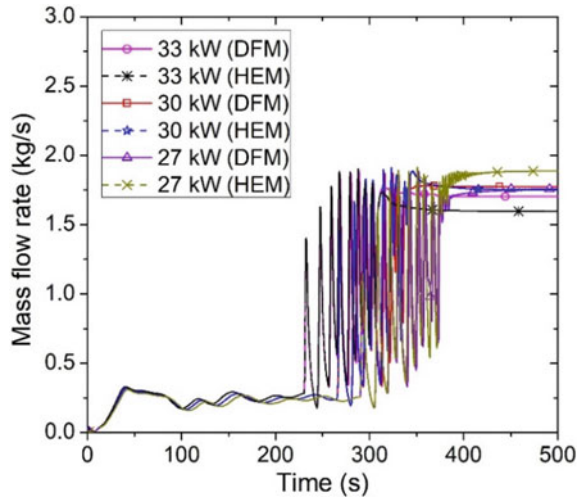
3.4.3 Input Power

The effect of input power is studied, and the results are depicted in Fig. 8. This figure shows DFM and HEM predictions for different input powers of 33, 30, and 27 kW. As shown, the influence of input power predicted by both models is similar. The flow rate is noted to decrease with an increase in input power. This can be attributed to the dominating friction region of the two-phase flow. The effect of input power predicted by DFM is comparatively higher than HEM. For higher power (33 and 30 kW), the predictions by DFM are higher than HEM. For 27 kW, the DFM predictions are lower than HEM. The relative change in steady flow rate predictions by DFM with respect to HEM ranges from (–) 7.01 to (+) 6.64%.

3.4.4 Comparison of Influence of Parameters

The effect of power, diameter, and height on steady mass flow rate employing DFM and HEM are plotted in Fig. 9. As shown, the trend predicted by both the models is same. However, the magnitude of the effect predicted by DFM is lower compared to HEM. For example, for ~ 8.1% increase in loop diameter, the mass flow rate increased by ~ 20.5% using HEM, whereas it is ~ 16.1% using DFM. This can be attributed to reduction in void fraction due to drift velocity. For the lower height and diameter, the DFM predictions are higher than HEM. At higher height and diameter DFM predictions are lower than HEM. This can be attributed to the role played by the dominant friction region and dominant gravity region.

Fig. 9 Comparison of
parametric effect on steady
flow rate
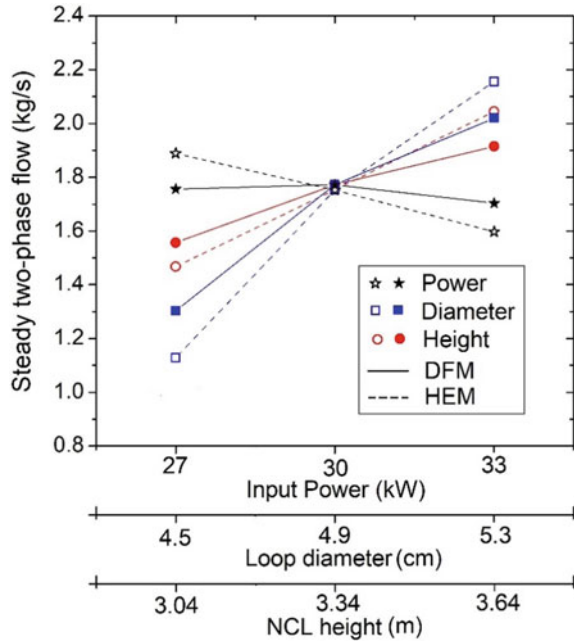
4 Conclusions

In this study, DFM- and HEM-based numerical models are developed to investigate the dynamics of two-phase NCLs. The models have features for capturing the flashing phenomenon. A water property program is used in place of the Boussinesq assumption. The key observations are listed below.

- The developed DFM and HEM models are benchmarked against three experimental loops. Results show that the models are capable of predicting two-phase NCL transients. Further, DFM predictions are relatively better than HEM.
- Flow regimes in two-phase NCL are investigated based on Mishima-Ishii, Bennett, and Taitel flow regime maps. Flow regime changes rapidly during transient phase, where the applicability of HEM is limited when beyond bubbly flow.
- DFM and HEM models could predict two-phase NCL start-up transients, in single-phase, transitions, and two-phase.
- The influence of power, diameter, and height on the dynamics of NCL is brought out using DFM and HEM models. The magnitude of effect of parameters predicted by DFM is observed to be lower than HEM.

Nomenclature

A	Area [m^2]
b	Constant [–]
C_p	Specific heat [J/kg. K]
C_o	Distribution parameter [–]
d	Diameter [m]
f	Friction factor [–]
G	Mass flux [kg/m^2 s]
$\underline{g}$	Acceleration due to gravity [m/s^2]
$\overline{h}$	Heat transfer coefficient [W/m^2 K]
h	Specific enthalpy [J/kg]
j	Superficial velocity [–]
K	Loss coefficient [–]
k	Thermal conductivity [W/m K]
L	Total length of the loop [m]
$\dot{m}$	Mass flow rate [kg/s]
P	Pressure [Pa]
$\dot{q}''$	Heat flux [W/m^2]
s	Length coordinates [m]
T	Temperature [K]
t	Time [s]
u	Velocity [m/s]
v	Specific volume [m^3/kg]
V	Drift velocity [m/s]
$\overline{V}$	Average drift velocity [m^3/kg]
x	Steam quality [–

Greek Letters

ρ	Density [kg/m^3]
μ	Viscosity [kg/m s]
θ	Angle w.r.t. horizontal axis [°]
Δ	Change in a variable [–]
ξ	Perimeter [m]
ϕ^2_{Lo}	Two-phase friction multiplier [–]
α	Void fraction [–]
σ	Surface tension [kg/s^2]

Subscript

e	Effective [–]
f	Circulating fluid [–]
g	Vapor [–]
in	Inner [–]
m	Mixture [–]
o	Outer [–]
si	Sink [–]
w	Wall [–]
∞	Atmosphere [–]

References

1. Dewangan KK, Das PK (2018) Assessing the effect of flashing on steady state behavior and Ledinegg instability of a two-phase rectangular natural circulation loop. Int J Heat and Mass Transfer 116:218–230
2. Bennett AW, Hewitt GF, Kearsey HA, Keeys RKF, Lacey PMC (1965–66) Flow visualization studies of boiling at high pressure. Proc Instn Mech Eng 180(3):260–283
3. Mishima K, Ishii M (1984) Flow regime transition criteria for upward two-phase flow in vertical tubes. Int J Heat Mass Transf 27(5):723–737
4. Taitel Y, Barnea D, Dukler AE (1980) Modelling flow pattern transitions for steady upward gas–liquid flow in vertical tubes. AIChE J 26:345–354
5. Zuber N, Findlay JA (1965) Average volumetric concentration in two-phase flow systems. J Heat Transf: 453–468
6. Hibiki T, Ishii M (2003) One-dimensional drift-flux model and constitutive equations for relative motion between phases in various two-phase flow regimes. Int J Heat Mass Transf 46:4935–4948
7. Rao NM, Chandra Sekhar C, Maiti B, Das PK (2006) Steady-state performance of a two-phase natural circulation loop. Int Commun Heat Mass Transf 33:1042–1052
8. Adinarayana KNV, Mangarjuna Rao P, Ali SM (2021) Development of numerical model for analysing transients of two-phase natural circulation loops. In: 4th international and 26th national ISHMT-ASTFE conference, 17–20 Dec 2021, IIT Madras, India
9. IAPWS (1997) Release on the IAPWS industrial formulation 1997 for the thermodynamic properties of water and steam. IAPWS Secretariat
10. Ishii M, Hibiki T (2011) Thermo-fluid dynamics of two-phase flow. Springer
11. Viet-Anh P, Kudinov P, Grishchenko D, Rohde M (2015) Input calibration and validation of RELAP5 against CIRCUS-IV single channel tests on natural circulation two-phase flow instability. Sci Technol Nucl 130741:1–14
12. Vijayan PK, Nayak AK, Saha D, Gartia MR (2008) Effect of loop diameter on the steady state and stability behaviour of single-phase and two-phase natural circulation loops. Sci Technol Nucl 672704:1–17
13. Dimmick GR, Chatoorgoon V, Khartabil HF, Duffey RB (2002) Natural-convection studies for advanced CANDU reactor concepts. Nucl Eng Des 215:27–38

Implementation of the Accurate Conservative Phase Field Method for Two-Phase Incompressible Flows in a Finite Volume Framework

Sahaj S. Jain and Danesh Tafti

1 Introduction

The development of computational fluid dynamics tools for multiphase flows has found many applications in recent times, including, but not limited to large-scale flows such as wave-energy harvesting [1–4], to flows at much smaller scales such as droplet impact on surfaces [5–7].

While many methods exist, one-fluid methods such as the Diffused Interface Method are considered in this paper. The Diffused Interface Methods involve discretizing the domain into two different phases using a phase variable ϕ, which varies smoothly but sharply over the interface. The material properties, such as viscosity and density, are then interpolated from the phase field. These methods are typically categorized either as, Level Set Methods or Phase Field Methods. While the Level Set Method involves a re-initialization step [8–10] which often results in a loss of accuracy, the Phase Field Method does not need a re-initialization step; instead, the phase convection and restoration are done at the same time. Typically, either Cahn and Hillard [11] or Allen and Cahn [12] equations are used to solve for the phase. However, both have their disadvantages. The Cahn-Hillard equation, while being mass conserving, involves solving for fourth-order terms, whereas the Allen–Cahn equation, which only has second-order terms, is not mass conserving in nature.

Chiu and Lin [13] formulated the conservative phase field based on the conservative Level Set Method [10] as follows:

S. S. Jain
Engineering Mechanics, Department of Biomedical Engineering and Mechanics, Virginia Polytechnic Institute and State University, Virginia 24060, USA

D. Tafti (✉)
Department of Mechanical Engineering, Virginia Polytechnic Institute and State University, Virginia 24060, USA
e-mail: dtafti@vt.edu

$$\frac{D\phi}{Dt} = \gamma \nabla \cdot \left(\epsilon \nabla \phi - \phi(1-\phi)\frac{\nabla \phi}{|\nabla \phi|} \right), \tag{1}$$

where $D(\cdot)/Dt$ is the material derivative, ϵ represents interface width, and γ, the re-initialization parameter is representative of the strength of the right-hand-side of Eq. (1), responsible for reinitializing and maintaining a hyperbolic tangent profile for the interface:

$$\phi = {}^{1}\!/_{2}\left(1 + \tanh\left({}^{\psi}\!/_{2\epsilon}\right)\right), \tag{2}$$

where ψ is the signed distance function varying which represents distance normal to the interface such that $\psi(\phi = 0.5) = 0$. While the knowledge of the hyperbolic tangent profile is derived from the thermodynamics of the interface, thermodynamics plays no further role in the mechanics of the advection of the phase field [13, 14]. The right-hand side, which contains a diffusion and an anti-diffusion term, for the hyperbolic tangent profile cancel each other out, ensuring that the phase is convected only by the flow.

Material properties Θ (such as density and viscosity) can be derived from ϕ as

$$\Theta(x, y, z, t) = \Theta_0 \phi(x, y, z, t) + (1 - \phi(x, y, z, t))\Theta_1, \tag{3}$$

where Θ_1 corresponds to material properties for the phase given by $\phi = 1$ and Θ_0 corresponds to material properties for the phase given by $\phi = 0$.

The Conservative Phase Field Method, which can be considered to be the one-step version of the conservative Level Set Method of Olsson and Kreiss [10], requires no pseudo time marching, has been shown to have excellent conservative [13] and boundedness properties [14], is easy to implement and has been shown to have lower computational costs than the, otherwise more accurate Volume of Fluid Method (VOF) for cases where the interface spans the entire domain [15].

However, it has been observed that the Conservative Phase Field Method introduces artificial distortions in the interface [16]. Jain [17] reformulated the anti-diffusion term in (1), using the signed distance function to introduce the *Accurate Conservative Phase Field Method (ACPF)*:

$$\frac{D\phi}{Dt} = \gamma \nabla \cdot \left(\epsilon \nabla \phi - \frac{1}{4}\left(1 - \tanh^2\left(\frac{\psi}{2\epsilon}\right)\right)\hat{\mathbf{n}} \right). \tag{4}$$

Since ψ varies linearly with the distance, as compared to the phase which has a sharp variation across the interface it becomes more convenient to calculate the normal vector field in terms of the signed distance function:

$$\hat{\mathbf{n}} = \frac{\nabla \phi}{|\nabla \phi|} = \frac{\nabla \psi}{|\nabla \psi|}. \tag{5}$$

The signed distance function can be obtained analytically from the phase:

$$\psi = \ln\left(\frac{\tilde{\phi} + \alpha}{1 - \tilde{\phi} + \alpha}\right), \tag{6}$$

where α is a very small number (10^{-50} in this paper) introduced to avoid 0 in the numerator, $\tilde{\phi} = \max((\alpha, \phi), 1 - \alpha)$, to limit the phase value within bounds. Further, the expression inside the bracket is constrained between α and $1/\alpha$ to avoid the calculations getting out of bounds.

The Accurate Conservative Phase Field Method has been shown to be more accurate than the Conservative Phase Field Method and demonstrates better boundedness and reduced truncation error for the calculation of the curvature [17].

2 Methodology

2.1 Accurate Phase Field Method

The Accurate Conservative Phase Field Method is solved in a collocated grid framework using the second-order Adams–Bashforth algorithm for time marching. The domain is first initialized using ones and zeros for the phase, and then the Phase Field Method solver is run to initialize the diffused phase field. The diffusion and convection terms are treated in a finite volume framework where, while the diffusion term is treated using the second-order central difference method, numerous schemes are available in the house code GenIDLEST for the treatment of the convection term, including second-order central difference, QUICK scheme, and TVD flux limiters. The anti-diffusion term is treated using the second-order central difference method in a finite difference framework, and the re-initialization parameter (γ) is updated every timestep as $\gamma = \gamma^* u_{\max}$ [13–15, 17], with a minimum value established as $\gamma = 0.1\gamma^* u_{\mathrm{ref}}$, where γ^* is a constant factor (typically chosen to be 1.0), $u_{\max}$ is the maximum velocity in the field, and u_{ref} is the reference velocity.

While a boundedness criterion has been well established by Mirjalili et al. [14], as a contingency, the phase is bounded by the limits $[\alpha, 1]$ to avoid any unforeseen division by zero errors, and the following treatment is provided to ensure phase volume conservation:

1. Calculate $\phi_d = \phi(1 - \phi)$ for each node.
2. Calculate phase volume:

$$V(t) = \underset{\Omega}{\int} \phi \, d\Omega, \tag{7}$$

where Ω is the volume of the domain and phase volume difference:

$$\Delta V(t) = V(t = 0) - V(t). \tag{8}$$

3. Apply the correction:

$$\phi^c = \phi + \frac{\Delta V \phi_d}{\int_\Omega \phi_d \mathrm{d}\Omega}. \tag{9}$$

This can be considered to be a first-order operation in moving the interface uniformly throughout the domain by a distance dL in the normal direction to incur a ΔV change in phase volume.

2.2 Conservation of Mass and Momentum

The dynamics of two-phase incompressible immiscible flows are determined by the incompressible Navier–Stokes Equations:

$$\nabla \cdot \boldsymbol{u} = 0, \tag{10}$$

$$\rho\left(\frac{\partial \boldsymbol{u}}{\partial t} + \nabla \cdot (\boldsymbol{u}\boldsymbol{u})\right) = -\nabla p + \nabla \cdot (\mu \nabla \boldsymbol{u}) + \rho \boldsymbol{g}, \tag{11}$$

where p is pressure, u is the velocity, $\boldsymbol{g}$ is the acceleration due to gravity, and density (ρ) and dynamic viscosity (μ) are approximated using Eq. (3). Capillary forces have been neglected in this paper.

These simulations are performed using the in-house FVM CFD code Generalized Incompressible Direct and Large Eddy Simulation of Turbulence (GenIDLEST) [18] using the fractional step method. A collocated grid framework is adopted, where phase, the signed distance function, velocity, pressure, density, and viscosity are stored at cell centers and a fully explicit second-order Adams–Bashforth algorithm is adopted for time marching. At each time step, the following steps are performed:

1. Predict a velocity field $\boldsymbol{u}^*$ using the momentum equation and interpolate to cell faces to calculate cell face fluxes $\boldsymbol{c}$ using the available pressure field, p_0.
2. Solve for the phase using the following steps:

   a. Calculate the signed distance function ψ and the term $\boldsymbol{S} = \frac{1}{4}\left(1 - \tanh^2\left(\frac{\psi}{2\epsilon}\right)\right)\hat{\boldsymbol{n}}$ at cell centers. Calculate the divergence of $\boldsymbol{S}$ to obtain the source term.

   b. Use cell face velocity fluxes to calculate the convection term and use second-order central difference to obtain the diffusion term.

   c. Find the new phase values by using the second-order Adams–Bashforth method. Adjust the phase between the limits [α, 1] and apply the correction for phase volume conservation. Update density and viscosity.

3. Use $\boldsymbol{u}^*$ interpolate to cell faces to calculate cell face fluxes c^*.

4. Using predicted cell face flux values c^*, calculate pressure correction with the variable coefficient Poisson equation using a preconditioned BICG-STAB solver:

$$\nabla \cdot \left(\frac{1}{\rho} \nabla (p' \Delta t) \right) = \nabla \cdot c^*. \tag{12}$$

5. Update the pressure as $p = p_0 + p'$, where p_0 is the pressure at the previous timestep. Use the pressure correction to update the velocity, u, field, and the cell face velocity fluxes, c.

3 Validation and Verification

Five generic test cases were considered for numerical verification of the Phase Field Method:

a. Droplet in Shear flow
b. Zalesak Disk
c. Rayleigh Taylor Instability
d. Solitary Wave
e. Dam Break Problem.

The first two are the standard test cases for evaluating advection schemes [19], whereas the latter involves solving the full Navier–Stokes coupled with the Phase Field Method.

3.1 Droplet in Shear Flow

In this standard test case introduced by Rider and Kothey [20], a droplet of radius 0.15 is introduced at the position (0.50, 0.75) in the domain of $[0,1] \times [0,1]$ with a prescribed velocity field given by the following stream function:

$$\psi = \frac{1}{\pi} \sin^2(\pi x) \sin^2(\pi y) \cos(\pi t / T), \tag{13}$$

where $T = 4$.

The droplet is allowed to deform as much as possible, and at $t = T/2$, the velocity field is reversed, and the circular droplet is restored. The initial and final shapes are compared to calculate the shape error as

$$\text{Shape Error} = \sum_{i,j} |\phi_{t=0}(i, j) - \phi_{t=T}(i, j)| \Delta x \Delta y. \tag{14}$$

Fig. 1 Shape errors for droplet in shear flow test case
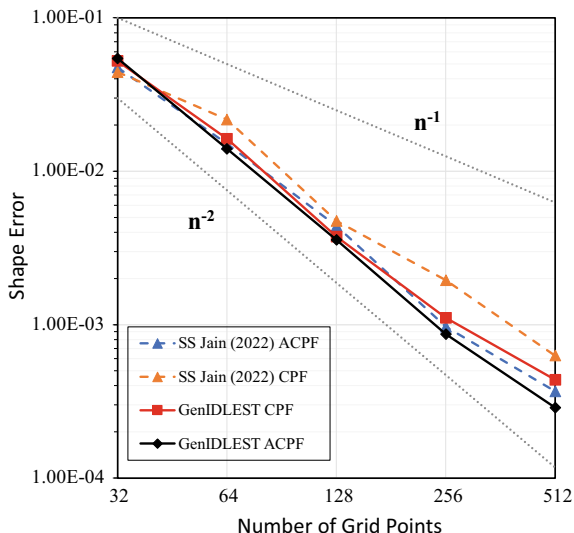
Table 1 Shape error comparison for droplet in shear flow test case between conservative phase field (CPF) and accurate conservative phase field (ACPF) methods

Grid size	Δt	Shape error	
		CPF	ACPF
32×32	$2.00e - 3$	$5.23E - 02$	$5.43E - 02$
64×64	$1.00e - 3$	$1.63E - 02$	$1.40E - 02$
128×128	$5.00e - 4$	$3.74E - 03$	$3.57E - 03$
256×256	$2.50e - 4$	$1.11E - 03$	$8.66E - 04$
512×512	$1.25e - 4$	$4.37E - 04$	$2.88E - 04$

Five simulations for grid sizes 32×32, 64×64, 128×128, 256×256, and 512×512 were performed with the parameters $\epsilon = 1.0\Delta x$, $\gamma = 1.0u_{max}$ using both the *Conservative Phase Field* (CPF) and *Accurate Conservative Phase Field Method* (ACPF). The shape errors were compared with the results of Jain [17], and a near second-order rate of convergence, comparable to previous studies (Fig. 1), is observed. It is also observed that the *Accurate Phase Field Method* is more accurate than the *Conservative Phase Field Method* (**Table 1**). The final shapes were also visually compared for different grid sizes (Fig. 2) to the exact solution and convergence is observed for higher resolutions.

3.2 Zalesak Disk

In this standard test case introduced by Zalesak [21], a circular disk of radius 15 with a notch of width 5 and height 25 is introduced at the position (50, 75) in the domain
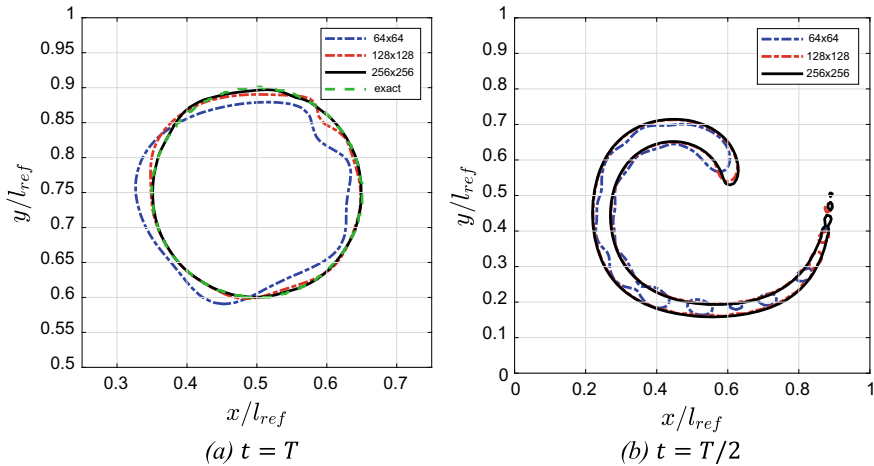
Fig. 2 Phase field contour line for $\phi = 0.5$ for the droplet in shear flow test case

of $[0, 100] \times [0, 100]$ with a prescribed rigid body velocity field:

$$u_x = \pi \frac{50 - y}{314}, u_y = \pi \frac{x - 50}{314}. \tag{15}$$

We set $\epsilon = 0.7\Delta x$, $\gamma = 2.5u_{\max}$. The problem is non-dimensionalized with $l_{\mathrm{ref}} = 100.0$ and $u_{\mathrm{ref}} = 1.0$. This test case is used to test the ability to preserve sharp corners; the slotted disk should be convected as it is by the flow field undergoing minimal possible deformations [19]. The initial and final shapes at $T = 0$ and $T = 628$ are compared in Fig. 3 for grid sizes 128×128, 256×256 and 512×512, with $\Delta t = 0.064\Delta x$, and it is observed that higher resolutions are able to preserve the sharp corners better.

3.3　Rayleigh Taylor Instability

The first dynamic test case considered is the evolution of Rayleigh Taylor instability for low Atwood numbers. Such instability occurs due to the action of gravitational forces when a heavier fluid sits on top of a lighter fluid.

The domain $[0, D] \times [-2D, 2D]$ is filled with two fluids in equal volumes of density ratio prescribed by Atwood number $At = (\rho_1 - \rho_0)/(\rho_1 + \rho_0) = 0.5$ and equal viscosity. For the phase, we use, $\gamma^* = 1.0$ and $\epsilon = 2.0\Delta x$. The interface is located at $y(x) = 0.1D \cos(2\pi x/D)$. The reference velocity is $u_{\mathrm{ref}} = \sqrt{gD}$ and time is non-dimensionalized using $t_{\mathrm{ref}} = D/u_{\mathrm{ref}}$. The Reynolds number is $\mathrm{Re} = \rho_1 u_{\mathrm{ref}} D/\mu = 3000$, the Froude Number is $\mathrm{Fr} = u_{\mathrm{ref}}/\sqrt{gD} = 1$ and surface tension forces are neglected. No-slip boundary conditions are used on the top and bottom

Fig. 3 Zalesak disk: final
shape for grid sizes 128 ×
128, 256 × 256, and 512 ×
512
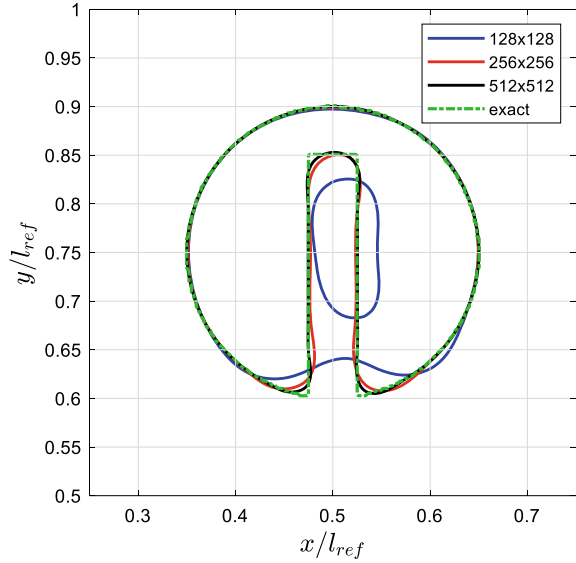
walls and periodic boundary conditions are used on the left and right sides of the
domain.

We studied this case for two grid sizes 200×800 and 400×1600. These simulations
were performed in a multi-block framework, with 16 blocks stacked over each other
in the $\hat{\mathbf{y}}$ direction.

The phase contour profile for the evolution of the instability is given in Fig. 5. We
also compare the y-coordinates of the top and bottom of the interface with previously
performed numerical simulations [13, 22, 23] and good agreement is observed, as
seen in Fig. 4. Here, the time is non-dimensionalized using Atwood Number, as
$t^* = (t/t_{\text{ref}})\sqrt{(\text{At})}$.

3.4 Solitary Wave Run-Up

This test case is used to quantify the effects of viscous damping and study the inter-
action of the interface with solid walls for high-density ratios. In a two-dimensional
domain $[-h, h] \times [0, 20h]$, the water free surface is prescribed using the following
elevation profile:

$$A(x, t = 0) = \frac{A_0}{\cosh^2\left(x\sqrt{0.75A_0}\right)}. \tag{16}$$

We use $h = 0.1$ m, and the theoretical wave speed is $C_w = \sqrt{gh} = 1$ m/s. We
use $g = 10$ m/s^2 for the sake of convenience. The density and viscosity of water and
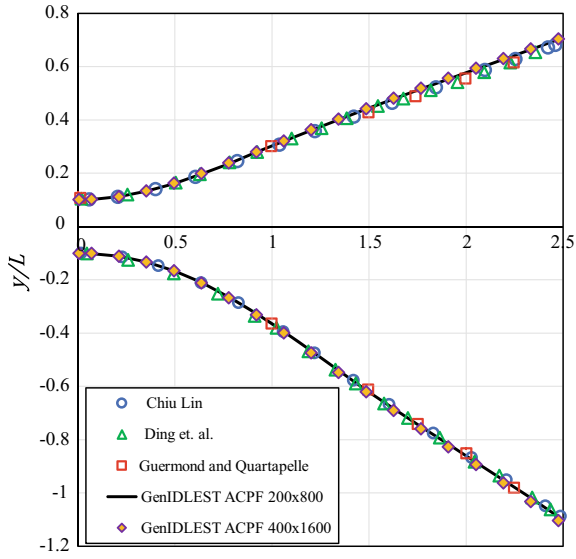
Fig. 4 Evolution of the *y*-coordinate of the top and bottom of the interface with time for Rayleigh Taylor instability

(a) $t/t_{ref} = 0$ (b) 2.0   (c) 2.5   (d) 3.0   (e) 3.5
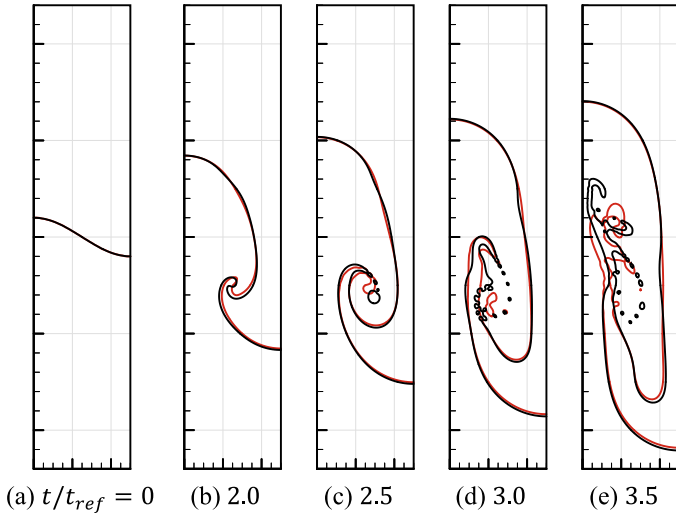
Fig. 5 Evolution of the interface for Rayleigh Taylor instability for grid sizes 400×1600 (black) and 200×800 (red)
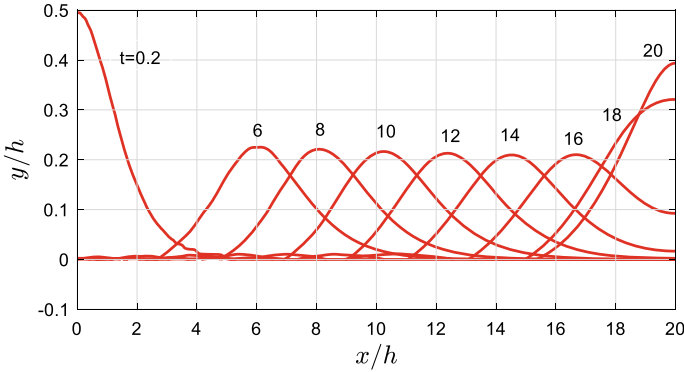
Fig. 6 Evolution of solitary wave for $A_0/h = 0.5$

air are prescribed as $\rho_a = 1.2 \, \text{kg/m}^3$, $\mu_a = 1.8\text{e} - 05 \, \text{Pa s}$, $\rho_w = 1000 \, \text{kg/m}^3$ and $\mu_w = 1.0\text{e} - 03 \, \text{Pa s}$, the Reynolds number is $\text{Re} = \rho_w C_w h / \mu_w = 1.0 \times 10^5$, and the Froude number is $\text{Fr} = u_{\text{ref}} / \sqrt{gh} = 1$.

A grid of 400×200 is employed with a fixed time step size $\Delta t / t_{\text{ref}} = 1.0 \times 10^{-4}$. These simulations were performed on 25 blocks in the $\hat{x}$ direction. For the phase, $\gamma^* = 1.0$ and $\epsilon = \sqrt{A_{\text{cell}}}$ are used. TVD flux limiters are used to calculate the density cell face values for pressure correction. Figure 6 depicts the evolution of the solitary wave for $A_0/h = 0.5$. For $A_0/h = 0.5$, a maximum phase volume change of $|\Delta V / V_0| \approx 5.15 \times 10^{-6}\%$ is observed, and the wave speed is $\sim 1.0625 \, \text{m/s}$, which is close to the theoretical wave speed.

We first study the wave run-up height (A_{runup}) as a function of the wave amplitude when the wave is at $x = 10$ (A_c) in Fig. 7. The results compare favorably against both, previously performed numerical simulations [24, 25], and the experiment by Chan and Street [26].

We also study the viscous damping effects, by comparing the evolution of wave amplitude for $A_0/h = (0.1, 0.3, 0.5, 0.7, 0.9)$, starting from $t/t_{\text{ref}} = 6$ (when the wave is free from the wall) to $t/t_{\text{ref}} = 14$, with the analytical solution predicted by Mei et al. [27]:

$$A_{\text{max}}^{-1/4} = A_{0\,\text{max}}^{-1/4} + 0.08356 \frac{C_w t^*}{h} \sqrt{\left(\frac{1}{\text{Re} h^{1/2}} \right)}, \qquad (17)$$

where $A_{0\,\text{max}}$ is the wave amplitude at $t/t_{\text{ref}} = 6$, $t^* = t - 6t_{\text{ref}}$ and A_{max} is the wave amplitude. The numerical solutions show good agreement with the perturbation solutions for low values of $A_{0\,\text{max}}$ (Fig. 8), while higher viscous damping is observed for higher amplitudes; this is expected as the small amplitude approximation is only valid for $A_{0\,\text{max}}/h \leq 0.1$.

Fig. 7 Wave run-up versus wave amplitude when the wave is at $x/h = 10$
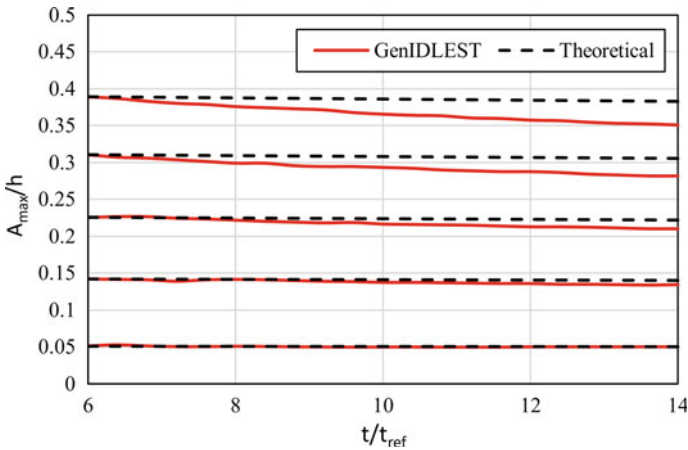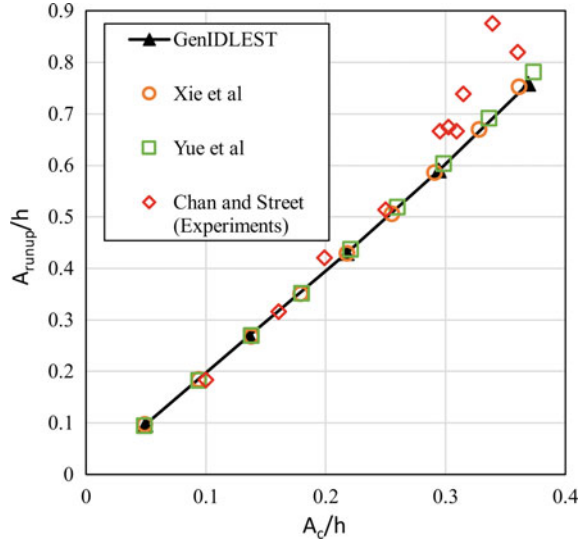
Fig. 8 Evolution of wave amplitude versus time to quantify viscous damping effects

3.5 Dam Break Problem

This free surface problem involves simulating the collapse of the water column. A water column of height $2L$ and width L is prescribed in the bottom left corner of the domain: $[0, 4L] \times [0, 4L]$. The same material properties as in the solitary wave example are used, surface tension forces are neglected, and acceleration due to gravitation is $g = -9.81$ m/s^2. $L = 0.146$ m is used as a reference length, $u_{ref} = \sqrt{g(2L)} = 1.6295$ m/s is used as a reference velocity which leads to the Reynolds

Number Re $= \rho_w u_{ref} L / \mu_w \approx 2.38 \times 10^5$ and the Froude Number Fr $= u_{ref} / \sqrt{gL} \approx$ 1.414. For the phase, $\gamma^* = 1.0$ and $\epsilon = 4.0 \Delta x$ are used.

TVD flux limiters are employed to calculate convective terms in both, phase and momentum equations, and density cell face values and a no-slip boundary condition are applied to all the domain boundaries. The simulation is first performed for a two-dimensional uniform grid of size 600×600 with a fixed time step size $\Delta t / t_{ref} = 2.5 \times 10^{-5}$.

This simulation was repeated on a non-uniform grid of size 400×400 with the grid refined to $\Delta x = 2L/600$ at the left, right, and the bottom walls, with a fixed time step size $\Delta t / t_{ref} = 0.625 \times 10^{-5}$. For the phase, $\gamma^* = 1.0$ and $\epsilon = 7.6808 \sqrt{\min(A_{cell})}$ is used. Both simulations were performed on 25 blocks (5 in each direction). We compare the position of the surge front versus time for both the simulations with previously performed numerical simulations [13, 28] and experiments [29, 30] and a good agreement is observed as seen in Fig. 9.

A maximum phase volume change of $|\Delta V / V_0| \approx 5.06 \times 10^{-4}\%$ and $9.23 \times 10^{-3}\%$ was observed for the uniform and non-uniform grids respectively between $t = 0$ and $t = 4t_{ref}$.
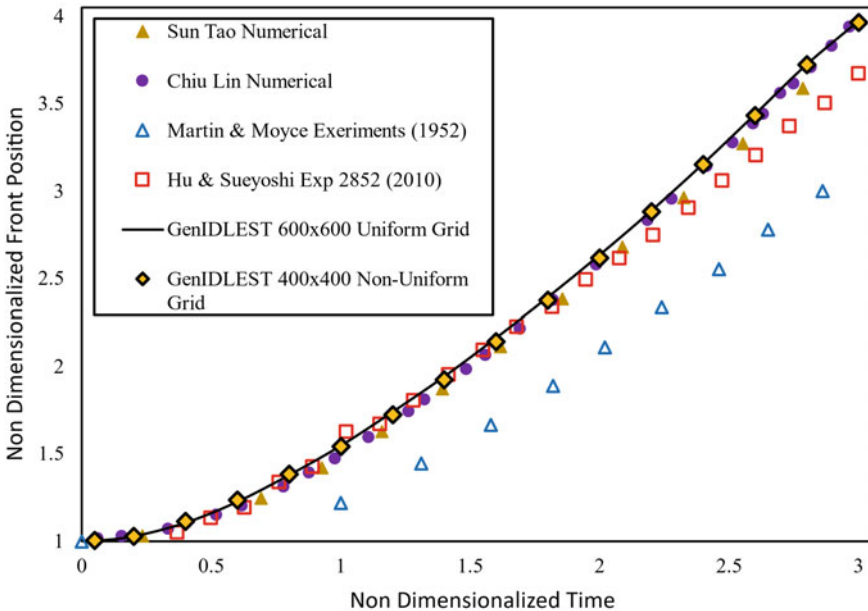
Fig. 9 Evolution of the wave front position of the collapsing water column with time

4 Conclusion

We implemented the Accurate Conservative Phase Field Method in a Finite Volume parallel multi-block collocated grid framework, and with the help of the droplet in shear flow test case and observed that it is more accurate than the Conservative Phase Field Method. The implementation was also verified against standard test cases such as Zalesak Disk, Rayleigh Taylor Instability, Solitary Wave, and the Dam Break Problem, and showed good agreement with theoretical, experimental, and previously performed numerical results. The method shows excellent phase volume conservativeness, even in cases where we have very high-density ratios.

Nomenclature

ϕ	Phase
ψ	Signed distance function [m]
ϵ	Interface width parameter [m]
γ	Re-initialization parameter [m/s]
γ^*	Scaled Re-initialization parameter
∇	Gradient operator [1/m]
Θ	Material properties
$\hat{\boldsymbol{n}}$	Normal vector field
$V(t)$	Phase volume [m^3]
$\boldsymbol{u}$	Velocity [m/s]
p	Pressure [Pa]
ρ	Density [kg/m^3]
μ	Dynamic viscosity [Pa s]
g	Acceleration due to gravity [m/s^2]
At	Atwood number
Re	Reynolds number
Fr	Froude number

References

1. Khedkar K, Bhalla APS (2022) A model predictive control (MPC)-integrated multiphase immersed boundary (IB) framework for simulating wave energy converters (WECs). Ocean Eng 260:111908
2. Benites-Munoz D, Huang L, Anderlini E, Marín-Lopez JR, Thomas G (2020) Hydrodynamic modelling of an oscillating wave surge converter including power take-off. J Mar Sci Eng 8(10):771
3. Schmitt P, Elsaesser B (2015) On the use of OpenFOAM to model oscillating wave surge converters. Ocean Eng 108:98–104
4. Wei Y, Rafiee A, Henry A, Dias F (2015) Wave interaction with an oscillating wave surge converter, part I: viscous effects. Ocean Eng 104:185–203
5. Luo L, Wang X-P, Cai X-C (2017) An efficient finite element method for simulation of droplet spreading on a topologically rough surface. J Comput Phys 349:233–252
6. Yada S, Lacis U, van der Wijngaart W, Lundell F, Amberg G, Bagheri S (2022) Droplet impact on asymmetric hydrophobic microstructures. Langmuir 38(26):7956–7964
7. Zhang Q, Qian T-Z, Wang X-P (2016) Phase field simulation of a droplet impacting a solid surface. Phys Fluids 28(2):22103
8. Sussman M, Smereka P (1997) Axisymmetric free boundary problems. J Fluid Mech 341:269–294
9. Sethian JA, Smereka P (2003) Level set methods for fluid interfaces. Annu Rev Fluid Mech 35(1):341–372
10. Olsson E, Kreiss G (2005) A conservative level set method for two phase flow. J Comput Phys 210(1):225–246
11. Cahn JW, Hilliard JE. Free energy of a nonuniform system. I. Interfacial free energy, p 11
12. Allen SM, Cahn JW (1979) A microscopic theory for antiphase boundary motion and its application to antiphase domain coarsening. Acta Metall 27(6):1085–1095
13. Chiu P-H, Lin Y-T (2011) A conservative phase field method for solving incompressible two-phase flows. J Comput Phys 230(1):185–204
14. Mirjalili S, Ivey CB, Mani A (2020) A conservative diffuse interface method for two-phase flows with provable boundedness properties. J Comput Phys 401:109006
15. Mirjalili S, Ivey CB, Mani A (2019) Comparison between the diffuse interface and volume of fluid methods for simulating two-phase flows. Int J Multiph Flow 116:221–238
16. Jain SS, Adler MC, West JR, Mani A, Moin P, Lele SK (2021) Assessment of diffuse-interface methods for compressible multiphase fluid flows and elastic-plastic deformation in solids
17. Jain SS (2022) Accurate conservative phase-field method for simulation of two-phase flows. J Comput Phys 469:111529
18. Tafti DK (2001) GenIDLEST: a scalable parallel computational tool for simulating complex turbulent flows. Fluids Engineering, American Society of Mechanical Engineers, New York, New York, USA, pp 347–356
19. Prosperetti A, Tryggvason G (eds) (2007) Computational methods for multiphase flow. Cambridge University Press, Cambridge
20. Rider W, Kothe D (1995) Stretching and tearing interface tracking methods. In: 12th computational fluid dynamics conference. American Institute of Aeronautics and Astronautics
21. Zalesak (1979) Fully multidimensional flux-corrected transport algorithms for fluids
22. Ding H, Spelt PDM, Shu C (2007) Diffuse interface model for incompressible two-phase flows with large density ratios. J Comput Phys 226(2):2078–2095
23. Guermond J-L, Quartapelle L (2000) A projection FEM for variable density incompressible flows. J Comput Phys 165(1):167–188
24. Xie Z, Stoesser T, Yan S, Ma Q, Lin P (2020) A Cartesian cut-cell based multiphase flow model for large-eddy simulation of three-dimensional wave-structure interaction. Comput Fluids 213:104747
25. Yue W, Lin C-L, Patel VC (2003) Numerical simulation of unsteady multidimensional free surface motions by level set method. Int J Numer Methods Fluids 42(8):853–884

26. Chan RK-C, Street RL (1970) A computer study of finite-amplitude water waves. J Comput Phys 6(1):68–94
27. Mei CC, Stiassnie M, Yue DK-P (2005) Theory and applications of ocean surface waves. World Scientific, Singapore
28. Sun DL, Tao WQ (2010) A coupled volume-of-fluid and level set (VOSET) method for computing incompressible two-phase flows. Int J Heat Mass Transf 53(4):645–655
29. Hu C, Sueyoshi M (2010) Numerical simulation and experiment on dam break problem. J Mar Sci Appl 9(2):109–114
30. Martin JC, Moyce WJ (1952) Part IV. An experimental study of the collapse of liquid columns on a rigid horizontal plane. Philos Trans R Soc Lond Ser Math Phys Sci 244(882):312–324

Numerical Investigation of Inertance Type Pulse Tube Cryocooler for Space Applications

R. Ashish, Raghuvara K. Hebbar, T. N. Prateek, Karthik R. Kashyap, and K. S. Rajendra Prasad

1 Introduction

Cryogenics is a highly operational technology in space missions for cooling sensitive electronic equipment that also finds applications in the military, medical, and other fields. Significant progress has been made in the last 50 years to develop cryogenic technologies and advance our knowledge of our surroundings. To enhance the performance and reliability of the cryocooler, it is necessary to focus on phase shift-imparting devices that improve the effectiveness of the pulse tube, regenerator and reservoir. In recent years, the IPTC has become extremely popular for its simplicity and compactness.

2 Literature Review and Objective

The numerical model of the IPTR was developed in Ansys Fluent by Cha et al. [1]. Flow straighteners have been attached with pulse tubes to suppress the streaming effect in the cryocooler. Kanao et al. [2] report to be one of the earliest uses of the IPTR. They measured performance as a function of the diameter and length of the tube, as well as frequency. Dodson et al. [3] conducted a study on the oscillating fluid flow in an inertance tube with varying geometries using CFD simulation. Their study involves solving nonlinear Ordinary Differential Equations (ODE) numerically with the Fluent software to predict the input acoustic power and the phase shift between the mass flow rate and pressure at the inlet of the inertance tube. Dang et al. [4] simulated a single-stage coaxial PTC, which achieved a cold end temperature of 29.7 K under no-load conditions, by integrating the inertance tubes with a gas reservoir. Chen [5]

R. Ashish (✉) · R. K. Hebbar · T. N. Prateek · K. R. Kashyap · K. S. Rajendra Prasad
Department of Mechanical Engineering, PES University, Bengaluru, India
e-mail: ashh164875@gmail.com

employed the CFD simulation method examine the thermodynamic cycles in an IPTR system. Ren and Dai [6] demonstrated an inline type single-stage IPTC operated by a linear compressor. A no-load temperature of 34.2 K at 35.2 Hz without a double-inlet phase shifter was achieved by their cryocooler model. Kumar [7] reported the numerical study of a 3D IPTR system from a design perspective. Liu [8] modeled a single-stage PTC, which achieved a cold end temperature of 26.9 K under no-load conditions and cooling power of 2 W at 35 K. It implemented an inertance tube and reservoir as the only phase shifters. In this work, it has been observed that the numerical analysis can be further developed in the below-mentioned aspects. 3D simulation of the cryocooler challenges the designer to analyze a cryocooler model within a given timeframe. In many situations, it becomes impossible due to high computational overheads. Hence, the 2D axis-symmetric model is easily adaptable. Modeling the compressor in a cryocooler assembly is complex; hence, a User-Defined Function (UDF) is developed to mimic the action of the compressor. A sinusoidal oscillating pressure pulse is given by the UDF which is coupled to the inlet of the transfer line, thereby eliminating the need for modeling a compressor. The system was simulated by keeping solid material properties constant. However, variable solid properties have been proved to yield a better cooling on further analysis. Initially, the piecewise linear scheme was employed to obtain the function for variable solid properties. On further research, polynomial regression predicts a possibility for better approximation of the variable solid properties. Changes in pulse tube geometry have been designed. Inward and outward tapering with varying angles have been simulated which eliminates the use of conventional flow straighteners. The objective of this study is to overcome the limitations associated with the recent numerical modeling trends of an IPTC using the Ansys/Fluent CFD platform. Specifically, the IPTC model proposed by Cha et al. [1] has been analyzed to address these limitations. Firstly, the obtained results have been subjected to validation to ensure the reliability and accuracy of the numerical methodology. Subsequently, the same IPTC assembly has been modeled and analyzed to overcome the encountered challenges, and the corresponding issues and difficulties have been consolidated and examined in detail.

3 Methodology

3.1 Geometry of the Cryocooler Components

A two-dimensional axis-symmetric, schematic of the modeled IPTC system is shown in Fig. 1. Three models of the pulse tube geometry are designed, which are, a straight pulse tube, inward tapered pulse tube of 1° taper and an outward tapered pulse tube of 1° taper. The detailed dimensions are given in Table 1. Wall thickness is neglected (Fig. 2).

Fig. 1 Schematic diagram of the IPTC

Table 1 Details of IPTC dimensions

S. No.	Components	Radius (m)	Length (m)
1	Transfer line	1.55E − 03	1.01E − 01
2	Aftercooler (AFT)	4.00E − 03	2.00E − 02
3	Regenerator	4.00E − 03	5.80E − 02
4	Cold heat exchanger (CHX)	3.00E − 03	5.70E − 03
5	Pulse tube	2.50E − 03	6.00E − 02
6	Hot heat exchanger (HHX)	4.00E − 03	1.00E − 02
7	Inertance tube	4.25E − 04	6.84E − 01
8	Reservoir	1.30E − 02	1.30E − 01
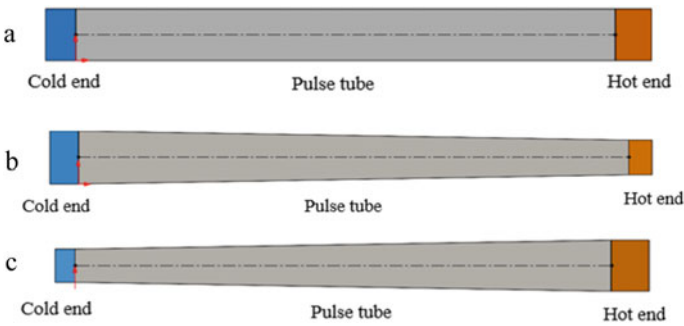
Fig. 2 Schematic of **a** the straight pulse tube, **b** 1° inward tapering pulse tube and **c** 1° outward tapering pulse tube

3.2   Discretization of the Present Models

Finite element mesh of IPTC assembly has been generated after designing the geometry of the proposed models. All the components of the cryocooler are meshed using 4-node quadrilateral elements. Number of elements and nodes obtained in each model is given in Table 2 (Fig. 3).

Table 2 Details of mesh

Geometric model	Elements	Nodes
Model 1	5493	6944
Model 2	43,083	47,431
Model 3	28,517	32,193
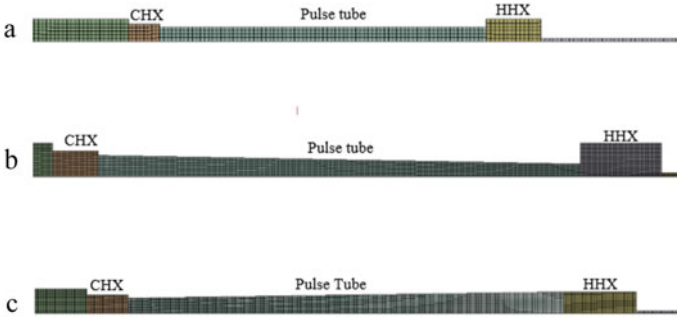
Fig. 3 Mesh diagrams of **a** the straight pulse tube, **b** inward tapering pulse tube, and **c** outward tapering pulse tube

3.3 Boundary Condition

The detailed boundary conditions of the models are given in Table 3. A UDF is developed using a C program to mimic the compressor action. Helium is chosen as the working fluid for the model owing to its lowest critical temperature, high volumetric heat capacity, and high thermal conductivity when compared to other available gases. Aftercooler (AFT), regenerator, cold-heat exchanger (CHX), and hot-heat exchanger (HHX) are modeled as porous zones and their boundary conditions are determined using viscous resistance and inertial resistance. The PISO scheme with a PRESTO option is used for pressure velocity coupling to correct the coupling equation. The IPTC with straight pulse tube model has been studied under two cases based on constant and variable solid material properties, individually. In the first case, constant theoretical values of thermal conductivity and specific heat of the solid materials are considered. In the second case, the material properties are depicted to vary as a function of temperature. In further cases, variable material properties are analyzed under piecewise linear scheme and polynomial function scheme, independently. Piecewise linear scheme incorporates a linear variation of material properties as a function of temperature.

```
User-Defined Function:
#include"udf.h"
DEFINE_PROFILE(unsteady_pressure, thread, position)
{
face_t f;
real t = CURRENT_TIME;
real freq =30.0;
real w = 2*M_PI*freq;
begin_f_loop(f,thread)
{
F_PROFILE(f,thread,position) = 101325.0*(16.0 + 5*sin(w*t));
}
```

Table 3 Details of boundary conditions

S. No.	Components	Wall material	Boundary conditions
1	Transfer line	Steel (SS304)	Adiabatic
2	Aftercooler (AFT)	Copper (OFHC)	Isothermal
3	Regenerator	Steel (SS304)	Adiabatic
4	Cold heat Exchanger (CHX)	Copper (OFHC)	Adiabatic
5	Pulse tube	Steel (SS304)	Adiabatic
6	Hot heat exchanger (HHX)	Copper (OFHC)	Isothermal
7	Inertance tube	Steel (SS304)	Adiabatic
8	Reservoir	Steel (SS304)	Adiabatic

    end_f_loop(f,thread)

    }

Sine wave is created with a mean pressure of 16 bar and amplitude of 5 bar representing the compressor action. Recurring loop of the sinusoidal pressure is applied with a frequency of 30 Hz.

3.4 Mathematical Modeling

Fluent solver solves the equation for conservation of mass, momentum, and energy for the transient 2D axis-symmetric model. Momentum equation is solved in both axial and radial direction. The energy equation for the solid matrix inside the porous and non-porous regions considered by neglecting the swirl assumptions. The general form of conservation equations is discussed.

Conservation of mass:

$$\frac{\partial \rho}{\partial t} + \nabla.(\rho \vec{v}) = S_m \tag{1}$$

Conservation of momentum:

$$\frac{\partial}{\partial t}(\rho \vec{v}) + \nabla.(\rho \vec{v} \vec{v}) = -\nabla p + \nabla.(\overline{\overline{\tau}}) + \rho \vec{g} + \vec{F}. \tag{2}$$

Energy conservation equation:

$$\frac{\partial}{\partial t}(\rho E) + \nabla.(\vec{v}(\rho E + p)) = \nabla.\left(k_{\text{eff}} \nabla \sum_j h_j \vec{\varphi}_j + (\tau.\vec{v}) \right) + S_h, \tag{3}$$

$$S_h = 0, \text{ for non - porous zones}, \tag{4}$$
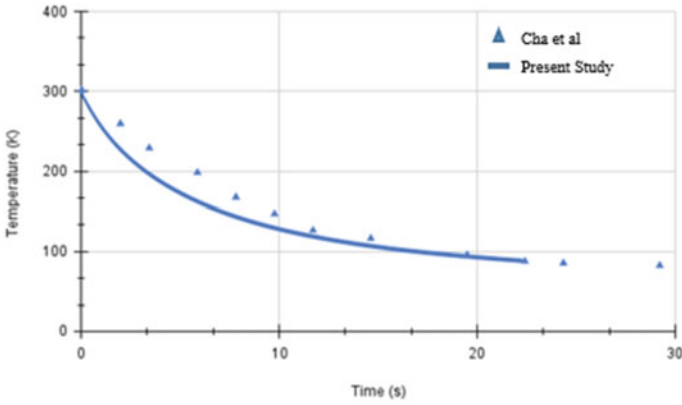
Fig. 4 Cooling curve obtained by validation of Cha et al. model

$$S_h = \frac{\mu}{\alpha}\vec{v} + 0.5C_2|\vec{v}|\vec{v}, \text{ for porous zones.} \tag{5}$$

In this study, $k - \varepsilon$ model is implemented to simulate the flow across the porous media. The corresponding $k - \varepsilon$ standard equations are taken from Ansys [9].

3.5 Validation

Validation test is carried out against the cryogenic journal published by Cha et al. [1] model. Cold end temperature of 87.2 K is achieved under no-load conditions. The results obtained from validation is in line with the experimental results of Cha et al. model as shown in Fig. 4.

4 Results and Discussion

Simulation of the mentioned geometric models of IPTC is carried out, results are analyzed, and the optimum angle of the pulse tube which provides better cooling is determined. Further, IPTC's performance characteristics are presented.

4.1 Role of Material Properties in Cryocooler Working

Thermal conductivity and specific heat of the solid materials are considered in the following cases.
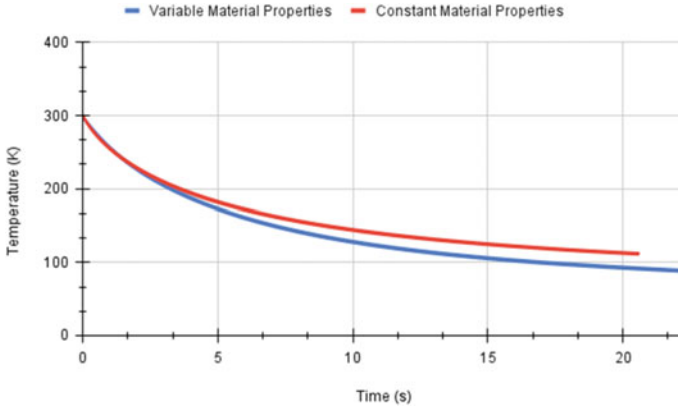
Fig. 5 Comparison of cooling curves of case 1 and case 2

Case 1: Constant Material Properties

Results are analyzed for constant material properties, and the cooling curve is shown in Fig. 5. Temperature of 110.7 K has been obtained at the cold end.

Case 2: Variable Material Properties

The variation of material properties, namely thermal conductivity and specific heat, as a function of temperature is implemented. The cooling curve is shown in Fig. 5. Temperature of 87.2 K has been obtained at the cold end.

The cooling effect obtained from the variable material properties provides better results in comparison with constant material properties.

4.2 Effect of Inward Taper in Pulse Tube on Cooling

In Model 2, an inward taper angle of 1° is applied to the pulse tube. Piecewise linear scheme and polynomial function scheme are implemented in the model, as two cases, independently.

Case 3: Effect of Piecewise Linear Scheme in Inward tapered Pulse tube

Piecewise linear scheme, that is, linear variation of material property as a function of temperature, has been applied to the setup. Cold end temperature of 86.1 K has been achieved in this case. The cooling curve is shown in Fig. 6.

Case 4: Effect of Polynomial Function Scheme in Inward tapered Pulse tube

Polynomial regression scheme, which obtains the best fitting curve, has been applied to the setup. The cooling curve is shown in Fig. 7. Cold end temperature of 45.3 K
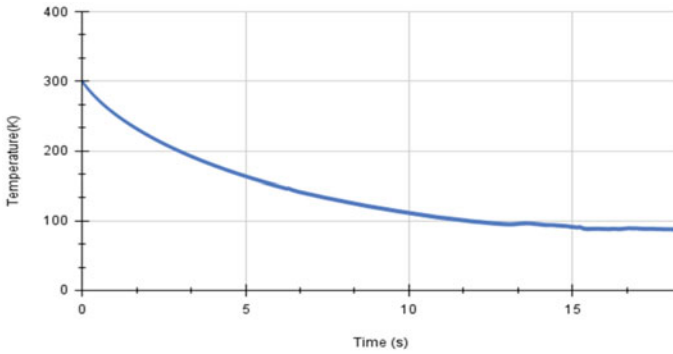
Fig. 6 Cooling curve of case 3
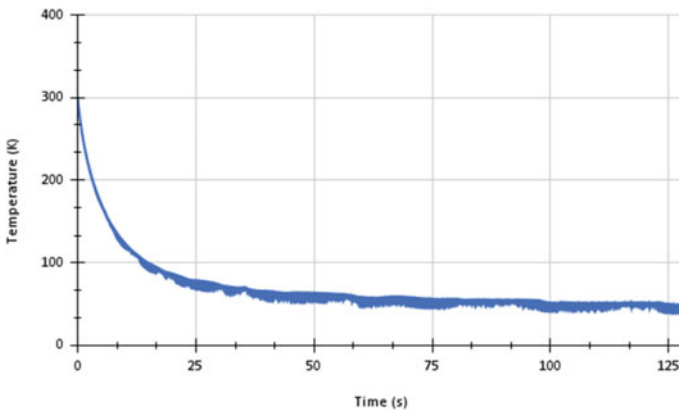
Fig. 7 Cooling curve of case 4

has been achieved in this case. This scheme produced better results compared to the piecewise linear scheme owing to its more precise curve fitting line.

4.3 Effect of Outward Taper in Pulse Tube on Cooling

An outward taper angle of 1° is given to the pulse tube in Model 3. The effect of outward taper is studied under two cases similar to the analysis of Model 2.

Case 5: Effect of Piecewise Linear Scheme Outward Tapered Pulse tube

Piecewise linear scheme, that is, linear variation of material property as a function of temperature, has been applied to the setup. The cooling curve is shown in Fig. 8. Cold end temperature of 157.2 K has been achieved in this case.
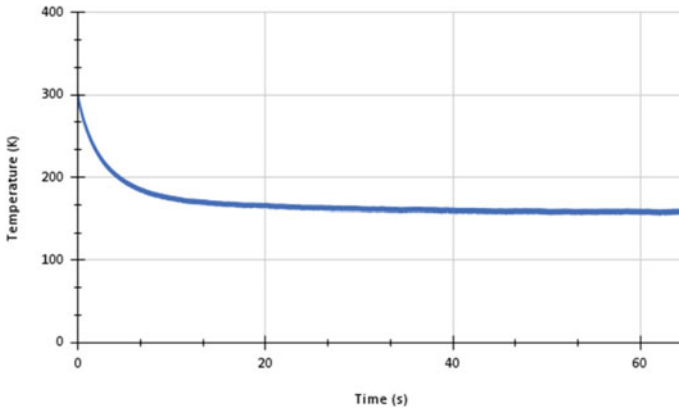
Fig. 8 Cooling curve of case 5

Case 6: Effect of Polynomial Function Scheme in Outward tapered Pulse tube

Polynomial regression scheme, which obtains the best fitting curve, has been applied to the setup. The cooling curve is shown in Fig. 9. Cold end temperature of 137 K has been achieved in this case.

The cooling performance obtained by inward tapering of the pulse tube is higher in comparison with that obtained by outward tapering.
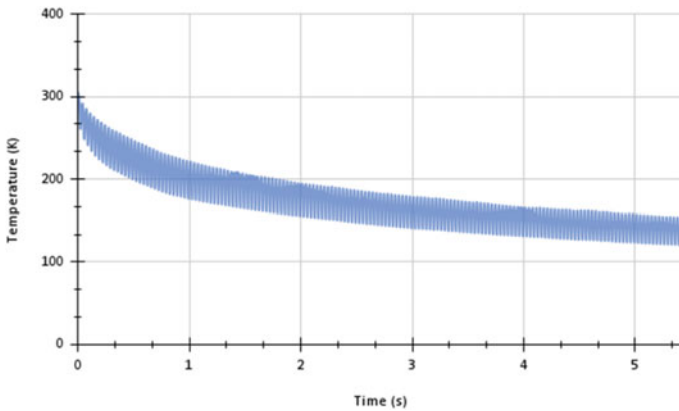
Fig. 9 Cooling curve of case 6

4.4 Effect of Vortex Formation in Pulse Tube

Vortex is a whirling formation in a fluid. The hydrodynamic and thermodynamic asymmetries along the cryocooler system induce pressure drops, which in turn leads to vortices. The generation, evolution, and shedding of these vortices lead to streaming. The pressure drops generated due to abrupt changes of the pulse tube cross sections at both hot and cold ends can be calculated.

Vortices in Straight Pulse tube

Vortices are formed in the straight pulse tube which hinders the performance of the cryocooler mainly due to minor losses and pressure drops. Generally, vortices are formed throughout the cryocooler components. However, the present work focuses on the vortices generated in the pulse tube region. Figure 10 shows the vortices formed in the straight pulse tube.

Vortices in Inward Tapering Pulse tube

Complete elimination of vortices in any cryocooler model is practically impossible, although one can try to minimize the vortex formation to a certain extent. Tapering of the pulse tube has been implemented in the present work by acknowledging this fact. Vortices appeared near the cold end of the inward tapered pulse tube and faded away across the length, as shown in Fig. 11. The time duration and the size of these vortices are very short.
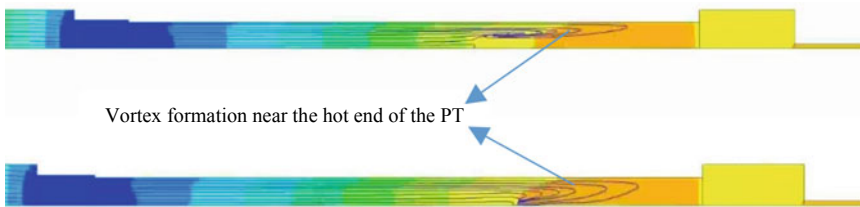
Fig. 10 Vortex formation in straight pulse tube
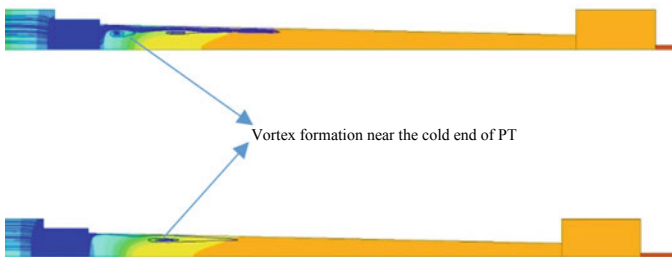
Fig. 11 Vortex formation in the inward pulse tube
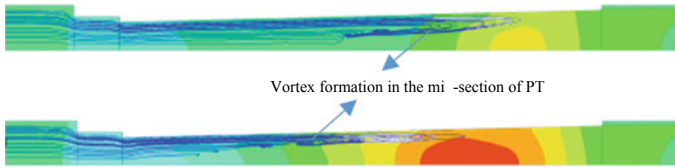
Fig. 12 Vortex formation in the outward pulse tube

Vortices in Outward Tapering Pulse tube

In outward tapered pulse tube, vortices are observed at the mid-section, as shown in Fig. 12, similar to the case of straight pulse tube. The intensity of these vortices hardly reduces across the length of the pulse tube. The vortices in this case exist dominantly throughout the cycle. Hence, this model of pulse tube geometry is least favorable.

5   Conclusions

In the present study, different cases are simulated by varying the pulse tube geometry and solid material properties to obtain optimum results. UDF, which mimics the compressor action and generates the oscillating pressure function, assisted in proper functioning of the system. Based on these inputs, results are analyzed and the pulse tube geometry which provides greater cooling is determined. It is observed that vortex formation is inevitable in all the cryocooler models that are studied. However, it is proved that vortex-induced streaming in inward tapering pulse tubes is significantly lower compared to that in straight pulse tubes and outward tapered pulse tubes. An operating frequency of 30 Hz and pressure oscillation between 11 and 21 bar is implemented to obtain a no-load temperature of 45.3 K using a 1° inward tapered pulse tube.

Nomenclature

ρ	Density [kg/m^3]
t	Time [s]
∇	Divergence Operator
F	External body forces
∂	Differential Operator

S	Generation of energy per unit volume of time
v	Velocity[m/s]
g	Gravity acceleration [m/s^2]
E	Total energy [J]
K	Thermal Conductivity [W/m-K]
S	Source Term
τ	Stress Tensor
h	Enthalpy [J/kg]
φ	Porosity
μ	Dynamic Viscosity [kg/m-s]
α	Permeability
C_2	Inertial Resistance [m^{-1}]
p	Pressure [Pa]
R_g	Universal Gas Constant [J/kg-K]
T	Temperature [K

References

1. Gu C, Zhou Y (2012) CFD analysis of nonlinear processes in pulse tube refrigerators: streaming induced by vortices. Int J Heat Mass Transf
2. Kanao K, Watanabe N, Kanazawa Y (1994) A miniature pulse tube refrigerator for temperature below 100 K. Cryogenics 34(ICEC Suppl.):167–170
3. Dodson C, Razani A, Roberts T (2010) Inertance tube modeling and the effects of temperature. AIP Conf Proc 1218:121–127
4. Dang H (2012) 40 K single-stage coaxial pulse tube cryocoolers. Cryogenics 52:216–220
5. Chen L, Zhang Y, Luo E, Li T, Wei X (2010) CFD analysis of thermodynamic cycles in a pulse tube refrigerator. Cryogenics 50(11):743–749
6. Ren J, Dai W, Luo E (2011) Experimental Investigation on a single-stage stirling-type pulse tube cryocooler working below 30 K. Cryocoolers 16, ICC Press, Boulder, CO, pp 51–55
7. Kumara P, Gupta AK (2019) Numerical investigation of a 3D inertance pulse tube refrigerator from design prospective. Cryogenics 98:125–138
8. Liu S, Jiang Z, Zhang A et al (2018) High efficiency 35 K single-stage pulse tube cryocooler for a space infrared detector. Cryocoolers 20, ICC Press, Boulder, CO, pp 57–61
9. ANSYS Inc. (2015) ANSYS fluent theory guide 12.0

CFD Modeling of High-Pressure Subcooled Flow Boiling in Vertical Pipes

Saikrishna Nadella and Naresh Kumar Maheshwari

1 Introduction

When the heat flux at a heated wall reaches to such a high value that forced convection and conduction solely cannot maintain the wall temperature below the saturation temperature of coolant, vapor bubble nucleation starts. Various local phenomena that occur near the wall during boiling enhances the heat transfer several folds making it an attractive option in many industries for component cooling. The overall heat transfer performance of boiling process depends on various parameters ranging from microscopic surface characteristics to macroscopic system variables (pressure, mass flux, etc.). Owing to the complex multi-parameter dependency of various multi-scale processes involved in this phase change process, the predictive models are still evolving.

Eulerian-Eulerian Two Fluid (EETF) model in conjunction with Wall Heat Flux Partitioning (WHFP) model are proven to provide suitable framework for component scale boiling flow simulation [1, 2]. However, this framework still need significant number of closure relations derived mechanistically/experimentally as input. Availability of validated correlations for high-pressure condition is scarce [2] due to difficulty in performing experiments and measurements at high pressure, high temperature conditions.

Evolving nature of the computational models brings the attention of researchers to open-source codes like OpenFOAM which have flexibility to incorporate and test new models. EETF and WHFP models along with various closure models proposed for simulation of subcooled boiling flows were incorporated in OpenFOAM. It is necessary to perform extensive evaluation studies of the present model and solver against experimental data to establish the capabilities and to identify the areas of improvement.

S. Nadella (✉) · N. K. Maheshwari
Bhabha Atomic Research Centre, Trombay, Mumbai 400085, India
e-mail: nskrishna@barc.gov.in

2   Literature Review and Objective

Krepper et al. [1] performed CFD studies of subcooled flow boiling in CFX solver with a set of closure relations and validated against the experimental data of [3, 4]. They observed that the proposed model has a general validity range from 30 to 110 bar, up to 1.2 MW/m^2 and at about 1000 kg/m^2/s. They also highlighted that lift and wall lubrication forces have negligible effect on cross-section averaged void fraction profiles, while they influence radial distribution of vapor. Rezhak et al. [5] performed a comparison of OpenFOAM with CFX for adiabatic air–water mixture flows. They noted that even with implementation of same CFD model in OpenFOAM as in CFX, the predictions from OpenFOAM could not be matched with CFX solver without fine-tuning of some model parameters. Fu and Anglart [6] implemented the EETF and WHFP models along with Interfacial Area Concentration Transport Equation in OpenFOAM and compared the results with few experimental data. They also noted that the requirement to fine-tune the turbulence dispersion coefficient to obtain accurate predictions of void fraction. Yang et al. [7] performed parametric studies in OpenFOAM to evaluate various nucleation site density models at near atmospheric pressure in vertical annulus.

Due to the complexity of the phenomena and uncertainty in applicability of various closure relations, the predictions of state-of-the-art CFD models also deviate from experiment to experiment. Fine-tuning of various model constants was necessary in various validation exercises [1, 5–8]. Therefore, unlike earlier studies with Open-FOAM, current study aims to investigate the performance of the solver on the experimental data of [3, 4] with large range of operating conditions, covering the pressure range of 15–150 bar, mass flux of 500–2000 kg/m^2/s and heat flux of 0.4–2 MW/m^2.

3   Materials and Methods

OpenFOAM version 7 [9] is used in current study. The EETF and WHFP models implemented in OpenFOAM7 along with all other necessary closure models are very briefly given in the following subsections. Specific details of implementation of these models may be referred from OpenFOAM7 source code.

3.1   Eulerian-Eulerian Two Fluid (EETF) Model

The conservation equations of Eulerian-Eulerian Two Fluid model are given below.

$$\frac{\partial \rho_l \alpha_l}{\partial t} + \nabla.(\rho_l \boldsymbol{U}_l \alpha_l) = \dot{m}_{vl} - \dot{m}_{lv}, \tag{1}$$

$$\frac{\partial \rho_l \alpha_l \boldsymbol{U_l}}{\partial t} + \nabla.(\rho_l \alpha_l \boldsymbol{U_l} \boldsymbol{U_l}) = -\alpha_l \nabla p$$
$$+ \nabla.(\alpha_l \boldsymbol{R}_{l,\text{eff}}) + \rho_l \alpha_l \boldsymbol{g} + \boldsymbol{F_{vl}} + \dot{m}_{vl} \boldsymbol{U_v} - \dot{m}_{lv} \boldsymbol{U_l}, \tag{2}$$

$$\frac{\partial \rho_l \alpha_l (h_l + K_l)}{\partial t} + \nabla.(\rho_l \alpha_l \boldsymbol{U_l}(h_l + K_l))$$
$$= \alpha_l \frac{\partial p}{\partial t} + \nabla.(\alpha_l \alpha_{l,\text{eff}} \nabla h_l) + \dot{m}_{vl}(h_{lf} + K_v)$$
$$- \dot{m}_{lv}(h_l + K_l) + H_{lf} A_f (T_f - T_l) + \rho_l \alpha_l \boldsymbol{g}.\boldsymbol{U_l}, \tag{3}$$

$$\frac{\partial \rho_v \alpha_v}{\partial t} + \nabla.(\rho_v \boldsymbol{U_v} \alpha_v) = \dot{m}_{lv} - \dot{m}_{vl}, \tag{4}$$

$$\frac{\partial \rho_v \alpha_v \boldsymbol{U_v}}{\partial t} + \nabla.(\rho_v \alpha_v \boldsymbol{U_v} \boldsymbol{U_v})$$
$$= -\alpha_v \nabla p + \nabla.(\alpha_v \boldsymbol{R}_{v,\text{eff}})$$
$$+ \rho_v \alpha_v \boldsymbol{g} + \boldsymbol{F_{lv}} + \dot{m}_{lv} \boldsymbol{U_l} - \dot{m}_{vl} \boldsymbol{U_v}, \tag{5}$$

$$\frac{\partial \rho_v \alpha_v (h_v + K_v)}{\partial t} + \nabla.(\rho_v \alpha_v \boldsymbol{U_v}(h_v + K_v))$$
$$= \alpha_v \frac{\partial p}{\partial t} + \nabla.(\alpha_v \alpha_{v,\text{eff}} \nabla h_v) + \rho_v \alpha_v \boldsymbol{g}.\boldsymbol{U_v}$$
$$+ \dot{m}_{lv}(h_{vf} + K_l) - \dot{m}_{vl}(h_v + K_v) + H_{vf} A_f (T_f - T_v). \tag{6}$$

Equations 1–6 are continuity, momentum, and energy conservation equations of liquid phase and vapor phase, respectively. Due to space constraints the meaning of all the symbols used in this paper are summarized in Nomenclature section. The symbols in bold face are vectors/tensors.

3.2 Wall Heat Flux Partitioning (WHFP) Model

WHFP model is used to maintain the heat balance at the wall considering various heat transfer mechanisms like evaporation, quenching, and forced convection. OpenFOAM7 has this model implemented in the form given below based on [10]

$$q = q_E + q_C + q_Q + (1 - f_{\text{Liquid}}) q_V, \tag{7}$$

$$f_{\text{Liquid}} = \begin{cases} 1 - \frac{1}{2} e^{-20(\alpha_l - \alpha_{\text{crit}})} & \alpha_l \geq \alpha_{\text{crit}} \\ \frac{1}{2} \left(\frac{\alpha_l}{\alpha_{\text{crit}}} \right)^{20\alpha_{\text{crit}}} & \alpha_l < \alpha_{\text{crit}} \end{cases}, \tag{8}$$

where $\alpha_{\mathrm{crit}} = 0.2$.

The functional forms of various heat flux components as implemented in OpenFOAM7 are given below

$$q_C = \alpha_{t,l} A_1 \left. \frac{\mathrm{d}h_l}{\mathrm{d}n} \right|_w, \tag{9}$$

$$q_E = \frac{1}{6} A_{2E} d_{\mathrm{dep}} \rho_{vw} f_{\mathrm{dep}} L^*, \tag{10}$$

$$q_Q = 2 A_2 \alpha_w C_{pw} f_{\mathrm{dep}} \sqrt{\frac{0.8/f_{\mathrm{dep}}}{(\pi \alpha_w)/\rho_w}} (T_w - T_l^*), \tag{11}$$

$$q_V = \alpha_{t,v} \left. \frac{\mathrm{d}h_v}{\mathrm{d}n} \right|_w. \tag{12}$$

$\alpha_{t,i}$ is calculated from turbulent thermal wall functions using formulation of [11]. The liquid temperature T^*_l in Eq. (11) is determined from turbulence thermal wall function at $y^+ = 250$ to avoid grid dependence [1]. The area fractions A_1, A_2 and A_{2E} are defined as follows:

$$A_2 = \min\left(\frac{\pi}{4} d_{\mathrm{dep}}^2 N A_l, 1\right), \tag{13}$$

$$A_1 = 1 - A_2, \tag{14}$$

$$A_{2E} = \min\left(\frac{\pi}{4} d_{\mathrm{dep}}^2 N A_l, 5\right), \tag{15}$$

$$A_l = 4.8 f_{\mathrm{Liquid}} e^{-\frac{Ja}{80}}; Ja = \frac{\rho_{lw} C_{pw} (T_{\mathrm{Sat},w} - T_l)}{\rho_{vw} L}. \tag{16}$$

The total wall heat flux is also given by Fourier law as

$$q = \frac{\alpha_l \gamma_{l,\mathrm{eff}} (T_w - T_l)}{\Delta l} + \frac{\alpha_v \gamma_{v,\mathrm{eff}} (T_w - T_v)}{\Delta l}. \tag{17}$$

The implementation of this wall boiling model in OpenFOAM7 is in such a way that the effective thermal conductivity of liquid phase at wall includes contributions from convection, evaporation, and quenching heat transfer mechanisms.

By inserting Eqs. (17)–(7), the latter is iteratively solved to obtain the heated wall temperature and partitioning of heat flux among the flux components given in Eq. (7).

For nucleation site density and bubble departure diameter, the correlations of Lemmert and Chawla [12] and Tolubinsky-Kostanchuk [1] are chosen as recommended by [1, 8]. They are given by

$$N = 210^{1.805}(T_w - T_{\text{sat}})^{1.805}, \tag{18}$$

$$d_{\text{dep}} = \min\left(0.6\,[\text{mm}] * \exp\left(-\frac{T_{\text{sat},w} - T_l}{45}\right), 1.4\,[\text{mm}]\right). \tag{19}$$

For bubble departure frequency the correlation given by Cole [1] is used.

3.3 Interfacial Forces

The interfacial forces represented by F_{lv} and $F_{vl} (= - F_{lv})$ in Eqs. (2) and (5) comprise of drag, lift, wall lubrication, turbulence dispersion, and virtual mass forces.

In the current study, only virtual mass, drag, and turbulence dispersion forces are taken into consideration based on observations from [1, 8].

3.3.1 Drag

The relative motion between bubbles and surrounding liquid leads to a resisting force on bubbles against the relative motion. This is accounted by drag force with following formulation.

$$F_{\text{drag}} = -\frac{3}{4d_b^2}C_D\text{Re}_{\text{rel}}\mu_l\alpha_v(\boldsymbol{U_v} - \boldsymbol{U_l}). \tag{20}$$

To determine the drag coefficient C_D in the above expression, the correlation of Ishii and Zuber [1] is used. This correlation takes into consideration large range of Reynolds number and Eotvos number and incorporates the effect of bubble distortion on the drag force.

3.3.2 Virtual Mass

Virtual mass force acts on bubbles accelerating in surrounding liquid. It is modeled as

$$\boldsymbol{F_{\text{vm}}} = -C_{\text{vm}}\rho_l\alpha_v\left(\frac{D_l\boldsymbol{U_l}}{dt} - \frac{D_v\boldsymbol{U_v}}{dt}\right). \tag{21}$$

C_{vm} is virtual mass coefficient given by 0.5.

3.3.3 Turbulence Dispersion

The liquid phase turbulence causes dispersion of vapor bubbles. This force is modeled by following relation given by [9]

$$F = \left(\frac{3}{4}C_{\mathrm{D}}\mathrm{Re}_{\mathrm{rel}}\frac{\rho_l \alpha_v \nu_l}{d_b^2}\right) \times \frac{\nu_{l,\mathrm{turb}}}{\sigma_t} \times \left(\frac{1}{\alpha_l} + \frac{1}{\alpha_v}\right)\nabla\alpha_v. \tag{22}$$

σ_t is taken as 0.7.

3.4 Interfacial Heat and Mass Transfer

Heat transfer across the interface between liquid and vapor phases is determined using two-resistance based formulation. In this method, every cell in computational grid contains three different temperature data, viz. liquid, vapor, and interface. Heat transfer resistance is offered on both liquid and vapor sides of the interface. Heat transfer from liquid and gas to interface is modeled as follows:

$$q_{lf} = H_{lf}A_f(T_l - T_f); q_{vf} = H_{vf}A_f(T_v - T_f). \tag{23}$$

Since the vapor phase predominantly exists in bubble form in subcooled boiling flow, these heat transfer coefficients are calculated by Ranz-Marshall correlation [1] on liquid side and by Nu = 10 on vapor side. T_f assumes the saturation temperature at local pressure. The heat transfer across the interface is utilized in phase change depending on the temperatures of liquid and vapor and saturation temperature corresponding to local pressure. Mass transfer rate is thus calculated as

$$\dot{m}_{vl} = \frac{H_{lf}A_f(T_f - T_l) + H_{vf}A_f(T_f - T_v)}{L^*}, \tag{24}$$

$$L^* = \begin{cases} h_{vf} - h_l & \text{heat trans. with evap.} \\ h_v - h_{lf} & \text{heat trans. with cond.} \\ h_{vf} - h_{lf} & \text{pure sensible heat trans.} \end{cases} \tag{25}$$

The above definition of L^* takes care of sensible heat transfer as well as phase change consistent to energy conservation equations (Eqs. 3 and 6).

Mass transfer due to evaporation of liquid at the heated wall is calculated based on WHFP model and given as source term to EETF model as follows:

$$\dot{m}_{lv} = \frac{q_E}{h_{v,\mathrm{sat}}(p) - h_{l,c}}. \tag{26}$$

This expression takes care of sensible heating of liquid in wall adjacent cell to saturation temperature and supply of latent heat for vaporization.

3.5 Turbulence Model

Turbulence of liquid phase is modeled with SST k-ω model [1], while vapor phase turbulence is assumed to be negligible in subcooled boiling flow. Contribution from bubble induced turbulence is accounted in the liquid phase effective viscosity by Sato et al. [1] model.

3.6 Bubble Diameter

The bubble diameter is a very important parameter which affects the interfacial forces and interfacial heat transfer between liquid and vapor phase. To determine the diameter of bubble surrounded by subcooled liquid, following expression [13] is implemented in OpenFOAM7 by the authors and used.

$$d_b = \begin{cases} 0.00015 & T_{\text{sub}} > 13.5 \\ -0.0001 T_{\text{sub}} + 0.0015 & 0 < T_{\text{sub}} \leq 13.5 \\ 0.0015 & T_{\text{sub}} \leq 0 \end{cases} . \tag{27}$$

4 Validation Data

The experimental data for the current study is obtained from [3, 4] for subcooled flow boiling in vertical pipes, because of large range of operating conditions investigated by [3, 4]. The conditions for which the simulations are performed are summarized in Table 1.

Maximum absolute error in vapor volume fraction was reported as $\pm$ 0.04 in full range of operating conditions.

Table 1 Experimental data [3, 4] used for validation

S. No.	ID (mm)	Pressure p (bar)	Mass flux G (kg/m^2/s)	Heat flux q (MW/m^2)
1	15.4	15	900	0.38
2		30	900	0.38
3		45	900	0.38
4	24	15	900	0.38
5		30	900	0.38
6		45	900	0.38
7		15	900	0.8
8		30	900	0.8
9		45	900	0.8
10	12	30.1	990	0.98
11		44.1	994	0.90
12		68.9	405	0.79
13		68.1	998	0.44
14		68.9	965	0.78
15		68.4	961	1.13
16		67.4	988	1.70
17		70.1	996	1.98
18		68.9	1467	0.77
19		67.9	2024	0.78
20		68.1	2037	1.13
21		108.1	966	1.13
22		108.1	1564	1.16
23		108.4	1959	1.13
24		147.9	1878	0.42
25		147.4	1847	0.77

5 Case Setup in OpenFoam

5.1 Geometry, Mesh, and Boundary Conditions

Three 2D-axisymmetric wedge models with included angle of 5° are prepared to cover both the experimental datasets, with 15.4, 24, and 12 mm inner diameters (ID) with uniform hexahedral mesh using *blockMesh* utility.

For the inlet, values are specified for velocity and other scalars. At outlet, pressure is specified and zero normal gradient boundary condition is used for all other scalars and velocity field. At wall, boiling model is enabled with specified heat flux. No slip condition is given for liquid, while slip is allowed for vapor at the wall.

5.2 Material Properties

The properties of water in both liquid and vapor phases are specified as constant, from [14], at saturation temperature (T_{sat}) corresponding to operating pressure. The enthalpy of both the phases at temperature other than T_{sat} is calculated based on specific heat capacity specified at T_{sat}.

5.3 Solver Settings

PIMPLE algorithm is used for pressure–velocity coupling. Local Time Stepping (LTS) technique of OpenFOAM is used to obtain steady state results. Second-order discretization schemes are used for all the terms in Eqs. (1–6).

6 Results and Discussion

6.1 Grid Independency Study

Multiple grids are generated with combinations of 10, 20, 40, and 80 cells in radial direction and 150 and 300 cells in axial direction. Cell size is maintained uniform in both directions. Experimental data of [3] with 15.4-mm-inner-diameter tube of 2 m length, 900 kg/m^2/s mass flux and 570 kW/m^2 heat flux is chosen for this study. Cross-section averaged vapor volume fraction, bulk liquid temperature and wall temperature are plotted for various grids in Figs. 1 and 2. It can be observed that grid variation in axial direction doesn't have any influence on the results. The grid variation in radial direction continues to show effect on cross-section averaged vapor volume fraction profiles, while its effect on temperature data is insignificant. As noted in literature earlier [2], grid dependency is one inherent problem of EETF and WHFP models due to various closure relations. It was also mentioned that different grid sizes perform well for different experimental datasets. So, an optimum mesh with respect to accuracy results for whole range of operating conditions and computational effort to be chosen. So, the grids 20 × 150, 32 × 150, 16 × 130 are chosen for 15.4, 24, and 12 mm ID test sections in the current study.

6.2 Validation with Experimental Data

Figures 3, 4 and 5 show the comparison of void fraction predictions from current study with experimental data of [3], while Figs. 6, 7, 8, 9 and 10 show the comparison of the predicted void fraction with experimental data of [4]. The legend entries in

Fig. 1 Grid independency
study: void fraction
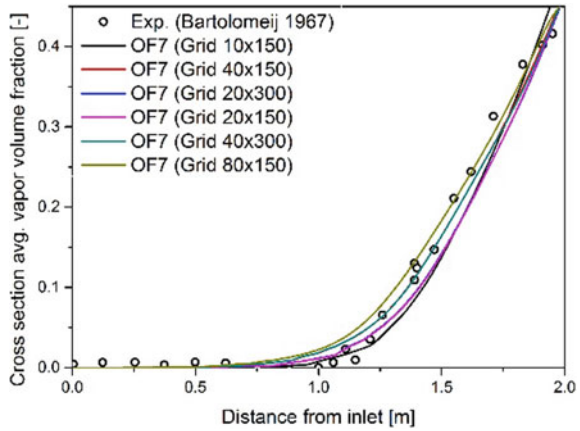
Fig. 2 Grid independency
study: temperature
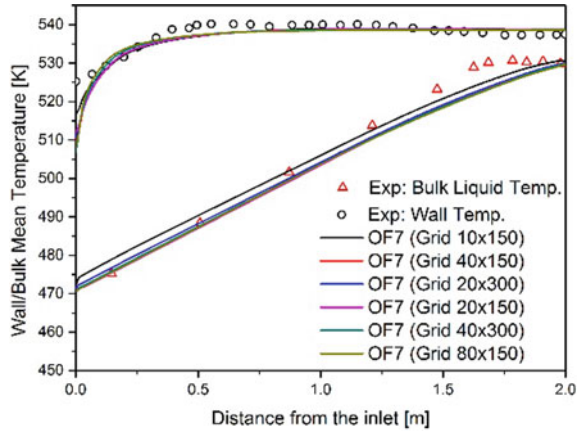
these figures can be read as G [kg/m^2/s]_q [MW/m^2]_p [bar]. The known principles
on effect of pressure on void fraction profiles and the quality at onset of intense
boiling [4] are well captured by the model. For example, with increase in pres-
sure, the void fraction at same thermodynamic quality, increases at the beginning
of non-equilibrium zone and decreases near the end of non-equilibrium zone [4].
This leads to cross-over in the void fraction profiles as can be seen in Figs. 3–5 and
10. With increase in pressure, the thermodynamic quality at which intense boiling
starts, decreases. Qualitative and quantitative accuracy of predictions are given by
correlation coefficient (r) and Root Mean Square Deviation (RMSD), respectively.
The qualitative trends in the data are well predicted by the model ($r > 0.95$ for 23
out of 25 cases and $r > 0.98$ for 16 out of 25 cases studied), while significant quan-
titative deviations observed (RMSD for 15.4 and 24 mm ID runs are 0.02–0.06 and
0.06–0.12, respectively, against reported maximum experimental error of $\pm$ 0.04
[4]).

Fig. 3 Effect of pressure on vapor volume fraction at $G = 900$ kg/m^2/s, $q = 0.38$ MW/ m^2 (ID = 15.4 mm)
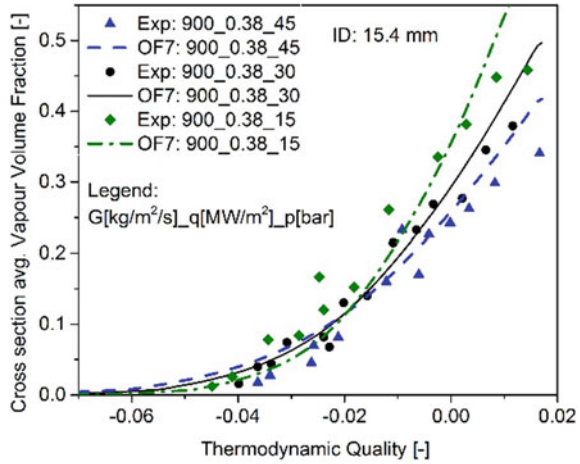
Fig. 4 Effect of pressure on vapor volume fraction at $G = 900$ kg/m^2/s, $q = 0.8$ MW/m^2 (ID = 24 mm)
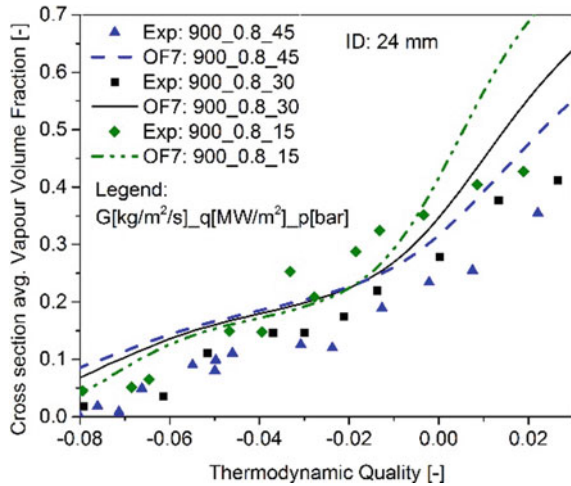
Figures 6 and 7 show the effect of heat flux on void fraction profiles at 70 bar and 150 bar, respectively. The general trends of void fraction profiles are predicted well at 70 bar ($r \geq 0.99$) and reasonably at 150 bar ($r = 0.96$–0.97). At 70 bar and ~ 1000 kg/m^2/s, the predictions are good (RMSD = 0.03–0.06) for $q \leq 1.13$ MW/m^2, while they become poorer with rise in heat flux (RMSD > 0.08). At 150 bar and ~ 1850 kg/m^2/s, void fraction is significantly (RMSD > 0.12) over predicted for both heat fluxes, 0.42 and 0.77 MW/m^2.

Figures 8 and 9 show effect of mass flux on void fraction at 70 bar and 110 bar, respectively. At 70 bar and ~ 0.8 MW/m^2, the void fraction predictions vary from under-prediction at 405 kg/m^2/s (RMSD = 0.07) to over-prediction at 2024 kg/m^2/s (RMSD = 0.05), with good match at 965 kg/m^2/s (RMSD = 0.03). At 110 bar and

Fig. 5 Effect of pressure on vapor volume fraction at $G = 900$ kg/m^2/s, $q = 0.38$ MW/m^2 (ID = 24 mm)
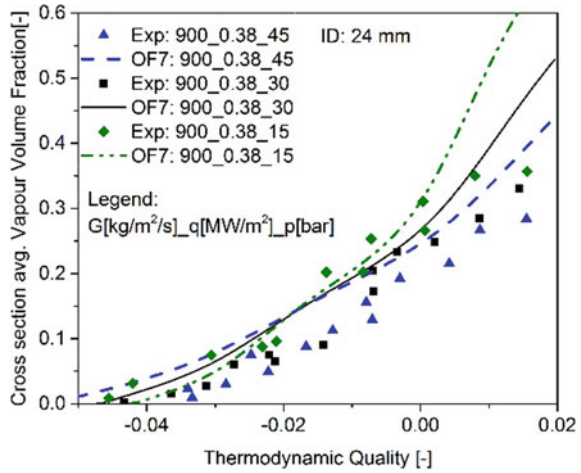
Fig. 6 Effect of heat flux on vapor volume fraction at about 70 bar (ID = 12 mm)
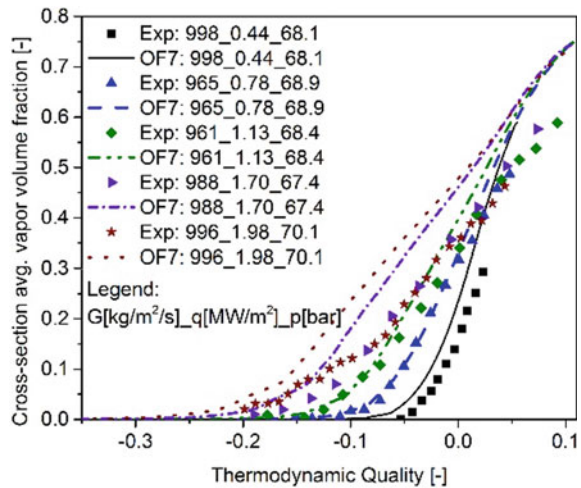
~ 1.13 MW/m^2 also, similar trend is observed. Predictions are good at 966 kg/m^2/s (RMSD = 0.03) and poorer with rise in mass flux (RMSD = 0.1 for 1959 kg/m^2/s).

From Figs. 7, 8 and 9, it can be seen that the thermodynamic quality at which onset of intense boiling is predicted, shifts toward lower values for mass fluxes above 1000 kg/m^2/s.

Figure 10 shows effect of pressure on void fraction profiles for ~ 1000 kg/m^2/s. The prediction accuracy improved with increase in the pressure, from RMSD = 0.09 at 30 bar to RMSD = 0.03 at 108 bar.

Fig. 7 Effect of heat flux on vapor volume fraction at about 150 bar (ID = 12 mm)
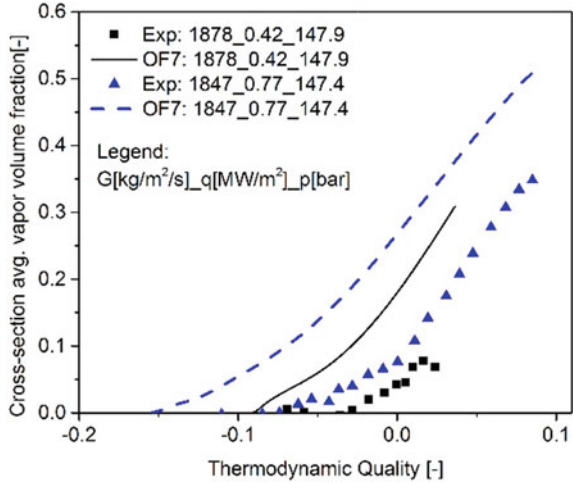
Fig. 8 Effect of mass flux on vapor volume fraction at about 70 bar (ID = 12 mm)
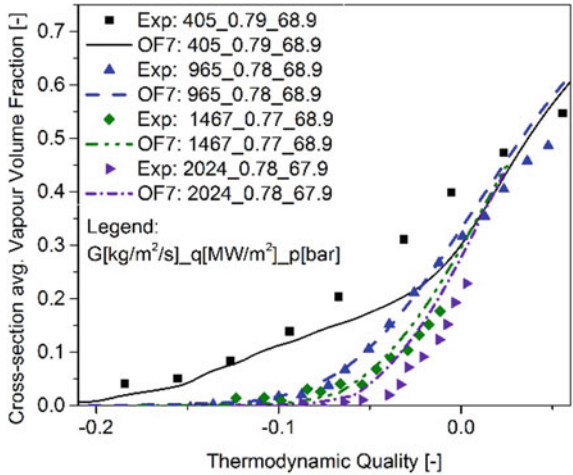
7 Conclusions

EETF and WHFP model framework available in OpenFOAM7 is evaluated with experimental data of large range of operating conditions using generally recommended closure models. It is found that the examined model gives good predictions ($r = 0.97$–0.999; RMSD = 0.02–0.06) in the common parameter range of, mass flux ~ 1000 kg/m^2/s, heat flux below 1.2 MW/m^2, and pressures from 30 to 110 bar for pipe diameters of 12 and 15.4 mm. Similar observations were reported earlier with ANSYS CFX [1]. The RMSD values need to be seen against the reported maximum

Fig. 9 Effect of mass flux on vapor volume fraction at about 110 bar (ID = 12 mm)
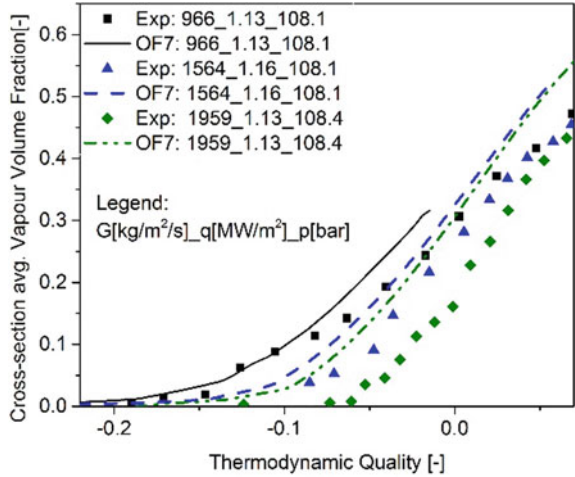
Fig. 10 Effect of pressure on vapor volume fraction at about 1000 kg/m²/s (ID = 12 mm)
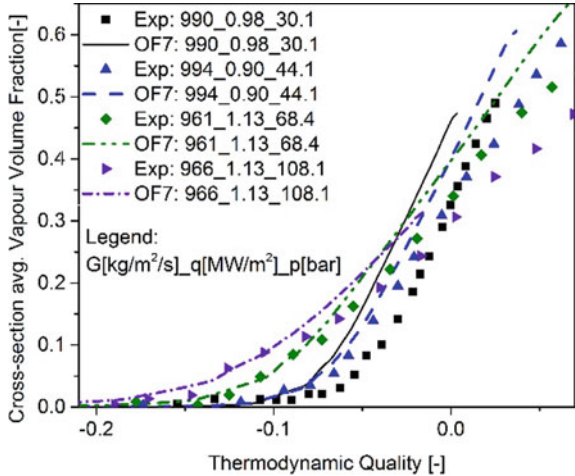
error of ± 0.04 in void fraction measurement [4], as experiment-wise uncertainties were not reported.

Further investigation is required with respect to grid dependency of these models and their implementation.

This study brings out the general applicability and accuracy of the investigated CFD model and OpenFOAM solver for subcooled boiling flows. This study is expected to serve as baseline for further research in improving the CFD model and their implementation and testing in OpenFOAM.

Nomenclature

U	Velocity [m/s]
p	Pressure [Pa]
p_{rgh}	Reduced pressure ($= p - \rho \boldsymbol{g}.\boldsymbol{z}$) [Pa]
g	Gravitational acceleration ($= 9.81$) [m/s^2]
F_{ij}	Force by phase i on phase j [N]
R_{eff}	Tensor with viscous and Reynolds stresses [N/m^2]
h	Enthalpy [J/kg]
q	Heat flux [W/m^2]
K	Kinetic energy [J/kg]
$\dot{m}_{ij}$	Mass transfer from phase i to phase j [kg/m^3/s]
H_{if}	Heat transfer coefficient between phase i and interface [W/m^2/K]
A_f	Interfacial area density ($= 6\alpha_v/d_b$) [1/m]
T	Temperature [K]
C_p	Specific heat capacity [J/kg/K]
C_D	Drag coefficient
f_{dep}	Bubble departure frequency [1/s]
d_{dep}	Bubble departure diameter [m]
N	Nucleation site density [1/m^2]
d/dn	Wall normal gradient [1/m]
D_i/dt	Total derivative with respect to phase i [1/s]
L^*	Ref. Eq. (26) [J/kg]
Eo	Eotvos number
Re	Reynolds number
r	Correlation coefficient
α	Volume fraction (as in α_l and α_v) [–] or γ/C_p (as in $\alpha_{t,l}$) [kg/m/s]
ρ	Density [kg/m^3]
ω	Turbulence dissipation frequency [1/s]
γ	Thermal conductivity [W/m/K]
μ	Dynamic viscosity [Pa s]
ν	Kinematic viscosity [m^2/s]

Subscripts

l	Liquid phase
v, V	Vapor phase
f	Interface
t	Turbulent
eff	Effective
w	Near wall properties
Q	Quenching

E	Evaporation
C	Convection
c	Wall adjacent cell center
sat	Saturation state
sub	Subcooling

References

1. Krepper E, Končar B, Egorov Y (2007) CFD modelling of subcooled boiling—concept, validation and application to fuel assembly design. Nucl Eng Des 237(7):716–731
2. Murallidharan JS, Prasad BVSSS, Patnaik BSV, Hewitt GF, Badalassi V (2016) CFD investigation and assessment of wall heat flux partitioning model for the prediction of high pressure subcooled flow boiling. Int J Heat Mass Transf 103:211–230
3. Bartolomej GG, Chanturiya VM (1967) Experimental study of true void fraction when boiling subcooled water in vertical tubes. Therm Eng 14:123–128
4. Bartolomej GG, Brantov VG, Molochnikov YuS et al (1982) An experimental investigation of true volumetric vapour con-tent with subcooled boiling in tubes. Therm Eng 29:132–135
5. Rzehak R, Kriebitzsch S (2015) Multiphase CFD-simulation of bubbly pipe flow: a code comparison. Int J Multiph Flow 68:135–152
6. Fu K, Anglart H (2017) Implementation and validation of two-phase boiling flow models in OpenFOAM. arXiv:1709.01783v1
7. Yang C, Cai J, He S (2021) Evaluation of various active nucleation site density models of subcooled flow boiling in a vertical tube using OpenFOAM. Prog Nucl Energy 138:103800
8. Vadlamudi SRG, Nayak AK (2019) Effect of boiling and momentum closures on the prediction of subcooled flow boiling. Multiph Sci Technol 31(4):319–344
9. OpenFOAM. https://openfoam.org
10. Lavieville J, Quemerais E, Mimouni S, Boucker M, Mechitoua N (2005) NEPTUNE CFD V1.0 theory manual. EDF
11. Jayatillaka C (1969) The influence of Prandtl number and surface roughness on the resistance of the laminar sublayer to momentum and heat transfer. Prog Heat Mass Transf 1:193–321
12. Lemmert M, Chawla LM. Influence of flow velocity on surface boiling heat transfer coefficient in heat transfer in boiling. In: Hahne E, Grigull U (eds) Academic Press and Hemisphere, New York, NY, USA (1977)
13. Anglart H, Nylund O, Kurul N, Podowski MZ (1997) CFD prediction of flow and phase distribution in fuel assemblies with spacers. Nucl Eng Des 177:215–228
14. NIST Webbook. https://webbook.nist.gov

Potential Flow Around Square Cylinder with Rounded Corners

Dhaval T. Solanki and Dharmendra S. Sharma

1 Introduction

The fluid flow around square-shaped structures are observed in wide range of applications such as offshore floating platforms, piers of bridges, skyscrapers and suspension bridges. In many of these applications, the square structures are furnished with sharp corners or modified corners. The corner modifications such as chamfered, recessed, and rounded corners of square structures are provided for the purpose of drag reduction, suppression of flow induced vibration, passive flow control, and enhancement of strength of structures by avoiding stress concentration.

Many researchers have studied flow behaviour around square cylinders with sharp corners by using different numerical [1–6] and experimental methods [7–11]. The effects of chamfered corner modification [12, 13] and recessed corner modifications [14] are considered by some of the researchers in their studies. While, the rounded corner modification on square structure is emphasised by many researchers in experimental [15–17] and numerical [18–20] studies. Hu and Zhou [21] considered square cylinder with radius at the corners in the study of wake behind the square bodies. The effect rounded corners on the heat transfer from the surface of square cylinder is investigated by Alam and Zafar [22]. Dey and Das [23] numerically studied the effect of different radius of corners on boundary layer thickness, velocity magnitude and pressure co-efficient distribution, and drag force acting on square cylinder. In their study, Dey et al. [24] have used Artificial Neural Network (ANN) to predict the aerodynamic behaviour of square cylinder with the radius at the corners in steady flow regime. Hinsberg et al. [25, 26] have conducted wind tunnel experiments on

D. T. Solanki (✉) · D. S. Sharma
Department of Mechanical Engineering, Faculty of Technology and Engineering, The Maharaja Sayajirao University of Baroda, Vadodara 390002, India
e-mail: dhaval.solanki-med@msubaroda.ac.in

D. S. Sharma
e-mail: dss_iit@yahoo.com; d.s.sharma-med@msubaroda.ac.in

rounded corner square cylinder to study the effect of roundness and incident angle on aerodynamic load.

The potential flow [27–29] model can also be adopted to investigate the effect of rounded corners on the flow parameters of flow over square cylinder at large Reynolds number. The potential flow around square cylinder can be obtained by mapping the area outside the circle to the area outside the square geometry. Such solution of potential flow around the square cylinder with sharp corners is attempted by Tian and Wu [30] by using Schwarz-Christoffel mapping along with complex potential function. Kim and Kim [31] gave the approximate analytical solution of potential flow around the square cylinder with sharp corners by using series multipolar expansion. The potential flow around rounded corner polygonal cylinder is given by Solanki and Sharma [32] using hypotrochoidal mapping [33–36].

In present research article, the potential flow around rounded corner square cylinder is investigated using complex variable method. The mapping function is developed from the parametric equations of hypotrochoid to map the area outside the circle to the area outside the rounded corner square geometry. The effect of corner roundness, flow angles, and vortex around the cylinder on the hydrodynamic parameters is studied. The comparison of the present results of velocity magnitude and pressure co-efficient with the results derived from ANSYS and available literature is done.

2   Mathematical Method

The mathematical formulation to obtain the potential flow around the square cylinder with the corner radius ρ is discussed in this section. The complex potential function $W_U(\zeta)$ for uniform flow, $W_c(\zeta)$ for circulatory flow, and $W_v(\zeta)$ for vortex around the cylinder are superimposed to obtain solution of potential flow. This solution is mapped around the square cylinder with different corner radius (ρ) by using the hypotrochoidal mapping function.

2.1   Mapping Function

The mapping function is developed here to map the square geometry with finite radius at the corners and sides of which are hypotrochoids. The hypotrochoid is the curve sketched by point fixed on a circle (rolling/generating circle) rolls inside another circle (directing circle) of larger relative size without slipping. For the directing circle of radius four time larger than the radius of rolling circle, the parametric equations of the of hypotrochoids are given as follow:

$$x(\theta) = 3r\cos(\theta) - h\cos(3\theta); \tag{1a}$$

$$y(\theta) = 3r \sin(\theta) + h \sin(3\theta), \tag{1b}$$

where r is the radius of rolling circle, h is the distance between the point tracing the curve and the centre of rolling circle. The radius at the corners of the mapped square geometry depends on the value of h. For $h = 0$, the circle, and for $h = r$, the square with sharp corners is mapped. For any other value of $0 < h < r$, the square is mapped with finite radius at the corners. Therefore, the corner radius 'ρ' can be defined which is the function of parameter h and r. The general formula for radius of curvature is

$$\rho_1 = \frac{\left[1 + \left(\frac{dy}{dx} \right)^2 \right]^{3/2}}{\frac{d^2 y}{dx^2}}. \tag{2}$$

The corner radius in above relation can be normalised as $\rho = \rho_1/c$, where $c = 3r$ is the radius of circle traced by the centre of rolling circle. By substituting derivatives of parametric Eq. (1) in above relation, the normalised corner radius is

$$\rho = \frac{(r - h)^2}{r(r + 3h)}. \tag{3}$$

By substituting the 'h' from above relation as a function of corner radius 'ρ' in the parametric Eq. (1) of hypotrochoid, the following mapping function is developed to map the area outside the square shape with finite radius at the corners from the area outside the circle (refer Fig. 1a),

$$Z = \frac{-4r\left(3\rho - \sqrt{\rho(9\rho + 16)} - 6\zeta^4 + 2 \right)}{8\zeta^3}. \tag{4}$$

For the corner radius $\rho = 1$ the circle is traced, and for $\rho = 0$ the square geometry with cusps is generated. For $0 < \rho < 1$, the square with finite corner radius can be mapped. Figure 1b shows the mapping geometries with different corner radius mapped using the mapping function (Eq. 4).

2.2 Complex Potential Function

The complex potential functions are presented here for uniform potential flow, point vortex flow, and circulatory flow around the circular cylinder.

(a)

(b)

$\rho=0$ $\rho=0.2$ $\rho=0.4$ $\rho=0.6$ $\rho=0.8$ $\rho=1$
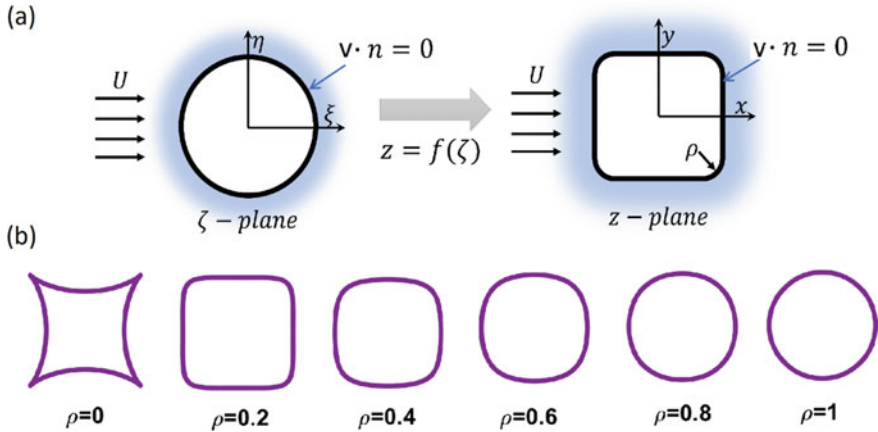
Fig. 1 **a** Conformal mapping of outer region of a circle to the outer region of a square with rounded corners and **b** the square geometries with different corner radius ρ

2.2.1 Uniform Potential Flow: W_U

The complex velocity potential function for uniform potential flow at an angle of attack α in complex ζ-plane around the circular cylinder is given as

$$W_U = U\left(\zeta e^{i\alpha} + \frac{a^2}{\zeta}e^{-i\alpha}\right), \tag{5}$$

where 'U' is a freestream velocity of uniform potential flow and 'a' is the radius of circular cylinder.

2.2.2 Point Vortex Around the Cylinder: W_v

The complex velocity potential for the vortex outside the circular cylinder can be obtained by means of Milne-Thomson circle theorem [37–40]. For the vortex element of strength γ_v at $\zeta_v = r_v e^{i\theta_v}$ outside the circular cylinder, the complex potential function is written as

$$W_U = -\frac{i\gamma_v}{2\pi}\log\left(\frac{\zeta - \zeta_v}{\zeta - \overline{\zeta}_v^{-1}}\right). \tag{6}$$

Above complex potential function produces the circulation $-\gamma_v$ around the cylinder.

2.2.3 The Circulatory Flow: W_c

To change the net circulation around the cylinder without changing the circulation γ_v of vortex at ζ_v, the point vortex of strength γ_c at $\zeta = 0$ can be placed. The complex velocity potential function for such circulatory flow is written as

$$W_c = -\frac{i\gamma_c}{2\pi}\log(\zeta). \tag{7}$$

The total complex velocity potential function is the superposition of complex potential functions for cases considered above and written as.

$$W = W_U + W_v + W_c. \tag{8}$$

The net circulation around the cylinder due to superposition of uniform, vortex and circulatory flow is $-\gamma_v - \gamma_c$.

By using above complex velocity potential and conformal transformation (Eq. 4) together, the potential flow can be obtained over the square cylinder with finite radius at the corners. The velocity around the square cylinder can be obtained by taking differentiation of total complex potential function as shown below,

$$V = v_x - iv_y = c\frac{dW}{d\zeta}\frac{d\zeta}{dZ}. \tag{9}$$

For the corner radius $\rho = 1$, the mapping function takes the form $Z = 3r\zeta$, which maps the circle in ζ-plane to the circle in Z-plane with reduced size by the factor of $3r$, and increases the velocity around the cylinder by the factor of $1/3r$ in Z-plane. To avoid the effect of size of cylinder on the velocity and other velocity dependent flow parameters, the factor $c = 3r$ is introduced in Eq. (9).

By substituting differentiation of complex potential function and mapping function in the Eq. (9), the velocity around the square cylinder is obtained as

$$V = -\frac{\frac{\zeta^4}{2r}\left(\frac{i\gamma_c}{2\pi\zeta} - \frac{Ue^{-i\alpha}\zeta^2(e^{i2\alpha}\zeta^2 - a^2)}{\zeta^2} + \frac{i\gamma_v\zeta_v(|\zeta_v|^2 - 1)}{2\pi(\zeta_v - \zeta)(\zeta_v - \zeta|\zeta_v|^2)}\right)}{\left(3\rho - \sqrt{\rho(9\rho + 16)} + 2\zeta^4 + 2\right)}. \tag{10}$$

The pressure distribution around square cylinder can be obtained in terms of non-dimensional pressure co-efficient Cp as given below,

$$Cp = 1 - \frac{\frac{\zeta^8}{4r^2}\left(\frac{i\gamma_c}{2\pi\zeta U} - \frac{e^{-i\alpha}\zeta^2(e^{i2\alpha}\zeta^2 - a^2)}{\zeta^2} + \frac{i\gamma_v\zeta_v(|\zeta_v|^2 - 1)}{2\pi U(\zeta_v - \zeta)(\zeta_v - \zeta|\zeta_v|^2)}\right)^2}{\left(3\rho - \sqrt{\rho(9\rho + 16)} + 2\zeta^4 + 2\right)^2} \tag{11}$$

3   Results and Discussion

In order to understand flow behaviour around square cylinder, the above mathematical relations are coded in MATLAB. The geometrical parameters (a, ρ, r) and the flow parameters (U, α) are the independent inputs and velocity V and pressure co-efficient Cp are the dependent output parameters. Some of the results obtained using present method are compared with the results obtained considering the inviscid flow model in ANSYS and with existing literature. The square cylinder of rounded corner in ANSYS Design Modeller is sketched by importing key-points extracted from MATLAB code.

3.1   Uniform Potential Flow

The streamlines of uniform potential flow of free stream velocity $U = 1$ with zero circulation ($\gamma_c = 0$) and without vortex flow ($\gamma_v = 0$) around circular cylinder and the square cylinder for the corner radius $\rho = 0.2$ are shown in Fig. 2.

The velocity and pressure contours for uniform flow around the square cylinder for the corner radius $\rho = 0.2$, obtained using mathematical method presented above and obtained through ANSYS are shown in Fig. 3a–d. The maximum velocity $V_{max}/U = 2.26$ and minimum value of pressure co-efficient $Cp_{min} = -4.13$ are obtained using present method which are in close confirmation with the results $V_{max}/U = 2.27$ and $Cp_{min} = -4.19$ obtained using ANSYS for same corner radius. The velocity and pressure co-efficient variation on the surface of square cylinder is shown in Fig. 3e, f.
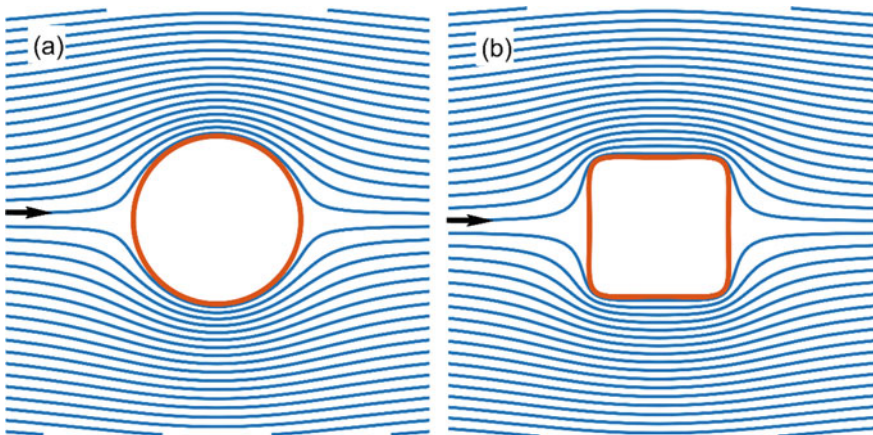
Fig. 2 Streamlines of uniform potential flow over **a** circular cylinder and **b** square cylinder with corner radius $\rho = 0.2$ ($U = 1$, $\boldsymbol{\gamma_v} = 0$, and $\boldsymbol{\gamma_c} = 0$)

The velocity and pressure distribution on the surface of square cylinder using present method is identical to that obtained using ANSYS.

The absolute velocity and co-efficient of pressure on the surface of square cylinder for different corner radius $\rho = 1, 0.8, 0.6, 0.4,$ and 0.3 is shown in Fig. 4. The
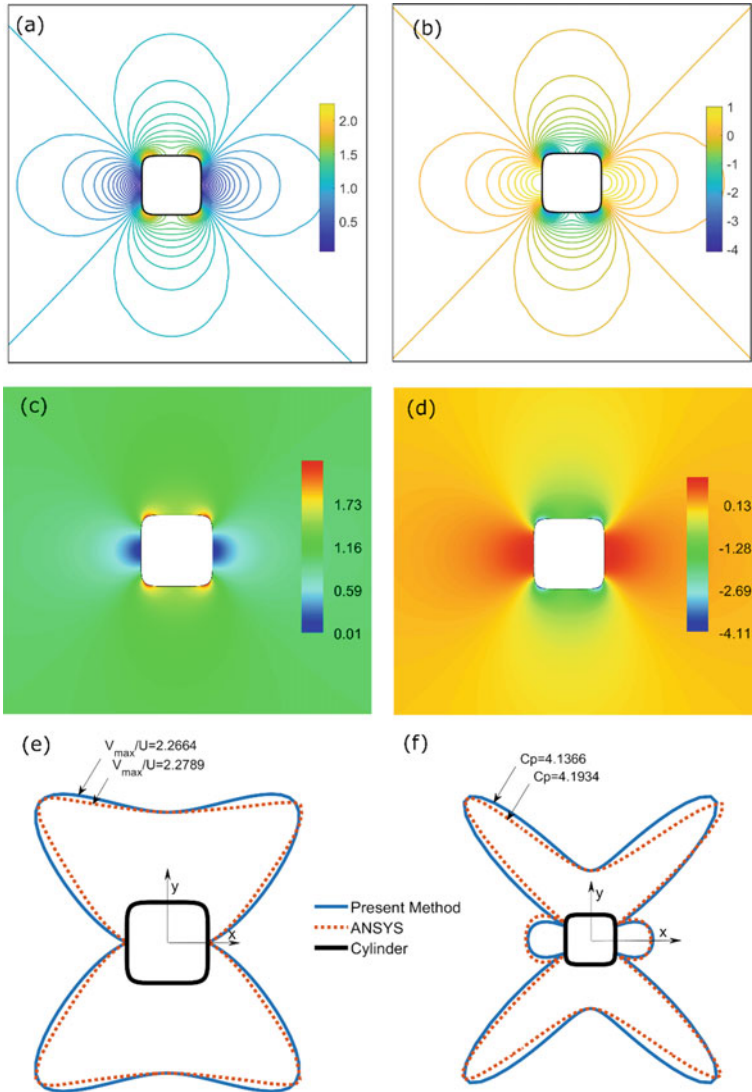
Fig. 3 Flow parameter contours around square cylinder with $\rho = 0.2$, **a** velocity contour (present method), **b** contour of pressure co-efficient (present method), **c** velocity contour (ANSYS), **d** pressure co-efficient contours (ANSYS), **e** comparison of velocity distribution, and **f** comparison of pressure co-efficient on square cylinder boundary ($U = 1, \gamma_v = 0,$ and $\gamma_c = 0$)

maximum values of velocity and pressure are found at the corners of cylinder. These extremum values of flow parameters decrease with increase of corner radius, and at corner radius $\rho = 1$, the velocity and pressure profile are found similar to that of circular cylinder. The velocity and pressure profiles for square cylinder with corners radius $\rho = 0$ are not shown, as the flow parameters attains the infinite value at the sharp corners (cusps) of the hypocycloidal cylinder.

The variation of maximum velocity and the minimum pressure co-efficient at the corners of square cylinder with the corner radius is shown in Fig. 5. For the corner radius $\rho = 0.01$, the flow parameter attained the values, $V_{\max}/U = 6.7052$, $Cp_{\min} = -43.9298$ at the corners of square cylinder, which converges to $V_{\max}/U = 2$, $Cp_{\min} = -3$ at the corner radius $\rho = 1$.
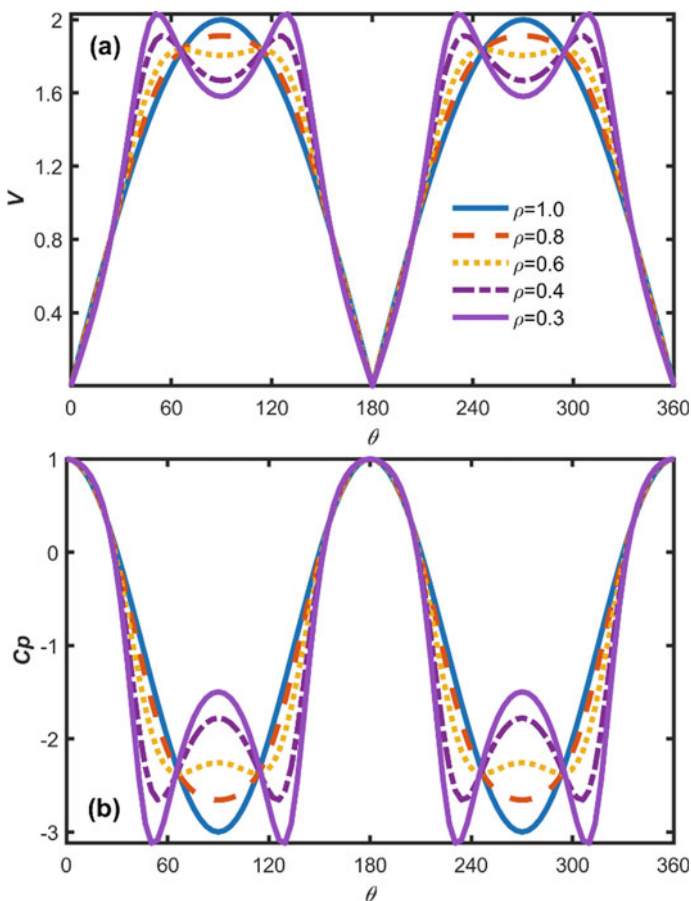
Fig. 4 Flow parameter distribution on square cylinder **a** absolute velocity and **b** pressure co-efficient

Fig. 5 Velocity V_{max} and pressure co-efficient Cp_{min} around square cylinder with the corner radius ρ
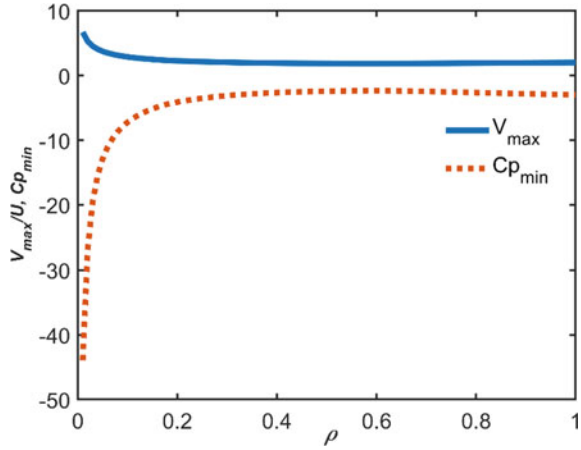
As the square cylinder is reduced to the circular cylinder for the corner radius $\rho = 1$, the result of pressure co-efficient at this corner radius using present method is compared with that obtained using ANSYS and results from existing literature for circular cylinder in Fig. 6. The results are quite identical, and such comparison of results at corner radius $\rho = 1$ validates the method used here for the flow around square cylinder with rounded corners.
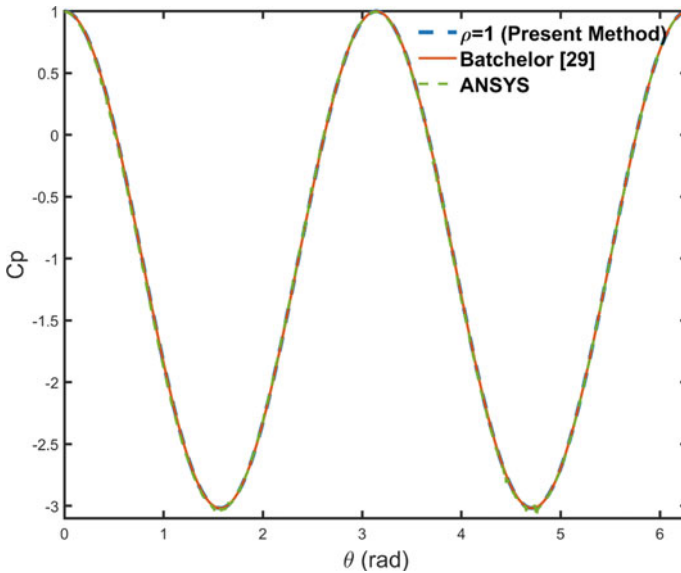
Fig. 6 Pressure co-efficient on cylinder surface for corner radius $\rho = 1$ using present method is compared with pressure co-efficient on the surface of circular cylinder using ANSYS and with results from existing literature

The flow angle 'α' is also one of the factors affecting the flow parameters around the cylinder. The extremum values of flow parameters on square cylinder with respect to the flow angle between $0° \leq \alpha \leq 90°$ is shown in Fig. 7.

The velocity V_{max}/U and pressure co-efficient Cp_{min} are found to increase with angle of attack α. For $\alpha = 45°$, the flow parameters attain the maximum values at the corners consisting the diagonal which is normal to the flow direction. At $\alpha = 45°$, the direction of freestream velocity is tangent to these corners. The stagnation points of the flow lie at the corners located at the end of diagonal aligned to the flow direction. The surface velocity distribution and pressure profile for angle of attack $\alpha = 45°$ is shown in Fig. 8.

For the flow angles other then $\alpha = 45°$, the direction of freestream flow is no longer remain normal to the diagonal (tangent to the corners) of square, and the extremum values of flow parameters are found lower than that obtained at $\alpha = 45°$.

Fig. 7 Variation of flow parameter **a** velocity V_{max} and **b** pressure co-efficient Cp_{min} with angle of attack α at different corner radius ρ
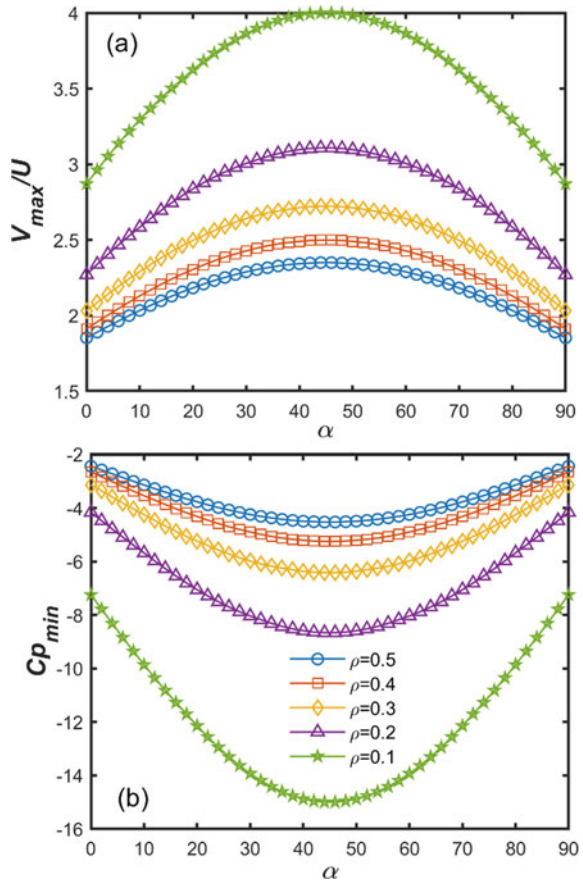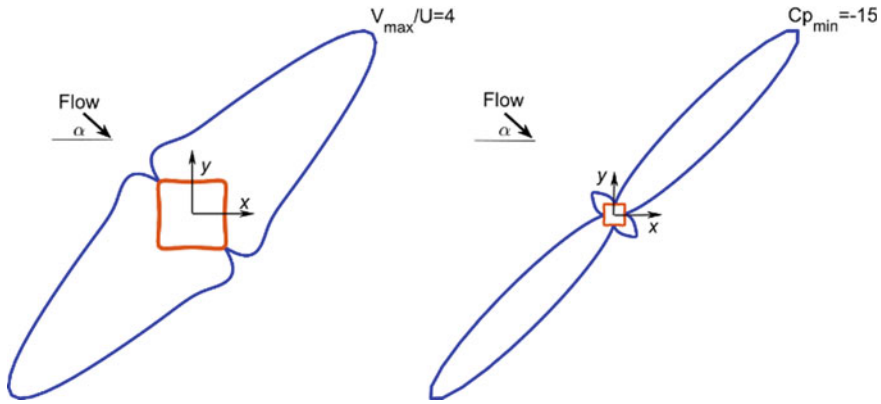
Fig. 8 Velocity profile (left) and pressure co-efficient profile (right) for $\rho = 0.1$ and $\alpha = 45°$

3.2 Effect of Presence of Vortex Around Square Cylinder

The effect of vortex around to the square cylinder on the flow parameters is investigated for different locations and strength of vortex. The streamlines of the flow around the square cylinder due to the vortex of strength $\gamma_v = 5$ located at $\zeta_v = 2e^{ipi/6}$ superimposed with uniform potential flow is shown in Fig. 9 ($\gamma_c = 0$). The presence of vortex near the cylinder not only changes the streamlines of flow but also changes the magnitude of velocity and pressure around the cylinder and the locations of extremum values of flow parameters.

The velocity distribution around the square cylinder for vortex of unit strength ($\gamma_v = 1$) located at different radial distances $r_v = 1, 1.2, 1.4, 1.6, 1.8, 2$ and $r_v = 50$, and at angle $\theta_v = 45°$ is shown in Fig. 10a. It is observed that the magnitude of velocity increases significantly at the corner of square cylinder near to the vortex. The changes in magnitude of velocity decrease as the vortex moves away from the cylinder, and at larger distance from the cylinder, the effect of presence of vortex vanishes and velocity distribution found similar as isolated square cylinder in uniform potential flow.

In Fig. 10b, the velocity distribution for the vortex of unit strength located at unit radial distance and different angular distance ($\theta_v = 0°, 30°, 45°, 60°,$ and $90°$) is shown. The magnitude of velocity increases significantly on the cylinder surface adjacent to the vortex. The maximum velocity is found for the vortex location $\theta_v = 45°$ at the corner of square cylinder ($\theta = 45°$).

The effect of change in vortex strength (γ_v) located at a fixed distance $\zeta_v = 5+5i$ ($\gamma_c = 0$) on the velocity distribution is shown in Fig. 11. The magnitude of velocity on the upper surface of square cylinder increases and at the lower surfaces decreases by the same magnitude while increasing the strength of vortex (γ_v).

The presence of vortex near the cylinder also changes the pressure distribution on the cylinder surface and as a result of it the hydrodynamic forces and torque are
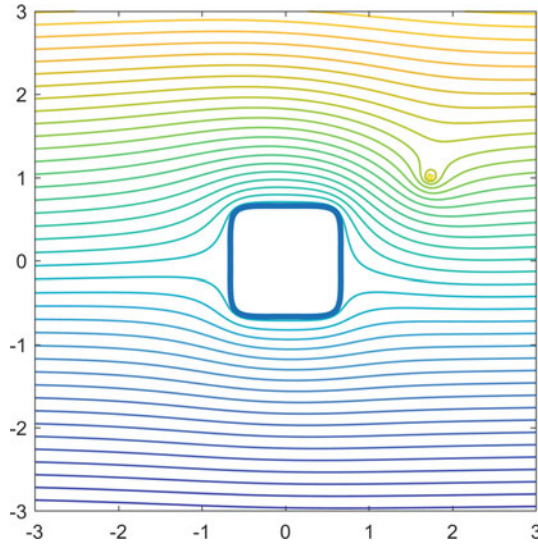
Fig. 9 Streamlines of uniform potential flow superimposed with vortex of strength $\gamma_v = -2$ located at $\zeta_v = 2e^{i\,pi/6}$ around the square cylinder ($\gamma_c = 0$)

induced on the square cylinder. Such results are not discussed and presented here to limit the length of paper.

The uniform potential flow around the finite corner radius square-shaped cylinder and the effect of vortex around the cylinder discussed above can be extended to the vortex street behind the cylinder as a representation of vortices separated from the surface of cylinder to capture some of the viscous effect. Also, the potential flow can be obtained around the square cylinder with flat sides and sharp corner with the application of Schwarz-Christoffel mapping.

4 Conclusions

The potential flow around the rounded corners square cylinder is obtained using complex variable approach. The mapping function is developed to map the area outside of circle to the area outside the square cylinder. Also, the mathematical formulation for the calculation of velocity and pressure around the cylinder is presented.

(1) The magnitude of velocity and pressure around the square cylinder are found to obtain the maximum values at the corners of cylinder and found increase with decrease of corner radius.
(2) The magnitude and location of flow parameters around the square cylinder are also found to be dependent on the flow direction (angle of attack).
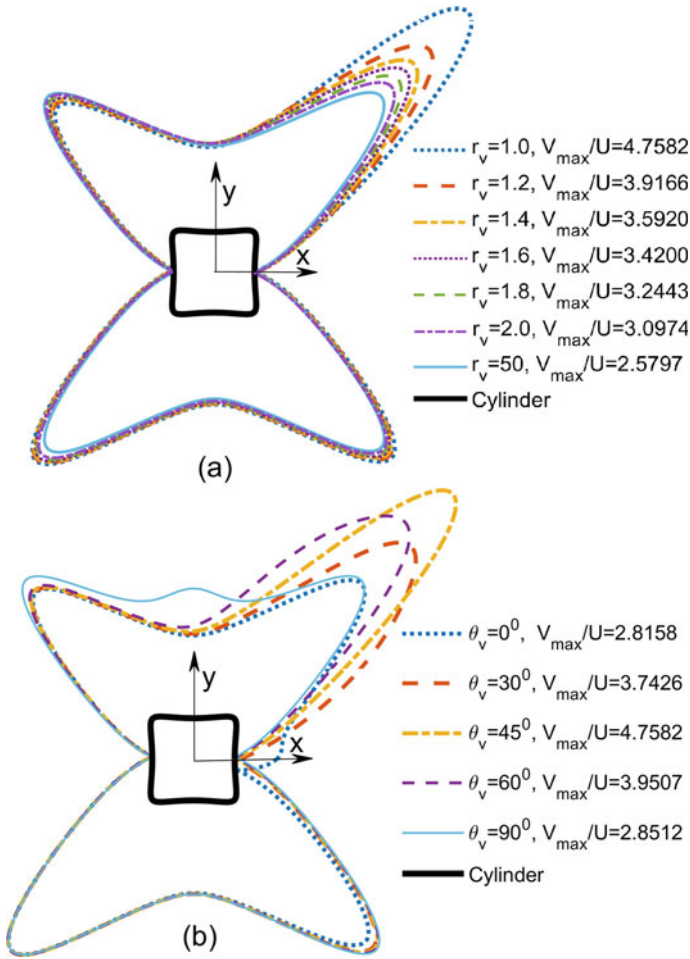
Fig. 10 Velocity distribution at the boundary of square cylinder due to the presence of **a** vortex of unit strength located at angles $\theta_v = 0°$, 30°, 45°, 60°, 90°, and at unit radial distance, **b** vortex of unit strength located at different radial distances $r_v = 1, 1.2, 1.4, 1.6, 1.8, 2, 50$, and at angle $\theta_v = 45°$

(3) The velocity and pressure attain maximum value for the flow direction normal to the diagonal of square cylinder (at

(4) $\alpha = 45^0$). These extremum values of flow parameters are found to be located at the corners at the end of the diagonal normal to the flow direction.

(5) The effect of presence of vortex around the cylinder is studied for different radial and angular locations of vortex around the cylinder. It is found that the magnitude of velocity and pressure increases significantly on the cylinder surface in the vicinity of vortex. The effect of presence of vortex decreases as the vortex moves
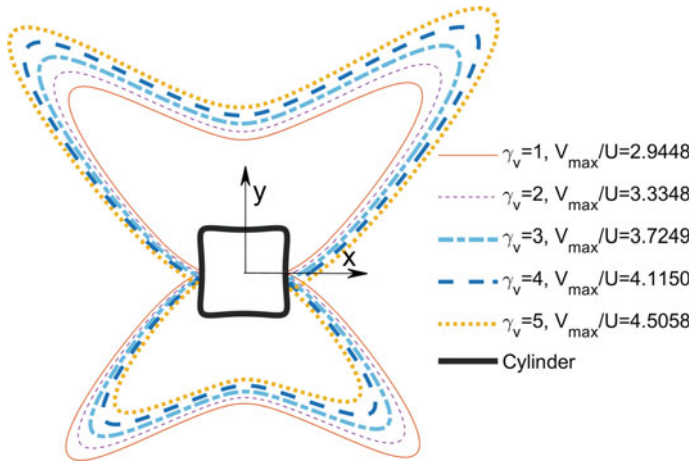
Fig. 11 Change in velocity profile on the boundary of square cylinder due to the presence of vortex of strength $\gamma_v = 1, 2, 3, 4,$ and 5 located at $\zeta_v = 5 + 5i$ and $\gamma_c = 0$ at the origin

away from cylinder and at large distance the effect die out and flow parameters around the cylinder are found similar as isolated single cylinder.

(6)   The magnitude of velocity and pressure on cylinder surface changes significantly with the change of vortex strength.

Nomenclature

Cp	Co-efficient of pressure
R	Radius of directing circle
U	Free stream velocity
V	Velocity around square cylinder
W	Complex potential function
Z	Complex plane
a	Radius of circular cylinder
h	Distance between curve tracing point and the centre of generating circle
r	Radius of rolling circle
u	Real part of velocity V
v	Imaginary part of velocity V
x, y	Parametric equations of mapping functions
θ	Angular dimension
α	Angle of attack
ρ	Radius at the corners of square cylinder
ζ	Complex plane
ζ_v	Location of vortex around cylinder

γ_v Strength of vortex around cylinder
γ_c Strength of vortex at origin of cylinder
r_v, θ_v Radial and angular location of vortex

References

1. Skerget L, Ravnik J (2007) Flow over a square cylinder by BEM. Trans Modell Simulation 44:161–168
2. Cao Y, Tamura T (2016) Large-eddy simulations of flow past a square cylinder using structured and unstructured grids. Comput Fluids 137:36–54
3. Mushyam A, Bergada JM (2017) A numerical investigation of wake and mixing layer interactions of flow past a square cylinder. Meccanica 52:107–123
4. Sen S, Mittal S, Biswas G (2011) Flow past a square cylinder at low Reynolds numbers. Int J Numer Meth Fluids 67:1160–1174
5. Jiang H, Cheng L (2020) Flow separation around square cylinder at low to moderate Reynolds numbers. Phys Fluids 32:044103
6. Sohankar A, Norberg C, Davidson L (1998) Low Reynolds-number flow around a square cylinder at incidence: study of blockage, onset of vortex shedding and outlet boundary condition. Int J Numer Methods Fluids 26:39–56
7. Bai H, Alam MM (2018) Dependence of square cylinder wake on Reynolds number. Phys Fluids 30:015102
8. Bearman PW, Obasaju ED (1982) An experimental study of pressure fluctuations on fixed and oscillating square-section cylinder. J Fluid Mech 119:297–321
9. Ali R, Hasan N (2020) Steady and unsteady flow regimes in two-dimensional mixed convective flow of air past a heated square cylinder. Int J Mech Sci 175:105533
10. Saha AK, Murlidhar K, Biswas G (2000) Experimental study of flow past a square cylinder at high Reynolds numbers. Exp Fluids 29:553–563
11. Dutta S, Panigrahi PK, Murlidhar K (2008) Experimental investigation of flow past a square cylinder at an angle of incidence. J Eng Mech 134:788–803
12. Tamura T, Miyagi T, Kitagishi T (1998) Numerical prediction of unsteady pressures on a square cylinder with various corner shapes. J Wind Eng Ind Aerodyn 74–76:531–542
13. Tamura T, Miyagi T (1999) The effect of turbulence on aerodynamic forces on a square cylinder with various corner shapes. J Wind Eng Industr Aerodyn 83(1–3):135–145
14. Gu M, Quan Y (2004) Across-wind loads of typical tall buildings. J Wind Eng Industr Aerodyn 92(13):1147–1165
15. Carassale L, Freda A, Marre-Brunenghi M (2013) Effects of free-stream turbulence and corner shape on the galloping instability of square cylinders. J Wind Eng Ind Aerodyn 123:274–280
16. Carassale L, Freda A, Marre-Brunenghi M (2014) Experimental investigation on the aerodynamic behavior of square cylinders with rounded corners. J Fluids Struct 44:195–204
17. Zhang W, Samtaney R (2016) Low-Re flow past an isolated cylinder with rounded corners. Comput Fluids 136:384–401
18. Miran S, Sohn CH (2015) Numerical study of the rounded corners effect on flow past a square cylinder. Int J Numer Meth Heat Fluid Flow 25:686–702
19. Cao Y, Tamura T (2017) Supercritical flows past a square cylinder with rounded corners. Phys Fluids 29:085110
20. Cao Y, Tamura T (2018) Aerodynamic characteristics of a rounded-corner square cylinder in shear flow at subcritical and supercritical Reynolds numbers. J Fluids Struct 82:473–491
21. Hu C, Zhou Y (2008) Aerodynamic characteristics of asymmetric bluff bodies. J Fluids Eng 131(1):011206

22. Zafar F, Alam MM (2019) Flow structure around and heat transfer from cylinders modified from square to circular. Phys Fluids 31:083604
23. Dey P, Das AKR (2017) A numerical study on effect of corner radius and Reynolds number on fluid flow over a square cylinder. Sadhana 42:1155–1165
24. Dey P, Sarkar A, Das AK (2016) Prediction of the aerodynamic behaviour of a rounded corner square cylinder at zero incidence using ANN. Ain Shams Eng J 7:767–775
25. van Hinsberg NP, Schewe G, Jacobs M (2017) Experiments on the aerodynamic behaviour of square cylinders with rounded corners at Reynolds numbers up to 12 million. J Fluids Struct 74:214–233
26. van Hinsberg NP, Schewe G, Jacobs M (2018) Experimental investigation on the combined effects of surface roughness and corner radius for square cylinders at high Reynolds numbers up to 10^7. J Wind Eng Ind Aerodyn 173:14–27
27. Hafez M, Wahba E (2004) Inviscid flow over a cylinder. Comput Methods Appl Mech Eng 193:1981–1995
28. Chen JT et al (2021) Applications of degenerate kernels to potential flow across circular, elliptical cylinders and a thin airfoil. Euro J Mech B-Fluids 90:29–48
29. Batchelor GK (1973) An introduction to fluid dynamics. Cambridge University Press, Cambridge UK
30. Tian ZW, Wu ZN (2009) A study of two-dimensional flow past regular polygons via conformal mapping. J Fluid Mech 628:121–154
31. Kim EJ, Kim I (2020) Approximate analytical solution of potential flow around a rectangle. Am J Phys 88:25–30
32. Solanki DT, Sharma DS (2022) Potential flow around polygonal shaped cylinders using hypotrochoidal mapping function. Int J Mech Sci 226:107395
33. Sharma DS (2016) Stresses around hypotrochoidal hole in infinite isotropic plate. Int J Mech Sci 105:32–40
34. Sharma DS, Dave JM (2015) Stress intensity factors for hypocycloidal hole with cusps in infinite anisotropic plate. Theoret Appl Fract Mech 75:44–52
35. Chauhan MM, Sharma DS, Dave JM (2015) Stress intensity factor for hypocycloidal hole in finite plate. Theoret Appl Fract Mech 82:59–68
36. Patel NP, Sharma DS (2017) On the stress concentration around polygonal cut-out of complex geometry in an infinite orthotropic plate. Compos Struct 179:415–436
37. Crowdy DG (2010) A new calculus for two-dimensional vortex dynamics. Theoret Comput Fluid Dyn 24:9–24
38. Crowdy DG (2006) Analytical Solution for uniform potential flow past multiple cylinders. Euro J Mech B/Fluids 25:459–470
39. Moura MN, Vasconcelos GL (2012) Vortex flow around a circular cylinder above a plane. Revista Cubana De Fisica 29:1E42
40. Vasconcelos GL, Moura M (2017) Vortex motion around a circular cylinder above a plane. Phys Fluids 29:083603

Numerical Simulation and Validation of NACA0012 Airfoil to Predict Its Performance During the Stalling Condition

Dishant Sharma and Rahul Goyal

1 Introduction

Current energy demand, decreasing fossil fuel reserves, and stringent environmental restrictions all contribute to the widespread adoption of renewable energy sources such as wind and solar. The most effective method for harnessing wind energy is the wind turbine. The advancement of vertical axis wind turbines (VAWTs) is crucial to the future of wind power because of its viability in low-wind environments, especially in urban areas [1–4]. VAWTs have advantages over horizontal axis wind turbines (HAWTs) in omnidirectional behaviour, higher scalability, better performance in chaotic, unstable, and turbulent flow conditions, lower maintenance, and higher overall efficiency for the entire wind farm [5–7]. In contrast, due to instability in terms of flow disturbances around the blade, rapid and cyclic changes in the angle of attack introduce dynamic stall.

The complicated chain of events known as dynamic stall occurs when an airfoil is subjected to rapid changes in angle of attack that go beyond the situation known as static stall. In the case of a two-dimensional flow, the dynamic stall processes during blade pitching involve the formation, growth, and shedding of the vortex structure. Qualitative characteristics of dynamic stall include the gradual reversal of the boundary layer from the trailing edge, the breakdown of the flow due to the bursting of laminar bubbles, and the emergence of a turbulent separation towards the leading edge. One common unwanted phenomenon in VAWTs is the appearance of a wake on the blade [8]. Downstream wind turbines experience an increase in aerodynamic loads due to the intense turbulent wake flow's influence on the development of dynamic stall characteristics [9]. Laneville and Vittecoq reported that for tip speed ratio (TSR, λ) less than or equal to 4, the dynamic stall phenomenon dominates for VAWTs [10]. As λ values fall below 4, the dynamic stall changes from a light to a

---

D. Sharma · R. Goyal (✉)

Department of Energy Science and Engineering, IIT Delhi, New Delhi 110016, India

e-mail: rahulgoyal@dese.iitd.ac.in

deep stall. The deep dynamic stall had four main stages: attached flow at a lower angle of attack (AoA), formation of leading edge vortex (LEV), shedding of LEV from the suction surface of the airfoil, and reattachment of the flow [11, 12]. This investigation on the dependence of λ on stall formation has uncovered a problem that will require further investigation. The formation and growth of LEV on suction side of the airfoil increases lift, and the shed off of this vortex from the surface of the airfoil causes transitory variations in the continuous torque delivery, lift, and drag performance metrics, resulting in decreased turbine power. It poses a severe problem to VAWTs since vibrations and induced noise reduce stability and efficiency [13].

The primary focus of the current work is to conduct a rigorous quantitative investigation of the performance characteristics, boundary layer flow features on the airfoil, lift and drag fluctuations, and angle of attack changes for a single-bladed rotor system. The dynamic stall phenomenon, which affects turbine efficiency, is given special attention. The current simulation runs at a moderate Reynolds number with a NACA0012 blade profile based on one of the Lee and Gerontakos [14] experiments' oscillating cases during the deep stall condition, where the AoA varies as $\alpha(t) = 10° + 15° \sin \omega t$ and the reduced frequency is 0.1. This case merited choice because it involved an investigation into deep stall regime conditions and yielded higher performance outcomes in comparison to other situations found in the literature [14]. The Lee and Gerontakos [14] experimental work serve as a basis for this numerical work's validity, and the observations drawn from the results are covered in the sections that follow. The work comprises of grid independency test (GIT), then followed by validation of numerical results with aforementioned experimental work. It was observed that the results obtained are in good agreement with experimental for all critical points except one. Details of which have been explained in the results section. Additionally, velocity vectors around the airfoil have been obtained to offer a visual depiction of the described underlying flow physics.

2   Numerical Methodology

The experimental work by Lee and Gerontakos [14] was performed numerically using commercial software ANSYS [15]. The available numerical model in the literature was re-developed using ANSYS-ICEM and ANSYS-Fluent solver. The experimental results of the literature [14] were used to validate the current results. The two-dimensional study that was conducted on the NACA0012 airfoil of 150 mm chord length consists of a computational domain, which was separated into two zones: the size of the stationary zone was $35D \times 20D$, and the size of the rotational zone was $1.5D$ for the current scenario, as shown in geometry Fig. 1. Here, D is typically the diameter of the turbine, but due to the single-blade rotor case, D is the chord length of the airfoil. The distance between the inlet of the domain to the rotor centre was $10D$, which is kept to avoid errors of overestimation [16]. In order to maintain the uniform pressure coefficient at the outlet, a distance of $25D$ was considered from the rotor centre. The domain width was calculated considering a less than 5% blockage
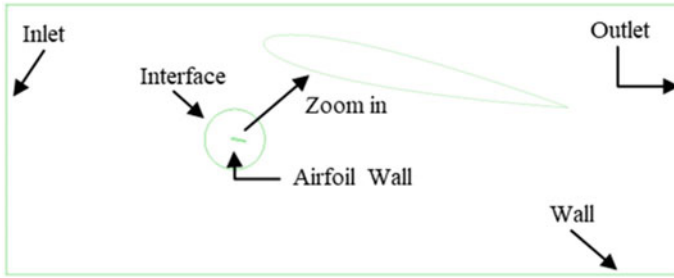
Fig. 1 Computational domain geometry of the NACA0012 airfoil comprises both fixed and rotating zones

ratio. The diameter of the rotating core was $1.5D$ for the present case to get a better grid generation capability. The dimensions of the flow domain were determined after taking into account the impacts of blockage ratio and the uncertainty caused by the boundary wall. A non-conformal interface with sliding mesh technique between the fixed and rotating domains allows the single-bladed rotor to rotate.

The moderate mainstream Reynolds numbers for the current cases are in the range of 100,000–150,000. The experimental static stall angle of the symmetric NACA0012 airfoil is around 13°.

$$\text{Re} = \frac{\rho V C}{\mu}.\tag{1}$$

The local coefficient of friction ($C_f\prime$) calculated using the empirical relation given by Eq. (2) [17]

$$C_{f\prime} = (2 \log \text{Re} - 0.65)^{-2.3}.\tag{2}$$

Equation (3) is used to compute the wall shear stress (τ_ω)

$$\tau_w = 0.5 C_{f\prime} \rho V^2.\tag{3}$$

The frictional velocity can be computed as

$$u_t = \left(\frac{\tau_w}{\rho}\right)^{0.5}.\tag{4}$$

An inflation with a first layer thickness of 0.01585 mm is given on the edge of the airfoil, ensuring precision at airfoil's boundary zone. Equation (4) is used to determine the blade's first layer thickness [18]

$$y+ = \frac{\rho u_t y}{\mu}.\tag{5}$$

ICEM grid generation software [15] was used to construct the grid for the entire domain. To accurately resolve the viscous sublayer and visualize the flow around the airfoil wall, the y+ is taken into account by refining the grid near the surface and keeping the value less than 1, which can be depicted numerically also as a range along the chord length as shown in Fig. 2b. The growth rate of 1.2 for the boundary layer mesh was considered. Turbulence models were also chosen depending on the y+ values. Grid-dependent investigations were conducted to determine the optimal grid size for the computing domain. Table 1 of the result section displays the findings acquired from the grid-dependent investigations for one of the critical angles. The mesh matrix for the present case, like skewness, orthogonal quality, aspect ratio and overall quality are in good agreement.

The transient, incompressible, two-dimensional flow condition with URANS equations and Reynolds stresses was modelled using a 5-equation turbulent model with 1-equation of intermittency. The current study employed the SAS-based SST k-ω turbulence model. The SST-SAS turbulence model exhibits scale adaptivity in

(a)

(b)
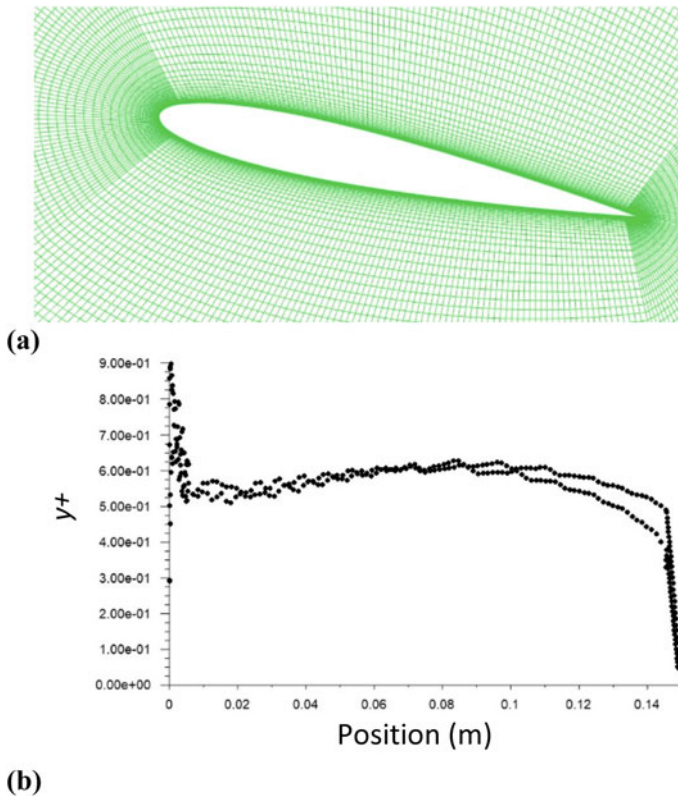
Fig. 2 **a** Close view of the structured mesh near to the airfoil and **b** variation of the wall $y+$ of the NACA0012 airfoil along the chord length position

contrast to conventional RANS models. It can dynamically resolve turbulent structures in an unsteady flow field while keeping URANS capability in steady flow regions. This can be achieved by including the von Karman length scale into the turbulence scale equation, which can be found in the reference [15].

For computation, the density of air and viscosity is taken as 1.225 kg/m^3 and 1.7894 × 10^{-5}, respectively. In the cell zone condition, the rotating and stationary mesh motion is provided with 18.535 rad/s rotational velocity. The boundary conditions consist of inlet as velocity type having 13.15 m/s magnitude and direction in the x axis. The turbulence intensity is kept 0.08 and turbulent length scale as 0.0105. The outlet boundary condition is pressure outlet and walls as no slip and stationary. For momentum, the spatial discretization technique is Bounded Central Differencing, while for other functions, it is QUICK. For the pressure–velocity coupling, the SIMPLE scheme is employed, and the transient formulation is done using the Bounded second-order implicit. All of the equations should meet the convergence criterion of less than 10^{-4}. To obtain reliable findings, the time step calculation needs to be carried out in consideration of CFL criteria. The time step size of 1.88 × 10^{-5} is computed considering the courant number less than unity and the rotational velocity of the rotating domain. The CFL number obtained for the present case using Eq. (6) is 0.36, ensuring grid and numerical stability [19]:

$$\text{CFL} = V\frac{\Delta t}{\Delta x}. \tag{6}$$

After ten revolutions, the data for the current case was obtained, and the findings of an additional four revolutions were analysed.

3 Results and Discussion

3.1 Grid Independence Test

The grid independent test was carried out for the present case. Three grids were generated and conducted the simulation for each one. Table 1 displays the findings that were acquired from the grid independent investigations for one of the critical angles (21°). Based on the observed values of lift and moment coefficient, Grid 2 is chosen for the remainder of the study due to the insignificant change in lift and moment coefficient values and the lower computational cost and time requirements.

Table 1 Details of the computational grid and its performance characteristics

Case	No. of cells	Moment coefficient (C_m)	Lift coefficient (C_L)
Grid I	74772	0.59	1.83
Grid II	149212	0.61	1.96
Grid III	301492	0.60	1.97

3.2 Validation of Numerical Model

The experimental findings of Lee and Gerontakos were used to validate the current numerical work and compared with the SAS-SST turbulence model results. The anticipated lift coefficient for the critical angle of attacks was plotted in Fig. 3a. The results demonstrate good agreement with the experimental values as stated in Table 2. The current numerical results showed good agreement on comparing with the experimental and numerical results of the literature [14, 20, 21]. The coefficients of lift obtained from this study for various angles of attack are close to the experimental values. The modelling predicts the onset of static stall around a 12° AoA, which is consistent with experiment. An increase in angle of attack up to 24° results in an increase in coefficient of lift. The onset of dynamic stall is noted around a 24° AoA. As the AoA reaches to 25° during upward motion, a reverse downward movement of the airfoil up to 0° AoA was commenced, resulting in a fall in predicted lift coefficient in accordance with experiment. It is important to note that the agreement to experiment failed during the transition from 24.9° to 24.5°. Although the experiment demonstrated an increase in lift coefficient during this event in an otherwise decreasing trend, simulation was unable to detect this rise and instead predicted a drop. However, the current results have significant improvement in prediction of aerodynamic forces compared to the numerical work of Rahman et al. [20] due to the better turbulence model, the structured mesh, the number of grid elements, the time step size, and the number of revolutions. Singh and Páscoa's [21] results are quite comparable to the current case, but the percentage of error is reduced for 7 critical points. This may be due to optimum geometry parameter selection and number of revolutions.

In the upward motion of the airfoil, the predicted values of the lift and drag coefficients by the SST-SAS turbulence model were in good agreement with the experimental findings. During the downward movement, secondary vortex formation causes an increase in lift for a small range of AoA that the current model unable to predict.

However, it is able to capture and better anticipate the events of post-stall, reattachment, and fully attached flow to the airfoil, as depicted in Fig. 3a. The current model manages to predict closely the drag coefficient for the onset of transition event at 12° AoA but overestimates the drag coefficient values for the event turbulence separation $\alpha \approx 17°$ and near to stall $\alpha = 24°$, as illustrated in Fig. 3b.

Figure 4 presents a comparison of the performance in terms of lift to drag coefficient ratio with the change in the angle of attack for upward motion case. The

(a)

(b)
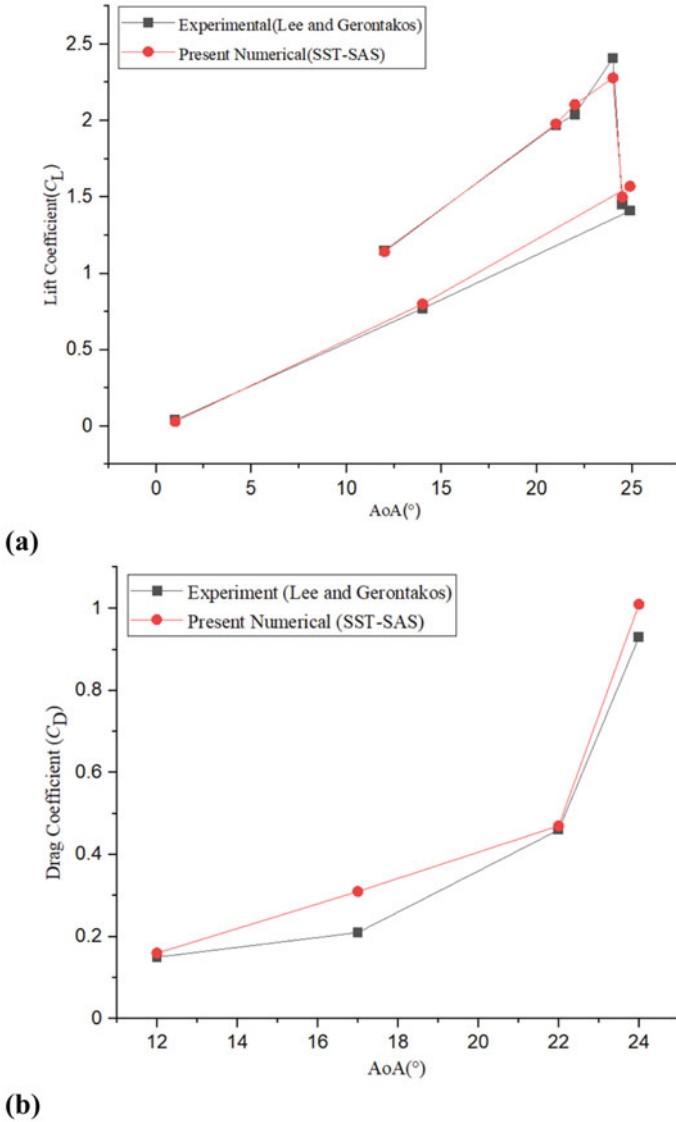
Fig. 3 **a** Variation of C_L with AoA and **b** variation of C_D with AoA of the NACA0012 airfoil

numerical values that are anticipated to occur during the pre-stall and dynamic stall conditions are underestimated up to 21°. This is because the drag coefficient values were overestimated, as can be seen in Fig. 3b. In comparison with the numerical results of Singh and Páscoa's [21], the present C_L/C_D numerical results demonstrate good agreement with the experiment at $\alpha \geq 21°$. This quantitative comparison of lift, drag, and lift to drag coefficients with experiment and numerical references [14,

Table 2 Comparing the experimental results of Lee and Gerontakos [14] at critical points with the current numerically calculated lift coefficient

AoA	Experimental	Present numerical	Error (%)
12	1.15	1.145	0.43
21	1.97	1.96	0.5
22	2.04	2.09	− 2.45
24	2.41	2.25	6.63
24.9	1.41	1.45	− 2.83
24.5	1.45	1.42	2.06
14	0.77	0.74	3.89
1	0.04	0.03	25

20, 21] demonstrates good agreement and the capabilities of SST-SAS turbulence model. Utilizing more advanced turbulence models in future research, such as LES, will allow more accurate prediction of important events such as turbulence separation, near-stall conditions, and the formation of secondary vortices.

The aforementioned performance matrices for the current case can be explained further with the velocity vector fields as shown in Fig. 5. The important observations of the flow physics involved for the pitching airfoil in deep dynamic stall condition are as follows:

For $\alpha < 12°$: Over the entire range of the AoA, the flow continues to be laminar and adhered to the suction surface of the airfoil. Figure 5a shows flow detachment
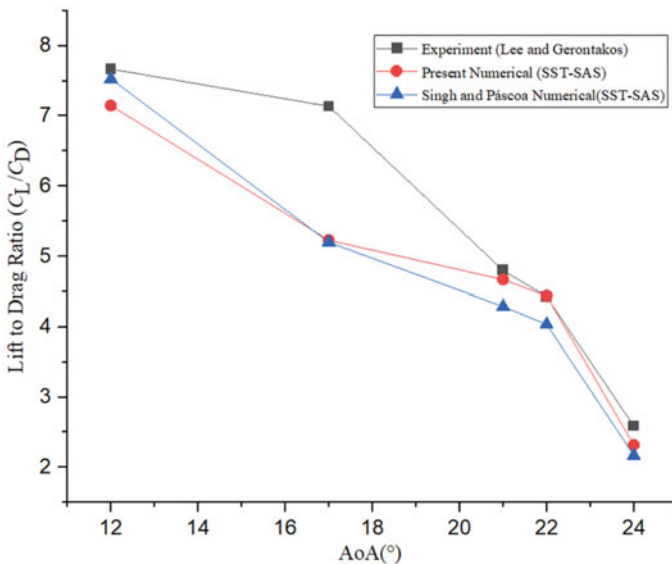
Fig. 4 Performance variation of C_L/C_D with AoA of the single-bladed rotor system
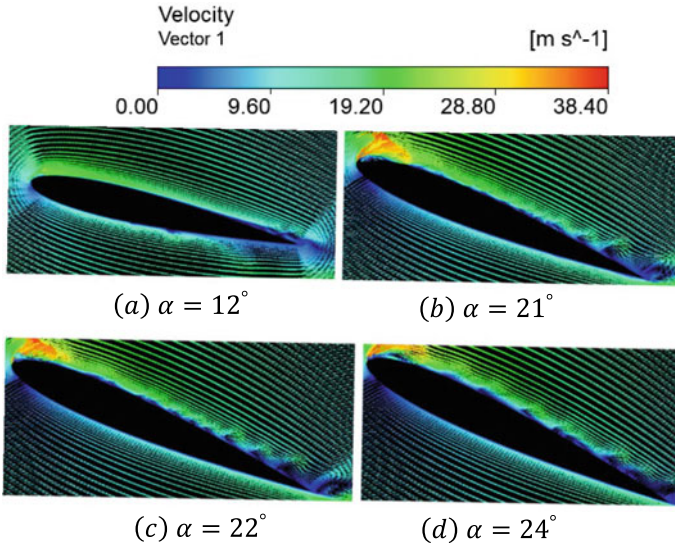
Fig. 5 Velocity vector plots during the upward motion of the airfoil for critical AoA

near the end of the trailing edge, which was previously confirmed experimentally by Lee and Gerontakos [14].

For $12° \leq \alpha \leq 21°$: The development of flow transition and reversal is observed with the increase in AoA. Flow reversal from trailing edge propagates towards the leading edge, as shown in Fig. 5b.

For $21° \leq \alpha < 25°$: With the increase in AoA, turbulent boundary layer breakdown can be visualized due to formation of dynamic stall vortex and adverse pressure gradient as shown in Fig. 5c, d. It rapidly increases the lift and drag coefficients which can be seen in Fig. 3a, b.

4   Conclusions

The current work presents an understanding of the flow dynamics, effect of change in angle of attack on aerodynamic performance in terms of lift and drag fluctuations for a single-bladed rotor. A rigorous quantitative investigation of the performance characteristics, boundary layer features, and the dynamic stall phenomenon on the airfoil which affects turbine efficiency is given special attention. For validating the experimental results and to visualize the vortex formation, Scale Adaptive Simulation is incorporated with SST k-ω turbulence model. The current numerical results of aerodynamic forces exhibit good agreement with the experiment for pre-stall events when compared to the numerical references [14, 20, 21]. Lift coefficient values are obtained with a percentage error of less than 4% for six critical AoA's out of eight.

The remaining two AoA's (24° during upward motion and 1° during downward motion) are observed with a percentage error of 6.63 and 25%. The flow reversal and progression depicted by velocity vectors aids in visualizing the crucial turbulent boundary layer events that occur over the airfoil. The generation, development, accumulation, and shedding of vortex structures from the suction surface of an airfoil are clearly observed using velocity vectors. It can be seen that the flow reversal started at around 12° AoA near to the trailing edge due to adverse pressure gradient. It is also observed from the velocity vectors that the flow reversal propagates from trailing edge to leading edge as the AoA increases but the boundary layer remains attached to the airfoil up to 21° AoA. Further increase in AoA results in turbulent boundary layer breakdown and formation of LEV, which further develops and convects over the suction surface of the airfoil, resulting in a rapid increase in lift. The shedding of vortex after further increment in AoA results in abrupt aerodynamic losses yielding a compromised airfoil performance. An important subject of application of the present analysis is the VAWT which relies on multiple airfoils for development of lift and consequent rotational shaft power. The analysis thereby serves to be a tool in performance prediction of VAWTs and may be used to identify, assess, and improve in future scope the optimal working conditions of these turbines.

Nomenclature

AoA(α)	Angle of attack (°)
CFL	Courant–Friedrichs–Lewy [–]
LEV	Leading edge vortex [–]
NACA	National Advisory Committee for Aeronautics [–]
SAS	Scale Adaptive Simulation [–]
SST	Shear stress transport [–]
SIMPLE	Semi-Implicit Method for Pressure Linked Equations [–]
QUICK	Quadratic Upstream Interpolation for Convective Kinematics
Re	Reynolds number
c	Airfoil chord [m]
C_L	Lift coefficient [–]
C_D	Drag coefficient [–]
C_m	Moment coefficient [–]
$C_{f'}$	Skin friction coefficient [–]
δ	Boundary layer thickness [mm]
λ	Tip speed ratio [–]
ρ	Density of air [kg/m^3]
D	Turbine diameter [m]
V	Free stream velocity [m s^{-1}]
μ	Dynamic viscosity [kg m^{-1} s^{-1}]
k	Turbulence kinetic energy [m^{2}s^{-2}]
ω	Specific turbulence dissipation rate [s^{-1}]

θ	Azimuthal angle (°)
τ_ω	Wall shear stress [N m^{-2}]
μ_t	Frictional velocity [m s^{-1}]
$y+$	Non-dimensional distance [–]
y	First layer thickness [mm]
κ	Reduced frequency [–]

References

1. Simic Z, Havelka JG, Bozicevic VM (2013) Small wind turbines—a unique segment of the wind power market. Renew Energy 50:1027–1036. https://doi.org/10.1016/j.renene.2012.08.038
2. Douak M, Aouachria Z, Rabehi R, Allam N (2018) Wind energy systems: Analysis of the self-starting physics of vertical axis wind turbine. Renew Sustain Energy Rev 81:1602–1610. https://doi.org/10.1016/j.rser.2017.05.238
3. Kant A (2020) India 2020—energy policy review. https://doi.org/10.1007/bf03404634
4. Lee J, Zhao F (2021) Global wind report 2021
5. Paraschivoiu I (2002) Wind turbine design: with emphasis on Darrieus concept
6. Islam MR, Mekhilef S, Saidur R (2013) Progress and recent trends of wind energy technology. Renew Sustain Energy Rev 21:456–468. https://doi.org/10.1016/j.rser.2013.01.007
7. Mohamed MH (2014) Aero-acoustics noise evaluation of H-rotor Darrieus wind turbines. Energy 65:596–604. https://doi.org/10.1016/j.energy.2013.11.031
8. Sanderse B (2009) Aerodynamics of wind turbine wakes (ECN-E--09-016). Energy Res Cent Netherlands. http://resolver.tudelft.nl/uuid:9f4dd67d-5fe2-4e86-b2b3-497852de4ea7
9. Leu TS, Yu JM, Hu CC, Miau JJ, Liang SY, Li JY et al (2012) Experimental study of free stream turbulence effects on dynamic stall of pitching airfoil by using particle image velocimetry. Appl Mech Mater 225:103–108. https://doi.org/10.4028/www.scientific.net/AMM.225.103
10. Laneville A, Vittecoq P (1986) Dynamic stall: the case of the vertical axis wind turbine. J Sol Energy Eng Trans ASME 108:140–145. https://doi.org/10.1115/1.3268081
11. Li S, Zhang L, Yang K, Xu J, Li X (2018) Aerodynamic performance of wind turbine airfoil DU 91-W2-250 under dynamic stall. Appl Sci 2018:8. https://doi.org/10.3390/app8071111
12. Jain S, Saha UK (2020) On the influence of blade thickness-to-chord ratio on dynamic stall phenomenon in H-type Darrieus wind rotors. Energy Convers Manag 2020:218. https://doi.org/10.1016/j.enconman.2020.113024
13. Crespo A, Hernández J (1996) Turbulence characteristics in wind-turbine wakes. J Wind Eng Ind Aerodyn 61:71–85. https://doi.org/10.1016/0167-6105(95)00033-X
14. Lee T, Gerontakos P (2004) Investigation of flow over an oscillating airfoil. J Fluid Mech 512:313–341. https://doi.org/10.1017/S0022112004009851
15. ANSYS Inc. (2015) ANSYS fluent theory guide 12.0
16. Rezaeiha A, Kalkman I, Blocken B (2017) CFD simulation of a vertical axis wind turbine operating at a moderate tip speed ratio: guidelines for minimum domain size and azimuthal increment. Renew Energy 107:373–385. https://doi.org/10.1016/J.RENENE.2017.02.006
17. Schlichting H, Kestin J (1961) Boundary layer theory
18. Sharma S, Sharma RK (2016) Performance improvement of Savonius rotor using multiple quarter blades—a CFD investigation. Energy Convers Manag 127:43–54. https://doi.org/10.1016/J.ENCONMAN.2016.08.087
19. Trivellato F, Raciti CM (2014) On the Courant–Friedrichs–Lewy criterion of rotating grids in 2D vertical-axis wind turbine analysis. Renew Energy 62:53–62. https://doi.org/10.1016/J.RENENE.2013.06.022

20. Hakim A, Rahman A, Ahmad N, Mohd RN, Lazim TM, Mansor S (2017) Aerodynamics of harmonically oscillating aerofoil at low Reynolds number. J Aerosp Technol Manag 9:83–90. https://doi.org/10.5028/jatm.v9i1.610

21. Singh K, Páscoa JC (2019) Numerical modeling of stall and poststall events of a single pitching blade of a cycloidal rotor. J Fluids Eng Trans ASME 2019:141. https://doi.org/10.1115/1.4040302/367361

Effect of Vent Position on Temperature Inhomogeneity Inside Apple Storage Package: A Numerical Study

Harshad Raghuwanshi, K. R. Aharwal, and Narendra Gajbhiye

1 Introduction

Special attention is needed to retain the shelf life, freshness, and quality of the food produce in post-harvest handling. Among the various methods of post-harvest handling, pre-cooling is one of the methods to maintain the quality and freshness of the food produce [1]. Temperature management is one of the crucial factors in the post-harvest handling of food produce. In the pre-cooling process, the field heat is removed from the harvested produce which reduces the metabolism of the product, hence retarded the deterioration process during storage and transportation. Low-temperature treatment of food produce also reduces microbial growth, moisture loss, enzymatic activities, and ethylene production. The low cost and high efficiency of the forced air pre-cooling technique make it widely accepted. This technique uses a fan to force the cold air over the produce package. This cold air takes the heat from the food produce and leaves through the ventilation in the packaging system. The packaging used to store the food produce hinders the direct contact of cold air with the product. Also, the design of the packaging complicates the airflow distribution. Thus, optimization of the packaging design is a crucial area to be explored.

H. Raghuwanshi · K. R. Aharwal (✉) · N. Gajbhiye
Department of Mechanical Engineering, MANIT, Bhopal 462003, India
e-mail: kraharwal@gmail.com

H. Raghuwanshi
e-mail: info4harsh@gmail.com

N. Gajbhiye
e-mail: nlgajbhiye@manit.ac.in

2   Literature Review and Objective

Vent area, shape, size, position, and stacking arrangement are some crucial design factors in the designing of food produce packaging. Han et al. [2] experimentally and numerically observed the effect on cooling heterogeneity inside the package by increasing the number of vent holes in the existing package filled with apples. In another numerical study, by the same authors cooling profile was observed after increasing the layers of the apples from two to four in a single package with varying the shape of the vents [3]. Wang et al. [4] numerically investigated the commercial packaging of strawberries by varying the shape of the vents for cold air and observed their effect on cooling performance. Han et al. [5] found that increasing the air inflow rate of cold air beyond a limit results in high energy consumption, excessive moisture loss, and chilling injury. To minimize moisture loss, plastic liners and poly liners can be used. Gruyters et al. [6] compared the cooling performance of traditional corrugated boxes with reusable plastic crates (RPC). Authors found that the performance of the RPC is better than the corrugated boxes for cooling uniformity and energy usage but they observed that the higher air flow rates result in chilling injury.

Apart from the packaging design, the tray placed in between the layers of the food produce also influences the airflow distribution inside the package. Gong et al. [7] numerically investigated the effect of the tray size placed between the apple layers. The complex package structure associated with the tray and food produce stacking results in complications of airflow distribution. This results in the cooling heterogeneity inside the package and consequently lowers the effectiveness of pre-cooling of the product. Bishnoi et al. [8–10] performed several experimental investigations on the airflow distribution and cooling heterogeneity in a cold room filled with products.

In the past few years, several experimental and numerical investigations are performed for optimizing the storage conditions of the food produce. Many researchers work on the optimization of vent shape, size, area, and stacking arrangement. The present study is focused on the effect of the position of the vent holes on the existing packaging of the apples. A 3-D CFD model of the package filled with apples is investigated numerically to find the optimum vent location on the package.

3   Numerical Models

3.1   Computational Domain

In the present study, a package filled with apples is placed in a 2.45 m long duct. The dimensions of the package are 0.27 m × 0.2 m × 0.45 m with 0.006 m thickness are considered. Four circular vents of 0.02 m diameter are kept at both sides of package perpendicular to the airflow. The schematic diagram of the duct with the apple filled package is shown in Fig. 1. A total of 24 apples are stored in each package in two layers. Each layer consists of 12 apples with a baffle plate in between them. The

baffle plate material assumed to be same material as of package with a 0.003 m thickness. Numerical simulations are conducted for three different positions of the vents on the package. The dimensions of the package with three different package designs termed A1, A2, and A3 are shown in Fig. 2.
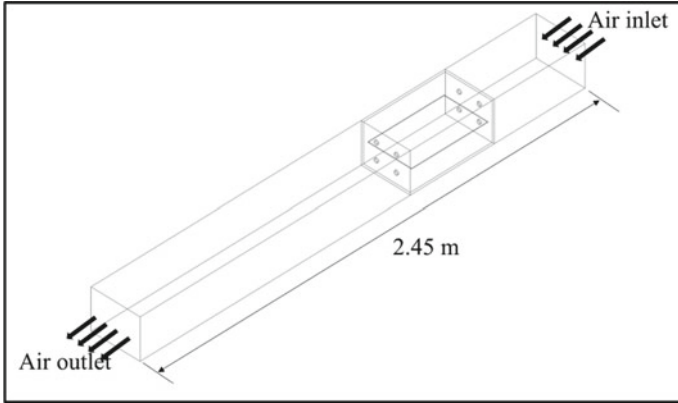
Fig. 1 Duct designed for the forced air pre-cooling with the package of apples
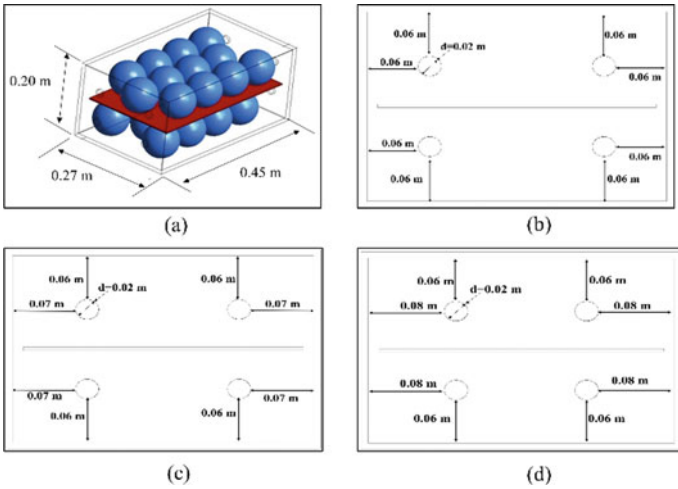
Fig. 2 **a** Dimensions of the package under study, **b** existing package design A1, **c** proposed package design A2, and **d** proposed package design A3

3.2 Governing Equations for Computational Domain

To solve the transient energy field and airflow in the computational domain, the Reynolds-averaged Navier Stokes (RANS) equations are used. The constant fluid properties are considered, and viscous heating is neglected in the present study. The governing equations used in the present study are as follows.

Conservation of Mass

$$\frac{\partial \rho_f}{\partial t} + \frac{\partial \overline{u_i}}{\partial x_i} = 0 \tag{1}$$

Conservation of Momentum

$$\rho_f \frac{\partial u_i}{\partial t} + \rho_f \frac{\partial \overline{u_i u_j}}{\partial x_j} = -\frac{\partial \overline{P_f}}{\partial x_i} + \frac{\partial}{\partial x_j} \left[\nu \rho_f \left(\frac{\partial \overline{u_i}}{\partial x_j} + \frac{\partial \overline{u_j}}{\partial x_i} \right) \right] - \rho_f \frac{\partial \overline{u_i' u_j'}}{\partial x_j} \tag{2}$$

Conservation of Energy

$$\frac{\partial \overline{T_f}}{\partial t} + \overline{u_i} \left(\frac{\partial \overline{T_f}}{\partial x_i} + \frac{1}{\rho_f C p_f} \frac{\partial \overline{P_f}}{\partial x_i} \right) = \frac{\partial}{\partial x_i} \left(\frac{\lambda_{\text{eff}}}{\rho_f C p_f} \frac{\partial \overline{T_f}}{\partial x_i} \right) \tag{3}$$

The Reynolds stresses in Eq. (2) can be expressed based on Boussinesq hypothesis:

$$-\rho_f \overline{u_i' u_j'} = \nu_t \rho_f \left(\frac{\partial \overline{u_i}}{\partial x_j} + \frac{\partial \overline{u_j}}{\partial x_i} \right) - \frac{2}{3} \rho_f k \delta_{ij} \tag{4}$$

where ν_t is the kinematic eddy viscosity and k is the turbulence kinetic energy.

$$k = \frac{1}{2} \overline{u_i' u_j'} \tag{5}$$

Effective turbulent thermal conductivity λ_{eff} is expressed as

$$\lambda_{\text{eff}} = \lambda_f + \frac{C_{P_f} \nu_t \rho_f}{\text{Pr}_t} \tag{6}$$

Here, Pr_t is the turbulent Prandtl number and it is taken as 0.85.

Published study suggests that two equation eddy viscosity SST $k - \omega$ turbulence model gives better accuracy and convergence compared with other turbulence models (Standard $k - \varepsilon$, RNG $k - \varepsilon$, Standard $k - \omega$ turbulence model) [2, 7]. Hence, two equation eddy viscosity SST $k - \omega$ turbulence model is used in the present study with RANS equations. Following are the transport equations of SST $k - \omega$ turbulence model [11] that are used.

Turbulence Kinetic Energy

$$\frac{\partial k}{\partial t} + U_j \frac{\partial k}{\partial x_j} = P_k - \beta^* k\omega + \frac{\partial}{\partial x_j}\left[(v + \sigma_k v_T)\frac{\partial k}{\partial x_j}\right] \tag{7}$$

Specific Dissipate Rate

$$\frac{\partial \omega}{\partial t} + U_j \frac{\partial \omega}{\partial x_j} = \alpha S^2 - \beta \omega^2 + \frac{\partial}{\partial x_j}\left[(v + \sigma_\omega v_T)\frac{\partial \omega}{\partial x_j}\right] + 2(1 - F_1)\sigma_{\omega 2}\frac{1}{\omega}\frac{\partial k}{\partial x_i}\frac{\partial \omega}{\partial x_i} \tag{8}$$

Kinematic Eddy Viscosity

$$v_t = \frac{a_1 k}{\max(a_1 \omega, SF_2)} \tag{9}$$

where F_1 and F_2 are blending functions and P_k is the production limiter and it is expressed as:

$$F_1 = \tanh\left\{\left\{\min\left[\max\left(\frac{\sqrt{k}}{\beta^* \omega y}, \frac{500v}{y^2 \omega}\right), \frac{4\sigma_{\omega 2}k}{CD_{kw}y^2}\right]\right\}^4\right\} \tag{10}$$

$$F_2 = \tanh\left[\left[\max\left(\frac{2\sqrt{k}}{\beta^* \omega y}, \frac{500v}{y^2 \omega}\right)\right]^2\right] \tag{11}$$

$$P_k = \min\left(\tau ij \frac{\partial U_i}{\partial x_j}, 10\beta^* k\omega\right) \tag{12}$$

$$CD_{kw} = \max\left(2\rho\sigma_{\omega 2}\frac{1}{\omega}\frac{\partial k}{\partial x_i}\frac{\partial \omega}{\partial x_i}, 10^{-10}\right) \tag{13}$$

where the values of the constants are
$\beta^* = \frac{9}{100}$, $\sigma_{k1} = 0.85$, $\sigma_{k2} = 1$, $\sigma_{\omega 1} = 0.5$, $\sigma_{\omega 2} = 0.856$.

3.3 Modeling Assumptions

The following assumptions are used in the present numerical study.

(1) The fluid is considered as incompressible.
(2) Apples are modeled as spherical object with 0.09 m diameter.
(3) The heat of respiration of apples is considered to be 60 W/ton [12].

4   Boundary and Initial Conditions

The following boundary conditions are used in present study.

4.1   Inflow Boundary

For the inlet air through the package vents, inlet velocity and temperature are kept at 2 m/s and 2 °C, respectively.

4.2   Outflow Boundary

At the outlet of the duct, pressure outlet condition is specified, while a zero gradient condition is applied for all the velocity components.

4.3   Wall Boundaries

No-slip boundary condition is specified for duct, package, baffle, and apple surface. The walls of the duct are considered insulated walls.

4.4   Initial Conditions

Since the product is pre-cooled before storing it in the cold room, the initial temperature of the duct and apples is considered as 27 °C before calculations. The properties of the material used in the present study are given in Table 1.

5   Simulation Procedure and Mesh

The ANSYS FLUENT 2020 R1 solver is used in the present study. First order implicit method and second-order upwind scheme is used for transient formulation and spatial discretization, respectively. The tetrahedral hybrid mesh is generated with ANSYS mesher. At the product's surface, boundary layer mesh is used with Y^+ value less than 0.95. To obtain the appropriate grid size, grid size independence test is carried for four different grid sizes as given in Table 2. The change in wall shear stress at fruits surface for grid M3 and M4 is found to be negligible. Therefore, M3 is used

Table 1 Properties of the materials

Input material properties [2]		
Material	Property	Value (unit)
Air	Density	1.286 (kg m^{-3})
	Dynamic viscosity	1.73 × 10^{-5} (Pa * s)
	Specific heat capacity	1004.8 (Jkg^{-1}K^{-1})
	Thermal conductivity	0.242 (Wm^{-1}K^{-1})
Apple	Density	837.22 (kg m^{-3})
	Diameter	0.009 (m)
	Specific heat	3821.96 (Jkg^{-1}K^{-1})
	Thermal conductivity	0.4508 (Wm^{-1}K^{-1})
Package material	Density	220 (kg m^{-3})
	Specific heat	1700 (Jkg^{-1}K^{-1})
	Thermal conductivity	0.05 (Wm^{-1}K^{-1})

in further numerical study. The enlarged view (near the wall boundary) with the full mesh of the duct is shown in Fig. 3.

Table 2 Grid size independence test

Grid name	Total number of grid elements	Wall shear stress on the fruit surface (Pa)	Change in %
M1	731,914	2.72 × 10^{-3}	---
M2	1,231,356	2.79 × 10^{-3}	2.50
M3	2,510,842	2.83 × 10^{-3}	1.41
M4	3,914,535	2.84 × 10^{-3}	0.35
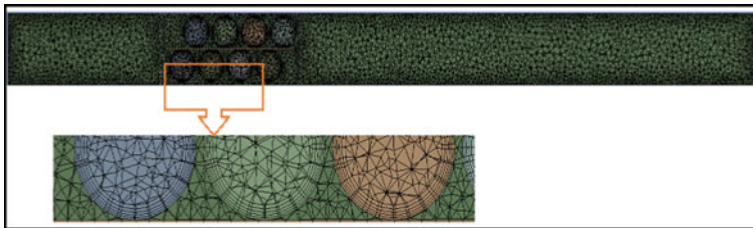
Fig. 3 Full and enlarged view of mesh
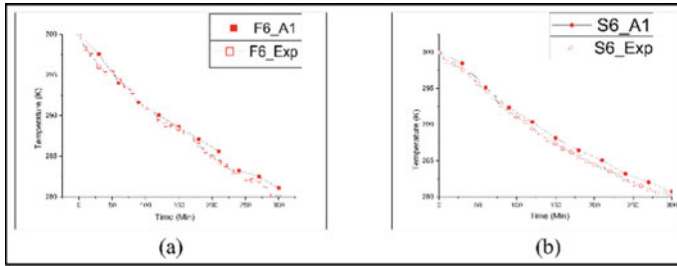
Fig. 4 Validation of the numerical model with the experimental results

6 Validation of the CFD Model

The present CFD model is validated with the experimental results from the published research [2]. The temperature of the product with respect to time is plotted for two different locations (F6 and S6) in plane 1 and plane 2. The numerical results show a good agreement with the experimental results, as shown in Fig. 4.

7 Results and Discussion

In the present study, the cooling profile for three different package designs is numerically simulated. A time step of 60 s with 20 iterations per time step is used for transient simulation. To observe the effect of different vent positions on the package, two horizontal planes and two product locations (one in each plane) are identified. The planes and locations are shown in Fig. 5a, b, respectively.
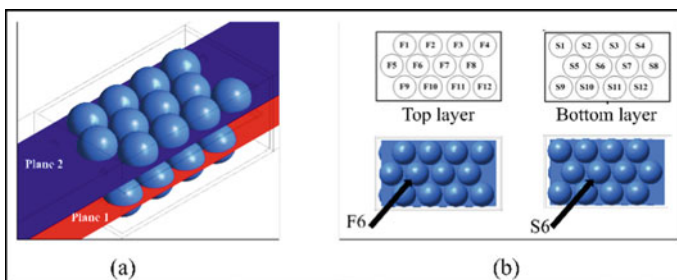
Fig. 5 a Location of the planes for temperature and velocity profile and **b** locations of temperature measurement
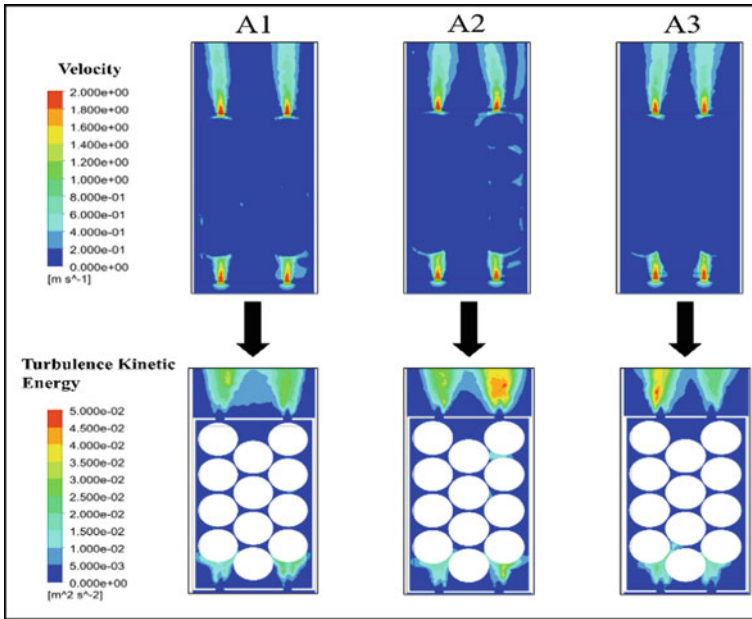
Fig. 6 Velocity contour and turbulence kinetic energy at plane 1 after 300 min of cooling time

7.1 Temperature and Velocity Distribution

The air velocity distribution and associated turbulence kinetic energy is shown in Fig. 6 at plane 1 after 300 min of cooling time. An insignificant difference in the velocity distribution is observed among all three designs (A1, A2, and A3) because of the compact stacking of the apples inside the package. The temperature contours after 300 min of cooling time are plotted at plane 1 and plane 2 for all three designs and shown in Fig. 7. It is seen from the Fig. 7 that the temperature of the product at the rear part of the package is cooled down to a lower temperature in A2 and A3 when compared with A1. A maximum cooling is reported in design A3 among other two designs.

7.2 Temperature Inhomogeneity

Dispersion degree of dimensionless temperature parameter Y_i is used to define the temperature inhomogeneity at any plane. This dimensionless temperature parameter has been reported in previous studies [5, 13].

$$Y_i = T_{i,t} - T_a / T_{in} - T_a \tag{14}$$
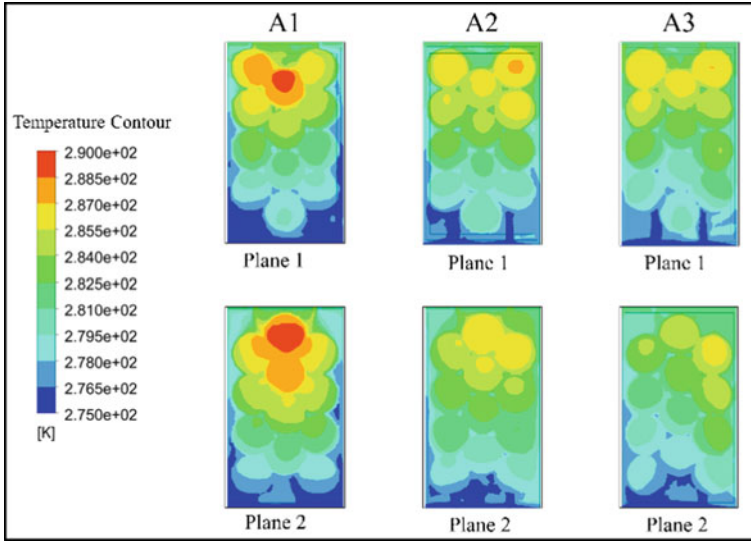
Fig. 7 Temperature contours at plane 1 and plane 2 after 300 min of cooling time

where

Y_i is the dimensionless temperature parameter,
$T_{i,t}$ is the temperature of the product at time t,
T_a is the air temperature,
T_{in} is the initial temperature of the product.

The above dimensionless parameter is used to calculate the temperature inhomogeneity as:

$$\sigma = \max\left\{Y_i - \frac{1}{n}\sum_{i=1}^{n}Y_i\right\} - \min\left\{Y_i - \frac{1}{n}\sum_{i=1}^{n}Y_i\right\} \tag{15}$$

The variation of product temperature with time is plotted in Fig. 8a and temperature inhomogeneity in three designs is shown in Fig. 8b. It is observed that changing the positions of the vent hole on the package changes the temperature inhomogeneity significantly. The maximum temperature inhomogeneity is observed in package design A1, while it is minimum for design A3. After 300 min of cooling time, the temperature inhomogeneity is found to be reduced by 25.8% in design A3 compared with design A1.
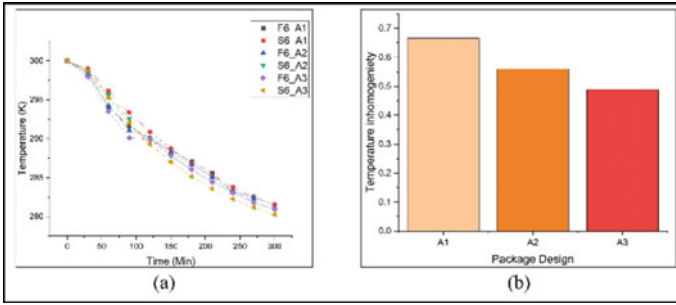
Fig. 8 **a** Temperature profile at F6 and S6 location for all the designs with respect to the time and **b** temperature inhomogeneity in all the three package designs after 300 min of cooling time

8 Conclusion

The temperature distribution inside the package filled with apples with different vent positions is investigated numerically. The obtained results of design A1 show good agreement with the experimental results. It is found that temperature inhomogeneity inside the package is dependent on the vent position and it reduces in design A3. After 300 min of cooling time, the temperature inhomogeneity is reduced up to 25.8% for A3 compared with existing package design A1.

Nomenclature

ρ_f	Density of fluid [kg m^{-3}]
λ_f	Thermal conductivity of fluid [Wm^{-1}K^{-1}]
C_{P_f}	Specific heat of fluid [Jkg^{-1}K^{-1}]
ν_t	Kinematic eddy viscosity [m^{2}s^{-1}]
k	Turbulence kinetic energy [m^{2}s^{-2}]
λ_{eff}	Effective turbulent thermal conductivity [Wm^{-1}K^{-1}]
Pr_t	Turbulent Prandtl number
Y_i	Dimensionless temperature parameter
$T_{i,t}$	Temperature of the product at time t [°C]
T_a	Temperature of air [°C]
T_{in}	Initial temperature of the product [°C]
σ	Temperature inhomogeneity

References

1. Duan Y, Wang GB, Fawole OA, Verboven P, Zhang XR, Wu D, Opara UL, Nicolai B, Chen K (2020) Postharvest precooling of fruit and vegetables: a review. Trends Food Sci Technol 100:278–291
2. Han JW, Zhao CJ, Yang XT, Qian JP, Fan BL (2015) Computational modeling of airflow and heat transfer in a vented box during cooling: optimal package design. Appl Therm Eng 91:883–893
3. Han JW, Qian JP, Zhao CJ, Yang XT, Fan BL (2017) Mathematical modelling of cooling efficiency of ventilated packaging: integral performance evaluation. Int J Heat Mass Transf 111:386–397
4. Wang D, Lai Y, Zhao H, Jia B, Wang Q, Yang X (2019) Numerical and experimental investigation on forced-air cooling of commercial packaged strawberries. Int J Food Eng 15(7):1–14
5. Han JW, Zhao CJ, Qian JP, Ruiz-Garcia L, Zhang X (2018) Numerical modeling of forced-air cooling of palletized apple: integral evaluation of cooling efficiency. Int J Refrig 89:131–141
6. Gruyters W, Defraeye T, Verboven P, Berry T, Ambaw A, Opara UL, Nicolai B (2019) Reusable boxes for a beneficial apple cold chain: a precooling analysis. Int J Refrig 106:338–349
7. Gong YF, Cao Y, Zhang XR (2021) Forced-air precooling of apples: airflow distribution and precooling effectiveness in relation to the gap width between tray edge and box wall. Postharvest Biol Technol 177:111523
8. Bishnoi R, Aharwal KR (2020) Experimental investigation of air flow field and cooling heterogeneity in a refrigerated room. Eng Sci Technol Int J 23(6):1434–1443
9. Bishnoi R, Aharwal KR (2021) Experimental evaluation of cooling characteristic, airflow distribution and mass transfer in a cold store. J Food Process Eng 44(2):1–11
10. Bishnoi R, Aharwal KR (2022) Experimental and theoretical analysis of mass transfer in a refrigerated food storage. Heat Mass Transf
11. Menter FR (1994) Two-equation eddy-viscosity turbulence models for engineering applications. AIAA J 32(8):1598–1605
12. Hoang HM, Duret S, Flick D, Laguerre O (2015) Preliminary study of airflow and heat transfer in a cold room filled with apple pallets: comparison between two modelling approaches and experimental results. Appl Therm Eng 76:367–381
13. Jia B (2021) The effect of alternating ventilation on forced air pre-cooling of cherries

RANS Simulations of Ground Effects on Flow Past Airfoils with Increasing Camber

Dilip Lalchand Parmar, Deepak Kumar Singh, and Arjun Sharma

1 Introduction

The surface pressure distribution and lift coefficient on an airfoil is affected by an impermeable wall placed in proximity below it [1, 2]. Under suitable conditions, a cushioning effect below the wings is produced which could be helpful in take-off or landing configurations. Such a ground effect also results in drag reduction and improved lift-to-drag ratios. Ground effect is beneficial for vehicles flying above ground or water [1, 3, 4, 5] as well as automotive applications.

Ground effects on flow around an airfoil are explained on the basis of flow induced by the image of the airfoil in the presence of an impermeable wall. More fluid is directed away from the wall towards the upper surface of the airfoil creating a region of high pressure between the lower surface and wall. There is also a strong dependence on surface profile of airfoil section [1, 6] and flow parameters such as angle of attack and Reynolds number.

2 Literature Review and Objective

There are several computational [7–10] and experimental [1, 3, 6] studies reported on the effects of the presence of an impermeable wall on the lift characteristics of an airfoil. Usually, ground effects are observed for gap ratios less than 1, where the ratio of wall distance from trailing edge to chord length is referred to as the gap ratio. The general observations are that, for a given airfoil section, there is an increase in lift coefficient above a certain angle of attack when gap ratio is decreased. The increase in lift occurs due to presence of large high-pressure region between the airfoil and

D. L. Parmar (✉) · D. K. Singh · A. Sharma
Department of Applied Mechanics, IIT Delhi, New Delhi 110016, India
e-mail: Dilipjainiitd@gmail.com

wall, which is primarily an inviscid effect of wall impermeability. A reduction in drag coefficient is also observed with a decrease in gap ratio. There could be non-monotonic trends in lift and drag coefficients as the gap ratio is decreased [6]. The surface profile on the lower side of airfoil forms a converging–diverging passage and has an effect on surface pressure distribution. At large angles of attack, flow separation on upper surface of airfoil can occur, which results in formation of a thick wake and large drag coefficient. In their computational study for a NACA4406 airfoil, at angle of attack of 4° and gap ratio of 0.1, Jung et al. [3] observe that there is an increase in lift coefficient and decrease in drag coefficient with increasing Reynolds number (in the range 2×10^5–2×10^9), which contributes to large values of lift-to-drag ratio at high Reynolds number. They also obtain the largest value of lift coefficient for an airfoil with least thickness (among four digit NACA44 series) at Reynolds number of 2×10^6 and gap ratio of 0.1 at angle of attack of 2°.

Previous study by the authors [8] on NACA4412 in ground effect shows that for an angle of attack of 0°, the values of lift coefficient remain almost constant for gap ratios above 0.4 and decrease when gap ratio is decreased below 0.4. For 10° angle of attack, an increase in lift coefficient is observed with decreasing gap ratio. Such trends are also noted in the experimental study of Ahmed et al. [1] at same flow configurations. The effects of airfoil camber on variation of lift coefficient with gap ratio at angles of attack of 0° and 10° are examined in the present study.

For wing-in-ground-effect studies, the flow results depend on boundary conditions imposed on the wall. Barber et al. [7] note that a moving wall boundary condition (with free-stream velocity imposed at the wall), in the frame of reference attached to the airfoil, is a realistic representation of the physical problem. In the present study, ground effects on airfoils of different camber are studied using steady Reynolds-averaged-Navier-Stokes (RANS) equations n two dimensions. A moving wall boundary condition is used. The Reynolds number considered in the study is 3×10^5 based on free-stream velocity and airfoil chord length. An airfoil section is characterized primarily by mean camber and thickness [2]. For the airfoil sections considered in the present study, only mean camber is varied; it increases progressively for NACA 0012, 4412 and 8412 sections. The presence of mean camber increases the value of effective angle of attack for the airfoil. The zero-lift angle of attack is zero for symmetric 0012 section, and negative for cambered sections, 4412 and 8412 [2].

3   Materials and Methods

Steady Reynolds-averaged-Navier-Stokes (RANS) simulations are performed to study the effect of presence of an impermeable flat wall on flow past cambered airfoils. Four-digit NACA airfoil sections with increasing camber, 0012 (symmetric), 4412 and 8412, are considered in the present study. The airfoil sections have a maximum thickness of 12%.

The Reynolds number based on airfoil chord length and free-stream velocity is $Re = U_\infty c/\upsilon = 3 \times 10^5$. The angles of attack considered in the present study are $\alpha = 0°$ and $10°$. The simulations are conducted for three different values of gap-to-chord ratio (h/c, , referred to as gap ratio in the remainder of this study): 1, 0.4 and 0.15.

A finite-volume based commercial solver, FLUENT [11], is used. A steady, pressure-based SIMPLEC algorithm [11] with two-dimensional solver setting is used with working fluid as air. A multi-block, structured grid around the airfoil surface is used for simulations. No-slip boundary condition is applied on the airfoil surface. A moving wall condition, with velocity same as the free-stream velocity, is applied at the wall. Uniform velocity inlet with pressure outlet condition is applied. The incoming turbulence intensity is set to zero. An approximate shear-free condition (using symmetry condition in fluent) is specified at the upper domain boundary. Spalart–Allmaras (SA) turbulence model [12] with standard model constants are used for RANS calculations. A second-order method with upwinding is used to solve the equations for momentum and modified turbulent viscosity. SA model has been used in a wide variety of turbulent flow simulations. The study of a laminar separation bubble formed at moderate Reynolds number using SA model is also reported [13].

A grid with approximately 4.75×10^5 quadrilateral volumes is used. Grid independence of results and model validation study, for flow past NACA4412 airfoil placed above an impermeable wall, are reported by the same authors in another study [8]. It is observed in the previous study [8] that RANS simulations using SA model yield results in good agreement with reference to experimental data [1] for the same flow configuration.

4 Results and Discussion

4.1 RANS Simulations

The pressure distribution around a symmetric NACA0012 airfoil, for free-stream angles of attack $\alpha = 0°$ and $10°$, are shown for varying values of gap ratio in Fig. 1. For $\alpha = 0°$ it is observed that when the airfoil is placed sufficiently far away from the wall ($h/c = 1$), the flow around airfoil remains symmetric resulting in net-zero lift. An asymmetry in pressure distribution on the upper and lower surfaces of the airfoil begins to appear when the airfoil is brought closer to the wall ($h/c = 0.4$). Considerably larger negative lift is generated (seen in Fig. 2), for gap ratio of 0.15, as pressure on the lower side decreases while pressure on the upper side remains almost unchanged. At a higher angle of attack, $\alpha = 10°$, , pressure on the lower surface of airfoil increases as the wall is approached. The pressure on the upper side of airfoil remains almost unchanged. The result is an increase in net lift coefficient (shown in Fig. 2) as gap ratio decreases when $\alpha = 10°$.

The surface pressure distribution for NACA4412 section is shown in Fig. 3. At $\alpha = 0°$, for all gap ratios, the pressure on the lower surface is higher than that on the upper surface, resulting in net positive lift. When gap ratio decreases, there is a slight decrease in pressure on the lower side, while pressure variation on the upper side remains unchanged. Thus, the lift coefficient decreases with decreasing gap ratio. At $\alpha = 10°$, the values of pressure coefficient increase on both upper and lower surfaces. However, the rise in pressure is asymmetric; it is larger on the lower side compared with the upper side, resulting in an increase in lift coefficient with decreasing gap ratio.

In case of NACA8412 airfoil section, for $\alpha = 0°$, an increase in lift coefficient is observed when gap ratio is decreased below 0.4 (refer to Fig. 2). This is in contrast to decreasing lift coefficients observed for 0012 and 4412 sections at $\alpha = 0°$ for gap ratios below 0.4. As shown in Fig. 4 at $\alpha = 0°$, the rise in pressure on the lower

Fig. 3 Values of surface pressure coefficient are shown for NACA4412 airfoil at $\alpha = 0°$ and 10° for gap ratios of 1, 0.4 and 0.15
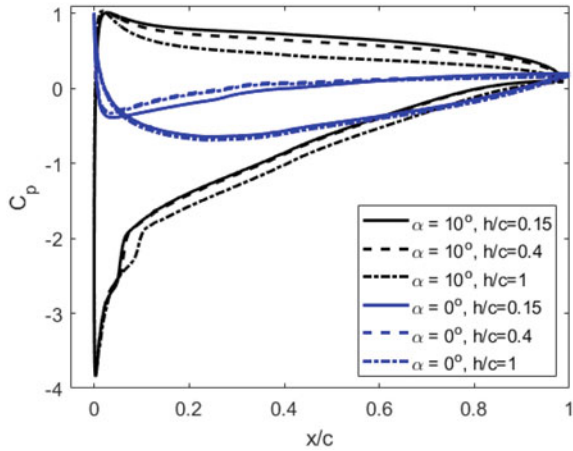
side is larger than that on the upper side when the wall is approached. Thus, there is an increase in lift coefficient with decreasing gap ratio. Similarly, at $\alpha = 10°$ a slightly larger increase in pressure is seen on both upper and lower surfaces. The pressure rise is asymmetric (more on the lower side), which results in an increase in lift coefficient when gap ratio is decreased.

Increase in values of lift coefficient at same α, for different airfoil sections, are consistent with an increase in effective angle of attack. The variations in surface pressure with gap ratio, for different airfoil sections, suggest a value of effective angle of attack, which determines increasing or decreasing trend in lift coefficients with decreasing gap ratio.

A comparison of surface pressure coefficients for the three airfoil sections is shown in Fig. 5 for $\alpha = 10°$ and gap ratio of 0.15. Gradually varying, higher pressure coefficients are seen on lower sides of 4412 and 8412 airfoil sections (with higher

Fig. 4 Values of surface pressure coefficient are shown for NACA8412 airfoil at $\alpha = 0°$ and 10° for gap ratios of 1, 0.4 and 0.15
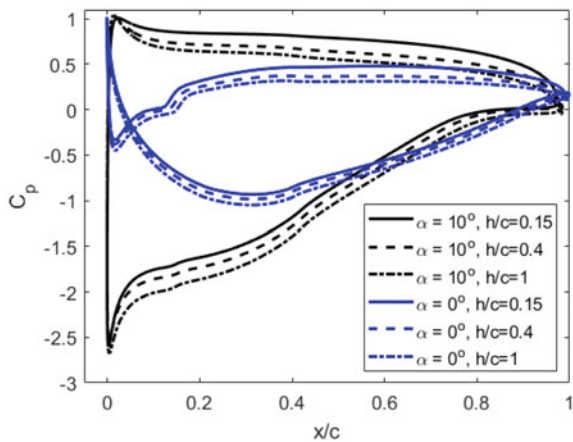
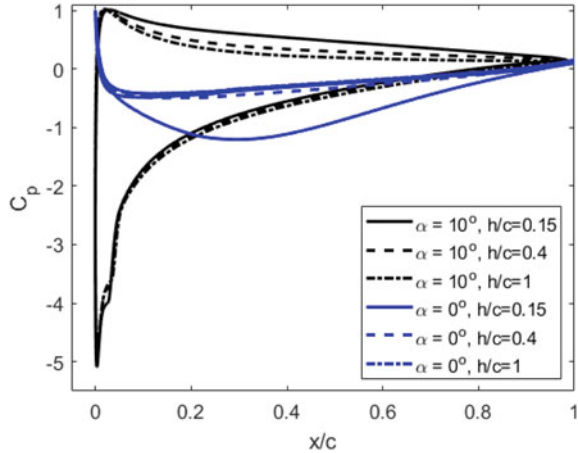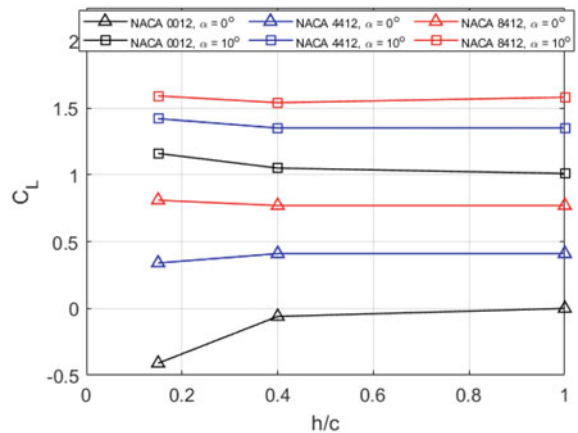**Fig. 5** Comparison of
surface pressure coefficients
is shown for NACA0012,
4412 and 8412 airfoil
sections at angle of attack of
$\alpha = 10°$ and gap ratio, $h/c =$
0.15
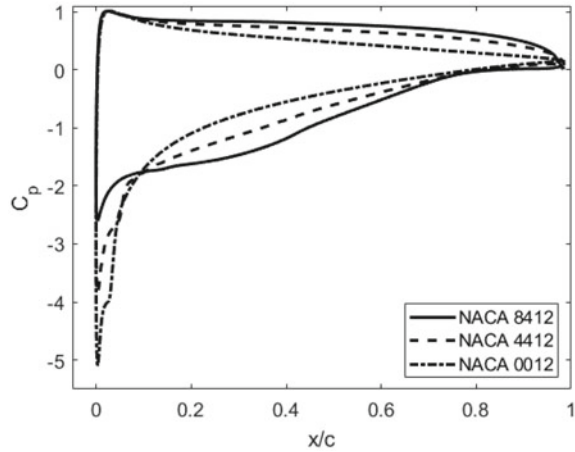
camber). A steepening of surface pressure gradient is observed near the leading
edge on the suction side as the gap ratio is decreased. The variations in surface
pressure on suction side are much more gradual in case of 8412 section. The minimum
pressure magnitude is much higher and pressure gradient much steeper for 0012
section compared with 4412 and 8412 sections, which makes the boundary layer
more susceptible to early separation if the angle of attack is increased further. For
$0.1 < x/c < 0.8$, the values of surface pressure coefficients on suction side are lower
for 8412 section compared with 4412 and 0012 sections. The factors described here
contribute to higher lift coefficient for airfoil sections with higher camber.

Pressure variations in the flow field around different airfoil sections are depicted
in Fig. 6, at $\alpha = 10°$ and gap ratio of 0.4. It is clear that a larger region of high
pressure exists in the gap between the airfoil and wall in case of 8412 section. The
minimum pressure magnitude is smaller and pressure gradient much gradual in case
of airfoil sections with higher camber. The presence of an impermeable wall has a
blocking effect on the wall-normal velocity component and creates a low-velocity
and high-pressure flow in the gap. NACA8412 airfoil section with higher camber
is more effective in decelerating the flow in the gap and redirecting the flow away
towards the upper side of airfoil surface. The values of surface pressure coefficients
are also affected by details of section profiles, e.g. laminar separation bubbles of
small size are observed on upper side of 4412 airfoil at $\alpha = 10°$ and on lower side
of 8412 airfoil at $\alpha = 0°$.

Pressure variations in the flow field, at $\alpha = 0°$, and same gap ratio of 0.4 are
shown in Fig. 7. A zone of negative pressure coefficient exists between the lower
surface and wall which contributes to negative lift in case of NACA0012 section. The
low pressure zone is smaller in case of NACA4412 section. The upward lift in case
of 4412 section is positive but decreases with decreasing gap ratio (Fig. 2). In case of
8412 section, the region between the lower surface and wall is a high-pressure zone
which contributes to an increase in lift coefficient with decreasing gap ratio.
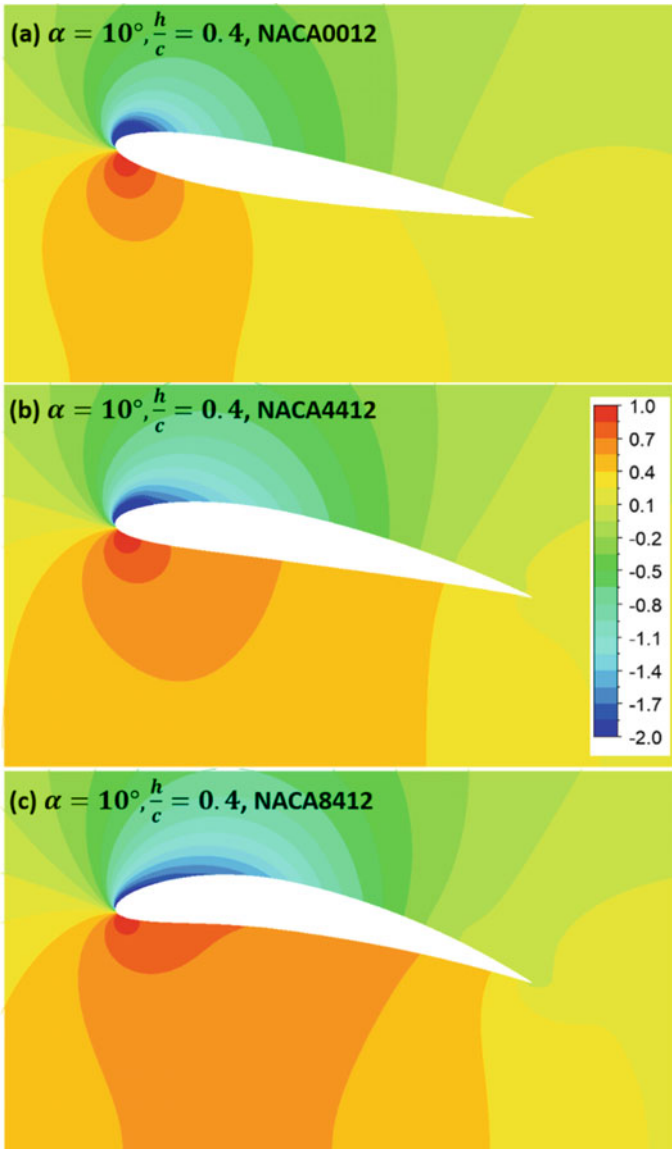
Fig. 6 Contours of pressure coefficient in the flow field are shown for NACA0012, 4412 and 8412 airfoil sections at angle of attack of $\alpha = 10°$ and gap ratio, $h/c = 0.4$
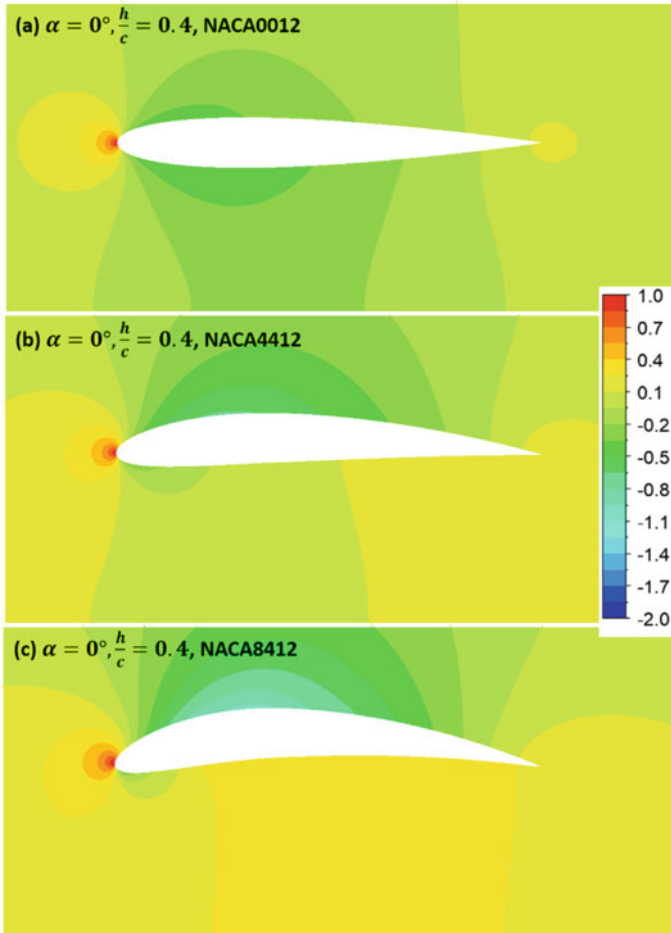
Fig. 7 Contours of pressure coefficient in the flow field are shown for NACA0012, 4412 and 8412 airfoil sections at angle of attack of $\alpha = 0°$ and gap ratio, $h/c = 0.4$

4.2 Irrotational Flow Calculations

Irrotational flow calculations are done for 0012, 4412 and 8412 airfoils at $\alpha = 0°$ to study the effect of proximity of wall, through the impermeability condition, on surface pressure distributions and lift coefficients. The method used in the calculations is the same as described in the previous study by the authors [8].

A gradual rise in pressure on both sides of airfoil surface is obtained with decreasing gap ratio, a trend also seen in RANS simulations [8]. The increasing or decreasing trend in lift coefficients with decreasing gap ratio depends on the asymmetry in pressure increase on the upper and lower sides of an airfoil. The lift coefficients obtained from calculations based on irrotational flow theory are shown

Fig. 8 Lift coefficients
obtained for NACA0012,
4412 and 8412 airfoil
sections from irrotational
flow calculations are shown
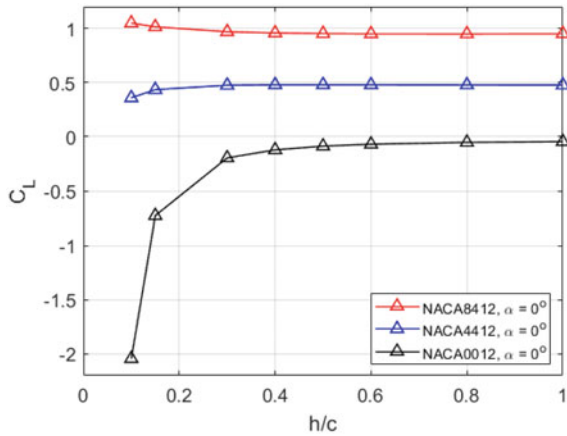
in Fig. 8. An increasing trend in lift coefficient with decreasing gap ratio is obtained
for 8412 airfoil at $\alpha = 0°$, same as that in RANS simulations. A decreasing trend in
lift with decreasing gap ratio at $\alpha = 0°$ is obtained for 0012 and 4412 airfoils which
is also noted in RANS simulations. However, the values of lift coefficient obtained
on the basis of irrotational flow theory are larger in magnitude than those obtained
from RANS simulations.

Since it is the asymmetry in the increase in pressure on the upper and lower sides
of the airfoil that contributes to increase in net lift coefficient, flow separation near
the trailing edge has a larger effect on surface pressure distribution at higher angle
of attack, $\alpha = 10°$.

5 Conclusions

A comparative study of ground effects on symmetric (NACA0012) and cambered
(NACA4412 and 8412) airfoils is performed using incompressible, steady Reynolds-
averaged-Navier-Stokes (RANS) simulations and calculations based on irrotational
flow theory. The effects of wall proximity on surface pressure distributions and lift
coefficients are studied. Reynolds number based on free-stream conditions is 3×10^5.
RANS simulations are conducted at two values of angle of attack, $\alpha = 0°$ and $10°$
for different gap ratios. As noted in prior study by the authors [8], the pressure
distribution obtained from RANS simulations for NACA4412 is observed to be in
good agreement with experimental data [1] available at same flow configurations.

For an angle of attack of $0°$, lift coefficients remain almost constant with changes
in gap ratio from 1 to 0.4 for NACA 0012, 4412 and 8412 airfoil sections. The asym-
metry in changes in surface pressure on upper and lower sides becomes increasingly
important when gap ratio is decreased below 0.4 for both symmetric and cambered
airfoils. For an angle of attack of $\alpha = 0°$, the lift coefficients are observed to decrease,

whereas for $\alpha = 10°$, lift coefficients increase with decreasing gap ratio for both NACA4412 and 0012 airfoils. For NACA8412 airfoil, an increasing trend in lift coefficient with decreasing gap ratio is noted at both angles of attack, $\alpha = 0°$ and $10°$. With increase in airfoil camber, a large reduction in minimum pressure magnitude and surface pressure gradients on upper side of airfoils is observed at different gap ratios. A high-pressure region develops between the lower airfoil surface and the wall with decreasing gap ratio, the extent of which increases with increase in airfoil camber.

Nomenclature

c Chord length [m]
h Trailing edge to wall distance (gap size) [m]
α Angle of attack (°)
C_L Lift coefficient
C_D Drag coefficient
C_p Pressure coefficient
ρ Density of air [kg/m^3]

References

1. Ahmed MR, Kohama Y, Takasaki T (2007) Aerodynamics of a NACA4412 airfoil in ground effect. AIAA J 45(1):37–47
2. Anderson JD. Fundamentals of aerodynamics, 5th edn. McGraw Hill
3. Jung JH, Yoon HS, Chun HH, Hung PA, Elsamni OA (2012) Mean flow characteristics of two-dimensional wings in ground effect. Int J Naval Archit Ocean Eng 4:151–161
4. Smith JL, Graham HZ, Smith JE (2008) The validation of an airfoil in the ground effect regime using 2-D CFD analysis. In: 26th AIAA aerodynamic measurement technology and ground testing conference, paper number AIAA-2008-4262
5. Chawla MD, Edwards LC, Franke ME (1990) Wind-tunnel investigation of wing-in-ground effects. J Aircraft 27(4):289–293
6. Ahmed MR, Sharma SD (2005) An investigation on the aerodynamics of a symmetrical airfoil in ground effect. AIAA J 29:633–647
7. Barber TJ, Leonardi E, Archer RD (1999) A technical note on the appropriate CFD boundary conditions for the prediction of ground effect aerodynamics. Aeronautical J: 545–547
8. Parmar DL, Singh DK, Sharma A (2021) RANS simulations of flow past a NACA4412 placed above an impermeable flat wall. In: National conference on fluid mechanics and fluid power (FMFP), paper number 137
9. Coulliette C, Plotkin A (1996) Aerofoil ground effect revisited. Aeronautical J 100(992):65–74
10. Barber T, Hall S (2006) Aerodynamic ground effect: a case study of the integration of CFD and experiments. Int J Vehicle Des 40(4):299–316
11. ANSYS, Inc. (2018) ANSYS FLUENT 18.0 theory guide

12. Spalart PR, Allmaras SR (1992) A one-equation turbulence model for aerodynamic flows. AIAA paper number AIAA-92-0439. American Institute of Aeronautics and Astronautics
13. Singh DK, Prajapati R, Sharma A (2019) RANS simulations of flow past a NACA0012 airfoil. In: National conference on fluid mechanics and fluid power (FMFP), paper number 80

Numerical Investigation to Study the Effective Position of Air Conditioner in an Office Room

Vikrant Narad, Pratik Malu, Pooja Giri, Sagar Borole, Aryan Naikare, and Pramod Kothmire

1 Introduction

In any office building, there are many heat sources like computers, laptops, led lights, etc. In most offices there is a problem regarding the thermal comfort of a person. A person expects to work in a comfortable environment. Scientifically, our bodies are designed to function within a very tight range around 37 °C. The person will shiver or sweat if the temperature changes a little also. An uncomfortable temperature in an indoor office room can affect the work speed and way of working. These all things can be done by HVAC for an office room. The CFD simulation and analysis for the problem is performed by applying different boundary conditions on the office room. Ansys software with version ANSYS2021 R1 is used for simulation. Ansys is a limited-scale analytics software used to mimic computer models of buildings, electrical appliances, or machine components to analyze power, durability, elasticity, temperature distribution, electromagnetism, fluid flow, and other features. A semi-coupled CFD model that combines the benefits of both completely coupled and totally segregated CFD models has been proposed by Zhang et al. This technique shortens the necessary time while maintaining the accuracy of the simulation [1]. Elhelw offered a design improvement strategy that took the uncertainties related to cooling load estimation into account. Consideration is given to the effects of the seven elements' uncertainty, including interior heat sources and exterior weather conditions [2]. Gagarin et al. have described a special way of heat load computing of heating and ventilation systems. This method allows refining the calculations of heat losses of the building [3]. In their modelling and analysis of an office building in a tropical climate, Kosonen et al. took into account how much energy the HVAC system and

V. Narad (✉) · P. Malu · P. Giri · S. Borole · A. Naikare · P. Kothmire
School of Mechanical Engineering, MIT Academy of Engineering, Alandi, Pune, Maharashtra 412105, India
e-mail: vikrant.narad@mitaoe.ac.in

lighting use. Window solar shading, interior air quality, and energy efficiency are all taken into account [4].

2 Literature Review and Objective

Computational fluid dynamics is used by Srivastava et al. to build and maintain air-conditioning systems while taking into account the various air flow patterns that influence system effectiveness. The entire set of geometry, meshing, and CFD simulation results are displayed [5]. With the help building simulator catherine et al.'s investigated the effects of inaccurate occupancy predictions on Hvac operation. Because SPOT operates on a finer temporal scale than MPC-based HVAC, it can decrease the effects of prediction errors on energy consumption and occupant comfort, which has been found to be true despite its effectiveness in increasing customized comfort [6]. In this research effort, Sung et al. created an indoor air quality control system utilizing the IoT smart house architecture. The objective of this study was to develop fast responses to elevated pollution levels and poor air quality in order to shield people from the physical and mental illnesses brought on by protracted exposure to an unfavourable environment [7]. A thorough strategy for making the most of the potential for energy savings in smart homes has been outlined by Christian et al. The knowledge base that serves as the foundation for the suggested system design enables the incorporation of previously unconsidered data. We were able to make certain decisions using the data, which made more difficult higher-level control jobs easier [8].

Becker et al. developed a simple approach for estimating how much energy may be saved in private residences by using an occupancy-based heating strategy. By using an unsupervised classification method to build an occupancy schedule, they were able to deduce occupancy patterns from unlabelled electricity usage data [9]. In this study paper, Ahmed et al. define passive design strategy as a method of building design that makes use of the architecture of the structure to cut energy use and enhance thermal comfort. In order to establish workable passive cooling solutions for structures with internal heat gains in a particular climate region, a chart for six Queensland towns was constructed by comparing the local climatic conditions with a standard chart [10]. A digital twin framework for MPC on actual and virtual buildings is described by Arendt et al. The study showed that the suggested system can enable the application of energy-saving measures while maintaining comfort levels equivalent to those maintained by current control strategies used by a commercial building management system [11]. Shaker et al. presented adverse condition and critical event prediction is an important subject in a variety of applications and is very closely related to the area of fault detection. ACCEPT was used in this paper to detect and predict faults in an actual commercial building. The proposed method employs PCA and has applications in a variety of fields, as well as being used to generate fault data for analysis purposes in this work [12]. Akata et al. describe the impact of a building-integrated photovoltaic system (BIPV) on room air temperature in a tropical region

has been investigated in this study. The primary parameter of BIPV is building orientation; openings that create a horizontal flow of air can significantly reduce the increase in building indoor air temperature caused by BIPV facade integration [13]. Leissner et al. introduced the NeGeV project which will provide a new solution that demonstrates the operation of the exhaust system by using phase switches to obtain effective heat during cooling needs. With the development of intelligent system controls, the project will demonstrate the integration capabilities of the system into a smart grid system to change the load and control efficiency [14].

Although many academics have worked on HVAC, this paper focuses exclusively on an office environment with various air velocities. This paper's unique objective is to create a comfortable environment in an office space by placing air conditioners in various locations throughout the space at various speeds. A heating, ventilation, and air-conditioning (HVAC) system's major goals are to offer thermal comfort and aid in maintaining acceptable indoor air quality through proper ventilation and filtration. Systems for controlling the temperature, airflow, ventilation, and air conditioning of an entire building are known as heating, ventilation, and air-conditioning (HVAC) systems. On hotter days the HVAC can provide the necessary cooling for the office staff to work properly and be comfortable.

3 Materials and Methods

It's an office room. It comprises four tables, on the top of tables there are four computers demonstrated in the shape of rectangle. The chair-like structure in the figure is of the person and there are four people in the office. Six led lights are mounted on the roof and has a square-like structure. It also has a central AC or the four-way cassette with four inlets. The square box at the centre is the outlet. The material used is aluminium. The dimensions of the office room are 7500 mm × 5500 mm × 3500 mm. There are in total three cases considering central air conditioning, side wall air conditioning and floor air conditioning, respectively. The case 1, 2, 3 denotes central A.C. geometry, side wall A.C. geometry, floor A.C. geometry of an office room, respectively (Figs. 1 and 2).

3.1 Meshing

Meshing is done to divide the figure into small square-like parts and then the equations are applied to get accurate results.

1. The first stage is adding the local sizing. The face-sizing is given to the inlet, light, computer, table and the person with a target mesh size of 0.02, and body sizing is given to the solid that is the office room with a target mesh size of 0.07 mm.

Fig. 1 Geometry creation of
an office room area
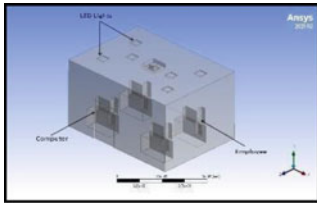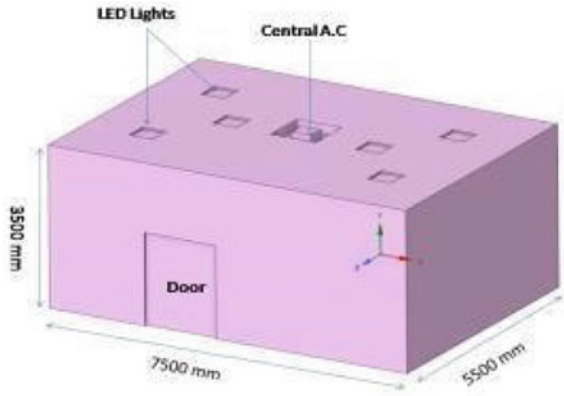
Case 1
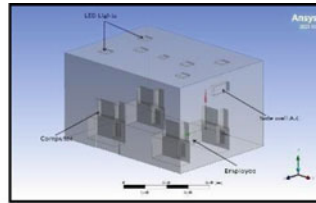
Case 2
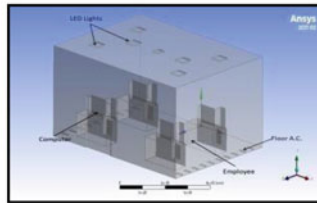
Case 3

Fig. 2 Different geometry cases to study the air- conditioning in office room

2. Surface meshing with a maximum size of 0.07 mm.
3. Created the boundary regions.
4. Followed by boundary creation comes the volume meshing. The office is filled with poly hex-core meshing with cell sizing 0.16. It uses polyhedral elements in the transition zone with a hexahedral element core, providing the optimal combination of mesh elements.
5. The next step is improving the quality of mesh by 0.5 (Fig. 3).

Fig. 3 Meshing performed on three different office rooms
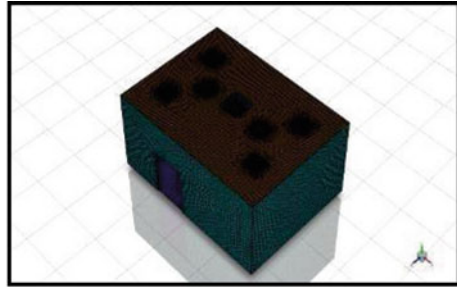
Case 1
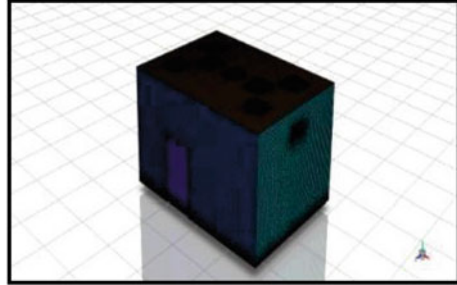
Case 2
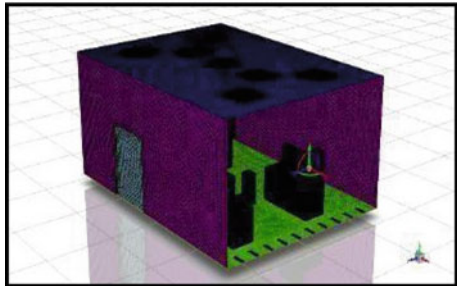
Case 3

3.2   CFD Simulation

Computational fluid dynamics (CFD) allows engineers to visualize flow speed, density, thermal impact, and chemical concentration in any region where flow occurs. Software is used for CFD simulation on ANSYS2021 R1. This helps developers to analyze problem areas and come up with better solutions. CFD is widely used in the construction industry to analzse and improve the structure of the HVAC system.

In an office environment, the thermal comfort is evaluated. Scalable wall functions are made possible by performing the analysis using the realizable k-epsilon model. The velocity and pressure are coupled using the SIMPLEC method. The emissivity ratio of every surface in the office space was close to 0.9. Due to the fact that they do

Table 1 Boundary conditions

S. No.	Conditions	Values
1	Temperature of room	17 °C
2	Velocity	0.5, 1.5, 2.5, 3, 4.5 m/s
3	Relative humidity	50%
4	Heat flux for person	50 W/m^2
5	Emissivity of person	0.98
6	Wall emissivity	0.9
7	Heat flux for light	120 W/m^2
8	Emissivity	0.85
9	Heat flux for computer	180 W/m^2
10	Emissivity of computer	0.9

not lose heat, the table and walls are regarded as adiabatic. 2000 iterations or so were completed. The solutions are then calculated and the outcomes. In the figure below, the temperature and velocity contours are displayed. The vector diagram displays the airflow in the office space.

3.3 Boundary Conditions

See Table 1.

4 Results and Discussion

With reference to the objective, the results are calculated and compared with the ASHRAE conditions. According to ASHRAE, temperature up to 22.2 °C and air speed low up to 0.1 m/s and occupants lightly clothed involved in activities like reading, the person will feel slightly cool. The recommended humidity should hover between 35 and 55 ± 5%.

4.1 Case 1

The office space is made comfortable by the air flow velocity of 3 m/s, which is taken into account by the four-way cassette design. By measuring the air's velocity and temperature around a person, the velocity and temperature contours can be utilized to observe how comfortable they are. The measurements for the temperature and velocity surrounding a person are 295.5 K (22.5°) and 0.1 m/s for a 3 m/s velocity

v = 2.5 m/s   v = 3 m/s
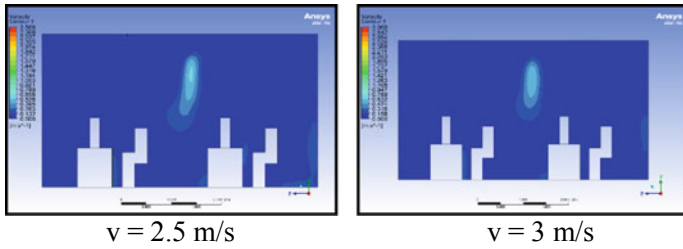
Fig. 4 Case 1 velocity contours

and 298 K (25°) and 0.13 m/s for a 2.5 m/s velocity. Therefore, in case 1, 3 m/s air flow velocity creates the most comfortable environment (Fig. 4).

4.2 Case 3

There are 20 ventilated paths in the floor AC ventilation system. As a result, it will reach the comfortable state quicker than in the other two scenarios. The simulation takes into account two air flow velocities of 0.5 and 1.5 m/s. Given that the air temperature and airflow velocity are 294.5 K (21.5°) and 0.1 m/s, respectively, the arrangement with 0.5 m/s airflow velocity offers a comfortable environment. When simulating airflow at 1.5 m/s, it is found that the office space becomes cooler than the comfortable level and the velocity surrounding one individual is larger than 0.1 m/s. The airflow's temperature and velocity are 290 K (17°) and 0.25 m/s, respectively (Fig. 5).

v = 2.5 m/s   v = 3 m/s
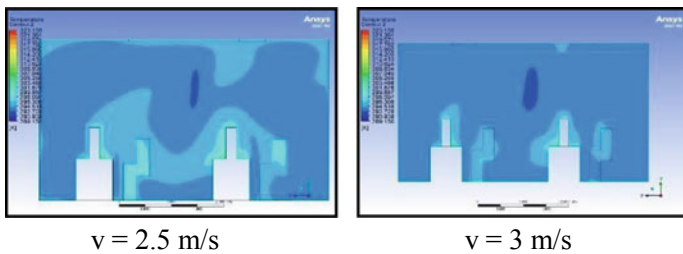
Fig. 5 Case 1 temperature contours

4.3   Case 2

For the side wall ventilation design, there are two air flow velocities: 3 and 4.5 m/s. As in instance 1, where we were able to attain the comfort condition at 3 m/s air velocity, case 2 begins with the same air flow velocity. Given that the air around a person has a velocity of 0.1 m/s and a temperature of 296 K (23°), the velocity of 4.5 m/s creates a comfortable environment. The room's temperature is not uniform throughout, more so for the area close to the AC and less so for the area far from the AC (Figs. 6, 7, 8 and 9).

v = 3 m/s   v = 4.5 m/s
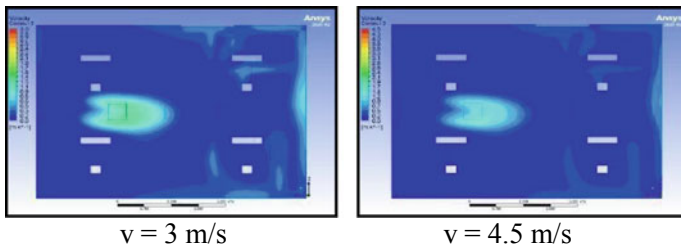
Fig. 6   Case 2 velocity contours

v = 3 m/s   v = 4.5 m/s
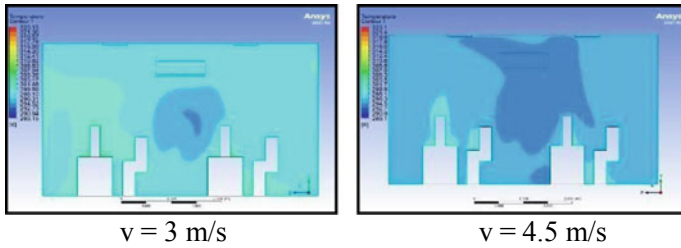
Fig. 7   Case 2 temperature contours

v = 0.5 m/s   v = 1.5 m/s
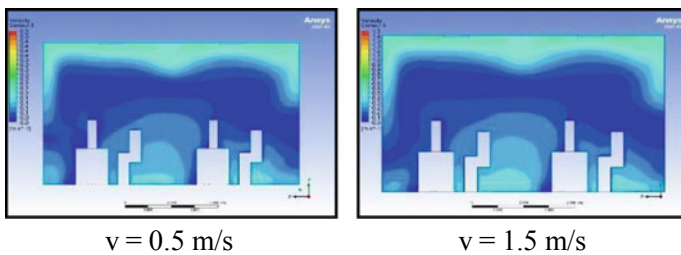
Fig. 8   Case 3 velocity contours

| v = 0.5 m/s | v = 1.5 m/s |
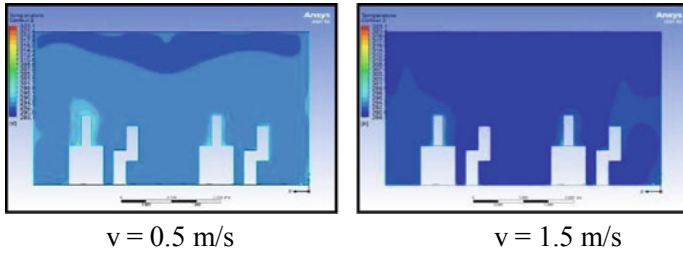
Fig. 9 Case 3 temperature contours

4.4 Comparative Analysis

The results have been quantified using the histogram graphs. Temperature is noted on the *X*-axis and the volume of air in that temperature. It also shows the volume covered by the air in the office room area. The volume of air in a particular temperature range is shown by the bar figures. It is easy to interpret from the above histogram graphs that the air flow in case 1 covers the maximum volume of room than the other two cases, i.e. around 88–90% of the volume in the temperature range of 293–295 K. In case 2, 62–64% of air volume ranges between 293 and 295 K. Similarly, the case 3 graph shows 68% of air volume in the range of 292–294 K.

From the above observations, the four-way air-conditioning system turns out to be the best ventilation system for the selected office area (Fig. 10).

5 Validation of Result

According to ASHRAE Standard 55-2017, thermal environmental conditions for human occupancy note that for thermal comfort purposes, temperature could range from between approximately 19–27 °C. From results the air flow in case 1 covers the maximum volume of room than the other two cases, i.e. around 88–90% of the volume in the temperature range of 20–22 °C which is best for human comfort.

Hence the results are validated with ASHRAE Standard.

Fig. 10 Histogram graphs of three cases demonstrating the distribution of air volume at different temperature ranges
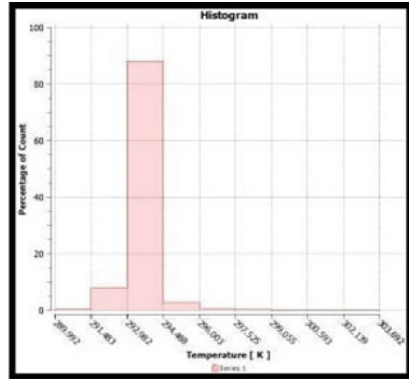
Case 1 four-way cassette design
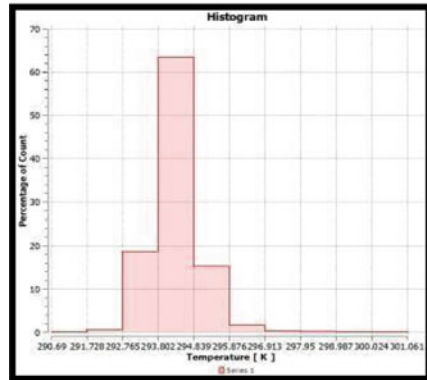
Case 2 Side wall ventilation design
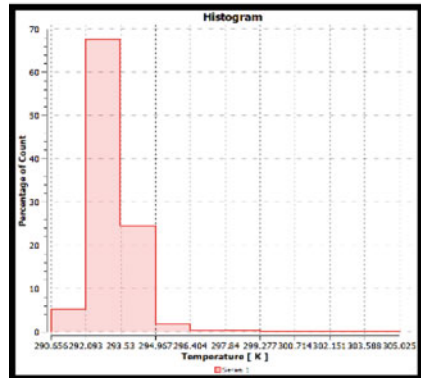
Case 3 floor AC ventilation system

6 Conclusion

CFD simulations in an office room area are calculated. Comfort conditions achieved by using different air flow velocities are evaluated and analyzed. The three designs of the office room area are similar but ventilated by different configurations of ventilated air conditioner. With reference to ASHRAE the air temperature and velocity around the person should be 295k and 0.1 m/s.

The observations produced by using CFD are as follows:

(1) Four-way cassette/central AC performed better than other ventilated configurations.
(2) Though the floor AC required low air flow velocity to attain the comfort condition, as it had ten air flow inlets, it cannot be considered as an energy efficient design.
(3) The sidewall AC attained the comfort condition in half of the office area, the other half had slightly high air temperature. The air flow velocity is not the same in both the parts. The people near AC will experience slightly higher temperature and air flow velocity than the people away from the side wall AC.
(4) The four-way cassette and floor AC have equal air flow distribution in the office area, hence the air velocity near the person is equal at all places. Whereas, the side wall AC is mounted at one side of the wall, hence the air temperature and velocity will not be the same in the office area.

References

1. Zhang L, Yu X, Lv Q, Cao F, Wang X (2019) Study of Transient indoor temperature for a HVAC room using a modified CFD method. Energy Procedia 160:420–427
2. Elhelw M (2016) Analysis of energy management for heating, ventilating and air-conditioning systems. Alexandria Eng J 55(2):811–818
3. Gagarin VG, Lushin KI, Kozlov VV, Neklyudov AY (2016) Path of optimized engineering of HVAC systems. Procedia Eng 146:103–111
4. Kosonen R. Sustainable office building: should I focus on HVAC-system design or building envelope
5. Srivastava G, Kumar A, Chandel D, Dabas H, Mishra SA (2019) CFD simulation of air conditioning system of the classroom. Int Dev 3(4):521–523
6. Catherine R, Jain M, Kalaimani R, Srinivasan K (2018) Using personal environmental comfort systems to mitigate the impact of occupancy prediction errors on HVAC performance. Energy Inform 60:1–21; Sung W, Hsiao S (2021) Building an indoor air quality monitoring system based on the architecture of the Internet of Things. Wireless Commun Netw: 1–41
7. Christian R, Felix I, Kofler M, Wolfgang K (2011) Think home energy efficiency in future smart homes. EURASIP J Embedded Syst 2011:1–18
8. Becker V, Coroama V, Kleiminger W, Mattern F (2018) Estimating the savings potential of occupancy-based heating strategies. In: Energy informatics. Springer, Corpus ID: 44199465, pp 1–18
9. Ahmed S, Khan M, Amanullah A, Rasul M (2014) Selection of suitable passive cooling strategy for a subtropical climate. Int J Mech Mater Eng 14(2014):1–11

10. Arendt K, Clausen A, Johansen A, Jorgensen N, Kjaergaard M, Sangogboye F, Veje C (2021) A digital twin framework for improving energy efficiency and occupant comfort in public and commercial buildings. Energy Inform 40:1–19
11. Egedorf S, Jorgensen N, Martin R, Shaker H (2018) Adverse condition and critical event prediction in commercial buildings: Danish case study. Energy Inform 10(2018):1–19
12. Akata M, Njomo D, Mempouo B (2015) The effect of building integrated photovoltaic system (BIPVS) on indoor air temperatures and humidity (IATH) in the tropical region of Cameroon. Future Cities Environ 4:1–10
13. Leissner J, Kilian R, Kotova L, Jacob D, Mikolajewicz U, Broström T, Smith JA, Schellen HL, Martens M, Schijndel JV, Antretter F, Winkler M, Bertolin C, Camuffo D, Simeunovic G, Vyhlídal T (2015) Climate for Culture: assessing the impact of climate change on the future indoor climate in historic buildings using simulations. Heritage Sci 3:38, 1–15
14. Hansen T, Jradi M, Kamuk K, Kieseritzky E, Lundi, Nicolaisen C, Veje C (2019) NeGeV: next generation energy efficient ventilation system using phase change materials. Energy Inform: 1–12

Prevention of Expansion Shock by the Control of Numerical Dissipation of Upwind Schemes

Abhishek Mondal, Anoop K. Dass, and Atul K. Soti

1 Introduction

Euler equations are frequently solved in the context of many aerospace design problems. These equations govern the dynamics of inviscid compressible flows. The unsteady Euler equations demand the design of a stable, robust and accurate scheme that works for a variety of challenging situations. The Euler equations allow discontinuous solutions in the forms of shocks, contact discontinuities, slip surfaces and expansion waves with sonic points [1]. The addition of artificial viscosity for the purpose of capturing shocks was first pioneered by von Neumann and Richtmyer [2]. With further research in this field, it became clear that the addition of explicit numerical diffusion is essential for numerical stability in case of central discretization of the flux terms. Pure central differencing of the Euler fluxes leads to instabilities because the direction of wave propagation is not respected, upwind schemes on the other hand are so designed as to respect the direction of signal propagation and hence they are generally stable because the strategy itself used to construct the schemes. They also provide better nonlinear stability near shocks. The FVS scheme of van Leer [3] is known to be highly robust but has high numerical diffusion which leads to smearing of discontinuities. Gudonov's scheme [4] laid the foundation for a variety of upwind schemes, the primary drawback of which was that it was computationally expensive as it involves an exact Riemann solver. The expansion shock phenomenon suffered by the Steger and Warming Scheme [5], the first major FVS scheme, was remedied by the dissipative van Leer scheme. Later, the quest for better accuracy gave rise to a number of FVS and FDS upwind schemes. A few important ones are Roe's FDS scheme [6], Liou and Steffen's AUSM scheme [7], Edward's LDFSS Scheme [8], Zha-Bilgen's scheme [9], Jameson's CUSP scheme [10], etc. Majority of these schemes have relatively low dissipation and the ability to capture shocks

A. Mondal (✉) · A. K. Dass · A. K. Soti
Department of Mechanical Engineering, IIT Guwahati, Assam 781039, India
e-mail: abhishek.mondal@iitg.ac.in

accurately. However, the question whether these schemes satisfy the entropy condition has received less attention. Merely not giving an expansion shock in a particular test problem is not a definitive proof of satisfying the entropy condition. However, if a scheme is seen to give expansion shock in a certain test case, we can justifiably say that it violates the entropy condition. In this paper, we experiment with two such schemes, namely, Roe's scheme and Zha-Bilgen scheme. Through a test case designed by Zha [11], we first demonstrate that for the quasi-one-dimensional nozzle flow through a convergent-divergent nozzle, both these schemes give expansion shocks at the throat, thus violating the entropy condition. Roe's FDS scheme is an important event in the development of approximate Riemann solvers as a natural progression to the Gudonov's scheme which involves an exact Riemann solver. Although, it provides high accuracy for a range of problems, Roe's FDS scheme suffers from limitations such as computational cost [7], carbuncle phenomenon and expansion shock [12]. Being a remarkable scheme with low dissipation, the Roe's scheme has received considerable attention from researchers and several so-called entropy fixes have been suggested [13–15]. We also demonstrate that one such entropy fix, namely, Hyman and Harten's [14] entropy fix rids the scheme of its entropy condition violation at the throat. It has been widely demonstrated that the entropy fixes cures Roe's scheme also of the strong-shock carbuncle phenomenon. Thus, the Roe's scheme gives a very accurate and powerful method when acting in conjunction with various entropy fixes.

In this paper, we observe that all these entropy fixes are based on the modification of the Roe's flux function and the strategy cannot be seamlessly extended to other schemes that violate the entropy condition. Not denying the effectiveness of these entropy fixes for the Roe's scheme, we ask ourselves—'Is it possible to adopt a general strategy that provides a common cure to all entropy condition violating upwind schemes'? The answer seems to be 'yes', and that is the problem we address in this paper. We first demonstrate that by adopting this general strategy the expansion shock given by the Roe's scheme can be eliminated as effectively as the entropy fixes found in literature. We then experiment with the other upwind scheme of Zha-Bilgen that violates the entropy condition. We first demonstrate that this scheme also gives an expansion shock at the nozzle throat and then go to show that the common strategy we propose remedies the problem effectively for this scheme as well. This, we feel justifies the claim that our strategy is likely to work with all entropy condition violating upwind schemes. The cure for entropy condition violation we propose has its roots in the dissipation regulation (DR-LLF) of a central scheme proposed in [1]. It has already been observed that an upwind flux function can be first cast in the form of a central flux function plus some dissipation term. The diffusion regulation strategy proposed in the DR scheme can be easily applied to the dissipation term inherently associated with an upwind scheme. In the next section, we explain the methodology adopted and then substantiate our claims with numerical results. It may be noted that we solve the nozzle flow problem using the quasi-one-dimensional (quasi-1D) version of the Euler equations using finite volume discretization.

2 Problem Definition and Numerical Procedure

2.1 Geometry

The Sod's problem [16] is a classic-bench-marking problem often used to test the performance of numerical schemes for hyperbolic conservation laws. Figure 1 shows a shock tube of length $L = 15$ m, in the middle there exists a diaphragm separating two gases of different pressures and densities into two sections, the driver with higher pressure and driven section with lower pressure. Initially, the gases on both sides of the diaphragm are at rest. Once the diaphragm is broken at $t = 0$ it leads to flow in the tube; the Mach number variation is studied numerically vs. analytically for validation. There are two problems, namely Sod's first and second problem. For the first problem the pressures in the driver and driven section are 1000 and 100 kPa, respectively while the densities are 1 and 0.125 kg/m³. For the Sod's second problem the pressures in the driver and driven section are 1000 and 10 kPa, respectively while the densities are 1 and 0.01 kg/m³. For both the cases the gases are at rest initially.

The geometry of the nozzle chosen for analysis is a converging–diverging nozzle designed and tested at NASA Langley Research Centre namely nozzle A2. The geometry is formed to be a converging and diverging section with slope angles of θ and β, respectively. The sections are connected via a circular-arc as shown in Fig. 1. The geometry is symmetric in nature. The mathematical equations describing the geometry [7] are given below:

$$y = x \tan \theta + h_t, \quad 0 \leq x \leq L_1 \tag{1}$$

$$y = -\sqrt{r_c^2 - (x - x_c)^2} + y_c, \quad L_1 \leq x \leq L_2 \tag{2}$$

$$y = (x - x_t) \tan \beta + y_t, \quad L_2 \leq x \leq L_3 \tag{3}$$

In the above equations, $\theta = -22.33°$, $\beta = 1.21°$, $L_1 = 4.74$ cm, $L_2 = 5.84$ cm, $L_3 = 11.56$ cm, $x_c = 5.7814$ cm, $y_c = 4.11$ cm, $r_c = 2.74$ cm, $x_t = 5.84$ cm, $y_t = 1.37$ cm. The minimum area of the nozzle is located at x_c where y_t is the throat radius (Fig. 2).
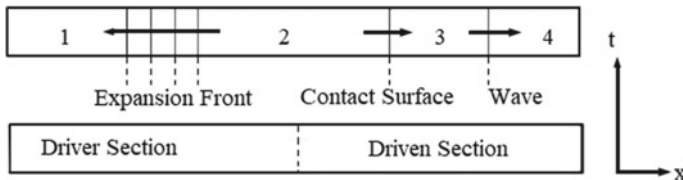
Fig. 1 Schematic of Sod's shock tube problem
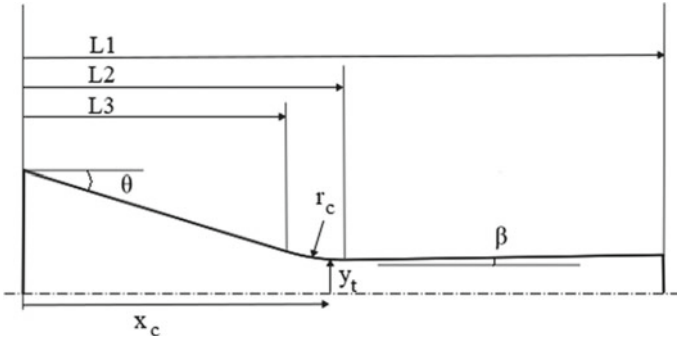
Fig. 2 A2 nozzle NASA

2.2 Governing Equations

In case of the quasi-1D nozzle problem, the physics is governed by the Euler equation. In the Cartesian coordinates it is expressed as:

$$\frac{\partial U}{\partial t} + \frac{\partial F}{\partial x} - H = 0, \tag{4}$$

where,

$$U = AQ, \, F = AE.$$

Here, U is the vector of conserved variables and F is the flux vector.

$$Q = \begin{bmatrix} \rho \\ \rho u \\ e \end{bmatrix}, \quad E = \begin{bmatrix} \rho u \\ \rho u^2 + p \\ (e + p)u \end{bmatrix}, \quad H = \frac{\mathrm{d}A}{\mathrm{d}x} \begin{bmatrix} 0 \\ p \\ 0 \end{bmatrix}.$$

Additionally, as we have three governing equations and four unknown's density, momentum, energy and also the pressure term. To close this system, we use the below equation.

$$p = (\gamma - 1)\left(e - \frac{1}{2}\rho u^2\right) \tag{5}$$

In the above equation, ρ is the density, u is the velocity in the x-direction, p is the static pressure, e is the total energy, i.e. the sum of internal and kinetic energy per unit volume and A is the cross-sectional area of the nozzle (Fig. 3).

We use the finite volume method (FVM) formulations to discretize the above governing equations and obtain the following formulation for cell 'I' and time level 'n'.

Fig. 3 Computational 1D
finite volumes with cell
interface

Fig. 3 Computational 1D finite volumes with cell interface
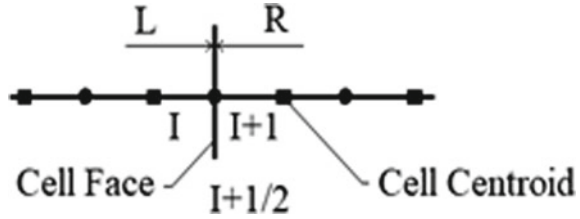
$$Q_i^{n+1} = Q_i^n - \Delta t \left(\frac{1}{\Delta x A_i} \left(F_{i+\frac{1}{2}} - F_{i-\frac{1}{2}} \right) - \left(\frac{H_i}{A_i} \right) \right)^n \tag{6}$$

It is to be noted that the same formulations are applicable to the Sod's shock tube problem with $A_i = 1$ and $H_i = 0$.

2.3 Artificial-Viscosity Form of Central Schemes

It is known that central discretization of the flux terms for the Euler equations which are hyperbolic in nature leads to numerical instabilities. The stabilization is achieved by the explicit addition of a numerical diffusion term. Hence, we solve a modified Euler's equation which contains second-order derivatives which exhibit viscous-like effects. The presence of excessive numerical diffusion smears out the discontinuities and therefore it becomes critical to control the diffusion term by the introduction of a diffusion regulation parameter. The flux expression in general can be derived as follows:

$$\frac{\partial U}{\partial t} + c \frac{\partial F}{\partial x} = 0. \tag{7}$$

In the above equation, c is the speed of wave propagation. Since, the direction of signal propagation is important for the discretization of the flux terms, we express c as the algebraic sum of two parts as shown in Eq. 6.

$$c = \frac{c + |c|}{2} + \frac{c - |c|}{2} \tag{8}$$

In the above equation, it is to be noted that if the magnitude of c is positive, the second term becomes zero, while in case c is negative, the first term becomes zero.

$$\frac{\partial U}{\partial t} + \frac{c + |c|}{2} \frac{\partial F}{\partial x} + \frac{c - |c|}{2} \frac{\partial F}{\partial x} = 0 \tag{9}$$

Now, the upwind scheme can be applied appropriately to each of the flux term. Expressing the flux terms as shown below allows us to apply upwind differencing

without concern about the direction of wave propagation.

$$\frac{U^{n+1} - U^n}{\Delta t} + \left(\frac{c + |c|}{2}\right)\frac{F_i - F_{i-1}}{\Delta x} + \left(\frac{c - |c|}{2}\right)\frac{F_{i+1} - F_i}{\Delta x} = 0$$

Finally, the flux terms can be collected to express the above as the sum of a central scheme and an additional diffusion term.

$$U^{n+1} = U^n - \frac{\Delta t}{2\Delta x}\{c(F_{i+1} - F_{i-1})\} + D, \tag{10}$$

where D is the numerical diffusive flux given by

$$D = |c|\frac{\Delta t}{2\Delta x}(F_{i+1} - 2F_i + F_{i-1}). \tag{11}$$

In the above equation, the diffusive flux term is regulated by the introduction of the diffusion regulation parameter Φ [1], this parameter is set based on the jump in Mach number across the cell interface and its magnitude in comparison with a parameter δ [1], the recommended value of which is 0.5.

$$U^{n+1} = U^n - \frac{\Delta t}{2\Delta x}\{c(F_{i+1} - F_{i-1})\} - \Phi D \tag{12}$$

2.4 Numerical Procedure

In case of the Sod's shock tube problem, the pressure, velocities and densities are known throughout the domain at the initial condition. The properties in the tube are uniform with a single discontinuity, therefore, it can be classified as a Riemann problem, the analytical solution to which is well-known [1]. It is to be noted that most of the analytical calculations needed are trivial, but numerical techniques need to be employed to find the pressure ratios across the shock as there is no straightforward way to solve the implicit equation relating the pressures p_1 and p_2 as shown in Eq. 13.

$$\frac{p_4}{p_1} = \frac{p_2}{p_1}\left[1 + \frac{\gamma - 1}{2a_4}\left\{u_4 - u_1 - \frac{a_1}{\gamma}\frac{\frac{p_2}{p_2} - 1}{\sqrt{\frac{\gamma-1}{2\gamma}\left(\frac{p_2}{p_2} - 1\right) + 1}}\right\}\right]^{\frac{-2\gamma}{\gamma-1}}, \tag{13}$$

where a is the speed of sound and the subscripts denote the corresponding region in the shock tube in Fig. 1.

For the nozzle problem, we assume that the inlet of the nozzle is connected to an infinite reservoir, for which the pressure and temperature are taken as the reservoir conditions of 101,325 Pa and 300 K, respectively. For the entry boundary condition for isentropic transonic flow, we apply the method of characteristics for specifying the correct number of boundary conditions, i.e. the inlet and outlet boundary conditions needed are specified based on the number of characteristics entering and leaving the corresponding boundary. The number of variables at the inlet is specified equal to the number of characteristics entering through the same, whereas, the number of variables to be extrapolated from the interior of the domain is equal to the number of characteristics leaving the domain.

In the quasi-1D nozzle problem, there are three characteristic waves crossing any point in the domain simultaneously. For the case considered, two characteristics enter and one leaves the computational domain. Therefore, we fix two variables at the inlet and extrapolate one from the interior. In the outlet for the supersonic case, three characteristics leave the domain. So, all the variables are extrapolated from within the computational domain.

The numerical formulation is done using FVM, while the two schemes chosen for study are the Roe and Zha-Bilgen scheme. For the purposes of comparison with the analytical case, the area-Mach number relation [17] mentioned in Eq. 14 is solved using Newton–Raphson method.

$$\left(\frac{A}{A_{\mathrm{t}}}\right)^2 = \frac{1}{M^2}\left[\frac{2}{\gamma+1}\left(1 + \frac{\gamma-1}{2}M^2\right)\right]^{\frac{(\gamma+1)}{(\gamma-1)}}, \tag{14}$$

where A_{t} is the area at the throat of the nozzle.

For the numerical solutions, we use a uniform structured 1D grid. The Roe's scheme involves solving the approximate Riemann problem for every grid point. The Zha-Bilgen scheme on the other hand involves splitting the fluxes into a convective and pressure parts.

2.5 Grid Independence Test

The grid independence test is performed on the Sod's second problem for a variety of grid sizes. We observe that the numerical results for $N = 200$ has reasonable accuracy. Here, for the purpose of resolving the entropy violation we choose lesser number of grid points. Although, choosing a large number of points may give better agreement with the analytical results, it also reduces the jump at the sonic point thus making it more difficult to identify and resolve the same (Fig. 4).
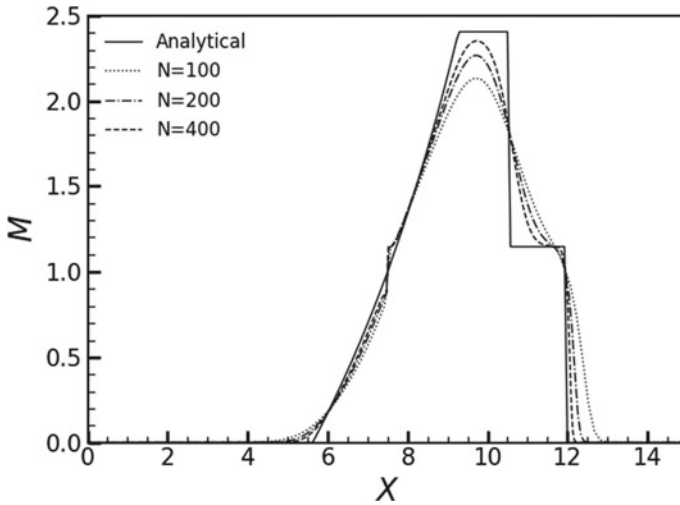
Fig. 4 Comparison of results for various grid sizes

2.6 Code Validation

The FVM formulations of the Zha-Bilgen and Roe's schemes are validated by comparing with the well-known Sod's shock tube problem [16] along with its analytical solution. For the shock tube problem, the time step at which the plots were verified is $t = 0.005$ s and the chosen value of Courant–Friedrichs–Lewy (CFL) number is 0.1. Additionally, it is also demonstrated that the analytical solution of the quasi-1D nozzle problem is in good agreement with the Roe's scheme when the well-known Hyman and Harten Fix is applied to the same as shown in Fig. 6.

We observe in the Fig. 5 that the numerical results are in good agreement with the analytical solution. Next, the code of the quasi-1D nozzle problem is also validated by plotting the analytical results along with the Roe's scheme with the incorporation of a well-known entropy fix name.

In the Fig. 6 for the plot without the fix, we observe that the Roe scheme exhibits a strong-shock at the throat of the nozzle. We choose one of the many well-known existing entropy fixes for the Roe scheme, namely Hyman and Harten Fix [14]. As expected this rids the scheme of its entropy violation condition and no jump is visible in the throat region.
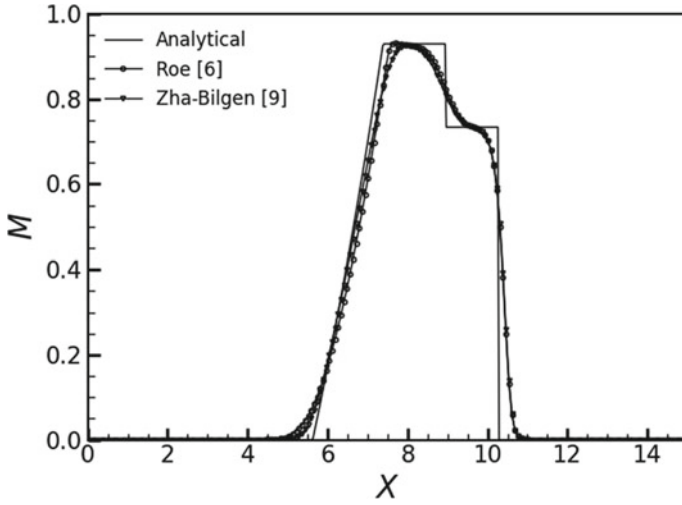
Fig. 5 Comparison with analytical results of Sod's first shock tube problem
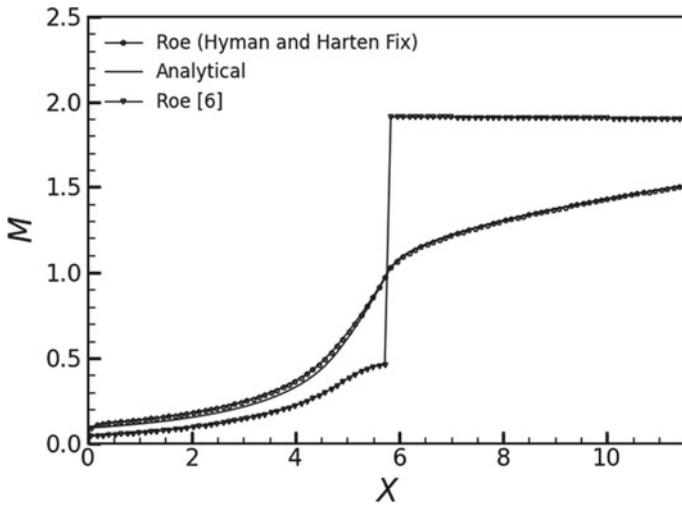
Fig. 6 Demonstration of Hyman and Harten's entropy fix for Roe's scheme

3 Results and Discussion

The numerical computations are performed on a structured 1D mesh using the FVM formulations using an in-house code written in C language. Firstly, Sod's second shock tube problem is implemented as it is expected that both the Zha-Bilgen as well as the Roe's scheme will produce a jump near the sonic region.
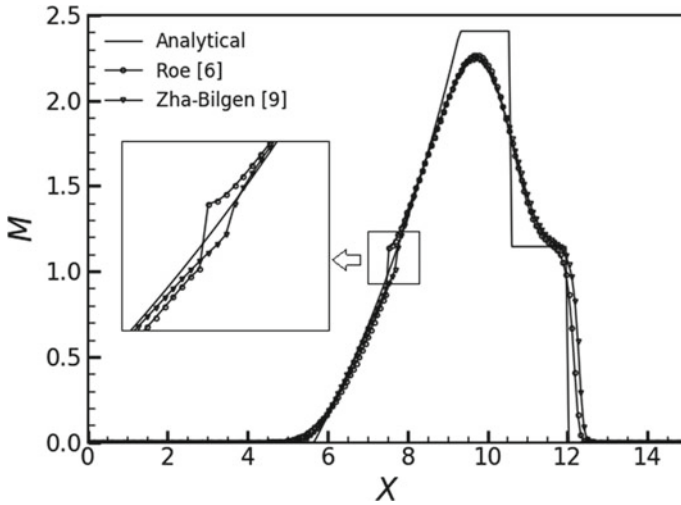
Fig. 7 Entropy violation for Roe and Zha-Bilgen schemes: shock tube problem

It can be observed from Fig. 7 that there is a jump in the expansion front near the sonic region where Mach number is equal to one. The results of the same is shown in Fig. 7.

It can be seen in the Fig. 7 that the violation of the entropy condition which caused a jump has been resolved upon incorporating the diffusion regulation parameter and setting the value optimally so as to minimize smearing, while simultaneously resolving the jump near the sonic point. It is also worth noting that reducing the dissipation regulation parameter any further would cause the schemes to become unstable (Fig. 8).

Secondly, the quasi-1D nozzle problem is addressed. For transonic flow, we observe a jump near the throat, i.e. the sonic point. For the isentropic transonic case, it is expected that the velocity or Mach number will gradually increase from subsonic to supersonic speeds without any jumps. However, at the sonic point the Zha-Bilgen and Roe's scheme is expected to show a jump in the throat near the sonic region due to the violation of the entropy condition as shown below in Fig. 9.

Finally, the present problem which involves the control of the diffusion regulation parameter to resolve the entropy violation is explored.

In the Fig. 10, a minimal amount of dissipation is added so as to handle the existing issues with minimal smearing of the results as diffusion inherently smooths out discontinuities and imparts stability to the numerical calculations.
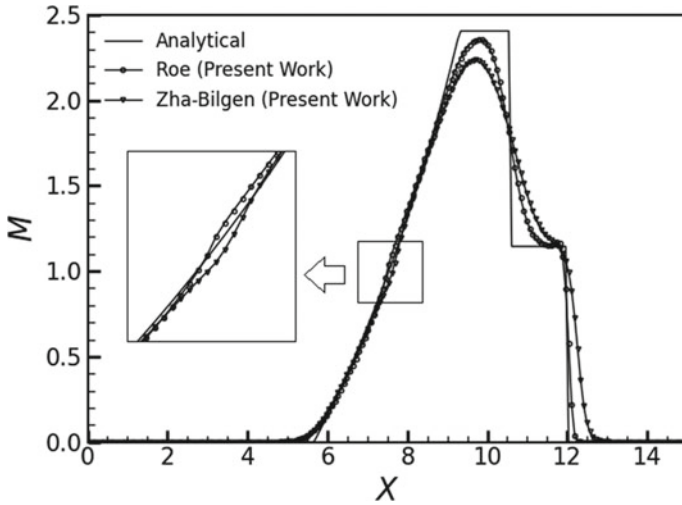
Fig. 8 Entropy violation fix for Roe and Zha-Bilgen schemes using dissipation regulation
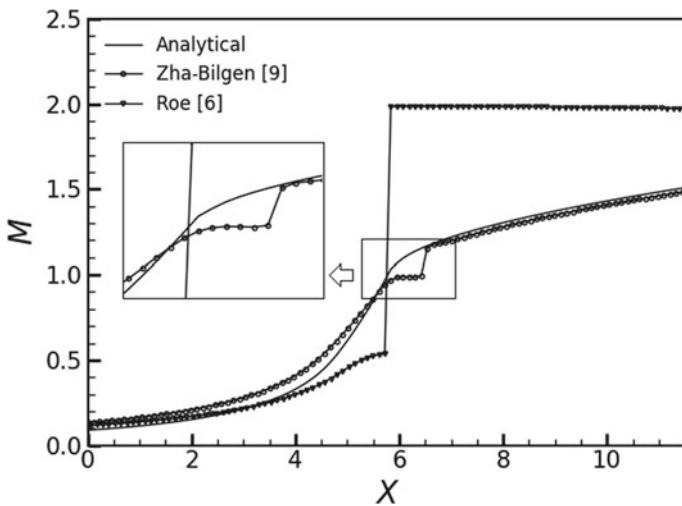
Fig. 9 Entropy violation for Roe and Zha-Bilgen schemes: nozzle problem

4 Conclusions

A number of upwind schemes are seen to give expansion shocks in some flow situations involving the Euler equations, which is a direct violation of physical laws. As the Euler equations are frequently used in the aerodynamic design of various objects such as wings, eliminating these nonphysical solutions is an extremely important
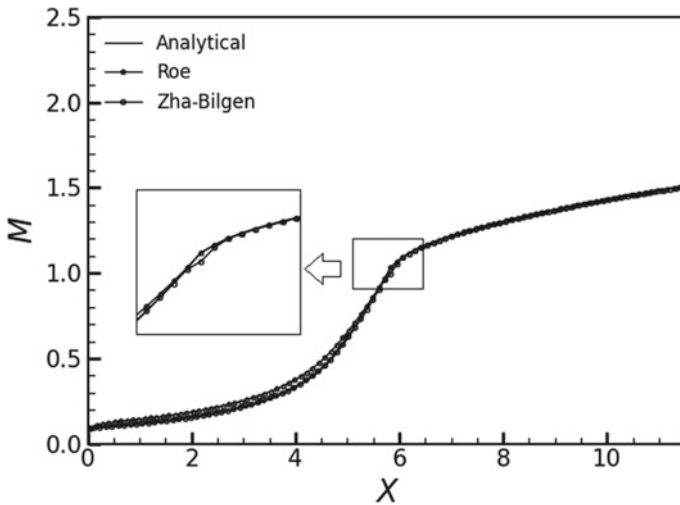
Fig. 10 Entropy violation fix for Roe and Zha-Bilgen schemes using dissipation regulation

CFD activity. This work proposes a general remedy to the problem of expansion shock demonstrated by some upwind schemes. To substantiate our claim, we take two well-known schemes that are known to violate the entropy condition, namely the Roe's scheme and the Zha-Bilgen scheme. We use these schemes to solve the quasi-1D Euler equations that govern the transonic flow in a convergent-divergent nozzle. As expected both these schemes give expansion shocks at the nozzle throat, where the flow turns supersonic from subsonic, thus violating the entropy condition. A number of entropy fixes have been proposed for the Roe's scheme, we use one of these to show that it remedies the problem of expansion shock at the throat. However, we observe that this remedy is not general in nature and is largely scheme-dependent. This motivates us to find a general cure for all upwind schemes that violate the entropy condition. This general strategy consists in first casting the upwind scheme in the form of a central-plus-dissipation scheme, and then regulating the diffusion proposed in a scheme named DR-LLF [1] scheme. Our numerical results clearly demonstrate that the expansion shock given by both Roe's and Zha-Bilgen schemes are completely eliminated by suitably adjusting the diffusion regulation parameter. In the case of Roe's scheme, the entropy fix proposed earlier and our diffusion regulation strategy are seen to be equally effective. In the case of Zha-Bilgen scheme our diffusion regulation strategy is highly effective in eliminating the expansion shock at the throat. As the method proposed in this work is likely to remedy the problem of entropy condition violation exhibited by any upwind scheme, the framework is very general. In this paper, we present case studies involving only two upwind schemes. Work is in progress to determine which other upwind schemes violate the entropy condition and then examine how our general cure remedies the problem.

Nomenclature

A	Cross-sectional area (cm^2)
A_t	Cross-sectional area of throat (cm^2)
D	Numerical diffusion (–)
F	Flux vector in the x-direction (–)
h_t	Throat radius (cm)
I	Cell number (–)
J	Flux Jacobian matrix (–)
L	Left side of cell interface (–)
SSSL$_1$	Length of converging section (cm)
L_2	Length of converging and curved throat region (cm)
L_3	Length of nozzle (cm)
M	Mach number (–)
P_o	Stagnation pressure (Pa)
r_c	Radius of curvature of the throat (cm)
R	Right side of cell interface (–)
T_o	Stagnation temperature (K)
U	Vector of conserved variables (–)
β	Angle of diverging section (°)
θ	Angle of converging section (°)
γ	Ratio of specific heats (–)
ρ	Density of fluid (kg/m^3)
Φ	Diffusion regulation parameter (–)

References

1. Jaisankar S, Raghurama Rao SV (2009) A central Rankine-Hugoniot solver for hyperbolic conservation laws. J Comput Phys 228:770–798
2. Von Neumann J, Richtmyer RD (1950) A method for the numerical calculation of hydrodynamic shocks. J Appl Phys 21:232–237
3. Van Leer B (1984) On the relation between the upwind-differencing schemes of Gudonov, Enguist-Osher and Roe. SIAM J Sci Stat Comput 5(1):1–20
4. Godunov SK (1959) A difference scheme for numerical computation of discontinuous solutions of the equations of hydrodynamics. Mat Sbornik 47:271–306
5. Steger JL, Warming FF (1981) Flux vector splitting of the inviscid gas dynamics equations with application to finite-difference methods. J Comput Phys 40:263–293
6. Roe PL (1961) Approximate Riemann solvers, parameter vectors, and difference schemes. J Comput Math Phys 1:267–279
7. Liou MS, Steffen CJ Jr (1993) A new flux splitting scheme. J Comput Phys 107:23–39
8. Edwards JR (1997) A low-diffusion flux-splitting scheme for Navier-Stokes calculations. Comput Fluids 26:635–659
9. Zha GC, Bilgen E (1993) Numerical solutions of Euler equations by using a new flux vector splitting scheme. Int J Numer Methods Fluids 17:115–144

10. Jameson A (1995) Analysis and design of numerical schemes for gas dynamics, 2: artificial diffusion, upwind biasing, limiters and their effect on accuracy and multi-grid convergence. Int J Comput Fluid Dyn 4(3–4):171–218
11. Zha GC (1999) Numerical tests of upwind scheme performance for entropy condition. AIAA J 37(8):1005–1007
12. Kim S, Kim C, Rho O, Hong SK (2003) Cures for the shock instability: development of a shock-stable Roe scheme. J Comput Phys 185:342–374
13. Harten A (1983) High resolution schemes for hyperbolic conservation laws. J Comput Phys 49:357–393
14. Harten A, Hyman JM (1983) Self-adjusting grid methods for one dimensional hyperbolic conservation laws. J Comput Phys 50:253–269
15. Le Veque RJ (2001) Finite volume methods for conservation laws and hyperbolic systems (to be published)
16. Sod GA (1978) A survey of several finite difference methods for systems of non-linear hyperbolic conservation laws. J Comput Phys 27:1–31
17. Laney CB (1998) Computational gas dynamics, 1st edn. Cambridge University Press, Cambridge

Numerical Investigations of Flow in Cuboidal Liquid Metal Battery

Kaustubh Thakurdesai and Avishek Ranjan

1 Introduction

Electrical grids operate by balancing the demand and supply levels and integration of renewables (solar and wind) which are inherently intermittent requires storage. Liquid metal battery (LMB) is a promising candidate for reliable and non-degradable energy storage at grid scale at low cost. Practical LMBs invented at MIT [1] and manufactured by a start-up AMBRI are already in use in the United States. A typical LMB consists of electrolyte, sandwiched in between two electrically conducting liquid metals or its alloys of different electronegativity, inside a casing as shown in Fig. 1(a). These layers are immiscible and self-segregate due to their densities, thus making LMB assembly simple and cost-effective.

During discharge, metal ions produced at the anode due to oxidation travel through the electrolyte and are reduced at surface of the cathode. The opposite happens during charging after which the negative electrode is replenished. Fluid flow inside the LMB can cause a short circuit, when the liquid metals separated by the electrolyte will come in contact with each other. Tayler instability (TI), MHD interface instabilities, electro-vortex flow (EVF) and thermal convection are some phenomena that may cause interface disruptions inside the LMB [2, 3]. EVF is generated inside an LMB due to converging or diverging current, which has a nonzero curl, thus driving the flow away from the sidewalls and forming vortices (Fig. 1(b)).

K. Thakurdesai (✉) · A. Ranjan
Department of Mechanical Engineering, IIT Bombay, Mumbai 400076, India
e-mail: kt541@cam.ac.uk

Fig. 1 LMB and EVF [2] representation

(a) LMB   (b) EVF
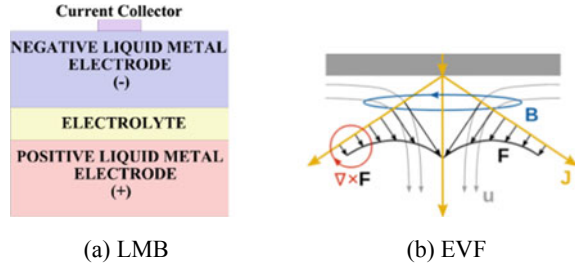
2 Literature Review and Objective

The structure of an LMB is simple to comprehend but its flow processes are complex due to the multiphysics coupling involved including interfaces. Hirt and Nicols [4] proposed the VOF algorithm to model interfaces and Deshpande et al. [5] presented a comprehensive study of the 'interFoam' solver and evaluated its performance on various test cases. Kelley and Weier [3] reviewed the fluid mechanics, challenges and opportunities associated with LMBs. Herreman et al. [6] used a multiphase MHD solver to study the EVF in cylindrical LMBs and concluded that it can lead to short circuits in moderately sized LMBs. Xiang and Zikanov [7] simulated the interfacial instability using OpenFOAM and studied the role of density differences across the interface in the stability of a cuboidal LMB. Mandrykin et al. [8] performed studies about EVF formation in cylindrical cell for varying electric current and cell aspect ratio. Liu et al. [9] proposed a new grid structure to be incorporated as part of LMB geometry for improving the LMB efficiency.

While the geometry considered by Xiang and Zikanov [7] had uniform current, in practical LMBs the current diverges from the current collector leading to EVF which can distort the interface. For this work, we have developed a solver in OpenFOAM to test the LMB safety with regards to interface disruption and short circuit due to the EVF. This solver was developed by modifying and merging two existing solvers, 'epotBFoam', which is an in-house MHD solver developed earlier in our group by Ranjan and Jindal [10] and 'interFoam', which is a VOF-based solver in OpenFOAM. The 'epotBFoam' solver is an extended version of the potential-based or induction-less MHD solver, 'epotFoam', developed by Tassone [11]. We describe the governing equations and numerical methodology below, after which we present our results and conclude.

3 Numerical Methodology

3.1 The 'epotBInterFoam' Solver

The 'epotBInterFoam' solver is based on the induction-less approximation approach to solve the MHD governing equations by using the Biot-Savart's law for calculating the magnetic field '**B**', coupled to 'interFoam' for simulating two fluid phases. MHD flow occurs when there is motion of an electrically conducting fluid, having velocity '**u**' in presence of magnetic field. During the flow, induced current '$\sigma (\mathbf{u} \times \mathbf{B})$' gives rise to a new induced magnetic field that augments the existing magnetic field. The total magnetic field interacts with the induced current density '**J**' to produce Lorentz force per unit volume equal to '$(\mathbf{J} \times \mathbf{B})$', which acts on the fluid to inhibit its relative movement with the magnetic field. Equations (1–3) represent the Maxwell's equations and the Ohm's law [12]. The Navier–Stokes (N–S) equation with Lorentz force and interfacial tension term is (4). Ampere's, Faraday's and Ohm's laws (1–3) with solenoidal **B** can be combined to give MHD induction Eq. (5). 'σ', 'μ' and 'μ_0' refer to conductivity, dynamic viscosity and permeability of free space, respectively.

$$\nabla \times \mathbf{B} = \mu_0 \mathbf{J} \text{ and } \nabla \cdot \mathbf{J} = 0 \tag{1}$$

$$\nabla \times \mathbf{E} = -\frac{\partial \mathbf{B}}{\partial t} \text{ and } \nabla \cdot \mathbf{B} = 0 \tag{2}$$

$$\mathbf{J} = \sigma(-\nabla \phi + \mathbf{u} \times \mathbf{B}) \tag{3}$$

$$\frac{\partial (\rho \mathbf{u})}{\partial t} + \nabla \cdot (\rho \mathbf{u} \mathbf{u}) = -\nabla p + \mu \nabla^2 \mathbf{u} + \mathbf{F_l} + \rho \mathbf{g} + f_\sigma \tag{4}$$

where,

$$\mathbf{F_l} = \mathbf{J} \times \mathbf{B} \text{ and } \nabla \cdot \mathbf{u} = 0$$

$$\frac{\partial \mathbf{B}}{\partial t} = \nabla \times (\mathbf{u} \times \mathbf{B}) + \lambda \nabla^2 \mathbf{B}, \quad \text{where } \lambda = (\mu_0 \sigma)^{-1} \tag{5}$$

$$\nabla^2 \phi = \nabla \cdot (\mathbf{u} \times \mathbf{B}) \tag{6}$$

$$\mathbf{B(r)} = \frac{\mu_0}{4\pi} \int \mathbf{J}(\mathbf{r'}) \times \frac{\mathbf{r} - \mathbf{r'}}{|\mathbf{r} - \mathbf{r'}|^3} dV' \tag{7}$$

In the induction-less approach, valid for liquid metals, we ignore the induced field and employ the potential (ϕ)-based formulation of the MHD equations, represented by Eqs. (3) and (6). Biot-Savart's integral is implemented for calculating the magnetic

Table 1 Details of six test cases

Case	Width (cm)	Depth (cm)	Voltage (V)
C1	2	1.5	0.0017
C2	2	1.5	0.003638
C3	0.8	0.6	0.00306
C4	0.8	0.6	0.00764
C5	1.2	0.6	0.00306
C6	1.6	0.6	0.00306

field due to applied current using Eq. (7).

$$\frac{\partial \alpha}{\partial t} + \nabla \cdot (\alpha \mathbf{u}) = 0 \qquad (8)$$

$$\rho = \alpha \rho_1 + (1 - \alpha)\rho_2 \qquad (9)$$

The Lorentz force calculated from the current density and magnetic field is added to the N–S equation. 'interFoam' solves Eq. (4) and the continuity Eq. (8) to calculate the phase fraction 'α', using which properties like density 'ρ', etc., are calculated by using Eq. (9). Separate files calculating the 'Alfven courant number', related to the MHD flow and the 'alpha Courant number' related to the multiphase flow are combined to calculate the Courant number which is monitored and kept <1. The six cases considered in this study at different applied voltages and geometries of current collectors are mentioned in Table 1.

3.2 Geometry and Details of Simulation

The LMB geometry constructed for our simulations is a thin cuboidal structure with a very small cuboidal protrusion provided at the top which represents the current collector of a practical LMB. Electric potential is applied on the top layer of this current collector. Henceforth, we will address this top layer as 'inlet'. The bottom layer or the LMB base will be called as 'outlet'. Case 3 geometry and mesh are shown in Fig. 2.

Geometry and mesh for all cases were created using 'blockMesh' utility. LMB dimensions for all the cases, excluding the inlet dimensions are 10 cm × 6 cm × 1.5 cm along the x, y and z axis, respectively. Electrolyte layer height along the vertical y-axis is 1 cm, above which there is 5 cm high negative liquid metal region. Current collector height for all cases is 0.1 cm. To capture the interface phenomena more accurately, elements near the interface are provided with finer resolution as shown in Fig. 2(b), using 'simpleGrading' mesh utility in 'blockMeshDict' file, for which the ratio of cell length along y-axis of the smallest cell to the largest cell for both the liquids is 0.1. As seen in Fig. 3, upper region (blue) is the negative metal electrode

(a) Geometry   (b) Mesh

Fig. 2 (**a**) Geometry and (**b**) Mesh of LMB for case 3
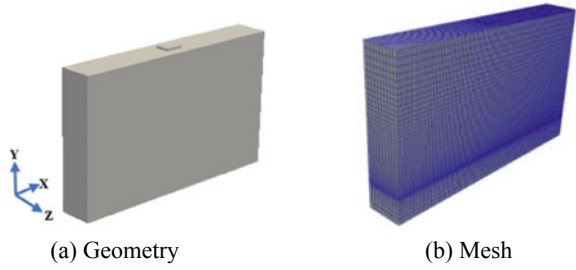
and lower region (red) represents the electrolyte. Short circuit or design failure of an LMB occurs when the two liquid metal electrodes come in contact with each other, which is equivalent to the situation when the negative metal electrode touches the outlet in our model. These two-layered simulations are less computationally intensive compared with the three-layered systems. To focus the study on EVF and save on the computational costs, the depth was kept to 1.5 cm. Any further reduction in depth along z-axis does not facilitate clear EVF formation, as it appears to be very feeble and is barely visible. An important issue for this simulation was about assigning conductivity to the domain. There is usually a large difference in the magnitudes of electrical conductivities of the liquid metal ($\sim 10^6$) and that of the electrolyte ($\sim 10^2$). This is a major issue from computation point of view. As a first step towards overcoming this problem, a single weighted average value [7] of the conductivity can be considered for all cells of the LMB as per Eq. (10).

$$\sigma_{\text{equivalent}} = \alpha_{\text{metal}}\sigma_{\text{metal}} + \alpha_{\text{electrolyte}}\sigma_{\text{electrolyte}} \tag{10}$$

The phase fractions of the liquids at initial time are 1/6th and 5/6th of the total volume of the LMB for the electrolyte and liquid metal, respectively. A concern with this weighted average approach is that the interface conductivity calculated using Eq. (10) is of $\sim 10^6$ range. As a step towards overcoming this problem, we have taken harmonic mean of conductivities [7] of both liquids for the cell boundaries adjacent to the interface as per Eq. (11).

$$\sigma_{\text{equivalent}} = \left(\frac{d_N/d}{\sigma_{\text{metal}}} + \frac{d_P/d}{\sigma_{\text{electrolyte}}} \right)^{-1} \tag{11}$$

Fig. 3 Conductivity at interface for solver 1
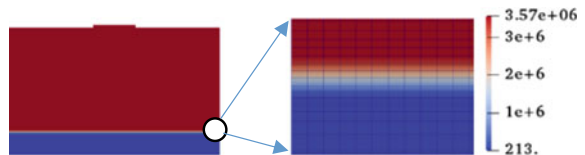
$$\sigma_{\text{equivalent}} = \frac{2 * \sigma_{\text{metal}} * \sigma_{\text{electrolyte}}}{\sigma_{\text{metal}} + \sigma_{\text{electrolyte}}} \tag{12}$$

'd_{N}' and 'd_{P}' are the distances from the interface to cell centres of elements adjacent to the interface. 'd' is the distance between cell centres of interface adjoining elements. For our cases, 'd_{N}' = 'd_{P}' = $d/2$, which reduces Eqs. (11)–(12). In 'epotBInterFoam', conductivity is modelled in a graded manner around the interface, as shown in Fig. 3. Since the deformations visible in our results were limited to maximum three or four layers adjacent to the interface, actual conductivity of the metal and electrolyte was assigned to the domain beyond these layers. Linear interpolation was used to define conductivity for layers adjacent to the interface, such that the interface has the harmonic mean conductivity value. Boundary conditions for 'α' and 'σ' are set using 'funkySetFields' utility. For the modelling of conductivity, we have developed two solvers. Our solver 1 models conductivity in a graded manner around the interface, using Eq. (12). On the other hand, our solver 2 assumes a constant weighted average value for conductivity calculated using Eq. (10) for all elements in the domain. Even though solver 2 models conductivity in a simpler manner but it may not be very ideal since it is likely to assign the electrolyte cells very high conductivity.

The 'funkySetFieldsDict' file contains code written to define conductivity in the domain, which is divided into four regions along the y-axis with different linear equations defining the respective conductivity in each region. The first region spans from the first cell layer above the interface till the third layer below the interface. The second region starts from the second layer above the interface till the fourth layer above the interface. The third and the fourth regions are the parts of the domain below and above the interface, respectively, which are not defined under first or second region and are assigned conductivity values of their corresponding liquids. Conductivity equation for first layer is defined such that the interface has the value of the harmonic mean, calculated using Eq. (12), while the boundary common to third region has electrolyte conductivity. Similarly linear equation for second region is defined such that its boundary adjacent to fourth region has liquid metal conductivity and the common boundary of first and second region has the same conductivity. Material properties are assigned using data from [6]. Magnesium (Mg) liquid metal has density and conductivity equal to 1577 kg m^{-3} and 3.57×10^6 S m^{-1}, respectively. Electrolyte (KCl–MgCl$_2$–NaCl), has density and conductivity equal to 1715 kg m^{-3} and 213 S m^{-1}, respectively. Table 1 describes the geometry of the inlet of the 6 LMB cases along with applied voltages.

(C1, C2) and (C3, C4) have same inlet dimensions. Thus, we have four different geometries. Figure 4 shows the inlet for different cases. Inlet for C3 and C4 is shown in Fig. 2(a).

To model conductivity in the LMB more accurately, we have also modified the 'epotBInterFoam' solver (S1) to implement dynamic modification of conductivity. We will refer to this modified solver as solver 3 (or S3). The implementation of dynamic model is done such that the conductivity of each individual cell changes during the simulation based on the composition of liquid metal and electrolyte present

(a) C1 and C2   (b) C5   (c) C6
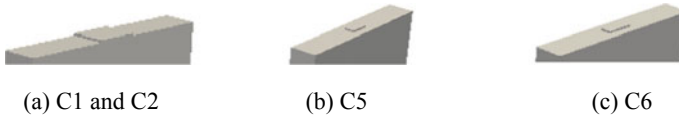
Fig. 4 Inlet protrusions

inside that cell by linear interpolation. Results of C2 simulated using solver 3 are presented at the end of next section and a comparison of the results is performed with C2 results obtained using the solvers 1 and 2. Following equation is implemented in solver 3 for carrying out the linear interpolation:

$$\sigma_{\text{equivalent}} = \sigma_m - \alpha_e * (\sigma_m - \sigma_e). \tag{13}$$

Here, 'σ_m' and 'σ_e' stand for the liquid metal conductivity and the electrolyte conductivity respectively. 'α_e' refers to the phase fraction of electrolyte. Equation (13) is used to modify the conductivity of all cells of the LMB during all iterations happening during the simulation run. As a result of implementation of Eq. (13), we have linked the current to conductivity of the domain, which in turn varies based on the phase fraction of the components of LMB. Mesh sensitivity analysis was performed on C1 and C3 by increasing the mesh along y-axis by 20% and 50% [represented in Fig. 5 by suffixes (I) and (II), respectively]. Instantaneous and time averaged velocity plots along jet centreline, on the vertical mid-plane of the LMB for C1 and C3 respectively at 10 s are shown in Fig. 5.

The mesh sensitivity for C1, as shown in Fig. 5(a), gives an error < 2% at all points. All other cases are unsteady in nature. They either are on the verge of short circuit or they have very feeble and diffused jets since the very beginning, thus giving more velocity fluctuations. The time averaged velocity profiles for C3 at 10 s are presented in Fig. 5(b). Since C3 is unsteady in nature, at this time instant we get maximum error of around 10% in this plot, which is likely to reduce when the simulation will

(a) C1   **(b) C3**
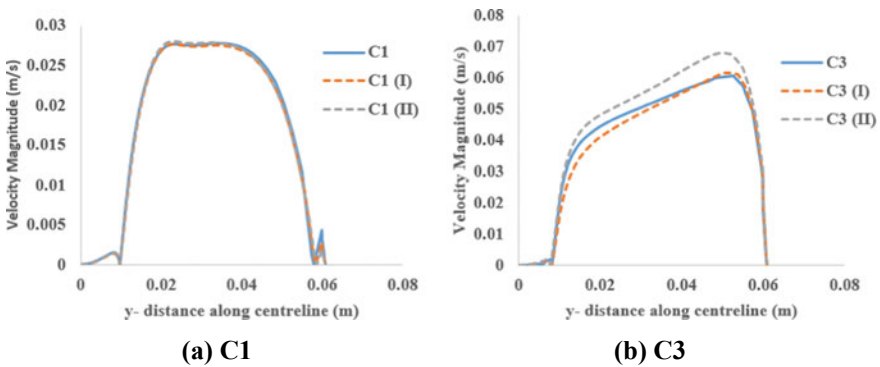
Fig. 5 Mesh sensitivity analysis for (**a**) C1 and (**b**) C3

be run for more number of time steps. Results obtained for the 'damBreak' case, using 'interFoam' matched to a very large extent with results obtained using solver 1 with no current and magnetic field.

4   Results and Discussion

All the results presented are along the jet centreline, on the vertical mid-plane of the LMB. Seven set of contours are presented for each case, where the images sequentially represent: jet emerging from inlet, jet just before striking the interface, jet impingement on the interface, beginning of significant vortex formation, vortex formation in final stages with solver 1, vortex formation in final stages with solver 2 and electrolyte phase fraction (α_e) showing significant interface deformation.

4.1   Case 1 (C1) and Case 2 (C2)

C1 and C2 have the same inlet width but with different electric potential and with the depth along z-axis equal to the LMB depth as seen in Fig. 4(a). Voltage supplied at inlet for C2 is increased to the extent that the current density observed for C1 at the interface is equal to current density at outlet for C2, which means current is larger at the interface for C2 leading to larger Lorentz force. Simulation results for C1 and C2 are shown in Fig. 6. High-speed jets just emitting out from the inlet can be seen in Fig. 6(a), (h). We can see the high-speed jet speeding towards the interface and eventually hitting the interface. After this, the flow is horizontal and along the walls to form a vortex. In Fig. 6(g), we can see minor deformation of the interface in phase fraction. LMB current collector design for C1 can be termed as safe since the liquid metal does not appear to touch the outlet at any time instant. However, this situation may drastically change when the voltage supplied is increased any further, as observed for C2 results.

Figure 6 (f), (m) show velocity profile computed by solver 2. We can observe from these results that the maximum and the overall velocity magnitude is in general higher and more chaotic for solver 1 than for solver 2 for the same inlet geometry. This may be due to relatively higher conductivity assigned to the liquid metal by solver 1, compared with solver 2.

4.2   Case 3 (C3) and Case 4 (C4)

Inlet sizes for C3 and C4 are reduced compared with C1 and C2. Electric potential for C3 at inlet is defined to get same current density at the interface as observed in C1. Voltage supplied at inlet for C4 is increased to give the current density observed

Fig. 6 C1, C2 velocity and phase fraction comparison

(a) **C1**: |**u**| at t = 2 s

(h) **C2**: |**u**| at t = 1 s

(b) **C1**: |**u**| at t = 3 s

(i) **C2**: |**u**| at t = 1.5 s

(c) **C1**: |**u**| at t = 4 s

(j) **C2**: |**u**| at t = 2 s

(d) **C1**: |**u**| at t = 5.5 s

(k) **C2**: |**u**| at t = 3 s

(e) **C1**: |**u**| at t = 10 s

(l) **C2**: |**u**| at t = 5 s

(f) **C1**: |**u**| at t = 10 s (solver 2)

(m) **C2**: |**u**| at t = 5 s (solver 2)

(g) **C1**: α_e at t = 10 s

(n) **C2**: α_e at t = 3 s
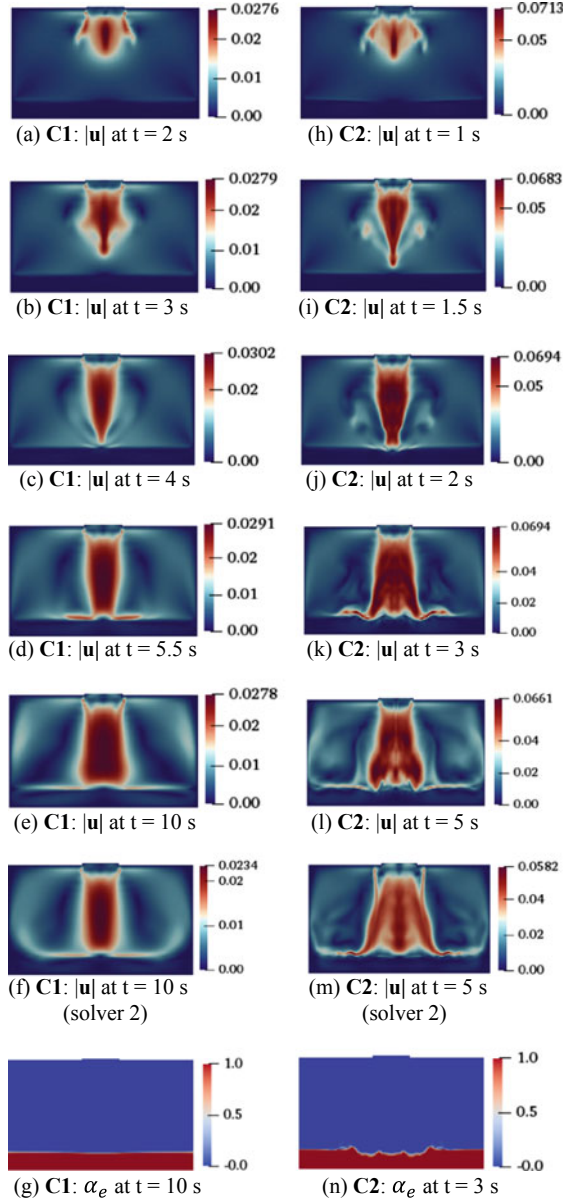
at C3 interface equal to the current density at C4 outlet. Short circuit happens in C4, which can be seen in Fig. 7 (l), (m), where the liquid metal pierces the interface and touches the outlet. It is observed from Fig. 7 that interface deformations for C3 and C4 are significantly more than C1. This is due to the reduction in inlet width which increases the strength of EVF. For C3, the LMB design appears to be safer than C2

as the liquid metal stays far from outlet most of the time. In Fig. 7 (i), (m), the jet can be seen piercing the interface at 0.75 s.

Thus, we conclude that LMB design for C4, at given voltage is unsafe and ought to be rejected. Solver 2 results for C4 also indicate short circuit at 0.75 s.

Fig. 7 C3, C4 velocity and phase fraction comparison

(a)C3: |**u**| at t = 0.5 s

(h) C4: |**u**| at t = 0.25 s

(b) C3: |**u**| at t = 1 s

(h) C4: |**u**| at t = 0.5 s

(c) C3: |**u**| at t = 1.5 s

(i) C4: |**u**| at t = 0.75 s

(d) C3: |**u**| at t = 4.5 s

(j) C4: |**u**| at t = 1.25 s

(e) C3: |**u**| at t = 7.5 s

(k) C4: |**u**| at t = 1.5 s

(f) C3: |**u**| at t = 7.5 s (solver 2)

(l) C4: |**u**| at t = 0.75 s (solver 2)

(g) C3: α_e at t = 2.5 s

(m) C4: α_e at t = 0.75 s
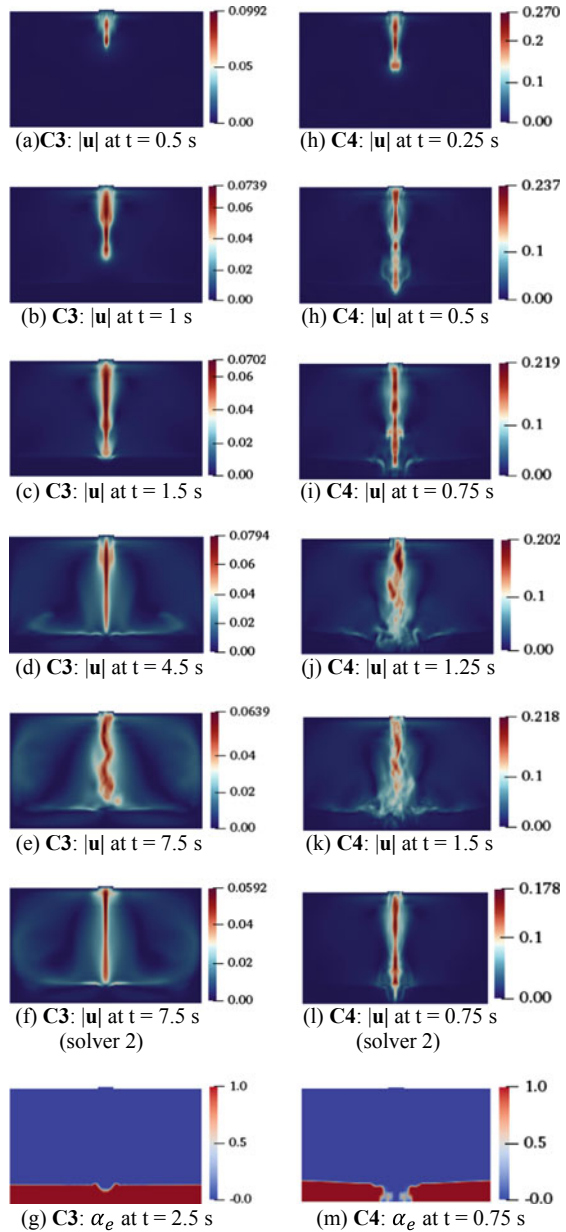
4.3 Case 5 (C5) and Case 6 (C6)

C5 and C6 have geometries similar to C3 but with an increment of 50% and 100% inlet width respectively along x-axis, when compared with C3. Inlet voltage remains same as in C3. This case is simulated to analyse the LMB stability when inlet geometry is changed for constant voltage.

Since inlet width along x-axis has increased, a lesser interface deformation is expected compared with C3. The interface deformation seen in Fig. 8 (g), (n) is much less than that in C3. This could be because the voltage supplied is same as in C2, but the inlet width has increased, giving a reduced jet intensity. It can be seen in Fig. 8 (k), the jet has started to become diffused just at 4.5 s. Once again this shows that voltage has significant effect on interface stability. It can be seen in Fig. 8 that C6 has feebler jet impingement and EVF than C5 due to further increase in inlet width with voltage remaining same. Results obtained from solver 2 for all cases are presented for fully developed EVF. Next, we perform comparison of velocity profiles from solvers 1 and 2 for C1, C2, C3 and C6 at time when jet strikes the interface, which is at 4, 2, 1.5 and 2.5 s, respectively, along the jet centreline on the vertical mid-plane is shown in Fig. 9. Solver 1 and 2 results are represented by suffixes (S1) and (S2), respectively.

It is observed that velocity predicted by solver 1 is larger than solver 2. This is expected since solver 1 assigns a higher conductivity value to the liquid metal than solver 2. During the simulation run, we observed solver 1 results to be more chaotic than solver 2, which is again likely due to difference in modelling of conductivity.

4.4 C2 with Dynamically Changing Conductivity

In the solvers 1 and 2, the conductivity in each cell remained constant throughout the simulation. This static behaviour of the conductivity model in solvers 1 and 2 does not consider the change in composition of cells near interface, happening due to interface deformation. As a result of this, the cells having very high composition of liquid metal may still represent the electrolyte conductivity and vice versa. This is undesirable since the conductivities of liquid metal and electrolyte differ by an order of $\sim 10^4$ magnitude. The modelling of conductivity in the solver 3 is implemented such that for all the cells at any given point of time during the simulation, if the value of 'α_e' (phase fraction of electrolyte) equals 1, then the conductivity of electrolyte is assigned to that cell. Similarly, if for any cell 'α_e' equals to 0, then the liquid metal's conductivity is assigned to that cell. Based on these two extremes, a linear interpolation is performed for all the cells for assigning the equivalent conductivity [Eq. (13)]. Based on the 'α_e' value during the simulation, conductivity is dynamically modified for each and every cell during all iterations, thus changing the current density. Images shown in Fig. 10 depict phase fraction, conductivity and velocity at mid-plane cross section

Fig. 8 C5, C6 velocity and phase fraction comparison

(a) **C5**: |**u**| at t = 1 s

(h) **C6**: |**u**| at t = 1 s

(b) **C5**: |**u**| at **t** = 1.5 s

(i) **C6**: |**u**| at t = 2 s

(c) **C5**: |**u**| at t = 2.5 s

(j) **C6**: |**u**| at t = 3 s

(d) **C5**: |**u**| at t = 4 s

(k) **C6**: |**u**| at t = 4.5 s

(e) **C5**: |**u**| at t = 7 s

(l) **C6**: |**u**| at t = 8.5 s

(f) **C5**: |**u**| at t = 7 s
(solver 2)

(m) **C6**: |**u**| at t = 8.5 s
(solver 2)

(g) **C5**: α_e at t = 5 s

(n) **C6**: α_e at t = 5 s
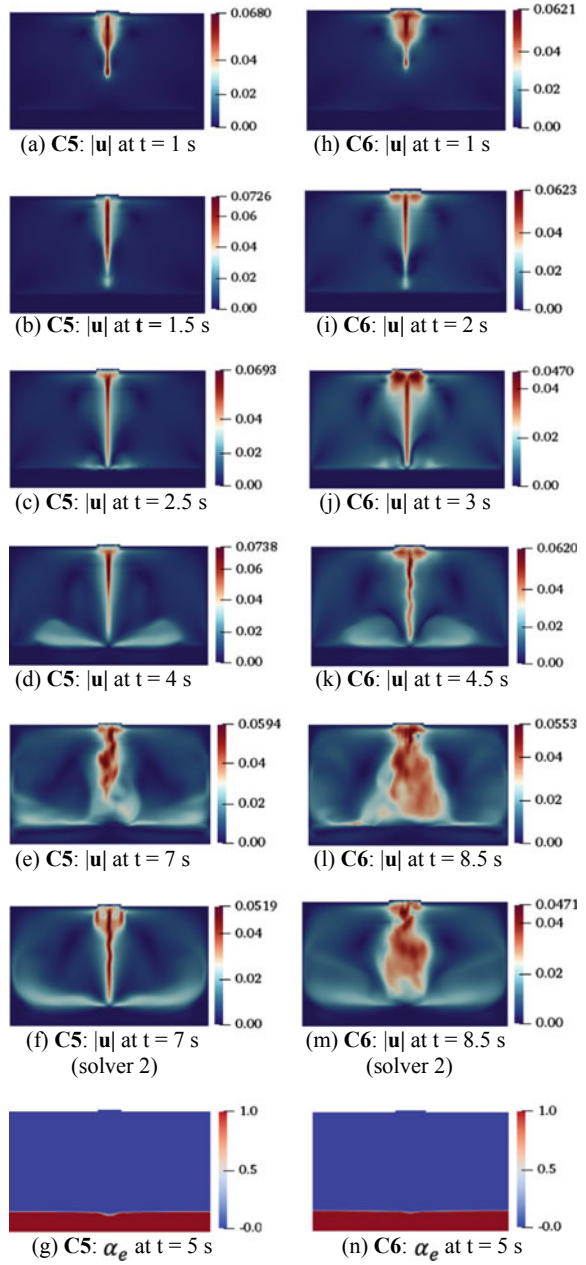
Fig. 9 Velocity magnitude along jet centreline on the vertical mid-plane for solvers 1 and 2. The black dashed line indicates the initial location of the interface
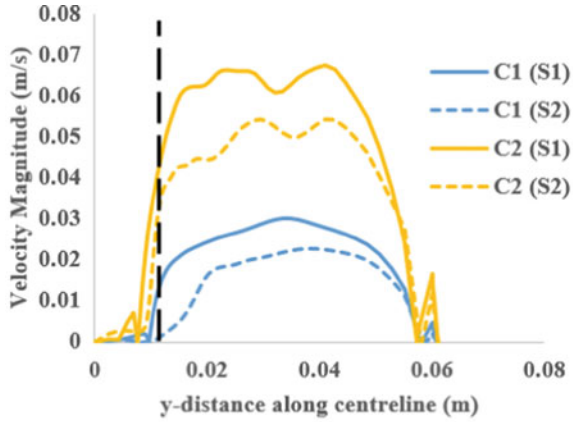
(a) C1 and C2
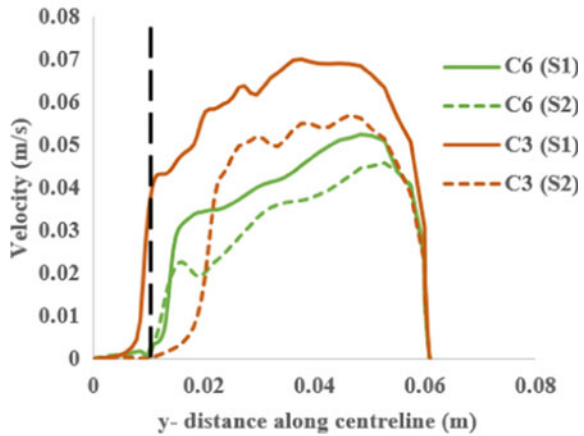
(b) C3 and C6

along z-axis for C2 using the dynamic conductivity modification model at time $t = 5$ s.

We can see by comparing the images in Fig. 10 that the shape of interface in (b) is exactly the same as in (a). This shows that the conductivity has been linked with the phase fraction for each cell and changes according to its values during the simulation. Following Fig. 11 compares the velocity profiles of C2 taken along y-axis of mid-plane of LMB along the z-direction, using all the three solvers: 'myInterFoam' (Solver 1), 'epotBInterFoam' (Solver 2) and the modified solver having dynamic conductivity model (Solver 3) at time $t = 5$ s.

We can see from Fig. 11 that different conductivity models predict different velocities for the same LMB geometry, with the same potential difference. Even though the overall shape appears to be similar, there are significant differences in the velocity

(a) **C2**: α_e at t = 5 s

(b) **C2**: $\sigma_{\text{equivalent}}$ at t = 5 s

(c) **C2**: |**u**| at t = 5 s

Fig. 10 Phase fraction, conductivity and velocity for C2 at $t = 5$ s using dynamic conductivity approach
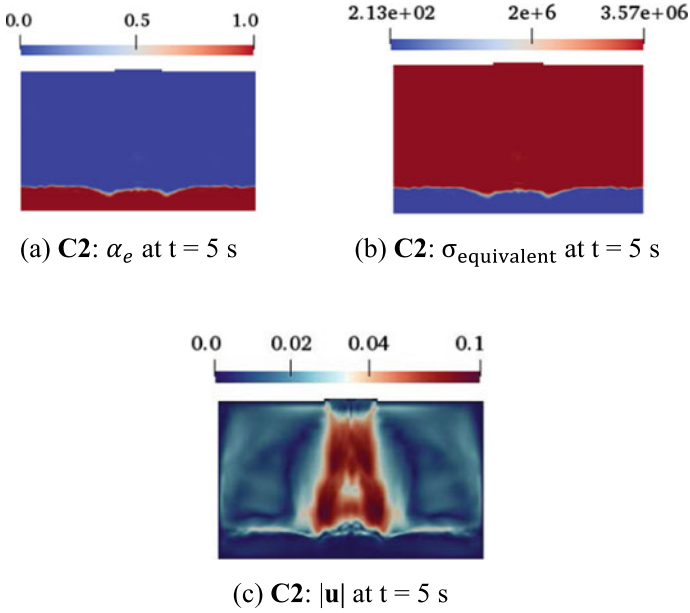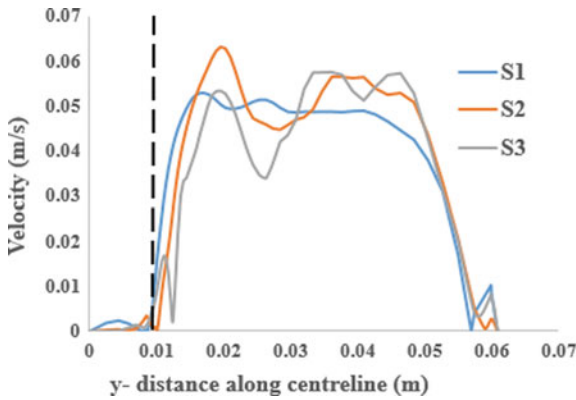

Fig. 11 Velocity comparison for C2 at time $t = 5$ s using results from solvers 1, 2 and 3. The black dashed line indicates the initial location of the interface

magnitudes, particularly near the interface. This is more pronounced for C2 since it is an unstable case on the verge of short circuit.

5 Conclusion

We have studied electro-vortex flow (EVF) in cuboidal LMB with different inlet (current collector) geometries and applied voltages. Results presented in this paper indicate that electric potential and the inlet width both contribute towards the stability of an LMB with respect to the EVF. We also developed a solver 'epotBInterFoam' in OpenFOAM and used this solver to test a given LMB geometry for its safety which can be used for other geometries as well. We have found that for constant width difference between inlet and outlet, the LMB becomes more unstable with increasing supply of electric voltage and similarly for constant electric voltage, LMB stability tends to increase with reducing difference between inlet and outlet widths. Short circuit occurred in the C4, where 0.00764 V was sufficient to disrupt the LMB functioning. Lastly, we also used a modified version of 'epotBInterFoam' to model the changing conductivity for case 2 (solver 3) and compare the results with those from solvers 1 and 2. Presently, we are trying to implement current continuity across the interface by including the conductivity jump across the interface while solving the Poisson's equation to obtain current distribution inside the LMB. This makes the problem numerically very stiff and therefore requires very fine mesh near the interface. We expect that most of our results before the electrolyte rupture should be valid even with the calculation of interface currents. However, if the interface becomes unstable, this can lead to interfacial instabilities.

Nomenclature

d Distance between cell centres (m)
f_σ Surface tension force (kg/m^{2}s^2)
g Acceleration due to gravity (m/s^2)
p Pressure inside fluid (N/m^2)
r Distance to cell centres (m)
u Fluid velocity (m/s)
B Magnetic field (T)
E Electric field (V/m)
F_1 Lorentz force per unit volume (kg/m^{2}s^2)
J Current density (A/m^2)
V Volume (m^3)
α Phase fraction of the liquid (–)
μ Dynamic viscosity (kg/ms)
μ_0 Permeability of free space (N/A^2)
ρ Density of fluid (kg/m^3)
σ Electric conductivity (S/m)
φ Electric potential (V)

References

1. Kim H et al (2013) Liquid metal batteries: past, present, and future. Chem Rev 113(3):2075–2099
2. Ashour RF, Kelley DH, Salas A, Starace M, Weber N, Weier T (2018) Competing forces in liquid metal electrodes and batteries. J Power Sources 28(378):301–310
3. Kelley DH, Weier T (2018) Fluid mechanics of liquid metal batteries. Appl Mech Rev 70(2):4038699
4. Hirt CW, Nichols BD (1981) Volume of fluid (VOF) method for the dynamics of free boundaries. J Comput Phys 39(1):201–225
5. Deshpande SS, Anumolu L, Trujillo MF (2012) Evaluating the performance of the two-phase flow solver interFoam. Comput Sci Discov 5(1):014016
6. Herreman W, Nore C, Ramos PZ, Cappanera L, Guermond JL, Weber N (2019) Numerical simulation of electrovortex flows in cylindrical fluid layers and liquid metal batteries. Phys Rev Fluids 4(11):113702
7. Xiang L, Zikanov O (2019) Numerical simulation of rolling pad instability in cuboid liquid metal batteries. Phys Fluids 31(12):124104
8. Mandrykin S, Ozernykh V, Kolesnichenko I (2020) Electro-vortex flow of liquid metal in a cylindrical cell with localized current supply and variable aspect ratio. Magnetohydrodynamics (0024–998X), p 56
9. Liu K, Chen L, Guo J, Li B, Huang L (2021) A new method to improve the efficiency of liquid metal batteries based on magnetohydrodynamic instability analysis. J Power Sources 31(495):229813
10. Ranjan A, Jindal S (2020) Electro-vortex flow in a liquid metal battery electrode with annular current collector. In: APS Division of Fluid Dynamics Meeting Abstracts 2020, pp J04–005
11. Tassone A (2016) Magnetic induction and electric potential solvers for incompressible MHD flows. In: Nilsson H (eds) Proceedings of CFD with OpenSource Software. https://doi.org/10.17196/OS_CFD#YEAR_2016
12. Shercliff JA (1966) A textbook of magnetohydrodynamics. Am J Phys 34(12):1204

Numerical Investigation on Effect of Appendage on Heat Transfer in a Backward-Facing Step (BFS)

P. Nagarajan and S. Soma Sundaram

1 Introduction

Separated flow over a step occurs in a many engineering problems and applications. The simple geometry has complex features, which has been studied by many researchers. The recirculation length, separation bubbles, reattachment points and coherent structures developed in the BFS are major areas where study has been focused on. The geometry generates a primary recirculation region downstream of the step. This region is of interest for heat transfer studies. Any modification in the BFS to enhance mixing increases the pressure drop across the channel. Hong et al. [1] examined the flow and heat transfer characteristics in a range of Prandtl numbers ($0.07 \leq \mathrm{Pr} \leq 100$). The influence of inclination angle was reported. They found that increasing the inclination angle enhanced the reattachment but decreased the wall friction coefficient. Barkley et al. [2] studied bifurcation analysis of the flow at a critical Reynolds number of 748 and found that critical Eigen mode of flat roll, localized at recirculation zone behind the step edge. A centrifugal instability was generated by secondary flow within separation zone. The main flow was found to be a Taylor–Gortler-type instability.

Biswas et al. [3] studied the effect of expansion ratios. The Reynolds number varied from, 1 to 400. A corner vortex with approximately constant size was obtained in concave corner behind the step. Nie and Armaly [4] compared the variation of two-dimensional analysis over a three-dimensional one on heat transfer studies in a BFS. The Reynolds number was varied from 150 to 450. The results of 2D case included short distance from step ($X/S = 30$). It was found that primary reverse flow was high and it developed strong vortices in span-wise flow. The strength of the vortex was maximum near the step as sudden expansion generated a higher velocity gradient.

P. Nagarajan · S. Soma Sundaram (✉)
Department of Mechanical Engineering, NIT Puducherry, Karaikal 609609, India
e-mail: somasundaram.s@nitpy.ac.in

Chen et al. [5] examined the velocity and temperature fields of incompressible steady flow in a low Reynolds number backward-facing step. Analysis was carried out with and without the insertion of a cylinder downstream from the step. Insertion of cylinder enhanced the convective heat transfer. The thermal performance is found to increase by approximately 33% at Reynolds number = 170. Yılmaz and Öztop [6] studied the effect of step heights, step length and the Reynolds number on the fluid flow. A second step had been used as a control device for enhancing heat transfer. The results showed that turbulent intensity and heat transfer rate were increased with increasing Reynolds number. Additionally, the ratio of step height was more effective parameter than the length of step for enhancement of heat transfer.

Kanna and Das [7] performed numerical analysis to study the local Nusselt number, interface temperature and average Nusselt number in the solid region for a conjugate heat transfer study of backward-facing step. The hydrodynamic solution was determined using stream function-vorticity formulation. To compare conjugate and non-conjugate case Reynolds number (Re), Prandtl number (Pr), thermal conductivity (K) and thickness of the slab (b) were varied. Reduced thermal layer thickness and high thermal gradients were reported in conjugate case. The Prandtl number increment caused the decrement in temperature gradient and increment in Nusselt number. In non-conjugate case the effect of thermal conductivity on Nusselt number was studied. It was found that when thermal conductivity increased, the Nusselt number also increased. When thickness of the slab was increased the Nusselt number reduced in non-conjugate case.

Kumar and Dhiman [8] numerically studied the heat transfer enhancement in laminar forced convection flow over a benchmark problem, with obstruction in form of an adiabatic circular cylinder. The effect of different cross-stream positions of the circular cylinder for various Reynolds numbers in the range of 1–200 was studied. The peak and average Nusselt number increased with Reynolds number. The heat transfer enhancement was up to 155% compared with the unobstructed case. Selimefendigil and Öztop [9] studied the forced convection of ferrofluid over a backward-facing step at a Reynolds number of 1–200. With increasing magnetic dipole strength, the flow field was directed downstream of the step and cylinder towards the bottom wall. The magnetic dipole strength was used to control the length and size of the recirculation zone. For Reynolds number under study the maximum and average Nusselt numbers increased as the magnetic dipole strength increased. Additionally, the external magnetic field acted in a way that decreased the local heat transfer in some locations. When the cylinder rotated clockwise, more flow was entrained in its wake and some of it was directed towards the bottom of the cylinder. At Re = 10, the maximum and average heat transfer increased with cylinder rotation, but at higher Reynolds numbers, the peak value of the Nusselt number and its location changed slightly with cylinder rotation compared with the motionless cylinder case.

D'Adamo et al. [10] observed that reattachment length caused by the shear layer, occurred at a natural frequency. When using plasma actuators to actively control a backward-facing step flow, power consumption was reduced since the flow was less sensitive to forcing amplitude. Hilo et al. [11] presented turbulent flow in BFS obtained by different parameters and conjugate shapes. At an amplitude height of

4 mm and Reynolds number of 5000, better heat transfer was observed in a trape-zoidal bottom wall. Ahmed et al. [12] studied the heat transfer in a micro-scale backward-facing step channel by using turbulators. The usage of rectangular wing vortex generator, enhanced the heat transfer providing low pressure.

Li et al. [13] performed studies on active control on BFS. The non-dimensionalized perturbation frequency at Strouhal number of 0.22 resulted in a minimized recircu-lation region and maximum heat transfer. Guo et al. [14] studied backward-facing rounded ramp with C-D riblets. It was observed that flow separation reduced, and the total pressure losses reduced to 3.75% times of riblets height. Talib and Hilo [15] examined the effect of corrugated wall in BFS. The Nusselt number and friction factor increased up to 40.7% and 46.2% in the study.

Based on the literature, it can be seen that both active and passive control methods have been studied on the BFS to enhance heat transfer. However, little researches have been done for passive control methods in step itself. This motivated the present study, to study the effect of inclusion of the appendages on the step. The height of the appendages and its orientation has been altered and its effect on heat transfer has been reported. The flow is considered to be laminar and the simulation has been carried out for four different Reynolds numbers (1, 10, 100 and 1000).

2 Simulation Methodology

The geometry considered for the simulation is taken from literature [8]. The height of the step is set as 'S'. The distance of step from the inlet is $10S$, while the distance from exit is $40S$. An expansion ratio of 2 is used in the present study. The length of the appendage has been varied from $0.16S$ to $0.84S$ in steps of $0.16S$. The computational domain for an appendage length $Y_A/S = 0.5$, placed vertically (90°) is shown in Fig. 1. The effect of varying the angle of appendage has also been studied, by placing the appendage horizontally (0°) and at an angle of 45°.
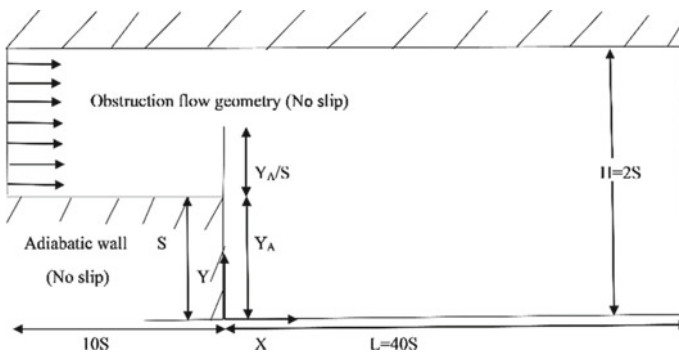

Fig. 1 Schematic diagram for BFS problem with obstruction case geometry

Table 1 Mesh details in backward-facing step

Mesh	Cells	X_1/S	Average Nusselt number
Coarse	19,000	2.58	2.153
Medium	40,000	2.80	2.147
Fine	93,000	2.78	2.155

The mesh has been created in a systematic manner. The computational domain has been divided into three regions. The primary region is close to the step while secondary and tertiary regions are far away. The primary region is given a fine mesh compared with secondary and tertiary regions. Grid independence study has been carried out on three different meshes with 19,000 cells, 40,000 cells and 93,000 cells. The length of the primary recirculation and average Nusselt number for the three meshes are given in Table 1. The results are found to be consistent to the mesh of 40,000 cells and it has been selected for further studies. The boundary conditions at the bottom wall after the step is considered as an isothermal wall with no-slip. The inlet of the computational domain is considered as mass flow inlet and mass flux corresponding to Reynolds number 1, 10, 100 and 1000 has been provided. The outlet boundary condition has been modelled as outflow. All walls except the bottom wall of steps are considered insulated and no-slip conditions.

Air with a density of 1.223 kg/m^3, viscosity of 1.7894 × 10^{-5} kg/ms, specific heat of 1006.43 J/Kg-K and thermal conductivity 0.0242 W/mk has been selected as the working fluid. The Prandtl number for air is 0.7.

Numerical simulation has been carried out in FLUENT software. The viscous model has been chosen as laminar flow and the energy equation has been turned on as heat transfer calculations are carried out.

The governing equations of continuity, momentum and energy have been solved for the effect of appendage on heat transfer in a backward-facing step under the conditions of steady flow, incompressible and Newtonian fluid, two-dimensional and constant flow. The governing equations are given below:

The continuity equation:

$$\frac{\partial U}{\partial X} + \frac{\partial V}{\partial Y} = 0.$$

The *x*-momentum equation:

$$\frac{\partial UU}{\partial X} + \frac{\partial VU}{\partial Y} = -\frac{\partial P}{\partial X} + \frac{1}{\text{Re}}\left(\frac{\partial^2 U}{\partial X^2} + \frac{\partial^2 U}{\partial Y^2}\right).$$

The *y*-momentum equation:

$$\frac{\partial UV}{\partial X} + \frac{\partial VV}{\partial Y} = -\frac{\partial P}{\partial Y} + \frac{1}{\text{Re}}\left(\frac{\partial^2 V}{\partial X^2} + \frac{\partial^2 V}{\partial Y^2}\right).$$

The conservation of energy equation:

$$\frac{\partial (UT)}{\partial X} + \frac{\partial (VT)}{\partial Y} = \frac{1}{\text{Re Pr}} \left(\frac{\partial^2 T}{\partial X^2} + \frac{\partial^2 T}{\partial Y^2} \right),$$

where U, velocity in X direction; V, velocity in Y direction; P, pressure; T, Temperature; Re is Reynolds number and PR is Prandtl number. Coupled equations have been used to solve the differential equations. The least-square cell-based method has been used for second-order accuracy in the finite volume method.

3 Results and Discussion

The results obtained by solving two-dimensional, steady, incompressible, laminar, non-reacting flow equations are explained in this section. The effect on varying the appendage length (Y_A/S) and its orientation, for various Reynolds number, on the convective heat transfer is explained. The variation in the Nusselt number, friction coefficient, pressure coefficient and performance evaluation criteria (PEC) is discussed.

Contours of streamlines are shown in Fig. 2. The contours are provided for a Reynolds number of 1000. The unobstructed case (a) is found to have a primary recirculation region of length $X_r/S = 1.833$. The secondary bubbles are formed on the top wall. The variation in the streamline upon inclusion of the appendage, with various Y_A/S is shown in Fig. 2b–f. It can be seen that there is not much variation in the length recirculation with an inclusion of appendage of $Y_A/S = 0.16$. However, upon increasing the appendage length further to $Y_A/S = 0.666$ and $Y_A/S = 0.833$, the length of the primary recirculation region increases. The effect of adding appendage results in increasing of the velocity at the step location. The increase in velocity has been observed by closing of streamlines. To study the effect of orientation of the appendage, two cases appendages ($Y_A/S = 0.3333$ and $Y_A/S = 0.5$) oriented to flow directions and one case with appendages ($Y_A/S = 0.333$) oriented at an angle of 45°.

It has been observed that the recirculation length is not much affected with the 45° orientations, but an increase in the recirculation length is noted in other two cases. With an increase in the primary recirculation length, a decrease in the secondary recirculation region is observed. The velocity streamline plots have the same expansion ratio, but the recirculating length increases as the Reynolds number increases. For other cases with Re < 1000, a recirculation region with lesser length has been observed.

The average Nusselt number has been obtained by the mean of the local Nusselt number determined in the bottom wall of the computational domain. The variation of average Nusselt number with Reynolds number is shown in Fig. 3. According to literature [8], the Nusselt number increases as the Reynolds number increases. The same trend has been observed in the present study. The appendages $Y_A/S = 0.84$ has highest improvement of Nusselt number compared with another appendages.

Fig. 2 Velocity streamlines
through backward facing
step with various
appendages: **a** Unobstructed
step; **b** $Y_A/S = 0.33$; **c** Y_A/S
$= 0.50$; **d** $Y_A/S = 0.84$;
e $Y_A/S = 0.33$ and 0°; **f** $Y_A/$
$S = 0.33$ and 45°
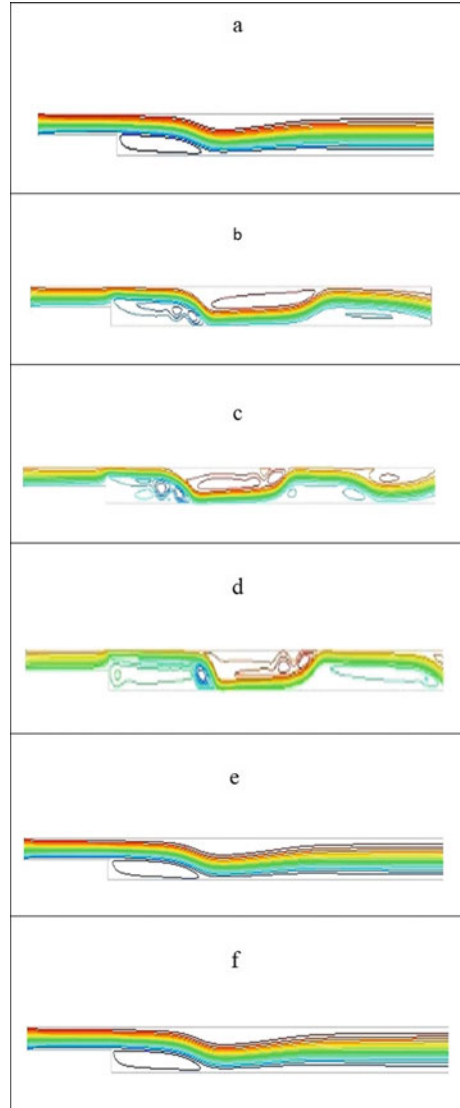
An increment of five times has been observed for Re = 1000. The increase in the
primary recirculation region formed in appendage $Y_A/S = 0.84$ causes better mixing
and hence an increase in the Nusselt number is observed.

Figure 4 presents the variation of pressure coefficient with Reynolds number along
with appendage. The Reynolds number is incremented from 1 to 1000. The variation
of pressure coefficient has been observed to occur at higher Reynolds number (Re
= 1000). The pressure coefficient increases with appendage length is increased. The
pressure coefficient for Re = 1000 is higher at $Y_A/S = 0.84$.

Fig. 3 Average Nusselt
number (Nu$_{avg}$) Reynolds
number for an appendage
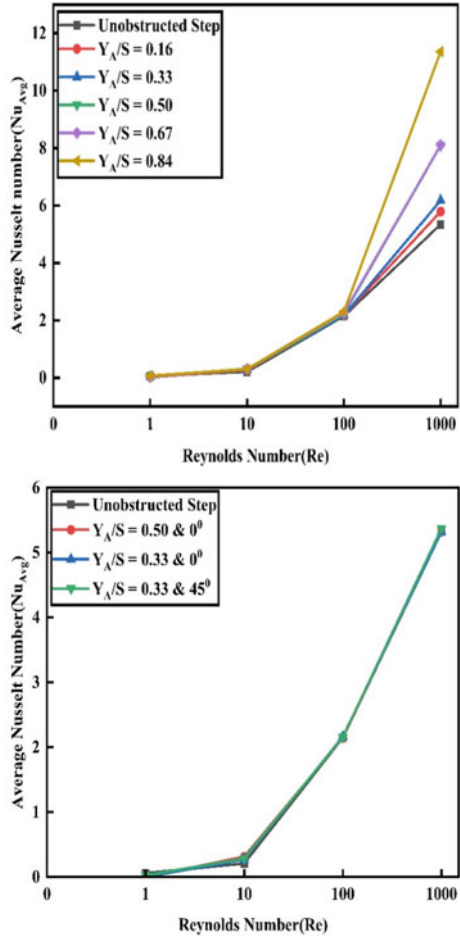
Figure 5 presents the variation skin friction coefficient with Reynolds number (Re) along the appendages. The skin friction has been observed to be highest at Re = 1000. The skin friction coefficient is found to be almost constant for variation in Reynolds number. However, for Reynolds number of 1000 a variation in skin friction coefficient has been observed with introduction of appendage. The skin friction coefficient increases when the appendage length is increased. The skin friction coefficient Re = 1000 is highest at $Y_A/S = 0.84$. The skin friction coefficient has been observed to be a constant for $Y_A/S = 0.50$ and 0°, $Y_A/S = 0.33$ and 0° and $Y_A/S = 0.33$ and 45°. The values are same as that of unobstructed and are not shown here for the sake of brevity.

Figure 6 shows the performance evaluation criteria (PEC) for variation of Reynolds number and appendage length. The heat transfer enhancement has been obtained by mixing, which generally causes the pressure coefficient to rise. It is one

Fig. 4 Pressure coefficient
Reynolds number for an
appendage
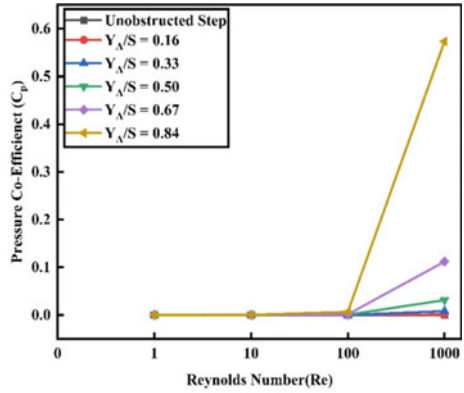
Fig. 5 Skin friction
coefficient (C_f) with
Reynolds number for an
appendage
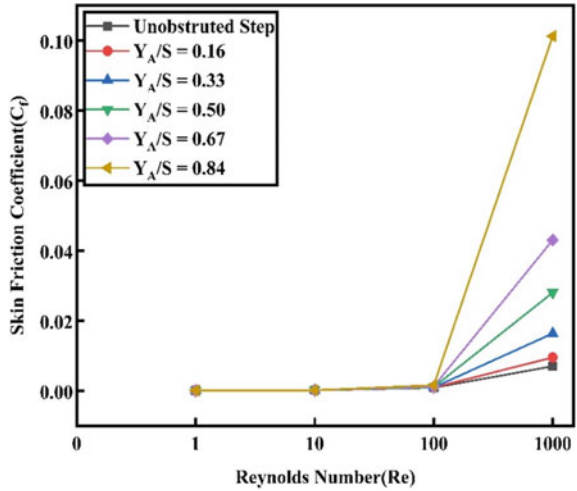
Fig. 6 Performance evaluation criteria with Reynolds number for an appendage
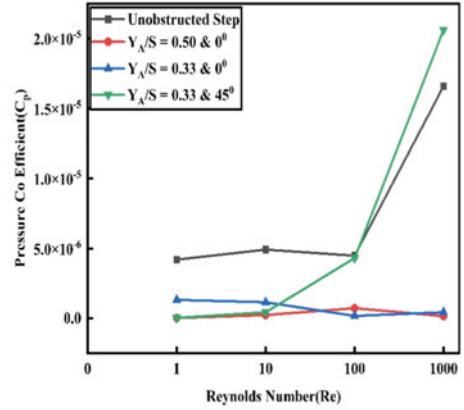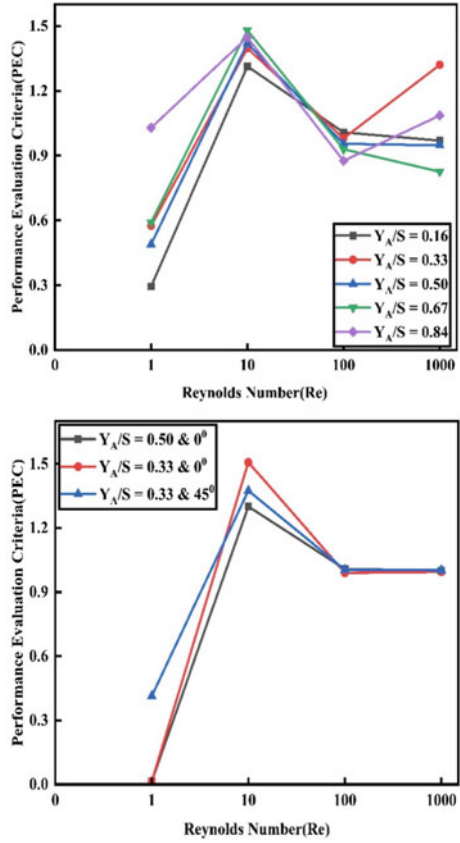
of the important characteristics to calculate the efficiency of utilizing an appendage
by the PEC.

$$\text{PEC} = \frac{\left(\frac{Nu}{Nu_0}\right)}{\left(\frac{f}{f_0}\right)^{\frac{1}{3}}},$$

where Nu is the Nusselt number and f is the factor of the new channel (backward-
facing step with appendage), while Nu_0 is the Nusselt number and f_0 is the friction
factor of the original channel (backward-facing step). The method of calculation of
PEC is obtained from literature [11]. When the PEC value is greater than 1, the heat
transfer improvement is higher than the rise of pressure efficient PEC value increases
with appendage length. However, the highest increase occurred at appendages of $Y_A/S = 0.33$ and 0° in a Reynolds number at 10. For a Re = 1, with the inclusion of
appendage the increment in heat transfer is lesser compared with pressure coefficient.
It can be seen in Fig. 3 that the better heat transfer is obtained for $Y_A/S = 0.84$ when
compared with $Y_A/S = 0.33$. However, it also has a higher friction coefficient as
shown in Figs. 4, 5. Correspondingly, the PEC of $Y_A/S = 0.33$ is higher than $Y_A/S = 0.84$, for a Reynolds number of 1000.

4   Conclusions

In this present study, the convection heat transfer in laminar two-dimensional BFS geometry is studied. The effect of various appendages and their orientation in the flow and the heat transfer enhancement of separated flow have been numerically explored. The numerical simulations have been carried out with air as working fluid.

Accordingly, the current findings are:

- Introduction of appendage improved heat transfer over the BFS.
- Appendage $Y_A/S = 0.84$, provided highest improvement of Nusselt number. The Nusselt number increased by five times than unobstructed step for a Reynolds number of 1000.
- However, it is found the appendage will cause higher pressure coefficient than increase in the heat transfer. The BFS with the appendage $Y_A/S = 0.84$ presented the highest average skin friction coefficient compared with other appendages.
- The Nusselt number gradually increases as Reynolds number increases.
- Appendage $Y_A/S = 0.33$ and $0°$ has the highest performance evaluative criteria PEC 1.507.

The turbulent flow over the modified in BFS with appendages and their influence on heat transfer will be considered for future work.

References

1. Hong B, Armaly BF, Chen TS (1993) Laminar mixed convection in a duct with a backward-facing step: the effects of inclination angle and Prandtl number. Int J Heat Mass Transf 36(12):3059–3067
2. Barkley D, Gomes MGM, Henderson RD (2002) Three-dimensional instability in flow over a backward-facing step. J Fluid Mech 473:167–190
3. Biswas G, Breuer M, Durst F (2004) Backward-facing step flows for various expansion ratios at low and moderate Reynolds numbers. J Fluids Eng 126(3):362–374
4. Nie JH, Armaly BF (2004) Convection in laminar three-dimensional separated flow. Int J Heat Mass Transf 47(25):5407–5416
5. Chen CK, Yen TS, Yang YT (2006) Lattice Boltzmann method simulation of a cylinder in the backward-facing step flow with the field synergy principle. Int J Therm Sci 45(10):982–989
6. Yılmaz II, Öztop HF (2006) Turbulence forced convection heat transfer over double forward facing step flow. International communications in heat and mass transfer 33(4):508–517
7. Kanna PR, Das MK (2006) Conjugate heat transfer study of backward-facing step flow–a benchmark problem. Int J Heat Mass Transf 49(21–22):3929–3941
8. Kumar A, Dhiman AK (2012) Effect of a circular cylinder on separated forced convection at a backward-facing step. Int J Therm Sci 52:176–185

9. Selimefendigil F, Öztop HF (2014) Effect of a rotating cylinder in forced convection of ferrofluid over a backward facing step. Int J Heat Mass Transf 71:142–148
10. D'Adamo J, Sosa R, Artana G (2014) Active control of a backward facing step flow with plasma actuators. J Fluids Eng 136(12):121105
11. Hilo AK, Iborra AA, Sultan MTH, Hamid MFA (2020) Effect of corrugated wall combined with backward-facing step channel on fluid flow and heat transfer. Energy 190:116294
12. Ahmed HE, Kherbeet AS, Ahmed MI, Salman BH (2018) Heat transfer enhancement of micro-scale backward-facing step channel by using turbulators. Int J Heat Mass Transf 126:963–973
13. Li ZY, Guo S, Bai HL, Gao N (2019) Combined flow and heat transfer measurements of backward facing step flows under periodic perturbation. Int J Heat Mass Transf 130:240–251
14. Guo T, Zhong S, Craft T (2020) Control of laminar flow separation over a backward-facing rounded ramp with CD riblets—the effects of riblet height, spacing and yaw angle. Int J Heat Fluid Flow 85:108629
15. Talib ARA, Hilo AK (2021) Fluid flow and heat transfer over corrugated backward facing step channel. Cases Stud Thermal Eng 24:100862

Accelerated CFD Computations on Multi-GPU Using OpenMP and OpenACC

Harshad Bhusare and Somnath Roy

1 Introduction

The computational fluid dynamics is an important branch of fluid mechanics for simulating fluid flows. The accuracy of those results depends on order of the numerical scheme, grid size, floating-point precision which is computationally expensive. Modern General Purpose Graphical Processing Units (GP-GPU) has higher floating-point computing capability (FLOPS) due to the large number of cores present when compared with a central processing unit (CPU). For carrying out a direct numerical simulation (DNS) with high Reynold's number (Re) the computational load is $N \sim \text{Re}^{9/4}$. The higher order finite difference method is computationally expensive and those solvers can be ported to GPUs for getting accurate results. Since the development of NVIDIA's CUDA architecture, the usage of general purpose GPU (GP-GPU) has increased drastically, due to its simple implementation and its capability of conducting highly parallel calculations. Thibault et al. [1] ported a 3D incompressible Navier–Stokes solver using CUDA programming language on multi-GPU. Thibault were able to get a speed-up of $21\times$ on two GPUs when compared with a single CPU. On a large-scale problem they were able to get 3x performance when compared with a single to a single GPU. The Jun-hui Wang et al. simulated surface water flow process with a higher resolution model and accelerated the computation using a single GPU [2]. The Ali Uzun et al. carried out direct numerical simulation based on a flow solver accelerated on GPU [3]. Chuang-Chao Ye et al. showed that their accelerated code on a Tesla V multi-GPUs were able to get a speed-up of $2000\times$ when compared with a CPU [4]. The Da-li Li et al. ported the Euler solver on central processing unit (CPUs) to three different CPU/GPU heterogeneous platforms which gave a highest speed-up of $260\times$ on their MUSCL Scheme [5]. There has been an

H. Bhusare (✉) · S. Roy
Department of Mechanical Engineering, IIT Kharagpur, 721302, Kharagpur, India
e-mail: harshad022@kgpian.iitkgp.ac.in

263

ease in programming and porting in-house codes onto a GPU platform due to emergence of OpenMP [6] and OpenACC [7], a directive-based programming model. The OpenACC architecture allows the user to divide the workload, making application porting more easier and efficient. Cappello et al. [8–10] proposed a hybrid programming model that combined MPI with p-threads using OpenMP. They showed that by combining shared memory and message passing models, it is possible to improve the efficiency of particular codes. Heterogeneous processors, which combine many CPUs and GPUs, are a popular choice for porting complicated scientific programmes [11]. The Jianqi Lai et al. were able to carry out hypersonic flow computations on a multi-GPU platform which are compute intensive tasks. They were able to get speed-up of $77\times$ for coarser mesh and $147\times$ speed-up for finer mesh on four GPUs. The compute unified device architecture (CUDA) + MPI was used for parallel computing platform and programming model for GPUs to implement the algorithm on heterogenous architecture [12]. The incompressible Navier–Stokes solver was implemented by Cohen and Molemaker based on the Boussinesq approximation with double precision [13]. Goddeke et al. [14] investigated finite element model for fluid mechanics computations on GPU platform. GPUs have also been widely reported for Euler solvers and incompressible Navier–Stokes solvers [1, 5, 15, 16].

In this present study, a hybrid programming model is implemented on Poisson solver of the in-house 3D incompressible Navier–Stokes code running on a single node based on OpenMP and OpenACC directive-based programming language utilizing multi-GPU. A direct numerical simulation (DNS) is performed on a simple 3D lid-driven cavity on this multi-GPU parallelized code.

2 Methodology

The conservation equations for mass and momentum for an unsteady incompressible flow of a Newtonian fluid in non-dimensionalized form are given by Eqs. (1) and (2) and are expressed as [17]

$$\frac{\partial u_i}{\partial x_i} = 0 \tag{1}$$

$$\frac{\partial u_i}{\partial x_i} + \frac{\partial u_i u_j}{\partial x_j} = -\frac{\partial p}{\partial x_i} + \frac{1}{\text{Re}} \frac{\partial^2 u}{\partial x_j^2} + F_i \tag{2}$$

where

x_i Spatial coordinates
u_i Velocity field
p Pressure
F_i Body force term

Fig. 1 Location of variables in staggered grid
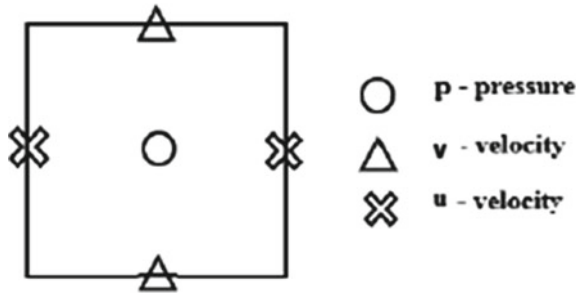
The Marker and Cell (MAC) algorithm were used to solve those Navier–Stokes equations [18]. The pressure values are located at cell centres, and the velocities are located at cell sides, in a staggered grid shown in Fig. 1. The solutions for the next time step are predicted directly by Eq. (3) and analogous y and z momentum equations.

$$\hat{u}_{i,j,k}^{n+1} = u_{i,j,k}^n - \delta t \left(\frac{p_{i,j,k}^{'} - p_{i+1,j,k}^{'}}{\delta x} \right)$$

$$- 0.5 * \delta t \left[3(\text{conv} - \text{diff})_{i,j,k}^n - (\text{conv} - \text{diff})_{i,j,k}^{n-1} \right] \tag{3}$$

Here, the projected velocity for the $(n + 1)$th time step is $\hat{u}$, which is not divergence free. The terms "conv" and "diff" denote discretized forms of $\left(u \frac{\partial u}{\partial x} + v \frac{\partial u}{\partial y} + w \frac{\partial u}{\partial z} \right) = 0$ and $\frac{1}{Re} \left(\frac{\partial^2 u}{\partial x^2} + \frac{\partial^2 v}{\partial y^2} + \frac{\partial^2 w}{\partial z^2} \right)$, respectively. The "convective" term is discretized using a second-order upwind technique, while the "diffusive" term is discretized using a second-order central difference method.

The pressure Poisson's equation is solved using Red-Black Successive Over Relaxation (SOR) algorithm.

Pressure Updation Step:

$$p_{i,j,k}^{n+1} = p_{i,j,k}^n + p_{i,j,k}^{'} \tag{4}$$

where $p_{i,j,k}^{'}$ is obtained from solution of Poisson Eq. (5).

$$\nabla^2 p^{'} = \frac{1}{\nabla t} \nabla . \hat{u} \tag{5}$$

$$(\text{Div})_{i,j,k} - \delta t \left[\frac{p^{'}_{i+1,j,k} - 2p^{'}_{i,j,k} + p^{'}_{i-1,j,k}}{\delta x^2} + \frac{p^{'}_{i,j+1,k} - 2p^{'}_{i,j,k} + p^{'}_{i,j-1,k}}{\delta y^2} \right.$$

$$\left. + \frac{p^{'}_{i,j,k+1} - 2p^{'}_{i,j,k} + p^{'}_{i,j,k-1}}{\delta z^2} \right] = 0 \tag{6}$$

where

$$(\text{Div})_{i,j,k} = \frac{\hat{u}^{n+1}_{i,j,k} - \hat{u}^{n+1}_{i-1,j,k}}{\Delta x} + \frac{\hat{v}^{n+1}_{i,j,k} - \hat{v}^{n+1}_{i,j-1,k}}{\Delta y} + \frac{\hat{w}^{n+1}_{i,j,k} - \hat{w}^{n+1}_{i,j,k-1}}{\Delta z}. \tag{7}$$

Velocity Correction Step

$$u^{n+1}_{i,j,k} - u^{n}_{i,j,k} = \delta t \left(\frac{p^{'}_{i,j,k} - p^{'}_{i+1,j,k}}{\delta x} \right) \tag{8}$$

Similarly, other two velocity components are determined using y and z momentum equations.

3 OpenMP and OpenACC

OpenACC [7] uses a directive-based approach to heterogeneous programming, where a programmer is required to add pragmas, i.e. compiler directives to the serial code to designate which parts of the function should be accelerated in a loop. The updated source code, including directives is subsequently processed by the OpenACC compiler, which generates programmes that can run on accelerators which is basically a GPU. There are a variety of other directives that allow for performance optimization and adjustments depending on the programmer. The OpenMP [6] is a shared-memory parallel programming model. The fundamental distinction between the two standards is that OpenMP permits ordinary OpenMP directives to be mixed with accelerator directives, whereas OpenACC directives are especially developed for offloading computation to accelerators. Data movement between the host and the device must also be carefully considered by the programmer otherwise, performance will be inefficient.

4 Parallelization: Strategy and Implementation

Parallel programming is further complicated by the diverse architecture of current computing clusters with accelerators. This is due to the differences in CPU and GPU hardware architecture, as well as the requirement to migrate data between the two and the requirement to perform the copy operations concurrently wherever possible [7]. In order to get the most out of the computer cluster, new techniques and algorithms must take advantage of the underlying architecture. To put it another way, algorithms that succeed on CPU alone may struggle on hybrid systems. As a result, prior to adopting a numerical method for heterogeneous systems, it is critical to analyze algorithmic bottlenecks. When a CPU algorithm is naively ported to a GPU, it may result in inadequate performance. Here, in our legacy code, the most time-consuming part was the solution of pressure Poisson equation which is based on Red–Black Successive Over Relaxation (RB-SOR) technique. Hence, the RB-SOR part was multi-GPU parallelized using hybrid programming model based on directive-based application porting interface (API), i.e. OpenMP and OpenACC. We use threads to operate a GPU and each thread is coupled with one GPU for parallelization of the Poisson solver on multiple GPUs. When the data directive of copyin/copyout/copy/create is used in a loop, the compiler creates the data memory allocation. The execution of several GPUs cannot be parallelized since memory allocation is a blocking operation. In OpenACC, this is inescapable because the compiler generates all runtime functions, and the placement of these procedures cannot be random. Our answer is to build a series of threads, each of which manages one GPU's context, is shown in Fig. 2. This implementation is task-based where, we have an nth GPU connected to a CPU host, and the host first spawns n-threads, each with its own GPU. The thread with the assigned sub-domain calls the attached GPU based on device-id assigned and the task within the loop is offloaded on that particular GPU. These tasks include memory allocation on GPU, memory freeing, data transmission, kernel/parallel constructs launch and so on.

For compiling flags passed to PGI compiler were *−fast −acc −mp -O3,* where *−acc* is required for invoking OpenACC directives and *−mp* for invoking OpenMP directive and the *O3* is for third-level optimization. The OpenACC Programming and Best Practices [19] Guide can be referred for more information on the OpenACC directives and programming.

5 Validation and Verification

A flow inside a 3D lid-driven cavity is simulated for Reynold's number Re=3200 and the configuration of the domain is as shown in Fig. 3. The geometry aspect ratio for *x:y:z* was chosen to be 1:1:3. The no-slip boundary conditions were applied at bottom and side walls with upper lid moving with a velocity U_{lid}.
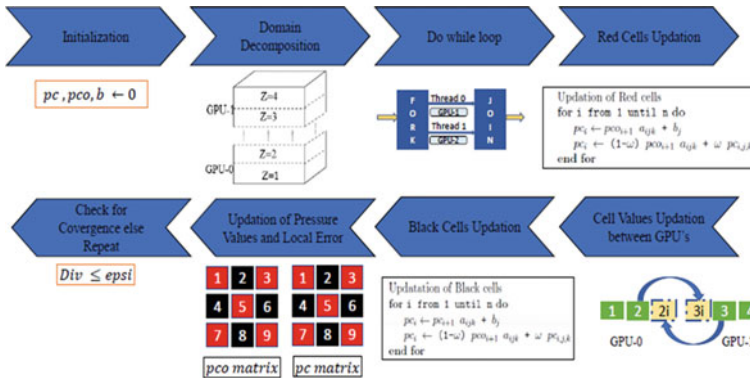
Fig. 2 Figure represents the flow chart of the computational algorithm along with domain decomposition and fork-join model of OpenMP with each thread been assigned to a GPU is also represented within the char
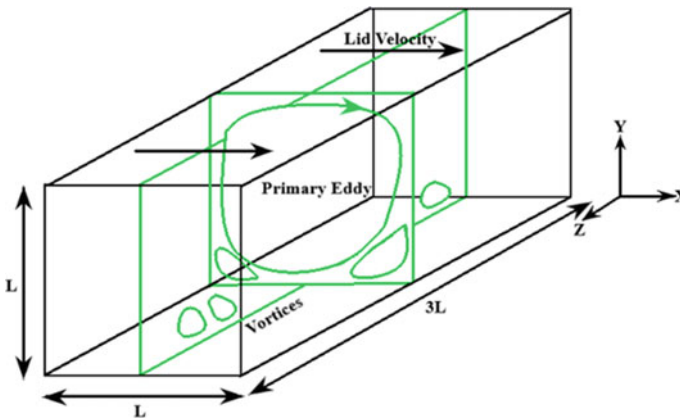
Fig. 3 Configuration of the domain

A. **Grid Independence Study**

Table 1 represents the grid independence study for the results obtained from the 3D lid-driven cavity at Re $= 3200$. Here, the results were represented for the u_{min} velocity at $y = 0.5$ along the centre plane. The results obtained for two different mesh sizes don't differ much and are within 0.5% range for the minimum u velocity. Further, the grid used for obtaining the results was $(100 \times 100 \times 300)$ cells.

B. **Validation**

The velocity profiles at the centre plane were validated with the experimental dataset. It can be seen that the simulated results were in good agreement with that of experimental data.

Table 1 Grid independence study for Re = 3200

Mesh			% Change
	$(100 \times 100 \times 300)$	$(160 \times 160 \times 480)$	
u_{min}	-0.333994	-0.337536	0.01061
y_{min}	0.040631	0.040625	0.00015

Fig. 4 Average u-velocity profile along symmetry plane and average v velocity along symmetry plane at Re = 3200
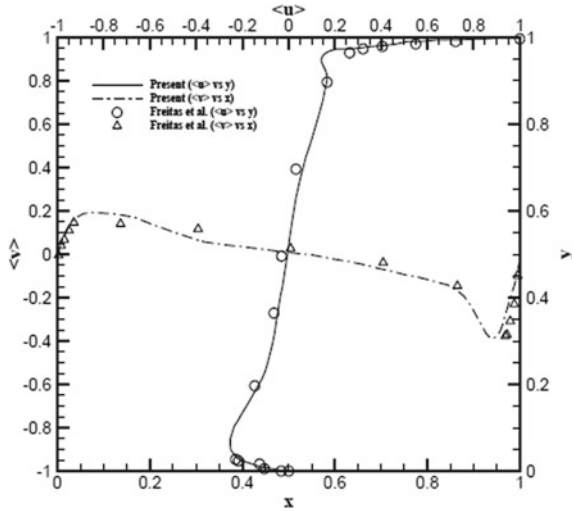
The velocity profile shown in Fig. 4 is the u velocity at the plane centre line $x = 0.5$ at $z = 1.5$, and v velocity at the plane centre line $y = 0.5$ at $z = 1.5$ and validated using experimental data from Freitas et al. [20].

6   Results and Discussion

A.   Performance Metrics

The HPC clusters are accompanied with large amount of resources, i.e. CPUs and GPUs and they consume a lot of energy. So it is advisable to use it efficiently and utilize the resource effectively. To analyze the performance of parallelized code, there are some parameters that can be calculated and compared for performance. Some of these parameters are defined below.

(1) **Speed-Up/Scalability**:

$$\text{Speed Up } (S) = \frac{T_s}{T_p}, \tag{9}$$

where

T_s Serial, timing
T_p Parallel, timing

(2) **Efficiency**:

$$\text{Efficiency}(E) = \frac{T_s}{p * T_p}, \tag{10}$$

where $p =$ No.of processors.

Tables 2 and 3 represent the performance of our parallelized code ran on single node on PARAM Shakti High Performance Computing cluster (Fig. 5).

B. **Flow Inside a Turbulent 3D Lid-driven Cavity**

Flow inside a 3D lid-driven cavity is simulated for Reynolds number Re = 10,000 and the configuration of the domain is as shown in Fig. 6.

(1) *Boundary Conditions.:* A Dirichlet type of boundary conditions were imposed on the walls for the cubic cavity as follows:

Table 2 Computation timings

Grid size [millions]	CPU [s]		GPU [s]	
	Single	Multiple	Single	Multiple
0.375	7.598	3.802	2.149	2.424
1.305	27.549	14.127	2.375	2.615
3.000	61.841	31.508	3.232	2.784
7.875	167.625	84.401	4.463	2.925
10.125	213.350	109.035	5.052	3.545
15.625	335.559	171.934	6.363	5.469

Table 3 Speed-up and efficiency

Speed-up				Efficiency (%)
Single versus multi-CPU	Single versus multi-GPU	CPU versus GPU	CPU vs multi-GPU	
1.999	0.886	3.536	3.134	44.31
1.950	0.908	11.601	10.535	45.40
1.963	1.161	19.136	22.211	58.04
1.986	1.526	37.560	57.302	76.28
1.957	1.425	42.234	60.185	71.25
1.956	1.689	52.735	61.354	84.48
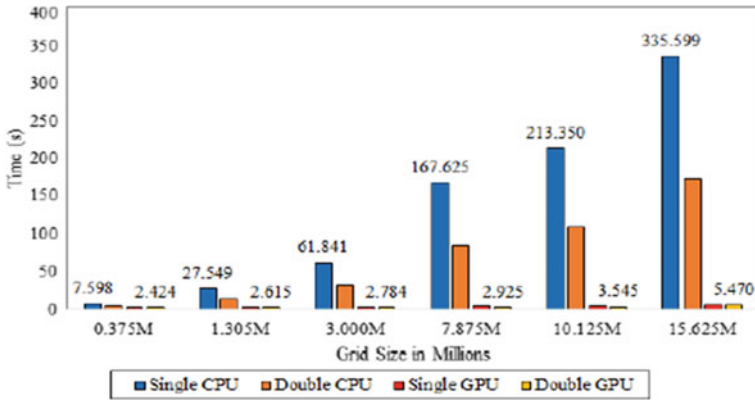
Fig. 5 Total runtime of the Poisson's equation solution is compared with CPU's timing for different domain sizes

Fig. 6 Configuration of the domain
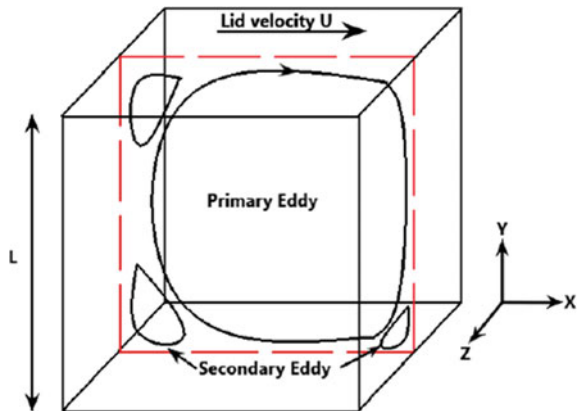
Right and left walls at $x = (0, nx) : u = v = w = 0$

Front and rear walls at $z = (0, nz) : u = v = w = 0$

The Bottom wall at $y = 0 : u = v = w = 0$

At the Top wall at $y = ny : u = U_{lid}, v = 0$

The above Fig. 6 shown is the geometry of the cubic domain with top lid moving with U_{lid} velocity. The Δx was chosen to be $4 * 10^{-3}$ and the number of cells in x, y, z direction as $(250 \times 250 \times 250)$, respectively. The time step Δt was taken as $1 * 10^{-3}$.

The time-averaged mean velocity profiles at the centre plane $z = 0.5$ are shown in Fig. 7 and those were averaged over a time period of 50 s and validated against the experimental data present from the paper Prasad and Koseff [21]. The mean u-velocity profile computed was able to capture the most values near the lower wall and

also captured well near the mid-section of the cavity, but it slightly under-predicted the upper wall rms values. The mean *v*-velocity profile closely matched experimental data, and were overall in agreement with the experimental data profile [21].

For turbulent statistics the urms and vrms velocities were normalized and averaged values are computed at the centre line at $y = x = 0.5$ and were compared with the experimental data from Prasad and Koseff [21]. The present simulation was able to compare well with the experimental rms values inside the cavity. The profiles are as shown in the Figs. 8 and 9.

Fig. 7 Average *u* velocity along y axis at $x = 0.5$ and average *v* velocity along x axis at $y = 0.5$ on the plane of symmetry at $z = 0.5$
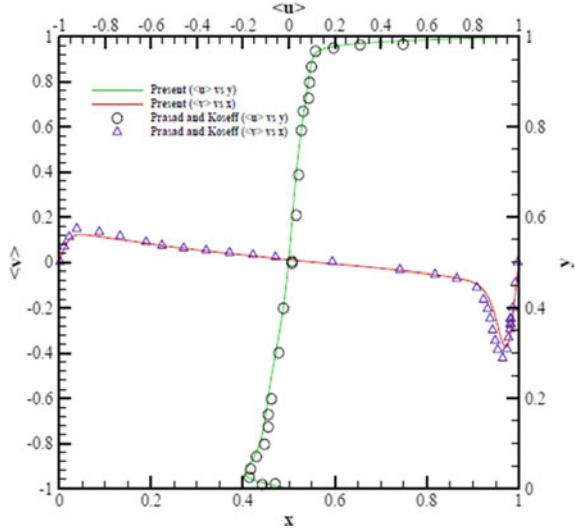
Fig. 8 Mean streamwise *u* rms velocity profile at $x = 0.5$ at Re = 10,000
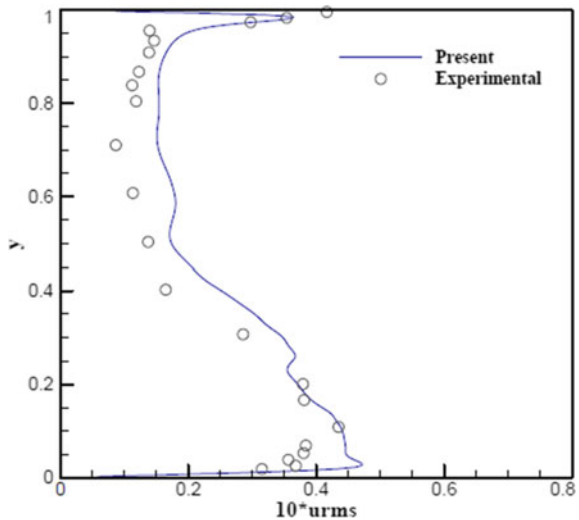
Fig. 9 Mean streamwise v rms velocity profile at $y = 0.5$ at Re $= 10,000$
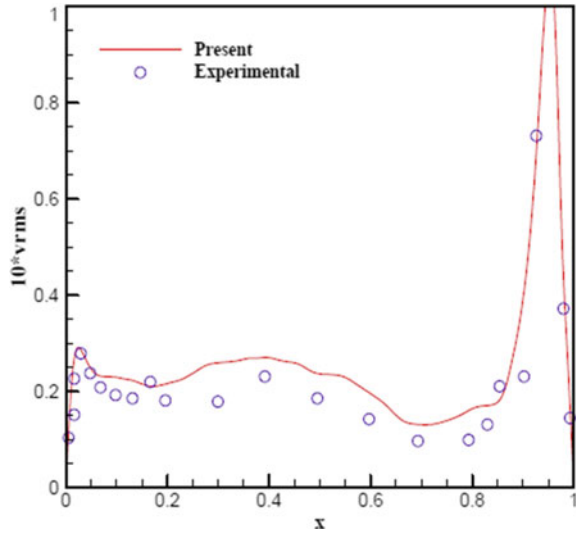
The Figs. 10 and 11 depicts the various averaged streamline plots at x and y mid-planes. In each plane there is a formation of corner vortices. The streamlines were examined in those cross-section planes of the cavity, where counter rotating vortices can be observed in the YZ-plane streamlines. The three dimensionality effects can be clearly observed as there is the formation of corner and Taylor Grtler like (TGL) vortices in the XZ-plane.

Fig. 10 Mean streamwise contour along mid x-plane
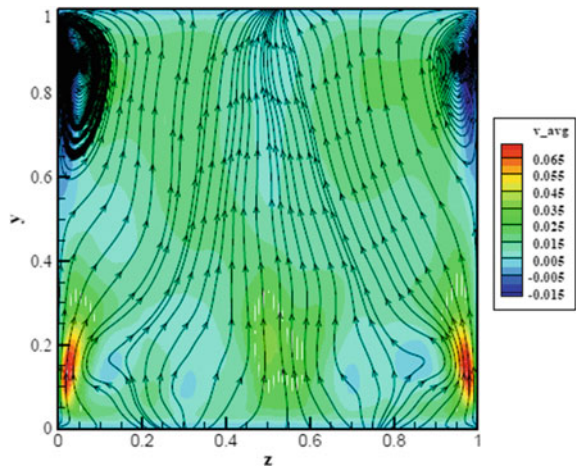
Fig. 11 Mean streamwise
contour along mid *y*-plane
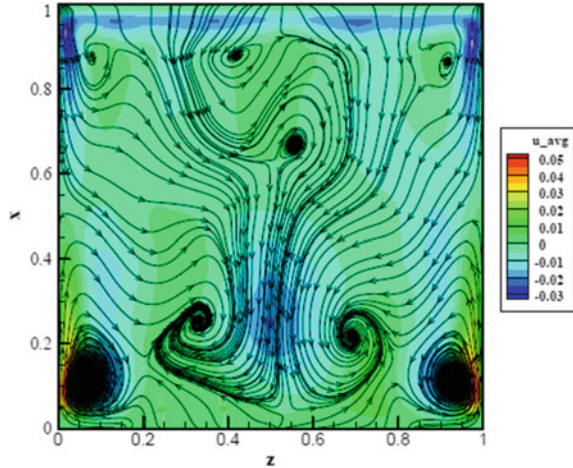
7   Conclusion

The hybrid programming strategy for multi-GPU within a single node using OpenMP
and OpenACC was investigated in this paper.

(1) We were able to get a speed-up of 61 × on two GPUs NVIDIA V100 when
    compared with Intel Xeon CPU and 1.6 × two GPU's speed-up when compared
    with a single GPU.
(2) The maximum efficiency we got for multi-GPU was 84% for the domain size
    of 15 million.
(3) On multi-GPU, we tested the hybrid architecture with these 3D lid-driven cavity
    case and saw a significant performance boost.

   We demonstrate the efficacy of our approach by exploring the 3D lid-driven cavity
results, where a large domain is decomposed into multiple sub-domains, after which
each sub-domain is offloaded to a GPU attached to a thread. We can simplify multi-
GPU programming while still getting considerably higher performance than the
hybrid paradigm by using the proposed directive modification. The parallelized code
was further validated by simulating 3D lid-driven cavity at Re = 3200, and the
results were in good agreement with the experimental data present in literature.
Turbulence was explored in a 3D lid-driven cavity at Re = 10,000, the mean and
rms velocity profiles were matched against the experimental data. The averaged
streamlines showed various vortices formation in the *x* and *y* mid-planes.

Nomenclature

Re	Reynolds number–
DNS	Direct Numerical Simulation–
CPU	Central Processing Unit–
GPU	Graphical Processing Unit–
PFLOPS	Peta Floating Points Operation–
HPC	High Performance Computing–
API	Application Programming Interface–
CUDA	Compute Unified Device Architecture–
FDM	Finite Difference Method–
MAC	Marker and Cell–
SOR	Successive Over Relaxation–
TGL	Taylor Görtler Longitudinal Vortices–
< . >	Averaged Quantity

References

1. Thibault J, Senocak I (2009) Cuda implementation of a navier- stokes solver on multi-gpu desktop platforms for incompressible flows. In: 47th AIAA aerospace sciences meeting including the new horizons forum and aerospace exposition, p 758
2. Wang J-h, Hou J-M, Gong J-H, Li B-Y, Shi B-S, Guo M-P, Shen J, Lu P (2021) A non-uniform grid approach for high-resolution flood inundation simulation based on gpus. J Hydrodyn 33(4):844–860
3. Uzun A, Malik MR (2021) Simulation of a turbulent flow subjected to favorable and adverse pressure gradients. Theor Comput Fluid Dyn 35(3):293–329
4. Ye C-C, Zhang P-J-Y, Wan Z-H, Yan R, Sun D-J (2022) Accelerating cfd simulation with high order finite difference method on curvilinear coordinates for modern gpu clusters. Adv Aerodyn 4(1):1–32
5. Lei J, Li D-l, Zhou Y-L, Liu W (2019) Optimization and acceleration of flow simulations for cfd on cpu/gpu architecture. J Braz Soc Mech Sci Eng 41(7):1–15
6. OpenMP Standard Home. https://www.openmp.org/
7. OpenACC Standard Home. https://www.openacc.org/
8. Cappello F, Richard O, Etiemble D (1999) Performance of the nas benchmarks on a cluster of smp pcs using a parallelization of the mpi programs with openmp. In: International conference on parallel computing technologies, Springer, Berlin, pp 339–350
9. Cappello F, Richard O (1999) Investigating the performance of two programming models for clusters of commodity smp
10. Cappello F, Etiemble D (2000) Mpi versus mpi+ openmp on the ibm sp for the nas benchmarks. In: SC'00: proceedings of the 2000 ACM/IEEE conference on supercomputing. IEEE, pp 12–12
11. Xu R, Tian X, Chandrasekaran S, Chapman B (2015) Multi-GPU support on single node using directive-based programming model. Sci Program
12. Lai J, Li H, Tian Z, Zhang Y (2019) A multi-gpu parallel algorithm in hypersonic flow computations. Math Prob Eng
13. Cohen J, Molemaker MJ (2009) A fast double precision cfd code using cuda. Parallel Comput Fluid Dyn Recent Adv Future Dir 414–429

14. Goddeke D, Buijssen SHM, Wobker H, Turek S (2009) Gpu acceleration of an unmodified parallel finite element navier-stokes solver. In: 2009 international conference on high performance computing and simulation. IEEE, pp 12–21
15. Brandvik T, Pullan G (2008) Acceleration of a 3d euler solver using commodity graphics hardware. In: 46th AIAA aerospace sciences meeting and exhibit, p 607
16. Jacobsen DA (2011) Methods for multilevel parallelism on gpu clusters: application to a multigrid accelerated navier-stokes solver
17. Tu J, Yeoh GH, Liu C (2018) Computational fluid dynamics: a practical approach. Butterworth-Heinemann
18. Harlow FH (1965) Mac numerical calculation of time-dependent viscous incompressible flow of fluid with free surface. Phys Fluid 8:12
19. OpenACC Programming and best practices guide. https://www.openacc.org/resources
20. Freitas CJ, Street RL, Findikakis AN, Koseff JR (1985) Numerical simulation of three-dimensional flow in a cavity. Int J Numer Methods Fluids 5(6):561–575
21. Prasad AK, Koseff JR (1989) Reynolds number and end- wall effects on a lid-driven cavity flow. Phys Fluids Fluid Dyn 1(2):208–218
22. Elsen E, LeGresley P, Darve E (2008) Large calculation of the flow over a hypersonic vehicle using a gpu. J Comput Phys 227(24):10148–10161
23. Schive H-Y, Tsai Y-C, Chiueh T (2010) Gamer: a graphic processing unit accelerated adaptive-mesh-refinement code for astrophysics. Astrophys J Suppl Ser 186(2):457

CFD Analysis of Different Designs of Greenhouse

Abhishek Pawar, Sachin Halikhede, Atharva Umbarkar, Aniket Kedar, Pratiksha Waghmode, and Pramod Kothmire

1   Introduction

A greenhouse is a structure with walls and a roof that is made of transparent material, such as glass. There are different designs of greenhouses which can be categorized into three types: unheated, heated, and refrigerated. Various techniques are used to manage air temperature, relative humidity, and vapor-pressure deficit. The climate which is created naturally in the greenhouses is used in the tropical and sub-tropical regions to produce food and commercial crops. The production of such crops is very much dependent on how much efficient the greenhouse is considering ventilation. The ventilation depends on the local climate of the region. The main objective of the greenhouse is to make the least possible disturbance in the environment of the plants. By controlling the environment in the greenhouse, we can maximize the yields of crops. This occurs due to the appropriate functioning of the photosynthetic process.

Natural ventilation in a greenhouse is a simple and efficient method that requires a much low level of maintenance when we compare the operating costs with forced ventilation greenhouses. By studying and finding the optimum design, we can maintain the temperature, control the ventilation, and also control the humidity which will facilitate the healthy growth of plants inside [1]. Natural ventilation is mainly dependent on the climatic conditions of the surrounding or outside environment as this type of ventilation requires the flow of air between two environments which in turn gives less control in maintaining the inside climate [2]. This problem mainly occurs in the summer season. This problem also occurs due to some fault in designs which generates an unsuitable environment inside the greenhouse.

The efficient working of greenhouse working on natural ventilation is mainly dependent on various factors such as the shape and size of the vents, the amount of slope of greenhouses, the geometry of the greenhouse, the direction and velocity of

A. Pawar (✉) · S. Halikhede · A. Umbarkar · A. Kedar · P. Waghmode · P. Kothmire
School of Mechanical Engineering, MIT Academy of Engineering, Alandi, Pune 412105, India
e-mail: ampawar@mitaoe.ac.in

wind, the distance between vent and ground, etc. [3]. In the case of natural ventilation, we can have configurations such as roof ventilation, side ventilation, or a hybrid of both. For the investigations of the study, various methods are used such as the experimentation method which is by directly setting up the required structure and analyzing it using sensors, but this method has limited applications as we cannot recreate any climatic region for experimentation. Another method is the use of computational fluid dynamics (CFD) which can provide fast and accurate results and simulations at a much lesser cost than an experimental setup. This method helps us to describe the temperature distribution and airflow in the greenhouse.

2 Literature Review and Objective

The goal of this project is to create a computer simulation of natural ventilation in greenhouses. To maximize the efficiency of natural ventilation, the design of greenhouses must be optimized. This can be done by creating a computer simulation that will analyze different designs and their respective effects on the environment inside the greenhouse. Different techniques are used to manage growing conditions, including air temperature, relative humidity, and vapor-pressure deficit. Different research papers showcased only the reduction of any one of the influencing parameters at a time, i.e., length or width but not simultaneously. Only a few research papers mentioned the concern of leakages of air through greenhouses [4].

To build an optimized design of a greenhouse that will allow efficient airflow with uniform temperature and velocity distribution. To perform analysis for different velocities in different directions of air. To build a leakage-proof design of the greenhouse. To increase the height of the side walls to get better temperature distribution and flow of air through the greenhouse. Additionally, in the ventilation process, humidity plays a major role in the analysis of the CFD model of the greenhouse but the buoyancy effect which is a major driving parameter for the humidity is yet to be analyzed which will be very fruitful for future purposes.

Edwin A. Villagrán, Esteban J. Baeza Romero, and Carlos R. Bojacá investigated the ventilation efficiency in three different greenhouses which were Colombian Wood (TG) and alternative types of multi-span greenhouses (Curved DMG and Gothic GMG) which have larger ventilation areas both on roof as well as sides. They found that the DMG and GMG greenhouses have 3.4 times higher ventilation rates than that of TG, also there was more uniformity in the average temperatures [1].

Sang-Yeon Lee, In-Bok Lee, and Rack-woo Kim studied the coastal reclaimed lands for the construction of single-span greenhouses which used natural ventilation, this was different than other researchers as the characteristics of winds in the coastal lands were different from the other places which called for careful evaluation. The validation of CFD results were done by wind tunnel experiments [2]. M. Vivekanandan, K. Periasamy, C. Dinesh Babu, G. Selvakumar, and R. Arivazhagan have used the greenhouse for drying it and stated that solar drying in greenhouse is much more effective than open air drying. The study is about choosing the best

shape for the optimum shape, while keeping the same volume in each of the shape considered [5].

To create the best possible environment for the crops inside, natural ventilation must be used as efficiently as possible. The management of growing circumstances involves a variety of methods, such as controlling air temperature, relative humidity, and vapor-pressure deficit. Different research studies solely focused on the lowering of one affecting parameter, such as length or width, at a time. Few research studies have discussed the issue of air leakages via greenhouses. To construct a greenhouse with an improved design that will enable effective airflow with consistent temperature and velocity distribution. To do analysis for various air velocities in various directions. Creating a greenhouse with a leak-proof design. Increasing the side walls height will improve temperature distribution and airflow through the building.

3   Materials and Methods

This analysis is done through CFD Software, ANSYS R22 R1 is being used for performing the analysis. In addition to it, Fusion 360 is also being used for sketching the different types of different greenhouses. The designs are created in Fusion 360 and are imported into Ansys Mechanical. The geometry created has a cuboidal environment consisting of four greenhouses of even type and peach type of which dimensions are specified in Table 1. For analyzing the system under Ansys, we cannot create the model in surfacing as Ansys Fluent has difficulty in detecting surfaces, so we have given a thickness of 0.1 m to the model so that it is easier for the analysis (Fig. 1a, b).

The model with the environment is created as shown in Fig. 2. As the model created has two regions fluid-air and solid-greenhouse, we subtract the solid greenhouse region so that we can work on the fluid region for the result [6]. This is done by using Boolean-Subtract in Ansys Mechanical. A comparative study was carried out on the even-type design consisting of the inlet of air firstly parallel to the greenhouse inlet and then at an angle of 45° to the greenhouse. This would determine which

Table 1 Specifications of greenhouse dimensions

Specifications of greenhouses (Unit—m)		
Parameters	Single span greenhouses	
	Even span type	Peach type
Width (W)	9	8.2
Ridge height (R)	4.95	3.9
Eave height (E)	2.7	1.6
Length (L)	45	45
Width of the side Vent (V)	1.35	1.2

(a)

(b)
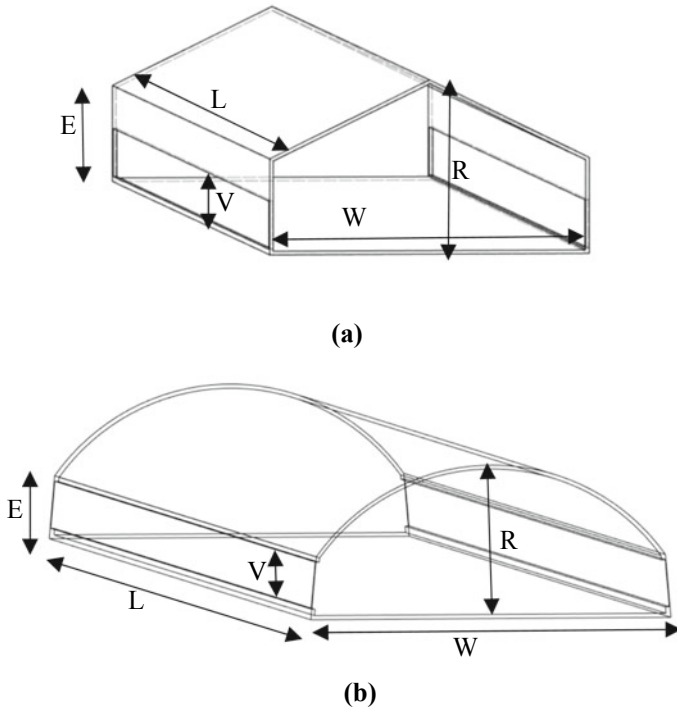
Fig. 1 Type of greenhouse **a** Even-span type **b** Peach type

alignment is better suited for the greenhouse and the result would be applied for the further temperature and velocity analysis.

For the comparative analysis between parallel and 45° flow, a separate geometry with an environment domain has been considered having arrangement of 2 × 2 for analysis. For the temperature and velocity analysis four closed greenhouses have
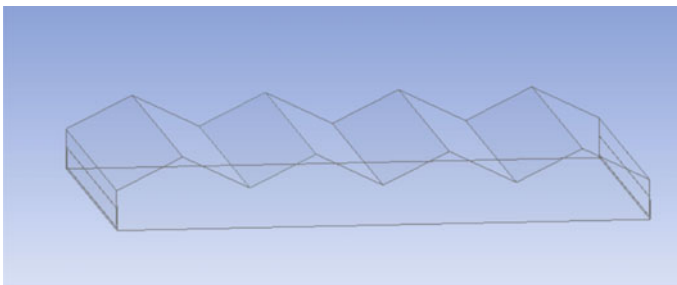
Fig. 2 Even span type model of greenhouse

been used for analysis. Figure 2 shows the model of even-type greenhouse in single span.

The model made here is to actual scale so, while meshing we used an element size of 1000, 900, and 800 mm. Edge sizing was applied on the inlets for finer meshing. The meshing was checked for quality. The named selections for the inlet and outlet were also specified for ease. The element size was varied to check for the mesh independence study. The mesh image is depicted in Fig. 3 and the element quality checking is in Fig. 4.

The mesh check shown in Fig. 4 shows the meshed element quality in even-type and peach-type greenhouse, respectively, observation shows that there are very few elements that are below the required quality, most of the elements pass the quality check having a value above 0.75.
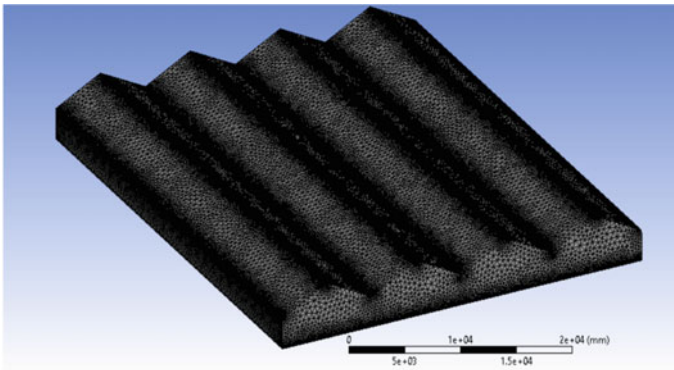
(a)
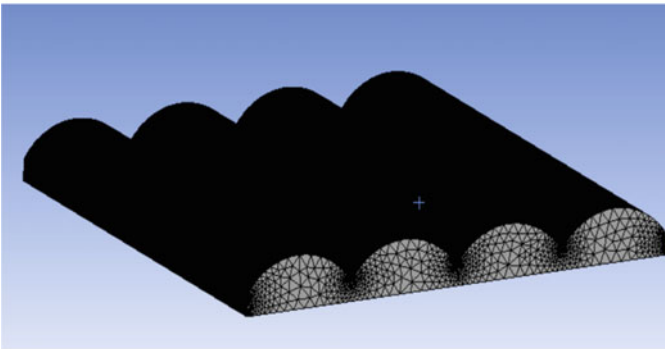
(b)

Fig. 3 Meshing result on two types of greenhouse geometries **a** Meshing on even-type geometry **b** Meshing on peach-type geometry
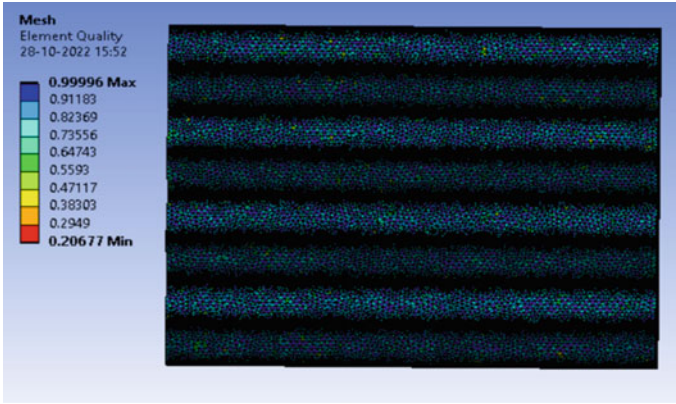
Fig. 4 Element quality check on even type of greenhouse **a** Top view **b** Isometric view

The boundary conditions were inlet velocity at the inlet of the environment created which was stated as 1 m/s considering normal airspeed. For the temperature analysis, air temperature was set to 305 K. For this study, energy model was turned on and the viscous realizable k-epsilon, standard wall function was used. The described model is depicted in Fig. 5.

Considering the greenhouse in open solar load on the walls of greenhouse, specific temperatures were assigned to the walls and light transmission of about 80% and temperature of 310 K were assigned to upper walls. The walls surrounding inlet and outlet were assigned a transmittivity of 50% and a temperature of 305 K. The other walls were also assigned transmission of 50% and temperature of 305 K. The bottom of the greenhouse, i.e., soil was assigned a temperature of 309 K and set as opaque.
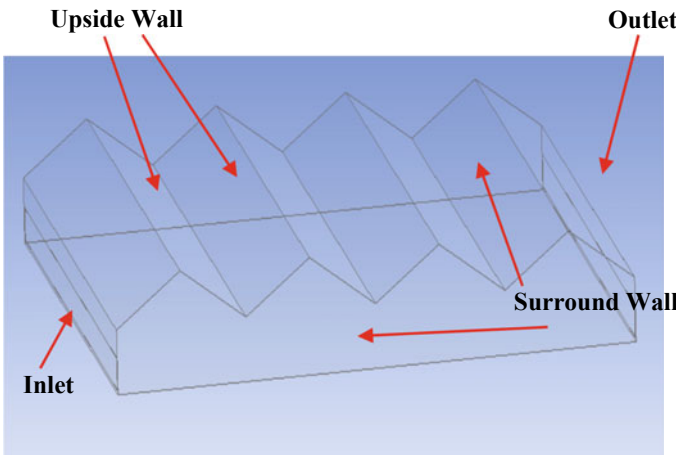
Fig. 5 Boundary conditions: Upwind wall, outlet, inlet, surround wall

The calculations were performed for 400 iterations. The resulting residual graphs are shown below. This study is based on the velocity and temperature analysis of the environment of the greenhouse and the internal velocity analysis of the greenhouse.

4 Results and Discussion

The results of the comparative study of the parallel and 45-degree flow for the even-type greenhouse are depicted below. This study depicts that the parallel flow is much better than the 45-degree flow as the velocity is reduced drastically, which is the most important requirement for the growth of plants in the greenhouse.

From the velocity contours, we can see that the even-type geometry having wind flow direction parallel to the greenhouse is having a more drastic reduction in the velocity than the 45-degree air flow model depicted in Fig. 6.
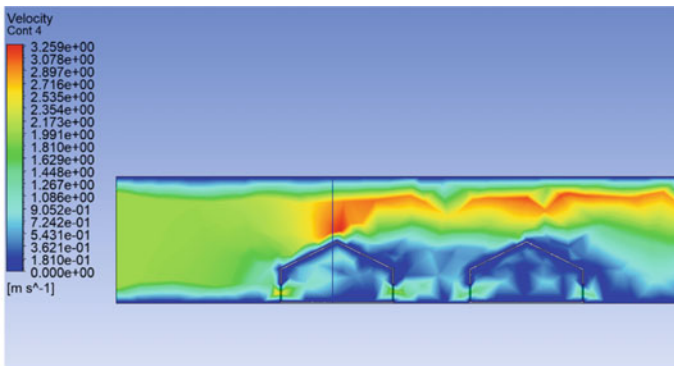
(a)
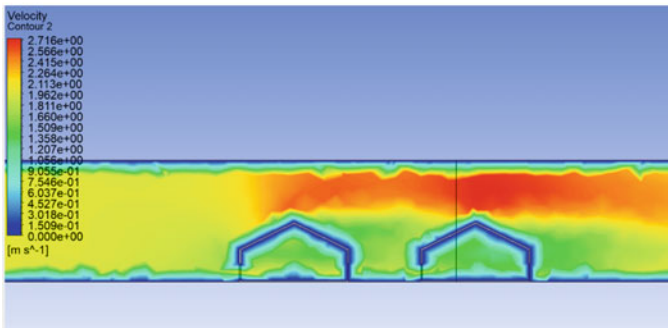
(b)

Fig. 6 Velocity contour of **a** Parallel flow and **b** 45-degree flow of even-type geometry of greenhouse

Table 2 Velocity comparison between different types of flows

Direction of air	Minimum velocity in m/s
Parallel	0.5–0.6
45°	1.1–1.4
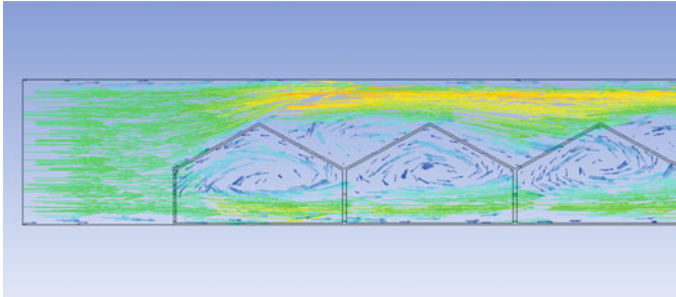
Fig. 7 Vector plot of the even-type geometry in an environment

Through the Fig. 6, we can analyze that the parallel flow of air in the greenhouse is best for the reduction of the speed of air in the greenhouse. Therefore, for the further analysis of peach-type geometry, we directly use the parallel flow of air as unlet to the greenhouse. The data obtained were compared at a particular point for velocity and the results are organized in the Table 2.

The even-type geometry when considered under an environment shows the direction of air flow as followed in Fig. 7, this states that the air going in not just goes into the nest greenhouse, some part of it strikes walls and flows again in the same greenhouse with a reduced velocity, the next greenhouse therefore has less entering velocity than the previous one and the air in inlet is mixture of direct air and some recycled air, thereby reducing the velocity of air as it moves through greenhouses.

The velocity contours and temperature contours of even-type geometry are shown below in Fig. 8. In these contours we can state that temperature of around 306 K dominates most of the even type of greenhouse, there is very little effect of the solar load and the soil temperature on the inside temperature of the greenhouse. Considering the velocity, it is varying from 0.5 to 0.7 m/s in the domain, there is a spike of greater velocity on the inlet varying almost 0.8–0.9 m/s.

In peach-type geometry, the yellow green zone of velocities 0.5–0.75 is less compared with the even type of greenhouse. The peach-type greenhouses in Fig. 9 show an even more decrease in the overall average velocities which is beneficial for healthy plant growth. The peach-type greenhouse while observing temperature contour shows the dominance of 305 K of temperature, also the peach-type greenhouse shows faster reduction in temperature than even type in Fig. 10. The temperature is also more uniform in peach-type greenhouse than in even type. This study shows that the peach-type greenhouse is better than the even-type greenhouse for
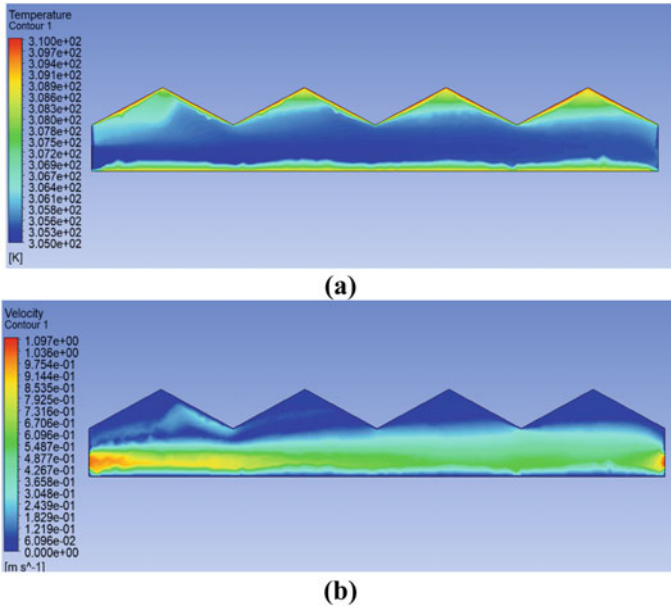
Fig. 8 Result of analysis as **a** Temperature contour and **b** Velocity contour for even-type greenhouse
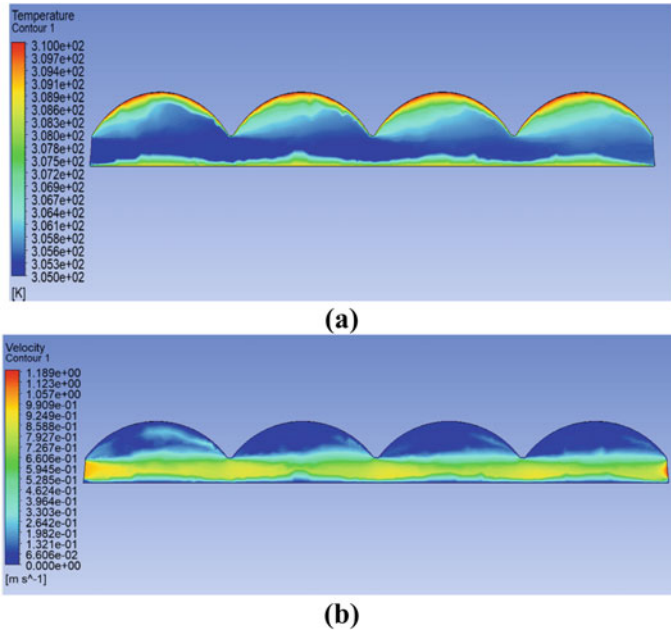
Fig. 9 Result of analysis as **a** Temperature contour and **b** Velocity contour for peach-type greenhouse

efficient plant growth. The peach-type geometry gives higher and even distribution of the lower velocity inside the greenhouse than the even type of geometry (Fig. 11).

This graph shows that, there is a very minute change in the velocities on changing the mesh element size, which shows that the results are not that much affected by the change in the mesh sizing

Fig. 10 Temperature vs. height graph of **a** Even-type and **b** Peach-type greenhouse
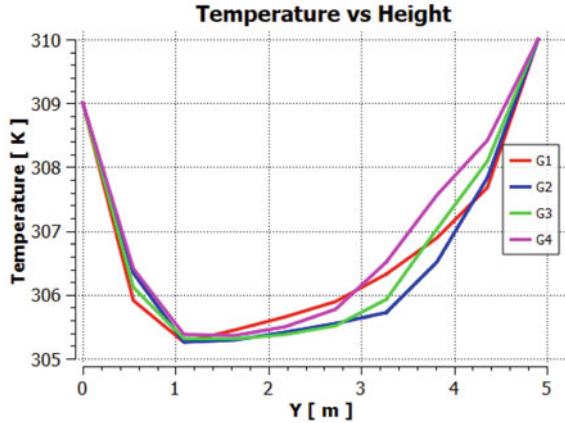
(a)
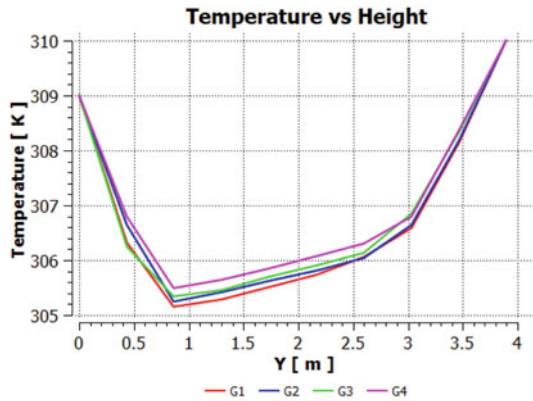
(b)

Fig. 11 Variation of velocity at a certain point concerning change in mesh element size for even-type greenhouse
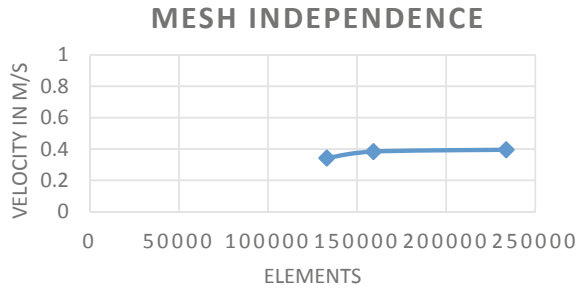
5 Conclusions

In this analysis study, we have considered some of the designs of greenhouses which are named as even—span and peach, which have different dimensions and uses that which they were differing from each other but giving some optimal results by taking all the designs mentioned above. In this study, we have performed the analysis on even–span type greenhouse and peach type where we have taken boundary conditions as velocity and the temperatures.

The analysis shows that the parallel type positioning is much better in reducing the velocity inside the greenhouse than the 45-degree alignment, which was compared for the even-type greenhouse and between the even type and peach type, the peach type shows more uniformity in velocity reduction and in distribution of temperature. The peach type gives lower temperature of almost 305 K over more area of the greenhouse, also the lower velocity is dominating more in peach-type greenhouse, giving it an advantage over the even-type greenhouse.

References

1. Villagrán EA, Romero EJB, Bojacá CR (2019) Transient CFD analysis of the natural ventilation of three types of greenhouses used for agricultural production in a tropical mountain climate. Biosyst Eng 188:288–304
2. Lee S-Y, Lee I-B, Kim R-W (2018) Evaluation of wind-driven natural ventilation of single-span greenhouses built on reclaimed coastal land. Biosyst Eng 120–142
3. Kim R-W, Hong S-W, Lee I-B, Kwon K-S (2017) Evaluation of wind pressure acting on multi-span greenhouses using CFD technique. Biosyst Eng 235–256
4. Kuroyanagi T (2017) Investigating air leakage and wind pressure coefficients of single-span plastic greenhouses using computational fluid dynamics. Biosys Eng 163:15–27
5. Vivekanandan M, Periasamy K, Dinesh Babu C, Selvakumar G, Arivazhagan R (2021) Experimental and CFD investigation of six shapes of solar greenhouse dryer in no load conditions to identify the ideal shape of dryer. Mater Today Proc 37:1409–1416
6. Saberian A (2019) Seyed Majid Sajadiye, The effect of dynamic solar heat load on the greenhouse microclimate using CFD simulation. Renew Energ 138:722–737
7. He X, Wang J, Guo S, Zhang J, Wei B, Sun J, Shu S (2018) Ventilation optimization of solar greenhouse with removable back walls based on CFD. Comput Electron Agric 149:16–25

8. Kim R-W, Kim J-G, Lee I-B, Yeo U-H, Lee S-Y, Decano-Valentin C (2021) Development of three-dimensional visualisation technology of the aerodynamic environment in a greenhouse using CFD and VR technology, part 1: development of VR a database using CFD. Biosyst Eng 207:33–58

9. Kim R-W, Kim J-G, Lee I-B, Yeo U-H, Lee S-Y, Decano-Valentin C (2021) Development of three-dimensional visualisation technology of the aerodynamic environment in a greenhouse using CFD and VR technology, Part 2: Development of an educational VR simulator. Biosys Eng 207:12–32

10. Zhang Y, Yasutake D, Hidaka K, Kitano M, Okayasu T (2020) CFD analysis for evaluating and optimizing spatial distribution of CO_2 concentration in a strawberry greenhouse under different CO_2 enrichment methods. Comput Electron Agric 179:105811. ISSN 0168-1699

11. Dhiman M, Sethi VP, Singh B, Sharma A (2019) CFD analysis of greenhouse heating using flue gas and hot water heat sink pipe networks. Comput Electron Agric 163:104853. ISSN 0168-1699

12. Franco A, Valera DL, Peña A, Pérez AM (2011) Aerodynamic analysis and CFD simulation of several cellulose evaporative cooling pads used in Mediterranean greenhouses. Comput Electron Agric 76(2):218–230. ISSN 0168-1699

13. Kim K, Yoon J-Y, Kwon H-J, Han J-H, Son JE, Nam S-W, Giacomelli GA (2008) In-Bok Lee, 3-D CFD analysis of relative humidity distribution in greenhouse with a fog cooling system and refrigerative dehumidifiers. Biosyst Eng 100(2):245–255. ISSN 1537–5110

14. Xu F-Y, Lu H-F, Chen Z, Guan Z-C, Chen Y-W, Shen G-W, Jiang Z (2021) Selection of a computational fluid dynamics (CFD) model and its application to greenhouse pad-fan cooling (PFC) systems. J Cleaner Prod 302:2021, 127013. ISSN 0959–6526

CFD Analysis of Catalytic Convertor to Optimise the Back Pressure and Velocity

Mahesh Shindge, Prathamesh Dhamnikar, Salman Tamboli, Rohit Fulzele, Omkar Gatlewar, Arpita Funde, and Pramod Kothmire

1 Introduction

The catalytic converter is a crucial element in lowering exhaust emissions from vehicles without modifying the engine's basic design. The stainless-steel container that holds the catalytic converter, which is attached along the engine's exhaust pipe, is made of a porous ceramic material. In converters, the ceramic is frequently a single honeycomb structure with several flow holes. Spark ignition engines exhaust emissions contain nitrogen oxides (NO_x) (20 g/kg of fuel), carbon monoxide (CO) (200 g/kg of fuel), and organic compounds such as unburned or partially burned hydrocarbons (UHC) (25 g/kg of fuel). The passages comprise of many shapes, including square, triangular, hexagonal, and sinusoidal [1]. The use of three-way catalysts to minimise combustion engine emissions is common. The majority of contemporary gasoline-powered cars employ a "three way" converter since it transforms due to the use of a catalytic convertor and advancements in IC engines.

The catalyst (alloys of high thermal stability materials) is introduced into the diesel oxidation catalyst (DOC), which results in an increase in back pressure. It is possible to argue that the presence of (DOC) results in an increase in the back pressure of the engine, which raises fuel consumption. Due to the positive impact catalytic converters have on engines, they serve as a considerable source of engine back pressure [2]. A ceramic monolith substrate is utilised to provide a standard shape and design for the catalytic converter's geometry. The catalytic converter's internal flow and pressure can be measured using CFD, with the transient 3D model of the monolith focusing on thermal effects and using the plug flow assumption for the channel flow [3]. CFD's primary objective is to select the ideal wire mesh grid size, canister material, shape, and size such that exhaust gases enter the catalytic converter with as low-pressure loss as is practicable, enhancing engine performance.

M. Shindge (✉) · P. Dhamnikar · S. Tamboli · R. Fulzele · O. Gatlewar · A. Funde · P. Kothmire
School of Mechanical Engineering, MIT Academy of Engineering, Alandi 412105, India
e-mail: mahesh.shindge@mitaoe.ac.in

The experimental catalytic converter result shows that the back pressure obtained is virtually identical to the result of CFD. We obtain decreased back pressure through both experimental testing and CFD analysis, and as a result, the engine's network production per cycle, which is reliant on the amount of pumping work required, is reduced when we employ DOC [4]. When using CFD, it can be observed that the engine's efficiency may be raised without compromising the emission requirement by using the appropriate simulated parameters, such as the inlet boundary condition, the optimum catalyst size, and the right positioning for the DOC [5].

A catalytic converter is crucial for reducing dangerous pollutants like NO_X, CO, unburned HC, and particulate matter that cause global warming. On the other hand, the catalytic converter generates exhaust back pressure, which reduces volumetric efficiency and increases fuel consumption. Therefore, it is essential to analyse the catalytic converter [6]. This comparison or analysis compares and contrasts full-scale with reduced-scale geometries. The primary distinction is the simultaneous resolution of the flow issue throughout the entire device with the catalytic reaction, diffusion, and heat effects. The fluid's qualities depend on the species and temperature. Piecewise polynomial fits from the FLUENT database are used to compute the specific heat and other thermodynamic properties.

2 Literature Review and Objective

These sections presented experimental study of catalytic convertor completed by different researchers mentioned below: CFD and Experimental Analysis of Catalytic Convertor to Optimise the Effect of Back Pressure, in this paper, Likesh A. Dahake works on the comparison of CFD with experimented result for validation. The main objective of the study is to design a diesel oxidation catalyst for the purpose of minimising the back pressure and pressure drop of DOC [1]. Design and Analysis of a Spiral Flow Catalytic Convertor: Pankaj Kumar gives a comparison between optimised design and conventional design by solving the Bernoulli equation. Aim of the study is to propose the design which contains arrangement of catalyst on the periphery, inclined at angle which will affect in greater surface area for catalytic reaction [2]. A Computational Flow Analysis for Optimising the Inlet Diffuser Design in Automotive Catalytic Converter: In this paper, S SRI Vaishnav studied the flow pattern and porous concentration in three-way catalytic converter with two catalysts separately by metallic plate of platinum and palladium to optimise the flow path of the exhaust which will affect in increasing the potency of the catalyst [3]. Catalytic Converter Design and Analysis Using Computational Fluid Dynamics (CFD): In this paper, K. Sathish Kumar has done the comparison of back pressure using CFD simulation on the various models of catalytic convertor. The study gives an alternative material like platinum, palladium, and rhodium, which are used as filler materials on surface of the ceramic honeycomb structure [4].

This section presented the results of numerical studies on catalytic converters completed by the researchers listed below. Modelling the Effect of Flow Maldistribution on the Performance of a Catalytic Converter: In this paper, Gaurav Agrawal conducted numerical study of the interaction between flow, reactions, and thermal effects in a planar two-dimensional model of a catalytic convertor. Also observed the effect of single and double channel monolith on the catalytic convertor [5]. Effect of Back Pressure Using Catalytic Convertor on the Lambarghini 340 Engine. In this paper, R.E. Hayes has done the CFD analysis on a full-size catalytic converter. The major focus of the study is on the optimisation of geometry by manipulating factors like monolith cell density, the diffuser angle, and the aspect ratio for better flow uniformity and a reduction in back pressure [6].

Hyes et al. [7] have done the CFD analysis to study the pressure drop and uniformity index of an existing exhaust system with a close-coupled catalytic converter. From his findings for better flow uniformity, he has suggested some improvement by analysing the individual flow contribution to the total pressure drop and flow uniformity [7]. Marcos et al. [8] work on simulation studies of nitrogen oxide catalytic reduction. Paper shows the CFD analysis on the monolith three-way catalyst and the validation of CFD results with experimental analysis. From the literature, author has studied the effect of temperature on emission of NOx, CO, and C_3H_6 [8]. The CFD analysis by different shapes done by S. Ramasubramanium [9] as well as numerical study for maldistribution on the performance of catalytic converter is investigated [10]. P. Thangapadian did the design and analysis of monolith for catalytic convertor and studied its effect on flow distribution and heat transfer [11].

It is evident from the literature that, the study on different diffusion angles of catalytic convertor and its effects on back pressure and velocity which affects the performance of catalytic convertor, is not yet completed. In current performance of catalytic convertor, it is noticed that back pressure increases, which mainly affects the overall efficiency of catalytic convertor and fuel economy of vehicle. The main goal of this study is towards increasing overall efficiency and check its effect on performance of catalytic convertor. The technical objectives and parameters for doing this study is to decrease back pressure and increase velocity. This study focuses on the investigation of back pressure and velocity by changing the diffusion angles.

3 Materials and Methods

3.1 Materials

The catalytic convertor material is selected as aluminium because aluminium has the properties to transfer heat into the environment. The cost of aluminium is minimum than other metals with same property. It has a lower weight, which will reduce the cost of transportation. Through the catalytic convertor, the fluid is passed. The carbon

monoxide fluid was selected because the exhaust gases contain maximum amount of carbon monoxide. Carbon monoxide enters from the inlet and exits from the outlet.

3.2   Geometry

The geometry created for catalytic convertor with different diffusion angles 34, 27, and 20 is named as model 1, model 2, and model 3, respectively. Model 2 is considered as the base model and geometry is modified by increasing and decreasing diffusion angle by 7-degree variation. Model 2 is considered for simulation and CFD analysis is performed. The geometry of the catalytic convertor has same dimensions with diffusion angle variation. Due to the change in the diffusion angle, length of the inlet section also is changed slightly.

The CFD simulation was performed for three different geometries with different angles and the results are summarised. Figure 1 presents the simulation geometry for model 1. The geometry is divided into three parts, the first part is the inlet, consisting of the inlet to the inlet porous area; the second part is the substrate, which is situated inside the porous area; and the last part is the outlet, which is from porous outlet to outlet section of the catalytic convertor.

Diffusion angles for different models are mentioned in Table 1. There are three models created with different diffusion angles. The angle formed by the converged section and the base line parallel to the central axis is known as the diffusion angle.

3.3   Mesh Selection

Meshing is the method of converting the big geometry into number of parts, which is known as an element. For catalytic converters, a simple mesh is generated and then used as mesh refinement tool. For simple meshing, the quality of the meshing is not suitable for analysis, so the mesh refinement option is used to enhance the quality of the meshing. In the mesh refinement, the size of the element is selected as fine. To enhance the element quality, the boundary portion is selected and it is divided into number of divisions. All the circular edges are divided into the 300 number of divisions, so that the mesh refinement can take place and the quality of the mesh element is enhanced. The quality of the meshing depends on various parameters like element quality, aspect ratio, Jacobean, etc. The Statics tool is used to check the quality of refined meshing and quality check parameters are presented in Table 2. For all the models, the same procedure is followed for the meshing. From the statics, it is studied that the aspect ratio has a range between 11.85 and 1.04, but the number of elements is at its minimum range. This shows that the mesh is accurate and able to solve the iterations.
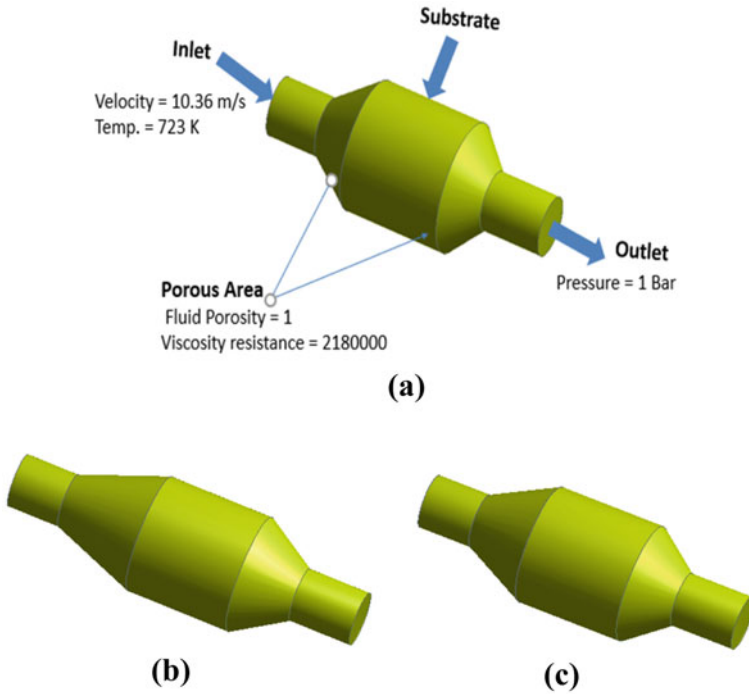
Fig. 1 Different geometry to study CFD analysis **a** Model 1 **b** Model 2 (base model) **c** Model 3

Table 1 Model name with diffusion angle

Model name	Diffusion angle (°)
Model 1	34
Model 2 (base model)	27
Model 3	20

Table 2 Quality check parameters for meshing

Sr. No	Mesh quality	Maximum value	Minimum value
1	Aspect ratio	11.857	1.0428
2	Element quality	0.99757	0.16756
3	Jacobian ratio	4.3257	1

3.4 Grid Independence Analysis

Figure 2 shows the grid independence test for the catalytic convertor. It is observed that for the fine grid, the computation time is greater than the coarse grid. The convergence criteria for the meshing element is shown in terms of pressure drop. Tests show that the by increasing number of divisions then the number of elements is

(a)

(b)
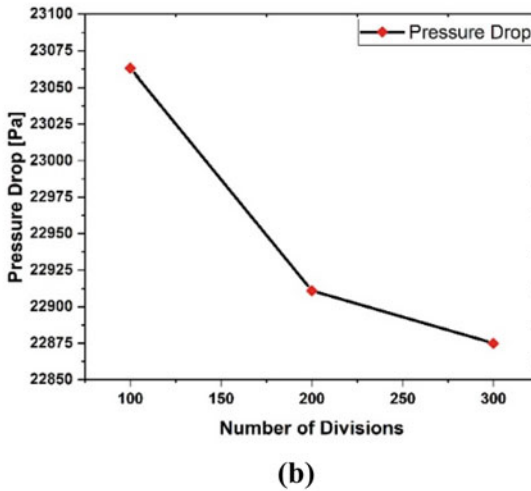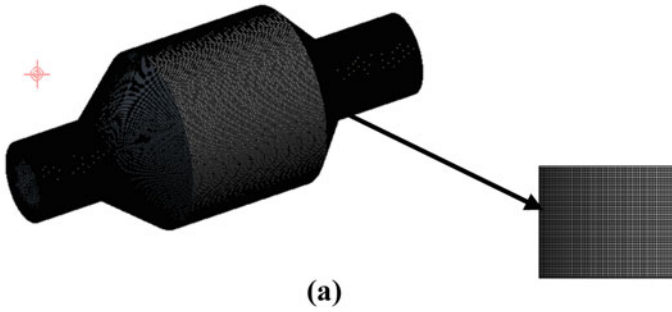
Fig. 2 **a** Meshing performed on catalytic convertor. **b** Variation of pressure with number of divisions

increasing, it results in reducing pressure drop at the greater number of the element. It means that the pressure drop is decreased by very less per cent. While increasing the number of divisions by 100, it reduces the pressure drop by 7.04% and time required for the computation is increasing by 30 min. From the test, it is observed that the results are changed with respect to change in the grid size.

It means that coarse mesh is best suited for the analysis, because it will be reducing the cost and time of the computation. The coarse mesh is selected for the simulation.

3.5 Boundary Conditions

The investigation of the numerical results is based on the model selection, given boundary conditions and number of iterations. The catalytic convertor is simulated

Table 3 Boundary conditions

Sr. No	Boundary condition	Magnitude
1	Velocity inlet	10.38 [m/s]
2	Pressure outlet	1 [bar]
3	Turbulence intensity	5%
4	Temperature at inlet	723
5	Fluid porosity	1
6	Viscosity resistance	2,180,000 [1/m]

by giving different boundary conditions. Table 3 presents the boundary conditions used to simulate the catalytic converter. At the inlet of the catalytic convertor, inlet is defined as a velocity inlet and the outlet is defined as a pressure outlet. For the velocity inlet, velocity is given as 10.34 and the turbulence intensity of gases is given as shown in Fig. 1 and table, 5% throughout the flow. For the outlet, the pressure is defined as atmospheric pressure.

The porous zone is defined separately by using cell zone conditions. The porous zone needs some parameters to define porosity in the fluent. The cell zone condition defined the porosity of the fluid as 1 and the viscosity resistance at porous area of 218000 1/m. At the porous area, the flow is selected as laminar and the porous material as solid.

3.6 Governing Equations

The steady state with pressure focused methodologies were used to carry out the numerical simulation. The values of mass and momentum under steady state conditions are determined using the partial differential equation. Basic methods are used to determine pressure and velocity, and second order discretion equations are employed. On the basis of all the governing equations, numerous experiments have been carried out using simulation. Since the k-epsilon model predicts well far from the boundaries (wall) and the k-omega model predicts well close to the wall, it was chosen for this analysis. Equations (1) and (2) are used to find the conditions for fluid flow in the catalytic convertor tube using continuity and Navier Stokes Eq. (3).

$$\frac{\partial \rho}{\partial t} + \frac{\partial \rho U_1}{\partial x_1} + \frac{\partial \rho U_2}{\partial x_2} + \frac{\partial \rho U_3}{\partial x_3} = 0 \tag{1}$$

Newton's second law is followed by the momentum balance. The body and surface pressures are under the influence of two forces. The momentum equation is given by CFD software

$$\rho \left(u \frac{\partial U}{\partial x} + v \frac{\partial v}{\partial x} \right) = -\rho g - \frac{\partial \rho}{\partial x} + u \frac{\partial^2 y}{\partial x^2}, \tag{2}$$

where ρ is the density kg/m^3, t is the time in s, U and V are velocity components, Cp is the specific heat in J/kgK, and u, v are velocities along x and y directions, respectively.

4 Results and Discussion

4.1 Validation of CFD Analysis

Om Guhan et al. [6] studied the pressure drop and flow uniformity of the LCV exhaust system. The total pressure drop for the exhaust system was 182 MPa. For catalytic converters, the pressure drop was analysed at 72 Mpa. The present study shows total pressure drop of around 27.188 Mpa, which is less than the Guhan et al. [6] study. From this study, it was concluded that a lesser pressure drop was achieved, which was efficient for the catalytic convertor. Guhan et al. [6] have obtained pressure at a porous inlet of 19.52 Mpa. The present study shows 14.13 Mpa and for the porous outlet, the pressure drop was 16.51 Mpa and this study presents 12.81 Mpa. It shows that the pressure drops which is analysed in the present study is less than the Guhan study and it is due to computational features.

Python code performs velocity validation. Python code has been generated to calculate velocity at various points. The continuity equation is used in the code to calculate the velocity at the catalytic convertor's outlet as well as at the porous area. The velocity validation is discussed in detail in the Fig. 3.
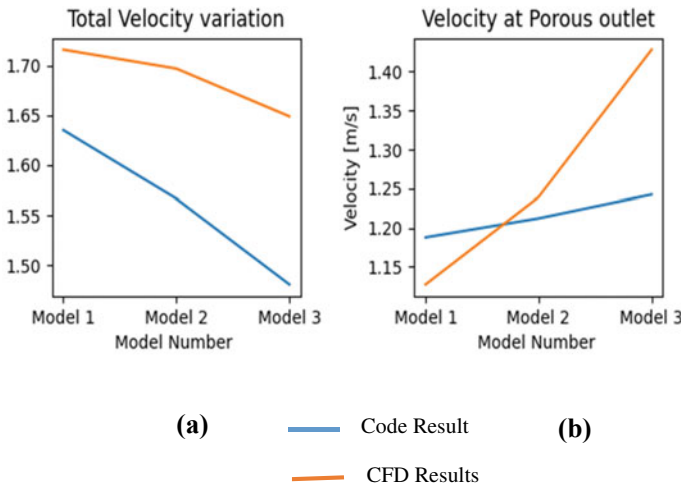

Fig. 3 a Validation of code result and CFD Results for total velocity. **b** Validation of code velocity and CFD velocity at porous outlet

The code results are shown in Fig. 3a above. The velocity for model 1 using code is 1.635 and 1.716 m/s using CFD analysis, which is also obtained for models 2 and 3. It has been discovered that by decreasing the diffusion angle, the length of the catalytic convertor may increase, causing the velocity to decrease. Some assumptions have been made in the code. Consider the fact that some constants are used in numerical analysis to solve governing equations. In numerical results, the velocity variation is greater. However, in the analytical coding, the value of constant added as a one is not considered for matching the trends. The velocity of a porous outlet is increased by a decrease in diffusion angle which results increase in velocity at porous outlet area.

4.2 Effect on Total Pressure

The back pressure is an important phenomenon because it affects thermal efficiency of the engine. When the back pressure increases, the thermal efficiency of the engine decreases. The back pressure depends on pressure drop in an exhaust system at the outside of engine. Figure 4 shows the variation of pressure in the catalytic convertor by increasing the diffusion angle. The pressure at the inlet of catalytic convertor is higher and at the outlet it is decreasing. It means that when the gases come from engine, they have high pressure and the pressure is reduced in the catalytic convertor. From the total pressure counter, it is calculated that when the diffusion angle is decreased by 7°, the total pressure is increased. It means that the pressure drops increased, but in the case of the increase in the angle by 7°, the total pressure is less and it will reduce the pressure drop inside the catalytic convertor.

Pressure drop is critical in determining engine power consumption. When pressure drops more at outlet of the exhaust system, it means that the fuel consumption by the engine is more due to the work required to exhaust the gases. Figure 4 shows the pressure drop for the different models with different diffusion angles. It is studied that the increase in diffusion angle got minimum pressure drop and decreasing angle results in maximum pressure drop. When the pressure drop is maximum, it should have a minimum work input to extract the gases.

4.3 Effect of Pressure at Porous Inlet and Outlet

In the case of the catalytic convertor, the maximum pressure drops happened due to the barriers of the porous materials used to convert the harmful gases into harmless gases. Figure 4 presents the pressure distribution over the porous inlet and outlet. At the porous inlet, the pressure is higher at the near wall of the catalytic convertor because of the divergent section. When the gases come from the engine, they directly bombard the porous material. At that time, the pressure acting on the wall of the catalytic convertor is greater than the centre pressure. But it is observed that at the outlet of the porous medium, the pressure is distributed over the porous surface. At
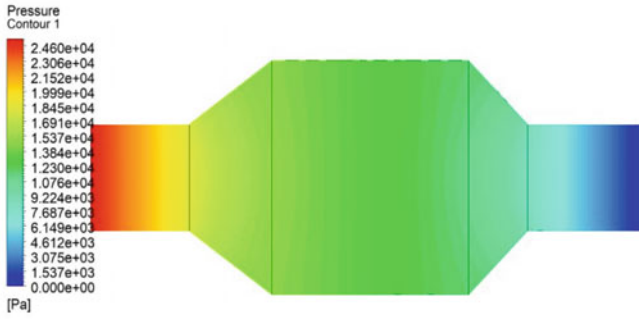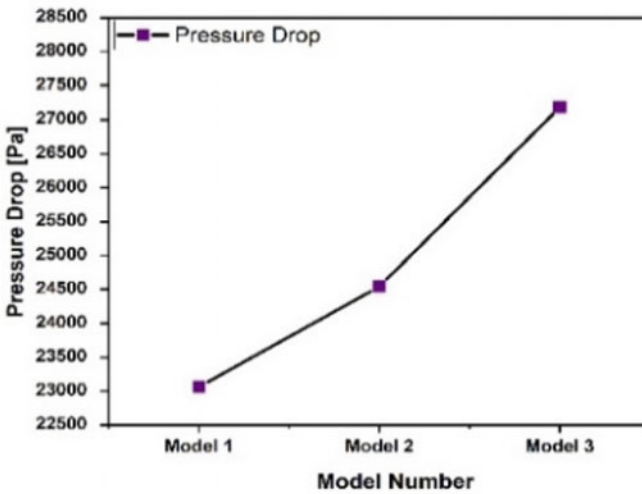
Fig. 4 a Contour for pressure distribution in the catalytic convertor. **b** Change in pressure drop at different models

a higher diffusion angle, the pressure at the porous inlet and outlet is high when compared with the base geometry and lower diffusion angle. It shows when gases come from the inlet of a catalytic converter, their velocity increases at the divergent section and their pressure decreases for the decrease in diffusion angle.

Figure 5 presents the pressure drop at the porous inlet and porous outlet. The pressure drop at the porous inlet and porous outlet is greater for the model no. 1, and the pressure drop is decreased with an increase in the diffusion angle at the porous inlet and outlet.
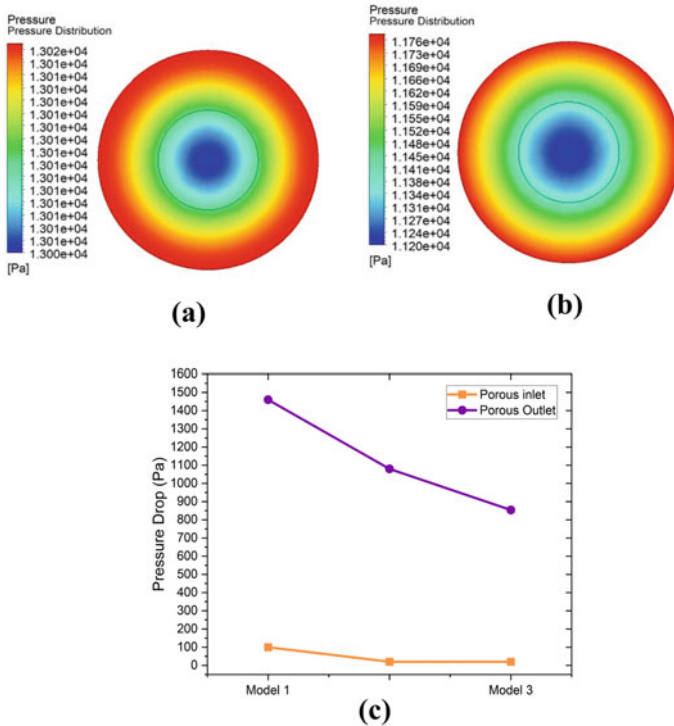
Fig. 5 a Contour for pressure distribution at porous inlet. **b** Contour for pressure distribution at porous outlet. **c** Pressure drop at porous inlet and outlet for different models

4.4 Variation of Velocity

Velocity variation is an important parameter in defining the performance of the catalytic convertor. When the velocity is high, the rate of passing gases through the catalytic convertor is greater. It means that there is a reduction in pressure drops inside the catalytic convertor. Model 2 shows the basic geometry with a 27-degree diffusion angle. Results for the velocity variation are compared with model 1, which has an increased diffusion angle by 7°, and model 3, which is designed with a decrease in diffusion angle by 7°. Figure 6 presents the change in velocity at the substrate section. For a decrease in diffusion angle, the velocity at the substrate is increased by 3.94% from the base model increased in diffusion angle, the velocity at the substrate is decreased by 4.6%. An increase in the diffusion angle has an effect on the velocity variation inside the substrate. When velocity inside the substrate is decreased, then the chemical reaction rate also decreases and the efficiency of the catalytic convertor decreases.

Total velocity variation is shown in the Fig. 6b. It shows that when the diffusion angle decreased, then velocity also decreased due to increase in the surface area.

Fig. 6 **a** Variation of
velocity at substrate area for
different models. **b** Total
velocity variation in the
catalytic convertor
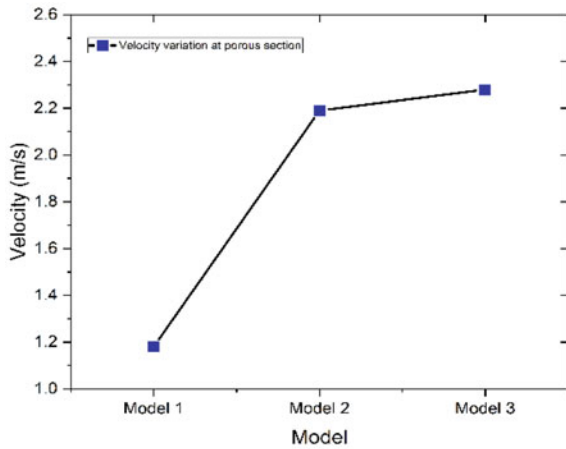
(a)
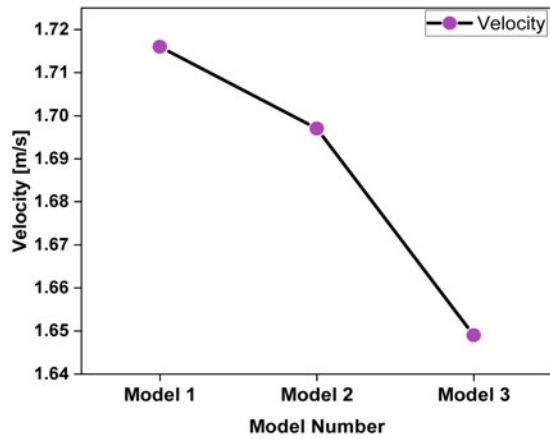
(b)

Also, increased in diffusion angle the velocity is increased and it is more efficient
for the catalytic convertor.

4.5 Variation of Velocity at Porous Inlet and Porous Outlet

Velocity variation at the porous inlet and outlet defines the rate at which the reaction
takes place at the substrate area. When the velocity is high at the porous inlet, it
means that the gases will be passed at a very high rate through the porous material.
It decreases the chances of proper chemical reaction taking place. Figure 7 presents

the velocity variation at the porous inlet and porous outlet. The velocity at the upper portion and lower portion is studied. The velocity at the lower section is studied more and it shows the direction of velocity from the inlet to the outlet. The uppermost portion of the section velocity is shown in negative. It means it shows the direction of the gases after striking on the porous section is less and the direction of the gases in reverse direction.

The velocity variation and the performance of the catalytic convertor are analysed. It is observed, velocity at the porous inlet and porous outlet for model 1 is higher than the base geometry and model 3. The greater the diffusion angle, the greater the gas strike rate on the porous material, but when the diffusion angle decreases gradually, the velocity also decreases. When the diffusion angle increases, then friction from the inlet to the porous inlet increases, so the velocity decreases. But as the diffusion angle increases, the harmful gases directly hit the porous inlet and having less friction, the velocity at the porous inlet is higher. At porous outlet, velocity increased slightly compared with the base model and model 1. After study, the velocity at the porous

Fig. 7 **a** Contour for velocity distribution at porous inlet. **b** Contour for velocity distribution at porous outlet. **c** Velocity variation at porous inlet and outlet for different models

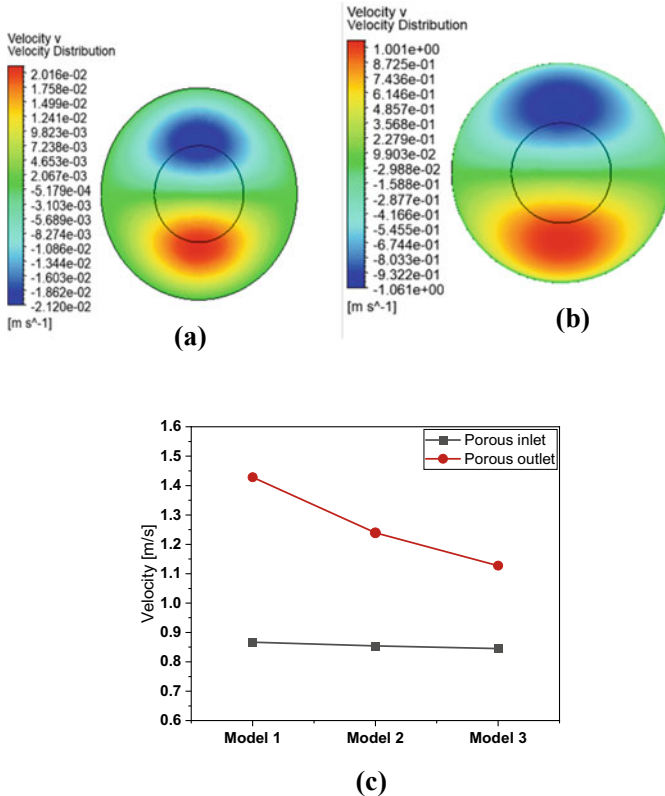inlet for model 1 was increased by 25.04% compared with the base model. The velocity at the porous outlet has decreased by 26.97%. In model no. 3, the velocity at the porous inlet decreased by 19.44%, and it decreased by 5.76 % at the outlet of the porous section.

5   Conclusion

The present study investigated the pressure drop and velocity change at the various locations of the catalytic convertor. The results are summarised below:

It is studied that for an increase in the diffusion angle by 7°, the pressure drop is increased by 6.03% in the base model. But when diffusion angle is decreased by 7°, then pressure drop is increased, then pressure drop is reduced by 9.72% in the base model. The pressure drops in the model 1 at the porous inlet is higher than the base model. But for model 3, the pressure drop at the porous inlet is decreased compared with the base model.

Velocity has changed with respect to various locations. At the porous inlet, the velocity is greater for model 1 than the base model and lower for model 3 than the base model. When the angle increased by 7°, the velocity increased by 25.04%, and when the angle decreased by 7°, the velocity decreased by 19.44%.

For the variation in the diffusion angle, the pressure and velocity also changed, but the change in the pressure drop for the increase in the angle is less and the velocity change is also less. It shows that an increase in the diffusion angle is suitable for the catalytic convertor up to standard particular limit.

References

1. Dahake LA (2017) CFD and experimental analysis of catalytic converter to optimize the effect of 932–939. https://doi.org/10.15680/IJIRSET.2017.0601057
2. Kumar P, Taneja N, Gaurav A, Singh V, Nath A (2015) Department of mechanical engineering, amity school of engineering & technology new Corresponding Author : pankajsinghps@gmail.com," no. September, 2015
3. Vaishnav SS, Vignesh V (2014) A Computational flow analysis for 3(6):1451–1463
4. Sathish Kumar K (2014) Design and analysis of catalytic converter using computational fluid dynamics (CFD) 3(11):768–780
5. Om Ariara Guhan CP, Arthanareeswaren G, Varadarajan KN (2015) CFD study on pressure drop and uniformity index of three cylinder LCV exhaust system. Procedia Eng 127:1211–1218. https://doi.org/10.1016/j.proeng.2015.11.466
6. Vaghela J (2018) CFD analysis of catalytic converter for mitigation of emission 4(10):181–184. https://doi.org/10.13140/RG.2.2.23868.13447
7. Hayes RE, Fadic A, Mmbaga J, Najafi A (2012) CFD modelling of the automotive catalytic converter. Catal Today 188(1):94–105. https://doi.org/10.1016/j.cattod.2012.03.015
8. Maros H, Juniar S (2016) "済無No title no title no title 1–23

9. Ramasubramanian S, Ganesh M, Karikalan L (2019) Design and analysis of catalytic converter model with shape change for overall improvement in fluid flow. Int J Sci Technol Res 8(11):3280–3284
10. Agrawal G, Kaisare NS, Pushpavanam S, Ramanathan K (2012) Modeling the effect of flow mal-distribution on the performance of a catalytic converter. Chem Eng Sci 71:310–320. https://doi.org/10.1016/j.ces.2011.12.041
11. Thangapandian P (2022) Design and analysis of exhaust manifold for multicylinder diesel engine with monolith catalytic converter using CFD. Int J Appl Sci Eng 19(1). https://doi.org/10.6703/IJASE.202203_19(1).003

Numerical Analysis of Solid–Liquid Disengagement in a Continuous Precipitator Relevant to Plutonium Reconversion

Saroj K. Panda, P. Vishnu Anand, Vivek K. Mishra, R. Rajeev, K. A. Venkatesan, and K. Ananthasivan

1 Introduction

In nuclear reactor operations, the fission of ^{235}U generates energy, neutrons and fission products which are radioactive in nature. During fission reaction, the fertile ^{238}U absorbs neutrons and produces ^{239}Pu which is a fissionable product. The spent fuel discharged from the nuclear reactor contains significant amounts of uranium and newly formed plutonium which can be reused as a fresh fuel to the reactor. The PUREX-based reprocessing which is an aqueous liquid–liquid extraction technology, used to recover Pu and U from the spent nuclear fuel. The radioactive nature of the materials involved in the process sets it apart from traditional chemical processes. After recovery of Pu and U nitrate solutions using solvent extraction, the nitrate solution goes through the reconversion processes that include precipitation, filtration and calcination processes to form plutonium oxide (PuO_2) for the deployment of plutonium-based fuels in nuclear reactors. However, presently used batch equipment, especially thickener/precipitator needs a thorough design optimization to convert it into glove-box adaptable continuous equipment to accommodate high throughput in the future big reprocessing plants. The change in design of the process equipment from batch to continuous operational would minimize the frequent human exposure to the radioactive material during loading/unloading operations.

S. K. Panda · P. V. Anand · R. Rajeev · K. A. Venkatesan (✉) · K. Ananthasivan
Process, Radiochemistry and Reprocessing R&D Division, Reprocessing Group, Indira Gandhi
Centre for Atomic Research, Kalpakkam, Tamil Nadu 603102, India
e-mail: kavenkat@igcar.gov.in

V. K. Mishra
Homi Bhabha National Institute, Anushaktinagar, Mumbai 400094, India

2 Literature Review and Objectives

The design and development of the continuous solid–liquid separation process for plutonium reconversion is a complex practice and requires rigorous experiments to understand the in detail hydrodynamics and robust computational models to predict the precipitation and separation (solid particles from liquid phase) characteristics.

Different methods are adopted over the years for the conversion of plutonium nitrate solution to plutonium oxide [1] for fresh fuel fabrication. Continuous process offers uniform product characteristics and processes higher throughput in comparison with the batch processes [1]. Lanthanides are considered as surrogate to plutonium for major development work in non-radioactive conditions [2]. In this regard, cerium is considered as a common surrogate to plutonium, often used for equipment testing and development [3, 4]. The experimental investigation of precipitation kinetics and dissolution characteristics of cerium (III) oxalate was carried out by Chang, 1987 [3] using continuous precipitation, whereas, Zhaogang, 2008 [5] investigated the effect of precipitation conditions (i.e. agitation speed, temperature and feeding mode of the phases. Further, Mei, 2009 [6] investigated the effect of different operating parameters such as concentration of reactant, impeller speed and temperature on particle size distribution (PSD) and morphology of cerium oxalate.

Alike the aforementioned experimental investigations, there is a paucity of research on the development of computational model and related research on the subject. In our preliminary investigations, we have performed experiments as well as CFD simulations to study the sedimentation of cerium oxalate particles [7, 8]. The aforementioned literature studies reveal that, no research has addressed in detail measurements and CFD analysis of the design optimization of glove-box adaptable continuous Pu reconversion equipment. Therefore, the present work is focused on the development of the computational model and performing simulation in a continuous precipitator using cerium oxalate as solid phase (dispersed) and mixture of oxalic + nitric acid as liquid phase (continuous). The parameters such as concentrations of cerium, oxalic acid, and nitric acid and impeller speed, etc., on the performance of precipitator/thickener for optimal operational condition to handle radioactive material are utmost important. The objective of the present work is the preliminary investigation of the solid–liquid disengagement process in a continuous precipitator to understand the detailed hydrodynamics and to use the predicted results from CFD as a guideline for further development of the equipment.

As mentioned earlier, Eulerian-Eulerian CFD simulations were performed to understand the solid–liquid hydrodynamic inside the precipitator. Initial predictions were compared with the experimental data which were obtained using mixture of nitric acid (HNO_3) + oxalic acid $(C_2H_2O_4)$ and cerium oxalate $[(Ce_2(C_2O_4)_3.10H_2O]$ to ascertain the predictive capability of the computational model.

3   Problem Statement

The solution domain consists of a continuous precipitator of height (h) 0.9 m, and diameter (d) 0.08 m was considered for solid–liquid simulations. The schematic of such a laboratory-scale precipitator and computational mesh is shown in Fig. 1. The column has two feed inlet pipes, one for cerium nitrate and other for oxalic acid. However, no reactions were considered while performing the simulations. Therefore, to mimic the solid–liquid slurry inside the precipitator, instead of feeding two liquids through inlets, both solid and liquid with proper stoichiometric proportions were fed to the precipitator. The mass flow rate of solid and liquid in both the inlets are different as per the plant condition. Initial dimension of the column has an overflow outlet situated at 0.85 m height from the bottom to collect particle overflow during operation. The column has a motor and shaft-pitch blade arrangement for mixing of the phases to form the precipitate.

Fig. 1 Schematic representation of **a** Laboratory-scale precipitator and **b** Meshing at different regions
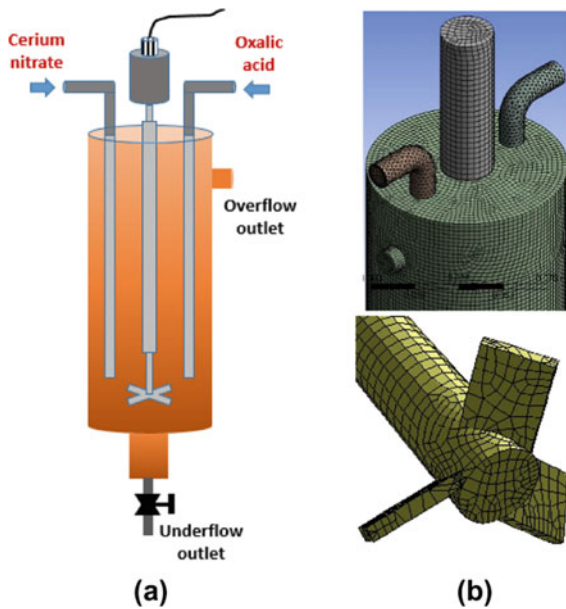
Table 1 Phase properties used for the simulation

Details of the fluid	Density (kg/m^3)	Viscosity (kg/m-s)
Cerium oxalate (solid)	2500	–
Mixture of oxalic acid and nitric acid (liquid)	1058	0.0009

4 Materials and Methods

4.1 Materials Used

The phase properties used for the simulations are mentioned in Table 1. Alike experiments where the two liquid phases getting mixed inside the precipitator and continuously formed cerium oxalate [(Ce$_2$(C$_2$O$_4$)$_3$.10H$_2$O] (as per Eq. 1), no liquid–liquid reaction was considered in the simulation. However, knowing the total weight of the solid recovered from each set of experiments at different cerium concentrations and liquid flow rate at both the inlets, the solid and liquid feed at both the inlets was calculated and used as the input parameters in simulations. Therefore, the mixture of oxalic acid and nitric acid was considered as continuous phase (liquid) and cerium oxalate as dispersed phase (solid).

$$2Ce(NO_3)_3 + 3H_2C_2O_4 + H_2O \leftrightarrow Ce_2(C_2O_4)_3 \cdot 10H_2O \qquad (1)$$
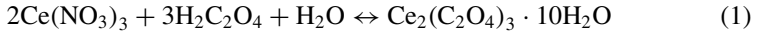
4.2 Computational Model and Boundary Conditions

The solid–liquid disengagement process was carried out using cerium oxalate as the solid phase and the mixture of oxalic + nitric acid as liquid phase in the column. Eulerian-Eulerian approach which is based on the interpenetrating continuum approach has been used to perform all the simulations. The two-fluid model was used by taking the constant average solid particle with drag as the interphase momentum exchange model.

The mass conservation equations are

$$\frac{\partial}{\partial t}(\alpha_l \rho_l) + \nabla \cdot \left(\alpha_l \rho_l \, \vec{U_l} \right) = 0 \qquad (2)$$

$$\frac{\partial}{\partial t}(\alpha_s \rho_s) + \nabla \cdot \left(\alpha_s \rho_s \, \vec{U_s} \right) = 0 \qquad (3)$$

The momentum conservation equations are

$$\frac{\partial}{\partial t}\left(\alpha_l \rho_l \vec{U}_l\right) + \nabla \cdot \left(\alpha_l \rho_l \vec{U}_l \vec{U}_l\right) = -\alpha_l \nabla P - \nabla \cdot \alpha_l \overline{\overline{\tau}}_l + \alpha_l \rho_l \vec{g} + \vec{M}_{l-s} \quad (4)$$

$$\frac{\partial}{\partial t}\left(\alpha_s \rho_s \vec{U}_s\right) + \nabla \cdot \left(\alpha_s \rho_s \vec{U}_s \vec{U}_s\right) = -\alpha_s \nabla P - \nabla \cdot \alpha_s \overline{\overline{\tau}}_d + \alpha_s \rho_s \vec{g} - \vec{M}_{s-l} \quad (5)$$

where the stress tensors were calculated as $\overline{\overline{\tau}} = -\mu\left(\nabla \vec{U} + \nabla \vec{U}^T\right)$ and $\vec{M}_{l-s}$ represents interphase momentum exchange terms between the phases and defined as

$$\vec{M}_{l-s} = K_{l-s}\alpha_l \alpha_s \left(\vec{U}_s - \vec{U}_l\right) \quad (6)$$

where

$$K_{l-s} = \frac{3}{4}C_D \frac{\rho_l \left|\vec{U}_s - \vec{U}_l\right|}{d_s}\alpha_l^{-2.65} \quad (\text{if } \alpha_l \geq 0.8) \quad (7)$$

$$K_{l-s} = 150\frac{\alpha_s(1-\alpha_l)\mu_c}{\alpha_l d_s^2} + 1.75\frac{\rho_l \alpha_s \left|\vec{U}_s - \vec{U}_l\right|}{d_s} \quad (\text{if } \alpha_l < 0.8) \quad (8)$$

Drag force was considered as the interphase momentum exchange $(\vec{M})$ between the phases. The Gidaspow drag model [9], which is one of the most widely used drag models for handling the solid particles in a multiphase flow system [10–12], was used in this work and defined as

$$C_{D_{l-s}} = \frac{24}{\alpha_l \text{Re}_s}\left[1.0 + 0.15(\alpha_l \text{Re}_s)^{0.687}\right] \quad (9)$$

where $\text{Re}_d = \left(\alpha_c \rho_c \left|\vec{U}_c - \vec{U}_d\right| d_d\right)/\mu_c$ is termed as the particle Reynolds number.

Different boundary conditions were implemented to perform the solid–liquid simulations. The pressure outlet boundary condition was specified at the top surface of the equipment, whereas mass flow outlet was considered at overflow outlet. Mass flow inlet was considered at both the inlets. The impeller blade was given the rotation condition to perform the mixing. The inner and bottom wall were specified as no-slip boundaries. The SIMPLE scheme was used for the pressure–velocity coupling, whereas discretization of the spatial derivatives in mass and momentum conservation equations was achieved using QUICK scheme. The temporal derivatives were discretized using the second-order implicit scheme to obtain better predictions.

5   Results and Discussion

The results are presented in terms of solid phase overflow (mass and volume fraction) from the precipitator, overall solid fraction along the height, pressure and radial velocity distributions inside the continuous precipitator. The aforementioned parameters were studied by varying the impeller speed (500 and 700 rpm), solid phase concentration in liquid phase (5, 15 and 20 g/l) and height of the overflow outlets (0.65, 0.75 and 0.85 m). To ascertain the correctness of the results, a thorough grid independent study was carried out before performing actual simulations.

5.1   Solid Phase Volume Fraction Distributions

The concentration of solid phase entering the precipitator through the inlets was varied and its effect was analyzed in terms of solid volume fraction distributions, mass and volume fraction at the overflow outlet. The solid phase volume fraction distribution at the mid-plane of the precipitator with solid concentration of 5 g/l and impeller speed of 500 rpm is presented in Fig. 2.

The solid particles enter the precipitator through the inlet tubes (at 100 s). Due to difference in mass flow rate between the two tubes, the variation in solid volume fraction was observed. It takes nearly 140 s for the solid–liquid mixture to enter the precipitator through both the pipes. The high solid volume fraction at certain locations in the pipe was due to low mass flow rate of solid particles and their accumulation

Fig. 2 Time evolution of solid phase volume fraction distributions along the height of the precipitator using solid concentration of 5 g/l at inlet and impeller speed of 500 rpm (overflow height = 0.85 m)

100 s   500 s   1000 s   1750 s   2000 s   4000 s   8000s   10000s
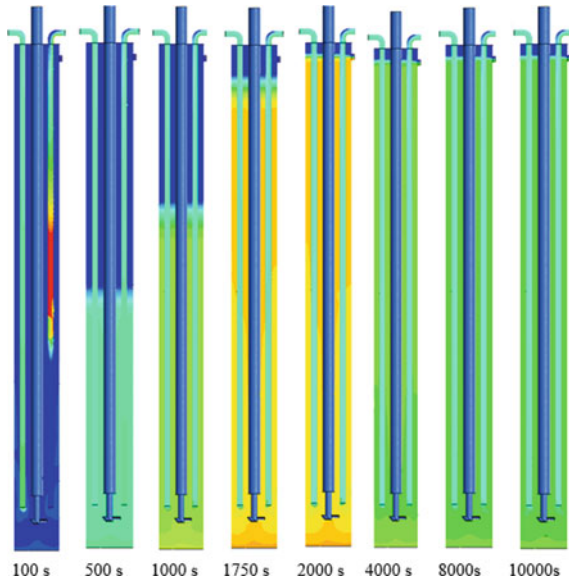
at the bends. As the accumulated mass flows down, high concentration of solid flow through the tube is seen. The solid particles entering the precipitator was gradually accumulated and concentration of solid particles was increased in the precipitator (from 100 to 2000s). With completely filling of the precipitator, the solid–liquid mixture flows out through the outlets. The concentration of solid particles in the precipitator starts to decrease with outflow of solid–liquid mixture and then becomes constant.

5.2 Effect of Impeller Speed

The impeller in the precipitator provides proper mixing of solid–liquid phases. The solid phase velocity vector and isotherm is presented in Fig. 3a and b, respectively. The effect of speed of impeller is investigated by rotating it at 500 and 700 rpm. The whirl which is generated below the impeller blade till the bottom centre of the precipitator and the effect of rotation is shown in terms of iso-surface. Vorticity is the curl of the fluid velocity and considered as the circulation per unit area at a point in a flow field. It is important to describe the detailed hydrodynamic inside a process equipment to understand the complex fluid flow phenomenon. Since the present study is based on Eulerian-Eulerian (EE) approach, individual particle phenomena cannot be presented. However, existence of solid particles was presented in terms of velocity vector and vorticity inside the settler. The effect of velocity is intense near the impeller blades and the outlet of the feed tubes.
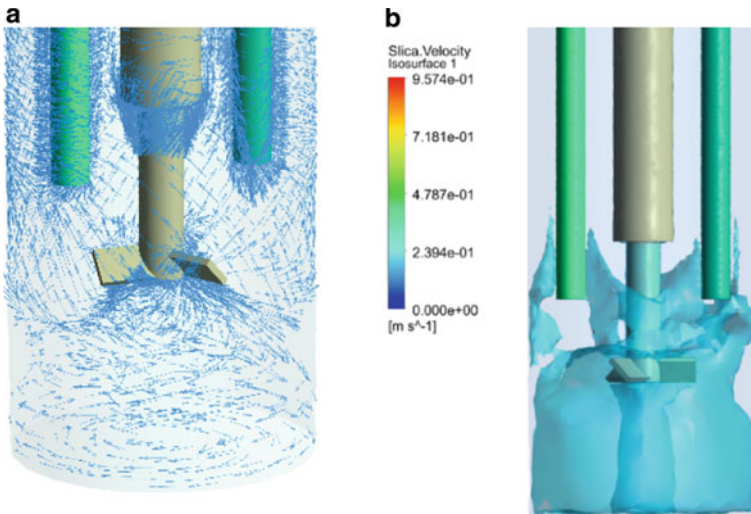
Fig. 3 a Velocity vectors and **b** Iso-surface around the impeller blades at rotating speed of 500 rpm

5.3 Mass Flow Rate and Volume Fraction Through Overflow Outlet

The time taken by the solid–liquid mixture to flow out from the precipitator is dependent on combined effect of concentration of solid particle and rotational speed of the impeller. The variation in mass flow rate and volume fraction of solid phase through the overflow outlet at 500 rpm impeller speed is presented in Fig. 4a and b, respectively.

It is seen that, as the solid phase concentration increases, the time taken for the solid–liquid mixture to come out of the precipitator also increases. The time taken for solid phase to flow out of precipitator from overflow outlet was nearly 1650 s for 5 g/l which was increased to 1850 and 1950s when concentration of solid particles was increased to 15 and 20 g/l, respectively. The increase in concentration of solid phase in the precipitator increases the solid–solid interactions. Thus, the resistance

Fig. 4 Comparison of solid phase **i** Mass flow rate and **ii** Volume fraction through overflow outlet at 0.85 m for different solid concentrations and at impeller speed of 500 rpm
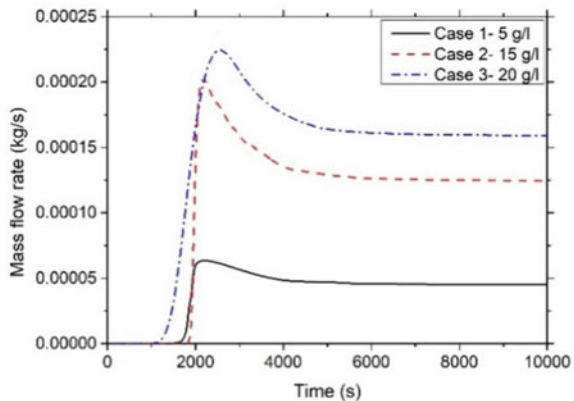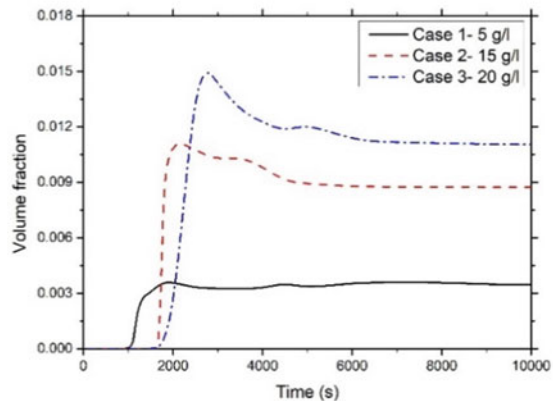
offered to rise in solid–liquid mixture was increased resulting in delay of outflow. The increase in rotational speed of the impeller from 500 to 700 rpm increases the lift in solid phase (particles). Consequently, the time taken for outflow of the solid particles was reduced.

Furthermore, once the overflow of solid phase started, a peak was seen in case of mass flow rate as well as solid volume fraction calculations. This initial peak in both the cases (see Fig. 4a and b) is due to the sudden release of concentrated solid mass from the outlet which was accumulated inside the precipitator. Thereafter, the release of the solid phase from the outlet decreases and attains a steady state pattern from 4000 s onwards. The overall solid concentration was checked inside the precipitator after the overflow started and found to be decreased from bottom to top.

5.4   *Effect of Overflow Outlet Height*

Since, the objective was to design a glove-box adaptable equipment, it is crucial to investigate the overflow height position so that all radioactive solid particles can be recovered in a stipulated time frame. Therefore, the solid volume fraction distributions along the height of the precipitator at a fixed interval (2000s) with overflow outlet height of 0.65 m, 0.75 m and 0.85 m are shown in Fig. 5a, b and c, respectively. As expected, due to increase in height of overflow outlet, the time taken for the solid phase to come out from the precipitator was increased. The solid phase started coming out from the overflow outlet was at 1250 s, 1300 s and 1750s when the outlet was located at a height of 0.65, 0.75 and 0.85 m, respectively. Due to increase in height of the outflow, the concentration of particles in the precipitator thus, increasing and drag offered to outflow of mixture. Therefore, the outflow of solid–liquid phase from the outflow was further delayed. The effect of variation in overflow height was also analyzed in terms of mass flow rate and volume fraction through the outlet.

6   Conclusions

The solid–liquid disengagement in a continuous precipitator with different solid concentration, impeller speed and varying overflow outlet position was investigated numerically. Based on the results obtained, it was found that the solid concentration was the most effective parameter compared with the change in impeller conditions.

The two-fluid Eulerian-Eulerian CFD model with appropriate boundary conditions and drag model is used for the simulations to predict the solid mass flow rate and volume fraction at overflow outlet and solid volume fraction distributions along the height of the precipitator. Variations in solid volume fraction was observed in the precipitator due to difference in mass flow rates between the two tubes. The high
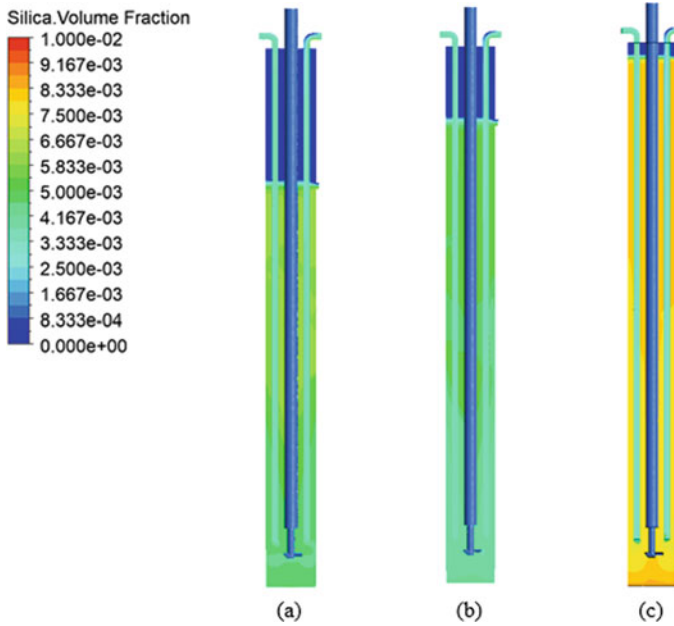
Fig. 5 Solid volume fraction distributions along the height of the precipitator with overflow outlet height of **a** 0.65 m, **b** 0.75 m and **c** 0.85 m at 2000s

solid volume fraction at certain locations in the pipe was due to low mass flow rate of solid particles and their accumulation at the bends.

As expected, the effect of solid phase velocity is maximum near the impeller blades and closer to the tube outlet inside the precipitator. The high rotational velocity near the blades causes the increase in solid phase axial velocity. However, the velocity of solid phase increases radially from the blades of the impeller and gradually decreases towards the wall. The mass flow rate and solid volume fraction were found to be more at lower over flow outlet compared with the outlet at the top of the precipitator.

In addition to the predictions using two-fluid model, a detailed simulation using multi-fluid model integrated with the population balance model is utmost important to have better improved predictions. Similarly, in detail experiments are required to understand the solid–liquid hydrodynamics quantitatively. The study will be beneficial for the development of the continuous Pu reconversion process for the upcoming large future reprocessing plants.

Nomenclature

C_D Drag coefficient –
d_s Particle diameter [μm]

g	Gravitational constant [m/s^2]
l	Liquid (continuous) phase –
$\vec{M}$	Interphase momentum exchange term [kg/m^3.s]
P	Pressure [N/m^2]
Re_d	Particle Reynolds number –
s	Solid (dispersed) phase –
$\vec{U}$	Phase velocity [m/s]
$\bar{\bar{\tau}}$	Stress tensor [Pa]
α	Phase hold-up –
ρ	Phase density [kg/m^3]
μ	Phase viscosity [kg/m.s].

References

1. Beede RL (1956) Continuous plutonium (IV) oxalate precipitation, hiltration, and calcination process. Hanford Atomic Products Operation, Washington, USA
2. Lalleman S, Bertrand M, Plasari E (2012) Physical simulation of precipitation of radioactive element oxalates by using the harmless neodymium oxalate for studying the agglomeration phenomena. J Cryst Growth 342(1):42–49
3. Chang TP (1987) Cerium oxalate precipitation (No. DP-1723). Du Pont de Nemours (EI) and Co., Savannah River Lab, Aiken, SC, USA
4. Rey G (1959) Plutonium oxalate disk filter and filter media studies. General Electric Co. Hanford Atomic Products Operation, Richland, Washington, USA
5. Ji P, Zhang J, Chen F, Anpo M (2008) Ordered mesoporous CeO$_2$ synthesized by nanocasting from cubic Ia3d mesoporous MCM-48 silica: formation, characterization and photocatalytic activity. J Phys Chem 112:17809–17813
6. Li M, Wang M, Liu Z, Hu Y, Wu J (2009) Cerium dioxide with large particle size prepared by continuous precipitation. J Rare Earths 27(6):991–996
7. Panda SK, Anand PV, Rajeev RP, Venkatesan KA, Ananthasivan K (2021) Experimental investigation of sedimentation behaviour using cerium oxalate particles in oxalic-nitric acid medium. Asia-Pac J Chem Eng 17(1):1–21
8. Panda SK, Anand PV, Aashranth BB, Pandey NK (2020) Disengagement of dispersed cerium oxalate from nitric-oxalic acid medium in a batch settler: measurements and CFD simulations. Ann Nucl Energ 144:107574
9. Gidaspow D, Bezburuah R, Ding J (1992) Hydrodynamics of circulating fluidized beds: kinetic theory approach, Report No. CONF-920502-1. In: 7th international conference on fluidization, 3–8 May 1992, Gold Coast, Australia
10. Lundberg J, Halvorsen BM (2008) A review of some existing drag models describing the interaction between phases in a bubbling fluidized bed. In: 49th SIMS conference on simulation and modelling, 7–8 Oct 2008, Oslo, Norway
11. Hassan M, Lu H, Liu G, Wang S, Rafique M (2018) Eulerian-Eulerian Simulations of the hydrodynamics of a binary mixture in an internally circulating fluidized bed. Braz J Chem Eng 35(4):1333–1342
12. Singh BK, Roy S, Buwa VV (2020) Bubbling/Slugging flow behavior in a cylindrical fluidized bed: ECT measurements and two-fluid simulations. Chem Engi J 383:123120

Fluid Flow Analysis in a Partially Filled Horizontal Channel with a Metal Foam Block—A Numerical Study

N. Aditya, N. Gnanasekaran, and Ajay Kumar Yadav

1 Introduction

The application of metal foams results in a better performance in terms of heat transfer but there is an increment in pressure drop [1]. So, channels partially filled with metal foam can be used instead of fully filled to achieve lower pressure drops along with the increment in the heat transfer performance over channels with no metal foam [2]. For channels fully filled with metal foam, convection heat transfer studies have been performed in detail [3, 4]. The numerical and analytical analysis is mentioned for channels fully filled with metal foam in [5, 6]. Several numerical studies have been performed on horizontal channels partially filled with metal foams [7], and further numerical studies are required to identify the effects of foam length, inlet velocity, and pore density on fluid flow behaviour.

2 Literature Review and Objective

Mancin et al. [8] investigated the air heat transfer and fluid flow through aluminium open-cell metal foam with different PPI ranging from 5 to 40 with almost constant porosity, two heights of foam core 20 mm and 40 mm, and heat fluxes 25, 32.5, and 40 kW with different inlet velocities. The effect of height, PPI, and velocity on global heat transfer coefficient and pressure drop was emphasized. Bidar et al. [9] numerically investigated the forced convection of airflow through a vertical channel. Metal foams of different materials were considered in a two-sided vertical channel

N. Aditya (✉) · N. Gnanasekaran
Department of Mechanical Engineering, NITK, Surathkal, Mangalore 575025, India
e-mail: adityabholu2@gmail.com

A. K. Yadav
 Department of Mechanical Engineering, IIT Patna, Patna, India

and results were compared with an empty channel. The pressure drop increased with velocity and decreased with porosity. Overall Nusselt number was higher for the filled channel when compared with the empty channel. Anuar et al. [10] studied fluid flow behaviour in a channel partially filled with metal foam. Effects of various pore densities 5–30 PPI, inlet velocities 3.9–6.2 m/s, and foam heights 0.004–0.05 m on fluid flow behaviour were investigated. Flow patterns outside and inside the metal foam block were visualized using particle image velocimetry and infrared thermography, respectively. For low PPI foam, more fluid flows straight through the metal foam but for higher PPI foam due to higher resistance to flow through the foam, fluid flowing through the metal foam tries to escape from the top surface of the foam. Different fluid flow patterns were reported for different values of foam height, pore density, and inlet velocity. Results show that the pressure drop increased with PPI but for very small foam heights this may not be true. Trilok et al. [11] investigated the numerical analysis of airflow through a vertical channel with metal foam at the centre of the channel. Here porosity, PPI, and length of foam are varied which resulted in different values of pressure drop and heat transfer. Moreover, Technique for Order of Preference by Similarity to Ideal Solution (TOPSIS) method was used to do a trade-off between pressure drop and heat transfer. Jadhav et al. [12] considered six different metal foam configurations for the enhancement of heat transfer in a circular conduit. Aluminium foam with PPI varying from 10 to 45 and almost the same porosity (0.90–0.95) was considered and they are partially filled in the conduit to reduce the pressure drop with constant heat flux. To do a trade-off between pressure drop and heat transfer, TOPSIS method was considered.

The present study used computational fluid dynamics to study the fluid flow behaviour in a channel partially filled with metal foam. This numerical study was conducted to investigate the effects of foam length, PPI, and inlet velocity on the fluid flow behaviour inside and outside the metal foam block.

3   Materials and Methods

A horizontal wind tunnel (WT) is considered with the dimensions of 1200 mm in length, 320 mm in width, and 320 mm in height. WT is partially filled with a metal foam block of varying lengths (l_f), 320 mm width, and 160 mm height attached to the bottom wall of the tunnel. l_f is considered as 0.25 $l_{f,max}$, 0.5 $l_{f,max}$, 0.75 $l_{f,max}$, and 1 $l_{f,max}$, where $l_{f,max}$ is 320 mm which is the maximum value of l_f considered in the present study. This way of defining l_f is extremely useful in the case, where a part of a bottom wall of a tunnel of length $l_{f,max}$ with constant temperature or constant heat flux, with different lengths of metal foams attached to it, is analyzed. Here, a three-dimensional domain is considered for better calculation of the pressure at the flow sections when compared with a two-dimensional domain for a channel flow, and the front view is shown in Fig. 1 for better understanding. The three-dimensional domain is discretized into a finite number of hexahedral cells to obtain a high-quality solution with fewer cells. The orthogonal quality and skewness are maintained close
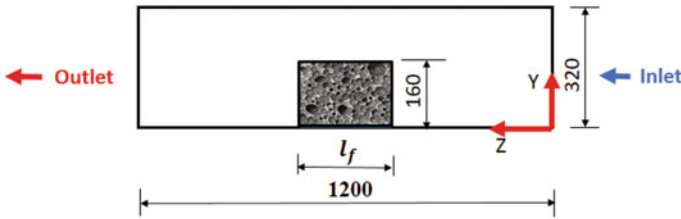
Fig. 1 Front view of computational domain

to 1 and 0 for good-quality mesh. The velocity and pressure of fluid are specified as inlet and outlet boundary conditions, respectively. In the present study, three different velocities 6.5, 9.5, and 12.5 m/s are taken at the inlet, and 1 atmospheric pressure at the outlet. No-slip boundary condition is applied for all the walls. At the clear fluid-metal foam interface, interior type condition is given, i.e. continuity in shear stress at the interface.

3.1 Numerical Simulations

The three-dimensional numerical simulation is carried out using commercially available ANSYS FLUENT software. Air is considered as the working fluid. Viscous-standard *k*-epsilon (two equation), standard wall function model is used for the clear fluid and metal foam region. Fluid flows through both the clear fluid and metal foam regions. The governing equations solved for the clear fluid region are similar to those of empty channel flow. For the metal foam region, the governing equation includes the terms of porosity, permeability, and foam drag to include the effect of metal foam on fluid flow. The governing equations considered for solving the metal foam region are as follows [13, 14].

Continuity equation:

$$\frac{\partial(\rho_f \emptyset u_i)}{\partial x_i} = 0. \tag{1}$$

Momentum equation:

$$\frac{\partial\left(\rho_f u_i u_j\right)}{\partial x_j} = -\emptyset \frac{\partial p}{\partial x_i} + \frac{\partial}{\partial x_j}\left((\mu_f + \mu_t)\left(\frac{\partial u_i}{\partial x_j} + \frac{\partial u_j}{\partial x_i}\right)\right)$$
$$- \emptyset\left(\frac{\mu_{\text{eff}}}{K} u_i + \frac{\rho_f C_F}{\sqrt{K}} u u_i\right). \tag{2}$$

Turbulent kinetic energy equation:

$$u_j \frac{\partial k}{\partial x_j} = -u_i' u_j' \frac{\partial u_i}{\partial x_j} + \frac{\partial}{\partial x_j} \left(\frac{K_m}{\sigma_k} \frac{\partial k}{\partial x_j} \right) - \varepsilon \tag{3}$$

Rate of energy dissipation equation:

$$u_j \frac{\partial \varepsilon}{\partial x_j} = -C_{\varepsilon 1} \frac{\varepsilon}{k} u_i' u_j' \frac{\partial u_i}{\partial x_j} + \frac{\partial}{\partial x_j} \left(\frac{K_m}{\sigma_\varepsilon} \frac{\partial \varepsilon}{\partial x_j} \right) - C_{\varepsilon 2} \frac{\varepsilon^2}{k}. \tag{4}$$

Effective viscosity:

$$\mu_{\text{eff}} = \mu_{\text{f}}, \tag{5}$$

where

$$\mu_{\text{t}} = \rho_{\text{f}} C_\mu \frac{k^2}{\varepsilon},$$

$$K_m = \nu \left[1 + \left(\frac{C_\mu}{\nu} \right) \frac{k}{\varepsilon^{0.5}} \right]^2.$$

The values of the constants of the above equations are:

$$C_\mu = 0.09; \ \sigma_k = 1.0; \ \sigma_\varepsilon = 1.3; \ C_{\varepsilon 1} = 1.44; \ C_{\varepsilon 2} = 1.92;$$

$$C_F = 0.00212 * (1 - \emptyset)^{-0.132} * \left(\frac{d_{\text{f}}}{d_{\text{p}}} \right)^{-1.63}. \tag{6}$$

The coupled scheme is used for pressure velocity coupling along with Green-Gauss Node based as a gradient for early convergence when compared with other schemes. So, the computational time is reduced with the same accuracy in final results when compared with other schemes. The convergence criteria for the residuals, i.e. continuity and velocities are set as 10^{-4}. The properties of metal foam selected for numerical study are given in Table 1.

Table 1 Metal foam microstructural properties [10]

Parameters	Values		
Pore density (PPI)	5	10	30
Porosity, $\emptyset(-)$	0.92	0.91	0.94
Permeability, $K * 10^{-7} (\text{m}^2)$	2.61	1.65	0.37
Fibre diameter, d_{f} (m)	0.0011	0.00044	0.00027
Pore diameter, d_{p} (m)	0.0058	0.0026	0.00087

Table 2 Grid independence study

Number of elements	Inlet pressure (pa)
176,640	302.60
207,360	302.78
253,440	303.16
316,800	302.96
423,720	302.4

Table 3 Validation with experimental results

Inlet velocity, $u_0\left(\frac{m}{s}\right)$	Pressure gradient, $\frac{\Delta p}{L}\left(\frac{pa}{m}\right)$	
	Present work	Experimental work [10]
6.5	52.5	47
9.5	110	100
12.5	188	180

4 Results and Discussion

4.1 Grid Independence Study

Grid independence study is an essential part of a numerical solution. For 5 PPI metal foam block with $\frac{l_f}{l_{f,max}} = 0.5$ and 12.5 m/s inlet velocity, 176,640, 207,360, 253,440, 316,800, and 423,720 number of elements are considered. The inlet pressure does not change much for this range of the number of elements as given in Table 2, so 253,440 elements have been considered to avoid higher computational time.

4.2 Validation with Experimental Results

To validate the methodology in the present work, a 5 PPI metal foam block of 270 mm length, 320 mm width, and 51.2 mm height with 6.5, 9.5, and 12.5 m/s inlet velocities are considered. Here, the pressure gradient is considered and validated against [10] and the validation is given in Table 3.

4.3 Velocity Profiles

U is defined as u_s/u_0, where u_s and u_0 are stream-wise velocity and inlet velocity, respectively. Figures 2 and 3 show that as the PPI increases, the normalized stream-wise velocity U increases in the top portion of the channel for any flow section, inlet velocity, and $\frac{l_f}{l_{f,max}}$ because as the PPI increases the resistance to flow increases and
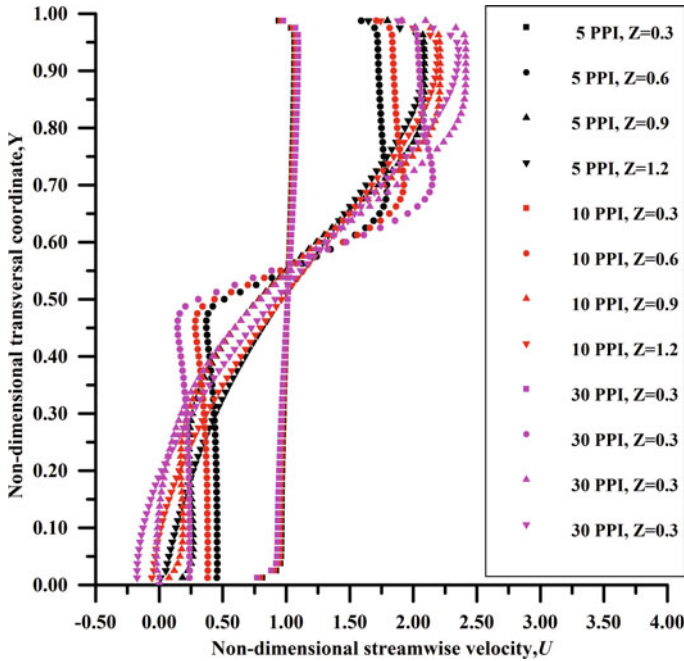
Fig. 2 Velocity profiles for different PPI at different axial location for $\frac{l_f}{l_{f,max}} = 0.5$ and $u_0 = 6.5$ m/ s

more quantity of fluid will flow from the clear fluid region above the metal foam. Figures 2 and 3 also show, as the $\frac{l_f}{l_{f,max}}$ increases, the normalized stream-wise velocity u_s/u_0 increases in the top portion of the channel for any flow section, inlet velocity, and PPI because resistance to flow by metal foam block increases.

4.4 Streamlines

Figure 4 shows the velocity contour, pressure contour, and streamlines for $u_0 = 6.5$ m/s and 30 PPI for different $\frac{l_f}{l_{f,max}}$. So for a particular PPI and inlet velocity as the $\frac{l_f}{l_{f,max}}$ increases, the deviation of fluid flow from the z direction occurs early and recirculation happens closer to the block. Figure 5 shows, for a particular $\frac{l_f}{l_{f,max}}$ and PPI the resistance offered by the block is the same. Here as the inlet velocity decreases, fluid has more time to bend and flow from above the block without entering it. So, more quantity of fluid tries to flow above the block without entering it due to which the fluid flowing through the metal foam is more deviated from the z direction resulting in the formation of eddies closer to the metal foam block.

Fig. 3 Velocity profiles for different PPI at different axial location for $\frac{l_f}{l_{f,max}} = 1$ and $u_0 = 6.5$ m/s

Fig. 4 Velocity contour, pressure contour, and streamlines for $u_0 = 6.5$ m/s and 30 PPI. **a–c** $\frac{l_f}{l_{f,max}}$ $= 0.25$, **d–f** $\frac{l_f}{l_{f,max}}$ $= 0.5$, **g–i** $\frac{l_f}{l_{f,max}}$ $= 0.75$
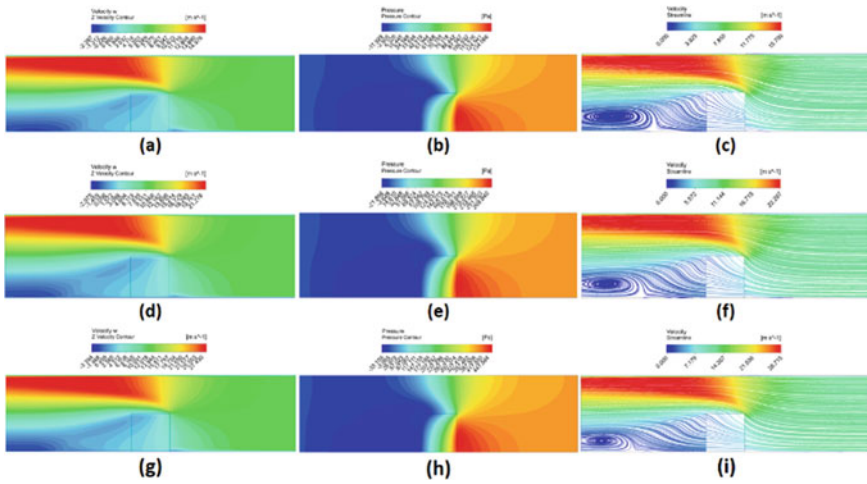
Fig. 5 Velocity contour, pressure contour, and streamlines for 30 PPI and $\frac{l_f}{l_{f,max}} = 0.5$. **a–c** $u_0 = 6.5$ m/s, **d–f** $u_0 = 9.5$ m/s, **g–i** $u_0 = 12.5$ m/s

Figure 6 shows, for a particular inlet velocity and $\frac{l_f}{l_{f,max}}$ as PPI increases more quantity of fluid tries to go from the top of the block without entering it, as resistance to flow from the block increases, due to which the deviation of the fluid flowing through the metal foam from the z direction increases resulting in the formation of eddies closer to the metal foam block.

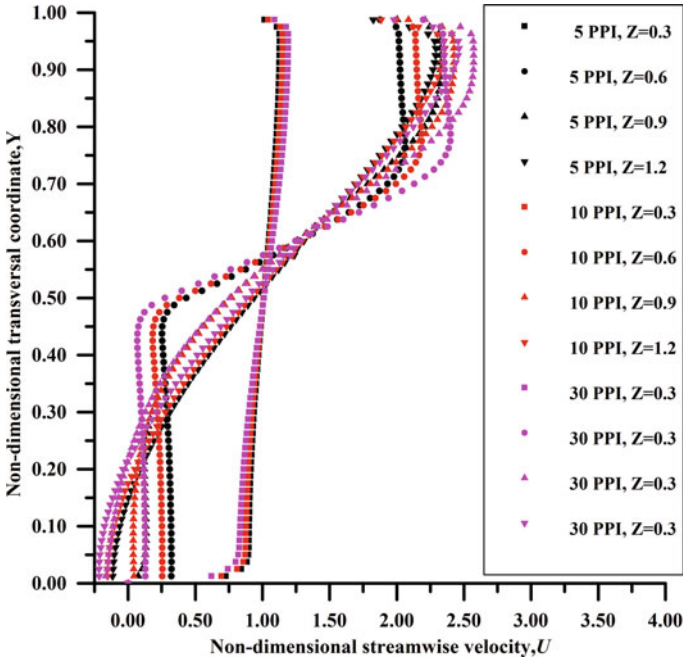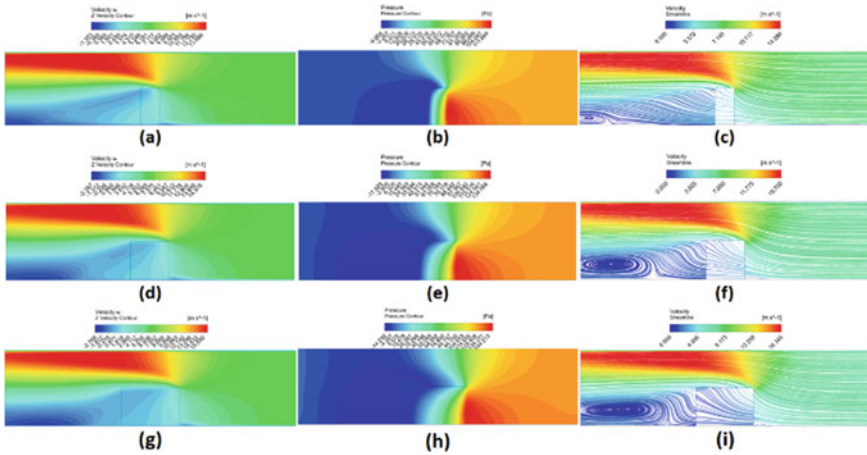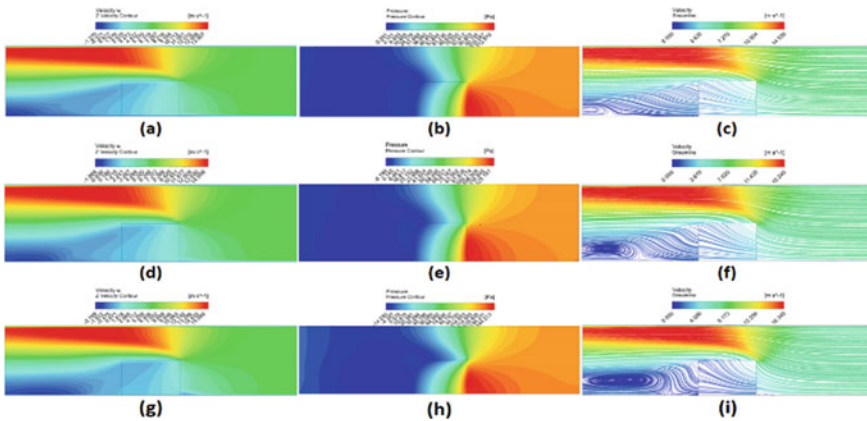**Fig. 6** Velocity contour, pressure contour, and streamlines for $u_0 = 6.5$ m/s and $\frac{l_f}{l_{f,max}} = 0.75$. **a–c** 5PPI, **d–f** 10PPI, **g–i** 30PPI
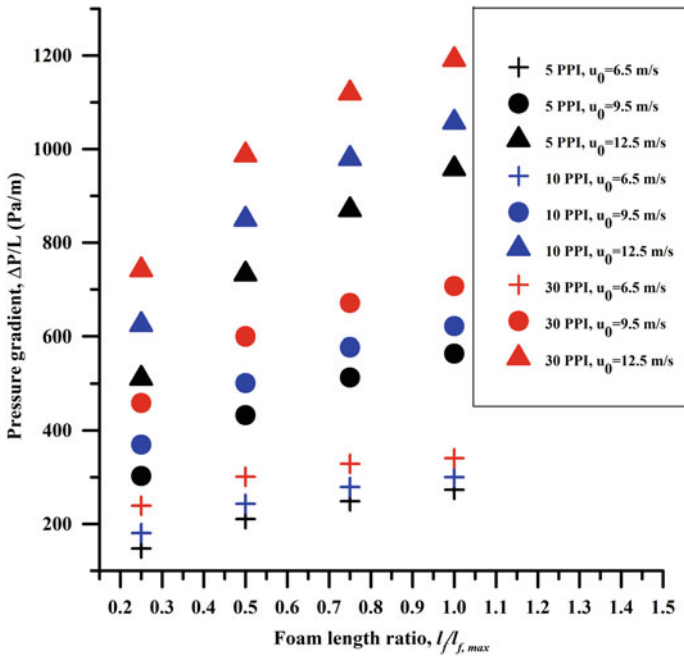
Fig. 7 Pressure gradient variation with $\frac{l_f}{l_{f,max}}$

4.5 Pressure Drop and Friction Factor

Figure 7 shows, the pressure gradient increases with inlet velocity for a particular $\frac{l_f}{l_{f,max}}$ and PPI, as the resistance to flow due to metal foam, channel walls, sudden contraction, and sudden expansion in the partially filled channel with metal foam increases. The pressure gradient increases with $\frac{l_f}{l_{f,max}}$ and PPI, as the resistance to flow due to metal foam increases. Here pressures are measured at $z = 0.395$ m and $z = 0.805$ m for the calculation of pressure drops. Figure 8 shows, the f reduces with an increase in inlet velocity for a particular $\frac{l_f}{l_{f,max}}$ and PPI, for the cases considered in the present study. The friction factor increases with $\frac{l_f}{l_{f,max}}$ and PPI.
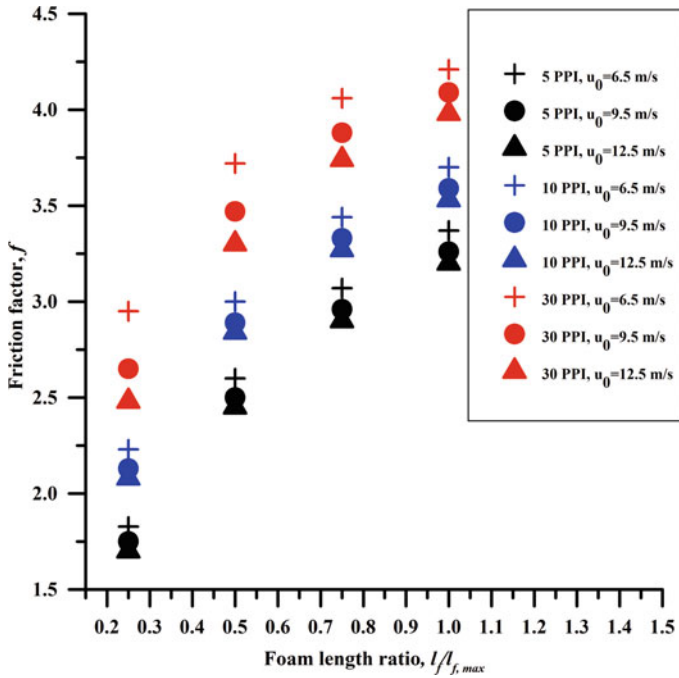
Fig. 8 Friction factor variation with $\frac{l_f}{l_{f,max}}$

5 Conclusion

Dimensionless velocity at the upper portion of the channel is higher for higher values of PPI and foam length for all the flow sections. The recirculation zones shift near to the metal foam block as inlet velocity reduces, PPI increases, and foam length increases. The pressure gradient increases with velocity, length and PPI with the highest value of 1190 Pa/m for the case of $\frac{l_f}{l_{f,max}} = 1$, 30 PPI, and 12.5 m/s inlet velocity. Friction factor reduces with velocity and increases with PPI and length of foam with the highest value of 4.2 for the case of $\frac{l_f}{l_{f,max}} = 1$, 30 PPI, and 6.5 m/s inlet velocity.

Nomenclature

C_F	Forchheimer coefficient (–)
d_f	Fibre diameter (m)
d_p	Pore diameter (m)
f	Friction factor (–)

k	Turbulent kinetic energy $\left(\frac{m^2}{s^2}\right)$
K	Permeability (m^2)
l_f	Length of foam (m)
$l_{f,max}$	Maximum length of foam (m)
L	Distance between the sections where pressures are measured for calculation of pressure drops (m)
Δp	Pressure drop across distance L (Pa)
p	Pressure (Pa)
PPI	Pores per inch (–)
u_s	Stream-wise velocity (m/s)
u_0	Inlet velocity (m/s)
u'_j	Fluctuation in mean velocity u_i (m/s)
U	Non-dimensionalized stream-wise velocity (m/s)
$\emptyset$	Porosity (–)
ε	Rate of energy dissipation $\left(\frac{m^2}{s^3}\right)$
μ_f	Viscosity of fluid $\left(\frac{N-S}{m^2}\right)$
μ_t	Turbulent viscosity $\left(\frac{Ns}{m^2}\right)$
μ_{eff}	Effective viscosity $\left(\frac{Ns}{m^2}\right)$
ν	Kinematic viscosity $\left(\frac{m^2}{s}\right)$
ρ_f	Density of fluid $\left(\frac{Kg}{m^3}\right)$

References

1. Anuar FS, Malayeri MR, Hooman K (2017) Particulate fouling and challenges of metal foam heat exchangers. Heat Transfer Eng 38(7–8):730–742
2. Kurtbas I, Celik N (2009) Experimental investigation of forced and mixed convection heat transfer in a foam-filled horizontal rectangular channel. Int J Heat Mass Transf 52(5–6):1313–1325
3. Mancin S, Zilio C, Cavallini A, Rossetto L (2010) Heat transfer during air flow in aluminum foams. Int J Heat Mass Transf 53(21–22):4976–4984
4. Mancin S, Zilio C, Diani A, Rossetto L (2013) Air forced convection through metal foams: experimental results and modeling. Int J Heat Mass Transf 62:112–123
5. Lu W, Zhang T, Yang M (2016) Analytical solution of forced convective heat transfer in parallel-plate channel partially filled with metallic foams. Int J Heat Mass Transf 100:718–727
6. Mahmoudi Y, Karimi N (2014) Numerical investigation of heat transfer enhancement in a pipe partially filled with a porous material under local thermal non-equilibrium condition. Int J Heat Mass Transf 68:161–173
7. Nithyanandam K, Singh P (2022) Enhanced forced convection through thin metal foams placed in rectangular ducts. Heat Transfer Eng 44(10):837–852
8. Mancin S, Zilio C, Rossetto L, Cavallini A (2010) Experimental and analytical study of heat transfer and fluid flow through aluminum foams. AIP Conf Proc 1254:305–310
9. Bidar B, Shahraki F, Mohebbi-Kalhori D (2016) 3D numerical modelling of convective heat transfer through two-sided vertical channel symmetrically filled with metal foams. Periodica Polytech Mech Eng 60(4):193–202

10. Anuar FS, Abdi IA, Hooman K (2018) Flow visualization study of partially filled channel with aluminium foam block. Int J Heat Mass Transf 127:1197–1211
11. Trilok G, Gnanasekaran N, Mobedi M (2021) Various trade-off scenarios in thermo-hydrodynamic performance of metal foams due to variations in their thickness and structural conditions. Energies 14(24):1–23
12. Jadhav PH, Trilok G, Gnanasekaran N, Mobedi M (2022) Performance score based multi-objective optimization for thermal design of partially filled high porosity metal foam pipes under forced convection. Int J Heat Mass Transf 182:121911
13. Kotresha B, Gnanasekaran N (2020) Numerical simulations of fluid flow and heat transfer through aluminum and copper metal foam heat exchanger—a comparative study. Heat Transfer Eng 41(6–7):637–649
14. Jadhav PH, Gnanasekaran N, Perumal DA (2021) Conjugate heat transfer study comprising the effect of thermal conductivity and irreversibility in a pipe filled with metallic foams. Heat Mass Transf 57(6):911–930

Numerical Simulation of Combined Natural Convection and Radiation Inside a Square Enclosure with a Horizontal Partition

Mariyam Ali and Anil Kumar Sharma

1 Introduction

Enclosures with different configurations having fluid flow and heat transfer have been studied for past several decades to understand the phenomenon of natural convection and radiation occurring inside it. While considering different configurations, enclosures with partition came into picture and many gap areas are observed as described in the following paragraphs. Thus, in this present research work a square cavity with a horizontal partition is considered to study the fluid flow and heat transfer.

2 Literature Review

Nag et al. [1] carried out a numerical investigation of natural convection inside a differentially heated square cavity. In his study, he considered a horizontal partition placed on the vertical hot wall inside the cavity for the analysis. Two types of thermal boundary conditions were considered for the horizontal partition. In the first case, the partition was considered to have infinite conductivity while in the second case it was considered to be adiabatic. It was observed that the material for the horizontal partition highly affected the rate of heat transfer inside the square enclosure. When the partition is infinitely conducting, the cold wall Nusselt number increases, while on the other hand when the partition is adiabatic, the rate of heat transfer decreases. Haghighi and Vafai [2] in their research considered a partial horizontal and vertical partition placed at hot vertical wall and bottom adiabatic wall, respectively. The partitions were assumed to be adiabatic and the Rayleigh number was taken between 10^3 and

M. Ali · A. K. Sharma (✉)

Department of Mechanical Engineering, Faculty of Engineering and Technology, Jamia Millia Islamia (A Central University), New Delhi 110025, India
e-mail: asharma1@jmi.ac.in

10^6. The purpose of this study was to find out the best position of the partitions for the maximum heat transfer reduction inside the cavity. After the numerical investigation, it was observed that the vertical partition is more effective in reducing the heat transfer inside the enclosure. Furthermore, with the horizontal partition the heat transfer rate increases to a great extent. Farah Zemani-Kaci and Sabeur-Bendhina [3] performed a numerical simulation of unsteady natural convection inside an enclosure with partition attached to the hot vertical wall. Air was considered as the working fluid and the study was carried out for Rayleigh number 10^9. The results were shown with the help of streamline and temperature contours. It was observed that the partition placed at the hot wall had a significant effect of heat transfer and enhances the overall heat transfer rate inside the enclosure. Xu et al. [4] carried out a numerical simulation of transient natural convection inside a differentially heated cavity with a thin fin on the side wall. The thin fin was placed at the center of the hot vertical wall. For the present study, the aspect ratio was considered to be 0.24. Also, the dimensions of the fin were fixed. The results were presented with the help of streamline and temperature contours. Kruger and Pretorius [5] in their research work considered a cavity with the vertical walls as adiabatic, bottom wall as hot wall and the top wall as cold wall along with conducting horizontal and vertical partitions. They carried out a computational study of natural convection inside the enclosure to study the effect of the partitions. The Rayleigh number for the study was taken as 9.1×10^7 to 1.9×10^9. The effect of these conducting baffles was shown with the help of temperature and velocity contour plots and average Nusselt Number. The observation made during the study was that the presence of partition inside the cavity affects the overall heat transfer rate to a great extent. Also, it was concluded that an enclosure with conducting partition can be used to represent an enclosed greenhouse. All these studies focus on natural convection characteristics in the enclosure with key influencing parameters such as partition material, length with isotherm and adiabatic boundary conditions. However, the interaction of surface radiation is not considered and these for the present study framed the objective of the present work.

3 Physical Model and Problem Description

The cavity considered here is a differentially heated partitioned square cavity with horizontal walls as adiabatic, left wall as hot wall considered at a higher temperature T_H and the right wall as cold wall considered at a lower temperature T_C as shown in Fig. 1. The fluid considered here is air having a Prandtl number of 0.71. The Boussinesq approximation is adopted for the working medium inside the cavity.

Fig. 1 Computational grid for partitioned enclosure
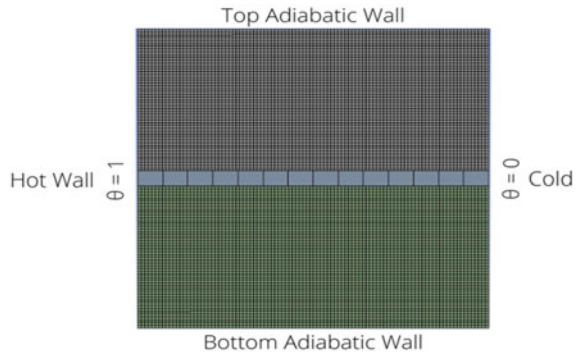
3.1 Solution Methodology

The study is carried out using ANSYS FLUENT 2022R1 to solve the governing equations of continuity, momentum and energy equations with the help of finite volume method. The pressure–velocity coupling is done by coupled algorithm and pressure interpolation is done by second-order scheme. For the momentum and energy equation, second-order upwind is adopted and for radiation equation first-order upwind is chosen. The value of surface emissivity for all the considered cases is taken as 1.

3.2 Calculation of Nusselt Number

The Nusselt number is evaluated based on heat flux obtained after analyzing the flow field and heat transfer characteristics inside the enclosure.

The local and average Nusselt number for hot and cold wall are defined as:

$$\mathrm{Nu_h} = -\frac{\mathrm{d}\theta}{\mathrm{d}x}\bigg|x = 0$$

$$\mathrm{Nu_c} = -\frac{\mathrm{d}\theta}{\mathrm{d}x}\bigg|x = 1$$

$$\overline{\mathrm{Nu_h}} = \int_0^1 \mathrm{Nu_h} \mathrm{d}Y$$

$$\overline{\mathrm{Nu}}_c = \int_0^1 \mathrm{Nu_c} \mathrm{d}Y$$

4 Results

The results are presented in the form of temperature and streamline contours in order to completely enumerate the combined effect of natural convection and radiation inside a differentially heated square cavity with a horizontal partition placed parallel to the adiabatic walls for Rayleigh Number 10^3 and 10^5. The effect of Rayleigh number, partition length and distance from top wall is studied. For this study, the partition thickness and thermal conductivity is assumed to be constant.

Four different cases 1, 2, 3 and 4 are considered in the present study with their subdivisions as a, b and c. In case 1 the length of the partition is taken as $l = L$. For case 2 the length of the partition is considered as $l = 3L/4$ maintaining a gap of $L/4$ between the cold wall and the partition. For case 3 two partitions are considered, one protruding from the hot wall and the other from the cold wall. The length of the partition attached to the hot wall is $L/2$, while the length of the partition attached to the cold wall is $L/4$ keeping a gap between them as $L/4$. Case 4 corresponds to the inverse situation where the length of the partition attached to hot wall as $L/4$ and length of partition attached to cold wall as $L/2$, maintaining a gap of $L/4$ between the hot and cold partition. In all the cases the subdivisions a, b and c correspond to the situations where the partition distances from the adiabatic top wall are $L/4$, $L/2$ and $3L/4$, respectively.

4.1 *Combined Natural Convection and Radiation*

The temperature and streamline contours are shown in Figs. 2 and 3 for Rayleigh number 10^3 and 10^5, respectively, for combined natural convection and radiation within a differentially heated square enclosure with a horizontal partition. The temperature contours for Ra 10^3 are almost parallel to the vertical walls as shown in Fig. 2. Also, from the streamline contours, it can be seen that the flow of fluid is in clockwise direction resulting in smooth circular curves. For Ra 10^5 the isotherm contours are somewhat distorted causing them to become parallel to the horizontal adiabatic walls as shown in Fig. 3. The streamline contours in this case also shows the clockwise rotation of fluid flow. The graphs in Fig. 4 show the variation of convective, radiative and total Nusselt number with Rayleigh number ranging from 10^3 to 10^6 for case 1 (a, b and c). It can be observed from the graph that the convective Nusselt number does not change much from 10^3 to 10^4, however at 10^5 there is a sharp increase of 217% to 10^6. The radiative Nusselt number vs Rayleigh number graph is almost a straight line with a continuous increase. The radiative Nusselt number increases to 925% for Ra increase from 10^3 to 10^6. Also, the value of convective Nusselt number is greater than that of radiative Nusselt number for considered Rayleigh number range. Both of these combined increases the total Nusselt number with increase in Rayleigh number.
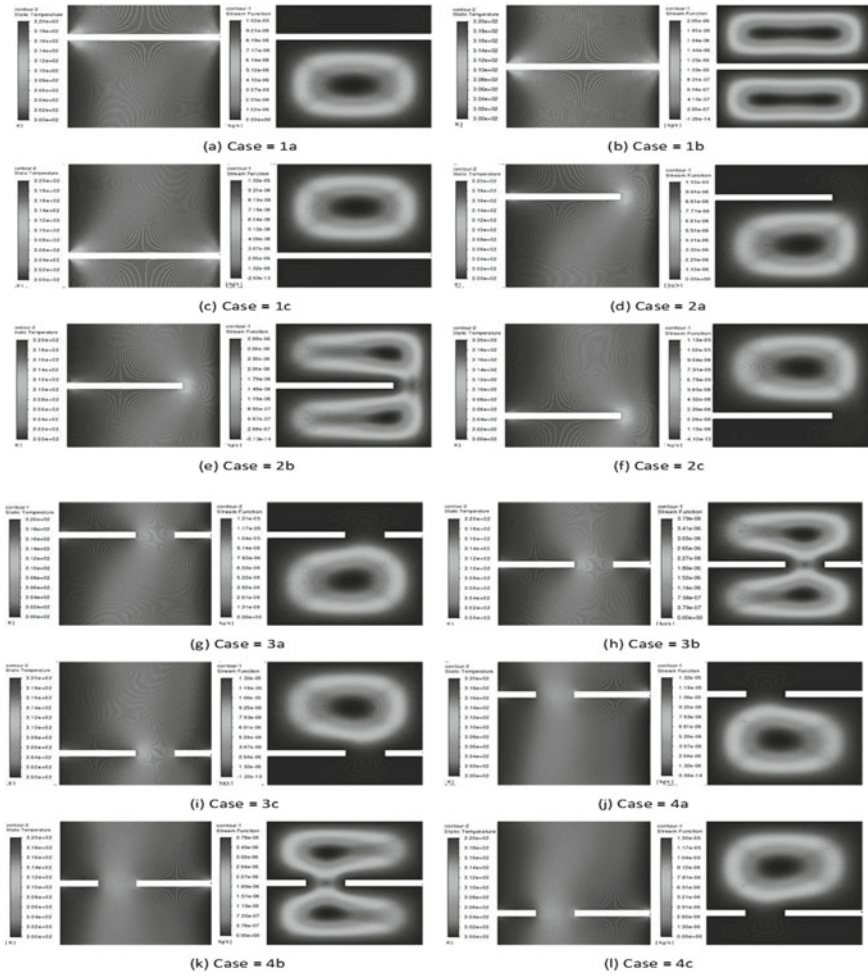
Fig. 2 Temperature contours and streamlines for Rayleigh number 10^3

4.2 Effect of Rayleigh Number

Figure 5 shows the effect of Rayleigh number on combined radiation and natural convection inside a differentially heated square enclosure with a horizontal partition. The graph shows the variation of total Nusselt number with Rayleigh number ranging from 10^3 to 10^6. It is observed that as the Rayleigh number is increased from 10^3 to 10^6 the NuT increases to 447% for case 1b.

(a) Case = 1a

(b) Case = 1b

(c) Case = 1c

(d) Case = 2a

(e) Case = 2b

(f) Case = 2c

(g) Case = 3a

(h) Case = 3b

(i) Case = 3c

(j) Case = 4a

(k) Case = 4b

(l) Case = 4c
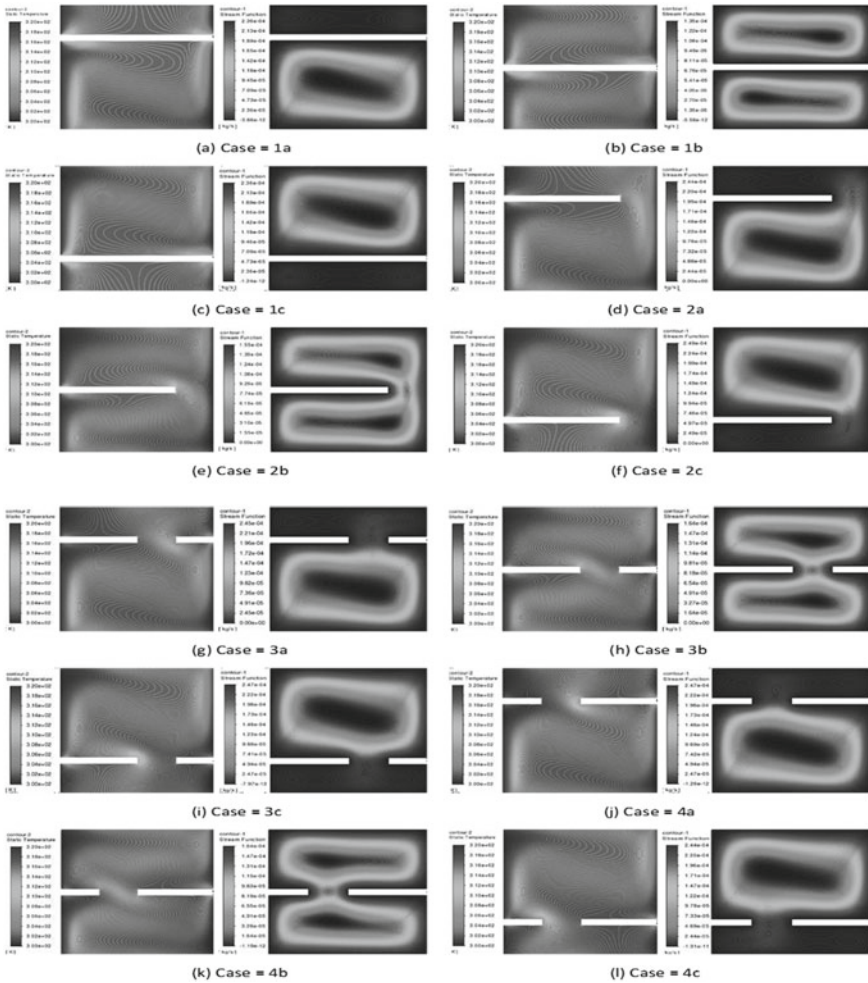
Fig. 3 Temperature contours and streamlines for Rayleigh number 10^5

4.3 Effect of Partition Length and Partition Distance

Figure 6 shows the variation of total Nusselt number with partition length for Rayleigh number 10^3 and 10^5. Four cases of partition length are considered for the analysis as mentioned above. By comparing the values of total Nusselt number for hot wall for all the four cases, it is observed that the maximum value of Nu_T is seen when the length of partition is equal to the length of the cavity, i.e., for case 1 when $l = L$. From the graph it can be seen that when the length of partition is varied from $l = L/4$ to L, the value of Nu_T increases to 75% and 16% for Ra 10^3 and 10^5, respectively. As for the partition distance from top wall, it can be seen from the graph for the three
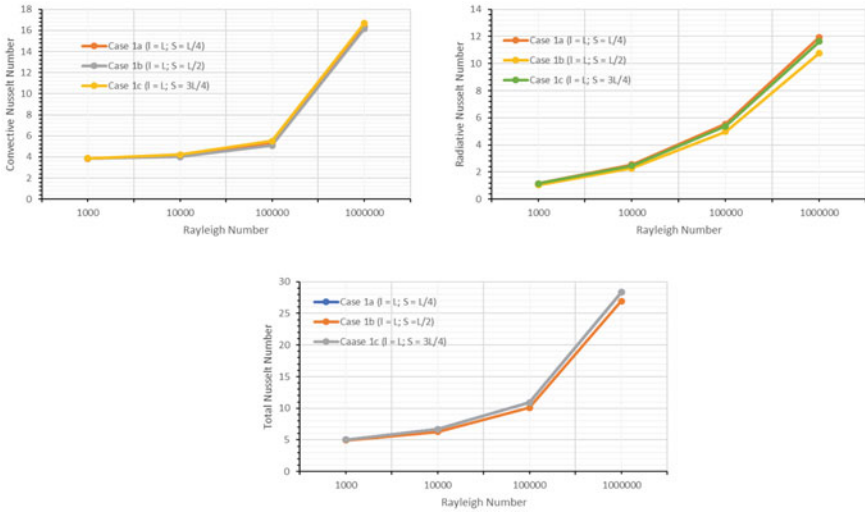
Fig. 4 Variation of convective, radiative and total Nusselt number for combined natural convection and radiation for hot wall for $\varepsilon = 1$ in r case 1 for Rayleigh number $10^3 - 10^6$

Fig. 5 Variation of total Nusselt number with Rayleigh numbers along the hot wall for central position of partition wall and different partition height
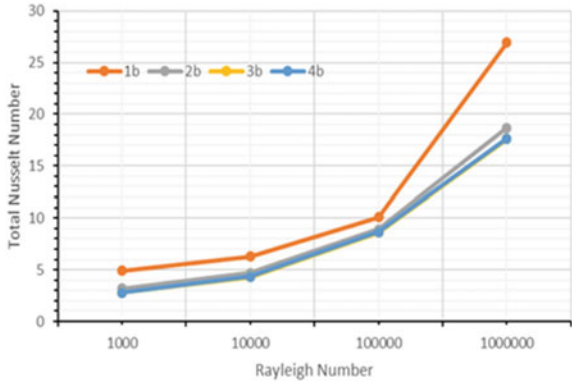
cases a, b and c that highest value of Nusselt number is observed for case c when the partition is farthest from top wall.
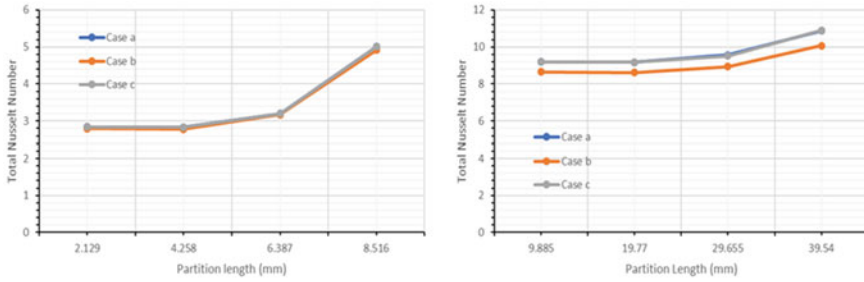
Fig. 6 Variation of total Nusselt number with partition length for different partition distances from hot wall for Rayleigh number 10^3 and 10^5, respectively

5 Conclusion

The present study of natural convection and radiation occurring inside an enclosure with horizontal partition leads us to certain conclusions which could be beneficial for future researches in this field. It can be concluded that the convection is almost equally participating in the total heat transfer phenomenon as the radiation and in some cases even more. It can also be concluded that as the Rayleigh number is increased that value of total Nusselt number increases. As for the partition length it is observed that greater the length, higher the Nusselt number value, as can be seen that when l is increased from $L/4$ to L the Nu_T increases to 75% and 16% for Ra 10^3 and 10^6, respectively. Also, as the partition distance is increased from the top adiabatic wall the NuT increases, however the change is not much significant.

Nomenclature

g	Gravity acceleration, ms^{-2}
L	Length of square cavity, m
h	Height of the partition, m
t	Thickness of the partition, m
S	Position of the partition from top wall, m
Nu_T	Total Nusselt number
P	Dimensionless pressure
Pr	Prandtl number
Ra	Rayleigh number
k_f	Thermal conductivity of the fluid adjacent to wall
T	Temperature, K
θ	Nondimensional temperature

References

1. Nag A, Sarkar A, Sastri VMK (1993) Natural convection in a differentially heated square cavity with a horizontal partition plate on the hot wall. Comput Methods Appl Mech Eng 110:143–156
2. Haghighi A, Vafai K (2014) Optimal positioning of strips for heat transfer reduction within an enclosure. Numer Heat Transf Part A 66:17–40. ISSN: 1040-7782
3. Zemani-Kaci F, Sabeur-Bendhina A (2017) Numerical simulation of unsteady natural convection in an air-filled cavity with partition. HAL Open Science. HAL Id: hal-03465622. https://hal.archives-ouvertes.fr/hal-03465622
4. Kruger S, Pretorius L (2013) The effect of vertical and horizontal partitions on natural convection in a heated enclosure. In: Proceedings of the ASME 2013 heat transfer summer conference HT2013
5. Xu F, Patterson JC, Lei C (2009) Transient natural convection flows around a thin fin on the sidewall of a differentially heated cavity. J Fluid Mech 639:261–290

Lateral Migration of Three Particles Through a Slit—An Immersed Boundary Computational Analysis

Manjappatta Pazhiyottumana Neeraj and Ranjith Maniyeri

1 Introduction

The slit microchannel is used in biological processes like DNA sequencing, protein translation, and gene therapy. The slit is present at the center of channel which helps in the sampling of biomolecules. For these procedures, normally electric field is applied to the channel. To reduce the cost of these procedures and to make them simpler, other methodologies rather than electric and magnetic field applications are being tested nowadays. Some techniques require pure fluid forces to drive the particles (known as passive techniques). The inertial migration of particles in fluid flow is such a transport technique. The combined effect of shear and wall induced lift forces generates a lateral lift over the particles flowing in the fluid. Both of these lift forces act opposite to each other, and this will create an equilibrium position for the particles [1]. The inertial migration is studied widely in literature. However, the effect of lateral migration in a slit channel is not much analyzed before.

2 Literature Review and Objective

In an experiment conducted by Segre and Silberberg [2], the spheres released in a tubular flow were found to be concentrating at 0.6 times the radius of the channel. This effect was further called Segre–Silberberg effect [3]. This effect is one of the basic characteristics of inertial migration. By observing interesting possibilities of inertial migration in biological fields and others, a number of experimental [4, 5] and analytical works [6, 7] were done by numerous researchers. The numerical methods

M. P. Neeraj · R. Maniyeri (✉)
Biophysics Laboratory, Department of Mechanical Engineering, National Institute of Technology Karnataka (NITK), Surathkal, Mangalore, Karnataka 575025, India
e-mail: mranji1@nitk.edu.in

seem to be more precise than analytical ones, and in this direction, a significant number of works have been done. The inertial migration of particles was simulated by using different computational schemes such fictitious domain method [8] and lattice Boltzmann method (LBM) [9]. However, the involvement of fluid–structure interaction (FSI) in inertial migration makes immersed boundary method (IBM) [10] a suitable methodology for the simulation of the same. We used another version of IBM with feedback forcing scheme [11] for studying the lateral migration of single cylindrical particle in stepped [12] and constricted [13] channels. The advantage of non-straight channels is that they can alter the inertial migration characteristics due to the presence of recirculation zones in them. The slit channel is such a type of non-straight channel. The slit is present at the center of the channel. It can be used for several biological processes such as protein transfusion and DNA sampling.

Considering the possibilities of a slit channel, the current work tries to explore the characteristics of lateral migration of three non-neutrally buoyant cylindrical particles in a slit channel. The residence time (time required for particles to pass the slit) and equilibrium position are computed from the simulation for different slit clearances and angles. The immersed boundary finite volume model constructed with the aid of feedback forcing scheme is incorporated to analyze the migration characteristics of the particles in the slit channel.

3 Methodology

Figure 1 shows the physical model of three particles migration in slit channel.

The channel is of length L and height H. The gap of slit is denoted by slit clearance (S_g). The angle of slit is also shown in Fig. 1 as Θ. The diameter of each particle is d, and F_{Sh} and F_W are induced shear and wall lifts, respectively. Fluid enters from left side with Poiseuille flow pattern and exits from the right side with zero-velocity gradient conditions. The bottom and top walls possess no-slip boundary conditions. The pressure gradient is kept zero at left side, bottom, and top wall, respectively.
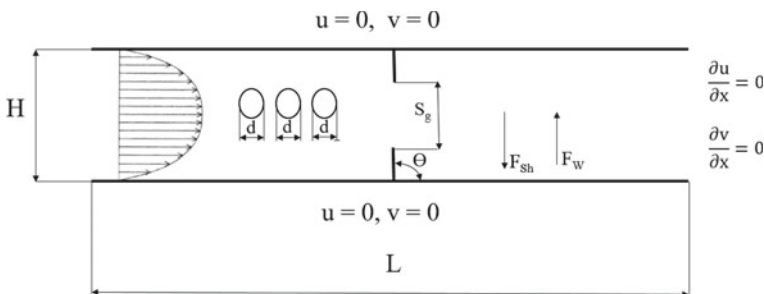

Fig. 1 Physical model

The particles are separated by a center-to-center distance of 0.25 initially. Both the particles and slit rods are modeled using IBM scheme.

The system of IBM carries two set of discrete grid systems. The Cartesian coordinates $\mathbf{x} = (x, y)$ are used to represent the fluid grids, while Lagrangian mesh system $\mathbf{X}_{P,K}(s, t)$ and $\mathbf{X}_S$ (position of Lagrangian coordinates on the particles and slit rods respectively) is utilized to denote the structure (particle and slit rod), where t and s indicate the time and structural point respectively. The terms $\mathbf{f}_{P,K}(\mathbf{x}, t)$ and $\mathbf{f}_S(\mathbf{x}, t)$ represent the Eulerian force density corresponding to particles and the slit rod (subscript K denotes the particle number, $K = 1, 2$ and 3). Velocity and pressure [$\mathbf{u}(\mathbf{x}, t)$ and $p(\mathbf{x}, t)$, respectively] of fluid are the other variables of flow, whereas the structural variables are the Lagrangian force densities $\mathbf{F}_{P,K}(s, t)$ and $\mathbf{F}_S(s, t)$ (particles and slit rod, respectively). It should be noted that all values are non-dimensionalized with respect to the height of channel H (characteristic length) and maximum velocity in the channel $\mathbf{u}_{\mathrm{ref}}$ (characteristic velocity in the channel). The Lagrangian force densities are computed by using feedback forcing scheme as shown in Eqs. (1) and (2) [11].

$$\mathbf{F}_{P,K}(s, t) = \alpha \int (\mathbf{U}_{\mathrm{ibP},K} - \mathbf{U}_{P,K}) \Delta t + \beta (\mathbf{U}_{\mathrm{ibP},K} - \mathbf{U}_{P,K}) \tag{1}$$

$$\mathbf{F}_S(s, t) = \alpha \int (\mathbf{U}_{\mathrm{ibS}} - \mathbf{U}_S) \Delta t + \beta (\mathbf{U}_{\mathrm{ibS}} - \mathbf{U}_S) \tag{2}$$

where $\mathbf{U}_{\mathrm{ibP},K}$ and $\mathbf{U}_{\mathrm{ibS}}$ are the velocity of immersed boundary points on the particles and slit rods, respectively, obtained from fluid velocity interpolation with the Dirac delta function δ [Eqs. (3), (4)]. α and β are negative constants of large magnitude, and $\mathbf{U}_{P,K}$ denotes the particle velocity [11].

$$\mathbf{U}_{i\mathrm{bP},K}(s, t) = \int \mathbf{u}(\mathbf{x}, t) \, \delta\big(\mathbf{x} - \mathbf{X}_{P,K}(s, t)\big) \, d\mathbf{x} \tag{3}$$

$$\mathbf{U}_{i\mathrm{bS}}(s, t) = \int \mathbf{u}(\mathbf{x}, t) \, \delta(\mathbf{x} - \mathbf{X}_S(s, t)) \, d\mathbf{x} \tag{4}$$

where $d\mathbf{x}$ denotes the Eulerian grid size. The four-point Dirac delta function is used here and it is given by [11],

$$\delta(\mathbf{x}) = \frac{1}{h^2} \Phi\left(\frac{x}{h}\right) \Phi\left(\frac{y}{h}\right) \tag{5}$$

The particle velocity $\mathbf{U}_{P,K}$ consists of both angular (Ω_K) and translational ($\mathbf{U}_K$) components as shown in Eq. (6) [14, 15]. Since the slit rods are fixed, $\mathbf{U}_S = 0$.

$$\mathbf{U}_{P,K} = \mathbf{U}_K + \Omega_K\big(\mathbf{X}_{P,K} - X_{C,K}\big) \tag{6}$$

where $X_{C,K}$ is the center of particle.

The particle positions are computed by [16]

$$\mathbf{X}_{P,K}^{n+1}(s) = \mathbf{X}_{P,K}^{n}(s) + \mathbf{U}_{P,K}\Delta t \tag{7}$$

The Lagrangian forces are interpolated with Dirac delta function δ to obtain the Eulerian force densities $\mathbf{f}_{P,K}(\mathbf{x}, t)$ and $\mathbf{f}_{S}(\mathbf{x}, t)$.

$$\mathbf{f}_{P,K}(\mathbf{x}, t) = \int \mathbf{F}_{P,K}(s, t)\, \delta\big(\mathbf{x} - \mathbf{X}_{P,K}(s, t)\big)\, \mathrm{d}s \tag{8}$$

$$\mathbf{f}_{S}(\mathbf{x}, t) = \int \mathbf{F}_{S}(s, t)\, \delta(\mathbf{x} - \mathbf{X}_{S}(s, t))\, \mathrm{d}s \tag{9}$$

where ds is the Lagrangian grid size. The Eulerian force densities are united into one single term $\mathbf{f}(\mathbf{x}, t)$ and are added to the non-dimensionalized Navier–Stokes equations as shown in Eq. (10). Equation (11) shows the dimensionless continuity equation.

$$\frac{\partial \mathbf{u}}{\partial t} + \mathbf{u} \cdot \nabla \mathbf{u} = -\nabla p + \frac{1}{\mathrm{Re}}\nabla^2 \mathbf{u} + \mathbf{f}(\mathbf{x}, t) \tag{10}$$

$$\nabla \cdot \mathbf{u} = 0 \tag{11}$$

where $\mathrm{Re} = \rho_{\mathrm{f}}\mathbf{u}_{\mathrm{ref}}H/\mu$. Equation (10) is discretized by finite volume method (FVM) and semi-implicit methodology on staggered Cartesian grid as given below. Equation (10) is discretized using semi-implicit scheme as written in Eq. (12).

$$\frac{\mathbf{u}_{i,j}^{n+1} - \mathbf{u}_{i,j}^{n}}{\Delta t} + N(\mathbf{u}^n) = -\left(\frac{\partial p}{\partial x_i}\right)^n + \frac{1}{2\mathrm{Re}}\big(\nabla^2\mathbf{u}^{n+1} + \nabla^2\mathbf{u}^n\big) + \mathbf{f}(\mathbf{x}, t) \tag{12}$$

where $N(\mathbf{u}^n)$ is the nonlinear convection term. The particle trajectory, fluid flow velocity, and pressure are computed using the above equations. The fractional step-based algorithm [17, 18] is aided to arrive at the solution of the discretized momentum equations. The momentum equations are solved with the aid of incomplete Cholesky conjugate gradient (ICCG) method for getting the intermediate velocity. Following this, the pseudo-pressure is determined which will further help in calculation of the actual pressure and velocity of fluid.

4   Results and Discussion

The feedback forcing scheme-aided IBM is employed to construct the computational model for cylindrical particle migration in a slit channel. The grid independence study is carried out by simulating rigid neutrally buoyant cylindrical particle migration in

a straight channel of 50×1 dimension. The Eulerian grids are 0.1, 0.05, and 0.025. The equilibrium positions (Y_{eq}) for each grid size are plotted as shown in Fig. 2.

The equilibrium positions are observed to be same for the Eulerian grid sizes 0.05 and 0.025. Hence, 0.05 is selected as the optimum grid. As part of validation, neutrally buoyant rigid cylindrical particle of diameter 0.25 and 0.35 is released in a straight channel of dimension 50×1 from same initial position of (1.0, 0.4). The Reynolds number is 50.0, and the value of α and β is -4000.0 and -40.0 [11]. The center trajectory of the particle is plotted in Fig. 3.

Fig. 2 Grid independence study [variation equilibrium positions with Eulerian grid sizes (h)]
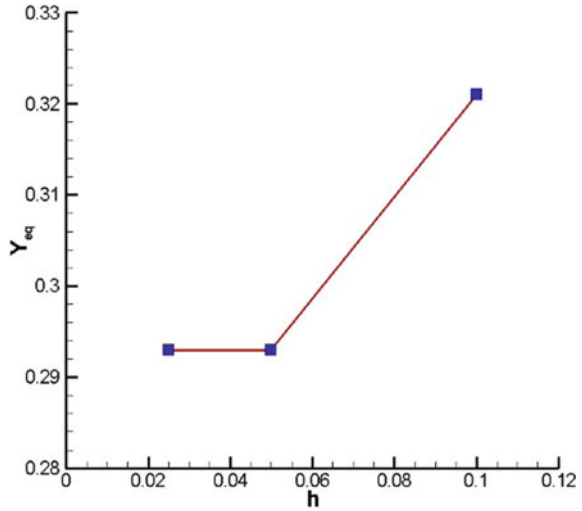

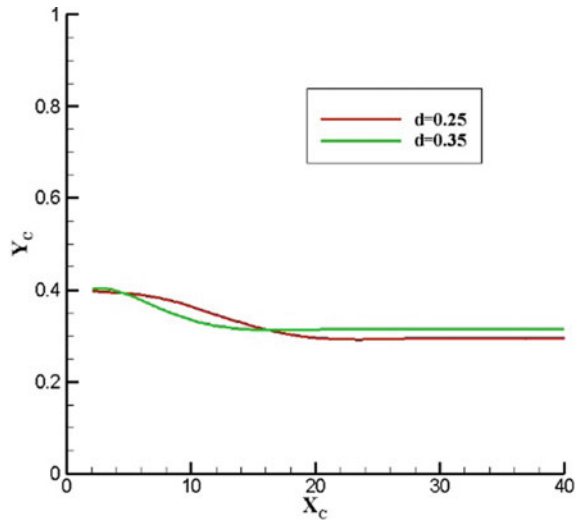**Fig. 3** Particle trajectory for two diameters 0.25 and 0.35 (Re = 50.0)

Table 1 Comparison of equilibrium positions Y_{eq} of particle in Poiseuille flow for two diameters observed in the present work with that of Huang et al. [19] (Re = 50.0)

D	$Y_{eq.}$ [19]	Y_{eq} (present study)
0.25	0.291	**0.293**
0.35	0.313	**0.316**

The particle terminates its lateral motion after a particular position, and this is called equilibrium position (Y_{eq}). The equilibrium positions are computed and shown in Table 1 along with the findings of Huang et al. [19].

It is observed that the values are in good agreement. Moving on, the non-neutrally buoyant particles migration in a slit channel of 20×1 dimension are simulated. The particle diameter is 0.2, and Reynolds number is 50.0. The density ratio (ρ) of particle to fluid is taken as 100.0. The slit clearance and angle are 0.5 and $\pi/2$. The particles are released from initial positions such as (5.0, 0.5), (5.25, 0.5), and (5.5, 0.5). The slit is present at a horizontal position of 10.0. The initial and final positions of three particles are shown in Fig. 4a, b.

The particles move past the slit and attain the equilibrium position. It is more evident from Fig. 5 where particle lateral trajectories are mapped against horizontal position and time.

The particle trajectory becomes parallel to horizontal axis after it passes the slit placed at 10.0 and attains equilibrium position. However, the equilibrium positions
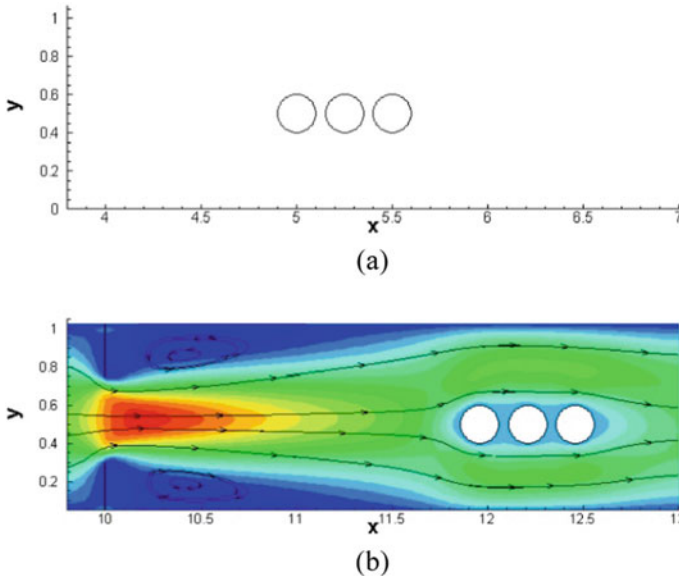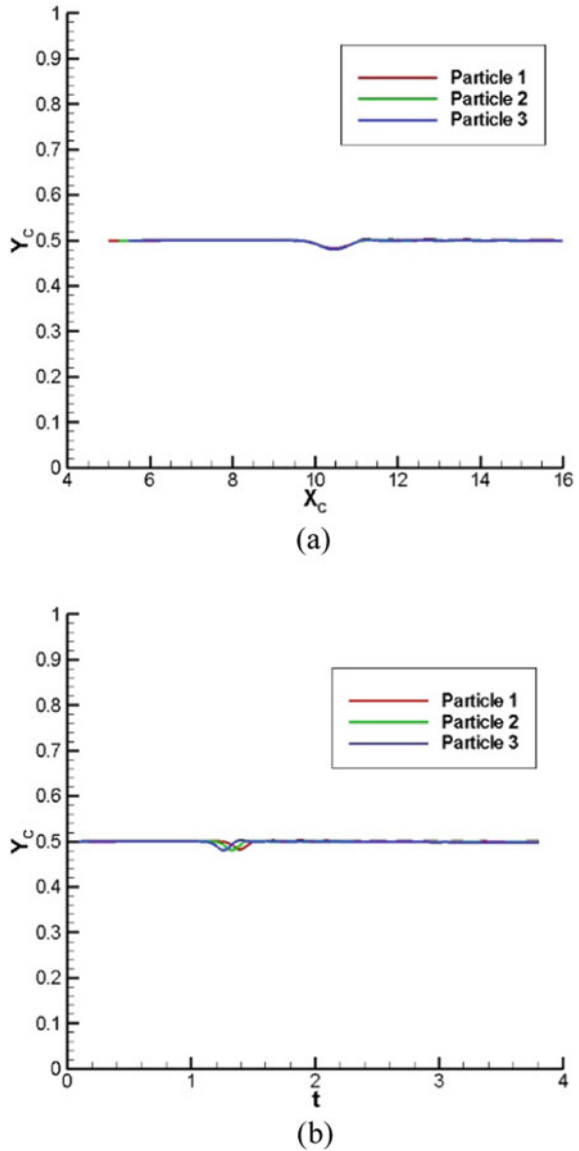

Fig. 4 **a** Initial positions of three particles. **b** Final position of particles ($d = 0.2$, Re = 50.0, $S_g =$ 0.5, and $\Theta = \pi/2$, $\rho = 100.0$).

Fig. 5 Variation of lateral positions of particles with **a** horizontal position, **b** time (Re $= 50.0$, $d = 0.2$, $S_g = 0.5$, $\Theta = \pi/2$, $\rho = 100.0$)

coincide for all three particles. This may be due to the same size and initial lateral release position of all the particles. From Fig. 5b it is clear that the particles pass the slit at different times. The particle which is placed very close to the slit (particle 3) passes the slit at the earliest. The time taken to pass the slit is called residence time (t_r). In the next stage, the slit clearance and angle are changed, and their importance in equilibrium position and residence time is studied.

4.1 Influence of Slit Clearance (S_g)

The slit clearance is varied in this section, while other parameters such as Reynolds number (50.0), particle diameter (0.2), density ratio (100.0), and slit angle ($\pi/2$) are kept constant. The particle trajectory with time is shown in Fig. 5 for different S_g (0.3, 0.4 and 0.5). To avoid complication, only the trajectory of particle 3 in each case is plotted. The particle trajectory with time is shown in Fig. 6.

The equilibrium position of particles stays unaltered with variation in slit clearance. The reduction in slit clearance increases the velocity at the channel center, and it should normally increase the effect of shear-induced lift which drives the particle equilibrium position toward either wall. However, the size of flow vortex plays an important role here. The strength and size of flow vortex increase with shortening of the slit clearance. Hence, this will act as a reverse force against the shear-induced lift, and hence, the additional effect of increased velocity gets canceled. This may be the reason for the unchanged equilibrium position. It is also noticeable from Fig. 6 that the particles take lower time to pass the slit for lower slit clearances. The size of the secondary flow vortex increases with reduction in slit clearance. Hence, the larger flow vortex deflects the particle in horizontal direction, and hence, the residence time decreases. The same behavior can be observed from Table 2 where the residence time for different slit clearances is tabulated.

Fig. 6 Particle trajectory with time for different S_g (Re = 50.0, $d = 0.2$ and $\Theta = \pi/2$, $\rho = 100.0$)
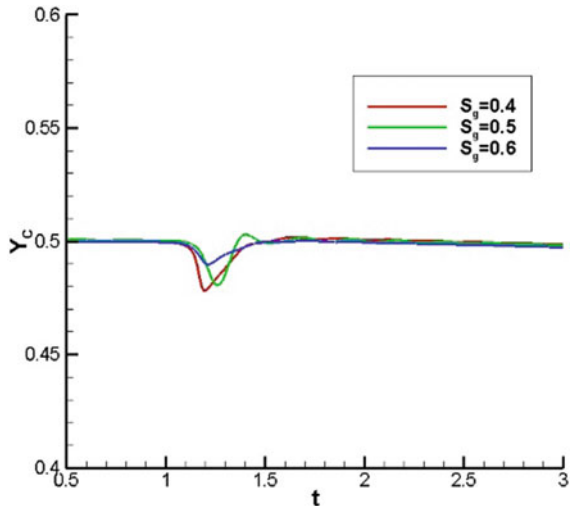
Table 2 Residence time (t_r) for different S_g

S_g	t_r
0.4	1.476
0.5	1.518
0.6	1.567

4.2 Influence of Slit Angle (Θ)

Here, the effect of different slit angles on the equilibrium position and residence time are analyzed. Three different slit angles such as π/4, π/2, and 3π/4 are selected for the study. In all three cases the particle diameter, Reynolds number, density ratio, and slit clearance are kept same (0.25, 50.0, 100.0, and 0.5, respectively). The particle trajectory with time for different slit angle is shown in Fig. 7.

The equilibrium position stays unaffected with slit angle. As the slit angle increases from π/4 to π/2, the size of secondary flow vortex increases. This will deflect the particle away from the wall. However, the same effect is canceled by the increase in flow velocity with change in slit angle from π/4 to π/2. When the slit angle is 3π/4, then the conditions are similar to that of π/4. The residence time is minimum for slit angle of π/2 since the flow velocity is highest and the vortex sizes are largest. To confirm the same, the residence time is given in Table 3.

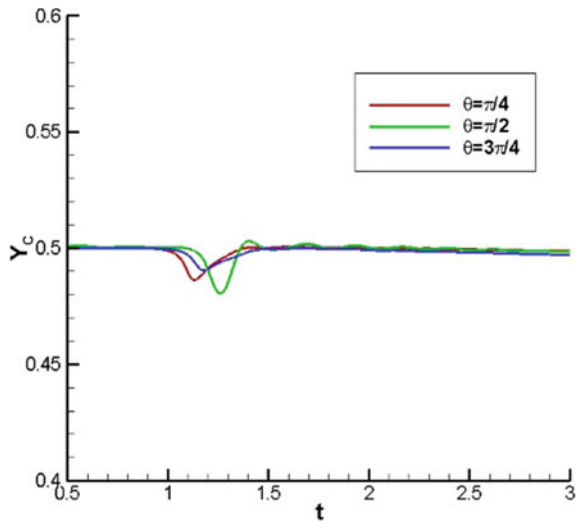**Fig. 7** Particle trajectory with time for different Θ (Re = 50.0, d = 0.2, S_g = 0.5, ρ = 100.0)

Table 3 Residence time (t_r) for different Θ (Re = 50.0, d = 0.2, S_g = 0.5)

Θ	t_r
π/4	1.583
π/2	1.518
3.0π/4	1.579

5   Conclusions

The migration of three rigid non-neutrally buoyant cylindrical particles in a slit channel is simulated by incorporating feedback forcing based immersed boundary finite volume method. The lateral migration of particles is studied by analyzing the equilibrium position and residence time. The particles initially released from left side of the slit separated by same center-to-center distance horizontally seem to move pass the slit and attain the equilibrium position. Further the effect of slit clearance and slit angle on equilibrium position and residence time is investigated. The equilibrium position stays unaffected with alteration in both slit clearance and angle. The velocity at the center of slit increases with reduction in slit gap and increase in slit angle from $\pi/4$ to $\pi/2$. However, the size of secondary flow vortices near the slit enlarges simultaneously. Both of these effects act in opposite direction and cancel out the effect of additional lift forces. On the other hand, the residence time reduces with shortening the slit clearance. The maximum velocity at slit center occurs for lowest slit clearance. The reduction in residence time may be due to this reason. It should be also noted that, the residence time is lowest for a slit angle of $\pi/2$. The flow velocity is highest, and secondary flow vortex size is largest for the same angle. Hence, the residence time seems to be lower.

Nomenclature

F_{Sh}	Shear-induced lift
F_W	Wall-induced lift
$\mathbf{u}$	Fluid velocity
t	Time
P	Pressure
Re	Reynolds number
$\mathbf{f}$	Eulerian force
$\mathbf{F}$	Lagrangian force
$\mathbf{U}$	Velocity of particle
Δ	Dirac delta function
$\mathbf{X}$	Lagrangian position
S	Lagrangian grid number
$\mathbf{U}_{ib}$	Velocity at immersed boundary point after interpolation
α, β	Large negative constants
Δt	Time step
$\mathbf{U}_P$	Translational velocity of the particle
$\mathbf{\Omega}_P$	Angular velocity of particle
X_C	Coordinate of center of cylinder
ds	Lagrangian grid size

References

1. Bazaz SR, Mashhadian A, Ehsani A, Saha SC, Krüger T, Warkiani ME (2020) Computational inertial microfluidics: a review. Lab Chip 20:1023. https://doi.org/10.1039/c9lc01022j
2. Segré G, Silberberg A (1962) Behaviour of macroscopic rigid spheres in Poiseuille flow: Part 1. Determination of local concentration by statistical analysis of particle passages through crossed light beams. J Fluid Mech 14:115. https://doi.org/10.1017/S002211206200110X
3. Rubinow SI, Keller JB (1961) The transverse force on a spinning sphere moving in a viscous fluid. J Fluid Mech 11:447. https://doi.org/10.1017/S0022112061000640
4. Abbas M, Magaud P, Gao Y, Geoffroy S (2014) Migration of finite sized particles in a laminar square channel flow from low to high Reynolds numbers. Phys Fluids 26:4902952. https://doi.org/10.1063/1.4902952
5. Frank M, Anderson D, Weeks ER, Morris JF (2003) Particle migration in pressure-driven flow of a Brownian suspension. J Fluid Mech 493:363. https://doi.org/10.1017/S0022112003006001
6. Saffman PG (1965) The lift on a small sphere in a slow shear flow. J Fluid Mech 22:385. https://doi.org/10.1017/S0022112065000824
7. Tam CKW, Hyman WA (1973) Transverse motion of an elastic sphere in a shear field. J Fluid Mech 59:177. https://doi.org/10.1017/S0022112073001497
8. Pan TW, Glowinski R (2002) Direct simulation of the motion of neutrally buoyant circular cylinders in plane Poiseuille flow. J Comput Phys 181:260. https://doi.org/10.1006/jcph.2002.7123
9. Inamuro T, Maeba K, Ogino F (2000) Flow between parallel walls containing the lines of neutrally buoyant circular cylinders. Int J Multiph Flow 26:1981. https://doi.org/10.1016/S0301-9322(00)00007-0
10. Peskin CS (1977) Numerical analysis of blood flow in the heart. J Comput Phys 25:220. https://doi.org/10.1016/0021-9991(77)90100-0
11. Shin SJ, Huang WX, Sung HJ (2008) Assessment of regularized delta functions and feedback forcing schemes for an immersed boundary method. Int J Numer Methods Fluids 58:263. https://doi.org/10.1002/fld.1706
12. Neeraj MP, Maniyeri R, Kang S (2022) Inertial migration of cylindrical particle in stepped channel—a numerical study. Lecture Notes in Mechanical Engineering, p 37–46. https://doi.org/10.1007/978-981-16-6928-6_4
13. Neeraj MP, Maniyeri R (2022) Lateral migration of cylindrical particle in a constricted microchannel—a numerical study. Can J Chem Eng. https://doi.org/10.1002/cjce.24473
14. Feng ZG, Michaelides EE (2004) The immersed boundary-lattice Boltzmann method for solving fluid-particles interaction problems. J Comput Phys 195:602. https://doi.org/10.1016/j.jcp.2003.10.013
15. Feng ZG, Michaelides EE (2009) Robust treatment of no-slip boundary condition and velocity updating for the lattice-Boltzmann simulation of particulate flows. Comput Fluids 38:370. https://doi.org/10.1016/j.compfluid.2008.04.013
16. Huang WX, Shin SJ, Sung HJ (2007) Simulation of flexible filaments in a uniform flow by the immersed boundary method. J Comput Phys 226:2206. https://doi.org/10.1016/j.jcp.2007.07.002
17. Maniyeri R, Suh YK, Kang S, Kim MJ (2012) Numerical study on the propulsion of a bacterial flagellum in a viscous fluid using an immersed boundary method. Comput Fluids 62:13. https://doi.org/10.1016/j.compfluid.2012.03.012
18. Maniyeri R, Kang S (2012) Numerical study on the rotation of an elastic rod in a viscous fluid using an immersed boundary method. J Mech Sci Technol 26:1515. https://doi.org/10.1007/s12206-012-0312-z
19. Huang L, Du J, Zhu Z (2021) Neutrally buoyant particle migration in Poiseuille flow driven by pulsatile velocity. Micromachines 12:2021. https://doi.org/10.3390/mi12091075

CFD Simulations for Thermal Qualification of a Radioactive Material Transport Cask

Sampath Bharadwaj Kota and Seik Mansoor Ali

1 Introduction

Radioactive materials are generally transported in shipping casks approved by the national regulatory body. The packages/casks are classified based on the activity and material it contains. Among the various types of casks, type B(U)/B(M) packages are used to transport significant activity radioactive material, such as teletherapy sources, gamma irradiators, and industrial radiography sources. Further, the spent fuel is also transported to a reprocessing facility in the type B(U) casks. Such packages are designed to withstand accident conditions during transport, and as part of compliance with the standards, these need to undergo a series of mechanical and thermal tests. The tests include, in sequence, a 9-m drop test, 1-m drop punch test, fire test, and an immersion test.

For thermal qualification of the casks, AERB [1] and IAEA [2] guidelines require the cask to be fire tested where the effects of a 30-min fire are to be considered. The criteria for the thermal test as stipulated in the [1] are outlined below:

- For steady-state analysis, the specimen should be in thermal equilibrium under an ambient temperature of 38 °C, subject to solar insolation and the maximum design internal heat generation rate within the cask from the radioactive contents.
- Further, the fire test analysis requires the cask to be tested for 30 min in a thermal environment that provides a heat flux equivalent to that of a hydrocarbon fuel–air fire in sufficiently quiescent ambient conditions to give a minimum average temperature of at least 800 °C.

Type B casks often use lead sandwiched between stainless steel/carbon steel shells to provide the necessary shielding from the gamma radiation emitted by the cask's contents. Since the melting point of the lead is low, i.e. 601 K, during the fire test, it is

S. B. Kota (✉) · S. M. Ali
Safety Research Institute, AERB, Mumbai, India
e-mail: ksb@aerb.gov.in

expected to melt. During the melting process, the lead could relocate, and shielding may be compromised [3]. Generally, compliance with the design standard is ensured either by subjecting the actual cask/its representative model to a fire test or by carrying out a detailed numerical study simulating the behaviour of the cask during the fire exposure period.

The behaviour of the lead melting process is a complex phenomenon, and the effect of Rayleigh convection on overall melting transient needs further investigation as it is crucial from the shielding perspective. As this issue is significant to the nuclear fraternity, this forms the motivation for the present work.

2 Brief Literature Review and Objective

The thermal qualification through analysis is often attempted by solving the 2-D or 3-D heat conduction equation [4–6], using the enthalpy formulation, ignoring the natural convection aspects. It is known that both diffusion and convection (due to the molten lead) processes co-occur, and they play an essential role in determining the actual fraction of molten lead. It is seen that most studies usually neglect the natural convection process associated with molten lead while modelling the fire test, which can lead to underestimation of the extent of melting. However, one of the studies modelled the convection process without accounting for the high Rayleigh number and associated turbulent natural convection expected during the fire test [7].

Further, a few authors reported CFD analysis using the porous media formulation of dry storage cask. Bae et al. [8] highlighted the packing fraction's effect on the cask's centreline temperature. Further, Herranz et al. [9] conducted sensitivity studies using CFD analysis for a spent fuel dry storage cask and found that heat load distribution is the most significant factor for the maximum fuel temperature in the cask.

Hitherto, the literature on thermal tests for transportation casks has not considered the more stringent hydrocarbon fuel–air fire curve for the analysis. Further, the analysis carried out by [3] has imposed convective boundary conditions based on forced convection. Therefore, in the present study, a detailed CFD analysis for thermal qualification of a typical type B(U) transport cask was carried out with a hydrocarbon fuel–air curve and a constant 800 °C ambient temperature in quiescent conditions, and the current study's findings are compared against the [3].

3 Modelling Aspects

A 2-D axisymmetric model was considered for the simulations, and geometrical details employed in the present study were adopted from [3]. The cask has lead material sandwiched between the inner stainless steel and outer mild steel. The geometrical details are shown in Fig. 1. The cylindrical cask has outer dimensions of 1785 mm in height and 715 mm in diameter. Further, the inner stainless steel cavity
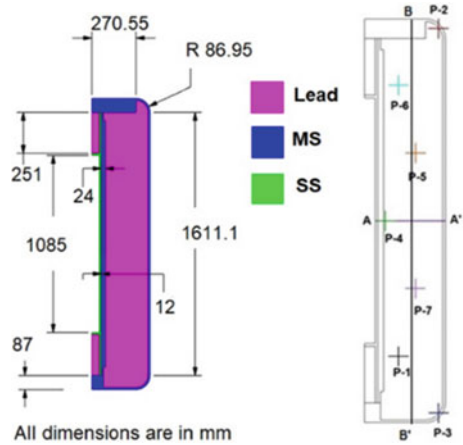
Fig. 1 Schematic diagram of the set-up

All dimensions are in mm

Table 1 Properties of the materials

Material	ρ (kg/m^3)	η (W/m K)	C_p (J/kg K)
Lead	10,768	40.28201–0.01853 × T (T < 601 K) 8.52726 + 0.01192 × T (T > 601 K)	140
Mild steel	7800	62.97356–0.03081 × T	510
Stainless steel	7800	10.21333 + 0.01517 × T	465

Table 2 Additional properties for lead

T_{ref} (K)	601
ρ_{ref} (kg/m^3)	10,768
β (K^{-1})	1.2234e−04
μ (kg/m s)	0.0032 at 601 0.00232 at 673.15 0.00154 at 873.15 0.00123 at 1073.15
L (J/kg)	26,000

is 1085 mm in height and 93 mm in diameter. The material properties employed in the present study are given in Tables 1 and 2.

3.1 Assumptions

- A 2-D axisymmetric domain is considered due to geometrical and thermal symmetry.
- Auxiliary components of the cask were not modelled.

- During the fire test, differential expansion of the molten lead and outer shell is neglected.
- The heat generation due to gamma interaction with structural materials is neglected.

3.2 Governing Equations

The conservation equations of mass, momentum, and energy are given by Eqs. (1), (2), and (3), respectively. In this study, the enthalpy-porosity technique was employed to study the melting of the shielding lead. Instead of explicitly tracking the interface, this technique calculates the interface based on an enthalpy balance.

$$\frac{\partial \rho}{\partial t} + \nabla \cdot (\rho \vec{v}) = 0 \tag{1}$$

$$\frac{\partial \rho \vec{v}}{\partial t} + \nabla \cdot (\rho \vec{v} \vec{v}) = -\nabla p + \nabla \cdot (\mu \nabla \vec{v}) + \rho \vec{g} - S_\phi \vec{v} \tag{2}$$

$$\frac{\partial (\rho H)}{\partial t} + \nabla \cdot (\rho \vec{v} H) = +\nabla \cdot (\eta \nabla T) \tag{3}$$

The energy equation takes into account both the sensible and latent heat as given in Eqs. (4), (5), and (6). For pure metals, as in the current case, both the solidus and liquidus temperatures are considered the same as the material's melting point, in this case, 601 K.

$$H = h + \Delta H \tag{4}$$

$$h = h_{\text{ref}} + \int_{T_{\text{ref}}}^{T} C_{\text{p}} dT \tag{5}$$

$$\Delta H = f_{\text{l}} L \tag{6}$$

As given in Eq. (7), appropriate momentum sink terms were added to the momentum equations to account for the pressure drop caused by the presence of solid material. The mushy zone constant (A_{mush}) is the measure of the damping associated with the solidification process. The higher the mushy zone constant, the faster material attains zero velocity upon solidification. The value ψ was considered as 0.001 to avoid division by zero while estimating the sink term. The value of the mushy zone constant was assumed as 10^6.

$$S_\phi = \frac{(1 - f_1)^2}{(f_1^3 + \psi)} A_{\text{mush}} \phi \tag{7}$$

The lead is expected to melt when the cask is exposed to a fire accident. The hot molten lead would rise inside the cask owing to its lighter density, and higher density lead would sink. Hence the density variation was modelled using the Boussinesq approximation to capture this phenomenon. The basis of this approximation is that though temperature-induced density variation is slight, the buoyancy-driven motion is significant. Thus, the effect of density variation is only considered in the buoyancy term of the momentum equation, as given in Eqs. (8) and (9) and is neglected elsewhere. The Boussinesq approximation is valid as long as $\beta(T - T_{\text{ref}}) \ll 1$. In the current set-up, for ΔT of 300 K, this value is around 0.0366.

$$(\rho - \rho_{\text{ref}})g \approx \rho_{\text{ref}} \beta(T - T_{\text{ref}}) \tag{8}$$

$$\rho = \rho_{\text{ref}}(1 - \beta \Delta T) \tag{9}$$

The magnitude of the Rayleigh number indicates whether the natural convection boundary layer is laminar or turbulent and is calculated using Eq. (10). In the present study, for a case where ΔT of 300 K and L of 1.5 m and the rest of the properties as given in Table 2, the Ra is around 8.3e11. So, it is safe to consider that the Rayleigh number would be on the higher side of 10^{11} during the fire test, which is in a turbulent regime.

$$\text{Ra} = \text{Gr} \times \text{Pr} = \frac{\rho g \beta \Delta T l^3}{\mu \kappa} \tag{10}$$

Therefore, the turbulence was appropriately modelled using the $k - \omega$ shear stress transport (SST) model to account for turbulent convection during the melting process. This model is apt for simulating moderate to high Rayleigh number convection-driven turbulent flows. The equations for the turbulence kinetic energy (k) and specific dissipation rate (ω) are given by Eqs. (11) and (12), respectively. This model combines $k - \omega$ formulation in the near wall region with a modified $k - \epsilon$ formulation in the far field by means of a suitable blending function. The parameters Γ_i, G_i, Y_i, S_i in the turbulence equations represent effective diffusivity, generation, dissipation, and source term, respectively.

$$\frac{\partial(\rho k)}{\partial t} + \nabla \cdot (\rho \vec{v} k) = -\nabla p + \nabla \cdot (\Gamma_k \nabla k) + G_k - Y_k + S_k \tag{11}$$

$$\frac{\partial(\rho \omega)}{\partial t} + \nabla \cdot (\rho \vec{v} \omega) = -\nabla p + \nabla \cdot (\Gamma_\omega \nabla k) + G_\omega - Y_\omega + S_\omega \tag{12}$$

3.3 Boundary Conditions

The simulations were carried out in two phases: normal conditions and heating due to exposure to fully engulfing fire representing hydrocarbon-air curve and average 800 °C ambient temperature.

3.3.1 Normal Conditions

A steady-state analysis was first carried out in which the outer cask surface was subjected to the convective heat transfer with an ambient temperature of 38 °C, along with the solar insolation of 800 W/m^2 and 400 W/m^2 for horizontal and vertical surfaces, respectively, as specified in the AERB safety code. The emissivity of the cask was assumed as 0.3, with a 7.4 kW heat flux imposed on the inner surface, accounting for the decay heat [3]. The boundary condition in a mathematical form is as shown in Eq. (13).

$$-\lambda_s \frac{\partial T_s}{\partial n} = \overline{h}_{s,\infty}(T_s - T_\infty) + \sigma \epsilon_s \left(T_s^4 - T_\infty^4\right) - \alpha_s q_{\text{solar}} \tag{13}$$

3.3.2 Fire Conditions

During the accidental fire condition, the cask is expected to be fully engulfed in the fire for about 30 min. To this end, four cases were simulated with the input conditions as given in Table 3. The first case corresponds to the scenario where the cask is exposed to the hydrocarbon fuel–air fire curve [as given in Eq. (14) in quiescent conditions]. The second case corresponds to the scenario where the average flame temperature was maintained at 800 °C for about 30 min. The third case was simulated to bring out the effect of convection in the melting process compared to the scenario where only diffusion was considered, as in the fourth case. The third and fourth cases were carried out at a constant heat transfer coefficient based on the Colburn relation with an assumed wind speed of 10 m/s and estimated to be 15 W/m^{2}K [3], except with a conservatively assumed surface absorptivity of 1.0. Further, the boundary condition on the outer surface of the cask exposed to accidental fire is as given in Eq. (15). During the fire exposure simulations, the surface-specific heat transfer coefficients are estimated based on the standard correlations available for the lower and upper surfaces of a cold and vertical plate [10]. The variation of surface-specific heat transfer coefficients for the top, bottom, and vertical surfaces of the cask is given in Fig. 2. Later on, this curve-fitted data was employed as a convective heat transfer coefficient as a function of ΔT in the form of Ansys Expressions.

$$T_f = T_\infty + 1080\left(1 - 0.325e^{-0.167t} - 0.675e^{-2.5t}\right) \tag{14}$$

Table 3 Simulation set-up conditions

Case	T_∞ (°C)	h (W/m^{2}K)	Effect	ϵ
1	HC-air curve	Figure 2	Diff + Conv	0.8
2	800	Figure 2	Diff + Conv	0.8
3	800	15	Diff + Conv	1.0
4	800	15	Diff	1.0

Fig. 2 Variation of heat transfer coefficients with respect to the temperature difference between the ambient and surface temperatures
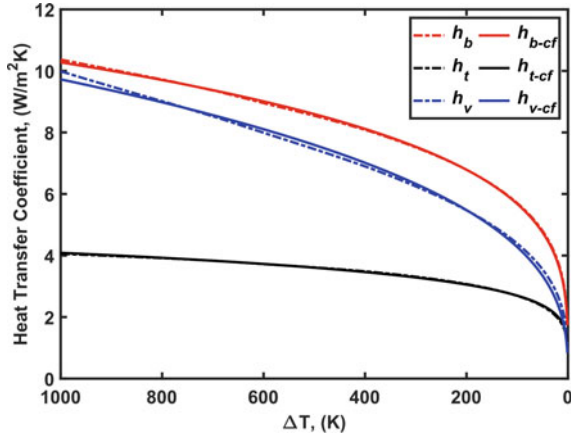
$$\lambda_s \frac{\partial T_s}{\partial n} = \overline{h}_{s,f}(T_f - T_s) + \sigma \epsilon_f T_f^4 - \sigma \alpha_s T_s^4 \tag{15}$$

3.4 Solution Procedure

The continuity and momentum conservation equations were solved using the coupled algorithm available in the Ansys Fluent. This algorithm is a fully implicit pressure-based solver, solving the momentum and pressure-based continuity equations together. Second-order upwind discretisation schemes were used for spatial discretisation of pressure, momentum, energy, and two-parameter turbulence equations. The continuity, momentum, and turbulence equations were considered fully converged when the sum of scaled residuals was less than 10^{-5} and energy was considered fully converged when the sum of scaled residuals was less than 10^{-8}. The adaptive time step was used for the current simulations, ranging from 1e−05 to 0.025 s.

At first, steady-state simulations were carried out for normal conditions in which the cask was exposed to solar insolation. After that, this steady-state solution was used as an initial condition for the fire test. During the fire test simulation, the boundary

conditions of ambient temperatures and surface-specific heat transfer coefficients for each case are given as inputs in the Ansys Expressions [11].

3.5 Mesh Sensitivity Study and Validation

Grid independence was carried out with an average mesh size of 2, 3, and 5 mm, and the respective cells were 146,000, 65,000, and 23,100. The temperature profiles plotted on the sectional line AA′ is shown in Fig. 3. The steady-state results yielded similar results for all three grid sizes; therefore, current simulations were carried out on a 3 mm mesh-size grid.

Experimental validation results for this large-tonnage cask may not be available in the literature due to the high expense of validation. Specifically, there are no experimental data about the exposure of this double-bundle radioactive transport cask to the hydrocarbon fire curve. As an alternative to these expensive tests, comprehensive simulations that account for all the physics involved in the melting process are performed. Nevertheless, the approaches and constants employed in this work are derived from the literature, and the current results are in excellent agreement with the numerical results [3] discussed in the following section. In fact, regulatory authorities recommend either numerical or experimental research for qualifying reasons [1].

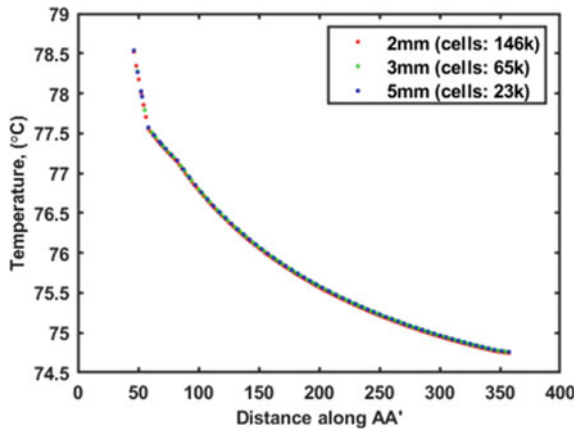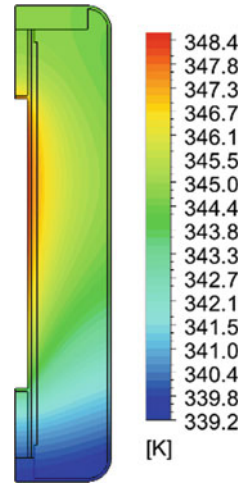**Fig. 3** Steady-state temperature profile in the radial direction along the line AA′ for various grid sizes

Fig. 4 Steady-state
temperature under normal
conditions

4 Results and Discussion

4.1 Normal Condition

The cask was subjected to solar insolation, convective heat transfer on the outer surface, and heat flux equivalent to the decay heat on the inner surface. It is seen from Fig. 4 that the steady-state temperature is maximum in the upper region of the inner surface and minimum on the bottom surface. This temperature variation could be attributed to the higher value of solar insolation on the top horizontal surface compared to zero insolation on the bottom horizontal surface. The minimum and maximum temperatures were found to be 339 and 349 K on the outer bottom and inner top surfaces, respectively. It could also be observed that the upper region of the internal surface is the hottest area because of the decay heat and maximum solar insolation on the top outer surface. The maximum temperature encountered in the study is lower than the stipulated temperature of 358.15 K.

4.2 Fire Test

4.2.1 Hydrocarbon Fuel–Air Curve

The temporal variation of molten during the fire test is shown in Fig. 5. During the hydrocarbon fuel–air fire test simulation, the lead started melting between 680 and 690 s.

It can be observed that the melting commenced in the edges of the cask, and then the melt front propagated into the interior of the domain as time progressed. It can
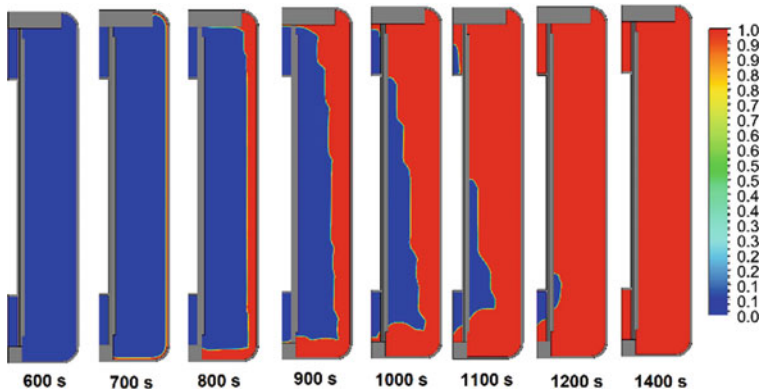
Fig. 5 Contours of the liquid fraction of molten lead at various time instances

also be observed that the molten lead quantity is similar in both upper and bottom regions up to about 800 s. After that, it can be observed that the quantity of molten lead was high in the upper region than in the bottom region. This variation can be attributed to the Rayleigh convection encountered in the present case.

Here, the hot and lighter molten lead adjacent to the outer mild steel wall would rise, whereas the denser molten lead in the interior region would sink. The hotter molten metal is relocated to the upper region of the cask, thereby significantly increasing the portion of the melted lead in the upper region. By the end of the 1240 s, it was observed that the entire lead melted when exposed to the hydrocarbon fuel–air standard curve.

4.2.2 Constant Ambient Temperature of 800 °C

Similar trends were observed for case 2, where the cask was exposed to a constant ambient temperature of 800 °C. However, as the test was less stringent than the hydrocarbon fuel–air test, the portion of molten lead by the end of 30 min was noted to be about 70% (Fig. 6).

4.2.3 Effect of Natural Convection

The effect of natural convection on the quantity of the molten lead present is brought out by comparing cases 3 and 4. In case 4, the Boussinesq approximation was neglected, effectively solving only the energy equation. It can be observed from Fig. 7 that by the end of 30 min, ~ 70% of the mass fraction is molten lead. However, when both convection and diffusion processes were considered in modelling, the
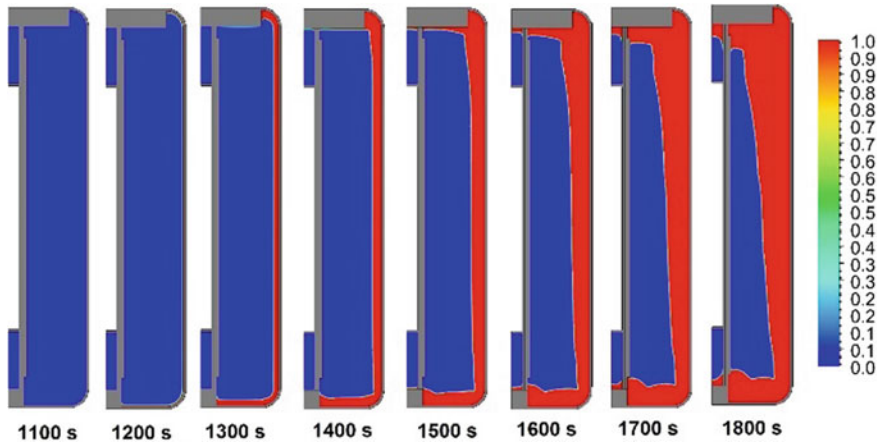
Fig. 6 Contours of the liquid fraction of molten lead at various time instances

amount of melting was ~ 95%. This increase in molten lead signifies the importance of modelling the convection process during phase change. Therefore, natural convection is vital in determining the amount of lead melting.

Further, the vertical velocities along the sectional line AA′ at various instances are shown in Fig. 8. It was observed that the vertical velocities are positive near the outer wall and negative for the inner region, indicating the circulation to be in a counter-clockwise direction. Further, the highest velocities were observed about 20 min into the transient fire test analysis. The magnitude of peak velocities was around ~ 75–80 mm/s, and the velocities were negligible for the intermediate zone, as shown in Fig. 8. Further, the negative peak velocities shift towards the inner region, representing the melting of the lead. However, the peak velocities start decreasing

Fig. 7 Temporal variation of the volume-averaged molten lead in the case of convection-conduction model and conduction-only model
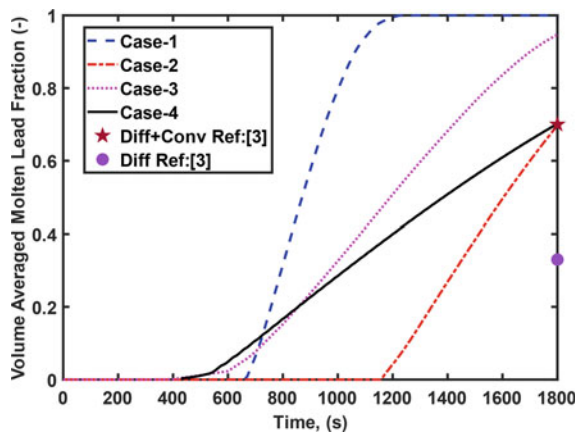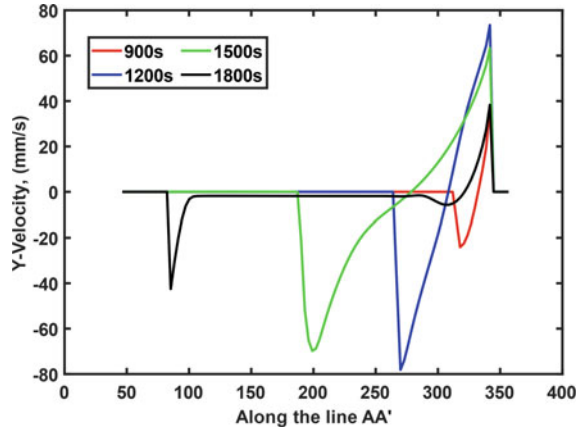
Fig. 8 *Y*-velocities along the AA′ line at various time instances

in magnitude, and this variation could be attributed to the decreased buoyant effect and increased frictional losses.

4.2.4 *Comparison with Sanyal et al.* [3]

Sanyal et al. [3] performed two simulations for the current cask design, with an average ambient temperature of 800 °C, either considering or ignoring the convection effect. It is observed from Fig. 7 that the fire test in case 2 (i.e. constant 800 °C) produces a similar amount of 70% molten lead as that of [3], though, in the current study, surface and temperature-dependent heat transfer coefficients were employed. Further, when the hydrocarbon fuel–air curve was employed, the lead was melted entirely even before the completion of the fire test. Therefore, one can consider the hydrocarbon fuel–air curve fire test as the most demanding thermal qualification test criterion compared to the one presented in [3].

Further, when cases 3 and 4 are compared with [3], it was observed that with an increase in absorptivity from 0.8 to 1.0, the total molten lead content increased from 70 to 95%, where convection effects are considered. Similarly, molten lead content increased from 33 to 70% for the cases with ignored convection effects, while absorptivity increased from 0.8 to 1.0

5 Conclusions

The following conclusions can be drawn from the present study:

(a) The shielding material was melted entirely when the cask was exposed to a hydrocarbon fuel–air fire test by the end of 1240 s.

(b) The volume-averaged molten lead was estimated to be 69.7% when the cask was engulfed in the constant ambient temperature of 800 °C in quiescent conditions.
(c) The buoyancy-induced natural circulation accelerated lead melting, which was observed to be 94.75% and 70.02% in cases 3 and 4, respectively.
(d) During the melting process, the Rayleigh convection imparted counter-clockwise circulations within the cask, thereby increasing the melting in the upper region.

Nomenclature

A	Surface area (m^2)
A_{mush}	Mushy zone constant
C_p	Specific heat (J/kg K)
f_l	Liquid fraction (–)
G	Generation
g	Acceleration due to gravity (m/s^2)
H	Enthalpy (J/m^3)
$\bar{h}$	Heat transfer coefficient (W/m^2 K)
k	Turbulence kinetic energy (m^2/s^2)
L	Latent heat (J/kg)
l	Length (m)
Nu	Nusselt number (–)
Pr	Prandtl number (–)
Q	Heat generation (W)
q	Heat flux (W/m^2)
Re	Reynolds number (–)
Ra	Rayleigh number (–)
S	Source ($–/m^3$)
T	Temperature (K)
t	Time (s)
V	Volume (m^3)
$\vec{v}$	Velocity (m/s)
Y	Dissipation
x, y, z	Coordinates

Greek symbols

α	Absorptivity (–)
β	Coefficient of volumetric expansion (K^{-1})
ϵ	Emissivity (–)

λ	Thermal conductivity (W/mK)
κ	Thermal diffusivity (m^2/s)
ρ	Density (kg/m^3)
σ	Stefan-Boltzmann constant $= 5.67e{-}08$ (W/m^2 K^4)
φ	Velocity/turbulence quantity (k, ω) in the source terms
Γ	Effective diffusivity
ω	Specific dissipation rate (1/s)
μ	Viscosity (kg/ms)

Subscripts

∞	Ambient
b	Bottom
f	Fire/flame
ref	Reference
t	Top
s	Surface
solar	Solar insolation
v	Vertical

References

1. AERB (2016) Safe transport of radioactive material. Atomic Energy Regulatory Board, Mumbai. https://www.aerb.gov.in/images/PDF/CodesGuides/RadiationFacility/Transport/1.pdf (accessed December 1, 2021)
2. IAEA (2006) Optimization strategies for cask design and container loading in long term spent fuel storage. IAEA, Vienna
3. Sanyal D, Goyal P, Verma V, Chakraborty A (2011) A CFD analysis of thermal behaviour of transportation cask under fire test conditions. Nucl Eng Des 241:3178–3189. https://doi.org/10.1016/j.nucengdes.2011.06.017
4. Ali SM, Verma V, Markandeya SG, Ghosh AK (2006) Transient thermal analysis of an exposure device for normal, fire and post fire test conditions. In: HMTC-2006-C226, IIT Guwahati, India
5. Goyal P, Verma P, Singh RK, Ghosh AK (2009) Thermal analysis of a spent fuel transportation cask
6. RD Manteufel, NE Todreas (1994) Effective thermal conductivity and edge conductance model for a spent-fuel assembly. Nuclear Technol 105:421–440. https://doi.org/10.13182/NT94-A34941
7. Heng X, Zuying G, Zhiwei Z (2002) A numerical investigation of natural convection heat transfer in horizontal spent-fuel storage cask. Nucl Eng Des 213:59–65. https://doi.org/10.1016/S0029-5493(01)00454-X
8. Bae J, Bean R, Abboud R (2020) CFD analysis of a dry storage cask with advanced spent nuclear fuel cask additives. Ann Nucl Energy 145:107610. https://doi.org/10.1016/j.anucene.2020.107610

9. Herranz LE, Penalva J, Feria F (2015) CFD analysis of a cask for spent fuel dry storage: Model fundamentals and sensitivity studies. Ann Nucl Energy 76:54–62. https://doi.org/10.1016/j.anucene.2014.09.032

10. Incropera FP, Dewitt DP, Bergman TL, Lavine AS (2003) Section 9.6: empirical correlations: external free convection flows. In: Fundamentals of Heat and Mass Transfer, 7th ed. Wiley, pp 604–613

11. Ansys Fluent User's Guide (nd) Release 19.2, Ansys, Inc

Numerical Study of Twin-Wall Jet Interacting with Different Surfaces

S. V. H. Nagendra and D. V. S. Bhagavanulu

1 Introduction

The concept of dynamics of the jet flows has been studied extensively as it is developed in different ways like a jet coming out horizontally out of an orifice, or a nozzle parallel and away from the surface is designated as a free turbulent jet. Wall-bounded jet flows are further classified into two different forms, i.e., plane wall jet and impinging jet. If the jet is parallel to the surface and wall-bounded, it is known as an offset jet; similarly, if the jet has a wall jet as well as offset jet configuration, it is known as a twin jet or dual jet. The application of twin jets is found in mixing processes in gas turbines, combustion chambers, vertical take-off aircraft, film cooling, HVAC, etc.

Initially reported work on flow characteristics of a wall jet was given by Forthman [1]. An extensive review of experimental work done until 1980 is presented by Launder and Rodi [2]. Numerical work during the 80s is reviewed by Launder and Rodi [3]. Gibson and Younis [4] presented a review on moderately curved jets. Flow over the strongly curved surfaces was given by Kobayashi and Fujisawa [5] and Gowda and Durbha on different convex cylindrical surfaces [6]. Similarly, a wall jet over a convex surface was also studied by Alcaraz et al. [7] and Wilson and Goldstein [8], while Neuendorf and Wygnanski [9] studied the effect of surface curvature on the development of a two-dimensional wall jet around a circular cylinder. Yukawa and Shakuochi [10], Sawyer [11], Rajaratnam and Subramanyam [12], Hoch and Jiji [13], and Nozaki [14] have studied the mean flow parameters. Davis and Winarto [15] and Agelin-Chaab and Tachie [16] worked on a three-dimensional round offset jet using a hot wire anemometer with different offset ratios. They found maximum decay rate, spread rates in the extent of 0–120d.

S. V. H. Nagendra (✉) · D. V. S. Bhagavanulu

Department of Mechanical Engineering, Gyan Ganga Institute of Technology & Sciences, Jabalpur 482001, India
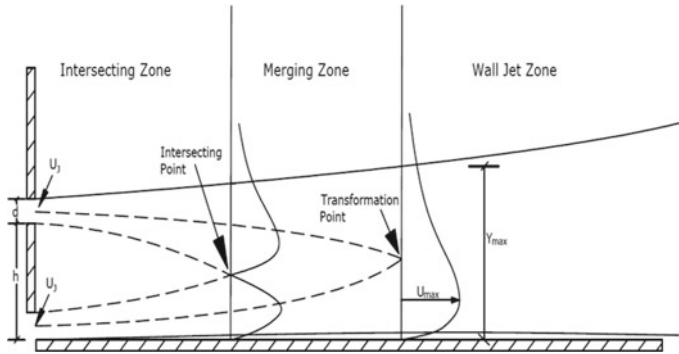
e-mail: svhnagendra@gmail.com

Fig. 1 Twin jet details generated over a plane surface

Twin jets as shown in Fig. 1 are studied by Wang and Tan [17], Assoudi et al. [18], Anderson and Spall [19], and Kumar [20] and found the mean flow parameters of twin jets like intersection point, vortex center, decay of maximum velocity, turbulent viscosity, jet half width, momentum flux, etc.

2 The Experimental Setup and Methodology

In this study, the mean flow parameters of the twin jet have been studied like mean velocity profiles, decay of maximum velocity, jet spread over three different types of surfaces, namely plane, inclined, and convex surface as shown in Fig. 2. The numerical modeling has been performed using a commercial computational tool. The inlet orifice has a diameter of "d"; there are eight stations of investigation where the velocity profile values are calculated. Three aspect ratios were selected for all three surfaces that are 2.0, 3.0, and 4.0 in the numerical investigation. Further, the results are compared with the existing experimental results of wall jet on a plane surface and convex surface (3.0 m radius), respectively. In the computational domain as well as experimental setup, initial straight portion is taken equal to 20d to provide sufficient length for the development of the flow [20], and the experimental setup is shown in Fig. 3. The two-dimensional computational domain uses unstructured triangular mesh. The RSM model is used for solving the flow regime using second-order advection scheme.

The exact transport equations for the transport of the Reynolds stresses $\rho u_i' u_j'$ may be written as follows:

$$\frac{\partial}{\partial t}\left(\rho \overline{u_i' u_j'}\right) + \frac{\partial}{\partial xk}\left(\rho u_k \overline{u_i' u_j'}\right) =$$

Local Time Derivative $C_{ii} \equiv$ Convection

Fig. 2 Inclined surface and convex surface

Inclined Surface with 10 Degree Inclination

Convex Surface with Radius 3.0m

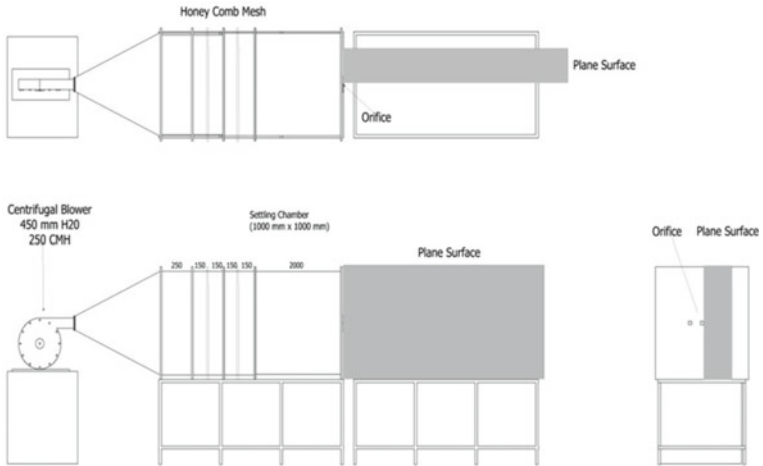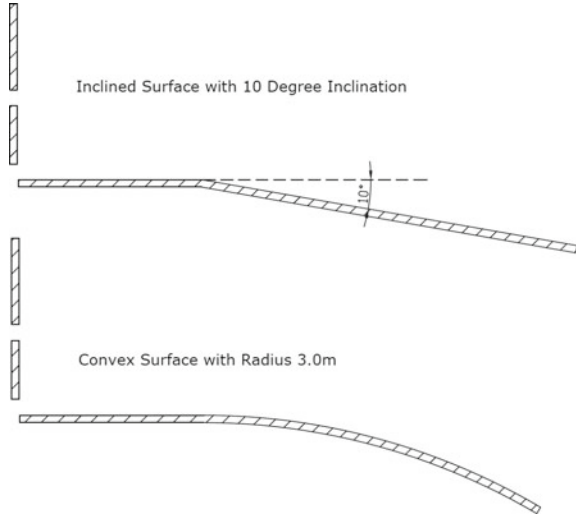**Fig. 3** Schematic diagram of the jet tunnel setup with plane surface

$$-\frac{\partial}{\partial xk} \cdot \left[\rho \overline{u'_i u'_j u'_k} + \overline{p \left(\delta_{kj} u'_i + \delta_{ik} u'_j \right)} \right]$$

$D_{T,ij} \equiv$ Turbulent Diffusion

$$+\frac{\partial}{\partial x_k} \left[\frac{\mu.\partial}{\partial x_k} \cdot \left(\overline{u'_i u'_j} \right) \right] - \rho\beta \left(g_i \overline{u'_j \theta} + g_j \overline{u'_i \theta} \right)$$

$D_{l,ij} \equiv$ Turbulent Diffusion $G_{ij} \equiv$ Buoyancy Production

$$+ \overline{p\left[\frac{\partial u_i'}{\partial x_j} + \frac{\partial u_j'}{\partial x_l}\right]} - 2\mu . \overline{\frac{\partial u_i'}{\partial x_k} . \frac{\partial u_j'}{\partial x_k}} -$$

$\Phi_{ij} \equiv$ Pressure Strain $\quad \in_{ij} \equiv$ Dissipation

$$2\rho\Omega_k\left(\overline{u_j'u_m'} \in_{ikm} + \overline{u_i'u_m'} \in_{jkm}\right)$$

$F_{ij} \equiv$ Production by system rotation

$\quad + S_{user}$ (Source Term) $\hfill$ (1)

The terms in these exact equations such as C_{ij}, D_{Lij}, P_{ij}, and F_{ij} do not require any modeling. However, D_{Tij}, G_{ij}, φ_{ij}, and $\in_{ij}$ need to be modeled to close the equations. D_{Tij} is a diffusivity term that is modeled using the gradient diffusivity model by Daly and Harlow.

The exit jet Reynolds number is taken as 57,285 for individual orifice. Pressure values at the outlet and open boundaries are taken as atmospheric pressure.

The convergence criteria set for the analysis are 1e−4. The grid independence test is also performed for the value of velocity at station 20d and 30d for all three surfaces, and the optimized grid size is selected accordingly.

3 Results and Discussion

The results are post-processed in the form of $X–Y$ dataset analyzed for different parameters like the intersection point of two jets, transforming points of two jets mean velocity profiles, and decay of maximum velocity.

3.1 Intersection and Transformation Point

The intersection point is the position where the outer layer of the two jets intersects each other, and the combination point is the position where the jets shows the characteristics of the wall jet. Table 1 shows the position of the intersection point over the different surfaces with different aspect ratios with respect to the diameter of the orifice. In the case of aspect ratio 2.0, the intersection point is very nearer to the orifice which is about $1d$, and the intersection point shifts toward downstream with the increase in aspect ratio.

As the fluid moves downward from the two orifices, it starts transforming from twin jet to wall jet and the profiles formed between 20 to 22d when the aspect ratio is 2.0; as the ratio increases to 3.0, the range changes from 22 to 25d. Similarly for aspect ratio 4.0, the position is near to 25d. After the transformation point, the velocity profile agrees well with the profile as shown in Fig. 13.

Table 1 Position of intersection point and combination point

Aspect ratio	Surface	Intersection point	Combination point
AR 2.0	Plane	Near 1d	20–25d
	Inclined	Near 1d	20–25d
	Convex	Near 1d	20–25d
AR 3.0	Plane	< 5d	20–25d
	Inclined	< 5d	22–25d
	Convex	< 5d	22–25d
AR 4.0	Plane	< 10d	25d onward
	Inclined	< 10d	25d onward
	Convex	< 10d	25d onward

3.2 Mean Velocity Profiles

Figures 4, 5, 6, 7, 8, 9, 10, 11 and 12 show the mean velocity profiles drawn between U by U_{max} and Y/Y_{max}. As two jets move forward, a vortex is formed, and it shows a reverse flow pattern before 1d in case of aspect ratio 2.0 and is extending upto10d at aspect ratio equal to 4.0.

At an aspect ratio 2.0, the maximum velocity position is 0.04 of all three surfaces. As the aspect ratio increases, the value shows a decreasing tendency, i.e., at 3.0 and 4.0; it is 0.035 and 0.03, respectively. From the velocity profiles, it is observed that with the increase in aspect ratio, the reverse flow occurs at the locations close the jet exit. As the jet moves downstream direction, the twin jet transforms in to a single jet and forms wall jet profile. This distance increases with the increase in aspect ratio. As it is stated earlier that at $x/d = 30$, the wall jet is formed in all the three cases considered in the present work (Fig. 13).

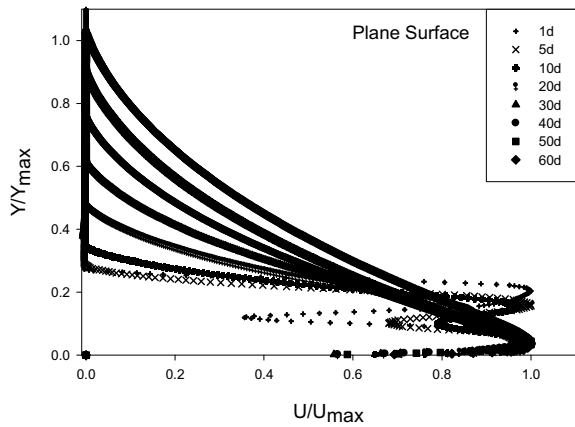**Fig. 4** Mean velocity profiles on plane surface with AR 2.0

Fig. 5 Mean velocity profiles on inclined surface with AR 2.0
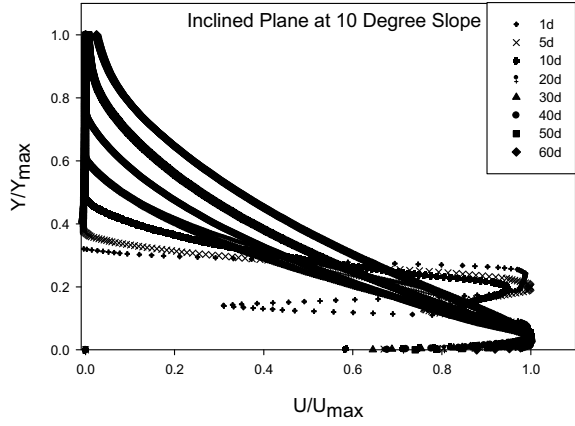

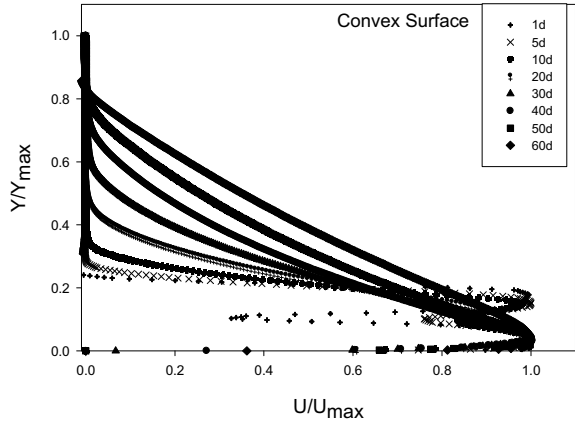**Fig. 6** Mean velocity profiles on convex surface with AR 2.0

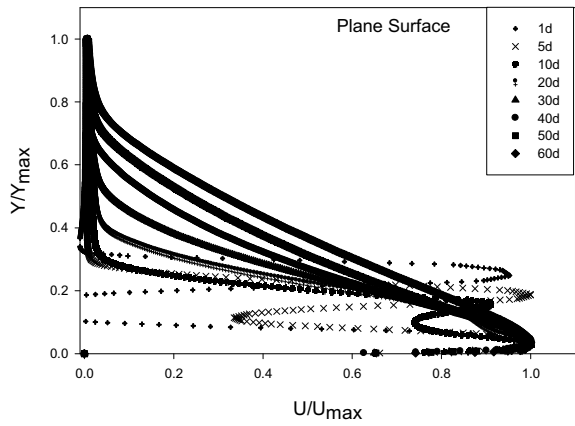**Fig. 7** Mean velocity profiles on plane surface with AR 3.0

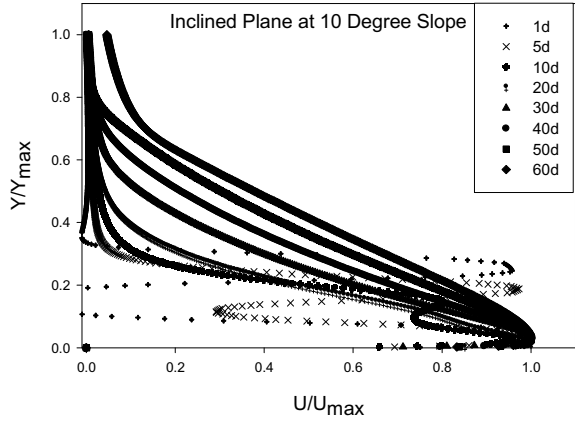**Fig. 8** Mean velocity profiles on inclined surface with AR 3.0

Fig. 9 Mean velocity profiles on convex surface with AR 3.0
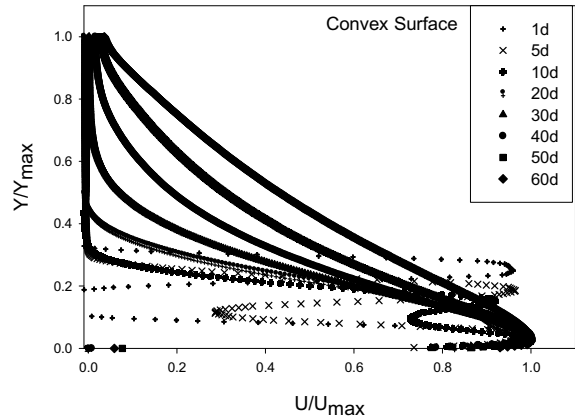

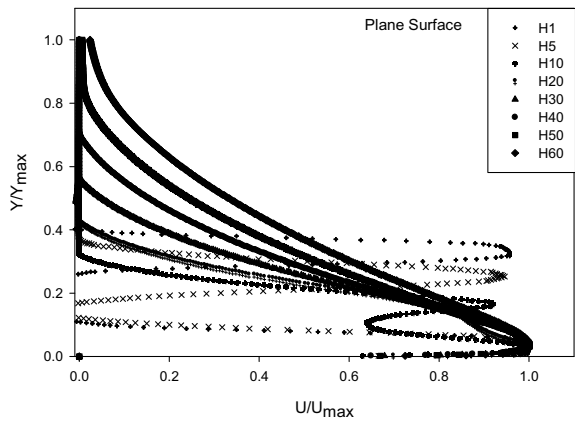**Fig. 10** Mean velocity profiles on plane surface with AR 4.0

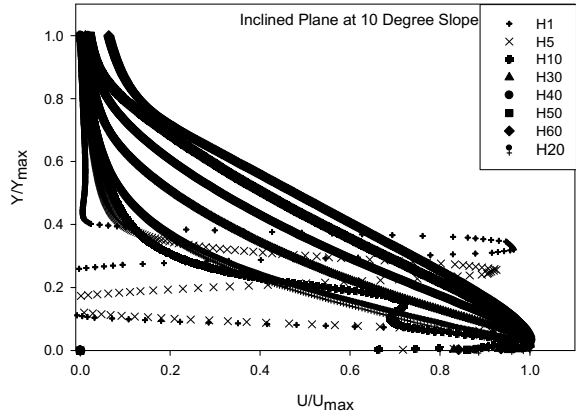**Fig. 11** Mean velocity profiles on inclined surface with AR 4.0

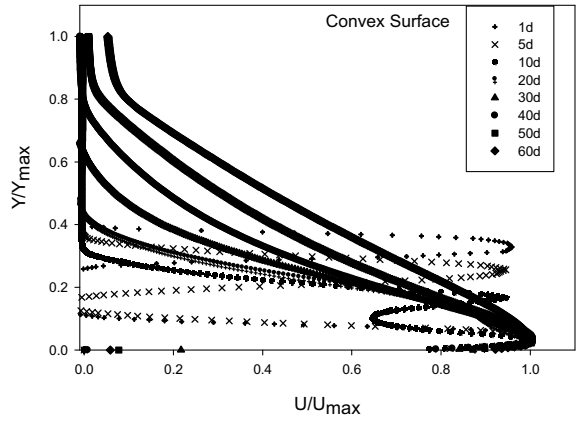**Fig. 12** Mean velocity profiles on convex surface with AR 4.0

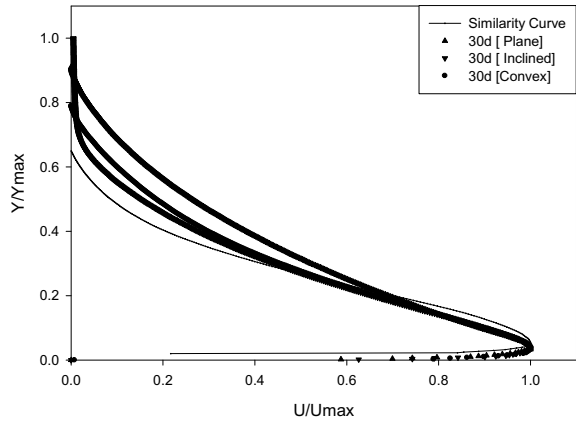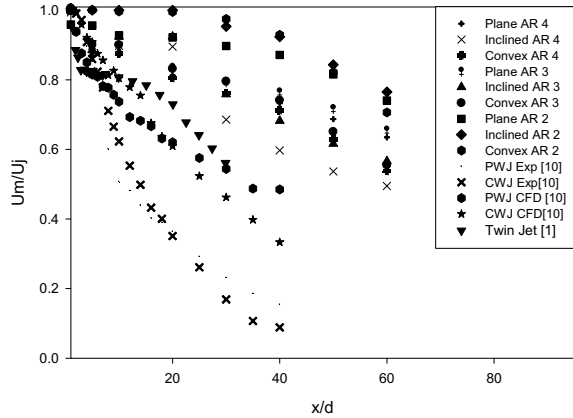**Fig. 13** Compares the velocity profile at 30*d*

Fig. 14 Decay of maximum velocity over all the surfaces

3.3 Decay of Maximum Velocity

Maximum velocity decay is plotted between x/d versus U_m/U_j, it exhibits the decay of maximum velocity at different stations of concern as shown in Fig. 14. At aspect ratio 2.0, the decay exponent is $- 0.18$, and it increases to $- 0.21$ at aspect ratio 4.0 for the plane surface; for the convex surface, it is $- 0.29$, $- 0.35$, and $- 0.43$, respectively. The decay of velocity is faster on an inclined plane when compared to plane and convex, and it is $- 0.29$ for aspect ratio 2.0, and it increases to $- 0.43$ and $- 0.53$ at aspect ratio 3.0 and 4.0, respectively. The decay of maximum velocity of the convex surface lies between the plane and inclined surface which is shown in Table 2. The decay on convex surface is faster when compared to plane surface, and it is slower when compared to inclined surface. This is mainly due to rolling vortices which are forming over convex surface. It is also seen that the decay rate of the twin jet is significantly slower than the plane wall jet.

Table 2 Details of decay exponent over different surfaces

S. no.	Type of surface	Aspect ratio (h/d)	Extent	Decay exponent
1	Plane	2	20–60	− 0.18
2	Inclined	2	20–60	− 0.29
3	Convex	2	20–60	− 0.29
4	Plane	3	20–60	− 0.2
5	Inclined	3	20–60	− 0.43
6	Convex	3	20–60	0.35
7	Plane	4	20–60	− 0.21
8	Inclined	4	20–60	− 0.53
9	Convex	4	20–60	− 0.43
10	Plane	Wall jet	20–40	− 1.19
11	Convex	Wall jet	20–40	− 1.45
12	Plane (CFD)	Wall jet	20–40	− 1.55
13	Convex (CFD)	Wall jet	20–40	− 1.3
14	Plane [17]	Dual jet	20–30	− 0.64

4 Conclusion

The present paper analyzed the twin jet flow for different surfaces, and flow charac-
teristics are compared with the wall jet. The intersection and transformation points
are efficiently located. The position of maximum velocity is also determined. The
mean velocity profile shows good agreement with existing literature at $x/d = 30$. It
is also observed that the decay of maximum velocity increases as the aspect ratio
increases from 2.0 to 4.0 in all three surfaces. Further decay rates also show that the
twin jets are slower when compared to plane wall jets and convex curved wall jet.
The decay rate is faster over inclined surface when compared to convex and plane
surfaces. The location of reverse flow was found closer to the exit for all the aspect
ratios considered in the present study.

Nomenclature

AR   Aspect ratio h/d (–)
PWJ   Plane wall jet
CWJ   Convex wall jet
d Diameter of orifice (mm)
h Distance between two adjacent orifice (mm)

References

1. Forthman E (1934) Turbulent jet expansion. Ingenieur-Arch 5:42
2. Launder BE, Rodi W (1981) The turbulent wall jet. Prog Aerosp Sci 19:81–128
3. Launder BE, Rodi W (1983) The turbulent wall jet. Annu Rev Fluid Mech 15:429–435
4. Gibson MM, Younis BA (1982) Modeling of curved turbulent wall jet. AIAA 20:1707–1712
5. Kobayashi R, Fujisawa N (1983) Curvature effects on two-dimensional wall jet along concave surfaces. Bull JSME 26:2074–2080
6. Gowda BH, Durbha VSB (2001) Turbulence measurements in three-dimensional wall jets on convex cylindrical surfaces. Indian J Eng Mater Sci 8:313–317
7. Alcaraz E, Charnay G, Mathieu J (1977) Measurements in wall jet over a convex surface. Phys Fluids 20:203–210
8. Wilson DJ, Goldstein RJ (1976) Turbulent jets with cylindrical stream wise surface curvature. J Fluids Eng Trans ASME 98:550–557
9. Neuendorf R, Wygnanski I (1999) On a turbulent wall jet flowing over a circular cylinder. J Fluid Mech 381:1–25
10. Ayukawa K, Shakouchi T (1967) Analysis of a jet attaching to an offset parallel plate (1st report, oscillation of a jet). Bull JSME 19:395–401
11. Sawyer RA (1960) The flow due to a two dimensional jet issuing parallel to a flat plate. J Fluid Mech 9:543–561
12. Rajaratnam N, Subramanya K (1968) Plane turbulent reattached wall jets. J Hydraul Div 94:95–112
13. Hoch J, Jiji LM (1981) Theoretical and experimental temperature distribution in two dimensional turbulent jet boundary interaction. J Heat Transf 103:331–335
14. Nozaki T (1983) Reattachment flow issuing from a finite width nozzle: effects of aspect ratio of the nozzle. Bull JSME 26(221):1884–1890
15. Davis MR, Winarto H (1980) Jet diffusion from a circular nozzle above a solid plane. J Fluid Mech 101:201–221
16. Agelin-chaab M, Tachie MF (2011) Characteristics of turbulent three-dimensional offset jets. J Fluids Eng 133(5):051203-1–051203-9
17. Wang X, Tan S (2007) Experimental investigation of the interaction between a plane wall jet and a parallel offset jet. Exp Fluids 42(4):551–562
18. Assoudi A, Said NM, Bournot H, Palec GL (2018) Comparative study of flow characteristics of a single offset jet and a turbulent dual jet. Heat Mass Transf 55:1109–1131
19. Anderson E, Spall R (2001) Experimental and numerical investigation of two-dimensional parallel jets. J Fluids Eng 123:401–406
20. Kumar A (2015) Mean flow characteristics of a turbulent dual jet consisting of a plane wall jet and a parallel offset jet. Comput Fluids 114:48–65

CFD Analysis of Data Center Using Open-Source Software: OpenFOAM

Hrishikesh Kulkarni and Dilshad Ahmad

1 Introduction

A data center is a facility that hosts information technology (IT) equipment such as computers, servers, and power distribution units inside it. While in operation, this equipment generates a large amount of heat which results in the reduction of the performance of this equipment. To operate this equipment effectively, the temperature of this equipment needs to be maintained within prescribed limits as specified by Ashrae [1, 2]. This necessitates the dissipation of heat generated during equipment operation from the data center to the outside. Generally, the air is used to carry heat from this equipment. A data center, therefore, is designed to supply cold air from chillers to this equipment and carry heated air away from them.

A typical data center has a raised floor arrangement which splits it into two parts [3]. The upper portion is called 'room', while the lower portion is called 'plenum'. The room hosts all types of IT equipment, while plenum facilitates flow of cold air from computer room air conditioners (CRACs) to the room through perforated tiles. The IT equipment are placed inside racks having multiple sections in it. They are provided with cooling fans to dissipate heat from these equipment. The tiles are placed near the suction side of the fans so that the cold air from the CRAC directly enters the IT equipment through the plenum. During operation of the data center, air, while passing through the IT equipment, gets heated up and exhausted at the other side of the rack through fan. This hot air is directed to the CRAC for cooling through ducts.

Generally, in a data center, about 40% of the total power consumed is contributed by the air conditioning system itself, and thus, cooling cost contributes to a major portion of the total cost of data center operation [4]. To reduce this cost, it is necessary to have an efficient cooling system for a data center. The most efficient cooling of the

H. Kulkarni · D. Ahmad (✉)
TCS Research, Sahyadri Park, Phase 3, Hinjawadi, Pune, Maharashtra 411057, India
e-mail: dilshad.ahmad@tcs.com

data center can be achieved by understanding details of the fluid flow and heat transfer phenomena occurring inside it. A detailed understanding of airflow and heat transfer inside data center is possible by modeling flow and heat transfer with computational fluid dynamics (CFD) approach [5].

2   Literature Review and Objective

A number of researchers have used CFD to understand flow and thermal profiles inside a data center and have come up with suggestions to improve cooling efficiency of the data center. For example, Gao et al. [6] have studied the effect of airflow patterns inside data center on cooling effectiveness using CFD simulation. Moreover, a CFD approach also provides ways to optimize different equipment arrangement, physical parameters, and geometric parameters for effective cooling of equipment inside data center [7]. A parametric CFD study of computer room air handling bypass in air-cooled data centers is done by Ahmadi et al. [8]. In this work, author has carried out CFD modeling and simulation using commercially available CFD software, Ansys Fluent version 18.1, and results are validated with an experimental data. This work also highlights high computational cost associated with CFD analysis and hence recommends reduced order modeling. To reduce computational expenses for CFD modeling, Summers et al. [9] has done CFD modeling of data center using open source and free tool OpenFOAM. This paper tries to demonstrate the effectiveness of modeling data center CFD using open-source software OpenFOAM.

Open Field Operation and Manipulation (OpenFOAM) is a CFD tool written in C++. OpenFOAM has good meshing capabilities such as snappyHexMesh, cfMesh, and blockMesh. It has number of solvers to model different physics. OpenFOAM also comes up with many post-processing capabilities [9]. Looking at the capabilities of OpenFOAM, it is an attractive substitute of commercial CFD software, provided OpenFOAM results are as good as that of commercial software such as Ansys Fluent™.

3   Comparison of Results by OpenFOAM and Ansys Fluent

To demonstrate the capability of OpenFOAM to capture the physics of the data center, a comparison between Ansys Fluent and OpenFOAM needs to be done. For this purpose, CFD analysis of prototype data center is performed using both Ansys Fluent academic version R.15 and buoyantBossinesqueSimpleFoam solver of OpenFOAM version 2.3.1. The prototype data center considered has one rack, one CRAC, and one tile component. A two-dimensional layout of the prototype data center is shown in Fig. 1.

A 3D STL file is generated for this prototype data center. The geometry is meshed using snappyHexMesh utility of OpenFOAM. The meshed geometry of the prototype

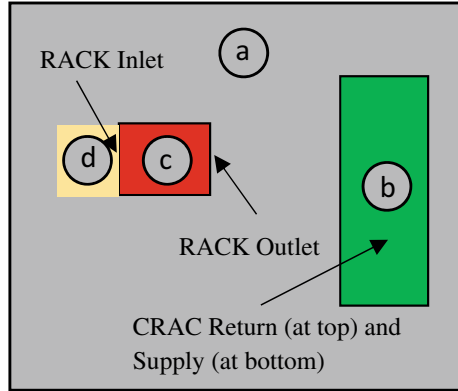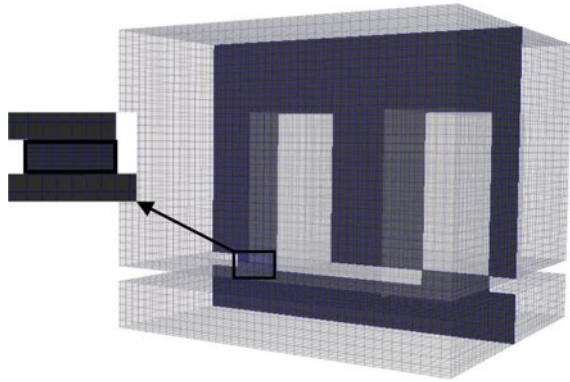**Fig. 1** 2D layout of prototype data center: **a** floor surface, **b** CRAC, **c** rack, **d** tile opening

RACK Inlet

a

d c b

RACK Outlet

CRAC Return (at top) and Supply (at bottom)

Fig. 2 Mesh with refined tile zone in inset

data center is shown in Fig. 2 through a section view of a mesh along with tile zone in inset.

3.1 Governing Equations

The flow and heat transfer are modeled using Navier Stokes equations with steady-state assumption as given by Eqs. 1, 2, and 3. To model the turbulence, k–ϵ model is used as shown by Eqs. 4 and 5. The flow resistance at the tile region is modeled by considering the tile as porous zone and then applying Darcy-Forchheimer equation (given by 6) to model the source term (S) in momentum equations.

$$\frac{\partial}{\partial x_j}\big[\rho u_j\big] = 0 \tag{1}$$

$$\frac{\partial}{\partial x_j}\left[\rho u_i u_j + \frac{\partial}{\partial x_j}\left[(\mu + \mu_t)\frac{\partial u_i}{\partial x_j}\right]\right] = \frac{\partial p}{\partial x_j}$$
$$- g\alpha(T - T_0) + S \tag{2}$$

$$\frac{\partial}{\partial x_j}\left[\rho u_j C_p T\right] = \frac{\partial}{\partial x_j}\left[\kappa\frac{\partial T}{\partial x_j}\right] \tag{3}$$

$$\frac{\partial}{\partial x_i}(\rho k u_i) = \frac{\partial}{\partial x_j}\left[\left(\mu + \frac{\mu_t}{\sigma_k}\right)\frac{\partial k}{\partial x_j}\right] + P_k - \rho\epsilon \tag{4}$$

$$\frac{\partial}{\partial x_i}(\rho\epsilon u_i) = \frac{\partial}{\partial x_j}\left[\left(\mu + \frac{\mu_t}{\sigma_\epsilon}\right)\frac{\partial\epsilon}{\partial x_j}\right] + C_{1\epsilon}\frac{\epsilon}{k}(P_k)$$
$$- C_{2\epsilon}\rho\frac{\epsilon^2}{k} + S_\epsilon \tag{5}$$

$$S = (\mu D_i u_i) + \frac{1}{2}\rho F_i|u_{kk}|u_i \quad \text{where } i, j = 1, 2, 3 \tag{6}$$

In Eqs. 4 and 5, σ_k, σ_ϵ, $C_{1\varepsilon}$, and $C_{2\varepsilon}$ are constants whose values are 1.00, 1.30, 1.44, and 1.92, respectively. The effect of buoyancy is considered in the momentum equation by adding hydrostatic contribution into the pressure term. Since the variation of the density induced by the temperature change is small, Boussinesq approximation is assumed.

3.2 Boundary Conditions

For the prototype data center, boundary conditions, as shown in Tables 1 and 2, are applied. For the velocity variable, mass flow rate of air at that boundary is specified and velocity is calculated using that specified mass flow rate internally.

The steady-state simulation is performed using both the simulation tools, namely Ansys Fluent and OpenFOAM, and results from both simulations were compared.

Table 1 Boundary conditions for mass flow rate, pressure, and temperature

Boundary name	Mass flow (kg/s)	Pressure	Temperature (K)
RACK inlet	− 0.3	Zero gradient	Zero gradient
Rack outlet	0.3	Zero gradient	Fixed value uniform 310
CRAC return	− 4	Zero gradient	Zero gradient
CRAC supply	4	Zero gradient	Fixed value uniform 293
Wall	0	Zero gradient	Zero gradient

Table 2 Boundary conditions for turbulent kinetic energy and dissipation rate

Boundary name	Turbulent kinetic energy (TKE)	Dissipation rate (epsilon)
RACK inlet	Zero gradient	Zero gradient
Rack outlet	Intensity 0.05 Uniform 0.09375	Intensity 0.05 Uniform 0.01
CRAC return	Zero gradient	Zero gradient
CRAC supply	Intensity 0.05 Uniform 0.09375	Intensity 0.05 Uniform 0.01
Wall	Wall function	Wall function

3.3 Validation Results, Discussions, and Conclusion

Figure 3 shows velocity contours at rack mid-plane for OpenFOAM, whereas Fig. 4 shows velocity contours the same location for Ansys Fluent. From the contours of these two figures, it is seen that velocity distribution is similar. The highest velocity of 3.0 m/s is observed at the tile outlet for both the cases. Apart from entire field, a slight variation in velocity magnitude of flow at the exit of tile is observed for the case of OpenFOAM compared to Fluent. This shows a well-qualitative match between both the cases.

To get a quantitative match, line plots of velocity and temperature were drawn as shown in Figs. 5 and 6. Here, a data on a line passing through a point (3.325, 1.25) and parallel to z (height) direction was extracted. Figure 5 shows the line

Fig. 3 Velocity contour at rack mid-plane using OpenFOAM
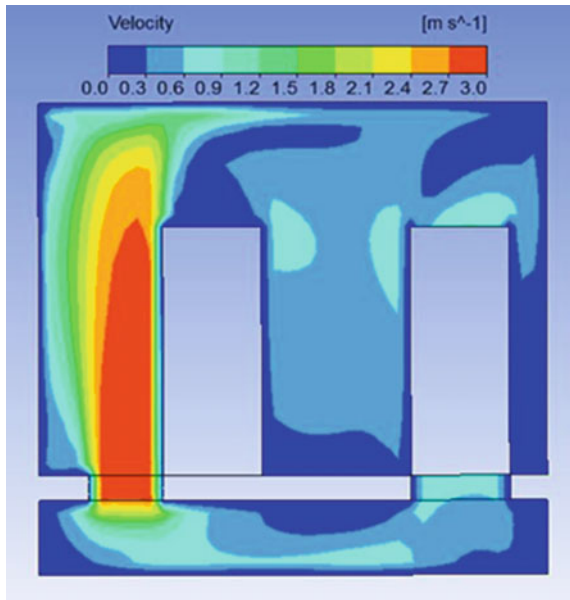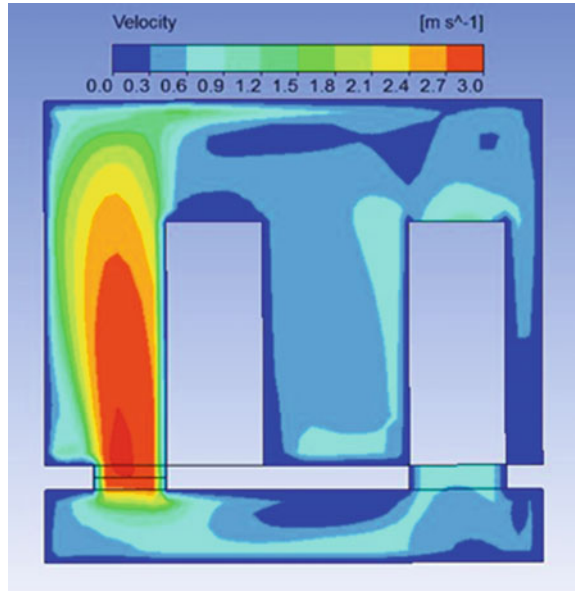
Fig. 4 Velocity contour at rack mid-plane using Ansys Fluent

plot of magnitude of velocity for OpenFOAM and Fluent, while Fig. 6 shows line plot of temperature for OpenFOAM and Fluent. A close match in the results by OpenFOAM and Fluent is seen for both the variables. From this study, it is clear that buoyantBossinesqueSimpleFoam of OpenFOAM is as good as Ansys Fluent. We can use OpenFOAM to model data center.

Unlike Ansys Fluent and other commercial CFD software, OpenFOAM does not have user interface. It is completely text based. In the absence of help, CFD modeling in OpenFOAM becomes very difficult.

Further, CFD modeling of a commercial data center with number of racks, CRAC, and tiles is time-consuming and difficult. A data center operator may not have required expertise and bandwidth to carry out such CFD modeling and simulation.

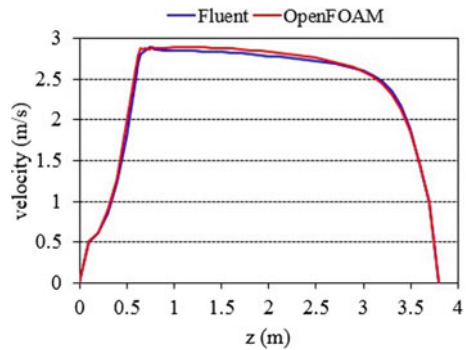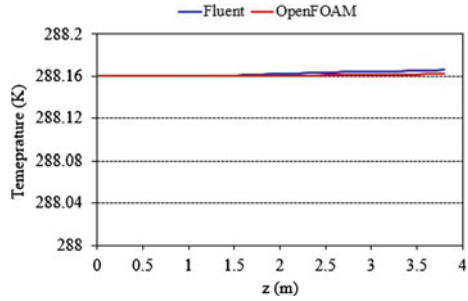**Fig. 5** Plot of velocity magnitude

Fig. 6 Plot of static temperature

For example, CFD simulation of an industrial data center of floor area of 1500 feet^2 floor area and containing 33 racks, 4 CRACs, and 39 perforated tiles takes a total of four weeks' time. Out of four weeks' time, geometry creation and mesh generation for this data center may take up to two weeks of man hour. Further, preprocessing along with simulation post-processing of the simulation results took another two weeks of time. Moreover, CFD simulations are generally carried out using commercial software due to simple GUI and easy to use features. They charge a huge amount as a license cost, for example, license cost of Ansys Fluent is about 1.8 million Indian rupees per annum (representative value). So, if a data center manager wants to improve cooling efficiency of their data center, manager needs to take help of a CFD expert for a month and purchase software for 3D modeling, meshing, and CFD simulation. This adds an additional task on data center manager along with his other responsibilities while adding cost to the total running cost of the data center. Therefore, it is desired to have thermal and fluid map of entire data center along with suggestion to operate data center optimally without incurring addition cost and manpower for running the data center.

Incidentally, data center components have standard geometry and function. A prior knowledge of these components with their location inside the data center can be used to create an algorithm to create entire geometry automatically. Further, using knowledge of functions of these components can further be used to come up with algorithm to automate these processes as well. Moreover, mesh generation and CFD simulation can be carried out on OpenFOAM to eliminate license cost as well completely. Therefore, with the use of automation of geometry creation, preprocessing, simulation, and post-processing eliminates the requirement of a CFD expert and use of free software reduces cost of CFD simulation to a great extent.

4 CFD Modeling for Real Data Center

In practice, the data center modeling starts with creating two-dimensional layout of the data center by physically moving through it and capturing geometric information of the components and physical set point details. There are various tools available for

Fig. 7 2D layout of the real data center
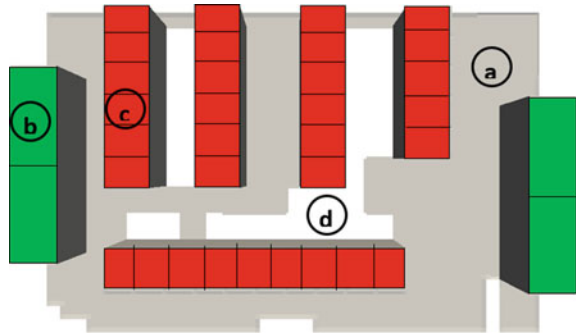
capturing this information. We have used Tata Consultancy Services (TCS) in-house access tool to capture this 2D layout. This tool captures layout by capturing component locations for CRACs, racks, tiles, any obstructions, etc. as on the Cartesian grid with 0.3 m × 0.3 m as smallest block.

In this file, the geometry of the entire data center is captured in a 2D layout. The height of different components and functional details are provided as a property of these components.

Figure 7 shows a 2D layout of an industrial-sized data center. In this layout, (a) shows the floor of the data center. The outer boundary of the floor is the outer layout of the data center. The data center contains 4 CRACs (b), 33 racks (c), and 39 tiles (d). The functional information of each component is provided inside a property box attached to that component.

4.1 Conversion of 2D Layout to 3D Mesh

Once the geometries for all the component with named surface are created, a bounding box for the entire geometry is prepared and background mesh is generated using blockMesh utility of OpenFOAM. Details of the bounding box and component geometry files are used to prepare snappyHexMeshDict. Finally, mesh is created using snappyHexMesh. Further manipulation of the mesh is done using different utilities such as createBaffles, splitMesh, and mergeMesh. To model tile as porous zone, cellZones are created using toposet utility of OpenFOAM. The total time required to prepare 3D geometry and meshing it with 0.36 million cells on a single core took about one hour as opposed to two weeks' time taken by a CFD expert. Figure 8 shows the sectional isometric view of this mesh with tile zone in an inset.

Fig. 8 Mesh generated using snappyHexMesh with tile zone in inset
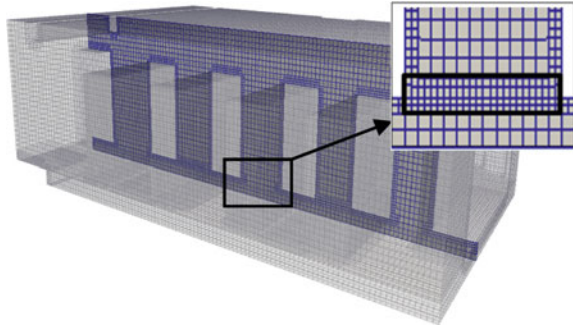
4.2 Simulation Using OpenFOAM

Before going ahead for simulation, fluid properties along with initial and boundary conditions need to be applied for all the variables over all the patches of the data center geometry. Fluid inside the data center is taken as standard air, and all the properties of standard air are used. Functional properties of all the components are used for application of initial and boundary conditions. Inlet of the CRAC is given a mass flow rate outlet, while the outlet of the CRAC is given as mass flow rate inlet with a fixed temperature captured in the 2D layout. A rack may have multiple sections with or without server in it. Presence of server is modeled as a fixed mass flow outlet from the domain at cold side and fixed mass flow inlet at the hot side with a jump in the average temperature as compared to the cold side. This jump in temperature is calculated based on the thermal load of the server and is applied using groovyBC [10]. Part of the rack without server is meshed so that the air can flow through it without a heating. Tiles on floor are modeled as porous zone using Darcy-Forchheimer law. A Darcy-Forchheimer law assumes homogenous porous media and pressure drop across zone are calculated using two scalar factors called as pressure loss coefficients. Pressure loss coefficients are related to amount of opening of the tile as given by Karki et al. [11].

5 Results and Discussion

Simulated results are post-processed using ParaView. Contour plots at specific planer locations are extracted for further analysis. Figure 9 shows a velocity vector for airflow inside domain, and vector color shows static temperature. These plots along with data for rack inlet temperatures and tile flow rates can be used further for obtaining optimum operation of data center.
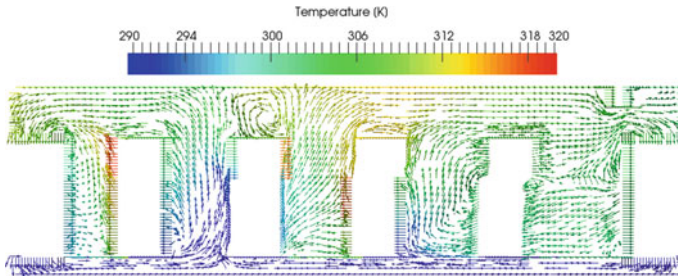
Fig. 9 Glyph vector and temperature (in K) at a plane

6   Conclusions

In conclusion, we have established that OpenFOAM is as good as Ansys Fluent in
modeling the physics of a data center. The algorithm is developed to create geometry;
mesh of the data center can create a mesh as good as that created by a CFD expert. The
simulation of the generated mesh is converged and provides a physically meaningful
result. Our solution is found advantageous in terms of cost, time, and human efforts
required in modeling an industrial-scale data center.

Nomenclature

ρ	Density of air (kg/m^3)
g	Gravitational constant 0f 9.81 (m/s^2)
u	Velocity (m/s)
T	Temperature (K)
μ	Dynamic viscosity (kg/ms)
μ_t	Turbulent viscosity (kg/m·s)
α	Coefficient of thermal expansion (/K)
C_p	Specific heat (J/kg K)
κ	Thermal conductivity (W/m K)
k	Turbulent kinetic energy (TKE) (m^2/s^2)
P_k	TKE production rate (m^2/s^3)
ϵ	TKE dissipation rate (m^2/s^3)

References

1. Ashrae TC (2011) Thermal guidelines for data processing environments—expanded data center classes and usage guidance. American Society of Heating, Refrigeration and Air-Conditioning Engineers, Inc.
2. Anandan SS, Ramalingam V (2008) Thermal management of electronics: a review of literature. Therm Sci 12(2):5–26
3. Sullivan RF. Alternating cold and hot aisles provides more reliable cooling for server farms. White paper, The Uptime Institute, Inc., Santa Fe, NM, USA
4. Song Z, Zhang X, Eriksson C (2015) Data center energy and cost saving evaluation. In: The 7th international conference on applied energy—ICAE2015. Energy Procedia 75:1255–1260
5. Patel CD, Bash CE, Belady C, Stahl L, Sullivan D (2001) Computational fluid dynamics modelling of high compute density data centers to assure system inlet air specifications. Proc IPACK 1:8–13
6. Gao C, Yu Z, Wu J (2015) Investigation of airflow pattern of a typical data center by CFD simulation. Energy Procedia 78:2687–2693
7. Mukaffi AR, Arief RS, Hendradjit W, Romadhon R (2017) Optimization of cooling system for data center case study: PAU ITB data center. Procedia Eng 170:552–557
8. Ahmadi V, Erden H (2020) A parametric CFD study of computer room air handling bypass in air-cooled data centers. Appl Therm Eng 166:114685. ISSN 1359–4311
9. Summers J, Kapur N, Thompson H (2013) Design of data centre rack arrangements using open-source software. In: 29th IEEE semiconductor thermal measurement and management symposium, pp 45–51
10. Gschaider BF (2013) The incomplete swak4foam reference. Tech Rep 131:202
11. Karki KC, Radmehr A, Patankar SV (2003) Use of computational fluid dynamics for calculating flow rates through perforated tiles in raised-floor data centers. HVAC&R Res 9(2):153–166

Picard and Newton-Based Preconditioned Nodal Integral Method for the Solution of Fluid Flow Equations

Nadeem Ahmed, Govind Maurya, Alok Kumar, and Suneet Singh

1 Introduction

Usually, nonlinear partial differential equations (PDEs) are used to model practical problems involving natural processes. Before the advent of computers, people generally relied on analytical or exact types of solutions to these PDEs. It is challenging to solve these PDEs analytically; therefore, finding solutions has long been challenging for researchers. To handle these PDEs, a variety of approaches, including finite difference methods (FDM), finite volume methods (FVM), and finite element methods (FEM) [1–4], are available in the literature. These approaches are more widely used and provide reassuringly accurate and straightforward solutions, making them more popular for solving PDEs. However, they have significant drawbacks because obtaining accuracy requires many mesh points (i.e., fine spatial discretization). Since each dimension needs a fine mesh to get a correct solution, these methods become unaffordably computationally expensive in multidimensional calculations. Methods for coarse mesh were developed in the late 1960s to avoid the necessity for fine mesh. Solving PDEs using coarser grids rather than fine ones was the primary motivation for developing these coarse mesh methods. Nodal methods were created among the varieties of coarse mesh techniques to address nuclear industry problems like the neutron diffusion equation. The Partial Current Balance Method [5] and the nodal green's function method [6] are the two predecessors of the nodal method. In

N. Ahmed (✉) · G. Maurya · A. Kumar · S. Singh
Department of Energy Science and Engineering, IIT Bombay, Powai 400076, India
e-mail: 26ahmedansari@gmail.com

G. Maurya
e-mail: rgovindm@gmail.com

A. Kumar
e-mail: alokpal541andc@gmail.com

S. Singh
e-mail: suneet.singh@iitb.ac.in

the 1970s, Dorning [7] and Lawrence [8] published a thorough analysis of the nodal approaches. Hennart [9] also provided the relationship between point-based and nodal approaches. The success of nodal methods in reactor kinetics has prompted nodal methods' application to fluid flow problems. Horak [10] and Doring [11] created nodal methods for the first time, utilizing the nodal green's function approach to solve the incompressible Navier Stokes problem. Later, Azmy [12] discovered that the Nodal Integral Method (NIM), which is conceptually more straightforward than the traditional nodal approach and requires fewer discrete unknowns per node, can yield similar results comparable to those produced by the nodal method.

The Transverse Integration Process (TIP), which transforms PDE into a series of ODEs, is the first step in practically all nodal approaches after discretization [7, 11, 13–16]. NIM captures the better physics of the system as a result of the ODEs being solved analytically within each cell. Despite these advantages, the application of NIM is only limited to weakly nonlinear problems. Picard-based solvers have only been used up till now to converge the NIM solution. The linear convergence prevents Picard-based solutions from exploiting the full potential of NIM. More effective nonlinear solvers are required to make NIM usable for problems with strong nonlinearity. The Newton method emerges as the best choice for solving nonlinear problems. Aside from NIM, the computational physics and the applied mathematical community generally preferred different solution strategies for the solution of nonlinear PDEs [17]. The community of applied mathematics highlighted Newton-based methods to find the solution to Boundary Value Problems (BVPs) [18]. In contrast, the computational fluid dynamics (CFD) community has more focused on Picard-based solvers [19]. The difference between the predominant approaches (Newton and Picard) seems more marked for implicit Initial Value Problems (IVPs). There is a slight difference between Picard's and Newton's implementations within the framework of NIM; therefore, knowing the required steps for implementing any approach is also essential. Picard-based methods are often preferred to solve nonlinear systems of equations because of their ease of implementation. In contrast, the Newton method is complicated to implement because of creating and storing the Jacobian matrix at each Newton iteration. The other difference between Picard and Newton methods lies in the fact that, with the Picard-based approach, an iterative method can be employed without the need to form matrices for solving the linear system. On the other hand, in the Newton-based method, although an iterative approach can also be utilized to solve the linear system, dealing with the Jacobian matrices remains challenging. Burgers' equation has recently been solved through the utilisation of Jacobian-Free Newton-Krylov (JFNK) method, an efficient version of the Newton method. This method, known as JFNK_NIM, employs a physics-based preconditioner specifically designed for addressing both one-dimensional (1D) and two-dimensional (2D) Burgers' and Navier-Stokes problems [20–23].

In the present work, a comparable methodology is used to understand the underlying convergence theory of both the systems (Picard and Newton). The current study uses modified nodal integral method (MNIM) [16] to discretize the two-dimensional Burgers' equation. With physics-based preconditioning, the final set of discretized equations is solved using the Picard and Newton methods. Iteratively solving the

linear system and effectively implementing the matrix-free approach are accomplished using the generalized minimal residual method (GMRES). The modified MNIM (M^2NIM) [15] is used here to construct the preconditioner because it has faster convergence with reduced accuracy. In other words, it has only been used to solve the weakly nonlinear (lower Reynolds number) problems, despite having a quicker convergence rate. As a result, the preconditioner used here is a linearized version of M^2NIM.

The solution of the two-dimensional burgers' equation is obtained at Reynolds number 5000. The results are compared with the exact solution to validate the different strategies (preconditioned Picard and preconditioned Newton). Numerical results are obtained at various Reynolds numbers and grid sizes to compare the convergence theory of both methods. Furthermore, spectral analysis is also given to demonstrate the effectiveness of Picard and Newton's preconditioning. The study reveals that, although the preconditioner is more effective in the Picard case, Newton's method should still be preferred due to its quadratic convergence.

2 Nodal Integral Method

The development of the Nodal Integral Method consists of various steps. A brief overview of the process is given in the following essential steps.

The first step is discretizing the domain in space and time into finite-size brick-like elements known as nodes. Each node has length, width, and height as $\Delta x = 2a$, $\Delta y = 2b$, and $\Delta t = 2\tau$, respectively. Following discretization, each node is subjected to the Transverse Integration Process (TIP), which converts each PDE into a set of ODEs. Transverse-integrated variables are the averaged variables in these ODEs. After that, the set of ODEs is divided into homogeneous and non-homogeneous parts. The part of the differential equation on the left side that can be conveniently integrated is referred to as homogenous. Contrarily, the component that is difficult to integrate is referred to as non-homogeneous and is positioned on the right side of the differential equation (also known as the pseudo-source term). The non-homogeneous terms are expended using the Legendre polynomial up to specific order. The expansion is truncated at the zeroth order (constant term) to achieve second-order accuracy. The set of ODEs is then solved analytically within each cell, capturing the physics of the system in greater detail. The fourth step applies the continuity conditions over each node's interface, which results in a three-point scheme. After that, some physically relevant constraint conditions are applied to eliminate the pseudo-source terms.

The steps in NIM are further elaborated by applying them to the two-dimensional Burgers' equation. The two-dimensional Burgers' equation is given as

$$\frac{\partial u}{\partial t} + u\frac{\partial u}{\partial x} + v\frac{\partial u}{\partial y} = \frac{1}{\text{Re}}\left[\frac{\partial^2 u}{\partial x^2} + \frac{\partial^2 u}{\partial y^2}\right] \tag{1}$$

$$\frac{\partial v}{\partial t} + u\frac{\partial v}{\partial x} + v\frac{\partial v}{\partial y} = \frac{1}{\text{Re}}\left[\frac{\partial^2 v}{\partial x^2} + \frac{\partial^2 v}{\partial y^2}\right] \tag{2}$$

Here u and v denote the x-direction and y-direction velocities, respectively, and 'Re' stands for the Reynolds number.

In the fluid flow community, the two versions of NIM are more popular, i.e., the Modified Nodal Integral Method (MNIM) [16] and Modified MNIM (M^{2}NIM) [15]. Before discretization of the space–time domain, the equations (Eqs. 1, 2) for MNIM are rewritten in the local coordinate system in the following form:

$$\frac{\partial u}{\partial t} + u_0\frac{\partial u}{\partial x} + v_0\frac{\partial u}{\partial y} = \frac{1}{\text{Re}}\left[\frac{\partial^2 u}{\partial x^2} + \frac{\partial^2 u}{\partial y^2}\right], \tag{3}$$

$$\frac{\partial v}{\partial t} + u_0\frac{\partial v}{\partial x} + v_0\frac{\partial v}{\partial y} = \frac{1}{\text{Re}}\left[\frac{\partial^2 v}{\partial x^2} + \frac{\partial^2 v}{\partial y^2}\right], \tag{4}$$

where u_0 and v_0 are the node averaged velocity at the current time step. The detailed definitions of these velocities are described later. MNIM is more implicit and gives a more accurate solution, whereas (M^{2}NIM) has some delayed effect in it, giving faster convergence. The different versions of NIM mentioned above (i.e., MNIM and M^{2}NIM) are used here to construct the framework of preconditioned Picard and Newton (i.e., JFNK) method for the solution of the 2D Burgers' equation. In both versions, the steps for the scheme's development are almost similar, and only the treatment of nonlinear convective terms in the Burgers' equation is different. In M^{2}NIM, the advection term based on the node averaged velocities at the previous time step has been added on both sides of the respective momentum equations. The first Burgers' equation (Eq. 3) can be rewritten after adding the advection term with the previous time step velocity as

$$\frac{\partial u}{\partial t} + u_\text{p}\frac{\partial u}{\partial x} + v_\text{p}\frac{\partial u}{\partial y} = \frac{1}{\text{Re}}\left[\frac{\partial^2 u}{\partial x^2} + \frac{\partial^2 u}{\partial y^2}\right] - \left(u_0 - u_\text{p}\right)\frac{\partial u}{\partial x} + \left(v_0 - v_\text{p}\right)\frac{\partial u}{\partial y} \tag{5}$$

where u_p and v_p are the nodes averaged velocities at the previous time step. The y-direction equation can also be written in a similar manner. The added term in the RHS is referred to as the correction term. It should be noted that there is no correction term in MNIM because convective velocities are calculated at the current time step. The sole difference between MNIM and M^{2}NIM is that MNIM provides a more accurate solution due to larger coefficient nonlinearity, whereas M^{2}NIM only contains nonlinearity in the source term, which results in faster convergence. In this paper, the Burgers' equation is discretized using MNIM, and the linearized version of M^{2}NIM is used to construct a preconditioner, which maintains both speed as well as accuracy.

The algorithm's complete discussion and their development process can be found in Kumar and Singh's [20] work. After all the development process, the final set of the algebraic equations for MNIM is given as

$$F_{37}\overline{u}_{i,j}^{xt} = F_{31}\overline{u}_{i,j-1}^{xt} + F_{32}\overline{u}_{i,j+1}^{xt} + F_{33}\left(\overline{u}_{i,j,k}^{xy} + \overline{u}_{i,j,k-1}^{xy}\right) + F_{34}\left(\overline{u}_{i,j+1,k}^{xy} + \overline{u}_{i,j+1,k-1}^{xy}\right)$$

$$(6)$$

$$F_{57}\overline{u}_{i,j}^{yt} = F_{51}\overline{u}_{i-1,j}^{yt} + F_{52}\overline{u}_{i+1,j}^{yt} + F_{53}\left(\overline{u}_{i,j,k}^{xy} + \overline{u}_{i,j,k-1}^{xy}\right) + F_{54}\left(\overline{u}_{i+1,j,k}^{xy} + \overline{u}_{i+1,j,k-1}^{xy}\right)$$

$$(7)$$

$$F_{37}\overline{v}_{i,j}^{xt} = F_{31}\overline{v}_{i,j-1}^{xt} + F_{32}\overline{v}_{i,j+1}^{xt} + F_{33}\left(\overline{v}_{i,j,k}^{xy} + \overline{v}_{i,j,k-1}^{xy}\right) + F_{34}\left(\overline{v}_{i,j+1,k}^{xy} + \overline{v}_{i,j+1,k-1}^{xy}\right)$$

$$(8)$$

$$F_{57}\overline{v}_{i,j}^{yt} = F_{51}\overline{v}_{i-1,j}^{yt} + F_{52}\overline{v}_{i+1,j}^{yt} + F_{53}\left(\overline{v}_{i,j,k}^{xy} + \overline{v}_{i,j,k-1}^{xy}\right) + F_{54}\left(\overline{v}_{i+1,j,k}^{xy} + \overline{v}_{i+1,j,k-1}^{xy}\right)$$

$$(9)$$

$$F_{77}\overline{u}_{i,j}^{xy} = F_{71}\overline{u}_{i,j}^{xt} + F_{72}\overline{u}_{i,j-1}^{xt} + F_{73}\overline{u}_{i,j,k-1}^{xy} + F_{74}\overline{u}_{i,j}^{yt} + F_{75}\overline{u}_{i-1,j}^{yt} \qquad (10)$$

$$F_{77}\overline{v}_{i,j}^{xy} = F_{71}\overline{v}_{i,j}^{xt} + F_{72}\overline{v}_{i,j-1}^{xt} + F_{73}\overline{v}_{i,j,k-1}^{xy} + F_{74}\overline{v}_{i,j}^{yt} + F_{75}\overline{v}_{i-1,j}^{yt} \qquad (11)$$

where all Fs are the coefficients that contain both linear as well as exponential terms in it with respect to the present-time velocities u_0 and v_0. For example

$$A_{91} \equiv \frac{-\dfrac{1}{\text{Re}} + \dfrac{b_j v_{0i,j}\left(1 + e^{\text{Re}v_{i,j}}\right)}{-1 + e^{\text{Re}v_{i,j}}}}{v_{0i,j}^2},$$

$$A_{92} \equiv \frac{e^{\text{Re}v_{i,j}}}{-1 + e^{\text{Re}v_{i,j}}} - \frac{1}{\text{Re}v_{i,j}},$$

$$F_{72} \equiv -\frac{A_{92}}{A_{91}}.$$

The definitions of the remaining coefficients are available in the referenced publications [15, 22]. The development process for M²NIM is the same as that of MNIM, and the final set of algebraic equations would also be the same as MNIM. However, it should be noted that in M²NIM, the exponential term in the coefficients depends on the previous time step velocities and therefore needs to be evaluated once at each time step, saving significant computational effort. Also, there would be a correction term as a source term in the final set of the algebraic equation for M²NIM. Since M²NIM is only required to construct a preconditioner, the source term will vanish during linearization.

The velocity at present and the previous time step are given as

$$u_0 = \frac{u_{i,j,k}^{xt} + u_{i,j-1,k}^{xt} + u_{i,j,k}^{yt} + u_{i-1,j,k}^{yt}}{4}$$

$$u_{\mathrm{p}} = \frac{u_{i,j,k-1}^{xt} + u_{i,j-1,k-1}^{xt} + u_{i,j,k-1}^{yt} + u_{i-1,j,k-1}^{yt}}{4}$$

where k denotes the node index in the direction of time. v_0 and v_{p} can also be written in a similar format.

3 Picard and Newton Preconditioning

The two-dimensional Burgers' equation is discretized using MNIM. The final set of discretized equations is solved using the Picard and Newton method with the help of physics-based preconditioning. The developed algorithm uses the linearized version of M²NIM for constructing the preconditioner. The preconditioning can be done in two ways: left preconditioning and right preconditioning. Generally, right preconditioning is often preferred due to its ease of implementation and intrinsic merit for comparing the strategies of different preconditioning approaches.

A linear system ($Ax = b$) can be written in terms of right preconditioning as,

$$AP^{-1}Px = b$$

where P is the preconditioning matrix, the right preconditioning described above is split into two parts. The linear system (($AP^{-1})w = b$) is repeatedly solved in the first part using Krylov subspace methods, and the second part uses $x = P^{-1}w$ to determine x. The GMRES method is used to iteratively solve the linear system of equations in the first portion, and each GMRES iteration calls for the action of P^{-1}. The abovementioned steps would remain the same for both methods (Picard and Newton). In the case of Newton's method, the linear system would be $J\delta(x) = -F(x)$, where $F(x)$ is a vector-valued function for a given state vector x and J represents the associated Jacobian Matrix at nth Newton iteration. In contrast, the linear system for the Picard method would be $Ax = b$, where A is a coefficient matrix. To make it a matrix-free approach, one can use the matrix–vector product approximation [17] because the GMRES method only requires the matrix–vector product as a vector to carry out the iteration.

In the present work, the preconditioning of both methods is matrix-free, and steps inside the GMRES method would remain the same for both cases. The detail of the development process can be found in the recent papers [20–23] on Newton-based preconditioners. However, Picard-based preconditioner is developed in the present work to understand the effectiveness of the preconditioner. There is a slight difference between the implementation processes of both approaches outside the GMRES loop. Therefore, it is essential to know the steps of the Picard and Newton-based method for an efficient implementation.

Algorithm 1 Picard algorithm for MNIM.

1: Time loop starts.
2:      Nonlinear iteration.
3:           **Compute u_0.**
4:           **Compute A using the value of u_0.**
5:           **Solve $Ax = b$ using GMRES.**
6:           **Update u_0.**
7:      Repeat until convergence.
8: Time loop end.

In Picard-based method, the present-time step velocity u_0 of MNIM is calculated explicitly after each nonlinear iteration and then computes the coefficient matrix A using the value of u_0 to make a linear system of equations. The linear system $Ax = b$ is then solved iteratively using the GMRES method, as shown in Algorithm 1. Note that the preconditioning step is present inside the GMRES iteration and does not affect to the implementation process.

Algorithm 2 Newton algorithm for MNIM.

1: Time loop starts.
2:      Nonlinear iteration.
3:           **Compute J and $F(x)$ of nonlinear system.**
4:           Solve $J\delta(x) = -F(x)$ using GMRES.
5:           **Update $\delta(x)$.**
6:      Repeat until convergence.
7: Time loop end.

In Newton-based method (i.e., JFNK), the Jacobian J is calculated from the original nonlinear system of MNIM instead of the explicit computation of u_0. The linear system $J\delta(x) = -F(x)$ is then solved using the GMRES method, as shown in Algorithm 2. As mentioned previously, there is a very slight difference in the implementation process, but this makes a massive difference in performance which will be clear in the following section.

4   Results and Discussion

The solutions to the 2D Burgers' equation are derived in this section for various Reynolds numbers and grid sizes. The comparisons between Picard's and Newton's preconditioning using MNIM are provided to understand the convergence theory. The clustering of eigenvalues of preconditioned Picard and preconditioned Newton are also provided to demonstrate that the preconditioner using M^2NIM is more effective in Picard than in Newton.
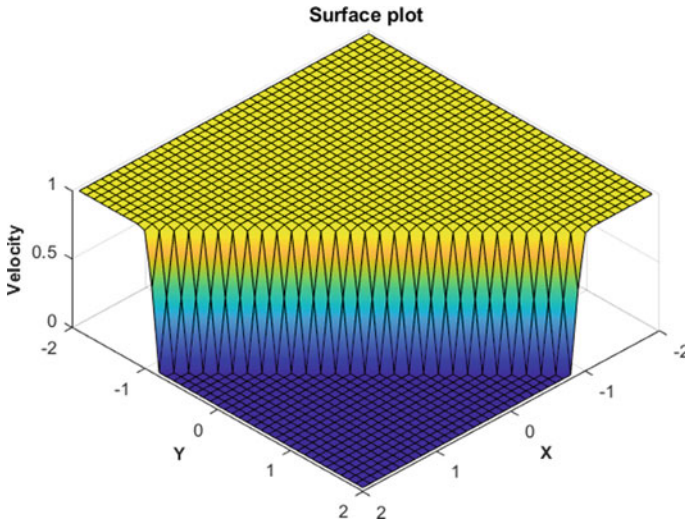
Fig. 1 Surface plot at time $t = 1$-unit for Re $= 5000$

4.1 Verification of the Results

The results of MNIM and PC-MNIM have already been discussed in detail in the previous work of Niteen and Singh [20]. The current work shows the results at a higher Reynolds number (Re $= 5000$) to demonstrate the effectiveness of Picard preconditioning.

Both a surface plot and a 2D line plot are used to display the results. The smooth wave pattern at $t = 1$ unit time is depicted in Fig. 1 by using the surface plot. In order to compare the numerical and analytical solutions for the velocity ($\overline{u}^{xy}$) at three different time steps ($t = 0.3$ unit in blue, $t = 1$ unit in magenta, and $t = 1.7$ unit in red), the 2D line graphic is provided (Fig. 2).

Note that the straight line indicates analytical solutions, whereas the dots represent all possible numerical solutions. Results are in excellent agreement with the analytical solution, proving that the preconditioned Picard is just as stable and accurate as Newton in offering the answer for a very high Reynolds number.

4.2 Comparison of Preconditioned Picard and Preconditioned Newton Methods

In this subsection, we will discuss the difference between Picard's and Newton's methods in detail. This study focuses on understanding whether Picard preconditioning works well with the developed preconditioner [21] or whether the Newton method will win the race again. After using both methods at different Reynolds
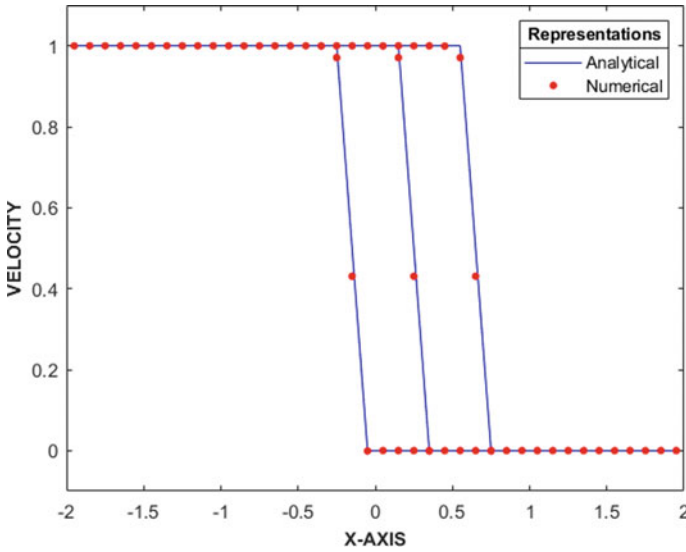
Fig. 2 Velocity ($\bar{u}^{xy}$) at three different time steps for Reynolds number 5000

numbers and grid sizes, a comparison of nonlinear iterations is given in Table 1. The comparison of the total number of nonlinear iterations is given in Table 1 to demonstrate the difference between linear and quadratic convergences of the Picard and Newton methods, respectively.

It is to be noted that these numbers of nonlinear iterations are independent of the preconditioning step. In other words, these numbers will remain the same for both preconditioned as well as non-preconditioned systems. However, the preconditioning step is essential for the comparisons of Krylov iterations. Therefore, a comparison of Krylov iteration for the same cases is given in Table 2.

The total number of Krylov iterations is more in the case of the Picard method because the nonlinear iteration is already high for Picard. However, the number of Krylov iterations per NI can be different, which is essential to know the difference

Table 1 Comparison of nonlinear iterations for Picard and Newton preconditioning for $dt = 0.01$ and $T = 1$ s

Reynolds number (Re)	Grid size ($n = m$)	Total nonlinear iterations (NI)		NI reduction factor (P/N)
		Picard (P)	Newton (N)	
500	12	2089	318	6.57
2500	24	3220	333	9.67
5000	38	3562	418	8.32
7500	48	3615	428	8.44
10,000	64	3814	443	8.61

Table 2 Comparison of Krylov iterations for Picard and Newton preconditioning for d$t = 0.01$ and $T = 1$ s

Reynolds number (Re)	Grid size ($n = m$)	Total Krylov iterations (KI)		KI reduction factor (P/N)
		Picard (P)	Newton (N)	
500	12	5914	2097	2.82
2500	24	10,516	2224	4.73
5000	38	13,423	2880	4.66
7500	48	14,805	2949	5.02
10,000	64	16,604	3137	5.30

Table 3 Comparison of Krylov iterations per nonlinear iteration for Picard and Newton preconditioning for d$t = 0.01$ and $T = 1$ s

Reynolds number (Re)	Grid size (n)	Picard preconditioning		Newton preconditioning	
		NI per time step	Krylov iterations per NI	NI per time step	Krylov iterations per NI
500	12	21	3	3	7
2500	24	32	3	3	7
5000	38	36	4	4	7
7500	48	36	4	4	7
10,000	64	38	4	4	7

between these two methods. It is assumed that the developed preconditioner is more efficient in the Picard method; therefore, a comparison of the total number of Krylov iterations per NI is given in Table 3.

Interestingly, the Krylov iterations per NI are less in the Picard preconditioning case, which means that the developed preconditioner is more effective in the Picard method. However, only this comparison is insufficient because the nonlinear iterations per time step are very high for the Picard case compared to the Newton method.

4.3 Spectral Analysis of Preconditioned Picard and Preconditioned Newton Methods

The Newton approach wins the race due to its quadratic convergence in nonlinear iterations, despite the developed preconditioner [21] being more effective in the Picard case. Additionally, the same idea can be represented using eigenvalues. The preconditioning method is said to be effective if the eigenvalues of the product JP^{-1}
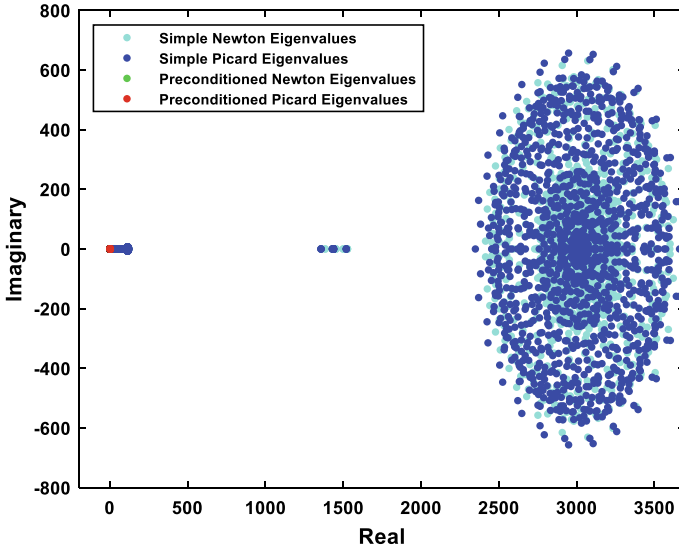
Fig. 3 Eigenvalues of simple Newton, simple Picard, preconditioned Newton, and preconditioned Picard for Re $= 3000$, $n = 20$, and d$t = 0.01$

(preconditioned Newton) or AP^{-1} (preconditioned Picard) cluster around one. The clustering capacity of the present algorithm is shown in Fig. 3.

In Fig. 3, the cyan dots represent the eigenvalues of J; blue dots represent the eigenvalues of A; green dots represent the eigenvalues of JP^{-1}; and red dots represent the eigenvalues of AP^{-1}. It is clear from Fig. 3 that the developed preconditioner [21] can cluster the eigenvalues in both cases (Newton and Picard).

The actual eigenvalue pattern can only be observed in the zoomed region, as shown in Fig. 4 (red dots shows the eigenvalues of preconditioned Picard and green dots illustrate the eigenvalues of preconditioned Newton) because the eigenvalues for the preconditioned matrix system are quite small. As expected, the clustering of eigenvalues for preconditioned Picard is better than the preconditioned Newton. Although the clustering looks good in the Picard case, it is also not bad for Newton. The improvement in Picard's case is there over Newton's method but not that significant. Therefore, preconditioned Newton wins the race.

5　Conclusions

The two-dimensional Burgers' equation is discretized using MNIM. The final set of discretized equations is solved using the Picard and Newton methods with the help of physics-based preconditioning. The developed algorithm uses the linearized version of M^{2}NIM for constructing the preconditioner. A comparison of nonlinear iterations
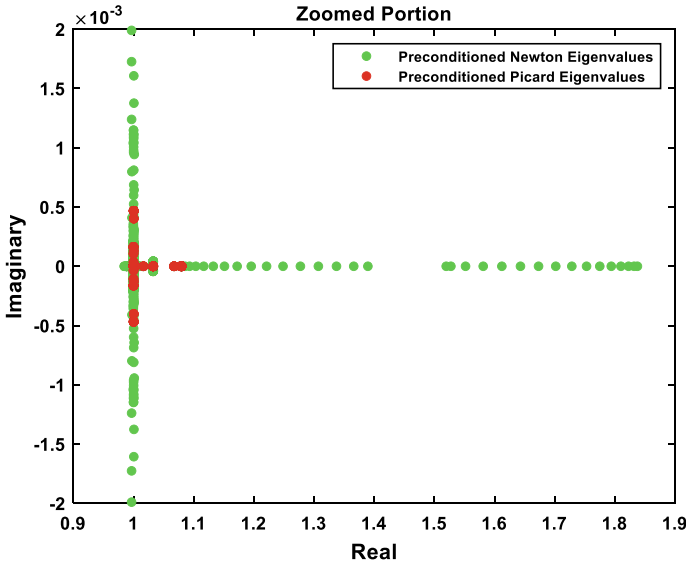
Fig. 4 Comparison of the eigenvalue clustering of preconditioned Picard and preconditioned Newton for Re = 3000, $n = 20$, and d$t = 0.01$

between Picard and Newton is given to illustrate the convergence of both methods. Relevant results in Table 1 show that the nonlinear iteration in Newton's method, due to its quadratic convergence, is roughly 8–9 times smaller than in Picard's case. However, when the preconditioner is applied in both cases, the number of Krylov iterations per Newton iteration in preconditioned Picard is nearly half that of preconditioned Newton. As a result, we can say that the preconditioner operates more effectively in the Picard case than in the Newton method. However, the net effect leads to the total computational time being lower for preconditioned Newton method due to its quadratic convergence.

Nomenclature

Δx	Spatial step size in x-direction
Δt	Time step size
τ	Temporal coordinate at a node interface
u^{xy}	Averaged u velocity in x and y directions
u^{xt}	Averaged u velocity in x and t directions
u^{yt}	Averaged u velocity in y and t directions
v^{xy}	Averaged v velocity in x and y directions
v^{xt}	Averaged v velocity in x and t directions
v^{yt}	Averaged v velocity in y and t directions

u_0 Averaged u velocity at current time step
v_0 Averaged v velocity at current time step
i Node index in the x-direction
j Node index in the y-direction
k Node index in the direction of time
NI   Nonlinear iterations

References

1. Thomas JW (1995) Numerical partial differential equations: finite difference methods. Springer, New York, p 1995
2. Kang F, Zhong-Ci S (1996) Finite element methods. Mathematical theory of elastic structures. Springer, Berlin Heidelberg, pp 289–385
3. Eymard R, Gallouët T, Herbin R (2000) Finite methods. Elseiver, Amsterdam, pp 713–1018
4. Ortega J, Rheinboldt W (1970) Iterative solution of nonlinear equations in several variables. Elsevier, Amsterdam
5. Burns TJ (1975) The partial current balance method: a local green's function technique for the numerical solution of multidimensional diffusion problems. Ph.D. Thesis. University of Illinois
6. Lawrence RD (1979) A nodal green's function method for multidimensional neutron diffusion calculation. Ph.D. Thesis. University of Illinois
7. Dorning JJ (1979) Modern coarse-mesh methods. A development of the '70's. Comput Methods Nuclear Eng 1:31–331
8. Lawrence RD (1986) Progress in nodal methods for the solution of the neutron diffusion and transport equations. Prog Nucl Energy 17:271–301
9. Hennart JP (1986) A general family of nodal schemes. SIAM J Sci Comput 7(1):264–287
10. Horak WC (1980) Local Green's functions techniques for the solution of heat conduction and incompressible fluid flow problems. Ph.D. Thesis. University of Illinois
11. Horak WC, Dorning JJ (1985) A nodal coarse-mesh method for the efficient numerical solution of laminar flow problems. J Comput Phys 59:405–440
12. Azmy YY (1982) A nodal integral method for the numerical solution of incompressible fluid flow problems. MS Thesis, University of Illinois
13. Ahmed N, Maurya G, Singh S (2023) A novel cell-centered nodal integral method for the convection-diffusion equation. Ann Nucl Energ 189:109858
14. Raj M, Ahmed N, Singh S (2022) Analytical nodal method for solution of neutron diffusion equation in polar coordinates. Ann Nucl Energ 165:108659
15. Wang F, Rizwan-Uddin (2003) A modified nodal scheme for the time-dependent incompressible navier–stokes equations. J Comput Phys 187(1):168–196. https://doi.org/10.1016/S0021-9991(03)00093-7
16. Wescott BL, Rizwan-Uddin (2001) An efficient formulation of the modified nodal integral method and application to the two-dimensional burgers' equation. Nucl Sci Eng 139(3):293–305. https://doi.org/10.13182/NSE01-A2239
17. Knoll DA, Keyes DE (2004) Jacobian-free Newton-Krylov methods: a survey of approaches and applications. J Comput Phys 193:357–397
18. Patankar SV (2018) Numerical heat transfer and fluid flow. CRC Press, Boca Raton
19. Oran ES, Boris JP (1987) Numerical simulation of reactive flow. Elsevier, New York
20. Kumar N, Majumdar R, Singh S (2019) Physics-based preconditioning of Jacobian free Newton Krylov for Burgers' equation using modified nodal integral method. Prog Nucl Energy 117:103104

21. Kumar N, Singh S (2021) A novel physics-based preconditioner for nodal integral method using JFNK for 2D Burgers equation. Prog Nucl Energy 134:103668
22. Ahmed N, Kumar A, Kumar N, Singh S (2022) A modified preconditioning approach for nodal integral method. In: Proceedings of the 8th WorldCongress on Mechanical, Chemical, and Material Engineering (MCM'22). International ASET, AVESTIA. https://doi.org/10.11159/htff22.173
23. Ahmed N, Singh S, Kumar N (2023) Physics-based preconditioning of Jacobian-free Newton–Krylov solver for Navier–Stokes equations using nodal integral method. Int J Numer Methods Fluids 1–24. https://doi.org/10.1002/fld.5236

Influence of Thermo-coupled Flowing Fluid on Cell Adhesion: Numerical Study

Arupjyoti Kakati, Saurabh Gupta, and Arindam Bit

1 Introduction

The knowledge of cell control and communication is important for the upkeep and processing of customised tissues. The extracellular matrix (ECM) to which cells are attached can significantly affect the functions of the cells. According to the "cell adhesion model," a cell has the most chemical connections on its surface the more it sticks [1]. Cell adhesion, which is involved in stimulating the signals, emphasises cell differentiation, cell migration, and cell survival. In cases of human malignancies, the adhesion of cells is reduced. Cancer cells are able to defy the social order due to a decrease in the ranges of intercellular adhesiveness, which leads to the loss of histological structure. Tumour cells are distinguished by alterations in their adherence to the ECM. The adhesivity of highly invasive cancer cells changes the biomechanics of endothelial cells. By affixing MDA-MB-231 cells, the stiffness of endothelial cells may be reduced by disabling the barrier function of the cells by remodelling of the actin cytoskeleton [2].

To ensure cell proliferation inside microchannel bioreactors, it is necessary to maintain estimated concentrations of solutes, such as dissolved gases, nutrients, and metabolic products [3]. Although the process of transferring heat and mass involves a high-pressure drop, microchannels are used in studies where exceptionally effective heat and mass transfer processes take place, like in the systems of lungs and kidneys.

A. Kakati · S. Gupta · A. Bit (✉)
Department of Biomedical Engineering, NIT Raipur, Raipur 492010, India
e-mail: arinbit.bme@nitrr.ac.in

2   Literature Review and Objective

In the case of laminar flows, obstructive elements can be used in a variety of designs and sizes to simulate surface roughness [3, 4]. Numerous problems exist with the regular element technique, including the influence of rough element shape or coordination on roughness [5–7]. With random-sized rectangular and triangular impediments, Croce and D'Agaro [6] also presented an alternative finding, and they discovered outcomes that are more in line with the experiment than homogenous rough parts.

The organisation of cellular adhesivity over a channel's substrate will be greatly aided by the presence of specific micropatterning configurations [8]. Compared to micro-wells, the effects on cellular adherence are more significant when the micro-configurations are in the shape of fins and pillars [5, 7]. In this paper, the modulation of the heat and velocity variations within the working fluid was mainly highlighted by the impacts of thermo-fluid coupling. Numerical research was done on how heat distributions affected the fluid flow with respect to the micro-fins inside the microchannel.

3   Materials and Methods

Rectangular topologies were used to build microchannels of two different types: positive fin associated and negative fin associated. With respect to time, these channels received a stationary input heat of 324 K as well as a time-dependent heat supply that varies from 301 to 324 K with an initial increment of 1 s to the second step, followed by an increment of 2 s up to the tenth step, and finally an increment of 5 s up to the hundredth step for each interval. Additionally, it was assumed that the input velocity was both stationary and time-dependent. The flowing fluid had a fixed fluid flow rate of 2e−6 m/s for constant input velocity. The magnitude of input velocity fluctuates for time-dependent fluid velocity according to the equation $v = v\sin(2ft)$, where $v = 2\mathrm{e}{-}6$ m/s, $f = 1.2$ Hz, and the time intervals are the same as for input heat. For the circumstances of transient input heat supply and spatially varying input heat supply to the fins, the central fin was given a maximum temperature of 324 K and transient heat supply as given, and the other fins were provided with temperature in accordance with the values as determined by Eq. 3 (for both positive fins attached and negative fins attached). Fins' physical characteristics were thought to be similar to those of graphene. Here, water was the working fluid under consideration.

The microchannels' height and width were determined to be 50 µm and 200 µm, respectively (Fig. 1). At the base of the channel, fins with dimensions of 25 µm by 15 µm were arranged for positive orientations in an outward manner from the substrate (Fig. 2a), and for negative orientations in an inward direction towards the substrate (Fig. 2b). The walls of the microchannels were kept warm using adiabatic heating, thermal isolation, and boundary conditions that prevented slippage.
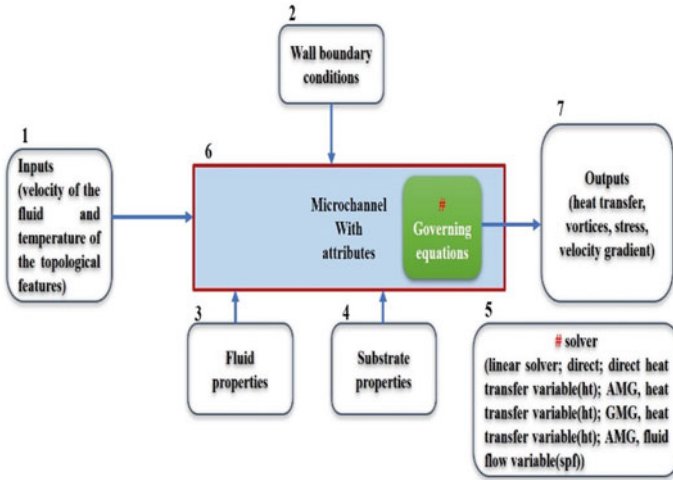
Fig. 1 Schematic of the problem (1: inlet for fluid flow; 2: boundary conditions for the walls; 3: material properties of the fluid; 4: material properties of the substrate; 5: solvers used for simulating the governing equations; 6: microchannel with topological features; 7: outlet)

Table 1 lists the mesh characteristics used for COMSOL microchannel designing in microchannels attached with positive and negative fins. For each construction, the fin placements were chosen to follow particular patterns or orders based on their distances from the central fins. Figure 2a shows the regular configurations that were taken into consideration for this investigation. The first and fourth fins were kept at an identical distance (47.5 μm) from the centre fin, while the second and third fins were kept at an equal distance (47.5 μm) from the central fin. The negatively oriented fin arrangements in the rectangular microchannels are shown in Fig. 2b. The placements of the fins were maintained at the same distances as those for positive fin orientation as well. For all of the simulations, the fin positions were tallied in clockwise directions.

Three basic forces that influence the flow pattern are taken into account in the study of fluid flow. These are the body force brought on by gravity, the pressure force brought on by friction, and the viscous force. The Navier–Stokes equation is the formula that governs incompressible Newtonian fluid flow for a given volume (Eqs. 1a and 1b).

$$\sum \vec{f} = \rho \vec{a} = \overrightarrow{f_{\text{grav}}} + \overrightarrow{f_{\text{press}}} + \overrightarrow{f_{\text{vis}}} = \rho \vec{g} - \vec{\nabla} P + \mu \nabla^2 \vec{V} \tag{1a}$$

$$\rho \left(\frac{\partial \vec{V}}{\partial t} + u \frac{\partial \vec{V}}{\partial x} + v \frac{\partial \vec{V}}{\partial y} + w \frac{\partial \vec{V}}{\partial z} \right) = \rho \vec{g} - \vec{\nabla} P + \mu \nabla^2 \vec{V} \tag{1b}$$
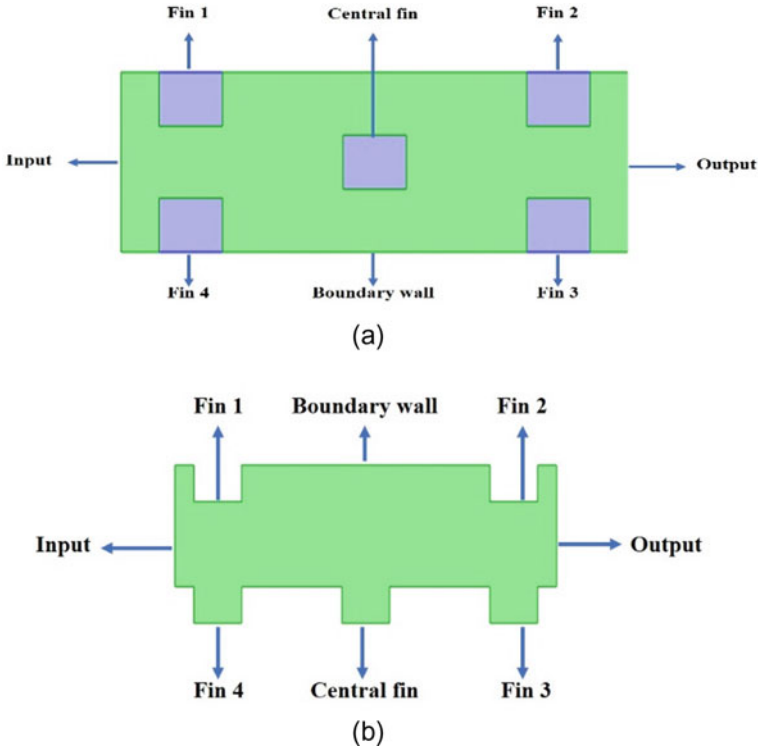
Fig. 2 Rectangular topology (regular configuration): **a** positive fins attached and **b** negative fins attached

And the energy equation for estimating temperature distribution can be expressed by Eq. 2.

$$\vec{\nabla}.\left(\vec{V}.T\right) = \frac{w}{\rho C_p}\nabla^2 T \tag{2}$$

The correlation for spatially varying input heat supply to the fins is given by Eq. 3.

$$T_{\text{fin\_4}} - T_{\text{fin\_1}} = T_{\text{fin\_2}} - T_{\text{fin\_3}} \tag{3}$$

Here, $\vec{V}$ is the velocity vector, **P** is the pressure, **T** is the temperature, μ is fluid viscosity, ρ is fluid density, and **w** is fluid thermal conductivity [5]. Discretisation of Eqs. 1 and 2 was made using finite volume method by utilising COMSOL Multiphysics 5.5.

Table 1 Mesh properties in microchannels of rectangular topology having positive and negative fins

Topology	Configuration	Mesh size	Triangular elements	Quad elements	Edge elements	Vertex elements	Minimum element	Average element quality	Element area ratio
Rectangular	Regular and positive	10,730 μm	14,131	1020	951	50	0.2387	0.8259	0.007651
	Regular and negative	13,200 μm	11,336	760	724	48	0.2392	0.8267	0.006997

4　Results and Discussion

The velocity fluctuations inside the microchannels were examined in this work with changes in the input heat supply. Here are the contour plots of the velocity amplitudes and heat transfer distributions for the arranged fins inside the microchannel (Fig. 3 corresponds to positive fins attached, and Fig. 4 corresponds to negative fins attached). Due to the existence of fin structures inside the microchannels, heat was distributed according to the second law of thermodynamics.

Observations revealed that, when the input fluid's velocity was independent of time, fluidic molecules obtained higher entropies near or between the flow-lines of the velocity profile than their corresponding magnitudes for the flow-lines near the boundary walls or in the points that were distant from the fin's walls (Fig. 3.A1, B1, and E1). The patterns of flow distributions remained the same, but there was a variation in the magnitudes of values obtained by fluid molecules when both input values (velocity of flowing fluid and temperature to the fins) were time-dependent functions, as demonstrated in Fig. 3.D1, and F1. When the input fluids' velocities varied over time, there was a moderate variation in the magnitudes of the velocities
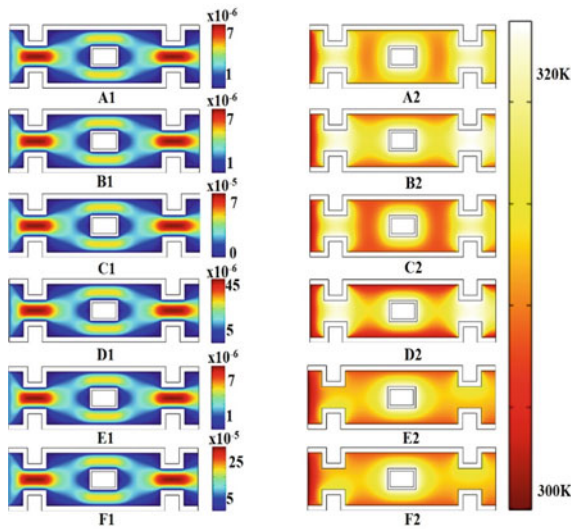
Fig. 3 For positive fins: velocity (m/s) contour (A1: constant input fluid velocity and constant fin temperature, B1: constant input fluid velocity and transient fin temperature, C1: transient input fluid velocity and constant fin temperature, D1: transient input fluid velocity and transient fin temperature, E1: constant input fluid velocity and spatially varying fin temperature, F1: transient input flu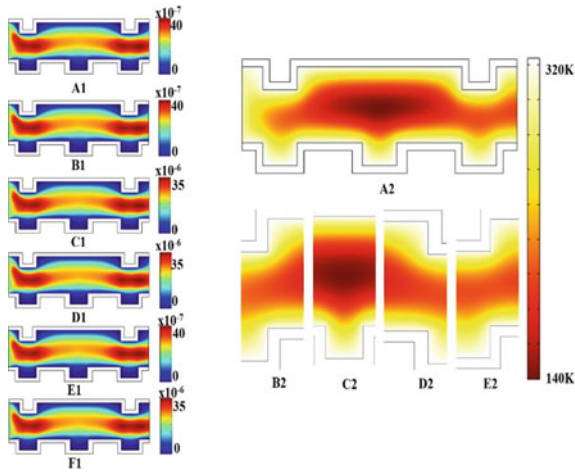id velocity and spatially varying fin temperature); heat distributions (A2: constant input fluid velocity and constant fin temperature, B2: constant input fluid velocity and transient fin temperature, C2: transient input fluid velocity and constant fin temperature, D2: transient input fluid velocity and transient fin temperature, E2: constant input fluid velocity and spatially varying fin temperature, F2: transient input fluid velocity and spatially varying fin temperature)

Fig. 4 For negative fins: velocity (m/s) contour (A1: constant input fluid velocity and constant fin temperature, B1: constant input fluid velocity and transient fin temperature, C1: transient input fluid velocity and constant fin temperature, D1: transient input fluid velocity and transient fin temperature, E1: constant input fluid velocity and spatially varying fin temperature, F1: transient input fluid velocity and spatially varying fin temperature); heat distributions (A2: constant input fluid velocity and constant fin temperature, B2: constant input fluid velocity and transient fin temperature, C2: transient input fluid velocity and constant fin temperature, D2: transient input fluid velocity and transient fin temperature, E2: constant input fluid velocity and spatially varying fin temperature)

for the fins' continuous heat supply (Fig. 3.C1). Additionally, it was found that for microchannels with positive fin characteristics, the rate of heat transfer is higher when the velocity of the flowing fluid inside the channel is constant (Fig. 3.A2, and B2) in contrast to the transfer rate for time-dependent input velocities (Fig. 3.C2, D2, E2, and F2).

Figure 4 demonstrated that the distribution of the fluid inside the microchannel with negative fins followed the same pattern of flow. When the temperature that was supplied to the fins was a function of time and the positions of the fins for transient velocities of input fluid, the values of flowing molecule velocities were marginally higher (Fig. 4.C1, D1, and F1) and lower when the velocities of the fluid remain constant over the course of flow (Fig. 4.A1, B1, and E1). The distribution of heat differed more for the microchannel with negative fins when the input fluid velocity was function of time, and the input temperature to the fins was constant with time (Fig. 4.B2) than when the input fluid velocity was constant with time and the input temperature was function of time (Fig. 4.C2). Figure 4.D2 demonstrated that the rate of heat transfer to the flowing fluid increased as both the velocity of the input fluid and the provided temperature to the fins varied with respect to time. Additionally, the rate of heat distribution transfer was higher in the areas close to the boundaries of the walls and fins when the input heat to the fins was a function of their positions for the constant velocity at the inlet, as opposed to the rate of heat transfer in the area midstream of the flow-lines (Fig. 4.E2).

It was discovered that positive fins exhibit more entropy fluctuations in the velocity distribution than negative fins. The cells that had been seeded had a stronger excitatory phase as a result. Furthermore, it was shown that in the case of positive fins, the impact of heat transfer on the velocity profile was minimal. The heat distribution profile had a dynamic transitory that positively aligned the fins around it.

This suggested that, without interfering with the patterns of velocity variations, it would be conceivable to have heat distribution that is heterogeneous in channels with positive fin alignments. However, the distribution of velocity in the channels with negative fins had a bigger impact on the rate of heat transfer. The presence of positive fins signals the possibility of a thermal effect that could cause stoichiometric alterations in the substrate's biomimetic topographical features through the heterogeneous distribution of heat transfer. As a result, cellular morphogenic activity may be spatially customised. The null influence of transient heat transfer rate on fluid flow characteristics in the channels having fins with positive alignments hints higher indications for mechanotransduction of flowing or floating cells near the fin circumference because of momentary fluctuations of entropy of the fluid flowing nearby these fins.

5 Conclusions

Surface and internal temperature variations result from the rapid heating of a substance. Thermal expansion is made possible by rapid heating, and the localised material movement that results in thermal strains. According to the energy conservation rule, the entropy changes were more pronounced close to or between the fins due to the distribution of heat transmission inside the microchannel. Because of the reduced internal energy shifts at specific places, the seeded cells were able to stick together better. In contrast to the case of negative fins, the presence of positive micro-fins had a greater impact on entropy.

As a result, the fluid around the fins with varied radii could generate local vortices. Due to the transmission of provided heat to the working fluid, fluidic molecules displayed a heterogenous entropy variation. The advantage of the suggested method is that it allows for the analysis of cell dispersion behaviours over the channel substrate. The obstacle of fabricating an inaccessible wavy pattern for various tissue profiles inside some annular structures, such as the trachea, blood arteries, and oesophagus, may be overcome using this technique.

Nomenclature

f Force (N)
ρ Density of fluid (kg/m^3)
$\vec{a}$ Acceleration (m/s^2)
P Pressure (N/m^2)
$\vec{V}$ Velocity (m/s^1)
T Temperature (K)
C_p Specific heat capacity (J/kg/K)
μ Viscosity (Pa s)

References

1. Ahmad Khalili A, Ahmad MR (2015) A review of cell adhesion studies for biomedical and biological applications. Int J Mol Sci 16(8):18149–18184
2. Mierke CT (2011) Cancer cells regulate biomechanical properties of human microvascular endothelial cells. J Biol Chem 286(46):40025–40037
3. Kandlikara G, King MR (2014) Heat transfer and fluid flow in minichannels and microchannels. https://doi.org/10.1016/B978-0-08-098346-2.00001-6
4. Lu H, Xu M, Gong L, Duan X, Chai JC (2019) Effects of surface roughness in microchannel with passive heat transfer enhancement structures, 26 Nov 2019. https://doi.org/10.1016/j.ijheatmasstransfer.2019.119070
5. Lu H, Xu M, Gong L, Duan X, Chai JC (2020) Effects of surface roughness in microchannel with passive heat transfer enhancement structures. Int J Heat Mass Transf 148:119070
6. Croce G, D'Agaro P (2005) Numerical simulation of roughness effect on microchannel heat transfer and pressure drop in laminar flow. J Phys D Appl Phys 38(10):1518
7. Zhang C, Chen Y, Shi M (2010) Effects of roughness elements on laminar flow and heat transfer in microchannels. Chem Eng Process 49(11):1188–1192
8. Li W, Joshi Y (2020) Capillary assisted evaporation/boiling in PDMS microchannel integrated with wicking microstructures, 02 Sept 2020. https://doi.org/10.1021/acs.langmuir.0c01711

CFD Analysis of Drag Reduction System (DRS) in Cars

Sandeep Kulkarni, Pranav Malasane, Nimesh Zanje, Yogesh Metkari, Niranjan Ghadge, Sneha Athawale, and Pramod Kothmire

1 Introduction

In 2011, a groundbreaking innovation known as the Drag Reduction System (DRS) was introduced in the Formula One domain. This technology allows the extension of the flap wing for overtaking assistance when engaged. During practice and qualifying, drivers have the freedom to utilize DRS within specified zones, provided they are within one second of the vehicle in front at the DRS detection point. The system automatically deactivates when the driver applies the brakes after activation, returning the rear wing flap to its original configuration. Since its debut, Formula One teams, including Formula Society of Automotive Engineers (SAE) teams, have adopted DRS to reduce drag in specific track zones [1]. The impact of vehicle design on Formula One car efficiency is also noteworthy. The rear wings of F1 cars, functioning oppositely to airplane wings, generate about 15–20% of the total downforce in conjunction with the back diffuser [2]. Utilizing a rear wing package concurrently reduces drag and increases downforce, influencing a sports car's top speed and acceleration.

A low-density zone develops behind an item when the fluid around it is moved. A low-pressure area was created as a result. To determine the drag force, use

$$F\,(\text{drag}) = \frac{C}{2\text{DAV}^2}$$

The front wing's construction prevents the automobile from rising off the ground. As a result, the front wing is made to have the airfoil's opposite form. The front wing endplates are of utmost significance. Because the wheels of F1 cars are mounted close to the chassis, downforce is boosted [7]. The vehicle can operate safely thanks

S. Kulkarni (✉) · P. Malasane · N. Zanje · Y. Metkari · N. Ghadge · S. Athawale · P. Kothmire
School of Mechanical Engineering, MIT Academy of Engineering, Alandi, Pune 412105, India
e-mail: sandeep.kulkarni@mitaoe.ac.in

to the rear wings, which counteract the detrimental effects of aerodynamic activity. In addition, it is shown that the connection between the coefficients of drag and downforce is suitable up to an angle of attack of 20 degrees. Furthermore, it is acknowledged that the dynamic performance of the F1 would be enhanced by the application of various composite materials like Kevlar or zylon-based [8]. A DRS would unquestionably be beneficial due to the huge drag reduction it causes at $15°$ and $-10°$ angles of attack [9]. This study looks at how the thickness and chord length of the wing flap affect airflow at the rear wing, as well as the aerodynamic behavior of airflow around the rear wing. The results demonstrate that decreasing downforce occurs as the flap wing aerofoil's thickness is increased. By optimizing the relative positioning of airfoil components, it is possible to achieve comparable downforce values while lowering drag for a certain configuration of a multi-element wing (number of elements in the wing). The objective of this research is to increase downforce while lowering drag on the vehicle [10]. In 2021, a comparison of several automobile attachments was done.

In 2021, a comparison of automobile attachments, including a GT spoiler with a diffuser, demonstrated a maximum drag reduction of 16.53%. While classical wind tunnel testing remains a reliable method for studying vehicle aerodynamics, Computational Fluid Dynamics (CFD) is recognized as a flexible and cost-effective alternative. Well-controlled CFD analysis can accurately predict a pre-designed vehicle's aerodynamic drag coefficient within 6–8%, providing a valuable tool for understanding and optimizing vehicle aerodynamics [3].

Observing existing literature, the study notes a lack of systematic investigations into the fundamentals of drag reduction processes, inspiring the researchers to address this gap. The current work focuses on systematically exploring how drag reduction contributes to increased vehicle efficiency using CFD techniques, addressing challenges outlined in the literature. The study specifically examines pressure and velocity while calculating drag coefficient, lift coefficient, drag force, and downforce, along with a comparative analysis of various NACA airfoils.

2 Literature Review and Objective

The research conducted by B. Vidhya Darshini, titled "Modeling and CFD Analysis of F1 Rear Wing," focuses on investigating the airflow dynamics through the rear wing of an F1 car using Computational Fluid Dynamics (CFD) modeling. The primary objectives of this study are to explore the aerodynamic behavior of the airflow around the rear wing and assess the impact of flap wing chord length and thickness on the airflow. The study reveals that an increase in flap wing airfoil thickness leads to a reduction in downforce. However, through careful optimization of the relative positioning of airfoil elements, it is possible to achieve comparable downforce values while concurrently minimizing drag for specific multi-element wing configurations. The aim is to maintain comparable downforce levels while alleviating drag on the vehicle [4]. Traditionally, the lower side of airfoils tends to be thicker. The downforce

exerted on the lower airstream decreases the surface area, resulting in increased flow speed and decreased pressure [5]. This study emphasizes two additional benefits of a spoiler on the overall pressure force: an augmented pressure force on the rear side of the vehicle due to the spoiler's diffuse impact and an increased pressure on the spoiler itself. The reduction of maximum lift is observed by using the same airfoil with a decreased attack angle [6]. F1 cars, distinguished by their advanced aerodynamics, effortlessly cut through the air and manipulate airflow toward the rear wings. This design minimizes drag and lift forces on the vehicle body, enhancing stability at high speeds. The study emphasizes the importance of reducing fuel consumption through a low-drag car body during straight-line travel, while acknowledging the challenge of common low-drag car body forms causing a decrease in downforce on the rear tires. The addition of rear diffusers or wings to sports vehicles mitigates these effects. Experimental and numerical studies on a passenger car model, specifically a 1/5th-scale model FIAT Linea, were conducted to examine pressure distributions and drag forces at different blockage ratios in wind tunnels at Uludag University and Ankara Wind Tunnel.

The literature review underscores the critical need for drag reduction to maximize both aerodynamic efficiency and fuel economy, especially considering the exponential rise in drag with increases in speed. Front wings, rear spoilers, and underbody design all contribute to the downforce a car produces. Adjustable rear spoilers, such as those in Formula One, play a crucial role in enhancing straight-line and turning speeds.

The subsequent sections of the research are organized into three segments post-literature review. The first focuses on CFD analysis of all airfoils, including contour examination. The second aims to calculate coefficients of drag, lift, downforce, and drag force. The third objective involves comparing the drag force and downforce of the three airfoils to determine the most effective design.

3 Methodology

Contemporary advancements in aerodynamics predominantly rely on Computational Fluid Dynamics (CFD) to facilitate cost-effective exploration of concepts and refinement of designs during the early stages of development. This study employs CFD analysis to investigate the impact of pressure on the airfoil and the variation in velocity around it, specifically focusing on National Advisory Committee of Aeronautics (NACA) airfoils—NACA 2408, NACA 2412, and NACA 2415. The analysis involves utilizing Ansys student software to assess drag and lift, while the geometry is designed using CATIA V5.

3.1   Geometry Creation

Various NACA airfoils are employed to configure the geometry for the double flap Drag Reduction System (DRS). Two airfoils, each with chord lengths of 250 mm for the main airfoil and 175 mm for the flap, are utilized to construct the 2D geometry. To establish a 10 mm gap between the two airfoils, the Y-axis coordinates of the flap are elevated by 10, and the airfoil coordinates are extracted from airfoil tools. Both airfoils are enclosed within a rectangular boundary with dimensions of 500 mm by 800 mm (height by width). The computational domain is set up with a front side extension of 8 times the width (w) and a rear side extension of 12 times the width when w equals 800 mm. For the analysis, conventional Drag Reduction System parameters, featuring a width of 1500 mm and a height of 500 mm, are considered. The impact area A, representing the frontal area of the object encountering air, is crucial for comprehending drag and lift, with a frontal area of 0.75 m^2 in this investigation. The material within the domain is maintained as air, a fluid characterized by standard parameters (density: 1.225 kg/m^3; viscosity: 1.7894e-05 kg/m s). Three NACA airfoils—NACA 2408, NACA 2412, and NACA 2415—are subjected to a CFD simulation, with identical gap positions of 10 mm. Despite the variation in chord lengths between the two airfoils, both adhere to the same standard (Fig. 1).

3.2   Mesh Selection

Meshing is the process of converting geometry into a collection of small elements, each referred to as an element. In this study, a straightforward mesh with linear order is employed for geometry meshing, and mesh refinement is applied to enhance accuracy. To achieve optimal results, a fine-element mesh is generated. The element size is maintained at a constant 50 mm for all cases in the study. Mesh quality is assessed through statistical data presented in Table 1 reports. The element quality spans from 0.2631 to 0.9994, and the aspect ratio ranges from 1 to 2.957, with all elements exhibiting the same value. Aspect ratios below 5 indicate that the generated elements possess high quality, affirming that the meshing is well-suited for the analysis (Fig. 2).

3.3   Grid Independence Analysis

The grid independence test is conducted on the NACA 2408 airfoil, utilizing the coefficient of lift to coefficient of drag (cl/cd) ratio as a pivotal parameter. The investigation focuses on observing how the results vary in response to changes in the element size. Figure 3 demonstrates the discernible impact of altering the element size on the cl/cd ratio. In the context of the Drag Reduction System, a higher cl/cd value signifies a superior outcome. Minimizing drag force during straight motion is crucial

(a)

(b)
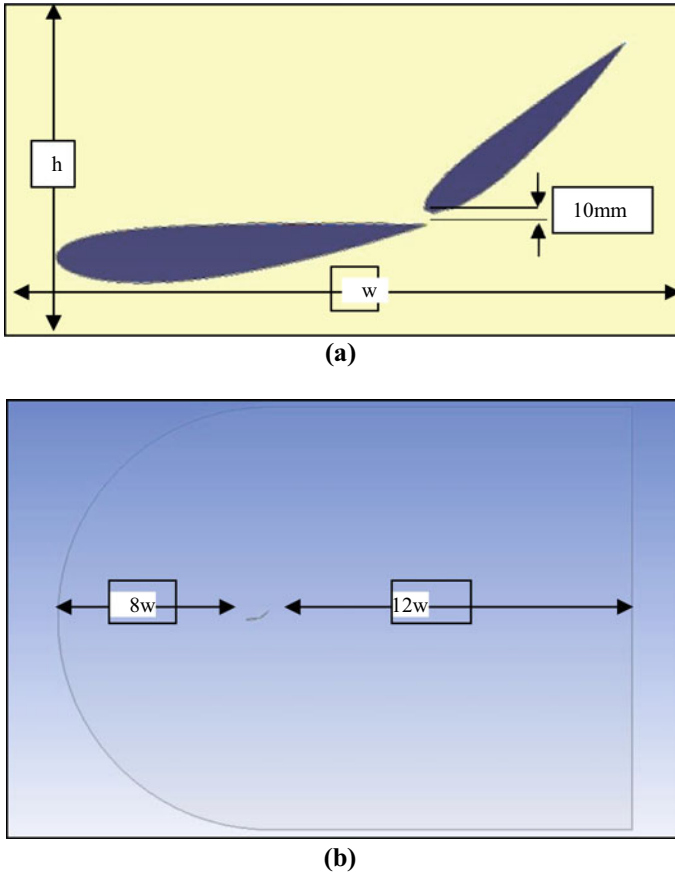
Fig. 1 a Double flap DRS geometry with 10 mm gap and **b** air domain around the geometry

Table 1 Quality check parameters

Sr. No	Parameter	Maximum	Minimum
1	Element quality	0.9994	0.2631
2	Aspect ratio	2.957	1
3	Jacobian ratio	4.8969	1

for achieving high speed, while increasing drag during cornering enhances traction. The cl/cd ratio experiences a noteworthy increase of 14.99% when the element size is reduced from 100 mm to 50 mm. It is important to note that this enhancement in performance is accompanied by a marginal increase in the computation time, approximately 0.5 seconds per iteration.
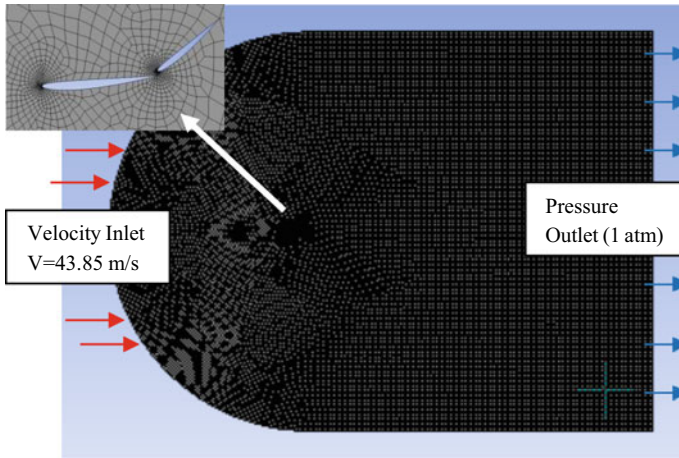
Fig. 2 Meshing around airfoil with 50 mm element size

Fig. 3 Variation of cl/cd ratio with respect to element size
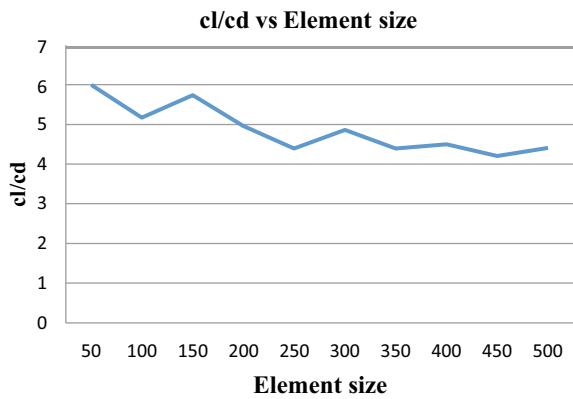
During the study, it is observed that more computational time is required for fine elements and observed spikes in residual graph. We determined that 50 mm element size is appropriate for this study. For all cases, the element size is kept at 50 mm.

3.4 Boundary Condition

To conduct a numerical study, modeling is carried out based on specified parameter values. The selection of the k-omega model is motivated by its demonstrated efficacy in boundary studies. The boundary conditions are outlined in Table 2 The focus of the study involves examining the airflow around the airfoil, for which the SST k-omega model is deemed more suitable compared to the k-epsilon model. Several crucial

Table 2 Boundary conditions

Sr. No	Condition	Value
1	Fluid	Air
2	Airfoil material	Aluminum
3	Model	SST k-omega
4	Solution method	Simple
5	Inlet velocity	43.85 m/s
6	Outlet pressure	1e+5 Pa

parameters, including impact area and air velocity, play a pivotal role in determining drag and lift values. The reference values for these parameters are as follows: area = 0.75 m^2, air velocity 7 = 43.85 m/s (in the A direction), ambient temperature 288.16 K, and a specific heat ratio of 1.4. The report definition encompasses the coefficient of drag (cd), drag force (downforce), coefficient of lift (cl), and lift force. To mitigate the occurrence of negative lift values, the force vector is set to -1 in the y direction, mirroring the conditions encountered in the Drag Reduction System (DRS).

4 Results and Discussion

The analysis results were obtained using Ansys Fluent 2022, encompassing evaluations on three distinct airfoils with the aim of attaining specific outcomes. These objectives involve the generation of pressure and velocity contours, alongside assessing various forces to facilitate airfoil comparisons. To ensure the robustness of our findings, reference has been made to previous research work, as guided in [1].

Both drag force and cl/cd values exhibit a consistent trend across the selected airfoils. Notably, the NACA 2415 airfoil emerges as the optimal choice, demonstrating superior performance characterized by low drag and high downforce Figure 4a illustrates the consistent decrease in drag force values across the different airfoils, with the magnitude in the current work slightly lower than in the referenced research due to variations in CFD models employed. Figure 4b depicts comparable cl/cd values between the two studies, with only the 2415 airfoil showing slight variations.

Pressure Contour

The pressure plot for the three airfoils reveals a circular pressure distribution at the upper side of the Drag Reduction System (DRS), positioned between the two airfoils. This pattern signifies that downforce is more pronounced when the DRS is in a closed position, affirming the underlying physics governing the DRS mechanism. Notably, the maximum pressure attained follows a proportional order: NACA 2415 > NACA 2408 > NACA 2412 (Fig. 5).

Fig. 4 Graph shows
a comparison of drag force
(research paper and current
work) and **b** cl/cd
comparison

(a)

(b)
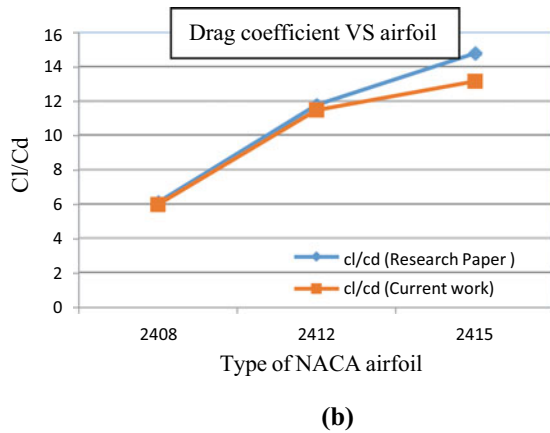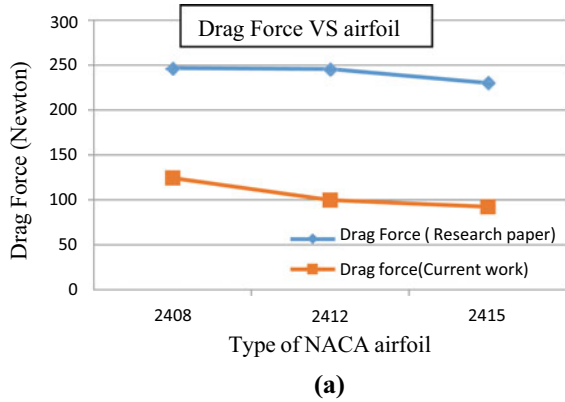
Velocity Contour

The velocity significantly decreases upon exiting the Drag Reduction System (DRS), as illustrated in Fig. 6a. In contrast, Fig. 6b depicts a reduction in velocity that eventually returns to normal Figure 6c demonstrates a swift recovery to normal velocity over a short distance. This observation implies that when a vehicle equipped with the DRS, as illustrated in Fig. 6c, continues its movement, the trailing air quickly reverts to its original velocity, minimizing the presence of turbulence or "bad air" left behind.

Coefficient of Drag and Drag Force

Figure 7a depicts a graph illustrating the drag coefficient plotted against the number of iterations. Notably, after 15 iterations, the drag coefficient stabilizes, indicating a consistent value. Turning off the Drag Reduction System (DRS) results in a loss of traction during turns, with a drag coefficient (Cd) value of 0.1128. Comparative Cd values for NACA 2408 and NACA 2415 stand at 0.1406 and 0.1044, respectively.
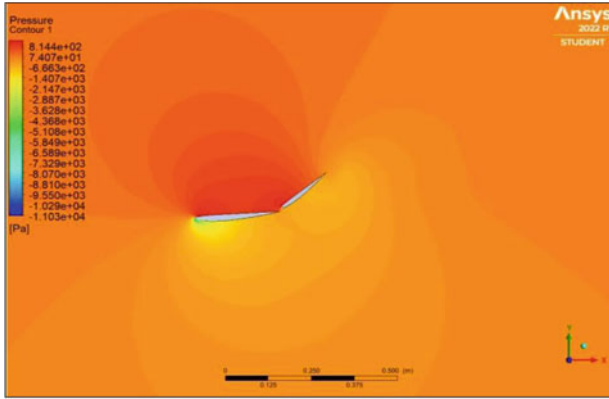
(a)
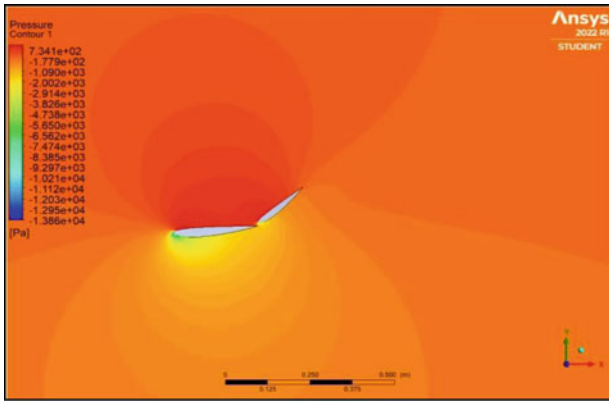
(b)
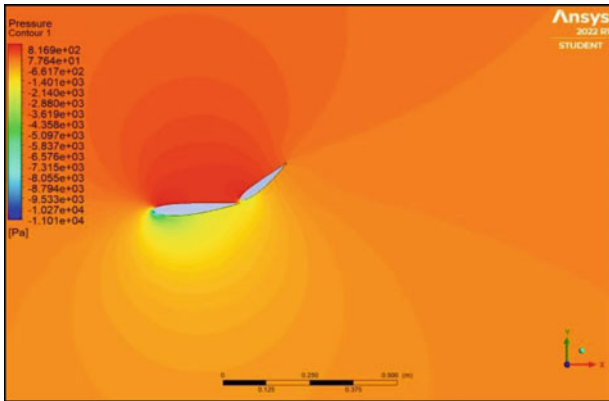
(c)

Fig. 5 Pressure plot for DRS geometry with **a** NACA 2408, **b** NACA 2412, **c** NACA 2415
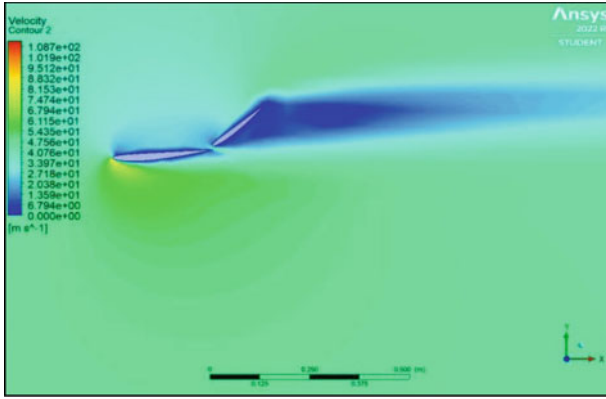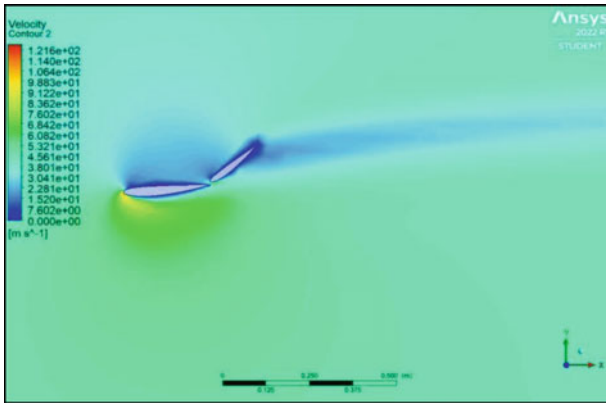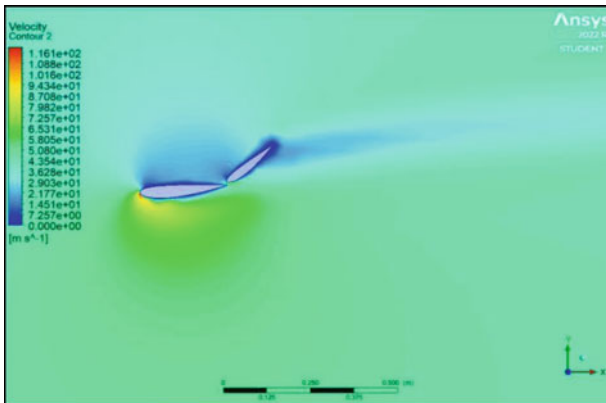
Fig. 6 Velocity contour of DRS with **a** NACA 2408, **b** NACA 2412, **c** NACA 2415
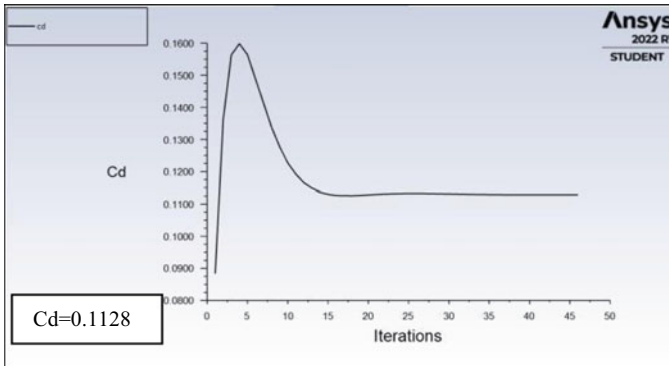
(a)
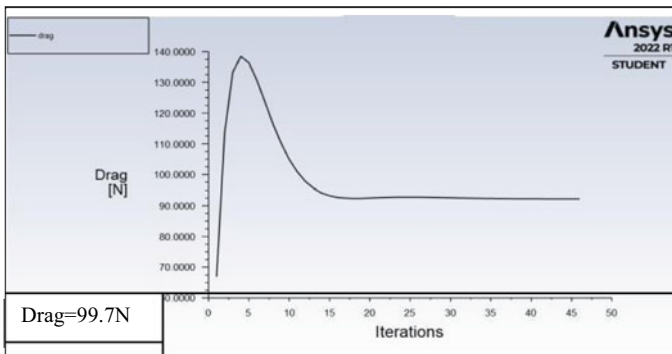
(b)

Fig. 7 Graph shows **a** coefficient of drag versus number of iterations (NACA 2412), **b** drag force versus number of iterations (for NACA 2412)

In Fig. 7b, the drag force values (in Newton) for NACA 2408, 2412, and 2415 are presented as 124.24, 99.70, and 92.24, respectively. These values provide insights into the aerodynamic performance of the different airfoils. Moreover, Figure 7c reveals the coefficients of lift for NACA 2408, 2412, and 2415, corresponding to 0.8431, 1.2983, and 1.3752, respectively. The downforce values (in Newton) for these airfoils are 744.79, 1146.85, and 1214.73, respectively.

5 Conclusions

The computational fluid dynamics (CFD) analysis employs the SST K-omega model to derive essential values for drag force, downward force, lift coefficient, and drag coefficient. In comparison to the NACA 2412 and NACA 2408 airfoils, the NACA 2415 airfoil exhibits a remarkable 8% reduction in drag and 34% less drag than

the NACA 2408 airfoil. Additionally, the NACA 2415 airfoil generates 6% more downforce than the NACA 2412 and 30% more than the NACA 2408 airfoil. The ratio of the coefficient of lift to the coefficient of drag is also higher for the NACA 2415 airfoil. Consequently, the descending order of airfoils based on performance is established as NACA 2415 > NACA 2412 > NACA 2408.While this study focuses solely on the rear wing, it is crucial to recognize that the side and front wings of racing vehicles play a significant role in aerodynamics, contributing to approximately 30% of the overall downforce. Future research endeavors should consider these additional elements, as various components of racing cars exert an influence on overall vehicle aerodynamics.

References

1. Azmi ARS, Sapit A, Mohammed AN, Razali MA, Sadikin A, Nordin N (2017) Study on airflow characteristics of rear wing of F1 car. IOP Conf Ser Mater Sci Eng. https://doi.org/10.1088/1757-899X/243/1/012030
2. Thomas P, O'Driscoll, Barron AR (2022) CFD analysis of the location of a rear wing on an aston martin DB7. In: Order to optimize aerodynamics for motorsports, vol 6, pp 608–620. https://doi.org/10.3390/vehicles4020035
3. Moujaes S, Armbya N (2006) CFD study of section characteristics of Formula Mazda race car wings
4. Penner DJ (2020) Aerodynamic design and analysis of a formula SAE drag reduction system (DRS). SAE Technical Paper 2020-01-0685. https://doi.org/10.4271/2020-01-0685.
5. Bhattacharjee S, Arora B, Kashyap V (2019) Optimization of race car front splitter placement using CFD. SAE Tech Paper 2019-01-5097. https://doi.org/10.4271/2019-01-5097
6. Deng Z, Sijia Y, Gao W, Yi Q, Wei Y (2020) Review of effects the rear spoiler aerodynamic analysis on ground vehicle performance. J Phys Conf Ser. https://doi.org/10.1088/1742-6596/1600/1/012027
7. Dey S, Saha R (2018) CFD Study on aerodynamic effects of NACA 2412 airfoil as rear wing on a sports car. In: International conference on mechanical, industrial and energy engineering
8. Darshini BV, Srija C, Srujana J, Sai DA, Suresh A (2021) Modeling and CFD analysis of F1 rear wing 7(4)
9. Ahsan M, Numerical study on aerodynamic drag reduction on a rear wing of a formula student car
10. Cakir M, CFD study on aerodynamic effects of a rear wing/spoiler on a passenger vehicle

CFD Analysis of Different Shape Rocket Nozzles

Pramodini Patil, Ashish Birajdar, Darshan Kuwar, Rugved Naigaonkar, Varad Madhavi, Vishal Gaikwad, and Pramod Kothmire

1 Introduction

Various new technologies are now available for the development of high-performance, safe, and reliable propulsion systems [1]. A nozzle commonly used in rocket engines is a device with a simple, specially shaped tube with a simple configuration that includes a fixed convergent section followed by a fixed divergent section and joined by an intermediate throat [2]. A jet plume with a high temperature is exhausted at supersonic speed when a rocket is launched, so the nozzle is designed such that the combusted hot exhaust converges after leaving the combustion chamber and then is entropically expands after the throat [3]. It is essential to understand the external and internal flow simulations of the rocket nozzle to develop a space launch vehicle with high reliability as, because of chemical erosion, the distribution of erosion rate and nozzle profile are changing with time [4, 5]. A rocket engine uses a propelling nozzle to accelerate hot exhaust to produce thrust by expanding and accelerating combustion products to high supersonic velocities. This is based on Newton's third law of motion [6].

Chemical thermal energy produced in the combustion chamber is transformed into kinetic energy by the nozzle. The nozzle converts the combustion chamber's low-velocity, high-pressure, and high-temperature gas into high-velocity, lower pressure, and lower temperature gas [7]. The internal nozzle flow development of a solid rocket is crucial to nozzle performance and design. Numerous physical processes taking place inside the nozzle are strongly and directly influenced by the mean velocity field, real pressure distribution, and turbulence characteristics, in particular [8]. A rocket engine nozzle begins by converging before being constricted in the middle, or throat, and finally diverging. Consequently, it is known as a converging–diverging nozzle. Primarily, the flow in the throat is sonic, which means that its Mach number

P. Patil · A. Birajdar · D. Kuwar (✉) · R. Naigaonkar · V. Madhavi · V. Gaikwad · P. Kothmire
School of Mechanical Engineering, MIT Academy of Engineering, Alandi, Pune 412105, India
e-mail: darshan.kuwar@mitaoe.ac.in

is one at the throat and becomes supersonic in the diverging section of the nozzle [9]. As a small angle enhances the actual component of exit velocity and generates a high specific impulse, which is a measure of rocket efficiency, it produces more thrust [10]. As the exhaust passes through the diverging section, its static pressure and temperature decrease, which results in exit velocity and directly affects the thrust produced at the end. The mass flow rate through the engine, the exit velocity of the flow, and the pressure at the exit of the engine all affect the amount of thrust the engine produces. The values of these three flow variables are all determined by the rocket nozzle design [11]. The pressure ratio increases with increasing discharge coefficient for small divergence angles, but the Mach number and other parameters vary with the angle of divergence [12]. The separation front enters an infection region, which is immediately downstream of the inflection point and is characterized by a negative wall pressure gradient produced by viscosity, identical to that of conventional nozzles, at the start of the transition [13]. High expansion resources are needed for increased high-altitude performance; however, this leads to over-expanded flow conditions at altitudes closer to sea level. The occurrence of significant side loads, or forces that act laterally to the actual direction of the thrust during the very transient startup and shutdown operations, is the most severe restriction on the over-expanded operation of conventional nozzles [14]. The De-Laval nozzle on the hybrid rocket motor causes overexpansion at small chamber pressure and thrust, and the hybrid rocket motor may easily adjust thrust by changing the oxidizer mass flow rate [15].

It is common practice to use either experimental or analytical results to determine the accuracy of the CFD models by comparing the results in the analysis of convergent–divergent nozzles using Computational Fluid Dynamics. The performance of any rocket nozzle in all practical approaches is always less than the theoretical approach [2]. In order to examine shockwaves and boundary layers and create shock-wave location as an analytical output, Stewart Keir studied a variety of theoretical and experimental data and analyzed them. Based on that analysis, new modifications to the studied designs were made in order to obtain a better output [16]. The expansion ratio of the nozzle has a direct impact on its efficiency. The structure of a fixed expansion ratio is provided by the conventional nozzle. Variable structure nozzles have emerged as a research hotspot in order to adapt to the maximum usage of solid rocket motor gas energy [17].

The major focus in the literature is addressed the work on the De-Laval nozzle. Literature reveals that the De-Laval nozzle, which is a convergent–divergent type nozzle, is the most efficient nozzle among all others. This is mainly because the Mach number and velocity of fluid flow are continuously increasing with continuously decreasing pressure. There is a lot of ambiguity in the literature as no one has systematically illustrated the fundamental science for estimating the performance of nozzles. So, we have tried to attempt the best geometry for a rocket nozzle, which is proposed in our work considering various parameters like Mach number and number of inlets. In this contest, the present scope of our work is CFD analysis of different rocket nozzles so as to achieve pressure, temperature, and velocity. For the present work, we have considered the geometry and boundary conditions of Falcon 9 as shown in Fig. 1. The Falcon 9 is a reusable, medium-lift launch vehicle that can

carry cargo and humans into Earth orbit. Also, a comparative study of nozzles is to be performed for different Mach numbers and exit velocities. This will help us to understand how the flow properties like turbulent intensity and thrust vary. Basically, different nozzles are analyzed to attain supersonic flow and to achieve the maximum thrust without flow separation by considering various parameters like velocity, turbulent intensity, Mach number, and geometry.

2 Materials and Methods

For carrying the analysis, many parameters are to be taken into consideration. Following parameters are deeply studied to achieve the final results.

2.1 Geometry

The geometry of the nozzle [7] of the hybrid rocket engine is shown in Fig. 2a. The total length of the nozzle is 2.547 m. The wire frame was designed to depict the cross-section of the nozzle. The convergent radius is 0.11 m and the divergent radius is 0.55 m. The oxidizer is injected through the combustion chamber inlet and reacts with the fuel to produce high-temperature and high-pressure gas, which is then passed through the nozzle to produce thrust. The nozzle throat radius is 0.064 m, with a convergence half-angle of 30.124° and a divergent half-angle of 13.4°. The design of the nozzle has been carried out using CATIA V5. The three-dimensional model designed in CATIA from the isometric view is shown in Fig.2b.

For the identical specifications of the inlet diameter, outlet diameter, and throat diameter, a bell-shaped nozzle is designed, but the length for this nozzle is 74% of the convergent–divergent nozzle, that is 1.98 m and the convergent angle of 24°. The same geometry is depicted in Fig. 2c.

Fig. 2 Two different geometries used for CFD investigation in the present work: **a** Nozzle Geometry [7], **b** 3D CAD model of C–D nozzle and **c** 3D CAD model of Bell-shaped nozzle

(a)

(b)

(c)
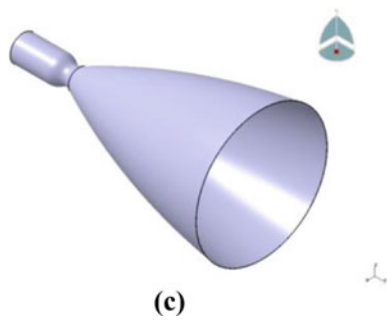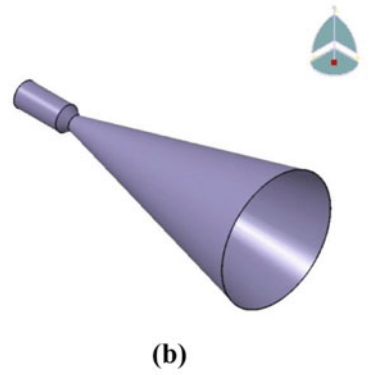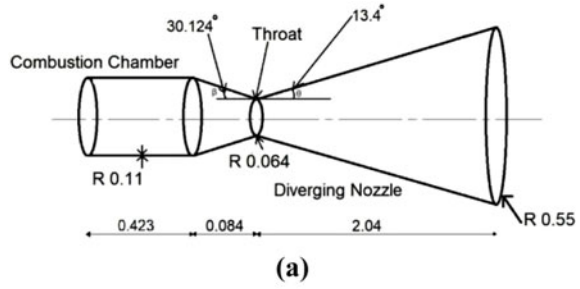
2.2 Meshing

After creating the geometry, the next step is to mesh it for the further CFD process. The meshing is done in ANSYS 22.0. Meshing is one of the important factors for doing the analysis. The inner wall is encrypted with a first layer mesh size of 15 mm and a growth ratio of 1.2, while Tetrahedron Mesh is used with the structured mesh for the computation. The mesh model is shown in Fig. 3. A mesh independence study is required to get the most accurate results over different mesh sizes. The geometry was meshed with five different sizes, and after comparing the results of each mesh, the best results were obtained at a 15 mm mesh, which is a finer one. Figure 4 shows
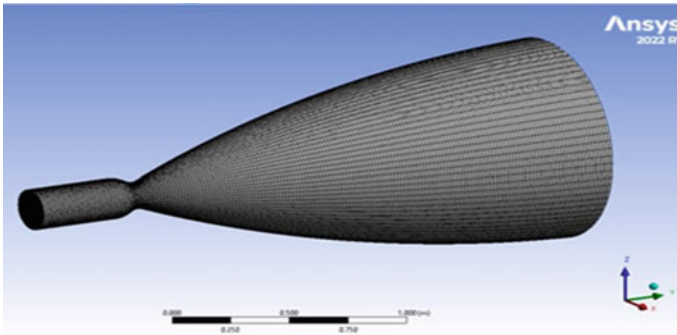
Fig. 3 Meshed geometry of bell-shaped nozzle
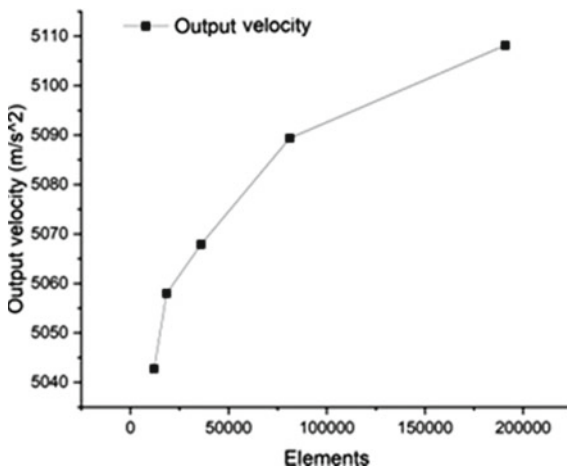
Fig. 4 Mesh independence graph

the graph of mesh independency with velocity as a result on the Y axis and the number of elements on the X axis.

2.3 Boundary Conditions

Firstly, the fluid domain model is established. As this paper is concerned with nozzle geometries, the nozzle part was taken for modeling. According to the Falcon 9 application, the nozzle inlet conditions used a mass flow inlet with a total mass flow rate of 2100 kg/s. The inlet temperature is 3500 K and the initial gauge pressure is 75 MPa. Ambient conditions were assumed at the outlet (the gauge pressure was taken as zero and the temperature as 300 K).

A density-based solver is used, taking into account the effects of viscous flow. The solution is done in an implicit formulation. In the case of fluid, the material type was designated as air, and solid titanium was used for the nozzle's wall. The energy equation was applied, and the standard k-epsilon viscous model was used for turbulence with a standard wall function.

2.4 Governing Equations

The following basic equations are used in one way or another to analyze flow characteristics since they let the user guess and calculate various flow variables including pressure, velocity, temperature, and turbulence [18].

Continuity Equation,

$$\frac{\partial \rho}{\partial_t} \times \frac{\partial}{\partial_{xi}} (\rho v) = 0 \quad \text{Momentum Equation}$$

$$\frac{D_{(\rho ui)}}{D_t} = \frac{\partial \rho}{\partial_{xi}} + \frac{\partial \rho}{\partial_{xj}} \left[\mu_{eff} \left(\frac{\partial_{ui}}{\partial_{xj}} + \frac{\partial_{uj}}{\partial_{xi}} - \frac{2\delta_{ij}\partial_{uk}}{3\partial_{xk}} \right) \right] + \frac{\partial(\rho ui uj)}{\partial_{xj}}$$

Pougatch et al. [21] advise assuming the overall enthalpy which is taken to be constant at this point in order to account for the conservation of energy. Therefore,

$$\text{Hg} = \text{Cp}T + \frac{V^2}{2} + k \quad \text{Constant}$$

At each location in the supersonic area, the features of the quasi-one-dimensional flow associated with the flow's Mach number can also be computed.

$$\rho = \rho_0 \left[1 + \left(\frac{y-1}{2} \right) M^2 \right]^{\gamma-1}$$

$$P = P_0 \left[1 + \left(\frac{y-1}{2} \right) M^2 \right]^{\frac{\gamma-1}{\gamma}}$$

$$T = T_o \left[1 + \left(\frac{y-1}{2} \right) M^2 \right].$$

3 Results and Discussion

This section compares the flow pattern of the bell-shaped nozzle to that of the convergent–divergent nozzle under various operating conditions. The calculation of thrust for each scenario also allows for a comparison of the performance of both nozzles under non-design situations.

The graph of the convergent–divergent nozzle as shown in Fig. 5 goes with the trend of the results of the mentioned paper [7], which validates our results for the velocity at various points over the length of the nozzle. The next graph shows the comparative study of the velocities obtained at five different points on the bell-shaped nozzle, which a little contradicts the trend after the throat area but matches for other regions, so the results we have obtained are true to the given constraint. For C–D and bell-shaped nozzles, the exit velocity available is 5694 and 44,793 m/s, respectively, from which it is observed that the bell-shaped is the most efficient to obtain more thrust and it matches the literature outcomes.

First, the fluid-domain steady-state results are determined. The pressure and temperature along the nozzle's central axis drastically drop as the majority of the heat energy in the nozzle are transferred to kinetic energy. It is observed that the velocity increases with the length of the nozzle. The velocity first dropped because of shocks in the nozzle, but it subsequently started to rise as the fluid expanded through the diverging part. In steady conditions, the gas velocity at the exit of the nozzle increases significantly to about 5694 and 44,793 m/s for the convergent–divergent nozzle and the bell-shaped nozzle, respectively. Figure 6a shows the distribution of gas velocity along the nozzle axis for the C–D nozzle and Fig. 4b shows the distribution of gas velocity for a bell-shaped nozzle.

All along the nozzle's length, the pressure progressively dropped, with the exception of a minor increase while shocking. In contrast to the overall drop in pressure, the increase was nevertheless insignificant. Bernoulli's equation predicts that pressure will decrease as expansion zone velocity rises. Figure 7a shows the distribution of gas velocity along the nozzle axis for the C–D nozzle, which gives 40,300 Pa outlet pressure, and Fig. 7b shows the distribution of gas velocity for the bell-shaped nozzle, which gives 18,901,000 Pa outlet pressure. So, as compared to the convergent–divergent nozzle, the bell-shaped nozzle design results in significantly higher outlet pressure.

Except for a minor uptick, the temperature is noted to have progressively declined. The minor increase arises in the shock zone, where fluid characteristics change quickly. However, compared to the overall reduction in temperature throughout the distance, the temperature increase was not substantial. The output temperature of the nozzle increases significantly to about 4895 and 4100 K for the convergent–divergent nozzle and the bell-shaped nozzle, as shown in Fig. 8a and b, respectively.
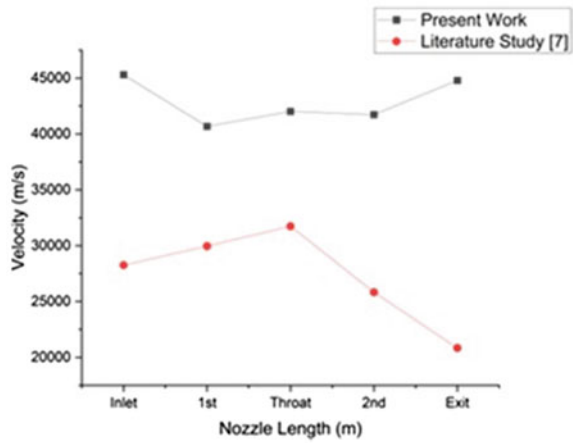
The simulated results and experimental findings [19] are in good agreement with each other. According to the thrust calculation formula,

$$Thrust = m.ve + Ae(Pe - Po).$$

Fig. 5 Velocity distribution graph over length of nozzle: **a** convergent–divergent nozzle and **b** bell-shaped nozzle
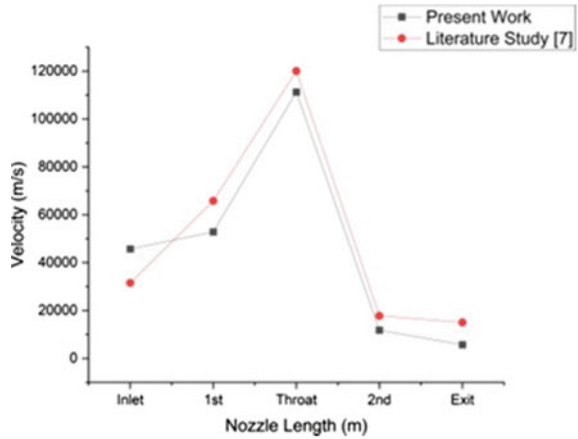

(a)

(b)

Among them, $\dot{m}$ is the outlet mass flow rate, ve is the exit gas velocity, Ae is the cross-sectional area of the outlet which is 0.4751 m^2 for all geometries, Pe is the outlet pressure, and P0 is the external pressure, here is 1 atm.

As Falcon 9 is the application considered for nozzle, the weight of the spacecraft is 525,000 kg against which the thrust force is applied

$$W = 5.15 \times 10^6 N.$$

Hence,

Fig. 6 Velocity distribution for two different rocket nozzles using CFD contours: **a** convergent–divergent nozzle and **b** bell-shaped nozzle

(a)

(b)
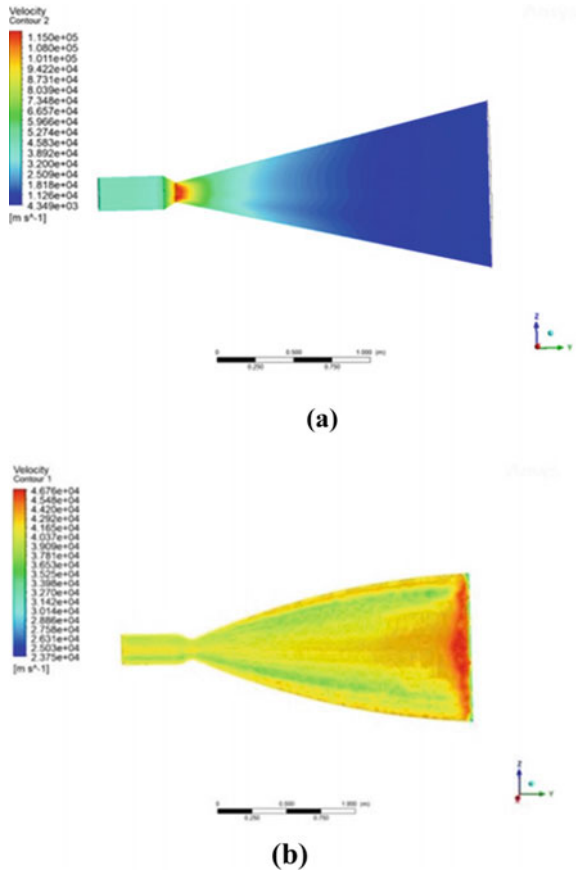
For cone nozzle (C–D type), the exit velocity and outlet pressure obtained during analysis are 5694 m/s and 40,300 Pa, respectively.

Thrust exerted by C–D nozzle,

$$Thrust = m.ve + Ae(Pe - Po)$$

$$Thrust = 2100 \times 5694 + 0.4751(40, 300 - 101, 325)$$

$$Thrust = 11.9284 \times 10^6 N.$$

And for the bell-shaped nozzle, exit velocity and outlet pressure obtained during analysis are 44,793 m/s and 18,901,000 Pa, respectively.

Thrust exerted by bell-shaped nozzle,

Fig. 7 Pressure distribution for two different rocket nozzles using CFD contours: **a** convergent–divergent nozzle and **b** bell-shaped nozzle
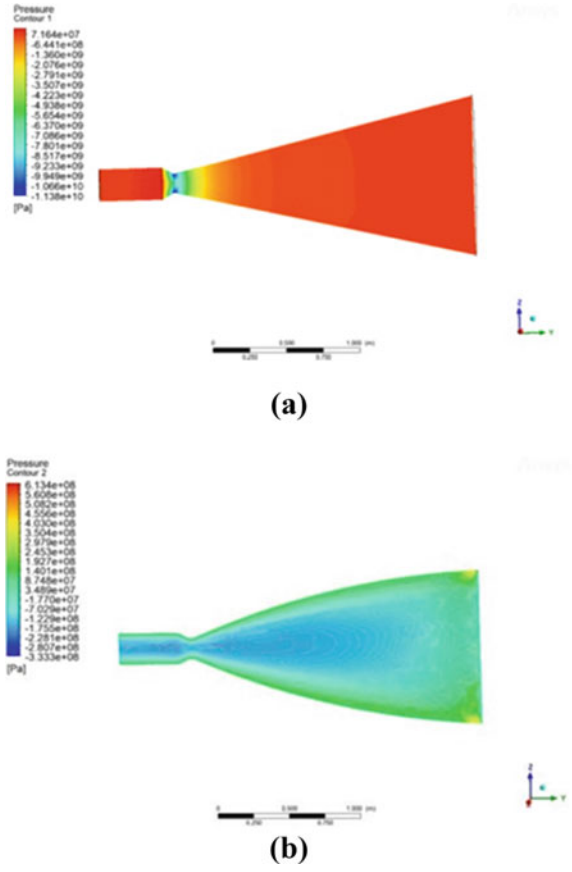
$$\text{Thrust} = \text{m.ve} + \text{Ae}(\text{Pe} - \text{Po})$$

$$\text{Thrust} = 2100 \times 44,793 + 0.4751(18,901,000 - 101,325)$$

$$\text{Thrust} = 10.2959 \times 10^7 \text{N}$$

The amount of thrust produced by both the nozzles is sufficient enough to propel the spacecraft against its gross weight. The thrust for a C–D nozzle is nearly 2.3 times the weight of the spacecraft, and the thrust of a bell-shaped nozzle is approximately 20 times the weight of the spacecraft. At high altitudes, less thrust is needed than at lower ones.

The results obtained are a little counterintuitive as compared to the literature results. Our CFD investigation reveals that for the bell-shaped nozzle, we got the maximum thrust as compared to the cone shape, which is inconsistent with the findings reported by Shivang et al. [20]. Basically, our understanding while doing

Fig. 8 Temperature distribution for two different rocket nozzles using CFD contours: **a** convergent–divergent nozzle, **b** bell-shaped nozzle


(a)

(b)
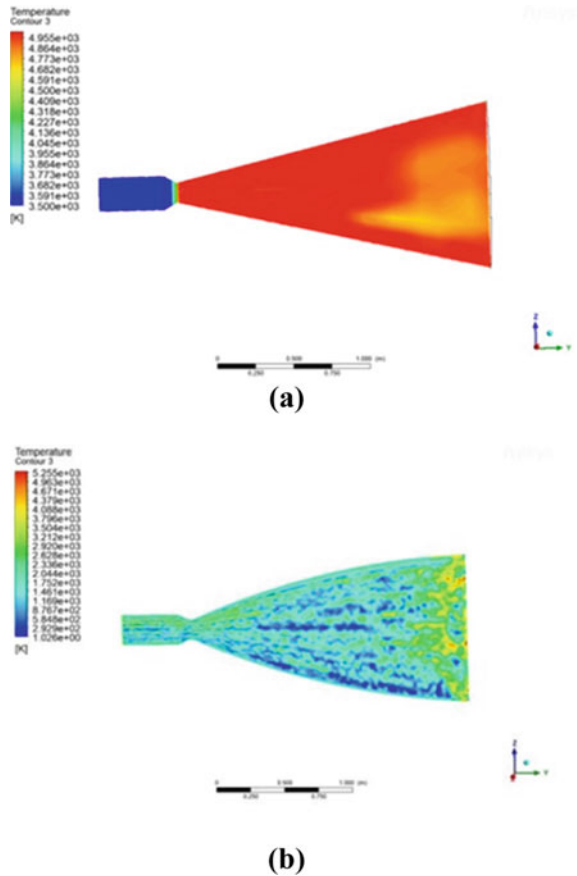
CFD investigation is that, in the bell-shaped nozzle, where the flow pattern is turbulent after the throat and spread all over the divergent section of the nozzle. And in the convergent–divergent nozzle, it develops a flow pattern that is more dense in the radially center area of the nozzle, and hence, the thrust imparted by the bell-shaped nozzle is inferred to be much greater than that of the convergent–divergent nozzle as shown in Fig. 9.

4 Conclusions

As soon as fuel and air are delivered into the combustion chamber, it burns immediately, and the temperature rises in the convergent and combustion chamber portions of the nozzle. The temperature then drops in the exit portion of the nozzle. It is observed that the velocity of the C–D nozzle is 5694 m/s and the thrust developed

Fig. 9 Velocity distribution for two different rocket nozzles using CFD streamline: **a** convergent–divergent nozzle, **b** bell-shaped nozzle
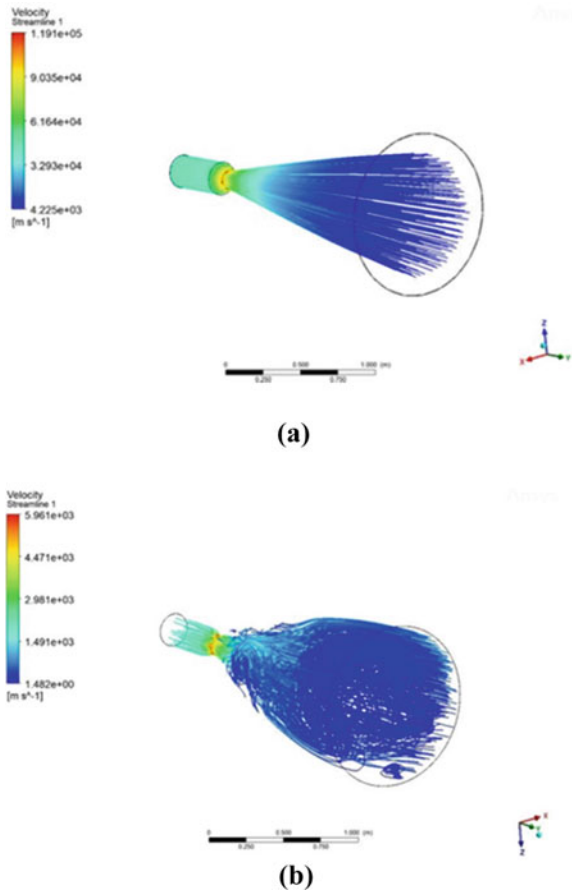
for it is 11.9284×10^6 N, which is 2.3 times the gross weight of Falcon 9. The bell- shaped gives a velocity of 44,793 m/s and a thrust of 10.2959×10^7, which is 20 times the gross weight of Falcon 9, from which it can be concluded that the bell-shaped nozzle produces more thrust compared to the C–D Nozzle.

The bell-shaped nozzles are well known because of their significant benefits in rocket engines due to their size and performance over the conical nozzle. Convergent–divergent nozzles experience thrust losses due to sudden changes in cross-section, but this drawback is overcome in the bell-shaped nozzle.

References

1. Stubbs RM, Kim SC, Benson TJ, Lewis N Computational fluid dynamics studies I of nuclear rocket performance prepared for the conference on advanced exploration initiative technologies cosponsored by AIAA, NASA, and OAI
2. Zhang X, Wang Z, Wang R, Lu C, Yu R, Tian H (2022) Numerical simulation of chemical ablation and mechanical erosion in hybrid rocket nozzle. Acta Astronaut 192(December 2021):82–96, 2022
3. Escarti-Guillem MS, Hoyas S, García- Raffi LM (2019) Rocket plume URANS simulation using OpenFOAM. Results Eng 4(October):pp 4–6, 2019.
4. Shimizu T, Kodera M, Tsuboi N (2008) Internal and external flow of rocket nozzle. J. Earth Simulator 9(March):19–26
5. Tian H et al (2021) Transient investigation of nozzle erosion in a long-time working hybrid rocket motor. Aerosp Sci Technol 118:106978
6. Zhukov VP (2019) The impact of methane oxidation kinetics on a rocket nozzle flow. Acta Astronaut 161(January):524–530
7. Belega B, Nguyen TD (2015) Analysis of flow in convergent-divergent rocket. Int Conf Sci Pap AFASES 2015
8. Balabel A, Hegab AM, Nasr M, El- Behery SM (2011) Assessment of turbulence modeling for gas flow in two-dimensional convergent-divergent rocket nozzle. Appl Math Model 35(7):3408–3422
9. Harikrishnan R, Lokavarapu BR (2020) Design and analysis of rocket nozzle. Mater Today Proc 38(xxxx):3365–3371
10. Sushma L, Udaya Deepika A, Kumar Sunnam S, Madhavi M (2017) CFD investigation for different nozzle jets. Mater Today Proc 4(8):9087–9094
11. Pandey KM, Yadav SK (2010) CFD analysis of a rocket nozzle with Fourinlets at Mach 2.1. Int J Chem Eng Appl 5(2):319–325
12. Srinivas G, Potti SR (2014) Numerical simulation of rocket nozzle. Adv Mater Res 984–985:1210–1213
13. Cimini M, Martelli E, Bernardini M (2021) Numerical analysis of side-loads reduction in a sub-scale dual-bell rocket nozzle. Flow Turbul Combust 107(3):551–574
14. Zhao X, Bayyuk S, Zhang S (2013) Aeroelastic response of rocket nozzles to asymmetric thrust loading. Comput Fluids 76:128–148
15. Hao Z, Tian H, Guo Z, Hedong L, Li C (2020) Numerical and experimental investigation of throttleable hybrid rocket motor with aerospike nozzle. Aerosp Sci Technol 106:105983
16. Cihan M (2019) Static structural and Cfd analysis of rocket nozzles made from, no. September
17. Keir AS, Ives R, Hamad F (2018) CFD analysis of C–D nozzle compared with theoretical & experimental data. INCAS Bull 10(2):53–64
18. Pougatch K, Salcudean M, Chan E, Knapper B (2008) Modelling of compressible gas-liquid flow in a convergent-divergent nozzle. Chem Eng Sci 63(16):4176–4188
19. Naghib-lahouti A, Nazarinia M, Tolouei E (2004) Design and Cfd analysis of an aerospike nozzle to compare its off-design performance with a conventional nozzle, no. March 2005, pp 244–261
20. Khare S, Saha UK (2021) Rocket nozzles: 75 years of research and development. Sadhana 46(2)
21. https://images.app.goo.gl/YCRqDCfT4MfVYZEd9

Numerical Analysis of Perforated Plate Use for Cooling Data Center and Server Room

Ankita Dawar and Beena D. Baloni

1 Introduction

The rising proportion, mass, complexity, and energy density of computer servers as a consequence of the rising in need for storage, networking, and processing include a significant power concern. Several ways to enhance energy efficiency are being researched, not just to provide for green rapid industrialization but also to minimize operational expenses. Inefficient cooling systems may contribute to up cooling energy consumption accounts for a massively disproportionate part of total energy consumption. The data center consumes 1% of the world's total power consumption. Almost all of the required electrical power in a data center is generated heat, which must be eliminated by a cooling system. Complex flow behavior through the tiles, such as flow acceleration via pores, jet–jet interactions, and downstream flow development, which simplistic models may fail to represent, must be taken into account to increase the correctness of the solution [1]. To achieve the needed gas flow homogeneity, perforated plates with a variety of open area ratios are used. Typically, plates with varying open area ratios are assemble into enormous panels whose total surface area might approach hundreds of square meter for large-scale industrial equipment [2]. An analysis of the thermal efficiency of an air-cooled data center using both raised-floor and non-raised-floor techniques an effort to address a specific thermal challenge [3]. The intricate structure of perforated plates complicates the mathematical modeling of system design and optimization. The impacts of a variety of factors on the flow pattern and pressure loss are explored. These parameters include Reynolds number, open porosity, orifice diameter, plate thickness, surface roughness, and plate

A. Dawar (✉) · B. D. Baloni
Department of Mechanical Engineering, Sardar Vallabhbhai National Institute of Technology, Ichchhanath, Surat, Gujarat 395007, India
e-mail: ankitadawar412@gmail.com

B. D. Baloni
e-mail: pbr@med.svnit.ac.in

inclination angle [4]. Focusing on incompressible fluids in the situation of totally turbulent flow, researchers examined the pressure drop that happens in correlation with a single-stage perforated plate. Typically, between upstream and downstream of a perforated plate is given by the pressure loss coefficient Eu. This dimensionless parameter expresses the ratio between the local pressure drop, caused by the restriction in the pipe due to perforated plates, and the kinetic energy per volume of the flow is given by equation, $Eu = \frac{\Delta P}{\frac{1}{2}\rho \times v^2}$ [5]. In this study, the dependence of the pressure loss on the Reynolds number, the porosity of the perforated plates, the number and distribution of holes under non-cavitating circumstances is explored at moderate Reynolds number range of 2500 to 9500. An expression, $Eu = 0.67 \times \beta^{-2.24}$ which gives the relationship between the pressure loss coefficient and the porosity of perforated plate is proposed with a mean deviation of 12% for practical usage [6]. The vast majority of data center employ the raised-floor design to feed server racks with cooling air. Providing the requisite airflow via the perforated tile(s) situated near the intake of each computer server is essential for proper thermal management [7]. The airflow through perforated tile limits the maximal equipment power density (e.g., power/rack or power/area) that may be placed in a standard raised-floor data center. Typically, in the design of a data center cooling system, a basic estimate of mean airflow per perforated tile is generated based on the number of CRACs and the number of perforated tiles [8]. CFD is an effective method for analysis the flow field in data centers. With a raised-floor arrangement, cold air is fed into an underfloor compartment and enters the room via perforated floor tiles placed in front of server racks. The results indicate that the cooling system's performance is greatly enhanced when the hard floor layout is replaced with a raised-floor configuration [9]. The kind of perforated tile and the present of plenum impediments have the most impact on airflow homogeneity. The floor layout, plenum depth, and airflow leakage rate have a moderate impact on uniform [10]. The generally used model for air flow through perforated plate is Porous jump model which specifies step pressure loss across the tile without considering the geometry of the tile. A recent proposed in the above model is body force model in these additional momentum source above the tile is taken into account. The aim of the present work is to evaluate the air flow rate through perforated tiles. A three-dimensional model with a plenum under uniform pressure is examined. Such studies are essential for evaluating the overall pattern of air supply in a data center to provide the right air flow rate according to the demands of the next rack. Three separate analysis is done for getting the precise result. The modeling of flow through sharp edge orifice, the parametric investigation of perforated plate and the numerical prediction of homogeneity of gas flow through perforated plate with different porosity results are analyzed.

2 Governing equation and Computational model

The flow field is governed by the three-dimensional Navier–Stokes equations and continuity equation, and the flow field under isothermal condition is examined using steady state is given as,

$$\frac{\partial u}{\partial x} + \frac{\partial v}{\partial y} + \frac{\partial w}{\partial z} = 0 \tag{1}$$

$$\rho \left(\frac{\partial u}{\partial t} + u\frac{\partial u}{\partial x} + v\frac{\partial u}{\partial y} + w\frac{\partial u}{\partial z} \right)$$
$$= -\frac{\partial p}{\partial x} + \mu \left(\frac{\partial^2 u}{\partial x^2} + \frac{\partial^2 u}{\partial v^2} + \frac{\partial^2 u}{\partial z^2} \right) + S \tag{2}$$

where u, v, and w are velocities in x, y, and z directions, respectively, p and t are pressure and time, respectively. The term S denote the source term in the momentum equation. The source term is

$$S_t = -\left[\sum_{j=1}^{3} D_{ij}\mu u_j + \sum_{j=1}^{3} C_{ij}\frac{1}{2}\rho|u|u_j \right] \tag{3}$$

where S_t is the source term in momentum equation ($i = x$, y, or z), u is the velocity module and D_{ij} and C_{ij} are the given matrices. Viscosity losses (Darcy's law), is the first term on the right-hand side of the equation and internal losses, is the second term on the right-hand side of the equation. The momentum loss in porous material is proportional to the pressure gradient. Pressure loss is proportional to the flow velocity. The pressure drop Δp across the plate δ was calculated by the following equation with Eq. (4). The pressure drop is calculated by Darcy–Forchimer equation in perforated plate is given by

$$\frac{\Delta P}{\delta} = \frac{\mu}{\alpha}u + \frac{1}{2}C_2\rho v^2 \tag{4}$$

2.1 Modeling of Flow Through Sharp Edge Orifice

Flow through each hole in a perforated plate is analogous to flow through an orifice, in which the flow accelerates and emerges as a jet owing to a lack of space, followed by a pressure decrease across the hole. To reduce the end effects, a comparable broad domain ($W = 10D$, $L = 10D$) is used for numerical simulations. The inlet direction is positive y direction, while the outflow direction is negative y direction. The diameter is considered for the analysis is 45.46 mm for sharp edge orifice plate with the plate

Fig. 1 **a** Computational
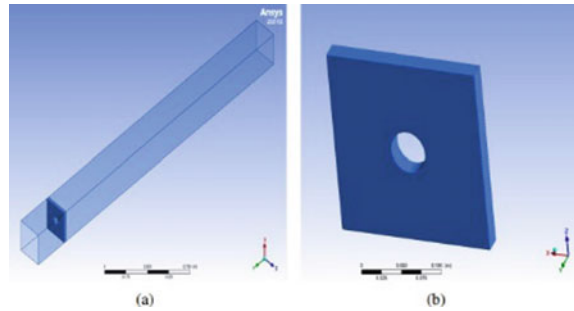fluid domain and **b** sharp
edge orifice plate

(a)   (b)

Table 1 Grid independence test of sharp edge orifice

Mesh elements	Pavg	Vavg	Pmax	Vmax
42,528	0.9491	1.1846	2.3293	1.9506
462,420	0.5613	1.3743	5.9393	3.3456
686,414	0.4450	1.1959	6.9375	3.4475
8,946,672	0.4452	1.1964	6.9379	3.4683

thickness is $t/d = 0.6$. The upstream $3D$ and downstream $10D$ is incorporated in the fluid domain to reduce the turbulence effect. The velocity inlet condition is set at the intake plane, while the pressure outlet condition is set at the outlet plate. On the sidewalls, symmetry boundary conditions are used. The three-dimensional fluid domain and orifice plate as shown Fig. 1. The meshing of the complete fluid domain and the orifice is structure mesh and it is done in ICEM CFD.

To find the least resolution or the number of cells required to obtain the accurate solution. Grid independence test is generally performed. Due to the complexity of flow behavior, a single grid cannot be considered. Therefore, the grid independence test for both the zone fluid domain and orifice plate is done at the reference plane $4D$ from the orifice plate. The parameter observed is the maximum velocity, maximum pressure, average velocity, and average pressure normal to the fluid flow is taken into analysis. It is observed that the parameters starts to converge considerably when the elements reaches 686,414. However for the present analysis, the number of elements is kept 686,414. The variation of the parameter is also shown in the Table 1.

3   Results and Discussion

A steady state, FVM method and the SIMPLE algorithm, the coupling of pressure and velocity in the flow field under isothermal circumstances are explored with ANSYS FLUENT. The intensity of inflow turbulence is measured to be 5%. To improve the mixing-length model k-epsilon model and k-omega model are used with inlet velocity 1 m/s. The stream line distribution over the fluid domain through sharp edge orifice

for different turbulence model are represented in Figs. 2, 3, 4 and 5. In the case of the flow from the sharp-edged orifice variation in velocity and variation in pressure in the potential core plane is listed below and the result compared with co-relation as well as experimental data also for all different turbulence model.

k-Epsilon model focuses on the mechanisms that alter the turbulent kinetic energy, in contrast to other turbulence models. The potential core lengths, though in this context would be seen as the distances from the exit planes beyond which the center-line mean stream-wise velocities decline gradually over time from an almost constant value. Just after the potential core region, which is characterized by a constant velocity, the mean stream-wise velocity begins to decrease to peak value in the adjacent flow field.
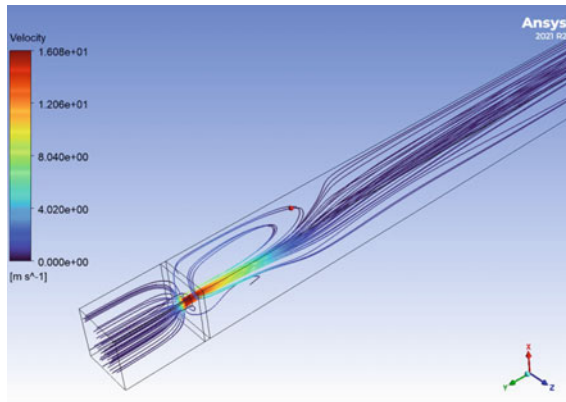
Fig. 2 Stream line distribution over fluid domain through orifice k-epsilon STD
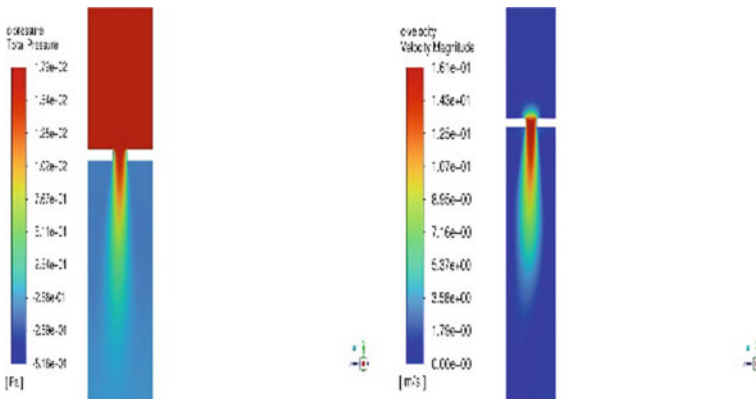
Fig. 3 Variation over the potential core plane k-epsilon STD model. **a** Pressure variation and **b** velocity variation
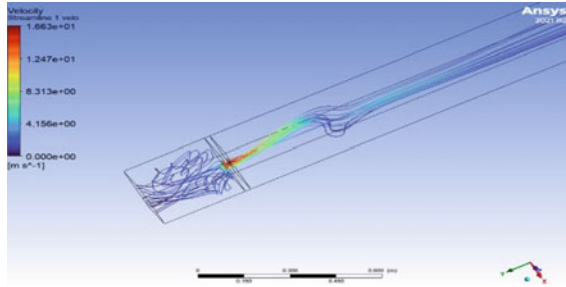
Fig. 4 Stream line distribution over fluid domain through orifice k-epsilon REL
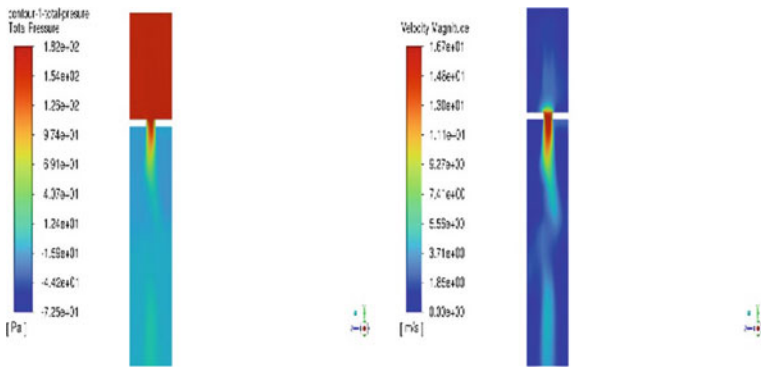
Fig. 5 Variation over the potential core plane k-epsilon REL model. **a** Pressure variation and **b** velocity variation

In k-epsilon STD and RNG turbulent viscosity is isotropic in nature, hence formation of swirling is observed in downstream. In k-epsilon REL model turbulent viscosity is anisotropic in nature though swirling is captured in upstream of the computational domain (Figs. 6, 7 and 8).

The major ways in which the SST model is gradual change from the standard k-omega model in the inner region of the boundary layer to a high Reynolds number version of the k-epsilon model in the outer part of the boundary layer modified turbulent viscosity formulation.

The non-dimensional mean stream-wise velocities at the jets center line are shown in Fig. 9. Vc is the mean stream-wise velocity, on the jet center line and Vexit is the mean stream-wise velocity at the center of the nozzle exit plane. In the case of the flow from the sharp-edged orifice, Vexit is the bulk-mean exit velocity. The numerical result is compared with experimental data and correlation for the complete fluid domain k-omega SST and k-epsilon RNG turbulence model give improved results up to $Y/D = 90$, after which the curve went back to a high peak due to significant experiment losses.
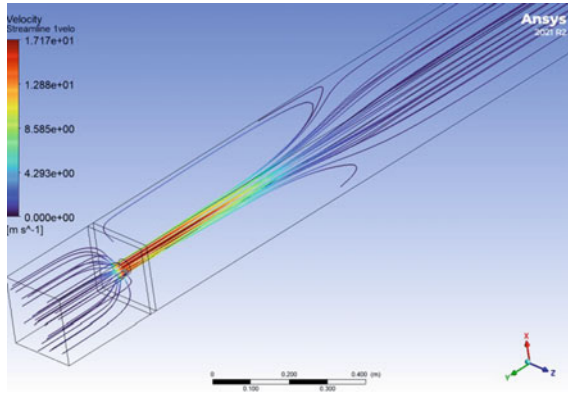
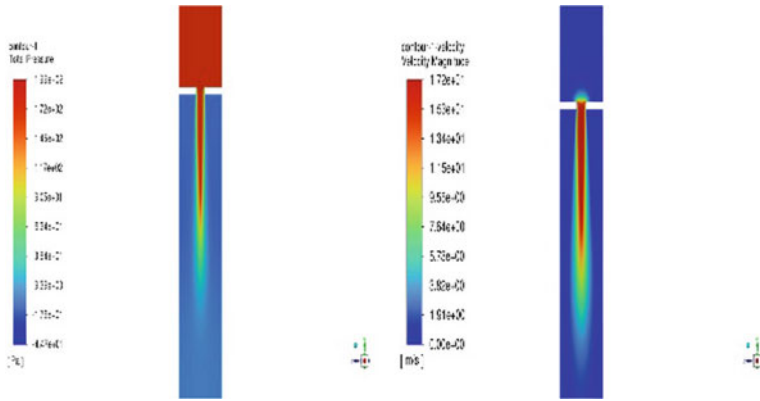**Fig. 6** Stream line distribution over fluid domain through orifice k-epsilon RNG

Fig. 7 Variation over the potential core plane k-epsilon RNG model. **a** Pressure variation and **b** velocity variation
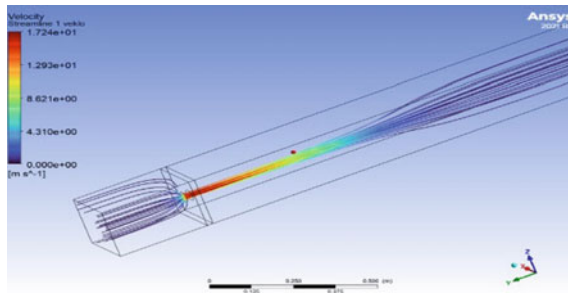

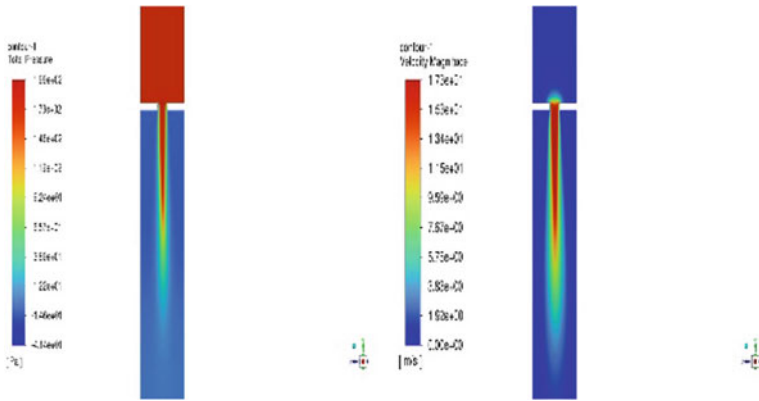**Fig. 8** Stream line distribution over fluid domain through orifice k-omega SST model

Fig. 9 Variation over the potential core plane k-omega SST model. **a** Pressure variation and **b** velocity variation

The effect of venacontracta zone, which results in the acceleration of the jet close to the exit plane, up to about $Y/D_e = 0.2$ Fig. 9b. In k-epsilon STD model, there is essentially no potential core because it fails to account for the flow's continued acceleration following the orifice plate. Formation of local eddies in the orifice is more in k-epsilon REL and k-epsilon STD model, whereas k-omega SST and k-epsilon RNG capture result close to the correlation and experiment data. Correlation of the center line velocity to the exit velocity for the sharp edge orifice in the region $18 < Y/D_e < 55$ is given by where U_{cl} is the center line velocity and U_{exit} is the exit velocity. Y/D_e is the distance measured from the orifice plate where D_e is the diameter of the sharp edge orifice plate $\frac{U_{cl}}{U_{exit}} = \frac{6}{\frac{Y}{D_e} - 2.15}$ (Figs. 10 and 11).

3.1 Parametric Investigation of Perforated Plate

Consequently, a more effective method for addressing the demand for flow dynamics through perforated tiles is required. Distribution, size, and shape of pores are taken into consideration. With varying pore distribution patterns, the flow field downstream are notably distinct. Taking into mind the geometrical length scales, pore holes for a perforated tile.

- **Effect of pore shape**—Pores into the perforated tiles may be any shape and have curved edges. Hence, we compare the flow field through a circular and square pore to examine the effect of pore shape on velocity field. Investigation is carried out with both the pore having same hydraulic diameter. The porosity of the tile is 25%. The one eight geometry of the cuboid domain is shown in Fig. 12.

In Fig. 13 indicates that the maximum velocity is 6.72 m/s for circular and 5.17 m/s for square shape perforated plate for the same inlet velocity 1 m/s.

Fig. 10 Comparison of the center line velocity decay by various models, correlation and experiment data. **a** Complete fluid domain and **b** vena-contracta
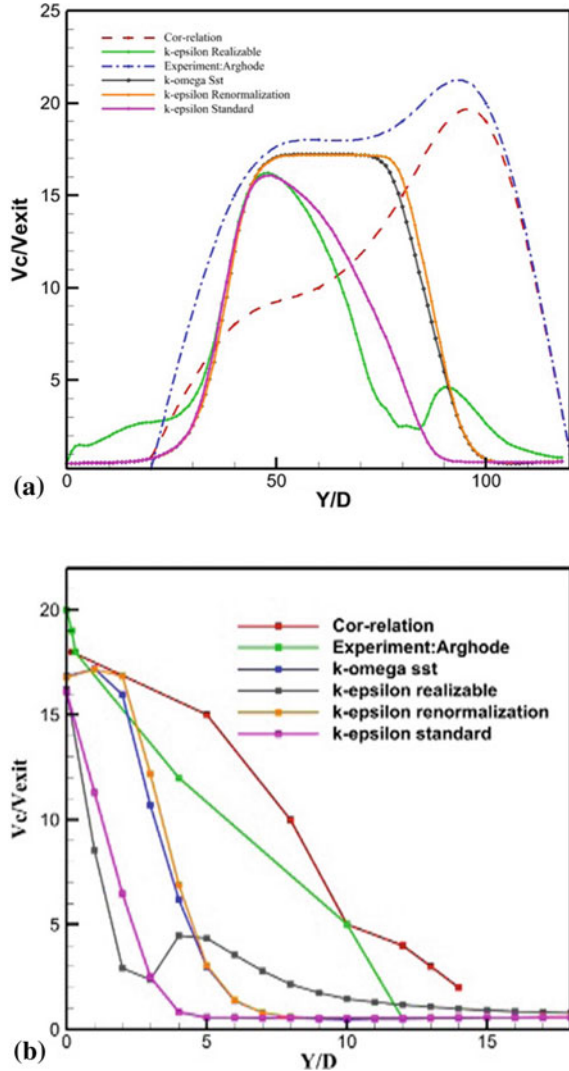
With the square pore shape jet interaction is ease compared with circular shape pore shape as demonstrated in Fig. 13. After the pore opening, the flow accelerates before eventually slowing in the downstream region and the negative pressure is there does the pressure at the outflow continuously following pore opening.

When the pressure fluctuated throughout the tile's surface based on the flow's acceleration, a lack of pressure is seen, and the head became the kinetic head as shown in Fig. 14.

On comparing the numerical result with mathematical model porous jump model and body force model The pressure loss predicted by CFD for circular and square

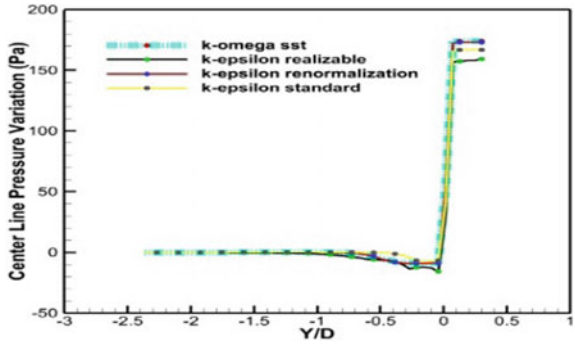**Fig. 11** Center line pressure variation with various model

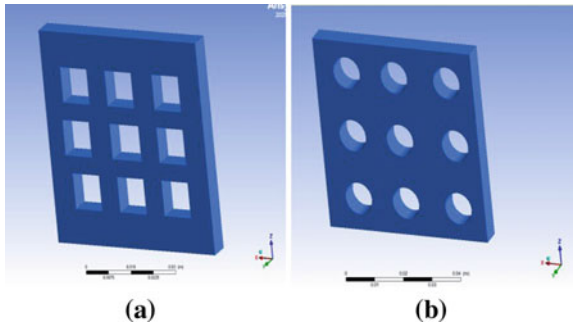**Fig. 12** Perforated plate with **a** square pore shape and **b** circular pore shape

Fig. 13 Velocity distribution over the potential core plane. **a** Circular perforated plate and **b** square perforated plate
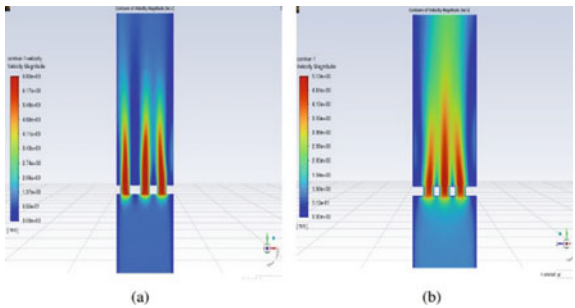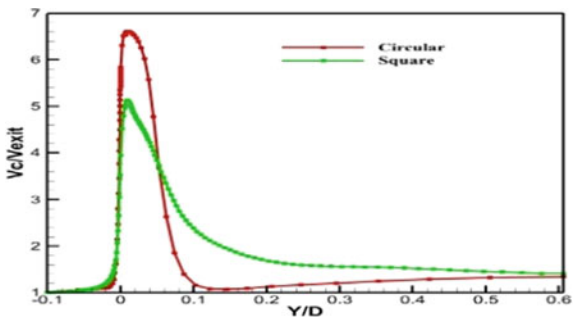

Fig. 14 Center line velocity variation with circular and square shape perforated plate

pores is $K = 39.18$ versus $K = 27.0$, respectively, and from the body force model calculated $k = 24$ and porous jump calculated $k = 29.69$ (Fig. 15). Hence, the pressure loss coefficient of square pore shape value close to the pressure loss coefficient value of body force model gives better result. This implies that square pores should be used to represent circular geometries with comparable hydraulic diameters.

- **Effect of pore length scale**—Pores length scale in perforated tiles may vary depend upon the application. Hence, we compare the flow field through a hydraulic diameter $D = 5$ mm of square pore shape and $D = 15$ mm of square pore shape and to examine the effect of pore length scale on velocity field. Velocity variation lying over the potential core plane through different pore length scale of perforated plate. It indicates that the maximum velocity is 12.1 m/s for $d = 5$ mm and 2.12 m/s for $d = 15$ mm of perforated plate (Figs. 16, 17, 18 and 19).

The pressure loss coefficient predicted by CFD for different pores length scale is $K = 45$ for $d = 5$ mm, $K = 27$ for $d = 10$ mm, and $k = 10.2$ for $d = 15$ mm, and the body force model calculated $k = 24$ and porous jump $k = 29.69$. This implies that $d = 10$ mm pores size might be used to represent circular or square geometries with comparable hydraulic diameters.

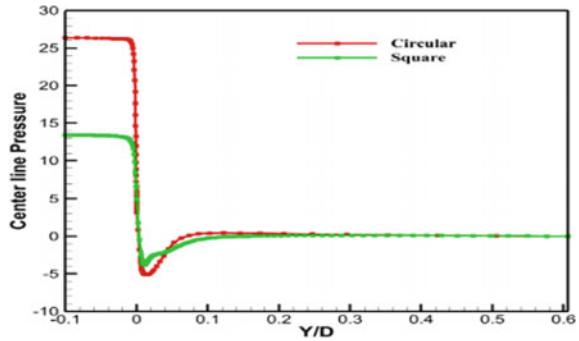**Fig. 15** Center line pressure variation with circular and square shape perforated plate

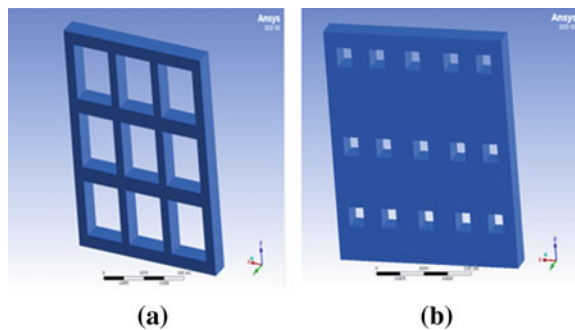**Fig. 16** Square pore perforated plate with hydraulic diameter of **a** 5 mm and **b** 15 mm

(a)   (b)

Fig. 17 Velocity distribution over the potential core plane: **a** $d = 5$ mm and **b** $d = 15$ mm
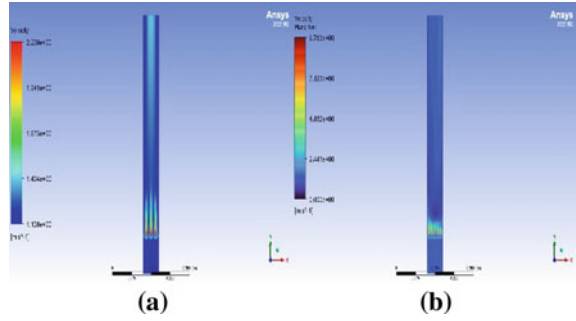

(a)   (b)

Fig. 18 Center line pressure variation in perforated plate for different pore length scale
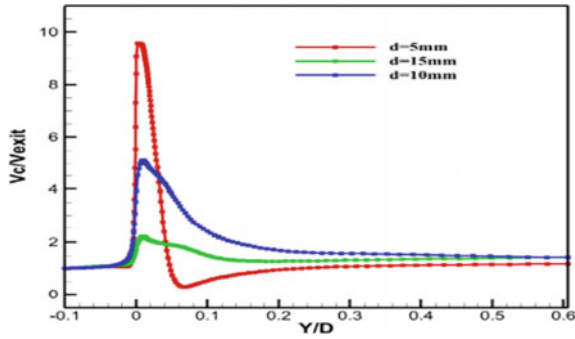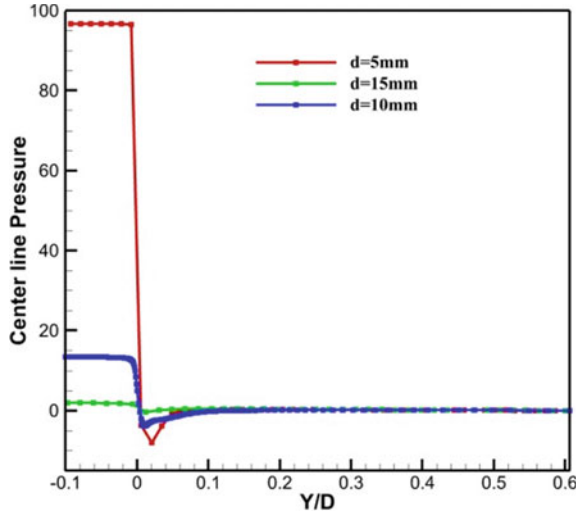

Fig. 19 Center line velocity variation in perforated plate for different pore length scale
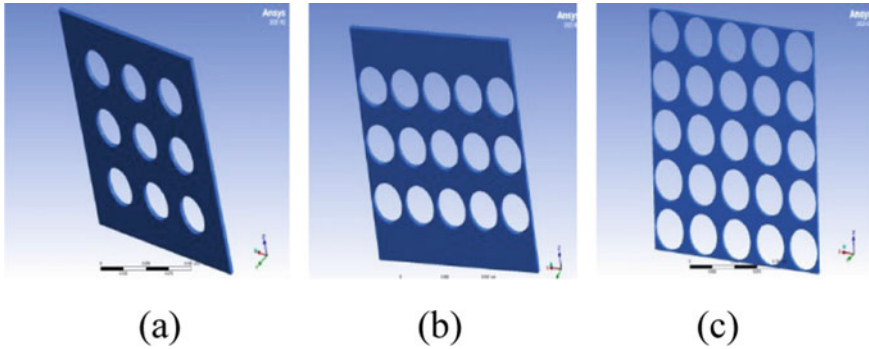
Fig. 20 Perforated plate with porosity: **a** 30%, **b** 40% and **c** 50%

3.2 Numerical Prediction Oh Homogeneity of Gas Flow Through Perforated Plates

The proposed modeling approach is tested for the plates with the following open area ratios: 0.3, 0.4, 0.5 (circle open area ratios, $D = 35$ mm), and $t/d = 0.6$. This geometrical model would need an incredibly fine computational mesh in order to correctly depict the boundary layer and the significant number of plate holes. The porosity is given by $f = \frac{A_o}{A_t}$, where A_o is overall surface area of holes and A_t is overall surface area of plate (Fig. 20).

From the Fig. 21 is observed that with the porosity is one of the important parameter for the homogeneous of the flow through perforated. With the increase in the open area ratio porosity the turbulence in the downstream is also enhanced hence formation of the local eddies after the flow through perforated is high which leads to non-homogeneous of the flow. Another point is also observed that with the same inlet velocity the downward flow vary with the variation in open area ratio. For the given inlet velocity 1 m/s the maximum velocity for $f = 0.3$ is $v = 6.5$ m/s, for $f = 0.4$ is $v = 4.1$ m/s, and for $f = 0.5$ is $v = 4.6$ m/s. However, the strength is also a decision factor while considering the porosity which is not included in the present analysis (Figs. 22 and 23).
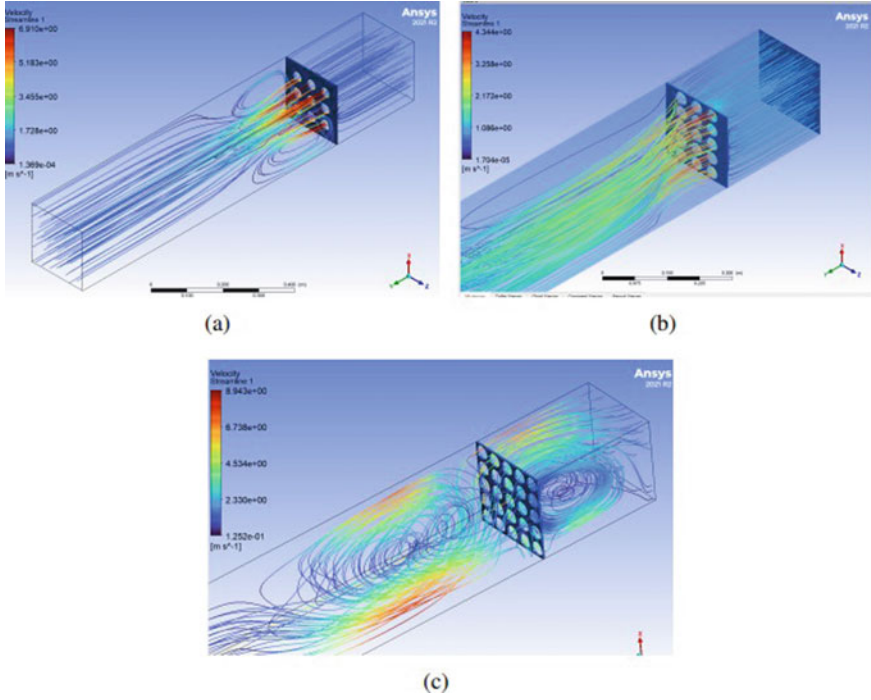
Fig. 21 Stream line distribution over fluid domain with $V_{in} = 1$ m/s through different porosity.
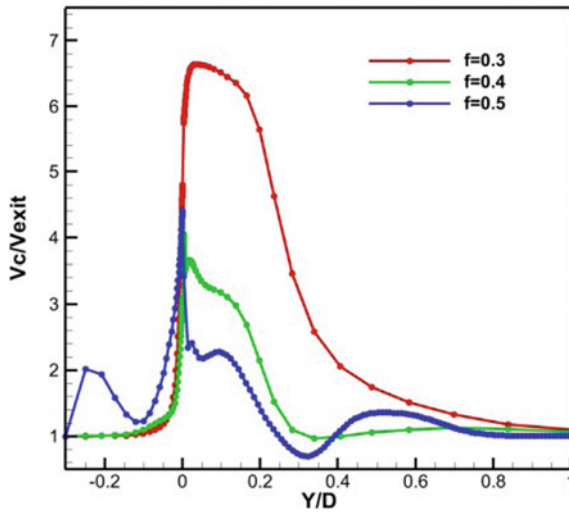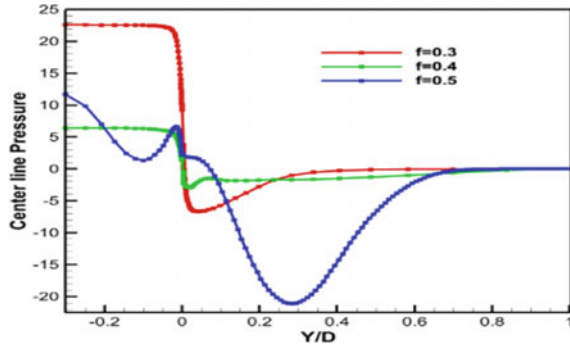**a** $f = 0.3$, **b** $f = 0.4$ and **c** $f = 0.5$

Fig. 22 Center line velocity distribution over fluid domain with $V_{inlet} = 1$ m/s through different porosity

Fig. 23 Center line pressure distribution over fluid domain with $V_{inlet} = 1$ m/s through different porosity

4 Conclusion

Accurate modeling of flow behavior above the tile surface requires close attention to tile geometrical characteristics and application of the proper computational model. Following are the conclusion are given below.

- In the sharp edge orifice plate the potential core plane is captured better by k-omega SST model. Hence compared to the commonly used STD k-epsilon model, k-epsilon REL, k-epsilon RNG for simulating flow through pores for flow through orifices.
- For the same hydraulic diameter square pore shape could be model to get precise result. Body force model give better result compared to porous jump model. Hence in porous jump model flow acceleration through pores, jet–jet interactions, and downstream flow development, which simplified models may fail to capture. In body force model in addition momentum is also incorporated in analysis as well as geometric detail of perforated plate is also incorporated.
- The jet decay proportionality with the pore length scale, hence larger size pore could results better in longer plenum and extended the flow development. Flow modeling for a perforated plate indicated that the CFD model overestimates the pressure loss and cannot reflect the impact of Reynolds number on the pressure loss. Geometric parameter also effects the flow through perforated plate, and it can be concluded that for the same hydraulic diameter, the square pore shape yields superior results when compared to the circular pore shape. With the variation in pore size, too tiny a pore size increases turbulence, resulting in greater losses, and too large a pore size decreases the flow rate, hence the size should be selected within an approximate range.
- Porosity is the dominant factor, higher the pressure loss lower the porosity of perforated plate. With the increase in the velocity local eddies formation is higher. As porosity grows the number of holes increases and the distance between holes decreases. For the use of high velocity in the design of perforated plate, further attention must be taken.

Abbreviation

CIR	Circular
SQR	Square
RNG	Re-normalization
REl	Realizable
STD	Standard
D	Hydraulic diameter
δ	Thickness of the plate
f	Porosity (open area ratio)
V_c	Center line velocity
V_{exit}	Velocity at the exit plane
k	Pressure loss coefficient
BDM	Body force model
FOU	First order upwind
SOU	Second order upwind
CFD	Computational fluid dynamics

References

1. Arghode VK, Joshi Y (2013) Modeling strategies for air flow through perforated tiles in a data center. IEEE Trans Comp Pack Manuf Technol 3(5):800–810
2. Chu W-X, Wang C-C (2019) CFD Investigation of airflow management in a small container data center. In: IEEE Trans Comp Pack Manuf Technol 9(11):2177–2188
3. Cloud Council (2014) Deploying big data analytics applications to the cloud: roadmap for success. Cloud Stand Cust Counc 35:384–397
4. Guo BY et al (2013) Numerical modelling of the gas flow through perforated plates. Chem Engineering Res Des 91(3):403–408
5. La Rosa DM et al (2021) On the pressure losses through multistage perforated plates. J Fluids Eng 143(6)
6. Özahi E (2015) An analysis on the pressure loss through perforated plates at moderate Reynolds numbers in turbulent flow regime. Flow Meas Instr 43:6–13
7. Schmidt R, Karki K, Patankar S (2004) Raised-floor data center: perforated tile flow rates for various tile layouts. In: The ninth intersociety conference on thermal and thermomechanical phenomena in electronic systems (IEEE Cat. No. 04CH37543), vol 1. IEEE, pp 571–578
8. VanGilder JW, Schmidt RR (2005) Airflow uniformity through perforated tiles in a raised-floor data center. In: International electronic packaging technical conference and exhibition, vol 42002, pp 493–501
9. Wang I-N, Tsui Y-Y, Wang C-C (2015) Improvements of airflow distribution in a container data center. Energy Proc 75:1819–1824
10. Wibron E (2018) A numerical and experimental study of airflow in data centers. PhD thesis. Luleå University of Technology

Heat Transfer and Fluid Flow Characteristics in a Two Pass Duct with Variable Rib Shapes: A CFD Analysis

Amir Yousf Sofi and Adnan Qayoum

1 Introduction

Gas turbines are combustion engines that work on the principal of Brayton cycle and play a pivotal role in operation of modern thermal power plants and aircraft industry. In gas turbines, increased thermal efficiency is extremely desirable and can be accomplished by increasing the turbine inlet temperature or by employing higher pressure ratios. Higher operating temperatures, on the other hand, may cause the turbine blade to fail owing to thermal corrosion and cracking. As a result, the need of effective cooling mechanisms in gas turbine blades is unavoidable. Rib turbulated cooling is one of the cooling techniques used to cool the gas turbine's centre portion. Jet impingement and pin fin cooling techniques are used to cool the gas turbine's leading and trailing edges, respectively. Flow separation and flow reattachment along with increased turbulence levels and modified boundary layer explain the heat transfer augmenting capability of the ribs. The heat transfer enhancing capability of the ribs generally depends on rib shape, rib angle of attack, rib pitch to rib height ratio (p/e), and the Reynolds Number (Re) of the working fluid. Ribs typically alter the near wall flow, therefore the tradeoff between heat transfer augmentation and the associated friction losses or pressure drop is acceptable.

The most remarkable and earliest work in the field of gas turbine cooling in general and rib turbulated cooling in particular is done by Han [1]. Pudake et al. [2] enunciated various turbine blade cooling technologies such as cooling by rib turbulators, pin fins, and jet impingement. Bunker et al. [3] have enlisted various innovative turbine blade cooling technologies. The heat dissipation technique in conventional gas turbine

A. Y. Sofi · A. Qayoum (✉)
Mechanical Engineering Department, National Institute of Technology, Hazratbal, Srinagar 190006, India
e-mail: adnan@nitsri.ac.in

A. Y. Sofi
e-mail: amir_2021phamec002@nitsri.ac.in

consist of 5 basic aspects comprising of conformal internal cooling, external surface cooling, choice of materials, component and systems thermal–mechanical designs and selection, and/or pre-processing of coolant fluid. Wang et al. [4] investigated the turbulent flow adjacent to ribs using Particle Image Velocimetry (PIV) technique. Lu et al. [5] experimentally and numerically investigated the effect of rib orientation on heat transfer rate and pressure loss characteristics in a rectangular single pass channel. Ribs with angle of attack of 60° showed highest heat transfer coefficient. In a single pass channel, Taslim [6] evaluated the influence of rib turbulators on the overall heat transfer performance. A correction factor was proposed in this research to compensate for the overvaluation of heat transfer coefficient due to the assumption that rib turbulators are 100% effective. Wang et al. [7] numerically investigated the effect of continuous wavy ribs on heat transfer and frictional loss characteristics in a single pass channel. The study concluded that in comparison to 45° V-shaped ribs, continuous wavy ribs showed a 33% increase in heat transfer rate and 9% decrease in associated pressure losses at a Reynolds Number of 25,000. In case of rib turbulated cooling extensive research on effect of rib shapes, rib angle of attack, and rib pitch to rib height (*p/e*) ratio has been carried out in case of stationary single pass channels with variable aspect ratios.

The comprehensive distribution of Nusselt Number ratios in case of a two pass square channel is presented by Ekad and Han [8]. The experimentally investigated rib shapes in the study were 90° parallel, 60° parallel, 60° V and 60° broken V. The Nusselt Number distributions were evaluated in the first pass, bend region and the second pass of a dual pass square channel. Singh et al. [9] numerically investigated the effect of rib shapes (V shape, W shape, M shape, and 45° angled ribs) on heat transfer enhancing capabilities of rib turbulators. It was found that V-shaped depicted better heat transfer characteristics but with increased pressure penalty. Rasool and Qayoum [10–12] numerically investigated the effect of rib shape on heat transfer and pressure loss characteristics in a two pass square duct. The study established that rib shapes had prominent effect on heat transfer enhancement in stationary two pass channels and boot shaped ribs depicted enhanced heat transfer characteristics as compared to conventional square ribs. The implementation of ribs in cooling gas turbine blades has been confined to single pass channels (except for conventional square ribs). There has been very limited research to study the effects of rib shapes (such as perforated ribs and wavy ribs) on heat transfer enhancement in two pass channels. Thus, the primary objective of this study is to investigate the effect different rib shapes on temperature distribution and frictional pressure drop characteristics in two pass channels.

2   Simulation Methodology

The current numerical analysis is carried out using the Conjugate Heat Transfer Module in COMOSOL Multi-physics 5.4, which integrates turbulent flow with heat transfer in solids and fluids. COMSOL Multi-Physics divides complex geometries into sub-domains termed as finite elements using the Finite Element Analysis (FEA)

Fig. 1 Simulation domain
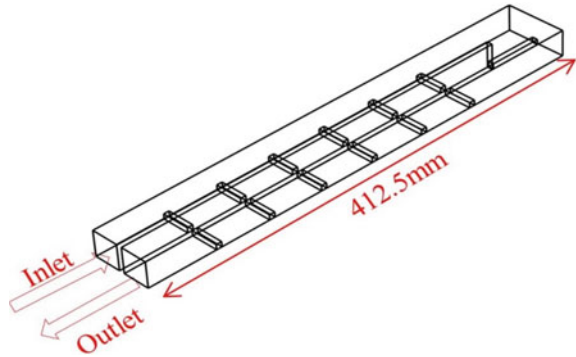
technique, and the associated finite element governing equations are produced using variational approaches.

2.1 Simulation Domain

The numerical analysis domain is comprised of a two pass ribbed channel with an aspect ratio (w/h) of 1:1 as illustrated in Fig. 1. The length of each pass is 412.5 mm and the thickness of the divider wall is 5 mm. The rib pitch to rib height ratio of the two pass ribbed channel is 10 with a blockage ratio of 0.2. Each pass contains 6 ribs with a square rib placed in the bend region. In the present numerical analysis, the heat transfer and friction loss characteristics of four rib shapes have been primarily investigated, viz., conventional square ribs, arched ribs, wavy ribs, and zig-zag ribs illustrated in Fig. 2. The Reynolds Number is varied from 10,000–40,000. All the relevant geometries have been developed either in the dedicated design module of COMSOL Multi-physics 5.4 or imported from SOLIDWORKS 2015.

2.2 Turbulence Model Selection

The current numerical analysis employs the conjugate heat transfer method, which combines heat transfer in solids and fluids with turbulent flow to investigate the heat transfer and pressure loss characteristics in ribbed two pass channels. There are numerous turbulence models available to simulate turbulent flow; however, the current numerical analysis considers three turbulence models to justify the use of a specific turbulence model in the study. The three turbulence models are k-ε turbulence model, k-ω turbulence model, and algebraic y + turbulence model. Table 1 enlists the average normalized Nusselt number ratios of a smooth two pass channel obtained from the aforementioned turbulence models and compared with the experimental results of Ekkad and Han [8]. It is clearly evident from the table that the normalized
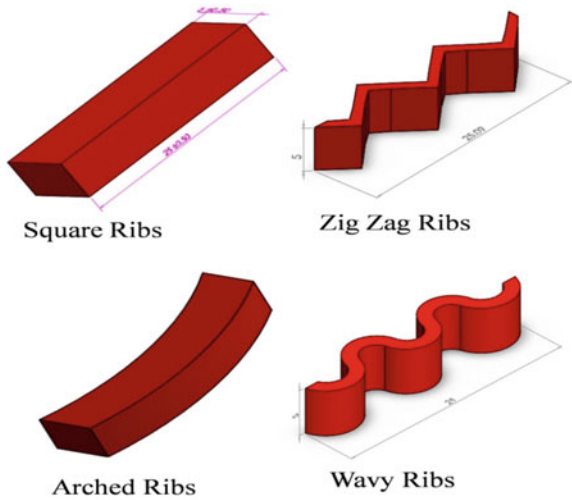
Fig. 2 Rib shapes (all dimensions in mm)

Square Ribs

Zig Zag Ribs

Arched Ribs

Wavy Ribs

Table 1 Turbulence model selection

| Turbulence model	Predicted average Nusselt number ratio	Experimental average Nusselt number ratio [8]
k–ε turbulence model	3.857	2.339
k–ω turbulence model	**2.456**	**2.339**
Algebraic y + turbulence model	3.924	2.339

Bold indicates the statistical significance of the k-omega turbulence model as its values are close to the experimental values. Therefore the k-omega turbulence model has been selected for the present numerical analysis and has been presented in bold

Nusselt number ratios simulated by k-ω turbulence model are close to experimental results.

2.3 Governing Equations and Boundary Conditions

The turbulent flow and the heat transfer in solids and fluids is governed by Reynolds Averaged Navier Stokes (RANS) Equations, continuity equation, momentum equation, and energy equation [11, 12]. Three-dimensional, incompressible, steady, and turbulent fluid flow is assumed. Because the current simulation domain features steep surfaces and a sharp bend of 180°, a turbulent intensity of 7% is specified at the dual pass channel's entrance. The inlet fluid velocity of the two pass channel is regulated by the Reynolds Number. As a result, the inlet velocity boundary condition is

Fig. 3 Unstructured mesh domain
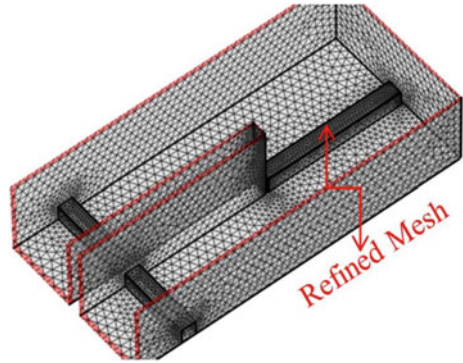
adopted in this investigation. The two pass ducts' entrance temperature is kept steady at 298 K. At the exit, the pressure boundary condition is specified.

3   Mesh Independence Study

The mesh independence study is carried out to assure that the simulation results obtained in the present study are independent of the mesh size. In a smooth two pass channel at a Reynolds Number of 10,000, three different mesh sizes are selected which consist of 0.5 million elements, 1 million elements, and 1.5 million elements. The three grid sizes are illustrated in Fig. 3 and are termed as coarse mesh, normal mesh, and fine mesh, respectively. The average normalized Nusselt number ratios obtained in each grid size are enlisted in Fig. 4. The percentage error in the obtained normalized Nusselt number ratios between fine and coarse mesh is 6.73%. Thus in order to reduce the computation time and increase the accuracy, a mesh size of one million elements is selected for the present study.

4   Data Reduction and Performance Evaluation

Data reduction generally involves the derivation and normalization of Nusselt number and friction factors. The heat transfer coefficient (h) is evaluated from the heat flux equation as:

$$h = \frac{Q^{''}}{T_{\mathrm{w}} - T_{\mathrm{f}}} \tag{1}$$

Fig. 4 Grid independence
study
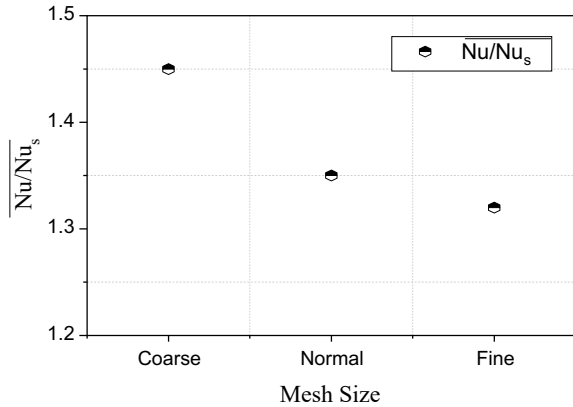
where Q'' is the applied heat flux, T_w and T_f denote the wall temperature and the bulk fluid temperature, respectively. The heat transfer coefficient is used to evaluate the Nusselt Number (Nu) as follows:

$$Nu = \frac{h D_h}{K} \qquad (2)$$

where D_h is the hydraulic diameter of the two pass channel, h is the heat transfer coefficient, and K denotes the thermal conductivity of the working fluid. The Dittus-Boelter Correlation for a smooth circular tube is used to normalize and standardize the calculated Nusselt numbers. The Dittus-Boelter Correlation is valid when $0.7 \leq Pr \leq 160$, $Re \geq 10{,}000$ and $L/D_h \geq 10$ [13]

$$Nu_0 = 0.023 Re^{0.8} Pr^{0.4} \qquad (3)$$

The friction factor to access the pressure loss in the two pass ribbed channel is evaluated by using the Fanning Friction Formula expressed as:

$$f = \frac{\Delta p D_h}{2 \rho u_{in}^2 l} \qquad (4)$$

The friction factor is normalized by the Blasius correlation expressed as:

$$f_o = \frac{0.316}{Re^{0.25}} \qquad (5)$$

The heat transfer enhancing capabilities of the ribs is accessed by evaluating the Nusselt number ratios and the associated pressure losses are accessed by calculating the friction factor ratios. Thus in order to justify the tradeoff between heat transfer enhancement and friction losses, it is essential to establish the thermal performance

index (η) of the different rib shapes and access their performance. The rib performance evaluation criteria was proposed by Gee and Web and is based on normalized Nusselt number ratios and friction factor ratios for smooth and ribbed channels. In general higher the Nusselt number ratios and lower the friction factor ratios, higher is the thermal performance index of the ribs and is expressed as:

$$\Delta = \left(\frac{\frac{Nu}{Nu_o}}{\left(\frac{f}{f_o} \right)^{\frac{1}{3}}} \right) \tag{6}$$

5 Simulation Results

This section illustrates various computational results associated with the heat transfer and fluid flow in a two pass ribbed channel. The span-wise normalized Nusselt number ratios, normalized friction factor ratios, thermal performance index, and variation of these parameters with Reynolds number of the working fluid has been evaluated in this section.

5.1 Validation of Numerical Analysis

The validation is carried out to establish the authenticity of the present numerical analysis. The validation is performed on a two pass smooth channel as investigated experimentally by Ekkad and Han [8]. The validation domain consists of a smooth two pass channel 609.6 mm in length with a hydraulic diameter of 50.8 mm. Figure 5 shows a comparison of the local normalized Nusselt number between Ekkad and Han's experimental analysis and the current numerical analysis in the case of a two pass channel. It is clearly evident that the variation of Nusselt number ratios predicted by current numerical analysis are similar to the trends observed in the experimental analysis of Ekkad and Han [8]. However, there is a slight over prediction of the Nusselt number ratios in the present numerical analysis because of different mesh size and different thickness of the divider wall of the two pass channel.

5.2 Heat Transfer and Pressure Loss Characteristics

The primary objective of the present numerical analysis is to reduce intra rib temperature hotspots, evaluate thermal performance index of different rib shapes and reduce rib associated frictional losses. The temperature profiles for the different rib shapes
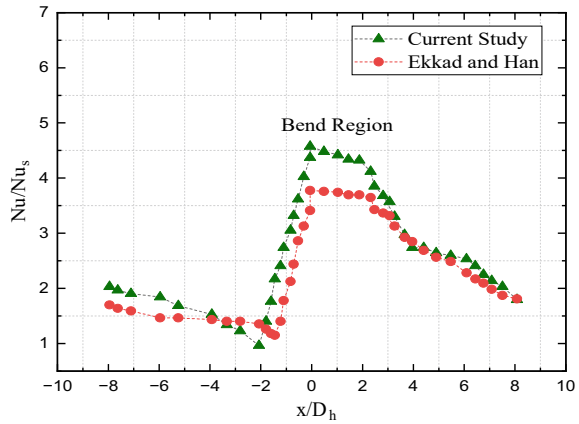
are illustrated in Fig. 6. It is clearly evident from the temperature profile plots that under similar boundary conditions, wavy ribs show minimum temperature hotspots followed by arched ribs, zig-zag ribs, and conventional square ribs.

Figure 7 shows the span-wise variation of normalized Nusselt number ratios in case of a ribbed two pass channel. The normalized Nusselt number plots depicts that wavy ribs exhibit better heat transfer augmenting capabilities as compared to other rib shapes at a Reynolds Number of 10,000. Zig-Zag ribs show poor heat transfer enhancing capabilities. Moreover from the normalized Nusselt number plot it is evident that the heat transfer enhancing capabilities of the ribs are much better

Fig. 6 Temperature profiles
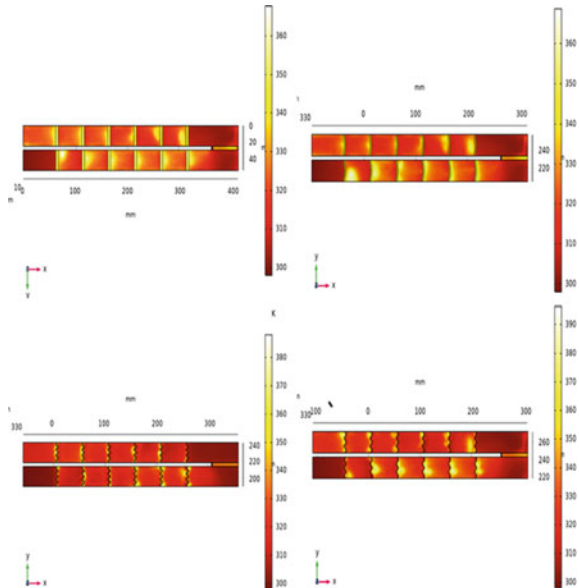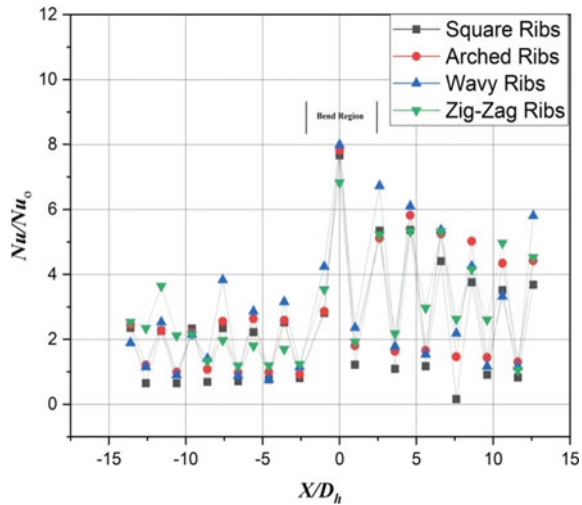of different rib shapes
(Kelvin)

Fig. 7 Span-wise
normalized Nusselt number
ratios

in the second pass and bend region of the two pass channel because of the generation of the secondary flows and dean type of vortices in the bend region. Figure 8 shows the variation of average normalized Nusselt number ratios with the Reynolds number. The average normalized Nusselt number ratios decrease with increase in Reynolds number of the working fluid. The Prandtl Number decreases with increase in temperature. As per Dittus-Boelter Correlation, it is evident that Nusselt number is directly dependent on Reynolds number as well as Prandtl number of the working fluid. Although with increase in Reynolds Number, Nusselt number should increase but the effect of increasing Reynolds Number is surpassed by decrease in Prandtl Number. Thus, the Nusselt Number in the present study decreases with increase in Reynolds Number.

The friction factor is normalized by Blasius correlation and the average normalized friction factor ratios for different rib shapes along with their variation with Reynolds Number is illustrated in Fig. 9. The frictional losses are evaluated by taking into account the pressure losses between the inlet and outlet of the dual pass channel. Generally higher the friction factor ratios, higher are the pressure drops between the inlet and outlet of the two pass channel. The frictional losses are minimum in case of wavy rib shape and with increase in Reynolds Number, the frictional losses also increase. At lower Reynolds Numbers, arched ribs exhibit higher pressure losses and at higher Reynolds Numbers, zig-zag ribs exhibit higher pressure losses.

5.3 Thermal Performance Index (η)

The tradeoff between the heat transfer enhancement and the associated pressure loss is justified by the thermal performance index (η) of different rib shapes. The

Fig. 8 Surface averaged
normalized Nusselt number
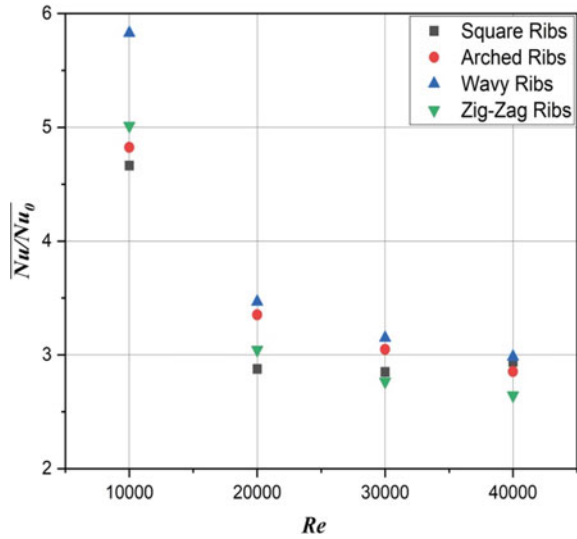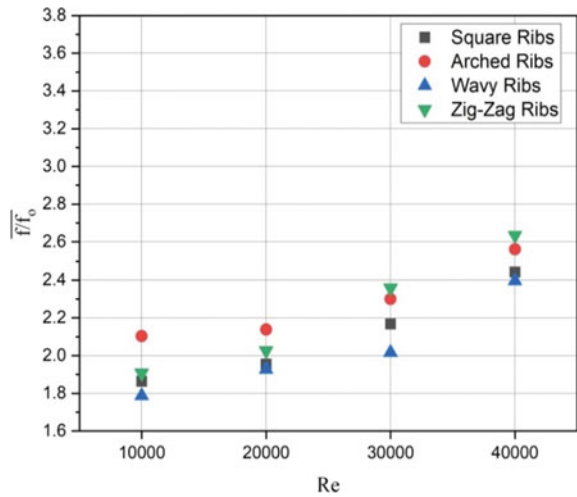vs Reynolds number

Fig. 9 Average friction
factor ratios variation with
Reynolds number

thermal performance index is the ratio of normalized Nusselt number ratios and
friction factor ratios. Higher the thermal performance index of a rib, higher is its heat
transfer augmenting capability and lesser are the associated frictional losses. The
thermal performance index for the rib shapes in present study is plotted in Fig. 10.
At a Reynolds Number of 10,000, the wavy ribs depict a 26.74% increase in thermal
performance index as compared to conventional square ribs. Moreover with increase
in Reynolds Number, the thermal performance index for all rib shapes decreases,
i.e., the heat transfer augmenting capability of the ribs decreases with increase in
Reynolds Number.

Fig. 10 Thermal
performance index versus
Reynolds number
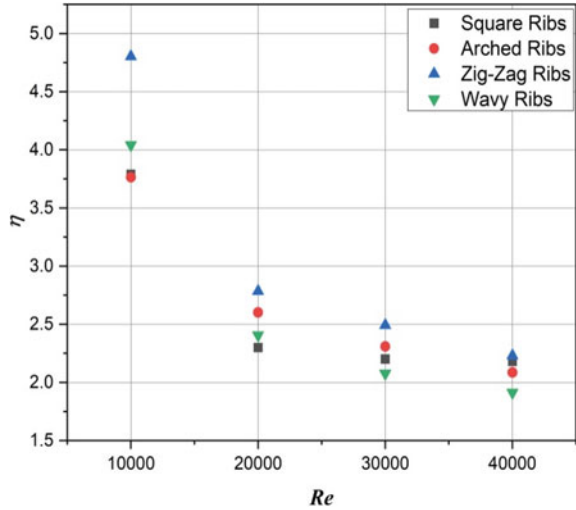
6   Conclusions

1. The numerical study of the ribbed dual pass channel indicates that the heat transfer enhancing capability of the ribs relies hugely on the shape of the ribs and the Reynolds Number of the working fluid.
2. The surface temperature profile plots exhibit that the temperature hotspots have been significantly reduced in case of wavy ribs.
3. The span-wise normalized Nusselt number plot obtained from the post processing of the numerical simulation clearly indicate that due to flow separation, flow reattachment, development of secondary flows, and dean type vortices the heat transfer enhancement in the second pass and bend region is higher as compared to first pass of the two pass channel.
4. At a Reynolds Number of 10,000, wavy ribs outperformed conventional square ribs by 24.96% in terms of normalized Nusselt number ratios and the thermal performance index (η) of the wavy ribs increased by 26.74% when compared to conventional square ribs.
5. The Nusselt number ratios (Nu/Nu_o) and thermal performance index (η) of all rib shapes decreased as the Reynolds Number increased. However, in the case of friction factor ratios, the contrary pattern emerged, i.e., friction factor ratios increased as the Reynolds Number increased.

Nomenclature

D_h Hydraulic diameter

p	Rib pitch
e	Rib height (m)
h	Heat transfer coefficient (W/m^{2}K)
k	Thermal conductivity (W/mK)
l	Length of channel (m)
Q''	Heat flux (W/m^2)
Nu	Nusselt number
$\overline{Nu}$	Average Nusselt number
Re	Reynolds Number
T	Temperature (K)
U	Velocity of fluid (m/s)

Subscripts

0	From Dittus-Boelter correlation
f	Fluid
w	Wall
in	Inlet

References

1. Han J-C (2004) Recent studies in turbine blade cooling. Int J Rotating Mach 10(6):443–457
2. Pudake P, Elgandelwar A, Lele M (2017) Gas turbine blade cooling technology—a case study. Int J Curr Eng Technol 195–201 (INPRESSO)
3. Bunker RS, Amano RS, Sunden B (2008) Innovative gas turbine cooling techniques. WIT Trans State Art Sci Eng 42:199–229
4. Wang L, Salewski M, Sundén B (2010) Turbulent flow in a ribbed channel: flow structures in the vicinity of a rib. Exp Therm Fluid Sci 34(2):165–176
5. Lu B, Jiang P-X (2006) Experimental and numerical investigation of convection heat transfer in a rectangular channel with angled ribs. Exp Therm Fluid Sci 30(6):513–521
6. Taslim ME (2005) Rib fin effects on the overall equivalent heat transfer coefficient in a rib-roughened cooling channel. Int J Heat Exch 6(2):135
7. Wang L, Wang S, Wen F, Zhou X, Wang Z (2018) Effects of continuous wavy ribs on heat transfer and cooling air flow in a square single-pass channel of turbine blade. Int J Heat Mass Transf 121:514–533
8. Ekkad SV, Han J-C (1997) Detailed heat transfer distributions in two-pass square channels with rib turbulators. Int J Heat Mass Transf 40(11):2525–2537. https://doi.org/10.1016/S0017-9310(96)00318-3
9. Ravi BV, Singh P, Ekkad SV (2017) Numerical investigation of turbulent flow and heat transfer in two-pass ribbed channels. Int J Therm Sci 112:31–43
10. Rasool A, Qayoum A (2018) Numerical analysis of heat transfer and friction factor in two-pass channels with variable rib shapes. IJHT 36(1):40–48. http//iieta.org/Journals/IJHT
11. Bhat AY, Qayoum A (2022) Viscosity of CuO nanofluids: experimental investigation and modelling with FFBP-ANN. Thermochim Acta 714. https://doi.org/10.1016/j.tca.2022.179267

12. Kamran M, Qayoum A (2022) Effect of ZnO nanofluids on thermo-hydraulic characteristic of flow in a heated duct. Energy Sour Part A Recover Util Environ Eff 44(4):10681–10693. https://doi.org/10.1080/15567036.2022.2154871
13. Tosun I (2007) "Evaluation of Transfer Coefficients: engineering correlations," in Modeling in Transport Phenomena, 2007, pp. 59–115. https://doi.org/10.1016/B978-044453021-9/50005-1

Numerical Simulations of AMRI Hospital Fire Accident 2011: A Case Study

Rajat Joshi and Sudheer Siddapureddy

1 Introduction

Fire research has led us to understand fire and its characteristics better. With a better understanding of fire, we can improve our investigations of the mishaps that have occurred in the past and make ourselves ready for fire accidents that might occur in the future. One of the tools that help the fire and safety research community in simulating and understanding these scenarios is fire dynamics simulator with evacuation (FDS + EVAC). Fire Dynamics Simulator (FDS) is an open-source computational fluid dynamics code widely used by the fire research community to simulate fire and combustion scenarios like open pool fires, compartment fires, etc. NIST added an open-source code, evacuation (EVAC), to the fire dynamics simulator. The EVAC model in conjunction with FDS, provides an advantage to numerically simulate fire, egress, and the effect of fire on the occupant simultaneously, with added reliability and user-friendliness of the FDS code. But, like any other simulation software, an evacuation simulation code/software also needs realistic input and actual building models to calculate required values and accurately simulate egress scenarios in the given environment. These input values are taken either from existing literature or found experimentally through various techniques. These experimental techniques include surveys, interviews, CCTV camera footage of drills or accidents, and conducting experiments with real people performing a routine executed under specified circumstances.

Identification and understanding the basic input parameters required by an egress model is essential to accurately model a fire accident or a building egress plan. An accurate depiction of the scenario requires an accurate input of the human parameters. Some of them are:

R. Joshi · S. Siddapureddy (✉)
Department of Mechanical, Material and Aerospace Engineering, Indian Institute of Technology Dharwad, Dharwad, Karnataka 580011, India
e-mail: sudheer@iitdh.ac.in

- Pre-Evacuation Time—The pre-evacuation time is the interval between the time a general alarm signal or warning is given (or other cues received) and the time at which the first deliberate evacuation movement is made [1]. This pre-evacuation time can be reduced using proper fire safety precautions, such as the installation of fire alarms and sprinklers in a building.
- Travel Time—It is the interval needed for an evacuee to reach a safe place once movement toward an exit has begun [1]. Travel time depends on agents' familiarity with the surroundings; agent velocity, which further depends on the physical characteristics of an occupant, mental fatigue, social influence, physical exertion, rise in the FED value of occupants, occupant density of the place, risk perception, fitness of occupant.
- Fire size and HRRPUA—This solely depends on the burning material and the location where the fire broke out in the building (i.e., the fire can lead to flashover or traveling fire if it is near windows, corridors, shafts, or vents).
- Smoke Yield—This influences agent FED and visibility directly, i.e., the higher the smoke yield, the rate of drop of visibility will be higher, and the rate of growth of FED for a single agent will be higher.
- Building Geometry—Geometrical Features of a building that affect evacuation, such as the width of the staircase, corridors, exits, and doors.

During its early years, evacuation research concentrated more on the environmental aspect of evacuation, i.e., exit door width, stairwell width, exit route recognition, etc. Work done by researchers such as Fruin et al. [2–4] enlightens us regarding the travel speed and travel density of the occupants during evacuation. This work led to the development of stair, corridor, and exit doors width of the optimum size. Sime et al. [5] introduced an Occupant Response Shelter Escape Time (ORSET) model, which brings together the aspects of both building fire safety and human behavior during a fire evacuation scenario. It was released during this time that fast and efficient evacuation relies not only on good building layout but also on social and behavioral characteristics of the evacuees and the relationship between them and their immediate environment within the building. Sime highlights that people do not respond in the same way in one physical (and social) location and circumstance as in another. Therefore, the response of an evacuee depends on various factors such as environmental, social, and situational features of their condition.

Kobes et al. [1] defined fire response performance as an individual's ability to perceive and interpret signs of danger and then carry out decisions to survive a fire. This parameter is considered to analyze the evacuation capability of the evacuees in case of fire. It has three stages: awareness of danger by external stimuli, validation of and response to danger indicators, and movement to/ refuge in a safe place. Proulx [6] observed that evacuation signals, such as alarms, sirens, are less impactful in most situations when compared to smelling or seeing flames and smoke, increasing the pre-evacuation time of the occupants. Even after realizing the building is under fire, the occupants may run back to their apartment or office to get valuables or try to warn or gather family or friends. The shoppers will continue shopping in a shopping center even after hearing an alarm. Jin [7] observed that the visibility of an individual is

hampered because of the soot and smoke that forms along with the fire, and reduced visibility will lead to poor tracking, which will further lead to longer escape times and that will finally lead to asphyxiation and death. Effects of exposure to smoke on evacuees in the short term are loss of reflexes, poor decision-making, and long-term physical effects such as cancer, lung damage. Purser et al. [8] suggest that a room becomes extremely inhabitable when any of the following thresholds are exceeded-

- Temperature exceeds 120 °C
- Heat Flux exceeds 2.5 kW/m^2
- O$_2$ levels drop below 12%

Proulx [9] observes that a person's decision-making ability gets hampered because of increased psychological stress. Psychological stress levels rise because of the inability to process information or due to confrontation with unfamiliar situations. Increased stress is very different from panic. Research shows no sign of panic in evacuees in cases of major disasters [10]. Building characteristics are divided into classes, i.e., situational features (ease of wayfinding, usage of proper preventive measures, etc.) and engineered features (width of exits, stairs, corridors, fire resistance installations, etc.), also critical factors influencing fire response performance.

The ability to move or degree of independent movement plays a significant role in evacuation from a building, especially when evacuating a hospital. Hostetter et al. [11], divides disability into four classes, i.e., functional independence (people using crutches or wheelchairs), sensory perception (people who can't respond to external stimuli such as fire alarms, exit signs, etc.), medical health (people with a dire medical condition such as heart or lung patients), and social cognition (It includes mental health disorders and interactions between occupants of the building). Therefore, it is essential to include such characteristics in our calculations.

After gathering data from experiments or interviews, it is entered into evacuation models such as FDS + EVAC, which use it to simulate the egress of agents.

Several literature articles were consulted to determine the speed, pre-evacuation time, known door probability, etc., of the patients and disabled people being simulated through the FDS + EVAC code. For instance, Peacock et al. [4] observed that the local movement speeds as occupants traverse down a high-story building through a stairwell vary widely within a given stairwell, ranging from 0.056 to 1.7 m/s. In their work, the authors presented a value of occupant velocity and their pre-evacuation times in a stairwell for 10, 18, 24, and 31-story buildings. In another study, Averill et al. [12] included firefighter counterflow movement on the stairs. They concluded that it has a significant impact on the velocity of occupants as the occupant velocity dropped from 0.83 ± 0.18 to 0.73 ± 0.26 m/s in the case of a 6-story building. Pauls et al. [3] experimentally concluded that the minimum stair width of 1120 mm. (44-in.) as recommended by the US building codes and standards, traditionally was flawed. The minimum nominal width of between 1400 mm (56 in.) and 1520 mm (60 in.) should be used for designing stairs where counterflow movements can be adjusted along with the regular activity of occupants. For even more efficient movement of the occupants, a stair width of approximately 1730–1750 mm (including

handrails) should be considered. Haghania et al. [13] planned experiments with different levels of urgency, several exits, spatial positions of doors and exit widths to get human behavior data in the form of occupant velocity, evacuation time, and density distribution.

All the data presented above is for regular fit evacuees associated with a building fire. Still, in the case of hospitals, a most vulnerable group, i.e., people with disabilities, are involved; therefore, utterly different evacuation studies are required for dealing with hospital fires [11]. Fire evacuation drills in hospitals are very typical to plan as hospitals are always filled with patients who have decreased mobility due to disability. Some patients are in critical condition and cannot be moved from their respective beds unless there is a real emergency. When evacuating hospitals, the administration or the evacuation group associated with a hospital must consider all groups of disabled people and act accordingly because each group requires different actions to be taken during an emergency [11]. Samoshin et al. [14] sub-categorized the mobility classification done by Hostetter et al. [11] by surveying several local hospitals in their area, after which they gave a total of 10 mobility groups along with their density distribution in a hospital. Later, they conducted experiments to get occupant velocity and density data for hospital evacuation scenarios concerning these groups. Wei et al. [15] collected actual patients' moving parameters belonging to the pediatric and orthopedic wards, i.e., velocity and exit familiarity, through observation and questionnaire investigation and divided the hospital populations into groups of administrative staff, nursing staff, doctors, patients in orthopedic wards, and patients in pediatric wards. Patients in orthopedic wards are physically disabled, considered this study's main population. Gwynne et al. [16] performed a drill involving outpatient and administrative staff of a hospital and collected pre-evacuation data using video equipment. The pre-evacuation times along with its standard deviation were given in their work.

Through this paper, FDS + EVAC needs to be validated. The authors tried to inculcate different features and parameters of the hospital and its occupants, such as the velocity and pre-evacuation times of various categories of patients. These parameters are essential because of the diverse disabilities that the patients suffer. Therefore, it becomes necessary to incorporate the effect of these disabilities into our calculations. Although it is tough to quantify all the disabilities separately, efforts were made to include as many types of patients as possible based on previous data. The distinction of patients based on their disabilities and the magnitude and distribution of their velocity and pre-evacuation time were taken from existing literature. In the end, the number of safe evacuees at various stair widths of the AMRI hospital building was studied and compared with the actual accident.

2 Details of the AMRI Fire Accident

Pal et al. [17] studied the AMRI fire accident scenario. They concluded that the hospital authorities were illegally using the hospital parking as a storage dump yard for used/unused LPG cylinders, used/unused mattresses, wooden crates, etc., which caused the fire to break out in the basement area. The smoke spread throughout the building via AC ventilation ducts. All deaths on that day were due to asphyxiation and intoxication of the patients from gaseous effluents of the fire. The hospital building's fire alarm and sprinkler systems were also not functional at the time of the fire. There was no way for the fire smoke to escape from the building as it didn't have any open windows (since the building was centrally air-conditioned and had glass façade walls). The hospital staff tried to control the fire by themselves, but all their efforts were in vain and when the situation got out of hand, the staff fled the scene. The chronology of the accident can be seen in Fig. 1. At around 11:00 AM another alarm was raised regarding radiation leakage from the lower basement as it had several machines like cobalt therapy, MRI, etc.

The fire department had to retort to rudimentary techniques (Fig. 2) to rescue the patients because of limited visibility inside the hospital building due to dense smoke accumulation.

The mishap led to 89 on-spot deaths and 57 injuries. The families or next of kin of the deceased were compensated for their loss with money and employment assistance by both the state and central government.
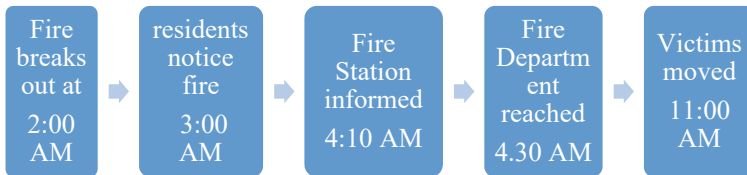

Fig. 1 Chronology of events in the fire accident [18]

Fig. 2 Firefighters forced to use rudimentary methods because of limited visibility inside the building [18]

3 Methodology

The details of the AMRI fire accident are gathered from the local newspapers and a few investigations that are reported [17, 18]. This data is incorporated in the simulation for the realistic calculations of the whole mishap. To understand the model accuracy of the model, the simulated results are compared with the actual scenario. Number of people able to evacuate the building in the stipulated time, maximum fractional effective dosage (FED), and visibility at different levels of the building are the quantities measured through the simulation. FED is a measure of airborne contaminants absorbed by an occupant. Hazards such as carbon monoxide and carbon dioxide are accumulated during the occupant's movement through a burning building. Each occupant has a specific FED counter and as soon as the FED counter reaches unity, the occupant is considered to be incapacitated and can no longer move. The FED is computed numerically using the following relation:

$$FED = \left(FED_{CO} + FED_{NO_x} + FED_{irr}\right) \times HV_{CO_2} + FED_{O_2} \tag{1}$$

where the suffix indicates the FED contribution from the corresponding gas, FED_{irr} is the FED contribution by irritant smoke effluents, and HV_{CO_2} is the hyperventilation factor. Each FED and HV coefficient in Eq. (1) are computed as given in the FDS + EVAC user's guide [19].

Visibility can be defined as the extent up to which a person can see without any visual aid. Here, the visibility is measured in a smoke or obscurant filled environment because smoke particles interact with visible light because of which the opacity of the medium increases and hence visibility decreases. Visibility (V) is computationally measured using the following equations:

$$V = \frac{C}{K} \tag{2}$$

$$K = K_m \rho Y_s \tag{3}$$

where K is the extinction coefficient, K_m is the mass specific extinction coefficient, which is fuel dependent, ρY_s is the density of a smoke particulate and, C is a non-dimensional constant which depends on the type of object being viewed through the smoke, i.e., $C = 3$ for a light reflecting sign and $C = 8$ for a light emitting sign. Visibility is computed at each stair entrance on all the levels.

The image of then hospital building is processed to identify the dimensions and other required geometrical parameters. The inferred building dimensions are $16.6 \times 25 \times 21 m^3$. The numerical domain is simulated with a gird size of $89 \times 134 \times 110$ in each direction, respectively. The building consists of 7 floors in total (1 basement + ground + 5 floors) with different rooms distributed all over as shown in Table 1. The simulation includes 2 stair widths, i.e., 1.0 and 1.4 m and their affect is studied through the simulation results.

Table 1 Floor-wise distribution of different rooms

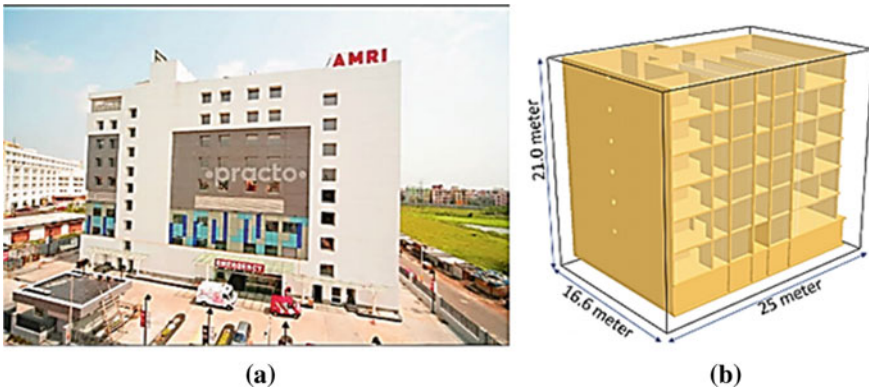| Floor	Facilities
Basement	CT scan, radiotherapy
Ground	Reception, MRI room, medical stores, main exit door
1st floor	Radiology, ultra sound, pantry, electric room
2nd floor	Female ward, deluxe suite
3rd floor	Utility ward, neurosurgeon station, general ward
4th floor	ICU, NITU
5th floor	Operation theatre, equipment and electric room

Fig. 3 AMRI hospital design layout **a** real. **b** In FDS + EVAC virtual environment

The building layout in real and virtual scenarios can be seen in Fig. 3. The actual blueprint of the building couldn't be found. Therefore, based on the comparison, the dimensions of the building and individual rooms were defined.

3.1 Evacuation Parameters

FDS + EVAC contains default properties for adults, women, children, and the elderly. Since we are simulating a hospital, we need to define the person (&PERS) properties of patients and persons with disabilities with as much accuracy as possible.

For our work, only four pedestrian classes as given by Hostetter et al. [11], were considered as they encompass most of the mobility conditions of patients in a hospital. Velocity data provided by Peacock et al. [4] for high-story building evacuation was considered and applied to adults situated on higher floors. For patient velocity and exit familiarity, data given by Wei et al. [15] was considered. Pre-evacuation time data

Table 2 Agent egress and evacuation parameters

Category	No. of occupants	Velocity (m/s)	Pre-evacuation time (s)	Mean time (s)	Standard deviation
Adult[1]	99	0.97 ± 0.2	183 ± 112	183	15
Adult[2]	48	0.44 ± 0.08	183 ± 112	232	15
Patient[1]	88	0.32 ± 0.05	375 ± 50	375	20
Patient[2]	46	0.51 ± 0.085	375 ± 50	375	20
Patient[3]	9	0.22 ± 0.11	437 ± 62	435	20
Patient[4]	26	0.015 ± 0.005	475 ± 25	435	20

provided by Gwynne et al. [16] was considered. The different parameters associated with agent egress and evacuation are shown in Table 2.

Normal distribution was used for assigning pre-evacuation time to the occupants because based on the alarm system of a building and common human behavior, most of the occupants will start evacuating in that time range based on a normal distribution of data. Velocity distribution was set as uniform distribution and values of velocities were taken based on Wei's data [15]. The known door probabilities were 1.0 for adult groups and 0.5 for all patient groups. There was only a single exit door from the hospital and because it was centrally air-conditioned, there were no windows for ventilation in the whole building [17].

Here, Adult[1] are predefined adult agents on lower floors of the building; Adult[2] are predefined adult agents on higher floors of the building with lesser speed; patient[1] are people with limited mobility using just one support (crutch) for walking; patient[2] are people with limited mobility using 2 supports (2 crutches) for walking; patient[3] are people who use a wheelchair; patient[4] are bed-ridden people who cannot move at all without external help/support from other people.

4   Results and Discussion

As the fire started evolving, the smoke engulfed all through the building from the lower ground to the top floor within 180 s. The occupants of the building started evacuating as per the pre-evacuation time and distribution given as input in the code. The pre-evacuation time distribution was given as normal distribution and the lower and upper limit of the time is as mentioned in Table 2.

From the above image, the spread of smoke throughout the building can be observed and it can be observed that visibility decreases at the stair entrance of lower floors first (Fig. 4).

The visibility drops significantly after 25–75 s in case of both stair widths, but it becomes zero for both the cases at approximately 100 s (Fig. 5). The visibility at the lower stair entrance starts dropping faster than that of the upper floors which happens because of the pattern of smoke development which can be observed from
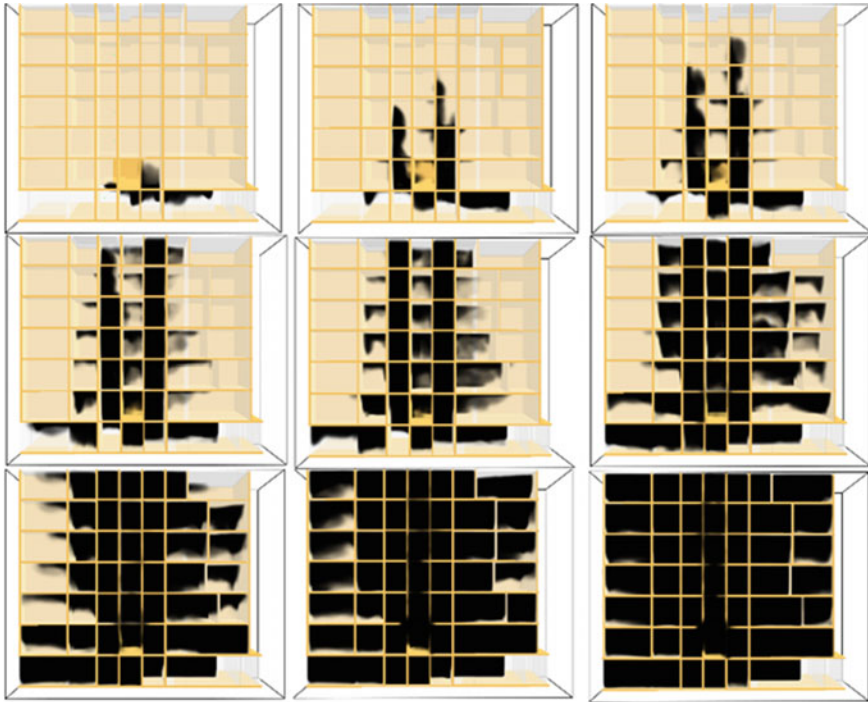
Fig. 4 Evolution of smoke inside the building

Fig. 4. It is also observed that stair width has a role to play in the rate of drop of visibility at the stair entrance. This is because larger stair width will lead to slower diffusion of smoke throughout the building as, in the current geometry, stairs are the only building feature responsible in its spread (Fig. 4).

The maximum FED value is the highest value of FED among all the agents present inside the building. In case of narrow stairs, the FED value increases faster than in the case of wider stair width which means that there is a faster spread of smoke in case of stairs of narrow width (Fig. 6).

Overall, 257 casualties in case of stair width of 1 m and 239 casualties in case of stair width of 1.4 m were observed. Therefore, the effect of stair width on evacuation can be seen clearly from the evacuation calculations (Fig. 7).

5 Conclusions

The ability of the FDS + EVAC code is verified by numerically simulating the AMRI hospital fire accident that occurred in 2011. From this case study, it is concluded that the model is robust and is capable of designing various ventilations, doors, windows,

Fig. 5 Visibility plot for different stair widths at different floors
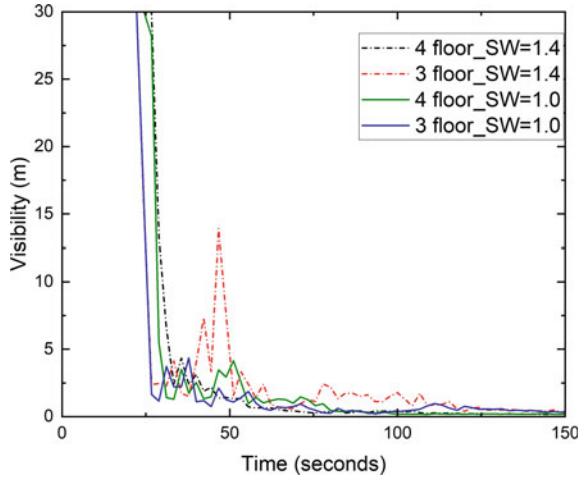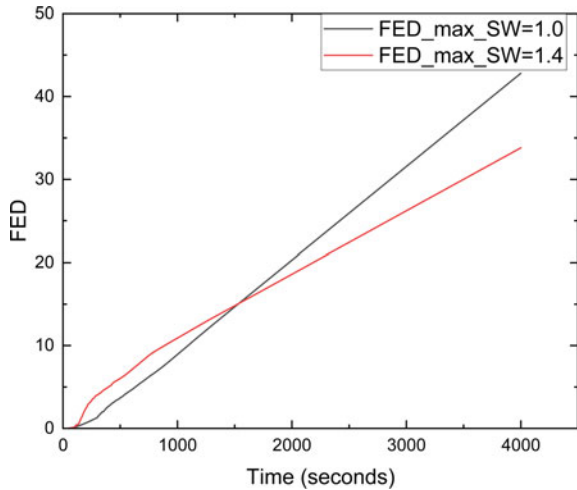

Fig. 6 Maximum FED value among agents in a domain

stairs, and other building geometry along with the fire and smoke movement. The major findings from this case study are:

1. The number of agents not able to evacuate the building were 239 (when stair width = 1.4 m) and 257 (when stair width = 1 m) out of a total of 316 agents in case of FDS + EVAC simulation as compared to 146 incapacitations (89 deaths + 57 injuries) in the actual mishap.
2. The number of deaths computed by the model (257) are higher than the actual number of deaths (92) that happened on the day of the accident.
3. In the real fire accident there were also injuries many occupants and they are captured in the model.

Fig. 7 Evacuation plot for different stairs width
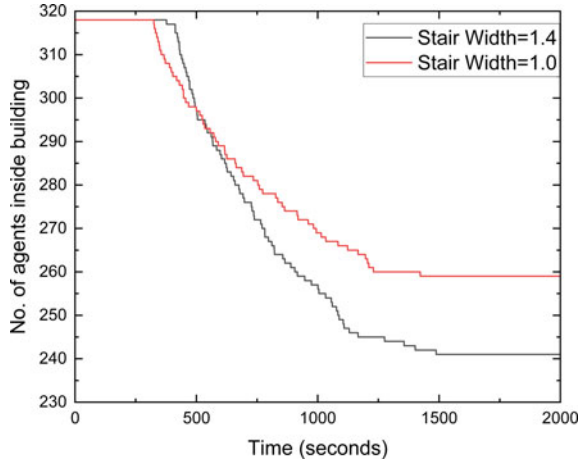
4. The higher number of evacuations in case of stair design of larger width is because overtaking and counter flow is possible in case of larger stair widths.
5. The higher rate of drop of visibility and higher rate of rise of FED in case of narrow stairs width is due to faster and larger accumulation of smoke due to narrow stairs.
6. The main reasons for the over calculation of the number of deaths are:

   a. insufficient fire and arson data from the accident (i.e., lack of HRR and soot yield values).
   b. exact Blueprint of the hospital building was unavailable
   c. patients' data was unavailable, i.e., the type of disabilities that the patients are suffering from and their number and floor-wise distribution. All this data was either assumed or taken from literature.

7. To the best of the knowledge of the authors, there is no/sparse literature available regarding the evacuation in Indian context: evacuee characteristics of the Indian crowd (occupant velocity and pre-evacuation time).

References

1. Kobes M, Helsloot I, De Vries B, Post JG (2010) Building safety and human behaviour in fire: a literature review. Fire Saf J 45(1):1–11
2. Fruin JJ (1971) Pedestrian planning and design (no. 206 pp).
3. Pauls JL, Fruin JJ, Zupan JM (2007) Minimum stair width for evacuation, overtaking movement and counterflow—technical bases and suggestions for the past, present and future. In: Pedestrian and evacuation dynamics 2005. Springer, Berlin, Heidelberg, pp 57–69
4. Peacock RD, Hoskins BL, Kuligowski ED (2012) Overall and local movement speeds during fire drill evacuations in buildings up to 31 stories. Saf Sci 50(8):1655–1664

5. BSI P (2004) The application of fire safety engineering principles to fire safety design of buildings. Part 6: human factors: life safety strategies—occupant evacuation, behaviour and conditions (sub-system 7974–6). British Standards Institute Google Scholar

6. Proulx G (2003) Playing with fire. ASHRAE J 45(7):33

7. Jin T (1997) Studies on human behavior and tenability in fire smoke. Fire Safety Sci 5:3–21

8. Purser DA (2010) Fire toxicity and toxic hazard analysis. In: 6th international seminar on fire and explosion hazards. Univesity of Leeds

9. Proulx G (1993) A stress model for people facing a fire. J Environ Psychol 13(2):137–147

10. Sime JD (1990) The concept of 'panic.' In: Canter D (ed) Fires and human behavior, 2nd edn. David Fulton Publishers, London, p 68

11. Hostetter H, Naser MZ (2022) Characterizing disability in fire evacuation: a progressive review. J Build Eng 53:104573

12. Peacock RD, Averill JD, Kuligowski ED (2010) Stairwell evacuation from buildings: what we know we don't know. In: Pedestrian and evacuation dynamics 2008. Springer, Berlin, Heidelberg, pp 55–66

13. Haghani M, Sarvi M, Shahhoseini Z (2020) Evacuation behaviour of crowds under high and low levels of urgency: experiments of reaction time, exit choice and exit-choice adaptation. Saf Sci 126:104679

14. Samoshin DA, Istratov RN (2013) The parameters of pedestrian flows in hospital during fire evacuation. In: Proceedings of 13th international conference, vol 2013. Interflam, pp 1003–1012

15. Wei X, Lv W, Song W, Wang D (2011) Evacuation analysis of a hospital based on fds+ evac software. In: 2011 international conference on remote sensing, environment and transportation engineering. IEEE, pp 3147–3150

16. Gwynne S, Galea ER, Parke J, Hickson J (2003) The collection of pre-evacuation times from evacuation trials involving a Hospital Outpatient area and a University Library facility. In: Fire safety science–proceedings of the seventh international symposium, pp 877–888

17. Pal I, Ghosh T (2014) Fire incident at AMRI hospital, Kolkata (India): a real time assessment for urban fire. J Bus Manag Soc Sci Res 3:9–13

18. Khare LL Learnings from Amri hospital fire. National Association of Fire officers, Case Studies. http://nafoindia.org/pdfs/kolkata_fire_report_AMRI.pdf

19. Korhonen T Fire dynamics simulator with evacuation: FDS+Evac technical reference and user's guide

20. Purser DA (2002) Toxicity assessment of combustion products. SFPE Handbook Fire Prot Eng 3:2–6

Influence of Double Fin Shape on Constrained Melting of PCM in a Spherical Capsule: A Numerical Study

Akhalesh Sharma, Jaykumar Joshi, Vivek Saxena, and Santosh Kumar Sahu

1 Introduction

Thermal energy storage (TES) system stores energy in latent, chemical, or sensible forms of energy. TES increases the effectiveness of thermal systems that use intermittent or variable-intensity energy sources. The high energy storage density linked to the change from the solid to liquid phase makes latent heat storage-based (LHTES) one of the most advantageous TES systems. A spherical capsule is frequently utilised in the LHTES system to store PCM due of its larger surface area per unit volume. The low thermal conductivity of the existing phase change materials (PCM) [1, 2] restricts the practical application of LHSU. The efficiency of (LHTES) can be improved by using fins. PCM melts in a SC either in constrained or unconstrained fashion. In the constrained melting [3], the unmelted PCM is held in its position by means of rod and cannot sink to the bottom whereas in unconstrained melting [4], solid PCM which is not melted because of its heavier weight than the liquid phase can sink to the bottom.

2 Literature Review and Objective

Various studies are being reported in the literature on the constrained melting of PCM in a SC with fins. Constrained PCM melting in a SC integrated with fins was studied experimentally and numerically by Fan et al. [5]. The authors reported that the induction of fin decreased the PCM melting time significantly which further decreases with the increment in fin insertion height. Meghari et al. [6] scrutinise the constrained melting of PCM in a spherical capsule integrated with solid and hollow

A. Sharma (✉) · J. Joshi · V. Saxena · S. K. Sahu
Department of Mechanical Engineering, IIT Indore, Indore 453552, India
e-mail: phd1901203007@iiti.ac.in

fins and reported the melting time decreases for both solid and hollow fins compared to the case without fin. Sinaga et al. [7] showed the effect of double fin having different position and shapes on the melting characteristics of PCM in a rectangular shaped container. Fins in the shapes of triangles, rectangles, and trapezoids were examined, and it was found that the triangle fin at the bottom location has the best melting efficiency. Samakoush et al. [8] numerically examined the melting of PCM in a vertical rectangular enclosure integrated with fins of a combination of rectangular and triangular shapes and found that various fin parameters such as internal fin schematics and triangular fin height have a significant effect on melting. Wang et al. [9] proposed a novel L-shaped fin for melting enhancement in a vertical PCM enclosure. Based on the numerical analysis, he concluded that the "L"-shaped fins' orientation and size had a major impact on the melting performance with upward L-shaped fins performing better than lower forms in terms of melting performance.

The majority of the research on constrained melting of PCM in a SC with fins is, it appears from the literature, focused on the influence of fin insertion depth. To the best of author's knowledge, no work is being reported on the effect of double on the melting of PCM in a SC. Thus, the current presents a numerical examination of the constrained melting of phase change material (*n*-octadecane) in a SC integrated with double fin is presented for various fin shapes while maintaining the area, base, and distance between the fins same for all.

3   Physical Model

The physical domain is a SC (t_w) whose internal radius (R) and thickness (t_w) are 50 mm and 2 mm, respectively. Figure 1 displays a double fin with 3 mm base thickness integrated with a spherical capsule constructed of Plexiglas, the fins are made of aluminium, and the PCM is *n*-octadecane. The PCM is held in place by a rod at the centre of the SC to maintain constrained melting conditions. Table 1 [5] lists the thermophysical characteristics of PCM (*n*-octadecane), aluminium, and Plexiglas.

Based on the shape of the fins, four different cases are being considered as shown in Fig. 1. For the comparison, SC without a fin is also studied. The area of each fin is kept constant as 50 mm^2 for all the cases. The spherical capsule's exterior wall is continuously heated to a temperature of $T_w = 40$ °C. Each fin's (H) distance from the capsule's centre is 6.25 mm.
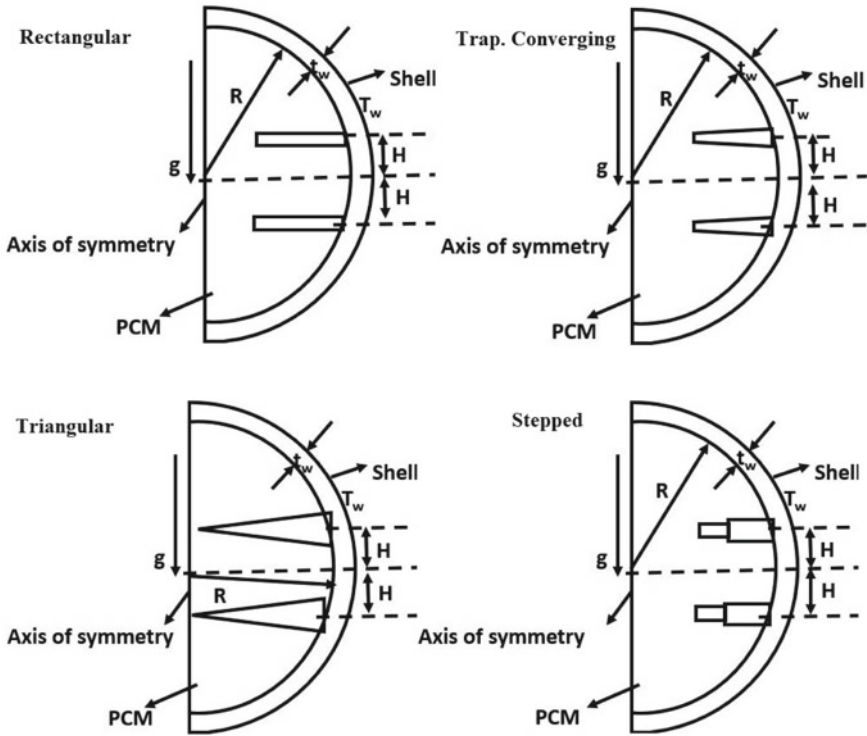
Fig. 1 Physical domain

Table 1 Thermophysical properties of various materials [5]

Properties	N-octadecane (PCM)	Plexiglass (capsule)	Aluminium (fin)
ρ	773	1200	2719
C_p	2410	1470	871
K	0.156	0.19	202.4
μ	0.00352	–	–
A	0.000932	–	–
T_m	301.15	–	–
L_f	241.8	–	–

4 Numerical Investigation

4.1 Governing Equations

The computational domain is two-dimensional and axisymmetric. The study disregards the distinction of density between the liquid and solid PCM owing to constrained melting conditions [3, 4] which prevents the sinking of solid in the numerical simulation.

Change of density in the governing equations is taken into consideration using the Boussinesq approximation. Throughout the whole melting process, the phase interface is kept at melting temperature (T_m) and is regarded as sharp. The study also makes the assumption that various thermophysical parameters remain constant. Radiation-based heat transfer is not taken into account. The PCM system is originally maintained at a constant temperature27 °C. Laminar and Newtonian flow describe liquid PCM. The following are the governing equations for mass, momentum, and energy in spherical polar coordinates:

Continuity Equation:

$$\frac{1}{r^2}\frac{\partial}{\partial r}\left(V_r r^2\right) + \frac{1}{r\sin\theta}\frac{\partial}{\partial\theta}(V_\theta\sin\theta) = 0 \tag{1}$$

Polar Direction Momentum:

$$\begin{aligned}
\frac{\partial V_\theta}{\partial t} &+ \frac{1}{r^2}\frac{\partial}{\partial r}\left(V_r r^2 V_\theta\right) + \frac{1}{r\sin\theta}\frac{\partial}{\partial\theta}(V_\theta\sin\theta V_\theta)\\
&= \vartheta\left(\frac{1}{r^2}\frac{\partial}{\partial r}\left(r^2\frac{\partial V_\theta}{\partial r}\right) + \frac{1}{r^2\sin\theta}\frac{\partial}{\partial\theta}\left(\sin\theta\frac{\partial V_\theta}{\partial\theta}\right)\right)\\
&\quad - \frac{1}{\rho}\frac{1}{r}\frac{\partial p}{\partial\theta} - g\alpha(T-T_m)\sin\theta - \frac{V_r V_\theta}{r} + \vartheta\frac{2}{r^2}\frac{\partial V_r}{\partial\theta}\\
&\quad - \frac{\vartheta}{r^2\sin^2\theta}V_\theta - \frac{C(1-\varphi)^2}{\rho\varphi^3}V_\theta
\end{aligned} \tag{2}$$

Radial Direction Momentum:

$$\begin{aligned}
\frac{\partial V_r}{\partial t} &+ \frac{1}{r^2}\frac{\partial}{\partial r}\left(V_r r^2 V_r\right) + \frac{1}{r\sin\theta}\frac{\partial}{\partial\theta}(V_\theta\sin\theta V_r)\\
&= \vartheta\left(\frac{1}{r^2}\frac{\partial}{\partial r}\left(r^2\frac{\partial V_r}{\partial r}\right) + \frac{1}{r^2\sin\theta}\frac{\partial}{\partial\theta}\left(\sin\theta\frac{\partial V_r}{\partial\theta}\right)\right) - \frac{1}{\rho}\frac{\partial p}{\partial r}\\
&\quad - g\alpha(T-T_m)\cos\theta + \frac{V_\theta^2}{r} - \vartheta\frac{2}{r^2}\frac{\partial V_\theta}{\partial\theta} - \vartheta\frac{2\cot\theta}{r^2}V_\theta\\
&\quad - 2\frac{\vartheta}{r^2}V_r - \frac{C(1-\varphi)^2}{\rho\varphi^3}V_r
\end{aligned} \tag{3}$$

Energy Equation (PCM):

$$\frac{\partial H}{\partial t} + \frac{1}{r^2}\frac{\partial}{\partial r}\left(V_r r^2 H\right) + \frac{1}{r\sin\theta}\frac{\partial}{\partial\theta}\left(V_\theta \sin\theta H\right)$$
$$= \frac{k}{\rho C_p}\left(\frac{1}{r^2}\frac{\partial}{\partial r}\left(r^2\frac{\partial H}{\partial r}\right) + \frac{1}{r^2\sin\theta}\frac{\partial}{\partial\theta}\left(\sin\theta\frac{\partial H}{\partial\theta}\right)\right) + S \quad (4)$$

where $S = -\frac{1}{\rho C_p}\left(\frac{\partial(\Delta H)}{\partial t} + \frac{1}{r^2}\frac{\partial}{\partial r}\left(V_r r^2 \Delta H\right) + \frac{1}{r\sin\theta}\frac{\partial}{\partial\theta}\left(V_\theta \sin\theta\,\Delta H\right)\right)$ (5)

Energy Equation (shell and fin):

$$\rho C_p \frac{\partial T}{\partial t} = K\nabla^2 \quad (6)$$

Total enthalpy is the sum of sensible ($H = C_p$) and latent heat (H). The relation between latent heat (H) and the liquid fraction (φ), is given as:

$$\Delta H = \varphi L \quad (7)$$

The latent heat for solid phase is 0 and L for liquid and in the mushy zone it is between 0 and L, φ is the liquid fraction of PCM which is defined as:

$$\varphi = 0 \quad \text{if} \quad T < T_{solidus}$$

$$\varphi = 1 \quad \text{if} \quad T > T_{liquidus}$$

$$\varphi = \frac{T - T_{solidus}}{T_{liquidus} - T_{solidus}} \quad \text{if} \quad T_{solidus} < T < T_{liquidus} \quad (8)$$

The temperature at which melting begins is known as $T_{solidus}$, whereas the PCM becomes fully liquid at a temperature called $T_{liquidus}$. This single-domain enthalpy-porosity formulation [3, 5] considers various phases as a porous medium. The equations for momentum include Darcy law damping terms $\left(\frac{C(1-\varphi)^2}{\rho\varphi^3}V_i, \quad i = r \text{ and } \theta\right)$ which will cause the velocity to arrest in solid phase. The value of C was set to 10^5 kg/ m^{3}s. The mushy zone constant is a measure of the damping amplitude of velocity. The results may oscillate if the mushy zone constant is set to a very high value. Commercial CFD code ANSYS Fluent [10] is used to conduct simulations. Second-order implicit time integration was used for time discretization. The PISO scheme is used for coupling velocity and pressure, and second order upwind scheme is used to discretize the velocity and temperature terms in the governing equations. Iterative solution for velocity, pressure, energy, and liquid fraction uses under-relaxation values of 0.3, 0.3, 0.9, and 0.95, respectively, while the convergence conditions for

Fig. 2 Grid independence study
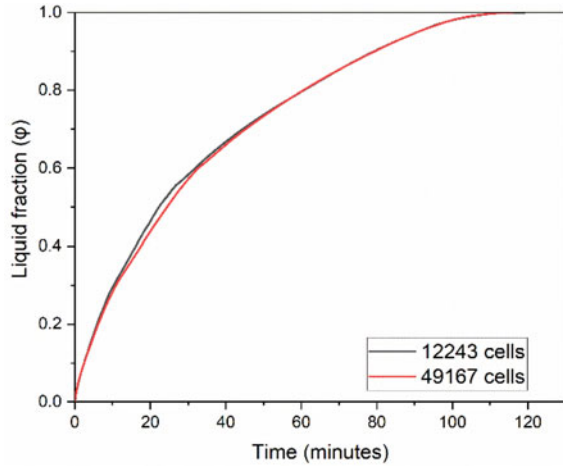
the continuity/momentum and energy equations were set to 10^{-6} and 10^{-6}, respectively. To satisfy this convergence criteria of 10^{-6}, 750 iterations per time step were chosen (Fig. 2).

4.2 Grid and Time Independence Study

Grid independence and time independence is being carried out considering PCM's overall melting time as a benchmark for comparison. Both quadrilateral and triangular cells are created in the meshed domain. Simulations with 12,243, 49,167 cells were performed to test the solution's mesh dependency. Figure 3 depicts how liquid fraction changed over time for these cells. There is no significant change in melting time between the two cases. We see no noticeable change in melting time when we increase the number of cells further. However, the overall computational time has increased noticeably. Based on this, 49,167 cells were considered in the computational domain. For the time independence study (Fig. 3, the time step sizes of 0.15, 0.25 and 0.5 s were used. Thus 49,167 cells and 0.25 s time step size is chosen, which provides the best compromise between resolution and CPU time.

4.3 Validation

To validate the computational model, the current numerical liquid fraction outcomes are compared with the experimental findings of Fan et al. [5].

The experimental setup is a SC integrated with fin whose internal radius and thickness are 50 mm and 2 mm, respectively. *n*-octadecane is used as the PCM.

Fig. 3 Time independence study
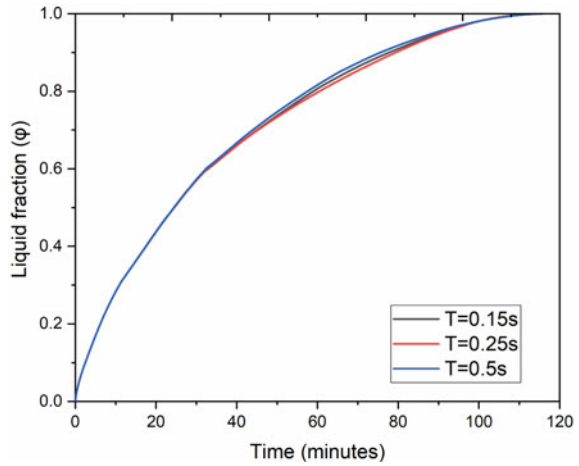
Melting conditions are constrained. Fin has a thickness of 2 mm with insertion into the SC of 37.5 mm. The exterior wall of the SC is continuously heated to 27 °C. In Fig. 4, the current investigation's melt fraction is compared to the findings of Fan et al. [5]. Figure shows that the percentage variance in estimating the entire melting time is 8.76%, which is in satisfactory accord with the results of the experiments.

Fig. 4 Comparison of liquid fraction between current model and experimental findings of Fan et al. [5]
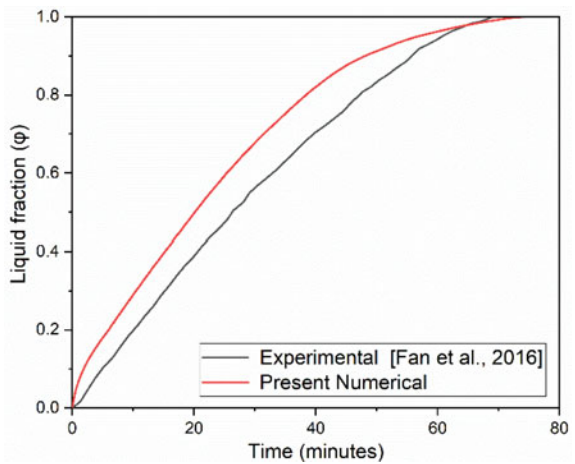
5   Results and Discussion

Here, we discussed the comparison of PCM melting in spherical capsules with and without fins. The fin's presence in the SC speeds up melting by creating a localised heating above and below the surface of fin. Such arrangements increase the phenomenon of conduction due to the increase in area as well as local natural convection in the vicinity of fin. The time when PCM melts completely is 116 and 175 min for finned and unfinned SC, respectively as depicted in Fig. 5. With the insertion of double fin to spherical capsule, it is observed that total melting time is decreased by 33.71%. PCM in the upper half portion of the SC melts at a faster rate than in the lower half portion for both finned and unfinned cases. Since the amount of latent heat stored is directly proportional to the liquid fraction. Thus, SC with fin can absorb the same of energy in a lesser period of time compared to the case of SC without fin. Also, latent heat stored by PCM in the upper half of the SC is higher than the energy stored at lower portion at any instant of time. Without fin temperature gradient persists at the lower portion of SC for a large interval of time, while the temperature decreases much earlier when the fin is integrated with SC due to which finned SC has better melting performance.

Figures 6 and 7 exhibit the melt fraction variation and average velocity magnitude variation with time for various fin shapes located at the centre. We see that for fin shapes other than triangular the melt fraction is nearly the same upto 10 min. Thus, during this time, we can say that the fin shape shows no effect on melting performance. After this the melt fraction for rectangular case also becomes distinct. Melt fraction variation with time remains similar for trapezoidal converging and stepped fin upto the completion of melting. Average velocity of molten PCM is an indicator of the magnitude of convection. It is noteworthy, that for large time interval triangular fin has the highest values of average velocity compared to other cases which is why it outperforms in terms of overall melting performance. While the rectangular case has

Fig. 5 Comparison of liquid fraction between finned and unfinned spherical capsule
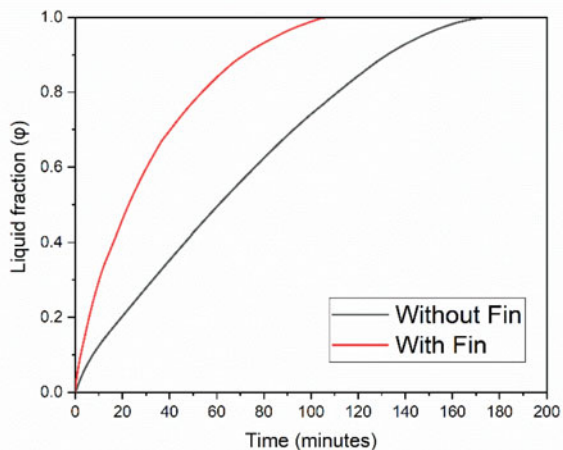
the least average velocity than all other cases from 30 to 50 min due to which it has worst melting performance. Followed by triangular fin trapezoidal converging and stepped fin case has the best melting performance overall. For all the cases average velocity rises to a maximum and falls which indicates conduction, strong convection and weak convection heat transfer regimes during the melting of PCM. The melting time for rectangular, trapezoidal converging, stepped fin, and triangular fin cases are 116, 107, 107, and 95 min, respectively (Fig. 8).

Overall fin effectiveness, which is a comparative measurement of the system's increased thermal performance over that of the unfinned system for an LHTES, is a system's performance to be considered. It is defined as:

Fig. 6 Comparison of melt fraction variation with time for various shapes of fins located at centre
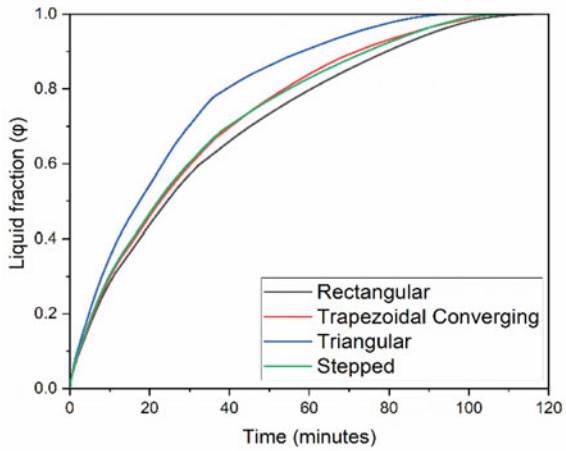

Fig. 7 Comparison of average velocity variation with time for various shapes of fins located at centre
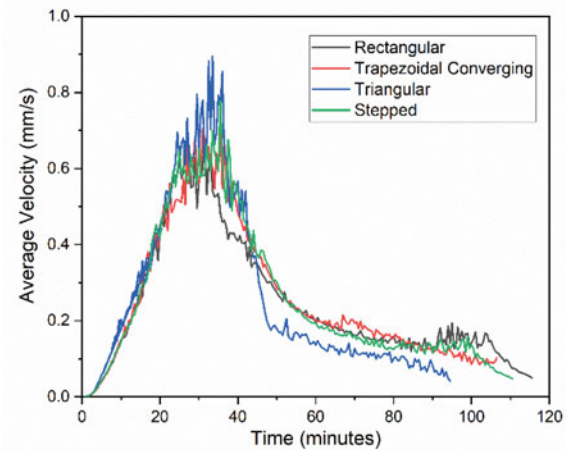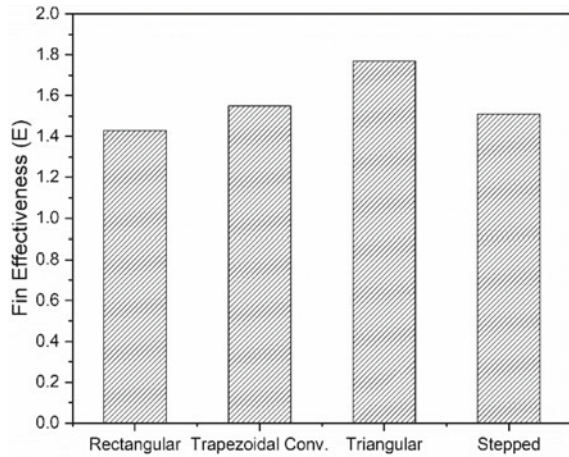
Fig. 8 Fin effectiveness for all considered cases

$$E = \frac{Q''_f S_f}{Q''_{nf} S_{nf}}$$

where Q''_f, S_f and Q''_{nf}, S_{nf} represents the heat transfer flux and surface area for finned and unfinned spherical capsules respectively and their product in the angle brackets is their time-averaged value upto the completion of melting.

Here the fin effectiveness is maximum for triangular case (1.77) which is attributed to the fact that it is having highest surface area which increases the local convection effects and thus increasing the rate of heat transferred to the PCM while it is minimum for rectangular fin case (1.43). Fin effectiveness for trapezoidal converging and stepped fin is nearly (1.55 and 1.51) same as both of them are having similar surface area and similar velocity magnitude variation with time and consequently same rate of convective heat transfer.

6 Conclusions

Constrained melting of PCM in a sphere integrated with a double fin of various shapes is being studied numerically. The current computational model was tested for conformity with the outcomes of earlier experimental results. According to the results, the integration of a fin reduces PCM melting time by 33% when compared to the no fin case. Among the various shapes of fin considered, the triangular case has the best melting performance (least melting time). Both trapezoidal converging and stepped fins achieve the second-best melting performance because they have similar surface area and velocity magnitude variation with time, and thus the same rate of convective heat transfer. In the present study changing the shape of the fin from straight has not affected the melting time significantly.

Nomenclature

C_p	Specific heat capacity (J/kg-K)
H	Fin insertion depth (mm)
PCM	Phase change material
S/V	Surface area/volume ratio (1/mm)
k	Thermal conductivity (W/mK)
L_f	Latent heat of fusion (kJ/kg)
R	Internal radius (mm)
T_m	Melting temperature (K)
t_w	Wall thickness (mm)
V_r	Radial velocity (m/s0
V_θ	Polar velocity (m/s)
SC	Spherical capsule
C	Mushy zone constant (kg/m³s)

Greek symbols

ρ	Density (kg/m³)
α	Thermal expansion coefficient (1/K)
λ	Liquid volume fraction
μ	Dynamic viscosity (kg/m-s)
ϑ	Kinematic viscosity (m²/s)

References

1. Kumar A, Kothari R, Sahu SK, Kundalwal SI, Paulraj MP (2021) Numerical investigation of cross plate fin heat sink integrated with phase change material for cooling application of portable electronic devices. Int J Energy Res 45:1–18
2. Kothari R, Das S, Sahu SK, Kundalwal SI (2019) Analysis of solidification in a finite PCM storage with internal fins by employing heat balance integral method. Int J Energy Res 43:1–23
3. Tan FL, Hosseinizadeh SF, Khodadadi JM, Fan L (2009) Experimental and computational study of constrained melting of phase change materials (PCM) inside a spherical capsule. Int J Heat Mass Transf 52:3464–3472
4. Tan FL (2008) Constrained and unconstrained melting inside a sphere. Int Commun Heat Mass Transf 35:466–475
5. Fan LW, Zhu ZQ, Xiao SL, Liu MJ, Lu H, Zeng Y, Yu ZT, Cen KF (2016) An experimental and numerical investigation of constrained melting heat transfer of a phase change material in a circumferentially finned spherical capsule for thermal energy storage. Appl Therm Eng 100:1063–1075
6. Meghari Z, Bouhal T, Benghoulam M, El Rhafiki T, Mohammed OJ (2021) Numerical simulation of a phase change material in a spherical capsule with a hollow fin. J Energy Storage 43:103024

7. Sinaga N, Moria H, Nisar KS, Vu CM, Heidarshenas B, Arsalanloo A, Youshanlouei MM (2021) Melting performance enhancement of thermal storage system by utilizing shape and position of double fin. Case Stud Therm Eng 23:100813
8. Masoumpour-Samakoush M, Miansari M, Ajarostaghi SSM, Arıcı M (2022) Impact of innovative fin combination of triangular and rectangular fins on melting process of phase change material in a cavity. J Energy Storage 45:103545
9. Wang G, Li F, Altanji M, Sharma K, Nisar KS, Khorasani S (2021) Proposing novel "L" shaped fin to boost the melting performance of a vertical PCM enclosure. Case Stud Therm Eng 28:101465
10. ANSYS FLUENT 12.0 User's guide

Effect of Shear Intensity on the Wake Characteristics of a Sphere

Abhishek Kumar, Shaligram Tiwari, and S. P. Das

1 Introduction

Flow past an isolated sphere has been the research of interest due to its vast engineering applications, such as transport phenomenon, internal combustion engines, games (football, cricket and golf), and multiphase flow. Due to the three-dimensional shape of the sphere, flow past it results in a complex wake structure even at the low Reynolds number. It has been known from past experimental and numerical studies that the flow behaviour in the wake of the sphere drastically depends on the various physical parameters. Non-uniform flow past sphere has many practical applications like solid particles flow in the pneumatic pipe, air bubble behaviour near the wall and snow particles motion near the ground. Particles' motion in such applications depends on the wake oscillation frequency and the dynamic forces (drag and lift). So, it is essential to know whether the intensity of non-uniform flow affects the wake frequency and the dynamic forces acting on the particles.

2 Literature Review and Objective

Flow past sphere has been investigated both numerically and experimentally by various researchers. Taneda [1] used the flow visualization technique to study the flow past sphere by varying the Re between 5 and 300. He found that the Reynolds number at which flow separation occurs is nearly equal to 24. The size of the vortex ring formed behind the sphere was found to be directly proportional to the logarithm of Re. He also observed faint oscillation of a large time period in the wake at $Re = 130$. Achenbach [2–4] measured the drag force and the vortex shedding frequency in

A. Kumar (✉) · S. Tiwari · S. P. Das
Department of Mechanical Engineering, IIT Chennai, Chennai 600036, India
e-mail: abhishek.nita98@gmail.com

the wake of the sphere at a high Reynolds number. He also determined the effect of surface roughness and the blockage ratio on the Strouhal number and the dynamic forces. Low and high modes of Strouhal number in the sphere wake were observed by Sokomoto and Haniu [5, 6] at a *Re* higher than 800. The low mode is associated with the vortex shedding frequency, and the high mode indicates the small-scale instability of the Kelvin Helmholtz type. Further, they experimentally examined the effect of non-uniform flow on wake oscillations. Kim and Durbin [7] determined the effect of acoustic excitation on the vortex shedding frequency and the drag force. Pao and Kao [8], Maxworthy [9], and Nakamura [10] also performed several experimental studies. An extensive numerical study on the flow past sphere at low and moderate values of *Re* has been carried out by Johnson and Patel [11] and Tomboulides and Orszag [12]. They reported that flow undergoes various transitions with change in the *Re*. Flow remains steady and axisymmetric up to $Re = 210$. In the range of *Re* between 210 and 270, flow becomes non-axis symmetric, and a double thread wake structure characterizes the flow. At $Re = 280$, the flow becomes completely unsteady, and the hairpin-shaped vortices continuously shed from the sphere at a constant frequency. Some authors [13–15] also examined the effect of particle sizes and the spacing between them at various *Re* values. They reported that the particle size and spacing between them greatly influence the wake and the dynamic characteristic of the particles.

Most of the studies in the past focused on the uniform flow past a sphere, and only a few experimental and numerical studies have been reported in the literature for a uniform shear flow past a sphere. In the present work, a numerical study on a uniform shear flow past sphere has been carried out using Open Source Field Operation and Manipulation (OpenFOAM). Effect of shear intensity (K) on wake structures is identified with the help of Iso-Q surfaces. Unsteady characteristics of the wake have been examined qualitatively by plotting the Hilbert spectrum of a transverse velocity signal. Variation of Strouhal number with K is determined with the help of the Marginal Hilbert spectrum of the transverse velocity signal at a point in the wake.

3   Problem Formulation

All the numerical simulations are performed by considering the domain, as shown in Fig. 1. Sphere of diameter (D) is positioned at a distance $L_u = 6D$ from the inlet. Here $L_1 = 20D$ is the size of the domain in the direction of the flow. $L_2 = 16D$ and $L_3 = 16D$ are the domain sizes in a direction transverse to the flow direction. A fixed Reynolds number $Re = 300$ has been chosen for all the computations, which is defined based on the centre line velocity $\left(U_c = \frac{U_1 + U_2}{2}\right)$ and the diameter of the sphere. Here U_1 and U_2 are the velocities at the bottom and top lateral surfaces. Uniform shear flow is specified at the inlet with the help of GroovyBC utility linked with the Swak4Foam. Shear constant $K = GU_c/D$ is varied from 0 to 0.125, where G is the gradient of velocity at the inlet.

Fig. 1 Schematic of the
computational domain
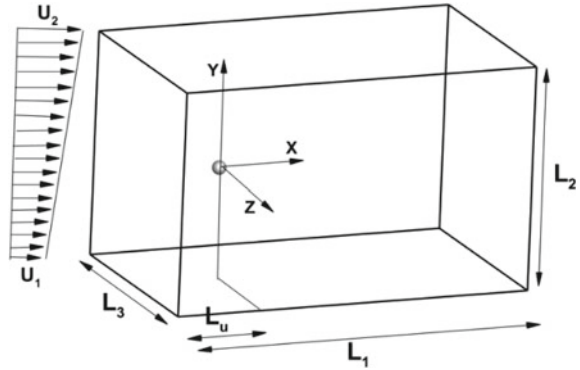
4 Governing Equations and Boundary Conditions

4.1 Governing Equations

Three-dimensional viscous, laminar, unsteady, and incompressible fluid flow is considered in the present study, governed by the three-dimensional continuity and Navier stoke equations. Centerline velocity U_c and the diameter of the sphere are chosen as the velocity scale and length scale to non-dimensionalize the governing equations. Non-dimensional mass and momentum equations are expressed below in the index notation.

$$\frac{\partial U_i}{\partial X_i} = 0 \tag{1}$$

$$\frac{\partial U_i}{\partial t} + U_j \frac{\partial U_i}{\partial X_j} = -\frac{\partial P}{\partial X_i} + \frac{1}{Re}\left(\frac{\partial^2 U_i}{\partial X_j \partial X_j}\right) \tag{2}$$

where U_i is the component of non-dimensional velocity along X_1, X_2, and X_3 coordinate directions. P is the non-dimensional pressure.

4.2 Boundary Conditions

Governing equations have been solved by employing suitable boundary conditions on the various surfaces of the computational domain.

Inlet

A linear velocity profile is employed at the inlet with the help of GroovyBC linked with Swak4Foam. For pressure, zero gradient is specified.

$$U = U_c + Gy \tag{3}$$

Outlet

Zero gradient is used for the velocity, and Dirichlet boundary condition $P = 0$ is specified for pressure.

Sphere

No-slip and impermeable boundary conditions for the velocity and zero gradient for the pressure.

Side and lateral surfaces

Fluid is allowed to slip on all these surfaces, and zero gradient is set for the pressure.

5 Numerical Technique and Grid Independent Study

5.1 Numerical Technique

Three-dimensional continuity and Navier-Stoke equations are solved by using a finite volume approach software Open Source Field Operation and Manipulation (OpenFOAM). Gaussian finite volume integration method is used to discretize the various terms of the governing equations. Unsteady terms are discretized using a first-order Euler implicit scheme. Gauss linear and Gauss cubic schemes are employed to discretize the gradient and the divergence terms of the governing equation, respectively. Laplacian terms of the governing equations have been discretized using Gauss linear corrected scheme. Pressure Implicit and Splitting Operator algorithm-based solver IcoFoam has been used to resolve the coupling between pressure and velocity. Convergence criteria are set to be 10^{-6} for both velocity and pressure.

5.2 Grid Independence Study

ANSYS ICEM CFD 18.1 is used to generate the three-dimensional hexahedral grid in the whole computational domain. O-grid with high grid resolution near the surface has been created around the sphere to resolve the large gradients near the wall, as shown in Fig. 2. Grid independence study has been performed by computing uniform shear flow past a sphere at $Re = 300$ and $K = 0.05$. Four different grids are chosen by changing the number of grids in radial and on the sphere's surface. In addition, the first cell height (Δr) varied from 0.02 to 0.005. Variation of Cd_{avg} and St with a change in the number of grids, and the first node height is depicted in Table 1. It can be noted that as the number of grids varied from *G1-G4* and the first cell height

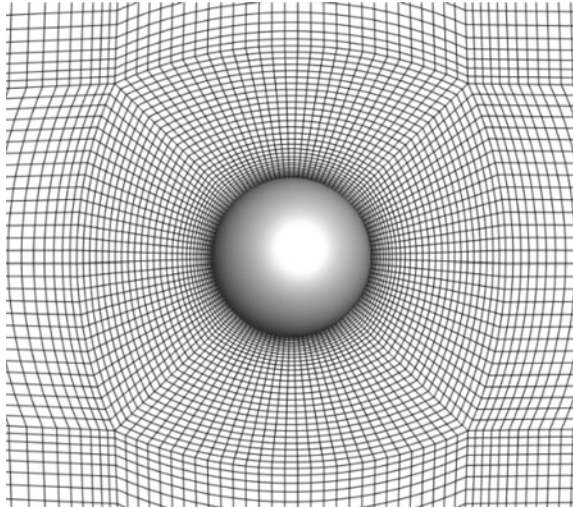**Fig. 2** Distribution of the grid near sphere surface

Table 1 Grid independence study

Grid (G)	Total number of grids (N)	Δr	Cd_{avg}	St
G1	293,132	0.020	0.698	0.154
G2	818,539	0.012	0.681	0.145
G3	**1,272,433**	**0.009**	**0.670**	**0.143**
G4	1,610,008	0.005	0.669	0.142

decreased from 0.02 to 0.005, the variation in Cd_{avg} and St becomes relatively very small, which ensures the reliability of the numerical method and the grid considered for the present study. All simulations are performed by considering the boldly marked grid.

6 Results and Discussion

6.1 Validation

Numerical validation is an essential part of the numerical study to confirm the accuracy of the numerical technique and the grids to capture the flow physics precisely. Validation is performed by computing uniform flow past an isolated sphere at various Reynolds numbers, and the results are compared with those reported in the literature. Figure 3. shows the variation of mean drag coefficient with *Re*. Variation of drag coefficient obtained from the present study indicates a good agreement with that reported by Johnson and Patel [11] and Roos and Willmarth [16].

Fig. 3 Variation of mean
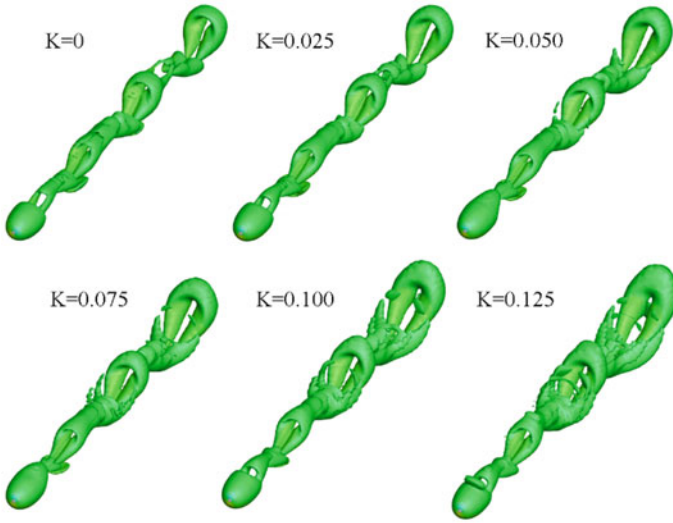drag coefficient with Re
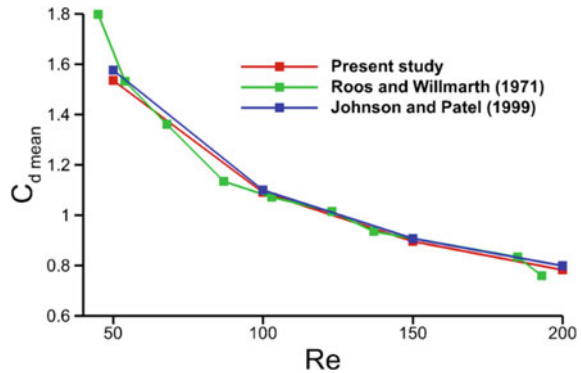
6.2   Wake Structure

The effect of shear intensity (K) on the three-dimensional flow structures is identified
qualitatively with the help of the Q-criteria proposed by Jeong and Hussain [17]. Q-
criteria define a vortex in terms of the eigenvalues of $S^2 + \Omega^2$, here S and Ω are the
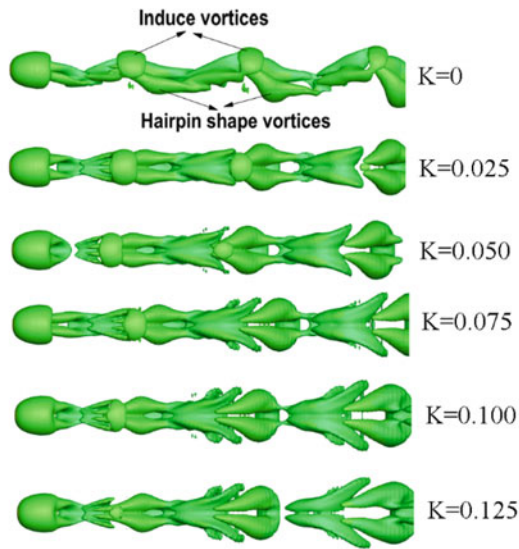strain and rotation rate tensors, respectively.

Wake structures for different values of K and $Re = 300$ are shown in Fig. 4. For
each value of the K, flow is unsteady and non-axis symmetric, and the hairpin-shaped
vortices are shed from the sphere. The strength of hairpin-shaped vortices increases
as the value of K varies from 0 to 0.125, as shown in Fig. 4a. Flow maintains a plane
of symmetry corresponding to each value of K. For non-zero values of K, symmetry
plane coincides with the X–Y plane because of the entrainment of more vorticity on
the high-velocity side of the sphere, due to which vortices are always shed from the
top of the sphere. On the other hand, in the case of $K = 0$, plane of symmetry is
different from that of the X–Y plane, as depicted in Fig. 4b. Sokomota and Haniu
[5] also experimentally observed that the vortices are shed from the high-velocity
side of the sphere for all non-zero values of K. Furthermore, the size of the induced
vortices becomes smaller and smaller as the value of the K changes from 0 to 0.125
and almost vanishes for $K = 0.125$, as can be observed from Fig. 4b.

6.3   Temporal Wake Characteristics

Unsteady behaviour of the wake is examined by taking a transverse velocity signal at
a point in the wake at $X = 3.5$ and $Y = 0.5$ for various values of the K, as presented
in Fig. 5. All the signals have been taken for the last 10 s physical time to avoid the
presence of initial transients. Amplitude of the signals increases as the value of K
varies from 0 to 0.075 and then decreases for $K = 0.1$. Signals amplitude increases
due to increased velocity at the top of the sphere as the value of K changes. Amplitude
of signals is maximum for $K = 0.125$ and minimum for $K = 0$. A sudden reduction

K=0 K=0.025 K=0.050

K=0.075 K=0.100 K=0.125

(a)

Induce vortices

K=0

Hairpin shape vortices

K=0.025

K=0.050

K=0.075

K=0.100

K=0.125

(b)

Fig. 4 Wake structures for different values of K and $Re = 300$. **a** Isometric and **b** Z–X plane
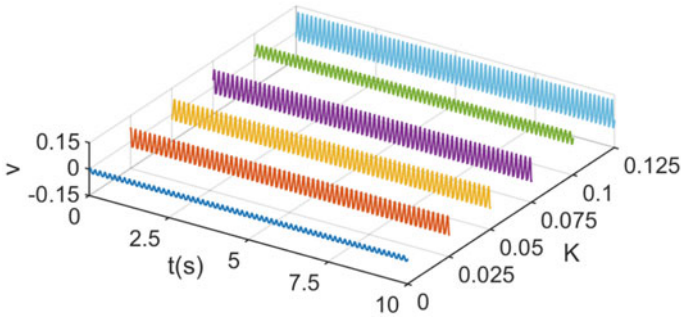
Fig. 5 Transverse velocity component time signal at $X = 3.5$ and $Y = 0.5$ in the wake for different values of K

in signal amplitude for $K = 0.1$ indicate the weaker unsteady wake. The waveform of the signals corresponding to each value of K does not significantly deviate from that of pure harmonics (sine or cosine). This indicates that the shear intensity (K) does not affect the non-linearity associated with the wake.

6.3.1 Hilbert Spectrum

Fourier transform is a very powerful time signal analysis method which expresses a time signal in terms of the linear combination of sine and cosine functions of constant frequency and amplitude. Fourier analysis provides actual physical information only if the time signals are linear and stationary. In the case of non-linear and non-stationary signals, Fourier analysis adds the spurious component of frequency to simulate the signal in the time domain, which results in wide energy frequency distribution in Fourier spectra. In contrast to the Fourier analysis, Hilbert Huang transform breaks a signal into some basic functions named intrinsic mode functions (IMFs), which are directly obtained from the original time signals by an algorithm EMD proposed by Huang et al. [18] (empirical mode decomposition). As the IMFs are obtained from the actual time data, they are adaptive to the local variation of frequency and amplitude in the time signal, as a result of which Hilbert Huang transform provides actual physical information in the case of non-linear and non-stationary data.

Hilbert spectrum is plotted for a transverse velocity signal at a point in the wake corresponding to each value of K. Frequency is plotted on the Y-axis and the time on the X-axis, as shown in Fig. 6. Colour contours represent the energy carried by each frequency component present in the wake, where blue and red colours indicate the minimum and the maximum energy, respectively. Waveforms in the Hilbert spectrum exhibit the variation of instantaneous frequency with time. Hilbert spectrum shows a straight horizontal line over time for a monocomponent IMF. Any deviation of the time signal from the sine or cosine function results in a frequency band in the Hilbert spectrum, which indicates the non-linear interaction between the wake structures.

Distinct frequency bands in the Hilbert spectrum represent the presence of intrawave frequency modulation, which indicate the strong periodic oscillations in the wake. Intermixing of frequency bands corresponding to each IMF represents the interwave frequency modulation which is a strong sign of aperiodic wake oscillations. Both intrawave and interwave frequency modulations reveal the strength of non-linearity associated with the wake.

Two frequency bands are observed for all values of K except $K = 0.1$, as depicted in Fig. 6. The lower frequency band associated with the vortex shedding frequency and higher frequency bands may correspond to variation in the vortices' strength as they move in the downstream direction. Distinct frequency bands for $K = 0.025$, 0.050, and 0.1 indicate the presence of intrawave frequency modulation, revealing the strong periodic oscillations and the non-linear interactions in the wake. Interwave frequency modulation for $K = 0, 0.075$, and 0.125 shows the non-linear interaction between the wake structures. However, the flow is still periodic for these values of K as reveals by the periodic waveform of the frequency bands. The bandwidth of the lower frequency band changes to a small extent with an increase in the value of K, which indicate that the variation of K does not much affect the non-linear interactions associated with wake. This is also confirmed by the pure harmonics type waveforms of the signals for all values of K, as depicted in Fig. 5.

6.3.2 Marginal Spectrum

The Marginal Hilbert spectra is similar to the Fourier spectra, which is obtained by integrating the Hilbert spectrum over the whole time span. Hilbert spectra provide information about how energy is distributed in the frequency domain.

Figure 7 shows the marginal spectra of a transverse velocity signal at a point in the wake for different values of K. Existence of distinct frequency peaks for all the values of K indicates the strong periodic oscillations in the wake. Very low-frequency peaks for $K = 0.075$ and 0.1 represent the energy carried by the mean flow. Two distinct dominant peaks for non-zero values of K show the lower and the higher limits of the frequency modulation amplitude. Presence of a single dominant frequency for $K = 0$ specifies the least intrawave frequency modulation, which indicates the weak non-linear interactions in the wake. It is interesting to note that as the value of K varies from 0 to 0.125, the Strouhal number ($St = fd/U_c$) increases from 0.1336 to 0.1528. Strouhal number increases due to the convection of more vorticity from the high-velocity side of the sphere relative to the low-velocity side.

7   Conclusions

In the present study, non-uniform flow past a sphere has been investigated numerically using Open Source Field Operation and Manipulation (OpenFOAM). A fixed Reynolds number equal to $Re = 300$ is considered in the present study. Shear intensity

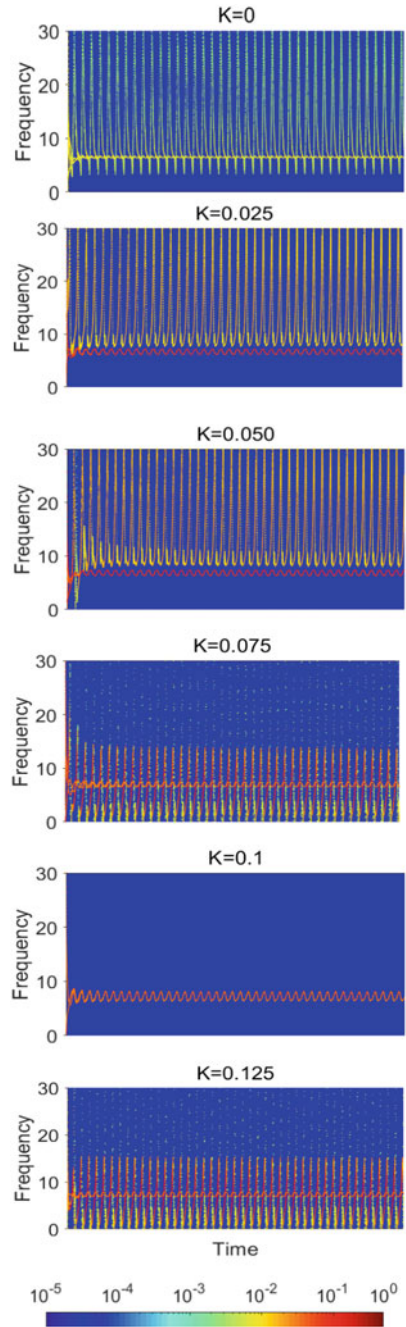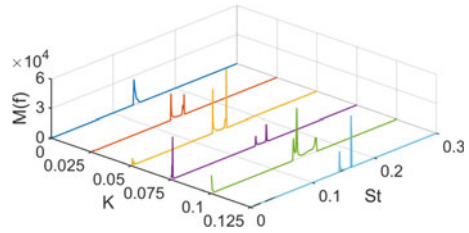**Fig. 6** Hilbert spectrum of a transverse velocity signal at a point in wake for different values of K

Fig. 7 Marginal spectrum of a transverse velocity signal at a point in the wake for different values of K

(K) takes the values between 0 and 0.125. Shear intensity is varied in such a way that the Reynolds number remains the same for all the computations. A linear velocity profile is employed at the inlet with the help of the GroovyBC utility linked with the Swak4Foam. The present study concludes that the flow past the sphere maintains a plane of symmetry corresponding to each value of K. Plane of symmetry coincides with the X–Y plane for non-zero values of K due to the convection of more vorticity on the high-velocity side of the sphere. For each non-zero value of K, hairpin-shaped vortices are constantly shed from the top of the sphere. The extent of non-linear interaction between the vortical structures has been analysed with the Hilbert spectrum of transverse velocity signal. Furthermore, the strength of hairpin-shaped vortices and their shedding frequency increase as the value of K varies from 0 to 0.125.

Nomenclature

Cd_{mean}	Mean drag coefficient
K	Shear intensity
$M(f)$	Marginal spectrum
Re	Reynolds number
St	Strouhal number

References

1. Taneda S (1956) Experimental investigation of the wake behind a sphere at low Reynolds numbers. J Phys Soc Japan 11:1104–1108
2. Achenbach E (1972) Experiments on the flow past spheres at very high Reynolds numbers. J Fluid Mech 54:565–575
3. Achenbach E (1974) Vortex shedding from spheres. J Fluid Mech 62:209–221
4. Achenbach E (1974) The effects of surface roughness and tunnel blockage on the flow past spheres. J Fluid Mech 65:113–125

5. Sakamoto H, Haniu H (1990) A study on vortex shedding from spheres in a uniform flow. Trans ASME J Fluids Eng 112:386–392
6. Sakamoto H, Haniu H (1995) The formation mechanism and shedding frequency of vortices from a sphere in uniform shear flow. J Fluid Mech 287:151–171
7. Kim HJ, Durbin PA (1988) Observations of the frequencies in a sphere wake and of drag increase by acoustic excitation. Phys Fluids 31:3260–3265
8. Pao HP, Kao TW (1977) Vortex structure in the wake of a sphere. Phys Fluids 20:187–191
9. Maxworthy T (1964) Experiments on the flow around a sphere at high Reynolds numbers. J Appl Mech Trans ASME 36:598–607
10. Nakamura I (1976) Steady wake behind a sphere. Phys Fluids 19:5–8
11. Johnson TA, Patel VC (1999) Flow past a sphere up to a Reynolds number of 300. J Fluid Mech 378:19–70
12. Tomboulides AG, Orszag SA (2000) Numerical investigation of transitional and weak turbulent flow past a sphere. J Fluid Mech 416:45–73
13. Schouveiler L, Brydon A, Leweke T, Thompson MC (2004) Interactions of the wakes of two spheres placed side by side. Eur J Mech B 23:137–145
14. Yoon DH, Yang KS (2009) Characterization of flow pattern past two spheres in proximity. Phys Fluids 21:073603
15. Kumar A, Tiwari S, Das SP (2023) Effect of size and spacing on the wake characteristics of two spheres placed in tandem. Phys Fluids 35:053601
16. Roos FW, Willmarth WW (1971) Some experimental results on sphere and disk drag. AIAA J 9:285–291
17. Jeong J, Hussain F (1995) On the identification of a vortex. J Fluid Mech 285:69–94
18. Huang NE, Shen Z, Long SR, Wu MC, Shih HH, Zheng Q, Yen NC, Tung CC, Liu HH (1998) The empirical mode decomposition and the Hilbert spectrum for non-linear and non-stationary time series analysis. Proc R Soc Lond A 454:903–995

CFD Modeling of Hydrodynamic Jet Breakup of Molten Nuclear Fuel in the Coolant

Ajay Rawat, A. Jasmin Sudha, V. Subramanian, and B. Venkatraman

1 Introduction

Although the hypothetical core disruptive accident in a Sodium Cooled Fast Reactor (SFR) is very rare [1], their implication on the reactor is considered during the design stage of a reactor. It is assumed that after the severe accident, the whole core could be in a partial or complete meltdown condition, which can breach the grid plate and threaten the main vessel's structural integrity due to its high temperatures. An in-vessel core catcher is placed at the bottom of the main vessel to avoid such instances. A gap of 2–3 m is provided between the grid plate and the core catcher so that the molten core jet does not fall upon the core catcher as a coherent jet, but it is sufficiently broken, fragmented, and dispersed before reaching the core catcher thus avoiding intense thermal load on the core catcher. Therefore, while doing an SFR safety assessment, the jet breakup length is an important parameter to be studied and analyzed.

Many researchers have recently performed jet breakup experiments with sodium as a coolant [2–5]. However, due to the opacity of the liquid sodium, the detailed jet fragmentation and breakup behavior could not be captured in these experiments. To overcome this difficulty, experiments have been performed with water as a coolant and metals or metal oxides as a simulant for molten core [6–9]. Although these experiments successfully captured the detailed morphology of jet fragmentation behavior and parameters like breakup length using a high-speed camera, the results of these experiments could not be directly extrapolated to the fuel/sodium system. These difficulties are circumvented by conducting numerical simulations of jet breakup behavior in sodium. The jet breakup is governed by the surface tension, inertial and

A. Rawat (✉) · A. Jasmin Sudha · V. Subramanian · B. Venkatraman
Aerosol Transport and Biodiversity Section, Radiological and Environmental Safety Division, Indira Gandhi Centre for Atomic Research, Kalpakkam, Tamilnadu 603102, India
e-mail: ajayrawat@igcar.gov.in

gravitational forces, and fluid instabilities like Kelvin–Helmholtz (KH), Rayleigh–Taylor (RT), and Rayleigh-Plateau (RP). The modeling of the jet breakup is mainly carried out using mesh-based and particle approaches. In the former case, Volume-of-Fluid (VoF) [10] and Level-Set (LS) [11] methods are used, and in the latter approach, Smooth Particle Hydrodynamics (SPH) [12] and Moving Particle Semi-implicit [13] schemes are favorably used by the reactor safety community. In addition to these two schemes, hybrid schemes like Lattice-Boltzmann Method (LBM) have found traction in the fast reactor safety community [14–16].

In the present study, the breakup of a molten fuel jet in a pool of liquid sodium is studied, the diameter of the jet (D) is varied from 1 to 25 mm, and the inlet velocity of the jet is fixed at 5 m/s. Following Saito et al. who has identified the boundary of the different regimes of jet fragmentation for a liquid–liquid system [17]. The cases considered in the present simulations primarily lie in the Atomization regime except for the case with 1 mm diameter, which is in a sinuous regime. The primary aim of the present study is to determine the jet breakup length due to the hydrodynamic instabilities for an isothermal condition.

2 Numerical Methods and Simulation Techniques

The numerical simulations were carried out using VoF scheme, which is available in the Ansys Fluent's multi-phase module. The VoF method in Tansy's Fluent solves the Navier Stokes equations for two immiscible fluids, where the participating fluids share a single set of momentum and conservation equations. The interface between the fluids is evaluated by keeping track of each phase's volume fraction in the computational cell.

2.1 Governing Equations

For an incompressible fluid with a constant density, the continuity equation is:

$$\nabla \cdot \boldsymbol{u} = 0 \tag{1}$$

The momentum equation follows from the conservation of momentum, and it is defined as follows:

$$\frac{\partial}{\partial t}(\rho \boldsymbol{u}) + \nabla(\rho \boldsymbol{u} \otimes \boldsymbol{u}) = -\nabla p + \nabla \left[\mu \left(\nabla \boldsymbol{u} + \nabla \boldsymbol{u}^T\right)\right] + \rho \boldsymbol{g} + \boldsymbol{F_s} \tag{2}$$

Here,

$\boldsymbol{u}$ the velocity of the fluid
$\boldsymbol{g}$ acceleration due to gravity

p pressure
μ dynamic viscosity
$\boldsymbol{F_s}$ surface tension force

The VoF model is helpful in predicting the jet fragmentation behavior and transient tracking of interface between the two fluids. The density and viscosity in a computational cell are defined as follows:

$$\rho = \alpha\rho_1 + (1 - \alpha)\rho_2 \tag{3}$$

$$\mu = \alpha\mu_1 + (1 - \alpha)\rho_2 \tag{4}$$

Here,

ρ_1, μ_1 density and viscosity of phase 1
ρ_2, μ_2 density and viscosity of phase 2
α volume fraction of phase 1
$1 - \alpha$ volume fraction of phase 2

The interfacial surface tension between the two fluids is modeled as continuum surface force (CSF) as proposed by Brackbill [18], and is evaluated using the following expression:

$$\boldsymbol{F_s} = \sigma\kappa\nabla\alpha \tag{5}$$

Here, σ is the interfacial surface tension constant, and κ is the curvature and is given in Eq. (6):

$$\kappa = -\nabla \cdot \hat{\boldsymbol{n}} \tag{6}$$

where $\hat{\boldsymbol{n}}$ is the unit vector normal to the interface.

Apart from the continuity and momentum equations an additional convection equation for volume phase fraction is solved for one phase, which will allow us to track the location of the interface between the two phases:

$$\frac{\partial\alpha}{\partial t} + \nabla \cdot (\alpha\boldsymbol{u}) = 0 \tag{7}$$

2.2 Boundary Conditions and Simulation Techniques

In the present study 2D geometry is chosen. Through a circular inlet of diameter (D) a liquid Mixed-Oxide (MOX) fuel is allowed to fall into a column of liquid sodium of width and height as 21 D and 50 D, respectively, the width and height is set in

Fig. 1 Schematic diagram of the computational domain with boundary conditions
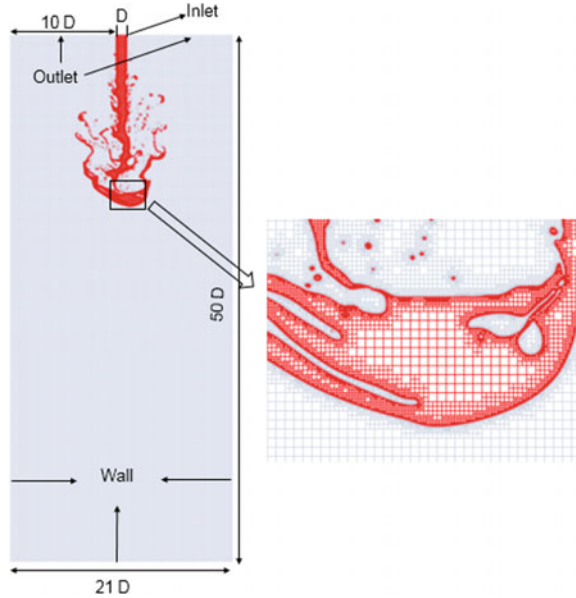
order to minimize the wall effect, see Fig. 1. The upper boundary of the tank is set as outlet, whereas the sides and bottom as no slip wall boundary condition. The jet breakup is a computationally challenging problem, because the range of scale we have to resolve ranges from tiny droplets to the nozzle diameter in mm range. To some extent this issue is circumvented by using the Adaptive Mesh Refinement (AMR) technique, which preferentially makes the fine cells in the region of interest, however the total number of cell counts can increase significantly. The quad mapped mesh was used in the simulations for a typical case with 10 mm of jet diameter and mesh width of 1 mm, and three level of mesh refinement one start with mesh count of ~ 1 lakh and at the jet breakup the total mesh count increased to ~ 4 lakh. AMR technique is utilized with up to three levels of refinement. This technique as seen in Fig. 1, shows that refinement is performed only on the jet surface. Thus, it avoids the usage of fine mesh throughout the whole domain and saves computational time. The stability of the numerical solution is achieved by constraining the interfacial Courant number below 0.25 and the global Courant number below 2. Semi-Implicit Method for Pressure Linked Equations-Consistent (SIMPLEC) scheme is employed for pressure–velocity coupling.

2.3 Simulation Condition

The hydrodynamic fragmentation of a liquid jet is mainly governed by the dimensionless numbers: density ratio $\gamma = \rho_j/\rho_c$, viscosity ratio $\eta = \mu_j/\mu_c$, for the present

Table 1 Properties of MOX fuel and liquid sodium [17]

Material	Surface tension (N/m)	Density (kg/m^3)	Viscosity (Pa s)
MOX fuel	0.465	8663	0.004
Liquid sodium		856	0.00028

Table 2 Properties of MOX fuel and liquid sodium

Diameter (mm)	Re	We$_a$	Fr
1	1.08×10^4	46	2548
5	5.41×10^4	230	510
10	1.08×10^5	460	255
15	1.62×10^5	690	170
20	2.17×10^5	920	127
25	2.71×10^5	1151	102

cases, $\gamma = 10.1$ and $\eta = 14.3$. Reynolds number Re, Ambient Weber number We$_a$, and Froude number Fr [19]:

$$\text{Re} = \rho_j V_j D / \mu_j, \quad \text{We}_a = \rho_c V_j^2 D / \sigma, \quad \text{Fr} = V_j^2 / gD \tag{8}$$

The physical properties of the materials used in the simulations are listed in Table 1, and the relevant dimensionless numbers are given in Table 2.

2.4 Grid Independence

A grid independence study has been carried out to determine the optimal grid size for simulating the melt jet breakup in a quiescent liquid sodium pool. The initial injection diameter of 10 mm (*D*) with an injection velocity of 5 m/s is considered for the study. The grid independence for the present system is carried out by simulating cases with three different mesh widths of *D*/5 (coarse), *D*/10 (medium), and *D*/20 (fine). The results of the study for various grid sizes are compared in Fig. 2. The jet morphology and the penetration depth are same for medium and fine mesh, see Fig. 2. Hence, domain with grid size of *D*/10 or medium mesh is chosen for the present study striking a balance between grid independence and computational cost.

D = 10 mm and t = 12 ms

| Coarse Mesh | Medium Mesh | Fine Mesh |
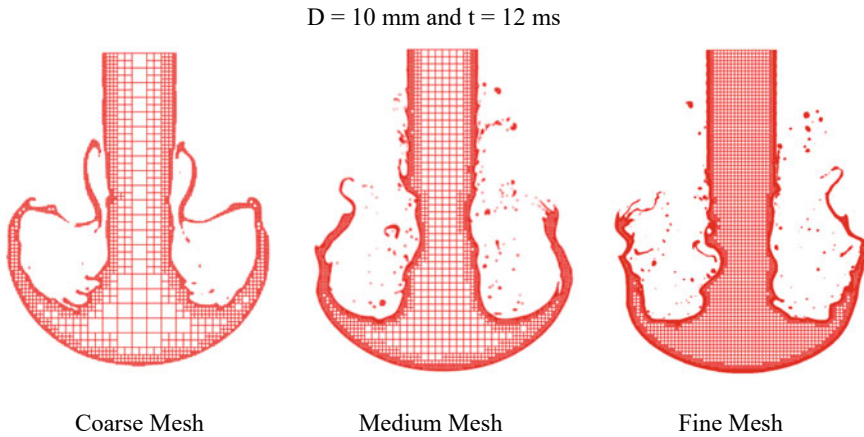
Fig. 2 Grid independence study

3   Results and Discussion

Figure 3 shows a molten fuel's phase-field map; the jet has a diameter D (= 10 mm) and a prescribed inlet velocity V_j (= 5 m/s). The appearance of an inverted mushroom-like structure at the leading edge is due to the RT instability, and from the leading edge of the mushroom we could see the formation of the ligament-like structures which breaks into fine droplets. Furthermore, as we travel downstream along the jet, surface instabilities appear on the lateral surface of the jet due to KH instabilities, mainly driven by the existing velocity difference between jet and liquid sodium. The velocity vectors superimposed over the jet shows that in the vicinity of the jet interface the coolant velocity increases in downward direction, as seen in Fig. 4, this increases the amplitude of the surface instabilities resulting in the formation of even more ligament-like structures from the sides of the jet. At higher velocities there is continuous striping of these ligaments from the jet interface, causing the jet to be surrounded by a cloud of fragmented droplets and eventually leading to its breakup.

The formation of the eddies near the leading edge of the jet also participates in its deformation, and because of increased coolant velocities it stretches the leading edge making it vulnerable to jet breakup. The jet breakup length is defined as distance between the points; where the jet enters the coolant and the point where the part of the lower portion of jet detaches from the main jet.

Figure 5 shows the time evolution of molten jet with different diameters. In the initial stages we could see the appearance of the mushroom-like head shape, and toward the later stages of the jet penetration it becomes asymmetric, and one could see the development of the droplets emerging from the jet sides. The location where the jet breaks is decided by the interplay between the continuous stripping from the jet sides and subsequent thinning of jet because of the KH instability, and the breakup near to the mushroom head due to the RT instability. As seen in Fig. 5, the
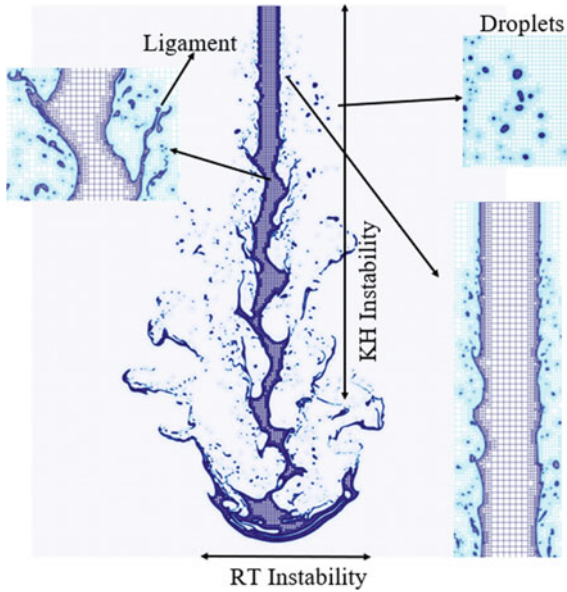
Fig. 3 Formation of ligaments and droplets due to the instabilities like KH and RT
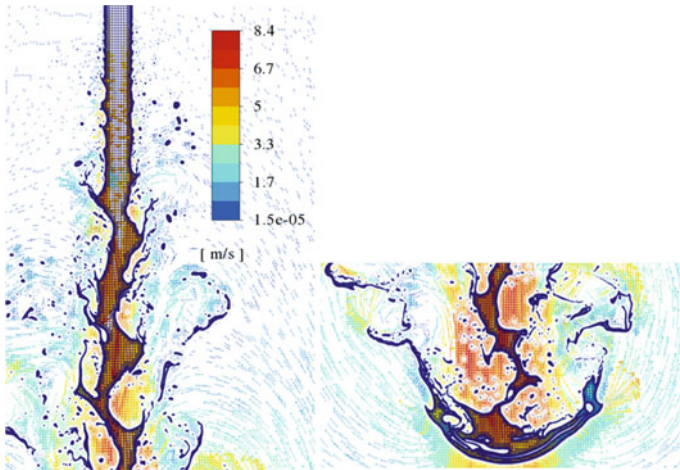

Fig. 4 Velocity field superimposed over a corium jet profile

jet with a diameter of 5 and 15 mm breaks close to the mushroom head, whereas for the other cases, it breaks somewhere in the middle. At present, we could not predict this seemingly random location of the jet breakup with greater certainty, and it is something which authors believe needs further investigation.
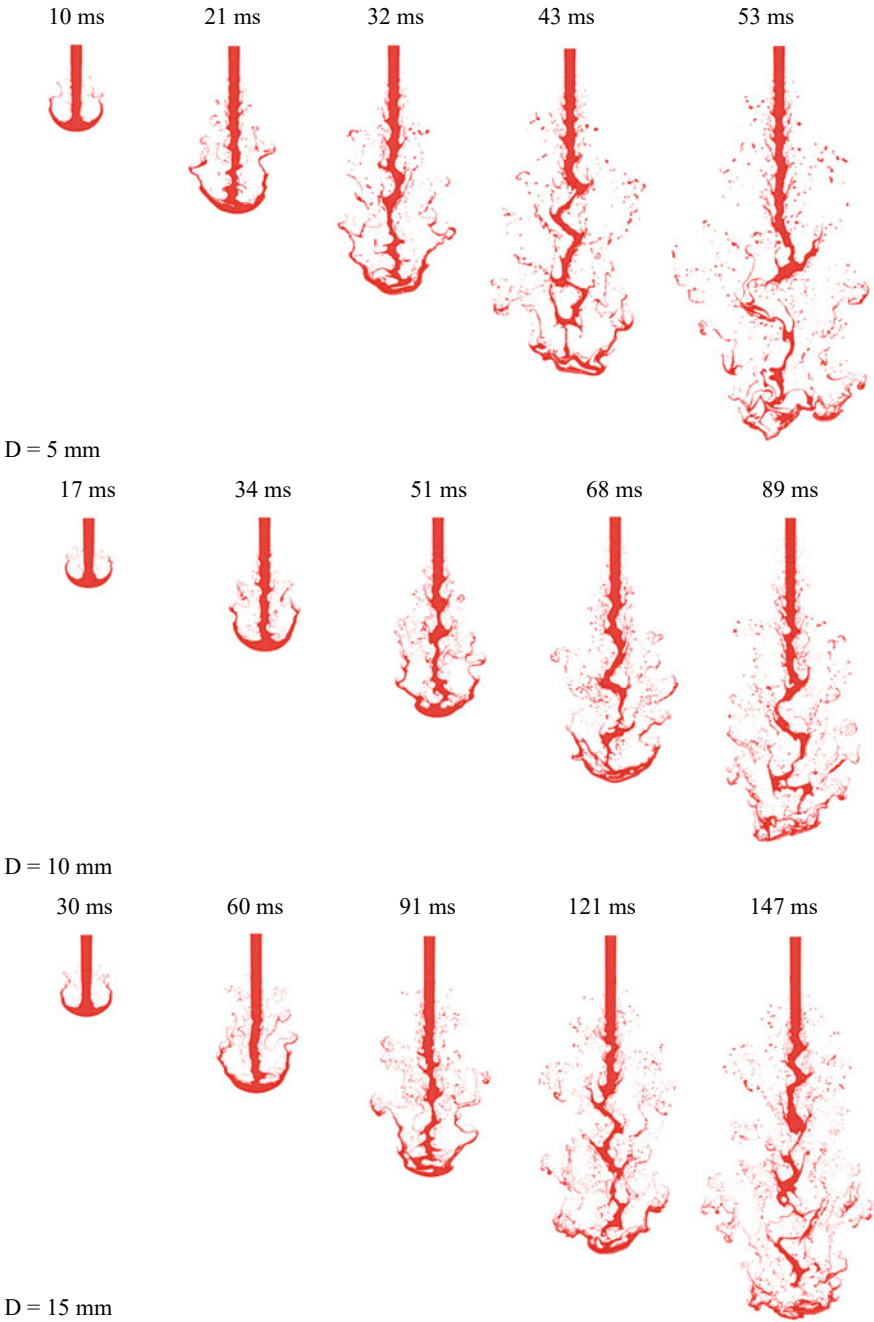
10 ms 21 ms 32 ms 43 ms 53 ms

D = 5 mm

17 ms 34 ms 51 ms 68 ms 89 ms

D = 10 mm

30 ms 60 ms 91 ms 121 ms 147 ms

D = 15 mm

Fig. 5 Snapshots of jet penetration for different initial diameters of the jet

D = 20 mm

D = 25 mm
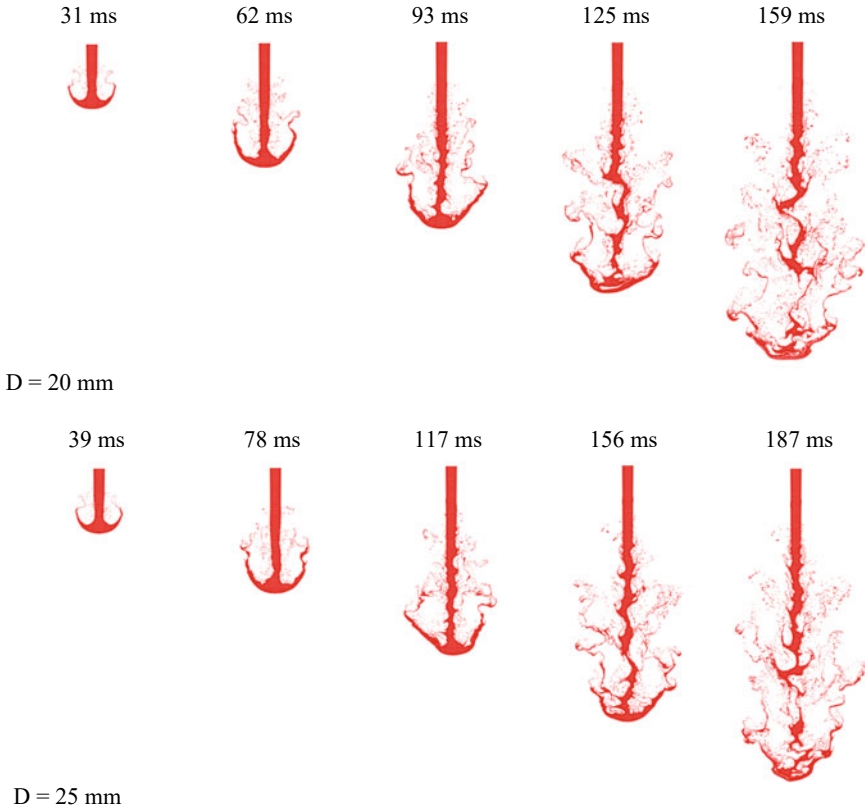
Fig. 5 (continued)

In the fast reactor community, the jet breakup length is also widely estimated using a correlation given by Epstein et al. [20]. The Epstein's correlation for dimensionless jet breakup length is defined as:

$$\frac{L_{\text{brk}}}{D} = \frac{1}{2E_0}\left(\frac{\rho_{\text{j}}}{\rho_{\text{c}}}\right)^{0.5}$$

Here, E_0 is the entrainment coefficient and its value ranges from 0.05 to 0.1. ρ_{j} and ρ_{c} are the mass densities of molten jet and coolant, respectively, the results are summarized in Fig. 6. It is found that the $L_{\text{brk}}/D_{\text{j}}$ for MOX-sodium system lies between Epstein's upper and lower bound for the chosen diameters and jet velocity.

Fig. 6 Comparison of
simulated jet breakup length
with Epstein's correlation
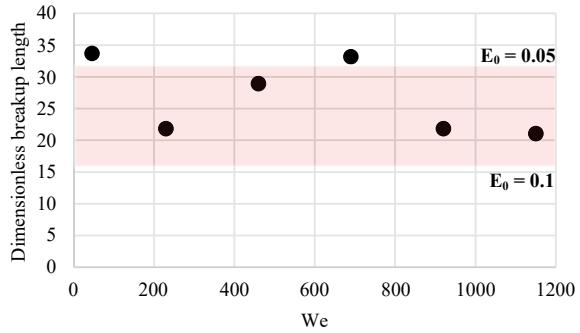
4 Conclusions

The molten fuel jet breakup and fragmentation analysis used a commercial CFD code,
Ansys Fluent. The study focuses on the identification of the jet breakup behavior as
well as the influence of jet diameter or We_a number on the jet breakup length. It is
found that the KH and RT instabilities strongly influence the breakup mechanism and
the droplet generation, and the breakup length estimated using the VoF simulations
is found to be in line with Epstein's correlation. It is to be noted that even though
for the cases under investigation the non-dimensional breakup length lies between
20 and 35 (Atomization regime), and with 1 mm diameter it is close to 35 (Sinuous
regime). However, in actual physical situation due to the thermal stress cracking and
the physical barrier such as core support structures the jet will break much ahead of
reaching this length.

Nomenclature

D Diameter of the jet (mm)
L_{brk} Jet breakup length (mm)
V_j Inlet velocity of the jet (m/s)
g Acceleration due to gravity (m/s^2)
p Pressure (Pa)

Greek symbols

μ Dynamic viscosity (Pa s)
ρ Density (kg/m^3)
σ Interfacial surface tension (N/m)

α Phase fraction
κ Curvature

Subscript

j   Jet
c   Coolant
brk   Breakup
a   Ambient

Non-dimensional

E_0 Entrainment coefficient
Re   Reynolds number
We_a Ambient Weber number
Fr   Froude number

References

1. Raj B, Chellapandi P, Vasudeva Rao PR (2015) Sodium fast reactors with closed fuel cycle. CRC Press
2. Chu TY (1982) Fragmentation of molten core material by sodium. In: Int. top. meet. LMFBR saf., Lyon, France, pp 487–496
3. Gabor JD, Purviance RT, Aeschlimann RW, Spencer BW (1988) Breakup and quench of molten metal fuel in sodium. In: Saf. next gener. power react., Argonne, IL (United States)
4. Magallon D, Hohmann H, Schins H (1992) Pouring of 100-kg-scale molten UO_2 into sodium. Nucl Technol 98:79–90
5. Nishimura S, Sugiyama KI, Kinoshita I, Itagaki W, Ueda N (2010) Fragmentation mechanisms of a single molten copper jet penetrating a sodium pool—transition from thermal to hydrodynamic fragmentation in instantaneous contact interface temperatures below its freezing point. J Nucl Sci Technol 47:219–228
6. Abe Y, Kizu T, Arai T, Nariai H, Chitose K, Koyama K (2004) Study on thermal-hydraulic behavior during molten material and coolant interaction. Nucl Eng Des 230:277–291
7. Abe Y, Matsuo E, Arai T, Nariai H, Chitose K, Koyama K, Itoh K (2006) Fragmentation behavior during molten material and coolant interactions. Nucl Eng Des 236:1668–1681
8. Magallon D (2006) Characteristics of corium debris bed generated in large-scale fuel-coolant interaction experiments. Nucl Eng Des 236:1998–2009
9. Mathai AM, Sharma AK, Anandan J, Malarvizhi B, Das SK, Nashine BK, Chellapandi P (2015) Investigation of fragmentation phenomena and debris bed formation during core meltdown accident in SFR using simulated experiments. Nucl Eng Des 292:87–97
10. Thakre S, Manickam L, Ma W (2015) A numerical simulation of jet breakup in melt coolant interactions. Ann Nucl Energy 80:467–475

11. Shahmohammadi Beni M, Yu KN (2019) Studies on hydrodynamic deformation and fragmentation of melt jet injected into water pool using level set method. Results Phys 13:102206
12. Jo YB, Park SH, Choi HY, Jung HW, Kim YJ, Kim ES (2019) SOPHIA: development of Lagrangian-based CFD code for nuclear thermal-hydraulics and safety applications. Ann Nucl Energy 124:132–149
13. Xu Y, Xu R, Cheng H, Liu X, Cheng S (2022) Numerical simulation of jet breakup phenomenon during severe accident of sodium-cooled fast reactor using MPS method. Ann Nucl Energy 172:109087
14. Saito S, Abe Y, Koyama K (2017) Lattice Boltzmann modeling and simulation of liquid jet breakup. Phys Rev E 96:013317
15. Saito S, De Rosis A, Festuccia A, Kaneko A, Abe Y, Koyama K (2018) Color-gradient lattice Boltzmann model with nonorthogonal central moments: hydrodynamic melt-jet breakup simulations. Phys Rev E 98
16. Cheng H, Zhao J, Saito S, Cheng S (2021) Study on melt jet breakup behavior with nonorthogonal central-moment MRT color-gradient lattice Boltzmann method. Prog Nucl Energy 136:103725
17. Saito S, Abe Y, Koyama K (2017) Flow transition criteria of a liquid jet into a liquid pool. Nucl Eng Des 315:128–143
18. Brackbill JU, Kothe DB, Zemach C (1992) A continuum method for modeling surface tension. J Comput Phys 100:335–354
19. Lin SP, Reitz RD (1998) Drop and spray formation from a liquid jet. Annu Rev Fluid Mech 30:85–105
20. Epstein M, Fauske HK (2001) Applications of the turbulent entrainment assumption to immiscible gas–liquid and liquid–liquid systems. Chem Eng Res Des 79:453–462

Numerical Estimation and Validation of Pressure Pulsation in Centrifugal Pump Discharge Pipes

Vishal V. Ghatbandhe, Pankaj P. Mahajan, Ranjit H. Gavhane, and Anmol Sharma

1 Introduction

Centrifugal pumps can handle a variety of liquids at relatively high pressures and/ or temperatures and were utilized in a wide range of applications. The current work focuses on the centrifugal pump having the single volute with single suction and double discharge. In industries, it is well known that the majority of vibrations occurred in the discharge pipes because of pressure pulsation in a centrifugal pump. Pressure pulsations were pressure fluctuations in the head developed by the pump. The transient fluid flow develops the variation in pressure that travels in the system with the speed of sound and generates noise and vibrations. This may lead to acoustic resonance and fracture of system components. Large pressure fluctuations in centrifugal pumps is one of the very problematic issues which occur as a result of the RSI between the rotor (Impeller) and stator (Volute/Diffuser). The fluid gets encompassed when the tip of the vane is away from the cutwater, i.e. the distance between the vane tip and cutwater is large and at any other point, the vane tip is adjacent to the cutwater because of the rotation of the impeller, the gap was getting reduced and large amount of kinetic energy of water impinged as wake on the cutwater. The sharp drop in pressure as the blade passes the cutwater as a result of the wake's impact on the cutwater and got minimum as the suction face of the impeller blade crosses the cutwater. The pressure then rises quickly as the impeller blade continues past the cutwater. This pressure pulse only lasts for a brief length of time less than half the duration of each blade. The change in minimum to maximum transfer of energy on the discharge side results in a variation of discharge pressure creating the pressure pulsation. Not only because of wake impingement, pressure pulsation is also formed due to the vortical flow structure, vortices forming downstream of trailing edge of vane, shear layers and flow separation, and discontinuities inflow [1].

V. V. Ghatbandhe (✉) · P. P. Mahajan · R. H. Gavhane · A. Sharma
Engineering—PPD, KSB Limited, Pune, Maharashtra 411019, India
e-mail: vishal.ghatbandhe@ksb.com

2 Literature Review and Objective

In 1978, Makay and Szamody [2] found the major causes for centrifugal pump failure. They suggested that for optimal efficiencies which were at designed conditions the undesirable flow was obtained. They have also suggested that internal pump clearances, i.e. Gap-B was more important since these are areas which have high pressure gradients. There are two types of flow phenomenon in RSI, i.e. Wake flow and Potential flow. Wake flow is flow associated with flow separation from the impeller resulting in impact and convective flows. The potential flow is obtained with the non-viscous fluid flow in the relative motion of the fluid between the rotor, i.e. impeller and the stator, i.e. diffuser [3]. Sudo et al. [4] provided some experiment information related to pressure fluctuations at discharge due to cutwater Gap-B and skew of cutwater tongue. Sun et al. [5] found that when the pump operated off-design conditions, i.e. deviates from design conditions then the distribution of fluid flow in the impeller was not uniform as the occurs in design conditions which makes instability of the pump and complex forces acting on the impeller. Also due to the relative motion of impeller and volute or diffuser, during off-design conditions and medium of fluid flow through impeller makes pressure to fluctuate rapidly with time and results in pressure pulsation. Shi and Tsukamoto [6] studied pressure pulsation and radial force in a centrifugal pump. The results showed that pressure pulsations was caused by RSI. The study of pressure pulsation characteristics mainly includes two methods, i.e. experimental and numerically. Since experimental methods required a high cost for the prototype pump so this method is useful for an experiment on scaled-down model of prototype pump. But the advancements in computational technologies the analysis of flow field inside 3D hydraulic models with transient state can be easily solved with low cost for prototype pumps with better accuracy results. Gonzáles et al. [7] studied effect of cutwater Gap-B on radial force characteristics of the impeller and found that Gap-B parameter has a great influence on the radial force. Shi et al. [8] performed CFD simulation to test the influence of Gap-B on pressure pulsation and radial force using k–ε turbulence model and SIMPLE algorithm. The numerical calculation results show that pressure pulsation at the monitor point at volute shows obvious periodicity. Main frequency of pressure pulsation was at blade passing frequency (BPF). For smaller Gap-B the pressure pulsation value was large and has greater amplitude at BPF. Spence and Amaral-Teixeira [9] studied effect of various geometric factors of the centrifugal pump such that cut water gap, vane arrangement, and the sidewall clearance on the pressure pulsations. The cutwater Gap-B and vane arrangement were found to be more influential than other parameters on pressure pulsation. Three cutwater gaps were considered based on the trimming of impeller diameter as per Gap-B requirement. Sparks and Wachel [10] studied the factors affecting pulsations and the effect of pulsation on the pipes. They found that pulsation problems were usually related to piping vibrations fatigue failure and pump internals. This can be controlled by modifying the generation of pulsation sources and pipes. Also researched that pulsation resonant frequencies can amplify the pulsation effects in discharge pipes resulting in fatigue failure. Thus, better treatment for these

vibrations was mismatching the resonances from major pump frequencies. Provided acoustic resonance configurations of half wave response and quarter wave response in pipes for locations of monitoring points.

Most of the research works focuses on pressure pulsations inside the centrifugal pump, not in discharge pipes. Additionally, there was less research on the impact of speed on pressure pulsation, i.e. VFD analysis. As per project requirements, the pressure pulsation analysis was performed and pressure fluctuations were measured in the discharge pipes.

3   Materials and Methods

3.1   Pump Geometry

The single suction, double discharge and volute casing centrifugal pump was used for analysis. Both the model and prototype of centrifugal pump were used for analysis. The model pump was tested using the experimental method and the prototype pump was analysed using CFD method. The specifications and geometric parameters are shown in Table 1. The centrifugal pump had 6 backward curved vanes. To reduce the size of the model from the prototype, a scale factor of 1.92 was utilized. The following formula of Gap-B% was used in calculation (Fig. 1),

$$\text{Gap-B\%} = \frac{D_3 - D_2}{D_2} \times 100 \tag{1}$$

The four Gap-B% were used for CFD analysis according to that impeller diameter was trimmed and keeping cutwater diameter constant. The four Gap-B% are shown in Table 2.

Table 1 Specifications and geometric parameters

Parameters	Prototype pump	Model pump
Stages	Single	Single
Suction	Single	Single
Discharge	Double	Double
No. of vanes	6	6
Density of fluid	$1000 \ \text{kg/m}^3$	$1000 \ \text{kg/m}^3$
Suction pressure	1 atm	1 atm

Fig. 1 Geometric
representation of Gap-B
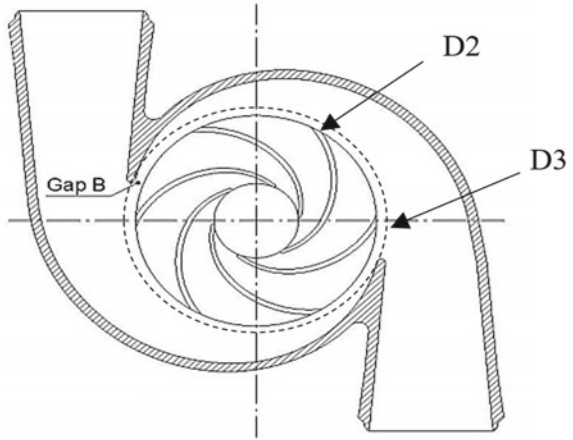
Table 2 Gap-B%
dimensions

Gap-B %
8
9
10
12
14

3.2 Simulation Domain

A 3D model was prepared in Siemens NX 1946 version. Fluid domain was extracted from the 3D model of prototype pump and repaired in the ANSYS 2022 R2 SPACECLAIM. The simulation domain or fluid domain is shown in Fig. 2.

A length of inlet pipe was added at the impeller inlet to prevent the inlet vortex zone from having an impact on the flow field and flow rate. Two discharge pipes of length 6 m each were used as outlet pipes for the pump.
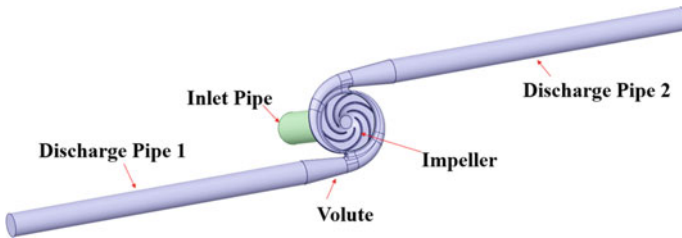
Fig. 2 Simulation domain

Fig. 3 Computational grids
of **a** impeller with suction
casing, **b** volute casing with
discharge pipes,
c computational domain
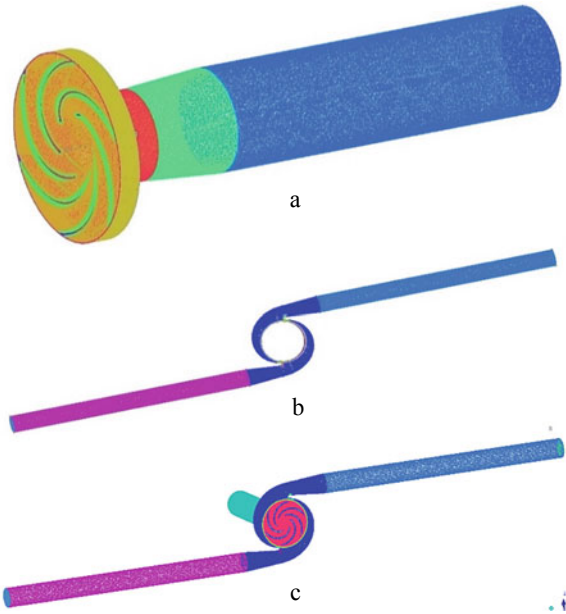
The simulation domain was assembly of fluid domains of impeller, volute, suction pipe, and discharge pipes. The mesh of above fluid domains was generated using ANSYS 2022 R2 ICEM CFD commercial software. To meet time limitation the all components were created using tetrahedral cells as shown in Fig. 3. To capture curvatures of fluid domain and meet the minimum orthogonal quality greater than 0.1 the refinement was given locally. Local sizing was given to parts of fluid domain to refined mesh. To meet the requirement of k–ε turbulence model the $Y+$ value maintained above 40–200.

The grid independence test was performed for centrifugal pump by considering the six cases with refinement of grid as listed in Table 3. The grid independence test was performed on pump with Gap-B of 8% with mesh refinement. The obtained head was comparable with experimental head having variation of 1.55%. To improve numerical calculation efficiency without reducing the calculation accuracy, the rated head point less than 2% was considered as the parameter of grid independence verification. Table 3 indicates the grid numbers having impeller and suction casing nodes, volute and discharge pipes nodes with corresponding percentage head variation with experimental head.

The fluctuation in rated head was small when number of grids were greater than 2.97 million. Considering parameters that affects the computational cost, i.e. computational time and configuration of computer, the grid number 4 was selected as follows for the different components were as follows, impeller and suction casing, 2,482,073; volute and discharge pipes, 493,187, i.e. total nodes, 2,975,260. To check mesh quality the parameter quality is used. The smaller value of quality represents the

Table 3 Grid independence analysis

Grid number	Impeller and suction casing nodes	Volute and discharge pipes nodes	Total nodes	Variation in head (%)
1	1,302,930	306,235	1,609,165	2.13
2	1,583,323	339,615	1,922,938	2.00
3	1,963,903	412,000	2,375,903	1.96
4	2,482,073	493,187	2,975,260	1.71
5	3,205,707	449,041	3,654,748	1.56
6	4,286,570	758,055	5,044,625	1.55

low quality and higher value represents higher quality. The quality of the mesh was found to be greater than 0.4 and also 70% of total number of elements are found with quality of 0.9–0.95.

3.3 Monitoring Points

To analyse the pressure pulsation characteristics, the different monitoring points were set on the both discharge sides of pump. Since in experimental test of model pump the measurement of pressure pulsation was taken on the discharge pipes so the monitoring points were set respectively using ANSYS 2022 R2 CFX software. To check half wave and quarter wave response the monitoring points were set at respective distance in discharge pipes. The monitoring points and their locations were shown in Fig. 4.

The location of monitoring points was same on both discharge pipes. $L1$ denotes monitoring point located at 1 m from the pump centreline, similarly other three monitor points were placed. All monitoring points were located from one reference
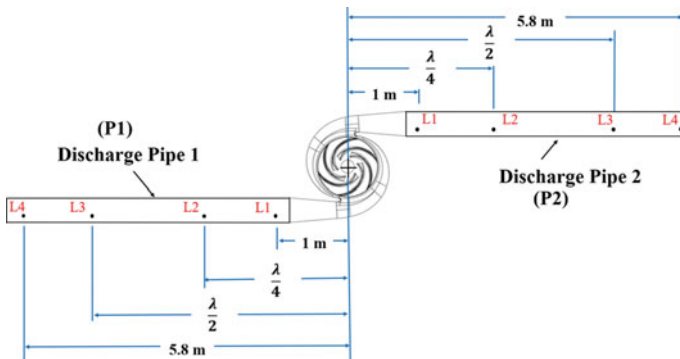
Fig. 4 Monitoring points

point, i.e. centre point of pump. The wavelength of standing wave was calculated as,

$$\text{Wavelength of standing wave } (\lambda) = \frac{\text{Sound velocity}}{\text{Vane passing frequency}} \tag{2}$$

The sound velocity considered in water was 1496 m/s [11]. So, wavelength of standing wave λ was obtained. Hence measurement location for quarter wavelength was λ/4 and λ/2 for half wavelength. Location *L*1 was selected on the both discharge lines at 1 m, additional location considered was at ~ 5.8 m selected approx. 0.2 m distance from end of discharge pipe to avoid the discharge effect at end point.

3.4 Governing Equations

To compute the fluid flow field inside the pump the Reynolds-averaged Navier–Stokes equations [12], used which are as follows as:

(1) Continuity Equation:

$$\frac{\partial \rho}{\partial t} + \frac{\partial (\rho u_i)}{\partial x_i} = 0 \tag{3}$$

(2) Momentum Equations:

$$\frac{\partial \rho_i}{\partial t} + \frac{\partial \left(\rho_i u_j\right)}{\partial x_j} = -\frac{\partial P}{\partial x_i} + \frac{\partial}{\partial x_j}\left[\mu\left(\frac{\partial u_i}{\partial x_j} + \frac{\partial u_j}{\partial x_i}\right) + \mu_t\left(\frac{\partial \overline{u_i}}{\partial x_j} + \frac{\partial \overline{u}_j}{\partial x_i}\right)\right.$$
$$\left. -\frac{2}{3}\left(\rho k + \mu_t \frac{\partial \overline{u_i}}{\partial x_j}\right)\delta_{ij}\right] + F_i \tag{4}$$

where ρ is density, μ is dynamic viscosity, μ_t is turbulent viscosity, F_i is source term, and k is the turbulent kinetic energy.

3.5 Boundary Conditions and Method of Solution

The boundary conditions were set such as inlet boundary was total pressure with reference to 1 atm, turbulent intensity at inlet was 5% and outlet boundary was mass flow rate in kg/s. The impeller was set to rotating domain and all other domains were set to stationary. The industrially most famous *k–ε* turbulence model was used for the analysis of pump. It is two transport equation model which solves transport equation for *k* (Turbulent Kinetic Energy) and *ε* (Turbulence dissipation rate). It is widely used since it is easy to implement, computationally cheap, convergence was better

than the other models, good for initial iterations and initial screening of alternative designs [1].

First steady calculation was performed in which the frozen rotor was selected as interface model. In unsteady calculation the dynamic (impeller) and static (volute) component were coupled with rotor–stator interface model. Steady-state results were used as initial conditions for unsteady calculation. Both interface types were fluid–fluid interface. The finite volume approach was used to spatially discretize the governing equations. The second order backward Euler implicit scheme was utilized for the time discretization in transient scheme. High resolution as advection scheme was used.

The time step size for unsteady calculation was selected such as it corresponds to changed angle of 0.5° of the impeller rotation. As it would provide 120 time steps per impeller blade passage, i.e. the total 720 time steps for one rotation of impeller and for reliable and accurate calculation of pressure pulsation, 4 cycles of impeller rotation, i.e. for 2880 time steps the numerical calculation was performed. The time step was choose based on the work of Spence [9] who conducted the unsteady analysis of centrifugal pump for calculation of pressure pulsation using time steps equivalent to 288 time steps for one impeller rotation and (48 time steps per impeller blade passage). The data of the 4th cycle was analysed used for further calculation of pressure pulsation percentage. The convergence criteria was set to 10^{-5}.

4 Results and Discussion

In industrial point of view the centrifugal pumps are widely used. These pumps are having the impeller as rotor rotating at high speed and vortical flow structure of volute serve as stator causing rotor–stator interaction. RSI was main reason for pressure pulsation which was maximum at blade passing frequency. Because interaction between the rotor and stator as the impeller blade is near to cutwater, the static pressure at edge of impeller blade and the corresponding increase in flow passage area results an uneven pressure distribution.

To analyse the pressure pulsation, the most widely used non-dimensional pressure pulsation coefficient C_P was used [9]. It was used to measure the magnitude of pressure pulsation the formula as follows:

$$C_P = \frac{P - \overline{P}}{0.5 * \rho u^2} \tag{5}$$

where P is the static pressure at the monitor point at particular time step, $\overline{P}$ is the average pressure of impeller in one rotation period, ρ is the density of fluid used, and u is peripheral speed of the impeller outlet. Also, the pressure pulsation can be measured with another non-dimensional formula as pressure pulsation percentage ($\Delta P\%$) which was non-dimensionalized by dividing Root Mean Square value (RMS)

value of ΔP with Pressure at Best Efficiency Point P_{BEP}. The formula is as follows:

$$\Delta P\% = \frac{\Delta P_{\text{RMS}}}{P_{\text{BEP}}} \tag{6}$$

where

$$\Delta P_{\text{RMS}} = \sqrt{\frac{\Delta P_1^2 + \Delta P_2^2 + \Delta P_3^2 + \Delta P_4^2 + \cdots + \Delta P_n^2}{n}} \tag{7}$$

$$\Delta P = P - \overline{P} \tag{8}$$

1, 2, 3, …, $n =$ are the time steps in 1 revolution of impeller.
P is the static pressure at the monitoring point.
$\overline{P}$ is the average pressure of the impeller in one rotation period.

The results were plotted with use of both C_P and $\Delta P\%$ to check variation of pressure pulsation with Gap-B %. The data of fourth cycle of rotation was considered for calculation of C_P and $\Delta P\%$. Figure 5 shows for monitor point $L1$ the variation of C_P with Gap-B% over the one period of impeller rotation. For all other monitor points the variation of C_P with time was minimal. The start time step of fourth rotation was 2160th time step and last time step 2880th, i.e. one rotation of impeller captured during 720 time steps. From the figure it was seen that for Gap-B of 14% the height of peaks and troughs were less. As the Gap-B% was decreases the C_P value increases. The fluctuations waves were periodic in nature having six waveforms appear in the one cycle which was equals to six impeller vanes.

The Gap-B of 8%, 9%, and 10% has highest C_P values in peaks and troughs both. Maximum value of C_P was found to be approx. -0.040. Pressure pulsation from
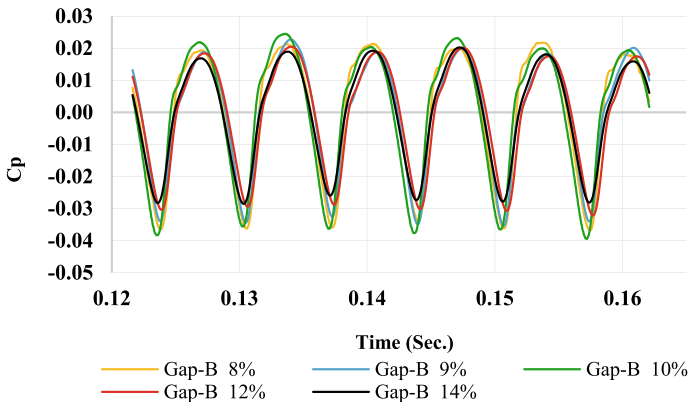
Fig. 5 Pressure pulsation (C_P) time domain diagram with Gap-B% for period of one rotation of impeller at L1 Monitor point

impeller inlet to outlet was gradually increases and pressure pulsation gets maximum at impeller outlet near cutwater. So this effects come in flow of discharge pipes.

The pressure pulsation percentage is criteria used for evaluation of pressure pulsation in pump since experimental testing results were recorded in $\Delta P\%$ format.

Figure 6 shows the variation of $\Delta P\%$ with Gap-B%. It was observed that the $\Delta P\%$ was decreases as Gap-B% increases and having negligible changes after Gap-B of 9%. For all other monitor points the variation was similar with respect to monitor point $L1$. There were negligible changes in pressure pulsation with respect to location and discharge pipes for respective Gap-B%.

At monitor point $L1$ the numerical results were also compared with experimental results in Fig. 7. From Fig. 7 it was observed that for Gap-B of 8%, 9% the results had some changes and after Gap-B of 9% the CFD results had negligible changes with increase Gap-B% since that decreases RSI interaction and subsequently decreases pressure pulsation. For all other monitor points the results were similar with monitor point $L1$. The appropriate Gap-B's therefore determined to be 9–12%, having low pressure pulsation for pump.
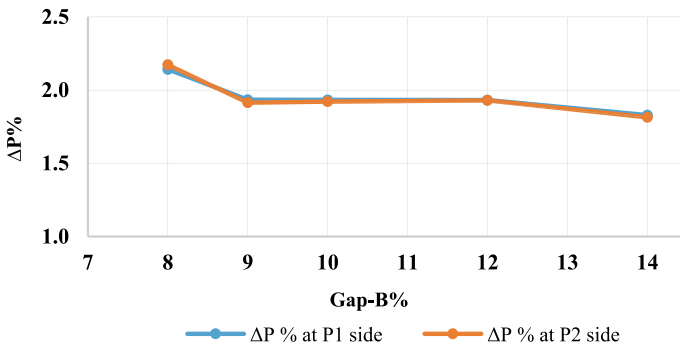
Fig. 6 Variation of pressure pulsation ($\Delta P\%$) with Gap-B% for both discharge pipes
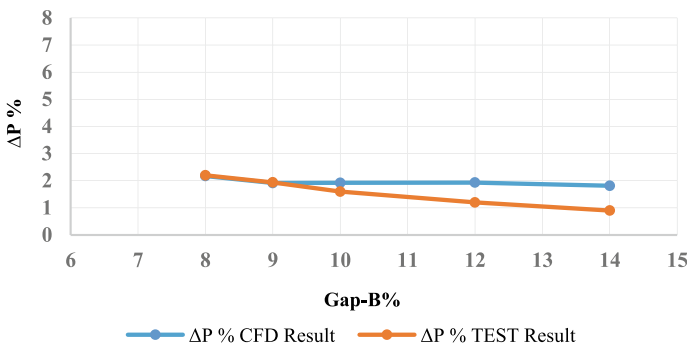
Fig. 7 Validation of CFD results with Experimental results
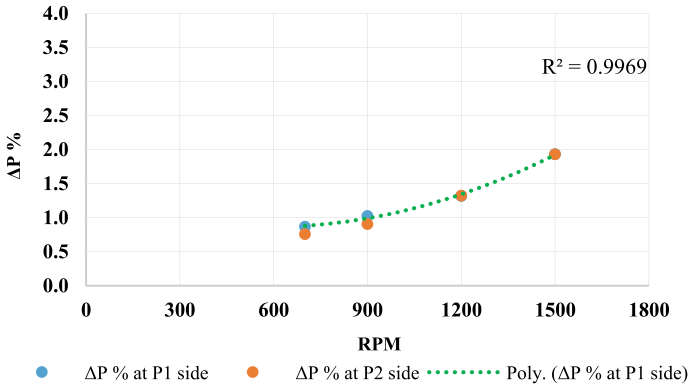
Fig. 8 Variation of pressure pulsation with impeller speed

The pressure pulsation was also checked with varying frequency drive, i.e. with increasing speed of impeller as shown in Fig. 8. The results were obtained for Gap-B of 12%. Since it had low pressure pulsation as shown in Fig. 7. The speed was varied as 700, 900, 1200, and 1500 RPM. As from affinity law the pressure head was directly proportional to square of speed. So, the pressure pulsation follows similar trend which showed quadratic variation of pressure pulsation with speed. Almost all points were fitting with 2nd order polynomial having accuracy $R^2 = 0.9969$ for both discharge pipes $\Delta P\%$.

5   Conclusions

In this study the pressure pulsation characteristics in a centrifugal pump were studied. Mesh of numerical model was first validated by grid independence test with rated head as parameter. The parameters such as cutwater Gap-B% and impeller speed in RPM were used for pressure pulsation analysis. A total 9 transient and 11 steady-state analysis were conducted to analyse pressure pulsation, performance of pump, and optimal grid by grid independence test. Transient analysis gives rise the major data set. The results were more focused and presented by concentrating on selected monitor points locations at discharge pipe. Pressure pulsation waveform shows six peaks and six troughs in one cycle consistent to number of impeller vanes. In general, the cutwater Gap-B was most affecting parameter on pressure pulsation but impeller speed also shows great influence on the same. The pressure pulsation data shown in terms of both coefficient of pressure pulsation (C_P) and $\Delta P\%$. The qualitative characteristic of pressure pulsations has been used, with the evaluation standard being "the lower the better". Additional desirable qualities include pump performance (i.e. pump generated head and hydraulic efficiency) could be its own evaluation criterion. Designers should find these guidelines helpful for their research work.

Nomenclature

Gap-B	Radial gap between the impeller tip and cutwater (%)
D_2	Impeller outlet diameter (mm)
D_3	Cutwater diameter (mm)
$L1$	Monitor point at 1 m length (–)
ρ	Density of water (kg/m^3)
C_P	Coefficient of pressure pulsation (–)
$\Delta P\%$	Pressure pulsation percentage (%)
P	Pressure (Pa)
$\overline{P}$	Average pressure of impeller in one rotation period (Pa)
μ, μ_t	Dynamic and turbulent viscosity (Pa s)
F_i	Source term (–)
k	Turbulent kinetic energy (J)
atm	Atmospheric pressure (Pa)
u	Peripheral velocity at impeller outlet (m/s)
ΔP	Pressure difference (Pa)
ΔP_{RMS}	Root mean square value of pressure difference (Pa)
P_{BEP}	Pressure at best efficiency point (Pa)

References

1. Gülich JF (2020) Centrifugal pumps. Springer, Switzerland
2. Szamody O, Makay E (1978) Survey of feed pump outages. Prepared for Electric Power Research Institute Research, Project 641, Report: FR-754
3. He X (1996) The mechanism on forming of the pressure pulse in vane pump. Mech Sci Technol Aerosp Eng 25(6):38–42
4. Sudo S, Komatsu T, Kondo M (1980) Pumping plant noise reduction: reduction of pressure pulsation in pump discharge pipe systems. Hitachi Rev 29(5):217–222
5. Sun Z, Zhang Y, Xia H, Chen S (2019) Radial force and pressure fluctuation analysis of axial flow pump rotor under different working conditions. J Irrig 38:122–128
6. Tsukamoto H, Shi F (2001) Numerical study of pressure fluctuations caused by impeller-diffuser interaction in a diffuser pump stage. J Fluids Eng 123(3):466–474
7. Gonzáles J, Santolaria C, Parrondo JL et al (2003) Unsteady radial forces on the impeller of a centrifugal pump with radial gap variation. In: Proceedings of the ASME/JSME 2003 4th joint fluids summer engineering conference, vol 45, pp 1173–1181
8. Shi W, Zhang, Chen B, Jiang T, Zhang H (2012) Effect of centrifugal pump clearance on pressure pulsation and radial force. J Drain Irrig Mech Eng 30(3):260–264
9. Spence R, Amaral-Teixeira J (2009) A CFD parametric study of geometrical variations on the pressure pulsations and performance characteristics of a centrifugal pump. Comput Fluids 38:1243–1257

10. Sparks C, Wachel J (1979) Pulsations in liquid pumps and piping systems. In: Proceedings of the fifth turbomachinery symposium, Turbomachinery Laboratory, Texas A&M University, College Station, Texas, pp 55–61
11. Lubbers J, Graaff R (1998) A simple and accurate formula for the sound velocity in water. Ultrasound Med Biol 24(7):1065–1068
12. Kang Y, Liu S, Zou W, Hu X (2019) Numerical investigation on pressure pulsation characteristics and radial force of a deep-sea electric lifting pump at off-design conditions. Hindawi Shock Vib 2019:16

CFD Analysis of Diesel Engine Intake Manifold

Rushikesh Thange, Tauhid Sheikh, Asha Honshette, Dhiraj Gangurde, Anuj Bhaskar, Ranjeet Bhosale, and Pramod Kothmire

1 Introduction

The performance of an IC engine depends on the components that make it up. The intake manifold is one such component. The function of the intake manifold is to provide air from the atmosphere in the engine block. An intake manifold consists of a plenum and a runner. The air from the atmosphere enters the manifold and passes through the plenum. From the plenum, the air travels through one of the runners to the engine cylinder head. The intake manifold ensures equal distribution of air to all the cylinders. Equal distribution of air is necessary for the safety of the engine and for obtaining maximum efficiency [1–3].

Throughout the years, experimental analysis was used to evaluate the performance of the engine with different intake manifolds. However, experimental analysis is time-consuming and expensive. Computational Fluid Dynamics (CFD) provides an alternative to experimental analysis. The change in performance can be evaluated without the need for prototyping. This increases the speed of product development and allows for more design variations.

The major use of Intake Manifold:

- Its purpose is to link the carburetor or throttle body to the cylinder head and aid in providing the air or air–fuel combination to all the cylinders in equal proportion.
- Avoid pressure loss.
- The runner sensor is positioned on the intake manifold, which regulates the flap's opening within the intake manifold to regulate the airflow.

An intake manifold is simple in design, but there are certain limitations in designing of diesel engine intake manifold as follows:

R. Thange · T. Sheikh (✉) · A. Honshette · D. Gangurde · A. Bhaskar · R. Bhosale · P. Kothmire
School of Mechanical Engineering, MIT Academy of Engineering, Alandi, Pune 412105, India
e-mail: tjsheikh@mitaoe.ac.in

  i. Runner length of the manifold runner should be as small as feasible to eliminate fuel supply lag.
  ii. The air is difficult to be pulled by the suction if indeed the diameter of the runner becomes too small in comparison to the combustion cylinders.
iii. The surface of a runner should not be too uneven and jagged which can produce resistance for air to go down.

The first model of the intake manifold is under standard geometrical parameters from the literature survey. A variable angle of the intake manifold used for pressure and volume flow rate variation is generated. All three designs of variable angles for the intake manifold have varying degrees of success. Identification of the different runner angles of the intake manifold and CFD analysis should be done. CFD analysis shows the flow distribution, pressure gradient, and velocity of the intake manifold. Afterward, in CFD analysis it is observed that the pressure gradient decreases with an increase in the runner angle.

2 Literature Review and Objective

The majority of Computational Fluid Dynamic studies on intake manifolds in IC engines give the air or air–fuel combination to all the cylinders in equal proportion. The information available on the intake manifold for different runner angles is very limited.

Extensive information on intake manifold designers is to attain a twin aim, strong performance, and low levels of emission. The role of the intake manifold is to provide the intake charge to all of the cylinders of the engine in an exact ratio. To achieve this double goal various design iterations have been carried out, ranging from modifications in existing designs to spiral intake manifolds produced using additive manufacturing [4]. The above-mentioned investigation available in the literature reveals the design of an engine intake system elaborates on techniques to define the new and better geometry of an intake runner, and presents an intake manifold system.

CFD methodology allows for quicker product development and design validation. Analysis can be carried out in a steady and unsteady state [5].

Various aspects of an intake manifold are tuned at the first design phase by carrying out a detailed analysis. Based on the 3D calculation, the engine flow is not correctly presented or is difficult to depict with finite volume modeling [6].

The geometry of the volumetric efficiency, mass flow rate, and pressure are investigated by using CFD and numerical analysis methods. The increase in torque and power is evident at 50% throttle position [7]. Simulation and experimental results of Brake thermal efficiency brake power, and brake torque are increased by 12.5% 16%, and 13.9% respectively. The effect of different designs of the intake manifolds from the papers shows a better prediction of the engine performance [8].

Studies have also implemented a 2D code to simulate the flow through an intake manifold [9]. Intake manifold design also affects fuel consumption. By optimizing the

intake manifold design and introducing additives, fuel consumption can be reduced as shown through studies [10].

However, the studies only showed the effect of change in plenum and runner lengths. There is future scope for determining the size of other engine components depending on the optimal plenum length [11]. The efficient design of intake manifold enables greater flow distribution to each cylinders and the elimination of pressure losses. The relation between design variations and the effect of the change in angles is not considered included only in the simulation of a particular design and also, not compared with the other possible iterations of the design.

Selection of runner angle of manifold:

(a) The small bending angle with a short straight pipe gives smoother and even airflow. To have an efficient engine system the pressure must be decreased across the system to promote even airflow.
(b) Also, nowadays the engine systems are getting compact with the short runner length and maximum bending angle for improving the Power-to-weight ratio.

Considering both conditions the angles for analysis are selected as 100, 110, and 120.

2.1 Objectives of the Present Investigation

The following objectives are identified for the present investigation:

- To design an optimal structure of the manifold for maximum efficiency.
- To analyze different types of designs of manifolds.
- To compare the mass flow rate and pressure of different manifold designs.
- To find the feasible solution/design among all six designs.

The main objective of the present investigation is to generate a reliable design of an intake manifold using a variable of angles and in late positions. It is essential to initially obtain data for designs of the intake manifold. This will accomplish several objectives; firstly, design an optimal structure of the Intake Manifold for varying angles. Secondly, analyze the different designs of intake manifolds to compare the velocity, pressure, and mass flow rate.

3 Materials and Methods

3.1 Methodology

3.1.1 Software

The 3D CAD Model of the intake manifold was designed in Autodesk Inventor. The CFD analysis is carried out in ANSYS R22. ANSYS R22 is based on the Finite Volume Method. The software is selected due to its computational use and familiarity with the user interface.

3.1.2 Geometry

A CAD model of a single plane intake manifold is created in Autodesk Inventor as shown in Fig. 1. The geometry of the Intake Manifold consists of a plenum and a runner. The plenum takes the input from the inlet and ensures equal distribution to the engine cylinders through the runner. Table 1 shows the various parameters used for designing the intake manifold.
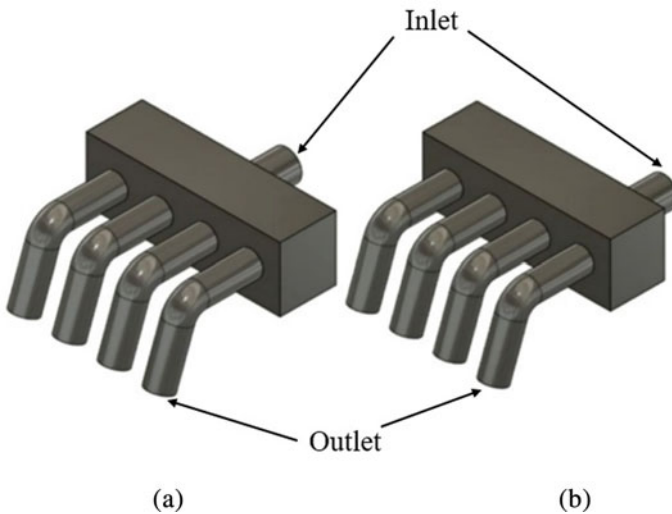
Fig. 1 Design of diesel engine intake manifold **a** geometry of intake manifold with center inlet **b** geometry of intake manifold with offset inlet

Table 1 Design values of the intake manifold

Parameters of manifold	Dimension
Diffuser diameter	38 mm
Diffuser length	70 mm
Runner diameter	30 mm
Runner length	100 mm
Plenum volume	1859.264 cm^3
Runner angle	80°
Thickness	3 mm (overall geometry)
Inlet position	(a) Center (b) Offset 71 mm from center
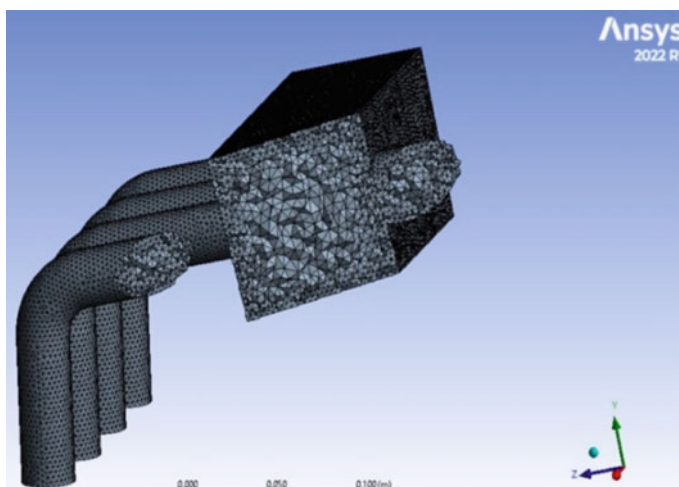
Fig. 2 Sectional view of mesh of intake manifold

3.1.3 Meshing and Material

Figure 2 shows the section view of the mesh. The mesh elements used are tetrahedrons. Figure 3 shows the mesh independence study. It is observed that there is no significant change in the pressure drop with an increase in the number of mesh elements.

3.1.4 Boundary Conditions

In order to carry out the analysis, the boundary conditions over the geometry are defined. The mass flow rate of air is defined at the inlet. Pressure condition is defined at the outlet as highlighted in Fig. 1a, b.
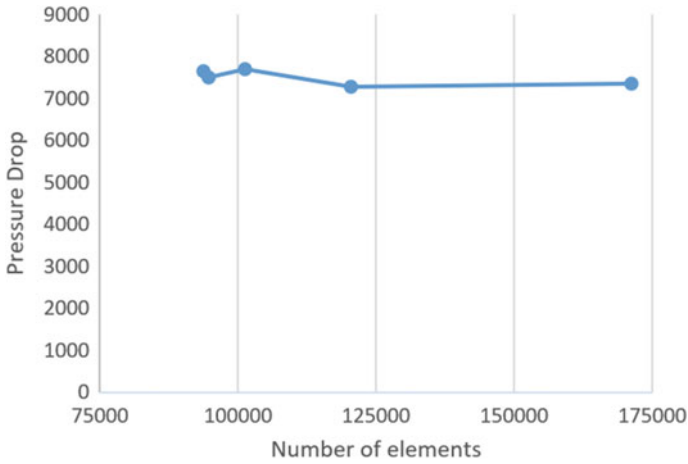
Fig. 3 Mesh independence study of the mesh generated on intake manifold

Inlet Mass Flow Rate: 0.067 kg/s
Outlet Pressure: 0 Pa.

3.1.5 Solver Model

Model: Realizable, *k*-epsilon
Physical Properties of Air
Time: Steady
Fluid: Incompressible ideal gas
Molecular Weight: 28.97 kg/kmol
Density: 1.128 kg/m^3
Dynamic Viscosity: 1.91E−05 kg m/s.

3.1.6 Governing Equations

a. Continuity Equation

$$\nabla \cdot \overrightarrow{V} = 0 \tag{1}$$

The mass continuity equation becomes a volume continuity equation if the fluid is incompressible (volumetric strain rate is zero).

This means that the divergence of the velocity field is zero everywhere. Physically, this is equivalent to saying that the local volume dilation rate is zero; hence a flow of water through a converging pipe will adjust solely by increasing its velocity as water is largely incompressible.

b. Momentum Equation

$$\rho \frac{D\overrightarrow{V}}{Dt} = -\nabla p + \rho \overrightarrow{g} + \mu \nabla^2 \overrightarrow{V} \tag{2}$$

Navier–Stokes equation, in fluid mechanics, a partial differential equation that describes the flow of incompressible fluids. By using Eq. (1) and vector notations above momentum equation is derived.

(Total derivative $= -$Pressure gradient $+$ Body force term $+$ Diffusion term)

$$\rho \left[\frac{\partial V}{\partial t} + (V \cdot \nabla)V \right]$$

(Change of velocity with time $+$ Convective term)

c. Transportation equation for standard k-epsilon model

For turbulent kinetic energy k

$$\frac{\partial(\rho\kappa)}{\partial \ell} + \frac{\partial(\rho\kappa u_i)}{\partial x_i} = \frac{\partial}{\partial x_i}\left[\frac{\mu_t}{\sigma_k} \frac{\partial \kappa}{\partial x_j} \right] + 2\mu_t E_{ij} E_{ij} - \rho\varepsilon \tag{4}$$

K-epsilon (k–ε) turbulence model is the most common model used in Computational Fluid Dynamics (CFD) to simulate mean flow characteristics for turbulent flow conditions.

For dissipation epsilon

$$\frac{\partial(\rho\varepsilon)}{\partial \ell} + \frac{\partial(\rho\varepsilon u_i)}{\partial x_i} = \frac{\partial}{\partial x_i}\left[\frac{\mu_t}{\sigma_\varepsilon} \frac{\partial \varepsilon}{\partial x_j} \right] + C_{1\varepsilon}\frac{\varepsilon}{\kappa}2\mu_t E_{ij} E_{ij} - C_{2\varepsilon\rho}\frac{\varepsilon^2}{\kappa} \tag{5}$$

In Eq. (5), the term turbulent kinetic energy (k) replace by dissipation (ε).

4 Results and Discussion

CFD analysis for three different runner angles is carried out. Figure 4a–c shows the pressure drop results for runner angles 100°, 110°, and 120°, respectively. Figure 5 shows the mass flow rate variance at each cylinder. Mass flow rate variation is carried out by opening all inlets to the cylinders. And pressure drop calculation is carried out by opening one inlet to the cylinder one by one. From the graph, it can be observed that the variance in mass flow rate with respect to angle is not that significant.

To study uniformness in the distribution of air, a parameter called Unevenness (E) is used [12].

$$E = (Q_{\max} - Q_{\min})/Q_{\text{me}} \tag{6}$$

Fig. 4 **a** Volume rendering
of pressure for 100º;
b volume rendering of
pressure for 110º; **c** volume
rendering of pressure for
120º
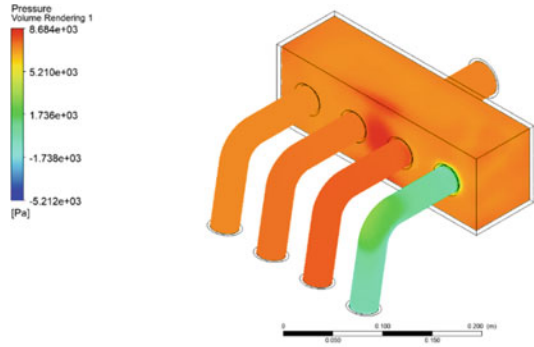
(a)
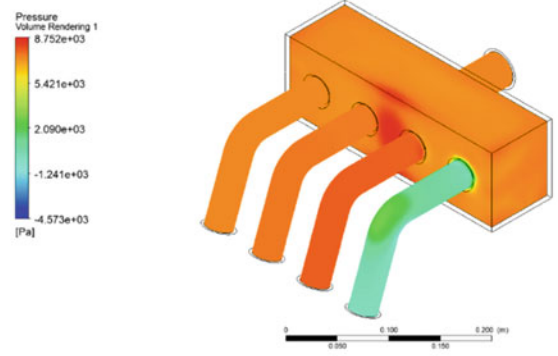
(b)
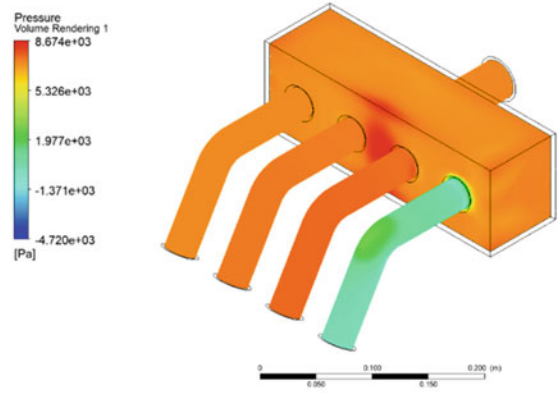
(c)
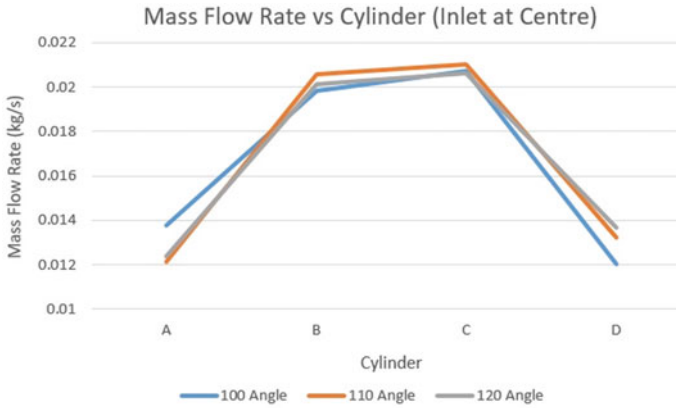
Fig. 5 Graph of mass flow rate versus cylinder of diesel engine intake manifold

where

Q_{me} = Average mass flow

Q_{max} = Maximum flow rate export quality

Q_{min} = Minimum flow rate export quality.

Equation (6) shows uneven air flow in cylinder which results in drop of pressure and increased fuel consumption.

For the angles, maximum unevenness is calculated as:

100°—0.5166
110°—0.5284
120°—0.4921

From the values, it can be observed that the unevenness is least in 120°. However, as there is not significant difference, another design iteration is carried out by changing the inlet position. The inlet is shifted to an offset position and CFD analysis is carried out as shown in Fig. 6.

CFD Analysis of two different designs, varying in inlet position is carried out. The analysis for both designs is carried out at a runner angle of 110°. Figure 7 shows the distribution of Mass Flow Rate with respect to the inlet position. It can be seen that the mass flow rate is more uniform over each cylinder when the inlet is located at an offset from the center.

A similar trend is observed for pressure drop concerning inlet position as shown in Fig. 8. It is observed that the pressure drop is even over all cylinders when the inlet is located at an offset. Therefore, it is showing that the inlet located at an offset is a better design than the inlet located at the center.

Figure 8 shows a similar trend observed for pressure drop concerning inlet position. It is observed that the pressure drop is even over all cylinders when the inlet is located at an offset. The offset design of the intake manifold gives a more optimal
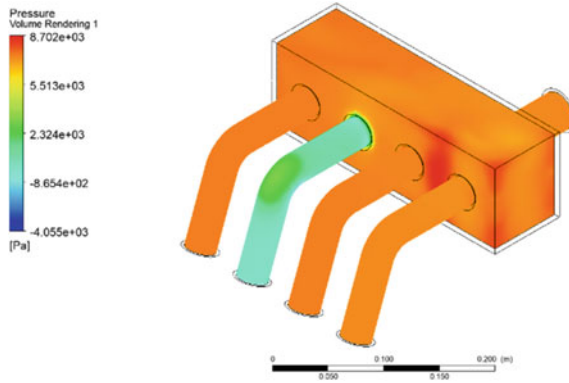
Fig. 6 Volume rendering of pressure for 110º (inlet at offset position of intake manifold)
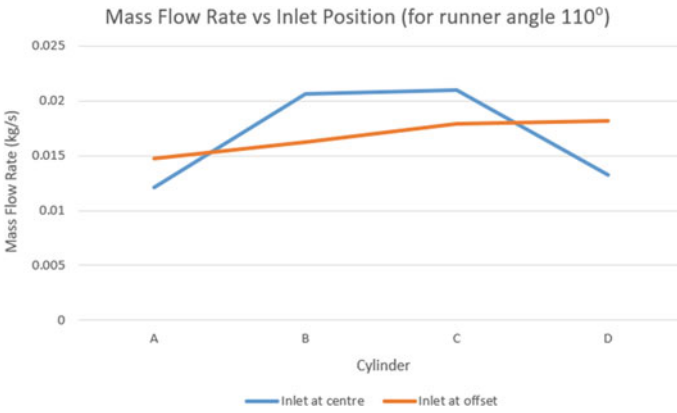
Fig. 7 Graph of mass flow rate versus inlet position (for 110º runner angle)
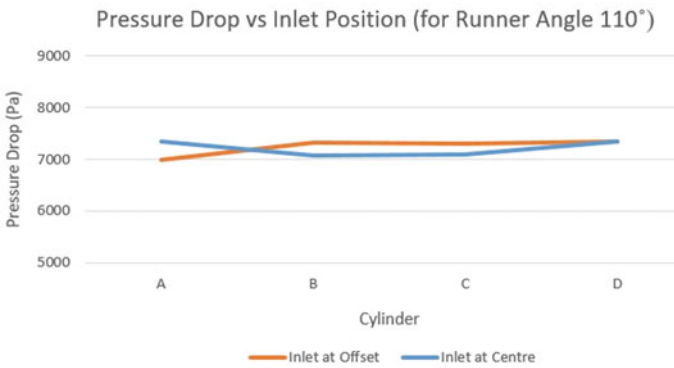
Fig. 8 Graph of pressure drop versus inlet position (for 110º runner angle)

comparison. Therefore, it is showing that the inlet located at an offset is a better design than the inlet located at the center**.**

5 Conclusions

The results of the CFD analysis show that the optimal intake manifold design is the one in which the runner angle is 120° and the inlet is located offset from the center. The maximum evenness is obtained in this case, therefore, demonstrating the best mixing. The least variation in pressure drop over each cylinder is observed in this case as well showing that there are the least fluctuations as the air passes over each cylinder. It ensures that the air coming into the engine is evenly distributed to all the cylinders and it is used in the excursion, expedition, F-250/F-350 super duty model which is at least a 5.4-L engine.

Nomenclature

k	Turbulent kinetic energy
u_i	Velocity component in the corresponding direction
ε	Rate of dissipation of turbulent kinetic energy
E_{ij}	Component of the rate of deformation
μ_t	Eddy viscosity
$\sigma_k, \sigma_\varepsilon, C_{1\varepsilon}, C_{2\varepsilon}$	Adjustable constants

References

1. Gurusamy P, Thirupathiraja S, Hari Krishna Raj S, Lokesh Kumar J (2021) Experimental investigation and CFD analysis of inlet manifold in internal combustion engine. Mater Today: Proc 37(2):840–843
2. Gocmen K, Soyhan HS (2020) An intake manifold geometry for enhancement of pressure drop in a diesel engine. Fuel 261
3. Alves L, dos Santos M, Urquiza A, Guerrero J et al (2017) Design of a new intake manifold of a single cylinder engine with three stages. SAE Technical Paper 0148-7191
4. Manmadhachary A, Santosh Kumar M, Ravi Kumar Y (2017) Design & manufacturing of the spiral intake manifold to improve volume efficiency of injection diesel engine by AM process. Mater Today: Proc 4(2):1084–1090
5. Al-Rousan AA (2010) Reduction of fuel consumption in gasoline engines by introducing HHO gas into the intake manifold. Int J Hydrogen Energy 35(23):12930–12935
6. Pai D, Singh H, Muhammed P (2011) Simulation-based approach for optimization of intake manifold. SAE Technical Paper 0148-7191
7. Saravanan D, Gokhale A, Karthikeyan N (2015) Design and development of a flow based dual intake manifold system. SAE Int J Engines 8(1)

8. Jemni MA, Kantchev G, Abid MS (2011) Influence of intake manifold design on in-cylinder flow and engine performances in a bus diesel engine converted to LPG gas fuelled, using CFD analyses and experimental investigations. Energy 36(5):2701–2715
9. Safari M, Ghamari M, Nasiritosi A (2003) Intake manifold optimization by using 3-D CFD analysis. SAE Technical Paper
10. da Silva Trindade W (2010) Use of 1D-3D coupled simulation to develop an intake manifold system. SAE Technical Paper 0148-7191
11. Ceviz MA, Akın M (2010) Design of a new SI engine intake manifold with variable length plenum. Energy Convers Manag 51(11):2239–2244
12. Xu J (2017) Flow analysis of engine intake manifold based on computational fluid dynamics. Phys: Conf Ser 916:012043

Computational Study of Unsteady Cavitating Flow on 3D NACA4412 Hydrofoil

Check for updates

Prabhakar Kumar, Srijna Singh, and Rajesh Reddy

1 Introduction

For over a century, cavitation has been a significant technological phenomenon and a difficult research problem in engineering science. Cavitation can occur in any equipment handling liquids. It may impact the performance of turbomachinery, causing the head and efficiency of pumps to decrease, lowering the power output and efficiency of hydro-turbines. Generally speaking, it is a highly complex vapor–liquid two-phase flow that includes phase shifts of the liquid when local pressure drops below vapor pressure (Knapp). The phenomenon of cavitation is classified based on the cavitation number. The cavitation number is given by $\sigma = \frac{p - p_v}{\frac{1}{2}\rho U_\infty^2}$, p is free stream pressure p_v is vapor pressure, ρ is liquid density, and U_∞ is the free stream velocity. Cavitation can be classified as initial, sheet, cloud, partial, and super cavitation. Partial and cloud cavitation regimes relate to a situation when the vapor phase covers a part of hydrofoil. Super cavitation is a condition where cavity length is more than the hydrofoil and closes in the liquid. Pumps, water turbines, and marine propellers are examples of hydraulic machinery where these phenomena can be seen. Cavitation may produce unwanted sounds, vibrations, and fluctuations, resulting in erosion [1].

P. Kumar · R. Reddy (✉)
Department of Mechanical Engineering, Shiv Nadar Institution of Eminence, Greater Noida, Uttar Pradesh 201314, India
e-mail: sathi.reddy@snu.edu.in

S. Singh
Department of Mechanical Engineering, Bennett University, Greater Noida, Uttar Pradesh 201310, India

2 Literature Review and Objective

For over a century, cavitation has been a significant technological phenomenon and a difficult research problem in engineering science. Huang et al. [2] used the state equations of the cavitation model combined with a linear viscous turbulent method to estimate the effect of cavitation on hydrofoils. They simulated the pressure distributions and vapor volume fractions at various cavitation numbers for the fixed angle of attack. They found that the numerical results on hydrofoil sections agreed well with the experimental data. In addition, with a larger attack angle, the vapor region moved to the front of the hydrofoil, and the cavity lengthened. Using computational and experimental methods, Fabula et al. [3] examined the lift and drag forces on cavitating hydrofoils at various cavitation numbers. Their computational findings closely matched the results of the experiments. Javadi et al. [4] examined two-dimensional cavitating flows around a hydrofoil. They found that the passive flow control strategy could reduce lift and drag oscillations. Jin et al. [5] numerically examined cavity generation on the 2D NACA0015 hydrofoil using RNG $\kappa-\epsilon$ turbulence model. It was claimed that configuration of bilateral tail wings distributes the turbulent kinetic energy from the leading edge to the wake and considerably reduces the cavitation.

Kumar et al. [6] numerically investigated the two cavitation model for compressible flow in a cavitating nozzle. In this investigation, a realizable $\kappa-\epsilon$ turbulence model was employed. Their findings state that the ZGB model is more accurate in predicting the cavitation flow than the Schnerr and Sauer models. Singh et al. [7] numerically investigated the hydrodynamic performance of the MHKF-180 and NACA4418 hydrofoil using realizable $\kappa-\epsilon$ turbulence model and ZGB cavitation model. The outcomes state that MHKF-180 has a higher lift coefficient in comparison to NACA4418 hydrofoil under various cavitating conditions. Wu et al. [8] investigated the flow around the Delft twisted hydrofoil using the LES technique and the Kunz cavitation model. It focused on the effect of mesh resolution on the outcomes. They argued that mesh resolution significantly impacts the ability to estimate cavity length, flow pattern, and fluctuation period.

Roohi et al. [9] utilized large eddy simulation (LES) with modified volume of fluid (VOF) method to study cavitation. Using the Kunz mass transfer model, they investigated the flows around several objects in a wide range of cavitation numbers. Their findings are reasonable prediction for cavitation length and drag coefficient compared with experimental data. Furuya et al. [10] examined the super cavitating hydrofoil. A three-dimensional nonlinear free streamline theory has been utilized to determine the effect of gravity on the cavity. It was concluded that the shape of the cavity is not strongly influenced by gravity. Cheng et al. [11] have studied the tip leaking cavitating flow around a NACA 0009 hydrofoil. Luo et al. [12] used a mass transfer cavitation model with the LES model to estimate the turbulent cavitating flow over a three-dimensional around a twist hydrofoil. It was argued that developing a grid-independent solution is difficult because the LES requires an extremely small mesh and has a high computational cost.

Considering past studies success, researchers often use numerical approaches to investigate cavitation phenomena. Many experimental and computational studies have been done on the NACA hydrofoil series. The essential advantage of the NACA44 series is its large leading edge radius and good cavitation resistance. The 3D investigation of the NACA4412 hydrofoil performance at low angle of attack and Reynolds number in the wide range of cavitation numbers has not been reported yet. With this motivation, investigation of the cavitating flow around a 3D NACA4412 hydrofoil is examined using a realistic and accurate simulation technique, at 4^0 in the range of super cavitation to non-cavitation zone. The range of cavitation numbers considered is from 0.3 to 1.3.

3 Governing Equations

The homogeneous mixture model has been used to resolve the cavitating flow, which assumes that the fluid is in a state of mechanical and thermodynamic equilibrium. This means that the pressure, velocity, and temperature are the same for each phase at the interface. As a result, this model only needs one set of conservation equations for the mixture. The continuity and momentum equation for the two-phase mixture [13] is given below:

$$\frac{\partial \rho_m}{\partial t} + \frac{\partial}{\partial x_j}\left(u_j \rho_m\right) = 0, \tag{1}$$

$$\frac{\partial}{\partial t}\left(\rho_m u_i\right) + \frac{\partial}{\partial x_j}\left(\rho_m u_i u_j\right) = -\frac{\partial p}{\partial x_i} + \frac{\partial}{\partial x_j}\left[\mu_{\text{eff}}\left(\frac{\partial u_i}{\partial x_j} + \frac{\partial u_j}{\partial x_i} - \frac{2}{3}\frac{\partial u_k}{\partial x_k}\delta_{ij}\right)\right], \tag{2}$$

where u_i is the instant velocity in direction i, ρ_m is the fluid mixture density, p is the mixture pressure, μ_{eff} is the effective viscosity which is given by

$$\mu_{\text{eff}} = \mu + \mu_t. \tag{3}$$

where is μ the molecular viscosity and μ_t is the turbulent viscosity, which is stated in terms of several turbulence models is illustrated by

$$\mu_t = \rho_m C_\mu \frac{\kappa^2}{\epsilon}. \tag{4}$$

Here, k is turbulent kinetic energy, ϵ is the rate of kinetic energy dissipation, and C_μ is the model parameter, in the equation above ρ_m is determined using

$$\rho_m = \alpha_v \rho_v + (1 - \alpha_v)\rho_l, \tag{5}$$

where α_v, ρ_v, and ρ_l represent the vapor volume fraction, vapor density, and liquid density, respectively.

The conservation between vapor and liquid yields the vapor volume fraction (α) as

$$\frac{\partial(\alpha_v\rho_v)}{\partial t} + \nabla \cdot (\alpha_v\rho_v u) = R_e - R_C \tag{6}$$

The mass transfer between vapor and liquid is described by the evaporation and condensation source terms, R_e and R_C, respectively.

The evaporation and condensation source terms in the Zwart–Gerber–Belamri cavitation model are as follows:

$$R_e = F_v \frac{3\alpha_{\text{nuc}}(1 - \alpha_v)\rho_v}{R_B} \sqrt{\frac{2}{3} \frac{(p_v - p)}{\rho_L}} \, (p \le p_v) \tag{7}$$

$$R_c = F_c \frac{3\alpha_{\text{nuc}}\rho_v}{R_B} \sqrt{\frac{2}{3} \frac{(p - p_v)}{\rho_L}} \, (p \ge p_v) \tag{8}$$

where vapor bubble radius is R_B, the nucleation site fraction is α_{nuc}. The saturated vapor pressure is p_v, and the static fluid pressure is p. The model constants for vaporization and condensation in the Zwart–Gerber–Belamri cavitation model are $F_v = 50$ and $F_c = 0.01$.

The realizable κ–ϵ turbulence model has been utilized for this investigation, where κ is the turbulent kinetic energy and ϵ is the of turbulent dissipation rate. The mathematical formulation for realizable κ–ϵ turbulence model is given by [6, 7].

$$\frac{\partial(\rho_m\kappa)}{\partial t} + \frac{\partial(\rho_m ku)}{\partial x_j} = \frac{\partial\left[\left(\mu + \frac{\mu_t}{\sigma_k}\right)\frac{\partial k}{\partial x_j}\right]}{\partial x_j} + G_k - \rho_m\epsilon - Y_M \tag{9}$$

$$\frac{\partial(\rho_m\epsilon)}{\partial t} + \frac{\partial(\rho_m\epsilon u)}{\partial x_j} = \frac{\partial\left[\left(\mu + \frac{\mu_t}{\sigma_\epsilon}\right)\frac{\partial\epsilon}{\partial x_j}\right]}{\partial x_j} - \rho_m C_2 \frac{\epsilon^2}{k + \sqrt{\nu\epsilon}} \tag{10}$$

where G_k is the turbulent kinetic energy resulting from mean velocity gradients, Y_M is the fluctuating dilatation factor in compressible flow. $C_2 = 1.9$, $\sigma_k = 1.0$, $\sigma_\epsilon = 1.2$ are the modal constants. PRESTO scheme has been used for the pressure, second order scheme has been utilized for momentum vapor fraction, turbulent dissipation rate, turbulent kinetic energy. The reference values used in the simulation are given in Table 1.

Table 1 Reference values

$U_\infty = 5$ m/s	$Re = 5.5 \times 10^5$
$c = 0.1$ m	$p_v = 3169$ Pa
$\rho_l = 997$ kg/m^3	$\mu_l = 0.894 \times 10^{-3}$ Pa s
$\rho_v = 0.023$ kg/m^3	$\mu_v = 9.84 \times 10^{-6}$ Pa s

4 Computational Domain and Numerical Methods

In the present work, the simulation has been carried out with 3D cambered NACA4412 hydrofoil. The chord length (c) of the hydrofoil is 100 mm, and its span length is 1.91c. The cubical domain has been generated around the hydrofoil. The domain inlet is located 6c from the leading edge. And the outlet is 12c downstream of the leading edge. The height and width in the computation domain are 10c and 1.91c. Boundary condition used are as shown in Fig. 1. Figures 2 and 3 respectively depict the meshing of hydrofoil with domain and meshing around the hydrofoil. The tetrahedral mesh has been generated around the 3D NACA4412 hydrofoil using ANSYS meshing tool. Total number of grids is the complete domain is kept 1.3 million. Skewness of the present mesh cells is having an average value of 0.27, which is in the acceptable skewness range of the tool manual. Skewness value one corresponds to low quality (skewed) cell and zero corresponds to excellent quality (unskewed) cell.
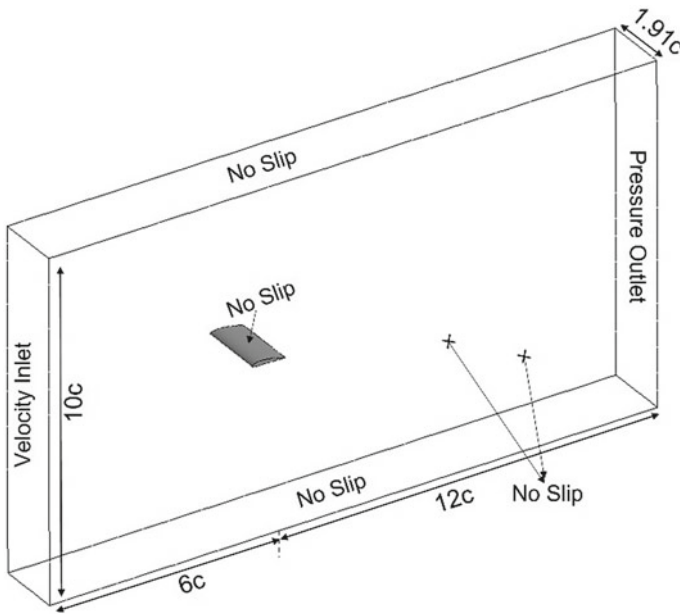
Fig. 1 NACA4412 hydrofoil geometry and computational domain
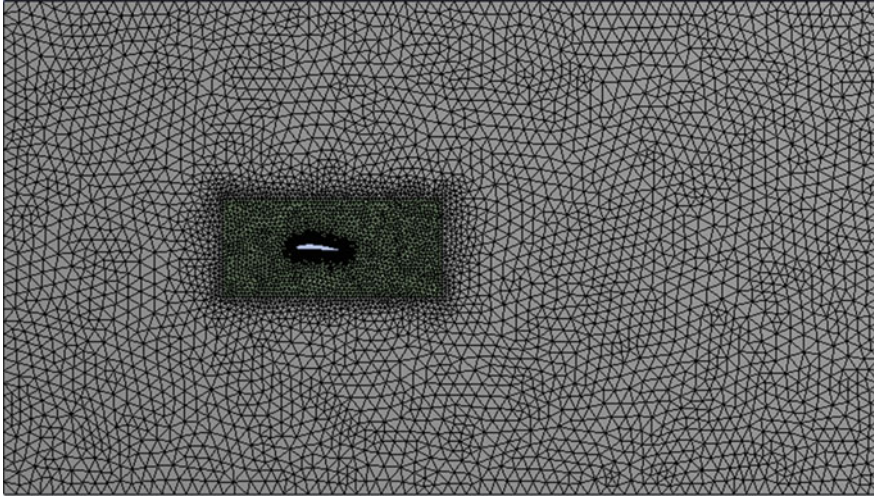
Fig. 2 Meshing around NACA 4412 hydrofoil with domain
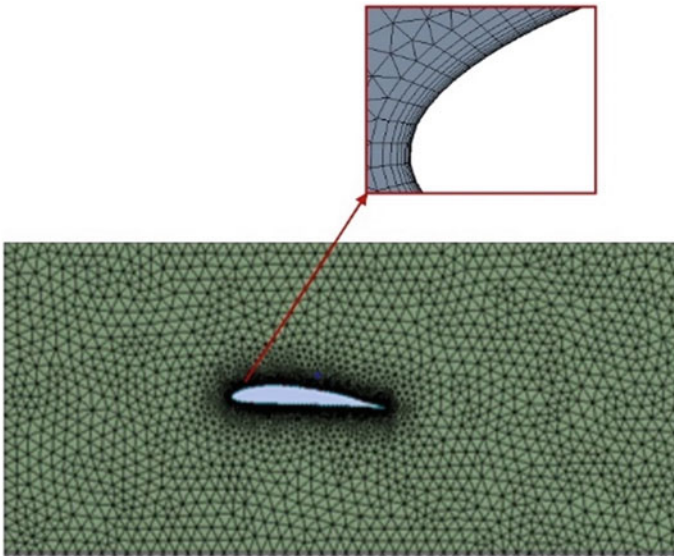
Fig. 3 Meshing around NACA 4412 hydrofoil

In order to capture the flow characteristics on the hydrofoil boundaries, the mesh is gradually refined in a cubical zone, and inflation layers are given around the hydrofoil to keep $y+ < 3$.

5 Results and Discussion

5.1 Grid Independence Test and Validation

The variation of the coefficient of lift with a different number of grids is shown in Table 2. In order to test the grid independence on the numerical simulations of the NACA4412 hydrofoil, three grids have been taken, at an angle of attack of 4^0 at $\sigma = 0.8$. Case A has 0.99 million grids, Case B has 1.3 million grids, and Case C has 1.52 million grids. From Table 2 and Fig. 4, it is observed that the percentage change in the value of C_1 for grid B is less than one percent with respect to grid C. Due to the fact the gird B is carried out for all the simulations.

To validate the numerical setup, computational results of NACA4412 hydrofoil has been compared with the experimental work by Kermeen at $Re = 0.7 \times 10^6$ for an angle of attack of 4^0 and at the cavitation number ranges between 0.3 and 0.8. A qualitative comparison of vapor fraction contour at $\sigma = 0.3$, $\alpha = 4^0$ represented in Fig. 5. Quantitative validation is performed by obtaining the variation of time averaged lift coefficient with cavitation number at angle of attack 4^0. Comparison of the present computational result with experimental work is presented in Fig. 6. The present numerical solver predictions are in close agreement with the experiment by Kermeen et al. [14].

Table 2 Time averaged lift coefficient (C_1) at different grid numbers

Serial number	Number of grids (million)	Time averaged lift coefficient (C_1)	Percentage change relative to grids C
A	0.99	0.6821	3.09
B	1.3	0.7037	0.02
C	1.52	0.7039	–

Fig. 4 Time averaged lift coefficient (C_1) at different numbers of grids at $\alpha = 4^0$ and $\sigma = 0.8$
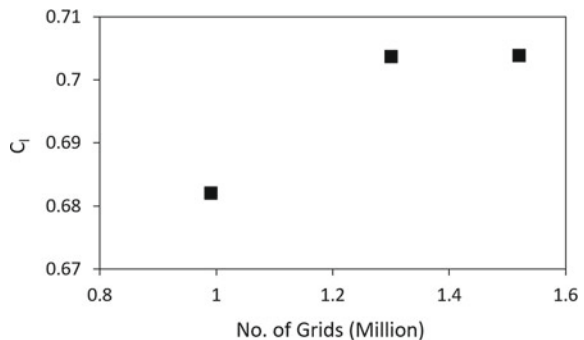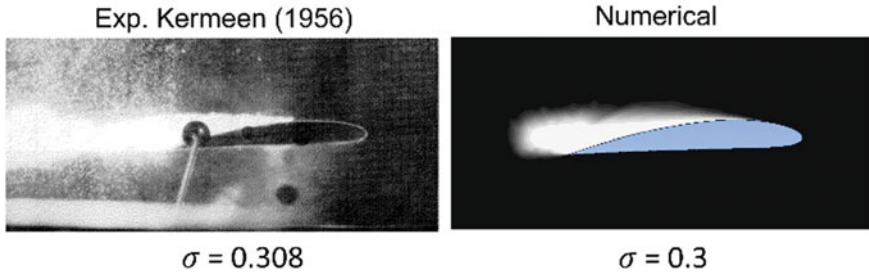
Fig. 5 Comparison of vapor volume fraction of present computational work and experimental work of Kermeen at $\sigma = 0.3$ for $\alpha = 4^0$ [14]
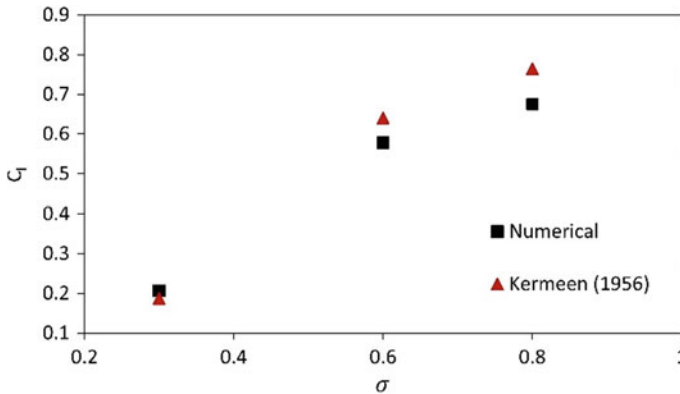
Fig. 6 Comparison of time averaged lift coefficient of present computational work and experimental work of Kermeen at $\alpha = 4^0$ [14]

5.2 Hydrodynamic Performance of NACA4412

Figure 7 represents y+ distribution on the NACA4412 hydrofoil at the mid span along the normalized chord length. The y+ < 3 is maintained on the hydrofoil to resolve the viscous sublayer of the turbulent boundary layer. Variation of time averaged lift coefficient at an angle of attack of $\alpha = 4^0$ at cavitation number ranges from 0.3 to 1.1 has been presented in Fig. 8. It is observed that lift coefficient is monotonically rising with cavitation number. At lower value of cavitation number for $\sigma = 0.3$, lift is lower due to the fact that the cavity starts forming on suction side of the hydrofoil near to the leading edge of the hydrofoil, and it extends till the trailing edge, which is called super cavitation condition. As a results there is decrease in difference in the pressure on the hydrofoil leads to reduction in C_l. However, on further increase in cavitation number results in decrease in cavity length, hence coefficient of lift increases. For $\sigma = 0.5$ and $\sigma = 0.8$, length of cavity is less than that of $\sigma = 0.3$.

Due to this fact coefficient of lift is larger than that of $\sigma = 0.3$. For $\sigma = 1.1$, cavity disappears, and for this condition maximum C_l has been observed.

Variation of time averaged drag coefficient with cavitation number ranges from 0.3 to 1.1, at $\alpha = 4^0$ has been presented Fig. 9. It is observed that with an increase in cavitation number C_d also grows and attains its maximum value which, corresponds to $\sigma = 0.5$. Furthermore, with an increase in σ results in a decrease in C_d. The drag of a 3D hydrofoil results from the pressure drag, skin friction, and lift induced drag. Pressure drag is due to the shape and size of the hydrofoil. Skin friction drag is due to the viscosity of the moving fluid. Lift-induced drag is the cause of the vortices. Vortices are formed due to pressure differences causing water to flow from the lower surface, around the hydrofoil tip, toward the upper surface. Larger the differences in pressure larger the strength of vortices. The vortices reduce the hydrodynamic ability to generate lift and increase the component of coefficient of drag. The larger the coefficient of lift, the greater the lift induces drag. A larger
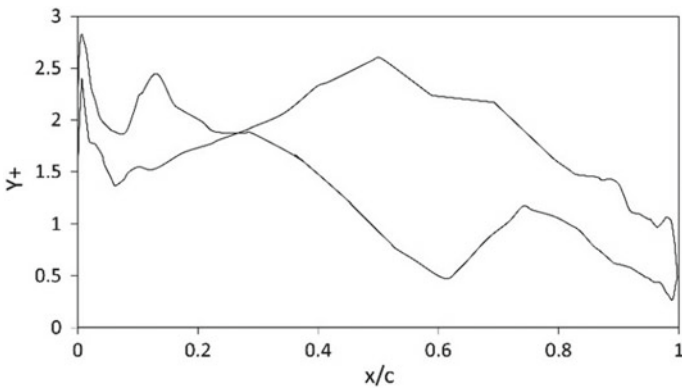
Fig. 7 $y+$ distribution on NACA4412 hydrofoil
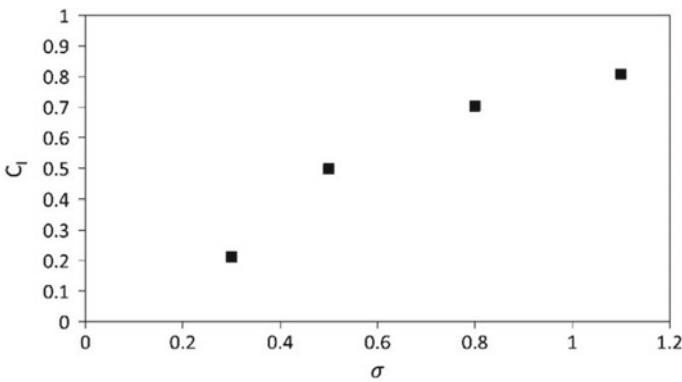
Fig. 8 Plot of C_l for NACA4412 hydrofoil for different σ
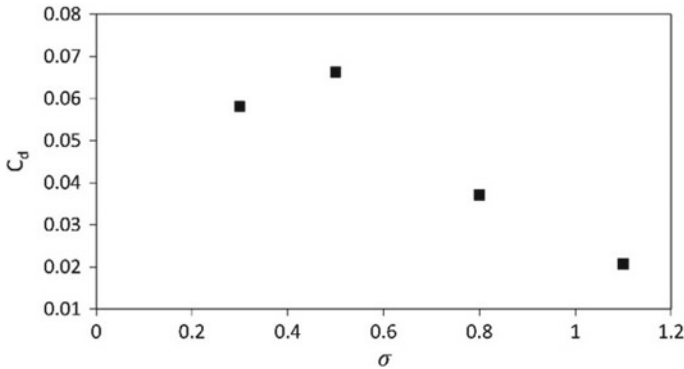
Fig. 9 Plot of C_d for NACA4412 hydrofoil for different σ

cavity length at a lower cavitation number of results in less skin friction drag. For $\sigma = 1.1$ corresponds to minimum value of coefficient of drag which corresponds to a non-cavitating condition.

Figure 10 shows the vapor volume fraction contours on NACA4412 hydrofoil at, $\alpha = 4^0$ for different cavitation numbers (σ). For $\sigma = 0.3$, the length of cavity covered the complete suction side of the hydrofoil which is called super cavitation condition. The length of the cavity covered along the chord length of the hydrofoil tends to decrease as the cavitation number rises and eventually approaches the state where there is no cavity formation, which corresponds to $\sigma = 1.1$. For, $\sigma = 0.8$ and $\sigma = 0.5$, the cavity respectively captures almost 55% and 75% of the chord and complete span of the suction side of the hydrofoil, which is termed as the trans-cavitation condition. For $\sigma = 0.3$ the cavity covers almost entire chord and span length of the hydrofoil, which is termed as super cavitation condition.

Figure 11 shows the pressure coefficient $(-C_p)$ curve along the normalized chord length at mid plane of the hydrofoil, for four cavitation numbers ($\sigma = 0.3, 0.5, 0.8$, and 1.1). The C_p is the fundamental variable that describes the pressure distribution on the hydrofoil surface and assists in the understanding of the formation of cavitation. Since the suction side of hydrofoil has lower coefficient of pressure as compared to pressure side so cavitation may occur in the suction side of the hydrofoil. The constant line of coefficient of pressure plot indicates the length covered by cavity on the suction surface of the hydrofoil. On comparing $(-C_p)$ for $\sigma = 0.3, 0.5, 0.8$, and 1.1, it is found that the minimum value of $(-C_p)$ has been observed corresponds to $\sigma = 0.3$ due to maximum pressure drop on the suction side of hydrofoil which may lead to occurrence of super cavitation phenomenon, and this can be seen in Fig. 7. The maximum value of $(-C_{p,})$ for cavitating flow has been observed at $\sigma = 0.8$, that leads to smallest cavity length out of these three cavitating cases, and for $\sigma = 1.1$, $(-C_{p,})$ is maximum out of these four cases, due to the fact there is no formation of cavity that leads to non-cavitating case.

Figure 12 shows the plot of Strouhal number (St) versus cavitation number (σ) on NACA4412 hydrofoil at $\alpha = 4^0$ along the normalized chord length at mid plane of
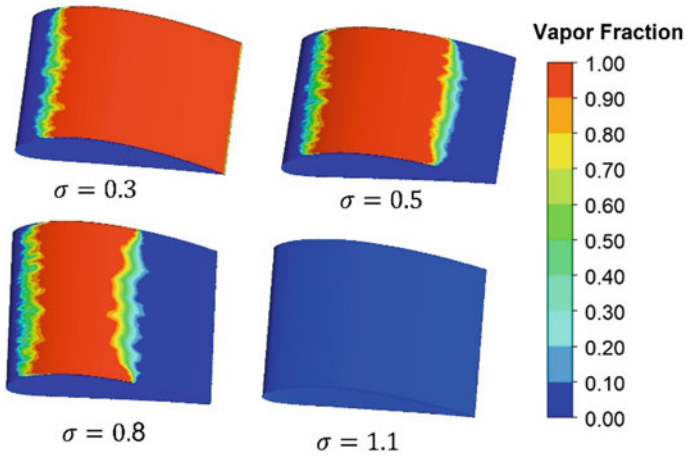
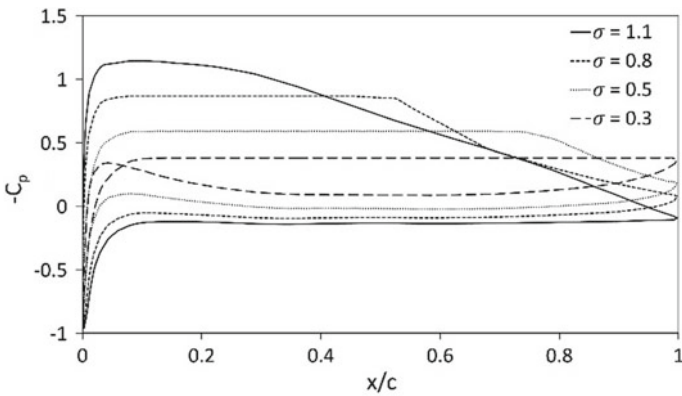Fig. 10 Comparison of vapor volume fraction on NACA4412 hydrofoil at different σ

Fig. 11 Comparison of the pressure coefficient on hydrofoil at different σ

the hydrofoil, for four cavitation numbers ($\sigma = 0.3, 0.5, 0.8$, and 1.1). To describe the pattern of the shedding of the cloud cavity, the Strouhal number (St) has been utilized, which describes how unstable oscillations affect the flow [15, 16]. The fast Fourier transformation (FFT) technique has been used to determine the Strouhal number, which transforms the signal from a time domain to a frequency domain. It has been noted that as the cavitation number increases, St gradually rises until it reaches its maximum value, which is at $\sigma = 0.5$. Minimum St has been observed corresponds to non-cavitating case for at $\sigma = 1.1$.
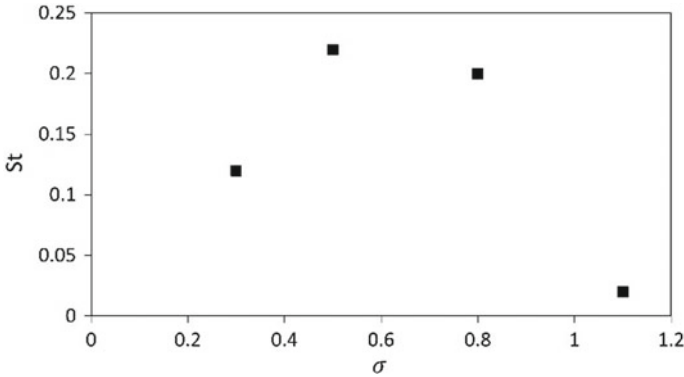
Fig. 12 Plot of St for NACA4412 hydrofoil for different σ

6 Conclusions

In the present investigation, the hydrodynamic performance of the 3D NACA4412 hydrofoil under cavitation numbers ranging from 0.3 to 1.1 has been investigated. Pressure coefficient, vapor volume fraction, lift coefficient, drag coefficient, and Strouhal number, all used to assess the performance. The turbulence effect is addressed by utilizing the realizable turbulence model, and the vapor volume fraction is estimated using the Zwart–Gerber–Belamri (ZGB) cavitation model. The major conclusions drawn from the investigation are as follows:

1. Among all the operating range of cavitation numbers, the super cavitation phenomenon has been observed for $\sigma = 0.3$. Trans-cavitation has been observed for $\sigma = 0.5$ and 0.8. Non-cavitation phenomena have been observed for $\sigma = 1.1$.
2. It is observed that increase in cavitation number results in a nonlinear increase in the coefficient of lift. Maximum coefficient of lift has been observed at $\sigma = 1.1$. The minimum coefficient of lift has been observed at $\sigma = 0.3$.
3. In the super cavitation to non-cavitating operating range, drag coefficient peaks at intermediate cavitation number. Maximum drag coefficient has been observed at $\sigma = 0.5$. The minimum drag coefficient has been observed at $\sigma = 1.1$.
4. In the super cavitation to non-cavitating operating range, Strouhal number peak is at intermediate cavitation number. Maximum Strouhal number has been observed at $\sigma = 0.5$. The minimum Strouhal coefficient has been observed at $\sigma = 1.1$.

Nomenclature

σ Cavitation number (–)
α Angle of attack ($\circ$)

U_∞ Free stream velocity (m/s)
ρ_l Density of liquid (kg/m^3)
p_v Vapor pressure of liquid (Pa)
c Chord length of hydrofoil (m)
Re   Reynold's number based on chord length (–)
C_l Lift coefficient (–)
C_d Drag coefficient (–)
C_p Pressure coefficient (–)
St   Strouhal number (–)
μ Molecular viscosity (Pa s)
μ_l Viscosity of water (Pa s)
μ_v Viscosity of water vapor (Pa s)
μ_t Turbulent viscosity (Pa s)
κ Turbulent kinetic energy (m^2/s)
ϵ Rate of dissipation of turbulent kinetic energy (m^2/s^3)

References

1. Christopher BE, Brennen CE (1995) Cavitation and bubble dynamics. Annu Rev Fluid Mech 9(1):145–185
2. Huang S, He M, Wang C, Chang X (2010) Simulation of cavitating flow around a 2-D hydrofoil. J Mar Sci Appl 9(1):63–68
3. Fabula AG (1962) Thin-airfoil theory applied to hydrofoils with a single finite cavity and arbitrary free-streamline detachment. J Fluid Mech 12(2):227–240
4. Javadi K, Dorostkar MM, Katal A (2017) Cavitation passive control on immersed bodies. J Mar Sci Appl 16(1):33–41
5. Jin W (2021) Cavitation generation and inhibition. I. Dominant mechanism of turbulent kinetic energy for cavitation evolution. AIP Adv 11(6)
6. Kumar A, Ghobadian A, Nouri JM (2020) Assessment of cavitation models for compressible flows inside a nozzle. Fluids 5(3)
7. Singh S, Danish M, Saha K (2021) Numerical simulation of unsteady cavitating flow around 2-D MHKF-180 and NACA4418 hydrofoils. J Ocean Eng Mar Energy 7(3):243–259
8. Wu XC, Wang YW, Huang CG (2016) Effect of mesh resolution on large eddy simulation of cloud cavitating flow around a three dimensional twisted hydrofoil. Eur J Mech B/Fluids 55:229–240
9. Roohi E, Zahiri AP, Passandideh-Fard M (2013) Numerical simulation of cavitation around a two-dimensional hydrofoil using VOF method and LES turbulence model. Appl Math Model 37(9):6469–6488
10. Furuya O (1975) Three-dimensional theory on supercavitating hydrofoils near a free surface. J Fluid Mech 71(2):339–359
11. Cheng HY, Bai XR, Long XP, Ji B, Peng XX, Farhat M (2020) Large eddy simulation of the tip-leakage cavitating flow with an insight on how cavitation influences vorticity and turbulence. Appl Math Model 77:788–809
12. Ji B (2015) Numerical simulation of cavity shedding from a three-dimensional twisted hydrofoil and induced pressure fluctuation by large-eddy simulation, vol 134 (2012)
13. Saha K (2014) Modelling of cavitation in nozzles for diesel injection applications, p 144

14. Kermeen RW (1956) NACA4412 and Walchner profile 7 hydrofoils in noncavitating and cavitating flows. Rep. No. 47-5, 220(47), pp 1–21
15. Hidalgo V, Luo XW, Escaler X, Ji B, Aguinaga A (2015) Implicit large eddy simulation of unsteady cloud cavitation around a plane-convex hydrofoil. J Hydrodyn 27(6):815–823
16. Dular M, Bachert R (2009) The issue of Strouhal number definition in cavitating flow. Stroj Vestnik/J Mech Eng 55(11):666–674

Numerical Investigation to Optimize Geometry of Hydrofoil Shaped Container Drone

Anashwara Binod, Bobin Saji George, Deepak G. Dilip, Ebel Philip Varghese, R. Abhishek, and Arjunlal Jawaharlal

1 Introduction

A lifting surface, or foil, that acts in water is known as a hydrofoil. They are similar in look and purpose to airfoils used by airplanes. Boats that utilize hydrofoil technology are also simply named hydrofoils. As a hydrofoil craft develops speed, the hydrofoils lift the boat's hull out of the water, minimizing drag and permitting greater speeds. The lifting body that produces high lift and low drag is a hydrofoil. Because it can now produce quicker and more accurate results for various flow parameters around the geometry or model, computational fluid dynamics (CFD) has recently grown to be very important to researchers. It is simpler to determine the flow on the hydrofoil model in detail using CFD calculations. Also, it is cost effective and it gives gaining the work time instead of the experimental research and have significant prices. Under addition, variation in flow regimes around submerged hydrofoils in different angle of attack (AOA), represents the major effect of environmental condition on hydrofoils performance. Thus, an appropriate prediction of 2D hydrofoil's hydrodynamic performance is a necessity to achieve an improved architecture of hydrofoils.

Force is applied to an object when fluid flows over its surface. This force that happens perpendicular to the direction of the incoming flow is defined as the drag force parallel to the lifting force. These forces are known as aerodynamic forces if the surrounding medium is air. ANSYS Fluent software was used for the numerical analysis to derive the velocity and pressure distribution on the model surface. The coefficients of lift and drag were computed using varying relative velocities. The NACA 0012 and NACA 4412 hydrofoils were subjected to a two-dimensional turbulent flow analysis investigation at varied angles of attack and velocities.

A. Binod · B. S. George (✉) · D. G. Dilip · E. P. Varghese · R. Abhishek · A. Jawaharlal
Department of Mechanical Engineering, MBCET (Autonomous), Thiruvananthapuram, Kerala, India
e-mail: bobin.george@mbcet.ac.in

2   Literature Review and Objective

In order to have a submerged hydrofoil with higher controllability, Rediniotis et al. [1] developed a shape-memory-alloy actuated bio-mimetic hydrofoil. This hydrofoil shape can be deforming to different shapes mimicking aquatic animal swimming to advance its performance. Vassalos et al. [2] and Matin et al. [3] formulated a numerical procedure based on potential panel method to analyze the 3D NACA4412 hydrofoil performance under the free surface. They found the pressure distribution, lift, drag, and wave generated profile to study various conditions of the 3D hydrofoil near to the free surface. The hydro structural optimization-framework used in the work is taken from previously developed framework, MACH. The CFD solver have used ADflow, it is a 3D finite-volume, cell-centered multiblock solver for the compressible flow equations. The hydrodynamic loads (pressure and shear stresses) calculated by ADflow are given to the structural solver, and the displacements from the structural solver, in fact, dictate the CFD mesh movement. To obtain a efficient and compact set of geometric design variable [4], the FFD volume approach parameterizes the geometric variations rather than the model itself. All the geometric variations are performed on the outside boundary of the FFD volume. The gradient-based optimization algorithm, SNOPT is used to rise the computational efficiency by lowering the number of function evaluations for cases with a large number of design variables [5].

A model of study is created using software like CAD and is analyzed using ANSYS to estimate the performance of device based on lifting bodies such as rudder or Marine current turbines. In this paper it explains the formation of laminar separation bubble when it subjected under various hydrodynamic condition. By varying the conditions and different properties by using numerical formulas various results are obtained when analyzed using software like ANSYS. The laminar to turbulent operations operated by the laminar separation bubble transition. The procedure occurs when a laminar boundary layer is under a sufficiently high adverse pressure gradient that give rise to separation of the boundary layer. The Kelvin–Helmholtz instabilities are formed and increased in the various shear layer and lastly lead to a break-down of the shear layer, that results in a turbulent flow that reattaches to the model. A close bubble is formed in between the separation and reattachment points [6]. Model composite structures along with orthotropic materials uses solid elements in a framework to give the hydro elastic result of composite hydrofoils with different unidirectional orientations and to analyze the influence of the fiber orientation on the response. An interior structure is needed for hydrodynamic rising of bodies cause of the higher fluid loading. The model the composite hydrofoils uses the orthotropic material properties. Having an idea of how the free vibration results to variations in fiber orientation [7, 8]. For the design to be efficient, the hydrofoil chosen needs to have a higher value of lift and low drag properties. NACA4412 and NACA0012 have been selected for this purpose. Ansys Fluent 19.2 commercial solver is used for analysis.
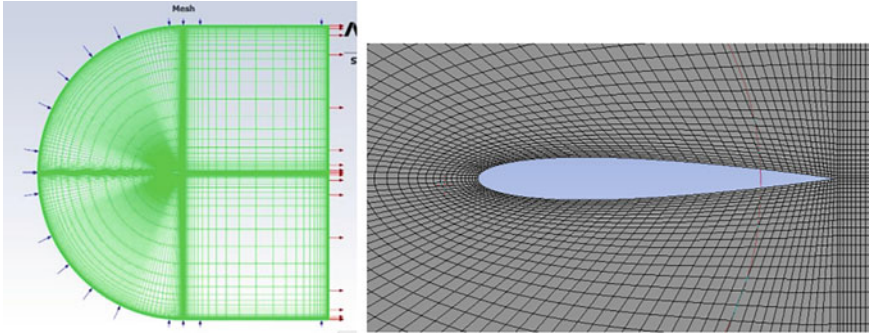
Fig. 1 Flow domain and mesh generated. The analysis has the flow around a hydrofoil at various angles of attack (4°, 8°, 12°) and varying velocities

3 Materials and Methods

The model coordinates were taken and prepared after references from the site [9], and structured mesh and un-structured mesh was created with different number of divisions and different number of elements. In order to obtain reliable resolution after trailing edge, as to attain tight cells in terms of mesh size. C-grid type is shown as structural mesh at which another node follows each of nodes consecutively. In present analysis, C type mesh with three-way velocity inlet method is used. The pressure-based implicit steady solver with realizable k-ε model turbulence model alongside second order upwind scheme is adopted for analysis. Mesh independency study was carried out and number of elements was fixed at 432,860. The domain and generated mesh is shown in Fig. 1.

4 Results and Discussion

Pressure coefficient contours at different values of attack angles were obtained for NACA0012 and NACA4412. Figure 2 depicts a general trend obtained.
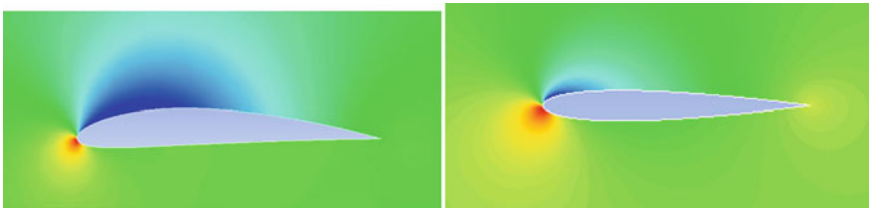
Fig. 2 Pressure contours of NACA 4412 and NACA 0012 for angle of attack 4° and velocity 5 m/s

The upper surface will be encountered by low pressure and the lower surface will be encountered by higher pressure. For this reason, the values of the lift coefficients will be rising and the values of the drag coefficients will also be rising, but the rise in drag value is less than the rise in lift values. The pressure on the lower side of each hydrofoil is higher than the pressure on the upper surface. Each hydrofoil is pushed upward more effectively into the incoming flow stream. Taking a look at the leading edge, we can see that the stagnation points where the flow velocity is almost zero for each hydrofoil. As the flow velocity accelerates over the upper surface of the hydrofoil, the velocity of the flow is completely opposite for lower surface of each hydrofoil. Figure 3 visualizes the velocity contour.

In Fig. 4, pressure coefficient distributions of the NACA0012 and NACA4412 hydrofoils at different attack angles is shown. It can be observed that the pressure coefficient varies vastly under different attack angles. Upper surface side of the hydrofoil has negative pressure coefficient and the lower surface side of the hydrofoil was positive, so the lift force of the airfoil is toward upward. When the attack angle rises, pressure coefficient difference between the lower and upper surface side is also raised. It is also found that the pressure difference coefficient is almost very lower at the trailing edge when it is much more at the leading edge. Thus, it also shows that the hydrofoil's lift force is mainly generated at the front.

Turbulent flow creates more friction drag than laminar flow due to its greater interaction with the surface side of the hydrofoil. In Fig. 5, since a turbulent boundary layer has more energy to oppose an adverse pressure gradient, it's often forces to the boundary layer to turn turbulent over fuselages to reduce overall drag. The two
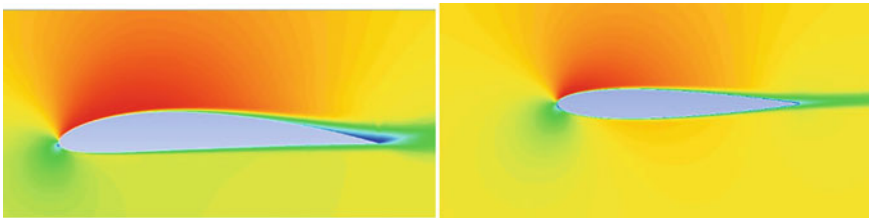
Fig. 3 Velocity contours of NACA 4412 and NACA 0012 for angle of attack 4° and velocity 5 m/s
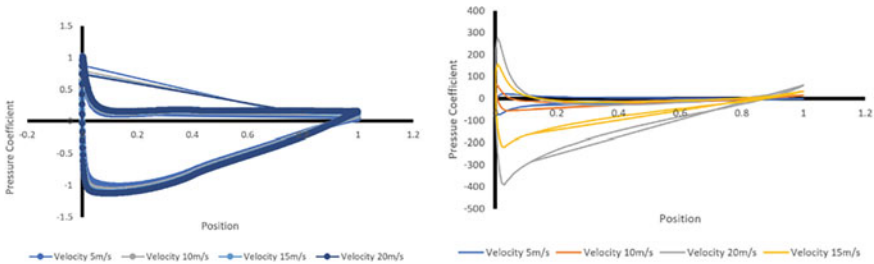
Fig. 4 Pressure coefficient values for NACA4412 and NACA0012
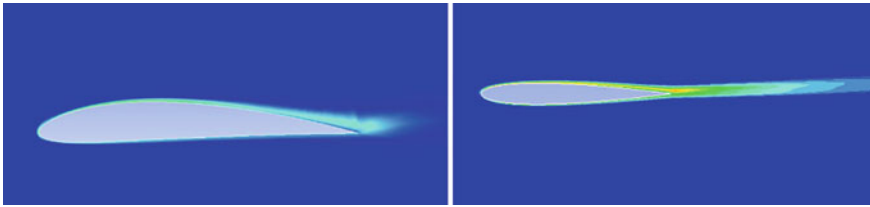
Fig. 5 Turbulence contour for NACA4412 and NACA0012 for angle of attack 4° and velocity 5 m/s
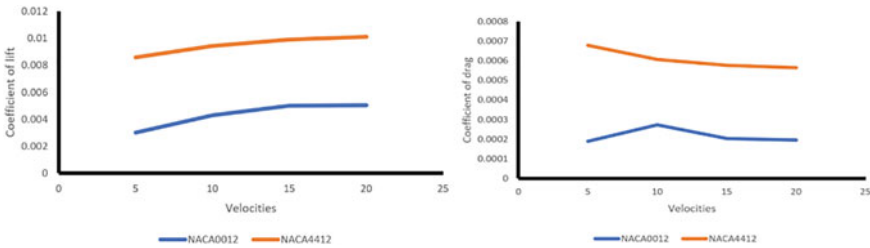
Fig. 6 Coefficient of lift and drag versus velocities

variables of turbulence effect are turbulent kinetic energy (k), it finds the energy in turbulence, and turbulent dissipation rate (epsilon), which finds the rate of dissipation of turbulent kinetic energy. So, k–epsilon model is used for having the turbulence model. With the increase in fluid free stream, the turbulence intensity causes delay of the stall angle and the maximum lift coefficient. However, it causes the increase in drag coefficient as shown in Fig. 6.

5 Conclusions

Analysis of hydrodynamic performance of NACA0012 and NACA4412 hydrofoils have been performed at different values of attack angles (4°, 8°, 12°), and using the Realizable k–ε turbulence model. The 2D analysis of the hydrofoil shaped models to navigate small and shallow waters is completed. The efficient design so that maximum performance can be obtained in an NACA0012 model. The effectiveness of the said is done by CFD. It can be seen that on the velocity magnitude figures, the upper surface side's flow velocity is higher than the lower surface's flow velocity and flow velocity of the upper surface rises with the rising of attack angles. It can be observed that from the pressure coefficient contours, pressure of the lower surface side of the hydrofoil increases with increasing attack angles. And also, the upper surface side of the hydrofoil has negative pressure coefficient and the lower surface of hydrofoil was positive, so the lift force of the hydrofoil is upwards. When the pressure

coefficient contours of NACA0012 and NACA4412 are observed, it can be taken that NACA4412 will have higher pressure gradient at each angle of attack. When the velocity magnitude contours of NACA0012 and NACA4412 are observed, it can be seen that the lower surface side of the asymmetric hydrofoil (NACA4412) provides more lift than the lower surface side of symmetrical airfoil (NACA0012). When the pressure coefficient of NACA0012 and NACA4412 is examined, it is realized that area of negative pressure for NACA4412 is larger than NACA0012. From the turbulence contour it is observed that after the leading edge of NACA0012, the effect of turbulence increases, then decreases at the tailing edge. From the coefficients of lift and drag changes with the angle of attack, it can be seen that the hydrofoil NACA0012 is more efficient shape than hydrofoil NACA0012 at every attack angles. Because of the lower coefficient of drag values observed in NACA 0012, it is opted as the more self-propelling model compared to NACA4412.

References

1. Rediniotis OK, Wilson LN, Lagoudas DC, Khan MM (2002) Development of a shape-memory-alloy actuated biomimetic hydrofoil. J Intell Mater Syst Struct 13(1):35-49. https://doi.org/10.1177/1045389X02013001534
2. Vassalos D, Xie N, Jasionowski A, Lee BS (2007) Dynamic stability of the air-lifted catamaran. Proc Inst Mech Eng, Part M: J Eng Marit Environ 221(4):137–146. https://doi.org/10.1243/14750902JEME97
3. Matin RK, Ghassemi H, Arzideh MH (2016) Numerical study of the effect of geometrical changes on the airfoil aerodynamic performance. Int J Fluid Mech Res 43:28–38. https://doi.org/10.1615/InterJFluidMechRes.v43.i1.30
4. Burrows CR (2000) Fluid power systems—some research issues. Inst Mech Eng Part C: J Mech Eng Sci 214:203–220
5. Garg N et al (2019) Experimental investigation of a hydrofoil designed via hydrostructural optimization. J Fluids Struct 84:243–262
6. Delafin P-L, Deniset F, Astolfi J (2014) Effect of the laminar separation bubble induced transition on the hydrodynamic performance of a hydrofoil. Eur J Mech B/Fluids 46. https://doi.org/10.1016/j.euromechflu.2014.03.013
7. Liao Y et al (2019) Viscous fluid–structure interaction response of composite hydrofoils. Compos Struct 212:571–585
8. Panigrahi DC, Mishra DP (2014) CFD simulations for the selection of an appropriate blade profile for improving energy efficiency in axial flow mine ventilation fans. J Sustain Min 13(1):15–21
9. https://airfoiltools.com/

Drag Computation on Rough Surfaces Using a Homogenised Model

Y. Sudhakar and Sahaj Jain

1 Introduction

Flows over rough walls are important in many practical applications including super-hydrophobic surfaces, wind turbines, ship hulls, and biomimetic drag-reduction methods. The existence of roughness elements significantly alters the surrounding fluid flow, and understanding them is important owing to the variety of applications mentioned above. One way of numerically studying flows involving rough surfaces is to resolve the roughness scales in the computational mesh. Such geometry-resolved simulations (called as DNS) are computationally expensive due to the multiscale characteristics: the microlength scale (l) is much smaller than the macrolength scale (H), leading to the scale separation parameter, $\eta = (l/H) \ll 1$.

Owing to the practical problems with DNS, effective models are being developed for numerical studies of fluid flows involving rough surfaces. In an effective model, the physical roughness elements are chopped off, and a fictitious interface above the crest plane of rough elements are introduced. On the fictitious surface, the effect of rough elements are expressed by means of interface conditions. The accuracy of effective models is dictated by how closely the interface conditions mimic the effect of physical roughness elements.

The most commonly used interface condition is the Navier-slip condition [2, 10], which relates the tangential velocity at the interface to the velocity gradient in the direction normal to the interface

$$u_1 = \lambda \frac{\partial u_1}{\partial x_2}, \tag{1}$$

Y. Sudhakar (✉) · S. Jain
School of Mechanical Sciences, IIT Goa, Farmagudi 403401, India
e-mail: sudhakar@iitgoa.ac.in

where λ is the slip length. Besides rough walls, the above condition is used in modelling superhydrophobic walls [9], liquid-infused surfaces [6], and flows over porous media [1, 7].

The Navier-slip condition, with a single scale value λ modelling the effect of roughness, is valid only for isotropic rough geometries. For a general anisotropic rough elements, the tensorial form of the above condition is proposed. Such a formulation replace the scalar λ with a second order mobility tensor [4].

Majority of the effective models use the Navier-slip condition or its tensorial form for the tangential velocity and zero wall-normal velocity as interface conditions. By investigating mass conservation over a control volume surrounding the rough elements, Lacis et al. [8] have demonstrated that the transpiration velocity is zero only when the slip velocity is constant throughout the interface length. They also derived a formula for transpiration velocity in their transpiration resistance (TR) model. Despite being much smaller in magnitude than the tangential velocity, transpiration dictates the physics of turbulent flows, as shown in [5]. Sudhakar et al. [11] rigorously derived the TR model using a multiscale homogenisation technique.

There are two limitations associated with existing effective models for rough surfaces: (1) They are derived only for flat interfaces aligned along one of the axes of Cartesian coordinates; the only exception is [12], which reported laminar and turbulent flows over a sphere coated with rough elements. (2) The main aim of the existing models is on capturing interface velocity. Although practically important, computation of drag on rough walls using homogenised formulations is not addressed.

In a recent work, Sahaj and Sudhakar [3] addressed the aforementioned limitations by deriving the TR model in polar coordinates. Moreover, they proposed two constitutive parameters, called stress correction factors, for computing components of drag on rough surfaces. In this paper, we provide additional results on flow over a rough cylinder and discuss the limitation of that model.

The paper is organised as follows. The effective interface conditions in Cartesian and polar coordinates are presented in Sect. 2. Section 3 discusses results on flow over rough cylinder, and the limitation of the model is demonstrated in Sect. 4 by considering a lid-driven cavity problem with rough bottom wall.

2 Effective Interface Conditions

This section details interface conditions of TR model in both Cartesian and polar coordinates. The conditions involve a shear-induced tangential velocity, and a transpiration velocity that is driven by the gradient of tangential velocity along the tangential direction.

In Cartesian coordinates, the TR model was derived by Lacis et al. [8]. The interface conditions are

$$u_1 = \mathcal{L}_{11}\left(\frac{\partial u_1}{\partial x_2} + \frac{\partial u_2}{\partial x_1}\right)$$
$$u_2 = -\mathcal{M}\left(\frac{\partial u_1}{\partial x_1}\right). \tag{2}$$

Here u_1 and u_2 are tangential and transpiration velocity at the interface. $\mathcal{L}_{11}$ and $\mathcal{M}$ are constitutive parameters that contain all information about the geometry of the roughness elements. These constitutive parameters can be computed by solving a Stokes problems in a microscale domain, thus making the formulations free of ad hoc parameters.

Sahaj and Sudhakar [3] extended the TR formulations to polar coordinates. They made use of the fact that the tangential velocity is proportional to the shear at the interface

$$u_\theta = \mathcal{L}\varepsilon \cdot n. \tag{3}$$

By substituting the rate of strain tensor ε in polar coordinates, the form of tangential velocity can be obtained. The transpiration or radial velocity formulation can be derived by applying the principle of mass conservation to a control volume surrounding the roughness elements as shown in Fig. 1. Complete details of the derivation can be found in [3].

The interface velocity conditions in polar coordinates can be summarised as

$$u_\theta = \mathcal{L}_{\theta\theta} \frac{1}{2}\left[r\frac{\partial}{\partial r}\left(\frac{u_\theta}{r}\right) + \frac{1}{r}\frac{\partial u_r}{\partial \theta}\right]$$
$$u_r = -\mathcal{M}\frac{\partial u_\theta}{\partial \theta} \tag{4}$$

Here u_r and u_θ denote velocity components along radial and circumferential directions, respectively. The constitutive parameters $\mathcal{L}_{\theta\theta}$ and $\mathcal{M}$ can be computed by solving the microscale problem in polar coordinates.

Fig. 1 Control volume around rough elements
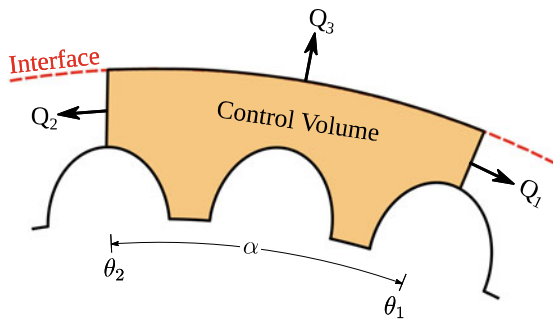
3 Flow Over a Rough Cylinder

In this section, we consider flow over a rough circular cylinder as depicted in Fig. 2. Roughness elements with height d are added to the baseline smooth cylinder of diameter *Db*. The rough cylinder is kept in a channel as shown in figure. Parabolic inlet velocity is specified at the inlet and a zero stress condition is applied at the outlet. No slip condition is applied on the rough cylinder surface and on channel walls. The Reynolds number, defined as $\mathrm{Re} = U\mathrm{max}Db/\nu$, is set to be 40. The scale separation parameter, $\eta(= d/Db) = 0.05$.

The constitutive parameters ($\mathcal{L}_{\theta\theta}$ and $\mathcal{M}$) as well as the stress correction factors ($\mathcal{S}_c$ and $\mathcal{P}_c$) can be computed from a single microscale problem. The geometry of roughness elements and the respective constitutive coefficients are given in [3]. Details of the partitioning of the total drag into pressure and viscous contributions are available in the stress correction factors.

We discuss the accuracy of interface conditions of TR model in polar coordinates (Eq. 4) by investigating the velocity components at the interface. Figure 3 shows comparison between DNS and effective of velocity components at the interface. It can be seen that along the entire length of the interface, the transverse velocity (u_θ) is predicted very accurately. The errors in radial velocity (u_r) is larger than u_θ. This is due to the fact that u_r represents a high order effect than u_θ [8, 11].

Having discussed the accuracy of interface velocities, we now analyse the applicability of stress correction factors in computing drag components. We perform DNS to get reference drag values, which can be directly obtained by integrating viscous and pressure forces on the rough surface. However, the drag components obtained from the effective model needs to be modified using stress correction factors.

$$F_v = \mathcal{S}_c F_v^{\mathrm{uncorr}}$$
$$F_p = F_p^{\mathrm{uncorr}} + \mathcal{P}_c F_v^{\mathrm{uncorr}} \tag{5}$$
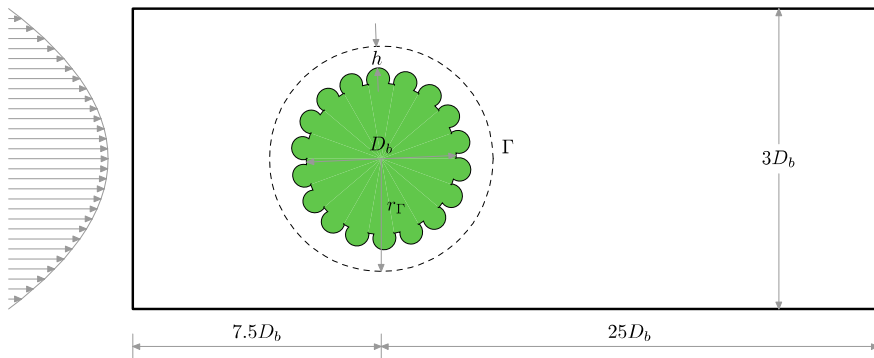
Fig. 2 Configuration of flow over a rough cylinder

Fig. 3 Velocity around the rough cylinder with elliptic roughness elements at $h = 0.1$. **a** Transverse velocity, **b** radial velocity. $\theta = 0$ corresponds to the rear end of the cylinder

(a)

(b)
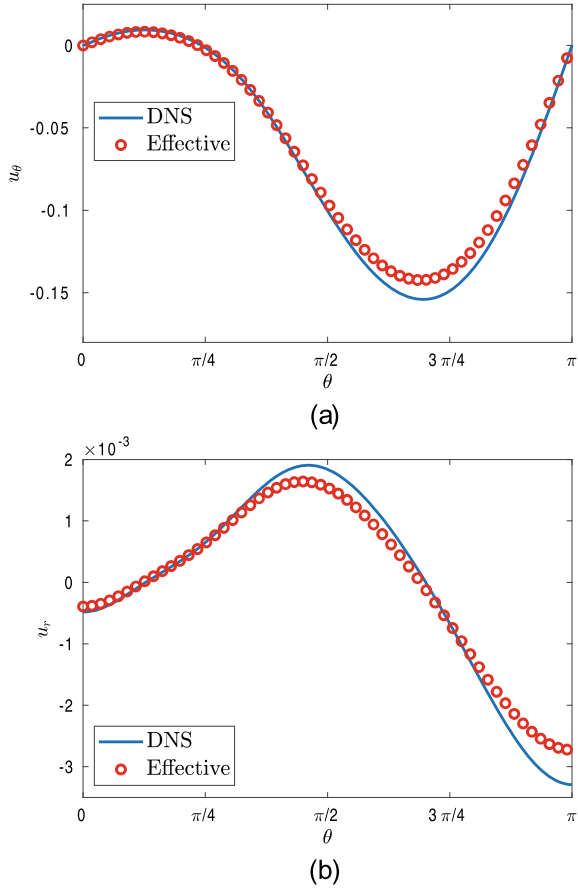
Here F_v and F_p denote viscous and form drag on rough surface, respectively. The superscript 'uncorr' implies forces computed directly on the effective interface.

Percentage of errors in drag components for square roughness elements at Re = 40 is presented in Table 1. It can be seen that uncorrected values show a large error, and after applying corrections, the accuracy of predicting drag components significantly improved. Additional results on the effect of Re and ellipse roughness elements are presented in [3].

4   Flow in a Driven Cavity

In the previous section, we have discussed a rough circular cylinder, and reported comparison of DNS and effective model. It is shown that the effective model can accurately approximate the interface velocity along the entire length of the interface.

Table 1 Percentage error in drag coefficients for flow over a cylinder with square roughness elements at Re = 40

h	Uncorrected		With correction	
	$C_{d,v}$	$C_{d,p}$	$C_{d,v}$	$C_{d,p}$
0.05	49.08	11.64	3.80	1.15
0.1	48.27	11.41	4.32	1.32
0.2	46.73	10.93	5.31	1.67
0.3	45.28	10.42	6.25	2.05

It can as well capture the drag components. One of the main assumptions used to derive transpiration-resistance model is that in the vicinity of the interface, the flow is viscous dominated. In this section, we report the performance of the model when it is used to compute drag components when the inertial effects are significant near the interface.

We consider the lid-driven cavity problem, but instead of all smooth walls as in the classical problem, the bottom wall is coated with semi-ellipse shaped roughness elements as shown in Fig. 4. The cavity size (H) represents the macroscale, while the microscale (l) is marked in the figure. We set the scale separation parameter, $\eta = (l/H) = 0.1$. The semi-major and semi-minor axis of the rough elements are set to be $0.3l$ and $0.6l$, respectively. The interface is positioned at a distance of 0.1 l from the crest plane of rough elements.

In the domain used for the effective model, a fictitious smooth interface is introduced and the roughness elements are chopped off. On the fictitious interface the

Fig. 4 Configuration of flow within a cavity with rough bottom
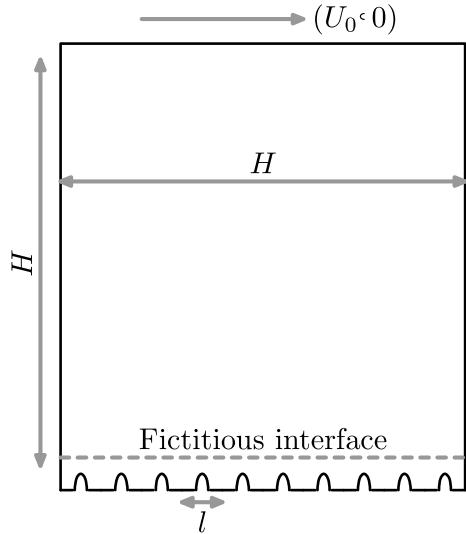
following effective boundary conditions, given by the transpiration resistance model, are applied (Eq. 2).

Reynolds numbers is defined as $Re = U_0 H / \nu$. Simulations are performed for Re of 1, 10, 100, 400, and 1000. For all five Re, both pressure and viscous component of drag are computed on the rough surface of the cavity. Due to the presence of rough elements, the pressure drag is non-zero in DNS. All simulations are repeated with the effective model; since the rough elements are discarded in the effective simulations, pressure drag is always zero. The viscous drag obtained from the model are multiplied with stress correction factors to get the pressure and viscous drag components, as given in Eq. 5.

Components of drag, computed using DNS and effective model, for different Re are presented in Fig. 5. It can be seen that for Re < 100, the model captures the drag components accurately. However, when the inertial effects becomes predominant in the interface region, the error produced by the effective model increases significantly. This is expected because the TR model is derived based on the following assumption: the viscous forces dominate the interface region.

Fig. 5 Comparison of drag components computed on the rough surface of the cavity: **a** viscous drag, **b** form drag
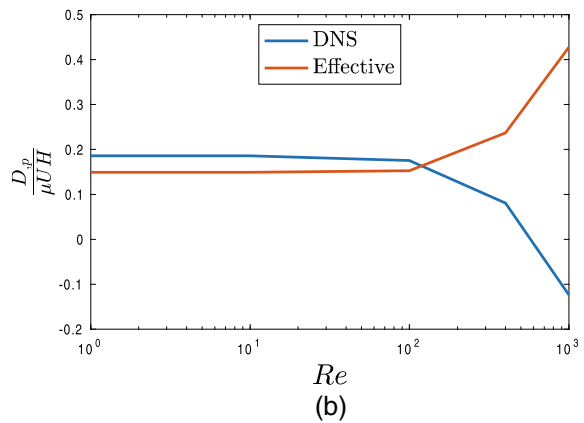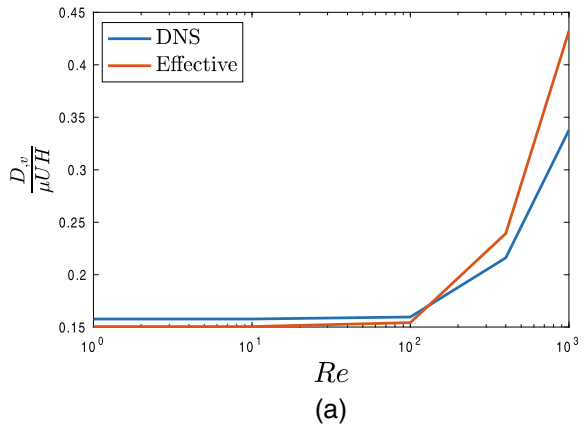
The dominance of inertial effects near the interface at high Re can be seen from two observations: (1) The drag is scaled with viscous forces; hence, if inertia were negligible both curves presented in Fig. 5 would have been a horizontal line. (2) Existence of viscous dominated flows near the interface implies that the fraction of total drag divided into pressure and viscous components remains the same, even if Re is increased. However, DNS results of pressure drag shows that at a larger Re, $D_{,p}$ becomes negative. This could be due to the presence of separated flow within the rough elements, which is a result of inertial effects.

5   Conclusions

We presented an effective model to simulate laminar flows over rough surfaces, in this paper. The flow over a rough cylinder is used as a baseline case to discuss the accuracy of the model. In addition to the interface velocities, the proposed model is able to capture drag components accurately, when the inertial effects can be neglected in the interface region. This limitation is demonstrated by considering a lid-driven cavity in which the bottom wall is coated with ordered roughness elements. In summary, the model presented here can accurately approximate interface velocities and drag components when the flow is viscous dominated in the interface regime.

Nomenclature

l	Microscopic length scale (m)
H	Macroscopic length scale (m)
η	Scale separation parameter (–)
Re	Reynolds number (–)
(u_1, u_2)	Velocity components (m/s)
U_0	Driving velocity in lid-driven cavity (m/s)
$D_{,v}$	Viscous drag (N)
$D_{,p}$	Pressure drag (N)
λ	Slip length (m)

References

1. Beavers GS, Joseph DD (1967) Boundary conditions at a naturally permeable wall. J Fluid Mech 30:97–207
2. Bolanos SJ, Vernescu B (2017) Derivation of the Navier slip and slip length for viscous flows over a rough boundary. Phys Fluids 29(5):057103
3. Jain S, Sudhakar Y (2022) Prediction of drag components on rough surfaces using effective models. Phys Fluids 34(7):073602
4. Kamrin K, Bazant MZ, Stone HA (2010) Effective slip boundary conditions for arbitrary periodic surfaces: the surface mobility tensor. J Fluid Mech 658:409–437
5. Habibi Khorasani SM, Lacis U, Pasche S, Rosti ME, Bagheri S (2022) Near-wall turbulence alteration with the transpiration-resistance model. J Fluid Mech 942:A45
6. Kim SJ, Kim HN, Lee SJ, Sung HJ (2020) A lubricant-infused slip surface for drag reduction. Phys Fluids 32(9):091901
7. Lacis U, Bagheri S (2016) A framework for computing effective boundary conditions at the interface between free fluid and a porous medium. J Fluid Mech 812:866–889
8. Lacis U, Sudhakar Y, Pashe S, Bagheri S (2020) Transfer of mass and momentum at rough and porous surfaces. J Fluid Mech 884:A21
9. Min T, Kim J (2004) Effects of hydrobhobic surface on skin-friction drag. Phys Fluids 16(7):L55–L58
10. Sarkar K, Prosperetti A (1996) Effective boundary conditions for Stokes flow over a rough surface. J Fluid Mech 316:223–240
11. Sudhakar Y, Lacis U, Pasche S, Bagheri S (2021) Higher-order homogenized boundary conditions for flows over rough and porous surfaces. Transp Porous Media 136:1–42
12. Zampogna GA, Magnaudet J, Bottaro A (2019) Generalised slip condition over rough surfaces. J Fluid Mech 858:407–436

Performance Analysis of Medium Specific Speed PAT for Back Cavity Filling Using CFD

Abhishek Namboodiri, Satish Dokiparti, Ashish Doshi, and Mukund Bade

1 Introduction

Large hydropower plants are the primary source of electricity in the majority of the world's nations. But as these plants are being built and developed, vast areas of productive land are submerged under water, resulting in the loss of ecosystems and a significant number of evacuations and rehabilitation of people. Overall, it is generally harmed by problems with the ecological balance, the socioeconomic system, and politics. A mini hydropower plant doesn't have these problems compared to this. Despite the lower power output, there are numerous benefits [1]. Micro hydropower plants (MHP) are small-scale power generation facilities that can be utilized to provide electricity in distant, off-grid places. Installing a turbine along a river or stream's course and diverting water so that it falls on the turbine can produce electricity. More than 6000 streams in India have been identified as possible locations for micro hydropower facilities [2].

Smaller hydraulic pumps can be used as turbines in MHPs to save plant costs overall. A pump that generates electricity when turning in the opposite direction is known as a pump as a turbine. The perennial streams are very difficult to locate in southern India. In this case, the pump can be operated in reverse mode to create electricity during the monsoon season when the inflows into rivers and streams are available, and in the pump, mode to pull water from deep wells or ponds during the dry season (when the stream level is very low or nil).

To enhance the performance of a PAT different geometrical modifications could be carried out. Research has been carried out on various modifications related to

A. Namboodiri · S. Dokiparti · A. Doshi · M. Bade
Department of Mechanical Engineering, SVNIT Surat, Surat 395007, India

S. Dokiparti (✉)
Mechanical Engineering Department, Sarvajanik College of Engineering & Technology, Surat 395001, India
e-mail: dsatish.3@gmail.com

impellers [3]. Also, the analysis of other flow and non-flow zones of the PAT domain was performed by some researchers both experimentally [4, 5] and numerically [6]. The analyses included the non-flow zones of the front, back, and side clearances.

In this research, back cavity filling, one of the newly proposed modifications of PAT shape [4, 5], is numerically investigated using computational fluid dynamics (CFD) software. The following hydraulic parameters would be used to assess the PAT's performance: total head, the turbine's power output, and efficiency.

2 Literature Review and Objective

The present work is focused on the numerical investigation of PAT. For any numerical analysis, it is always important to reduce the error percentage when validating with the corresponding experimental results. This mainly depends on the methods followed in the simulation, like boundary conditions, turbulence models, etc. In this section, different CFD-related works performed on the pump as turbine (PAT), by various authors across the world have been discussed.

Emma [7] carried out a performance analysis of PAT using CFD. The analysis was done for three different pumps (Ns = 37.6, Ns = 20.5, Ns = 64). Boundary conditions used were velocity at the inlet and static pressure at the outlet and the k–ε turbulence model was used because other models like Large Eddy Simulation (LES), RANS, etc. take more computational time. Multiple reference frame (MRF) was used for simulations, with the impeller being kept as a rotating zone and the casing, inlet, and outlet as a stationary zone. Simulation results matched well with the experimental results, showing an error of 4% at the Best Efficiency Point (BEP). It was observed that the power range in turbine mode was higher than that in pump mode.

Rosi et al. [8] developed a predicting model for PAT's performance in off-design operating conditions. The analysis was done using Ansys CFX for a pump with 6 backward swept blades and outlet diameter of 281 mm. The boundary conditions used were, the volume flow rate at the inlet and average static pressure at the outlet. It was observed that at slightly off-design operating conditions, the error was negligible, but at higher off-design conditions the error increased further.

Santolaria Morros [9] performed numerical modeling and flow analysis of a centrifugal pump running as a turbine for unsteady flow structures and also found the effects of unsteady flows on the global performance of the PAT. The pump modeled had 7 backward swept vanes, an outer diameter of 200 mm, and a specific speed of 0.52 rpm. The pump was analyzed in Fluent with inlet boundary condition as static pressure and outlet boundary condition as zero total pressure. The results obtained showed a good match with the experimental data deviating by approximately 10%.

Derakhshan [10] studied experimental and numerical analysis of propeller pump as turbine. The analysis was performed using the k-ε turbulence model with average static pressure as an inlet and mass flow rate as an outlet. For the walls in the fluid

domain, a roughness of 50 μm was assumed. The residual was set to 10^{-6} for convergence. The fluid domain was split into three parts: pump inlet pipe, impeller, and outlet. To get a relatively stable inlet and outlet flow. The relative error of predicted head, shaft power, and efficiency to experimental data at BEP was 4.8%, 3.8%, and 1.3%, respectively, showing an acceptable level of accuracy at BEP.

Lei [11] studied the effect of axial clearance on the efficiency of a shrouded centrifugal pump. The performance analysis was done for 3 sets of front and back clearances. Modeling of the pump was done in Pro-E and simulation in Ansys CFX with boundary conditions as mass flow rate inlet and static pressure outlet, turbulence model as shear stress transport (SST) k–ω turbulence model. The interfaces were connected using a frozen rotor MRF interface with an impeller and shrouds in the rotating zone and the remaining domain in the fixed zone. The efficiencies showed an error of 3% compared to experimental results. It was concluded on increasing the clearance size, head, and efficiency decrease, resulted in a reduction in hydraulic and overall efficiency. Also, with an increase in clearance space, the turbulence backflow increases at the impeller inlet.

Ayad [12] studied the effect of semi-open impeller side clearance on centrifugal pump performance using CFD. The CFD simulations were carried out for side clearances of 0, 1, 2, 3 mm. The impeller contained 6 backward swept blades with an eye diameter of 50 mm and an outlet diameter of 130 mm. Ansys CFX was used for analysis, with total pressure as an inlet boundary condition and mass flow rate as an outlet boundary condition. MRF was used with a frozen rotor interface, in which the impeller was considered as a rotating zone and the casing as a stationary zone. The CFD results varied by 10% from the experimental results. It was concluded that on increasing the side clearance space, head and efficiency decrease, resulting in the shifting of BEP toward the left.

Wang et al. [3] performed a numerical analysis of PAT with a specially designed impeller. The impeller had forward curved vanes and its performance was compared with a regular PAT with backward curved vanes. For CFD analysis the boundary conditions taken were inlet mass flow rate and outlet static pressure with k-ε turbulence model and convergence criteria of 10^{-6}. The results showed that the change in geometry gave an improvement of about 8% in the overall efficiency of PAT.

2.1 Objectives of the Work and Problem Definition

Based on the literature review, the objectives of this work would be:

- To perform 3D numerical analysis of a centrifugal pump of a specific speed of 54 rpm, running in reverse mode (turbine mode) at 1000 rpm.
- To determine numerically, the performance characteristics of the selected pump in PAT mode with and without back cavity filling.

As previously performed experimental results [4] for medium-specific speed PAT of 54 rpm is available through one of the authors of this paper, it is selected for CFD analysis. Further, for the given PAT, using CFD software Ansys Workbench, validate the model with basic characteristics.

3   Numerical Analysis

The geometry of a centrifugal pump with a specified speed of 54 rpm was created by using a Coordinate Measuring Machine (CMM), as shown in Fig. 1. Once the fluid models of impeller and volute were generated, inlet and outlet pipes were added using the Design Modeler module in Ansys Workbench, and then they were joined to the volute casing using the Boolean command.

The meshing model in Ansys Workbench was utilized to mesh the entire domain as shown in Fig. 2. The unstructured mesh was chosen even though structured mesh produces results that are more accurate due to computational power limitations. To better capture the flow and ensure a smooth transition of flow from the volute to the impeller, the contact/interface zone between the impeller and the volute was given using multiple frame references.

Figure 3 shows the meshing of two different fluid models of the same geometry.

As shown in Fig. 4, the boundary conditions used were: inlet-mass flow rate and outlet-static pressure. The turbulence model used was a $k–\varepsilon$ model. The wall function is considered scalable, l. The convergence criterion was set to a residual value of 10^{-4}. The steady-state analysis was used with the upwind advection schemes.

Fig. 1 Geometrical model of the selected pump
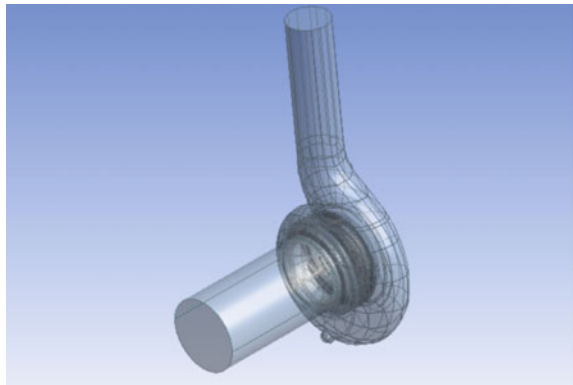
Fig. 2 Meshed model
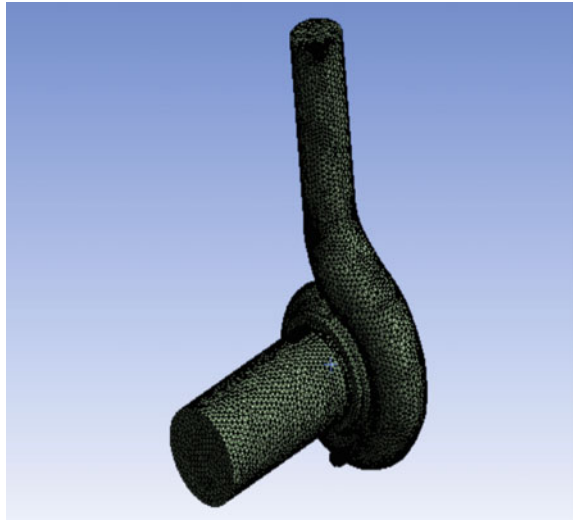
Fig. 3 Meshed fluid model **a** backside of initial geometry **b** backside of modified geometry (with BCF)
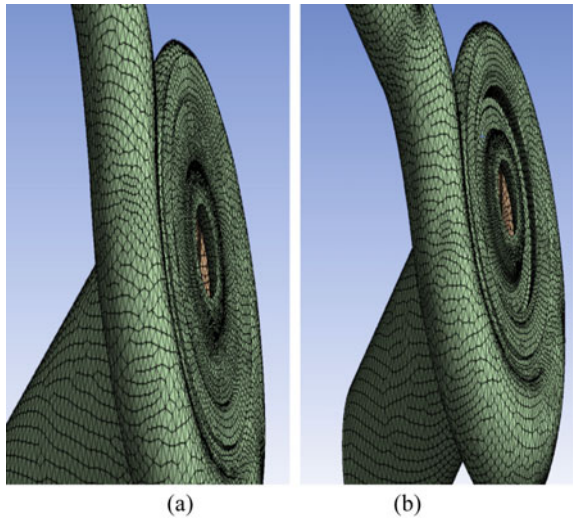
(a)   (b)

4 Results and Discussion

4.1 Grid Independence Test

The grid independence study was carried out at BEP for a shaft speed of 1000 rpm, taking element sizes as 10, 9, 8, 7, 6, and 5 mm. As shown in Fig. 5, it was seen that once the element size was less than 7 mm, there was not much change in the output

Fig. 4 Boundary conditions
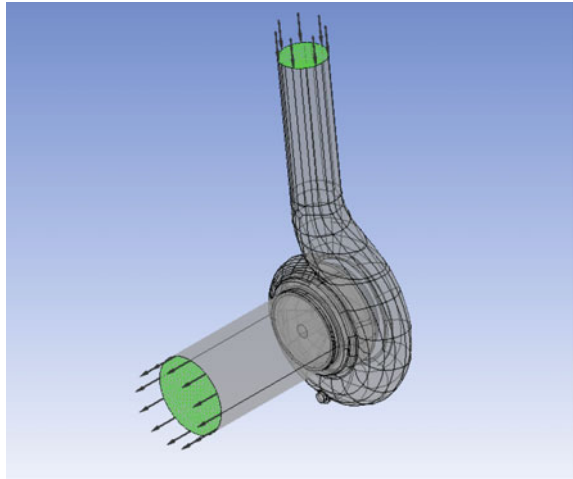
Fig. 5 Grid independence test
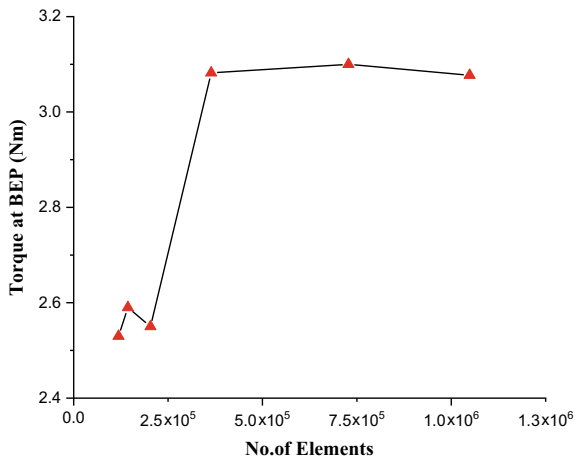
torque. Hence, 7 mm was considered the optimum element size, and the grid for that element size was chosen as the independent grid size. All the simulations on PAT were performed at this grid size.

4.2 Performance Characteristics of Initial Geometry

The performance characteristics of PAT are plotted at 1000 rpm. The results obtained from the CFD simulations were validated with experimental results [4].

The parameters taken for validation are Total Head, Mechanical Power, and Overall Efficiency.

The total head on the turbine can be calculated in the simulation as [13]:

$$H_T = \frac{p_1 - p_2}{\rho g} + \frac{v_1^2 - v_2^2}{2g} \tag{1}$$

Subscripts 1 and 2 represent the inlet and outlet of PAT.

Mechanical Power can be calculated as [5]:

$$P = \frac{2\pi NT}{60} \tag{2}$$

The overall efficiency of the turbine can be calculated as [5]:

$$\eta = \frac{P}{\rho g Q H_T} \tag{3}$$

Figures 6, 7 and 8 show the characteristics curve of Total Head, Mechanical Power, and Overall Efficiency with flow rate. The graphs generated from the numerical results follow the correct trend as that of the general characteristic curves of a turbine. When compared to the experimentally obtained results, the CFD results for 1000 rpm, show absolute average percentage errors of 17%, 4%, and 11% for the head, output power, and efficiency, respectively. The BEP obtained from CFD lies at a flow rate more than that of the experimental BEP.

Fig. 6 Total head (H_T) versus flow rate (Q) curve
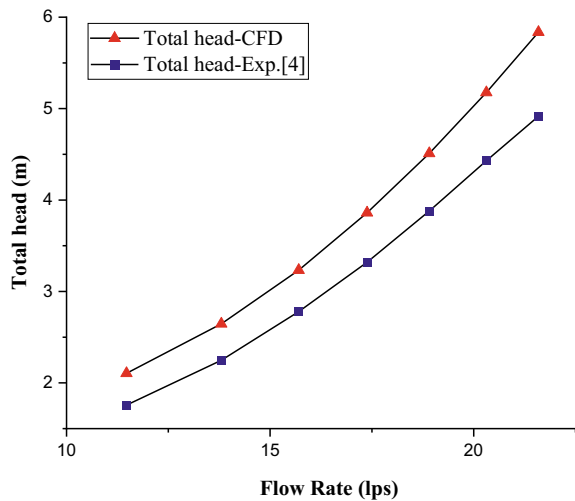
Fig. 7 Mechanical power (*P*) versus flow rate (*Q*) curve
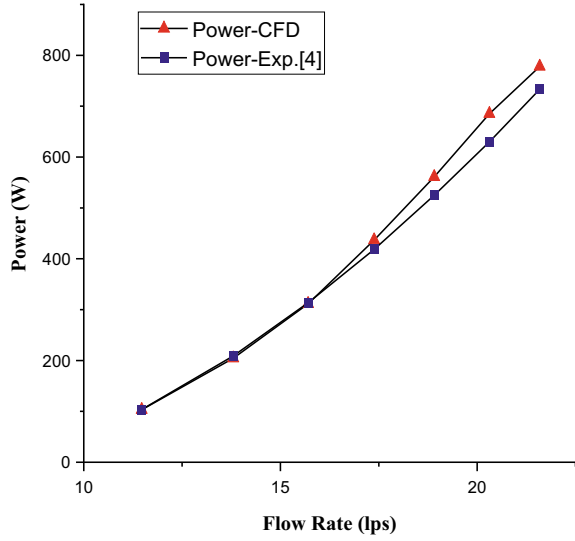
Fig. 8 Overall efficiency (η) versus flow rate (*Q*) curve
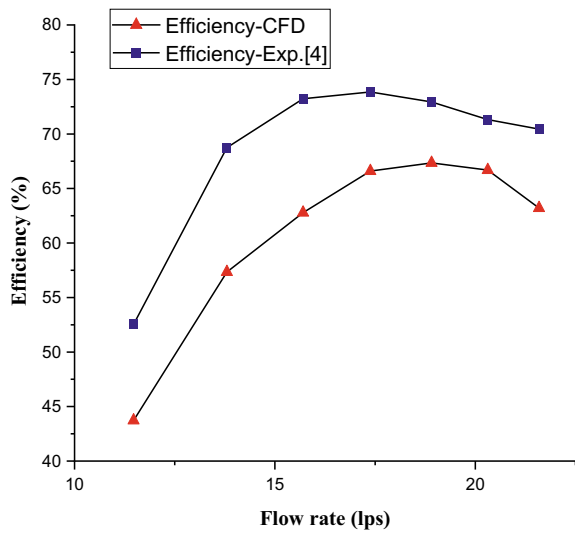
This could be because of the slight error in geometry modeling, occurring due to inaccuracies in the CMM. Since the errors are in and around 15%, the numerical method adopted can be considered an effective tool in the performance prediction of PAT.

4.3 Internal Flow Study and Comparison

To study the internal flow physics of PAT, pressure and velocity contours are plotted on two planes. Firstly, the contours are plotted on the mid-plane of the domain, which shows the velocity and pressure variations near the impeller blades and also the inlet pipe, and secondly, they are plotted on the meridional plane of the domain, showing the pressure and velocity changes along the outlet pipe and the back cavity region as shown in Figs. 9, 10, and 11.

From Figs. 9, 10, and 11, it can be seen that the pressure inside the volute is lesser for the modified geometry. As the pressure is less, the velocity is higher than in the initial case. Since the back cavity is filled, most of the fluid goes through the actual flow path (Flow Zone). Hence, the flow rate in the flow zone slightly increases, which also increases velocity in the flow zone, since the area of the flow zone remains constant in both cases.

From Fig. 12, i.e., the contours on the meridional plane, it can be noticed that the thickness of the boundary layer along the top and bottom walls of the outlet pipe is reduced as compared to the initial case. Due to this, the mean velocity in the outlet pipe has increased, resulting in higher outlet velocity, and reduced total head. Also, the wake regions that appeared in the back cavity region (seen in the initial geometry) are no longer visible, indicating negligible entry of fluid into the back cavity. Therefore, the losses that occurred due to large boundary layers and undesired wake regions are eliminated, resulting in an increased overall efficiency of PAT.

It was found that the efficiency improved by 2% (approx.) at BEP when the geometry was modified whereas the efficiency improved by 3.5%, at off-loading conditions.

5 Conclusions

Steady-state numerical analysis using Ansys Workbench was carried out on a medium-speed centrifugal pump (specific speed—54 rpm), running in reverse mode for different flow rates. The performance characteristics were predicted using CFD and validated using available experimental data [3]. Apart from validation, the CFD simulations were performed on a modified geometry of the same pump. A back cavity filling was added, and the performance characteristics were plotted to compare the results with the initial simulation and check for improvement. The internal flow analysis was also performed for both cases. The simulations were carried out at flow rates ranging from 11 to 21 lps for both the geometric modifications, i.e., with and without back cavity filling (BCF).

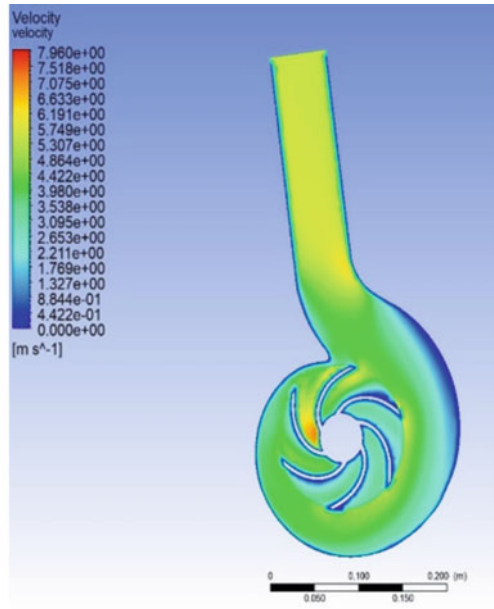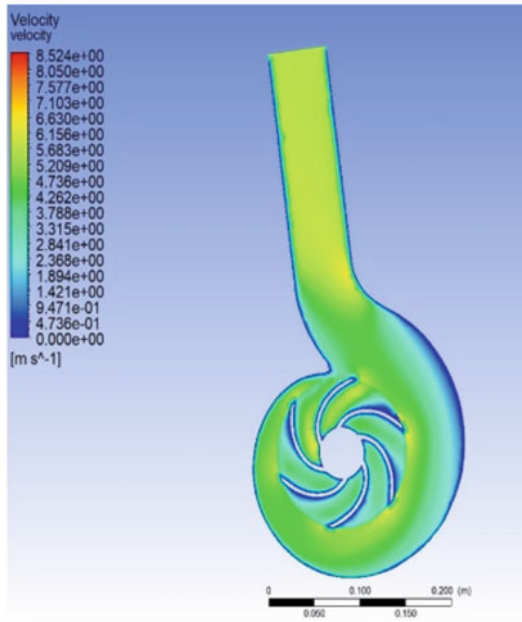**Fig. 9** Pressure contours along a mid-plane at BEP **a** with BCF **b** without BCF
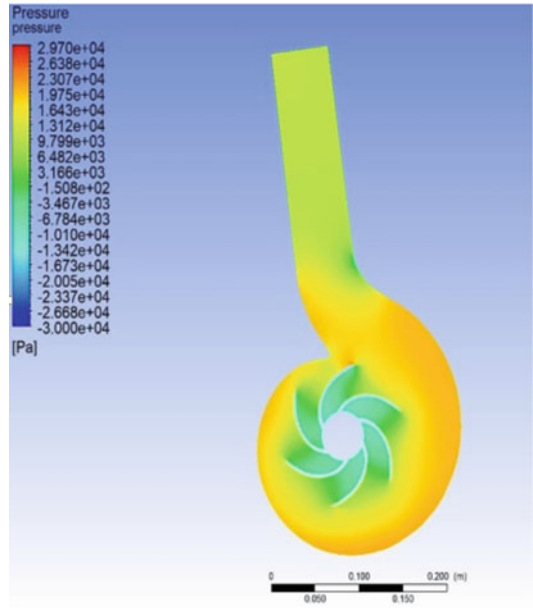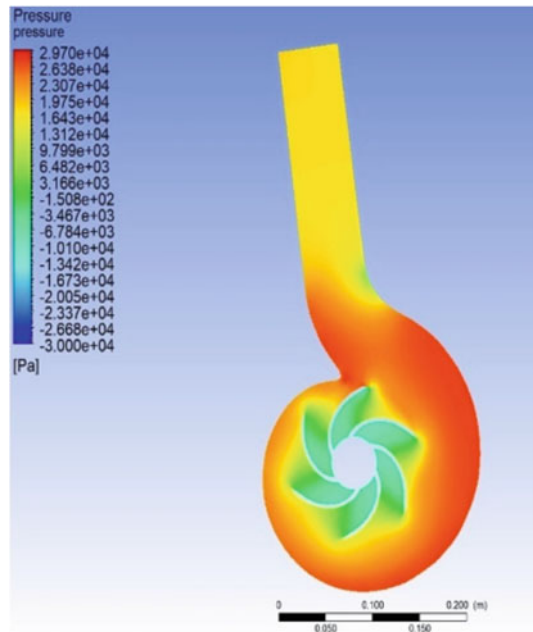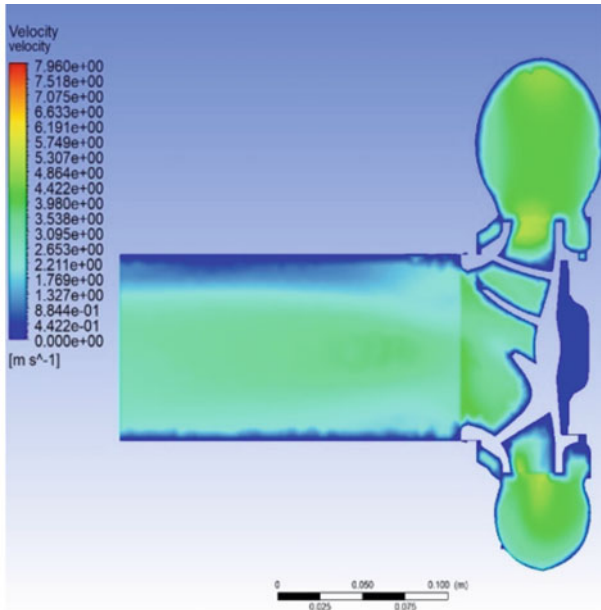
Fig. 10 Velocity contours
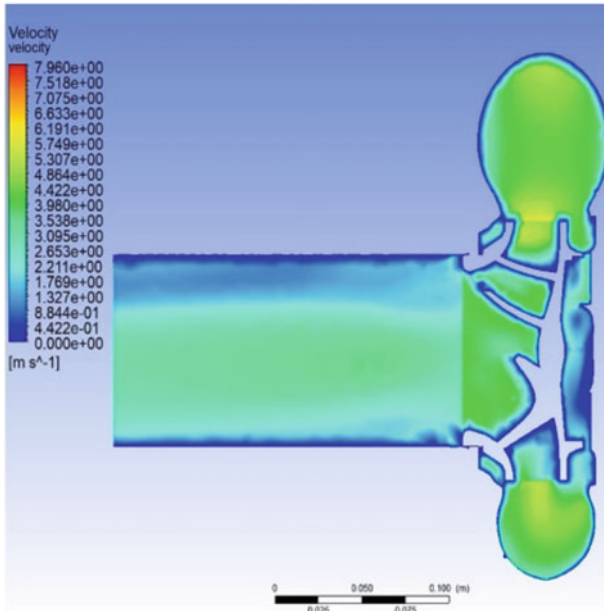along a mid-plane at BEP
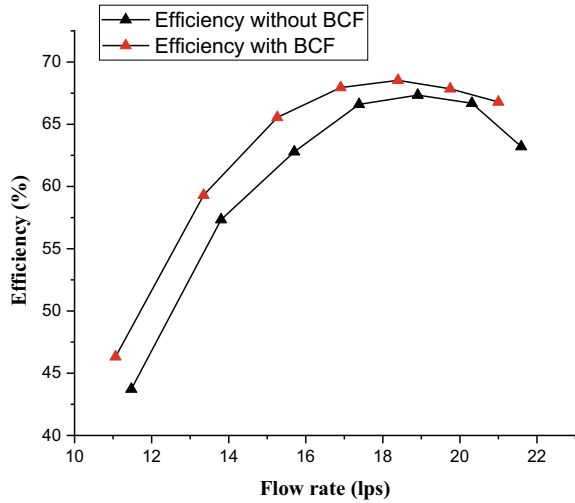**a** with BCF **b** without BCF

(a)

(b)

(a)

(b)

Fig. 11 Velocity contours along a meridional plane at BEP **a** with BCF **b** without BCF

Fig. 12 Efficiency comparison of two geometries

The following conclusions were drawn:

- The CFD simulation results for Total head, Mechanical power, and Overall efficiency had an average absolute deviation with respect to experimental results of 17%, 4%, and 11%, respectively, at 1000 rpm.
- The performance analysis was done on the back cavity-filled geometry and a 2% rise in overall efficiency was observed when compared with the initial geometry's results.
- The internal flow physics was studied for both cases by plotting pressure and velocity contours on two planes at BEP. It was observed that the losses occurring due to higher turbulence in the back cavity region and thicker boundary layers in the outlet pipe, were reduced, resulting in improved efficiency of the PAT.

Nomenclature

k	Specific turbulent kinetic energy (m^2/s^2)
g	Acceleration due to gravity (m/s^2)
H_T	Total head (m)
N	Rotational speed (rpm)
P	Output power (W)
Q	Flow rate (m^3/s)
T	Output torque (Nm)
ε	Turbulent kinetic energy dissipation rate (m^2/s^3)
η	Efficiency (%)

ρ Fluid density (kg/m^3)
v Velocity (m/s)
p Pressure (Pa)

References

1. Binamaa M, Sua W-T, Lia X-B, Lia F-C, Weia X-Z, Anc S (2017) Investigation on pump as turbine (PAT) technical aspects for micro hydropower schemes: a state-of-the-art review. Renew Sustain Energies
2. Jain SV, Patel RN (2014) Investigations on pump running in turbine mode: a review of the state-of-the-art. Renew Sustain Energy Rev
3. Wang T, Wang C, Kong F (2017) Theoretical, experimental, and numerical study of special impeller used in turbine mode of centrifugal pump as turbine. Energies
4. Doshi A, Channiwala S, Singh P (2018) Influence of nonflow zone (back cavity) geometry on the performance of pumps as turbines. J Fluids Eng
5. Doshi A, Channiwala S, Singh P (2016) Inlet impeller rounding in pumps as turbines: An experimental study to investigate the relative effects of blade and shroud rounding. Exp Therm Fluid Sci
6. Singh P, Nestmann F (2011) Internal hydraulic analysis of impeller rounding in centrifugal pumps as turbines. Exp Therm Sci
7. Frosina E (2017) A performance prediction method for pumps as turbines (PAT) using a computational fluid dynamics (CFD) modeling approach. Energies
8. Rosi M, Nigro A, Renzi M (2018) A predicting model of PaTs' performance in off-design operating. Hong Kong, China
9. Santolaria Morros C (2019) Numerical modelling and flow analysis of a centrifugal pump running as a turbine: unsteady flow structures and its effects on the global performance. Power Energy
10. Derakhshan S (2014) Optimization, numerical and experimental study of propeller pump as turbine
11. Lei C (2015) Effect of axial clearance on the performance of pump. Fluids Eng
12. Ayad AF (2020) Effect of semi-open impeller side clearance on the centrifugal pump. Aerosp Eng Technol
13. Lal J (2008) Hydraulic machines. Metropolitan Book Co. Private Ltd., New Delhi

Investigation of the Flow Physics in an Oscillating Lid-Driven Cavity with a Concentric Square Obstacle Using the Lattice Boltzmann Method

Prabir Sikdar, Sunil Manohar Dash, and Kalyan Prasad Sinhamahapatra

Nomenclature

Re   Reynolds number
Ls^* Dimensionless size of the square obstacle
ω Dimensionless Oscillation frequency
L Length of the square cavity (LBM unit)
U Maximum horizontal velocity of the top lid (LBM unit)
T Time interval of an oscillating cycle
ρ Fluid density (LBM unit)
$\boldsymbol{u}$ Flow velocity (LBM unit)
f Density distribution function
τ Single relaxation time factor
α Lattice direction

1 Introduction

Flow inside a lid-driven cavity (LDC) is a fundamental problem in fluid mechanics in which the top wall moves with a constant velocity, and the remaining cavity walls are generally stationary. Typical industry applications of LDC involve mixing of solid particles in the fluid domain [1] and polymer processing [2], etc. In general, the top lid's uniform motion results in poor fluid mixing within the cavity. There have been many studies where an oscillating lid is used to enhance fluid mixing. In this study, an oscillating top lid-driven cavity with a concentric square obstacle has been

P. Sikdar (✉) · S. M. Dash · K. P. Sinhamahapatra
Department of Aerospace Engineering, IIT Kharagpur, Kharagpur, West Bengal 721302, India
e-mail: iamprabirsikdar@gmail.com

investigated to further characterise the fluid mixing in the enclosed annular space of the cavity.

2 Literature Review and Objective

The flow regime inside the LDC usually consists of one primary vortex and several counter-rotating corner vortices [3, 4]. It is found that at higher Re, the position of the primary vortex shifts towards the cavity centre, and the size of the corner vortices grow. In order to enhance fluid mixing in the enclosed cavity space, many studies have suggested the use of an oscillating lid motion [5–7]. Note that an oscillating lid creates enhanced instability in the fluid domain, facilitating better flow mixing. Mendu and Das [5] numerically investigated the effect of oscillating frequency (ω) of the cavity lid and Re on the development of vortices inside the LDC. It was found that at a fixed Re, as the ω increases, the number of vortices inside the cavity decreases, resulting in poor fluid mixing. Nishimura and Kunitsugu [7] studied the effect of ω and cavity aspect ratio and observed that the degree of fluid mixing increases for a higher aspect ratio of the cavity.

Interestingly, the presence of an obstacle inside the LDC can considerably modify the fluid mixing [8, 9] within the enclosed cavity space. Yaswanth and Maniyeri [9] placed a circular obstacle of fixed size in an oscillating LDC to increase the fluid mixing within LDC. They noticed that the oscillating lid generates the vortices, and the internal obstacle breaks them into multiple sub-vortices, and consequently, fluid mixing is enhanced. Rajan and Perumal [8] investigated the effect of various shapes of internal obstacles on the flow structure inside the cavity. They observed that secondary vortices near the obstacle improve mixing within the cavity.

The above literature review shows that the oscillating lid in the LDC with an internal obstacle can substantially augment the flow mixing in the cavity. To the best of the authors' knowledge, the effects of the size of the internal obstacle on the fluid mixing in the square LDC are unexplored. In the present study, we have attempted to address this research gap by investigating the flow physics in the square LDC with an oscillating top lid for the different-sized concentric square obstacles. Note that the annular space in the square LDC is modified with a change in the size of the internal square obstacle. In addition, we have varied the oscillating frequency (ω) of the moving top lid and Re to assess their effects on the mixing and vortical structures in the cavity. This numerical study is performed using our in-house solver based on the Lattice Boltzmann Method (LBM). Recently, the Lattice Boltzmann Method (LBM) has been extensively followed for simulating complex fluid flow problems [5, 6, 10, 11] since it has several computational advantages, including ease in parallelization and simplicity[12], etc., over the conventional CFD methods.
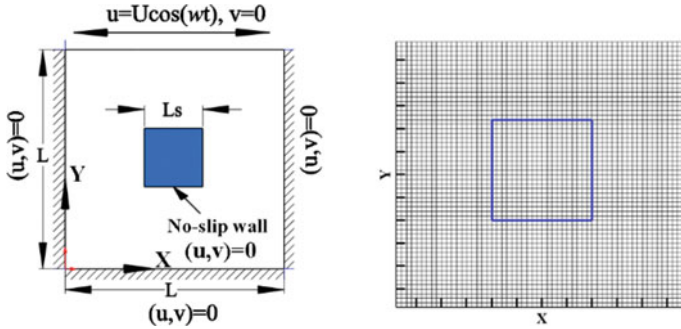
Fig. 1 Schematic diagram of the oscillating LDC with a square obstacle (left) and computational mesh (right)

3 Materials and Methods

3.1 Problem Definition and Computational Domain

The schematic diagram of the oscillating LDC and followed boundary conditions is shown in Fig. 1. Here, L represents the length of the square cavity. A square obstacle of length Ls is placed at the centre of the cavity. We have varied the square obstacle's non-dimensional length (Ls* $=$ Ls/L) from 0 to 0.5 at an interval of 0.1 without varying its central location. The instantaneous velocity of the oscillating top lid is selected as $u = U \cos(\omega t)$, U being its maximum horizontal velocity. The oscillating frequency of the lid is ω which is varied as $2\pi/6$, $4\pi/6$, and $6\pi/6$. The corresponding time interval of the oscillating cycle can be expressed as $T = 2\pi/\omega$. In this study, the Reynolds number (Re) can be defined using two different length scale: Ls and L. If we use the obstacle length Ls to define Re, for the simple LDC (Ls $=$ 0), the Re approaches zero value which is obviously not the case we are evaluating. Further, to make a fair comparison between a simple LDC and one with an obstacle, Re must be same for both the cases, which is only possible if we define Re based on the cavity length L. Hence, Re $= UL/\upsilon$ and simulations are conducted for Re $=$ 100, 400, and 1000.

3.2 Numerical Methodology

The unsteady, incompressible, laminar, and viscous flow inside the oscillating LDC can be represented using the governing Eqs. (1) and (2).

$$\frac{\partial \rho}{\partial t} + \nabla \cdot (\rho \boldsymbol{u}) = 0. \tag{1}$$

$$\frac{\partial(\rho\boldsymbol{u})}{\partial t} + \nabla \cdot (\rho\boldsymbol{u}\boldsymbol{u}) = -\nabla p + \upsilon\nabla \cdot \left[\rho\nabla\boldsymbol{u} + (\nabla\boldsymbol{u})^T\right]. \tag{2}$$

The variable ρ, $\boldsymbol{u}$, p, and υ denotes the fluid density, flow velocity, pressure, and kinematic viscosity of the fluid, respectively. Instead of solving Eqs. (1) and (2) using a conventional numerical scheme like FDM or FVM, here we have adopted the lattice Boltzmann method due to its several computational advantages, as discussed in the introduction. In the LBM framework, Eqs. (1) and (2) are solved using Eq. (3).

$$f_\alpha(\mathbf{x} + \boldsymbol{c_\alpha}\Delta t, t + \Delta t) - f_\alpha(\mathbf{x}, t) = -\frac{f_\alpha(\mathbf{x}, t) - f_\alpha^{\text{eq}}(\mathbf{x}, t)}{\tau} \tag{3}$$

The density distribution function and the corresponding equilibrium distribution function in Eq. (3) are represented by f_α and f_α^{eq}. Here α is the lattice direction, and for the D2Q9 model, it varies from 0 to 8 [5]. The variable τ is called the single relaxation time factor and is defined using BGK approximation [5, 12]. The macroscopic density and velocity are computed using Eq. (4) expressions.

$$\rho = \sum_{\alpha=0}^{8} f_\alpha \quad \text{and} \quad \rho\boldsymbol{u} = \sum_{\alpha=0}^{8} f_\alpha \boldsymbol{c}_\alpha. \tag{4}$$

Note that in the present LBM solver, the bounce-back condition is imposed at the stationary cavity walls as well as on the surface of the square obstacle to attain the no-slip velocity condition. However, for the oscillating lid, the equilibrium distribution function is modified [13] to satisfy the moving wall condition. In case of corner points, a second order accurate extrapolation is employed to determine the unknown density distribution function. Additional details of the followed LBM solver and its implementation steps can be found in the ref. [5].

3.3 Grid Independence Test

In order to ensure that our observations are independent of grid size, a grid independence study was carried out on a square lid-driven cavity with $\text{Ls}^* = 0.3$ and $\omega = 2\pi/6$ at Re = 1000. The grid sizes varied between 101×101, 201×201, and 301×301. In Fig. 2, the vertical velocity component along the horizontal centreline of the cavity is plotted for different grid sizes. The deviation in the observation is insignificant when the grid sizes are finer than 201×201. So, the grid size of 201×201 is followed in the remaining simulations of the present study.

Fig. 2 Comparison of vertical velocity component (v) along the horizontal centreline for various grid sizes at Ls* = 0.3, $\omega = 2\pi/6$ and Re = 1000. Here, U is the maximum velocity of the oscillating lid
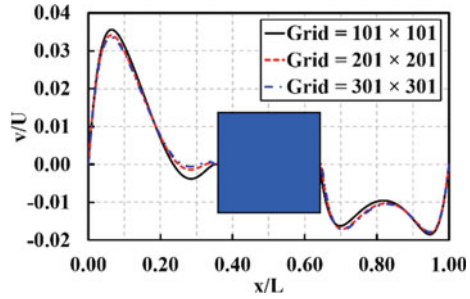
4 Results and Discussion

4.1 Validation Study

We have validated the developed LBM solver using two different cases. The first validation considers a square LDC where its top lid moves with a steady uniform velocity. Here, the Re is defined using the top lid velocity and it was varied as 400 and 1000. The u-component velocity along the vertical centreline and v-component velocity along the horizontal centreline for Ls* = 0 and $\omega = 0$ at Re = 400 and 1000 obtained in the present solver are compared with that of the Ghia et al. [3], as shown in Fig. 3a, b. They are found to be in excellent agreement.

Our second validation study considers the square LDC with an oscillating top lid at the frequency of $\omega = 2\pi/6$. The streamlined patterns in the cavity obtained in the present simulations are in good agreement with that of Mendu and Das [5] for Ls* = 0.0 and Re = 1000 at t = 0.4 T. These validations further confirm the accuracy and capabilities of the presently developed LBM solver.

In the following section, we have investigated the effects of the Reynolds number (Re) and the oscillating frequency (ω) of the top moving lid on the evolution of the flow structure in the square LDC in the presence of the square obstacle of length Ls*.

4.2 Effect of Reynolds Number (Re)

To determine the effect of the Re on the flow structures in the square LDC with an oscillating top lid, we have fixed $\omega = 2\pi/6$ and Ls* = 0.3. Re is varied as 100, 400, and 1000. The streamline pattern in Fig. 5 shows the evolution of the flow field in the cavity at different instances. Note that the flow field in the cavity is predominantly unsteady with several vortical structures. This is because of the time-varying velocity of the top lid (see Fig. 5) that substantially affects the vortex formation inside the cavity. Further, the number of vortices within the cavity considerably increases with Re (compare Fig. 5a–c), creating more unsteadiness in the enclosed space, which augments the fluid mixing.

Fig. 3 Comparison of **a** u-velocity and **b** v-velocity along the vertical and horizontal centreline, respectively of the square LDC
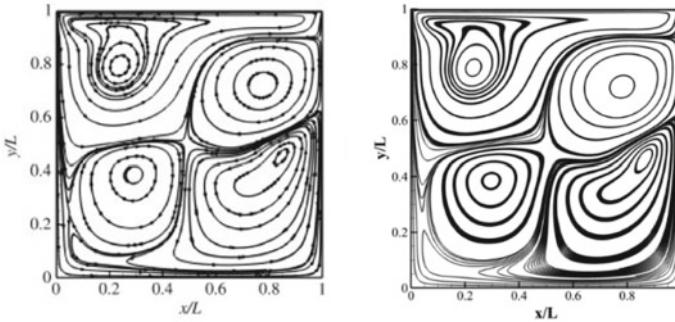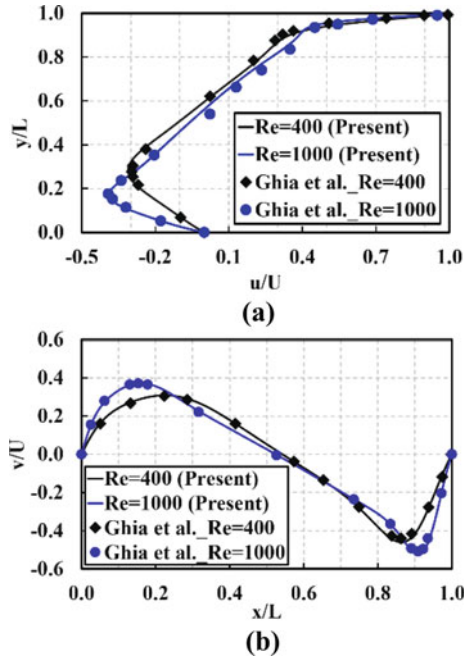

(a)

(b)

Fig. 4 Comparison of streamline pattern in the square LDC for Ls* = 0.0, $\omega = 2\pi/6$ and Re = 1000 at $t = 0.4$ T, Mendu and Das [5] (left) and present (right)

Therefore, Re = 1000 is the optimum Reynolds number producing the fluid mixing in the considered parametric space. Thus the impact of other parameters (ω and Ls*) on the evolution of the flow structures and fluid mixing rate will be discussed at this Re.
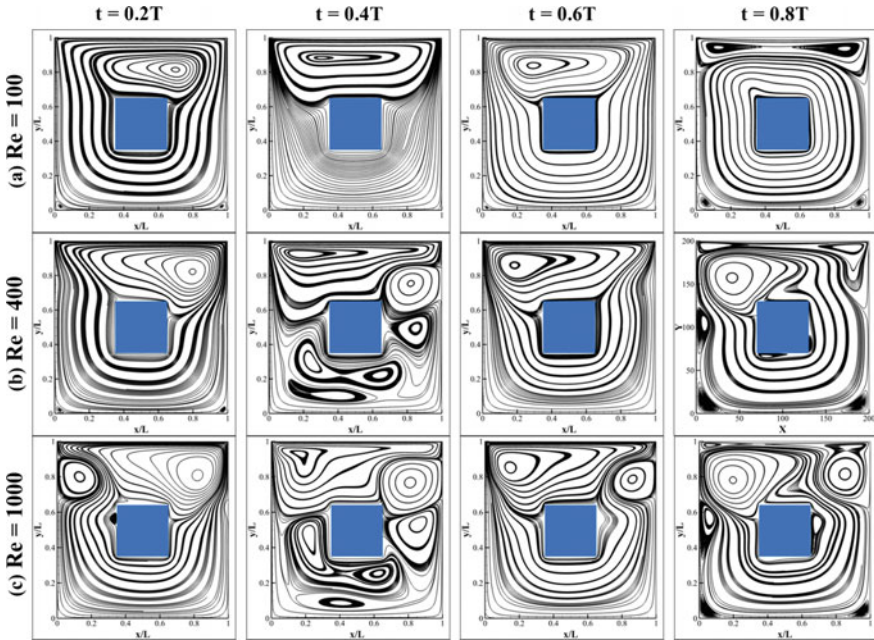
Fig. 5 Streamline plots in the square LDC at different time instances for **a** Re = 100, **b** Re = 400, and **c** Re = 1000. Here, $\omega = 2\pi/6$ and Ls* = 0.3

4.3 Effect of Oscillating Frequency (ω)

In Fig. 6, the streamlined pattern within the square LDC at oscillating frequencies of $\omega = 4\pi/6$ and $6\pi/6$ is plotted for fixed Re = 1000 and $Ls^* = 0.3$. It is noticed that the vortical structure within the square LDC is substantially modified with the variation in the oscillating frequency. The comparison of Figs. 5c and 6 shows that the number of vortices inside the cavity are more at a lower frequency ($\omega = 2\pi/6$), leading to better mixing in the enclosed cavity region. In the subsequent section, we have additionally investigated the effects of the inner square obstacle size on the evolution of the flow structures and fluid mixing rate at Re = 1000 and $\omega = 2\pi/6$ since, at this Re and ω, the unsteadiness and mixing in the fluid domain is maximum in the square LDC.

4.4 Effect of Size of Inner Obstacle (Ls*)

Figure 7 shows the variation of the streamline pattern inside the oscillating LDC for different sizes of the square obstacle ($Ls^* = 0.2$ and 0.4). Notice that the gap between the cavity wall and obstacle reduce with the increases of Ls^*, modifying the
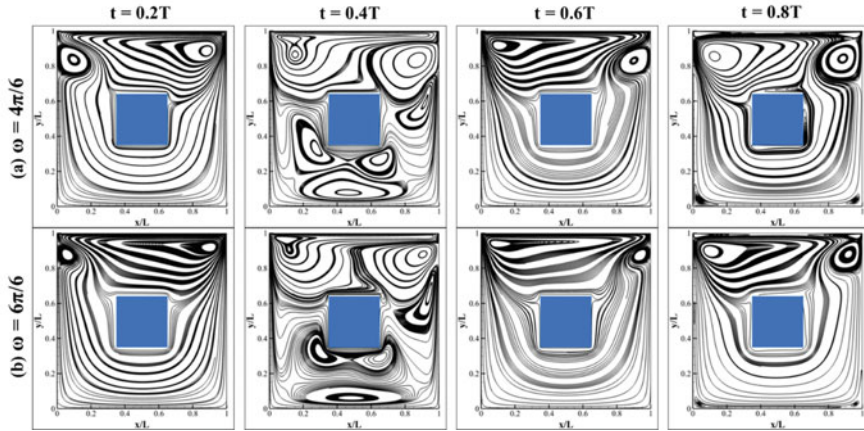
Fig. 6 Streamline plots in the square LDC at different time instances for **a** $\omega = 4\pi/6$ and **b** $\omega = 6\pi/6$. Here, Re = 1000 and Ls* = 0.3

flow structure within the cavity. Typically, densely packed streamlines are seen in the annular region of the enclosed cavity. Moreover, when Ls* increases, the vortex close to the square obstacle splits and forms secondary vortices (see in Fig. 7), leading to increased circulation and fluid mixing within the cavity. In other words, we can conclude that better fluid mixing is achieved in the smaller annular region of the cavity.
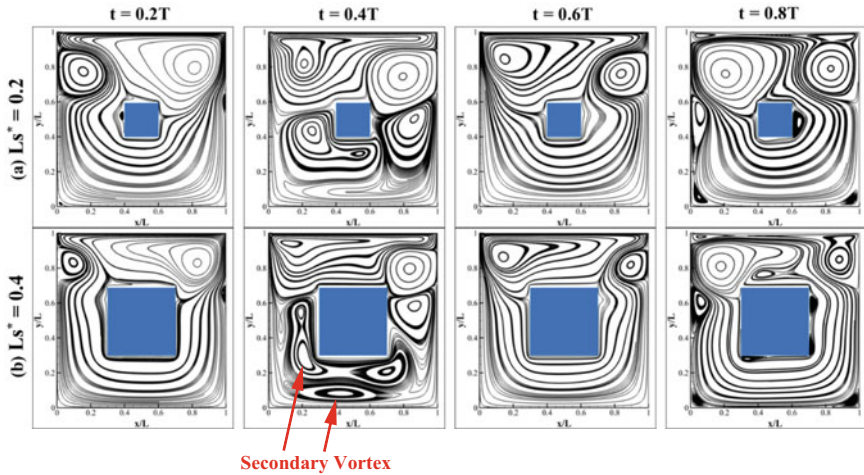
Fig. 7 Streamline plots in the square LDC at different time instances for **a** Ls* = 0.2 and **b** Ls* = 0.4. Here, $\omega = 2\pi/6$ and Re = 1000

5   Conclusions

In this study, the fluid flow inside an oscillating lid-driven cavity in the presence of the square obstacle is investigated for different Reynolds numbers (Re = 100, 400, and 1000), the oscillating frequencies of the moving top lid ($\omega = 2\pi/6$, $4\pi/6$, and $6\pi/6$) and size of the inner obstacle (Ls* = 0.0 – 0.5). It is seen that the number of vortices within the cavity is increased for higher Re and lower ω and increased Ls* consequently, the fluid mixing in the cavity region is considerably enhanced.

In the future, the study will be extended to other geometric shapes and size of the obstacle and cavity. It would be fascinating to do a thorough investigation of the flow within the lid-driven cavity using the vorticity contour and Urms plot. However, due to the conciseness of this work, we have refrained from doing so. As such, we want to include these variables into future studies in order to more precisely characterise the mixing process.

References

1. Kosinski P, Kosinska A, Hoffmann AC (2009) Simulation of solid particles behaviour in a driven cavity flow. Powder Technol 191(3):327–339
2. Canedo EL, Denson CD (1989) Flow in driven cavities with a free surface. AIChE J 35(1):129–138
3. Ghia UK, Ghia KN, Shin CT (1982) High-Re solutions for incompressible flow using the Navier-Stokes equations and a multigrid method. J Comput Phys 48(3):387–411
4. Burggraf OR (1966) Analytical and numerical studies of the structure of steady separated flows. J Fluid Mech 24(1):113–151
5. Mendu SS, Das PK (2013) Fluid flow in a cavity driven by an oscillating lid—a simulation by lattice Boltzmann method. Eur J Mech-B/Fluids 39:59–70
6. Bhopalam SR, Perumal DA, Yadav AK (2021) Computational appraisal of fluid flow behavior in two-sided oscillating lid-driven cavities. Int J Mech Sci 196:106303
7. Nishimura T, Kunitsugu K (1997) Fluid mixing and mass transfer in two-dimensional cavities with time-periodic lid velocity. Int J Heat Fluid Flow 18(5):497–506
8. Rajan I, Perumal DA (2021) Flow dynamics of lid-driven cavities with obstacles of various shapes and configurations using the lattice Boltzmann method. J Therm Eng 7(2):83–102
9. Yaswanth D, Maniyeri R (2022) Numerical study of oscillating lid driven cavity with the presence of an obstacle using immersed boundary method. Mater Today Proc
10. Sikdar P, Dash SM, Sinhamahapatra KP (2021) Lattice Boltzmann simulations of a lid-driven cavity at different moving lengths of the top lid. Fluid mechanics and fluid power. Springer, Singapore, pp 203–211
11. Sikdar P, Dash SM (2020) A numerical study on the lid-driven cavity with power-law fluids at different moving lengths of the top lid. CFD Lett 12(6):107–117
12. Succi S (2001) The lattice Boltzmann equation for fluid dynamics and beyond. Oxford University Press, Oxford, England
13. Hou S, Zou Q, Chen S, Doolen G, Cogley AC (1995) Simulation of cavity flow by the lattice Boltzmann method. J Comput Phys 118(2):329–347

CFD Analysis of Exhaust Gas Flow Through Muffler

Akash Damdhar, Saurabh Gunturkar, Sandip Dhumal, Krantisinha Jagtap, Aditya Pathak, Shubham Malkunjikar, and Pramod Kothmire

Nomenclature

P	Pressure (Pa)
V	Velocity (m/s)
T	Temperature (k)
X	Inlet tube length (mm)
ITR	Iteration

1 Introduction

A muffler serves as a crucial component in reducing the noise emanating from the exhaust of an internal combustion engine. The primary objectives of an exhaust system include the rapid and effective reduction of engine noise through the implementation of a muffler, as well as the safe release of hot and toxic exhaust gases into the atmosphere. These gases are produced in pulses, with three-cylinder engines generating three distinct pulses for each complete engine cycle. The swift movement of these pulses results in the creation of low pressure behind them. However, the back pressure generated by the exhaust system can adversely impact engine performance, leading to a reduction in pumping power. Maintaining minimal back pressure is essential for optimal engine operation. In modern automotive exhaust systems, consisting of multiple sections from the engine side to the tailpipe, the material properties of each section are directly linked to operating temperatures. These temperatures can range from 100 to 350 °C for components close to the engine, such as mufflers and

A. Damdhar · S. Gunturkar · S. Dhumal · K. Jagtap · A. Pathak (✉) · S. Malkunjikar · P. Kothmire
School of Mechanical Engineering, MIT Academy of Engineering, Alandi, Pune 412105, India
e-mail: pathak.aditya@mitaoe.ac.in

tailpipes (considered the cold section), to 600–900 °C near the engine (considered the hot section) [1].

2 Literature Review and Objective

Within the market, three main types of mufflers exist: reactive, absorptive, and hybrid. Wave cancellation, the first type, is a method employed for noise reduction. Numerous researchers have explored various muffler designs and conducted analyses on noise levels. Transfer matrix methodology has been used, incorporating an expression-based model centered on the velocity ratio concept, considering convective effects [2]. Additionally, experiments have been conducted on hybrid pressure-based compressible solvers for low Mach number acoustic flow simulation [3]. Research efforts have focused on reducing muffler weight and exploring the impact of design variations on back pressure, noise level, sound quality, and exhaust gas temperature [4]. Investigations into modifying muffler geometry have been conducted, analysing the effects of back pressure, chamber temperature, and velocity on different designs [5]. Other studies have delved into pressure drop and uniformity index of exhaust systems, considering close-coupled catalytic converters [6]. Verification of muffler configurations has been undertaken using finite element methods [7]. Further exploration involves the effects of upstream flow distribution during the cold-start period on catalytic converter performance, examined through CFD simulation [8]. Researchers have predicted the multidimensional performance of catalysts coupled with turbulent reacting flow simulations, emphasizing thermal durability through mechanical and thermal properties [9]. Numerical studies using a conservative unstructured finite-volume approach have simulated laboratory-scale catalytic converters, encompassing implicit heat and fluid flow coupling, heterogeneous chemical processes, mass transfer, and transfer [10]. A comprehensive CFD study of full-size catalytic converters has been conducted, revealing strong dependencies on converter properties, density, diffuser angle, and aspect ratio under reacting and non-reacting conditions [11]. Theoretical and experimental studies on the 3-D steady and unsteady compressible non-reacting flow inside double flow of monolith catalytic converter systems attached to 6-cylinder engines have been explored [12]. However, it is evident from the literature that the predominant focus lies on the design analysis of models with typical geometry and a single material. The literature lacks emphasis on various thermal parameters such as velocity, pressure, and temperature for different materials. Moreover, researchers have not thoroughly investigated designs by varying the inlet tube length and observing the associated parameters using different materials. In the present work, our focus is on understanding the effects of velocity, pressure, and temperature variations during gas flow by altering the inlet tube length and material composition of the muffler, thereby contributing to a more comprehensive understanding of flow distribution.

3 Materials and Methods

In this paper the study on exhaust muffler has been carried out, by changing the inlet pipe length, i.e. *X* for Steel and Aluminium material.

3.1 Materials

Nowadays, most automobiles typically use Steel and Aluminium as a material in mufflers. According to that survey, we have to examine which of the material gives optimum results in pressure drop and heat rejection rate, etc. parameters which are available at minimum cost.

1. Aluminium
2. Steel.

A loud vibrating sound is produced as the engine's exhaust valves open to release pressurized gas. Every minute, several little noises emerged and bounced down the exhaust pipe. The result is a loud and potentially unpleasant sound. The solution is to find a way to lower this sound level before it exits the exhaust system. Muffler is located in line with the exhaust pipe at the end, usually just before the tip. It has number of perforated tubes or chambers with baffles that are intended to optimize and reduce the sound output from engine. The sound waves that enter the muffler bounce off the baffles and creates opposing sound waves that cancel each other out. The baffles and chambers in mufflers can be "tuned" to provide the desired sonic impact.

The main focus of study is dependent on the following approaches:

(1) Using different materials of muffler

In this paper, Steel and Aluminium is used as a material while designing of the muffler.

Steel

Steel was first employed as an excellent review material in automobiles. Moreover, though the past years, this has mainly been utilized as a material for exhaust systems. Since Steels with better high-temperature performance and excellent corrosion resistance to encounter social objectives for spotless exhaust gases and compact design for better fuel economy [13]. As a result, the materials used to produce exhaust system components have started to shift from traditional cast metals and aluminized carbon Steel sheets to Steels, and from overall Steels to specialty Steels with higher performance.

Aluminium

The exhaust system of a vehicle should be made of a resilient, long-lasting metal because it commonly experiences dangerous chemicals and severe temperature changes. Exhausts have typically been made of cast iron or mild Steel, and although modern Plain Carbon-Steel alloys are much probably more suited to the conditions that your exhaust system must sustain.

(2)   Varying the tube length of muffler (X distance)

In first case, the inlet tube of muffler is placed within the chamber at 150 mm from inlet side of the shell. Then the boundary conditions are applied and analysis has carried out. In future work by varying the tube length of the muffler (x distance) will update and come up with proper results.

3.2 Geometry

The CAD modelling is done with CATIA V5 software for the CFD study. It consists of 1 inlet tube and 1 outlet tube and a baffle with a smaller hole in the middle of the muffler. The design of muffler is prepared using a circular shell of 250 mm diameter and thickness of 2 mm by using Aluminium and Steel. Table 1 indicates the entire dimensions of the geometry to be designed (Figs. 1, 2 and 3).

Table 1 Dimensions of designed geometry

S. No	Parameters	Measurement (mm)
1	Inlet pipe diameter	50
2	Baffle hole diameter	40
3	Thickness of muffler	2
4	Length of shell	600

Fig. 1 The length X shows the variation in inlet tube length inside the shell
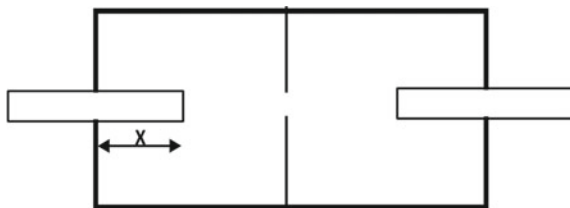
Fig. 2 Geometry of muffler with CATIA V5 software without changing inlet tube length (X)

(a)

(b)
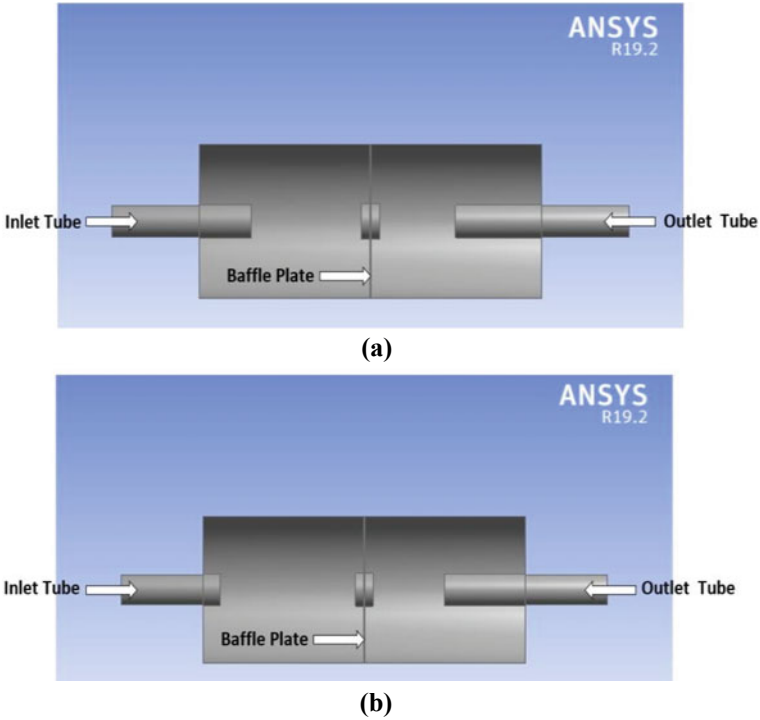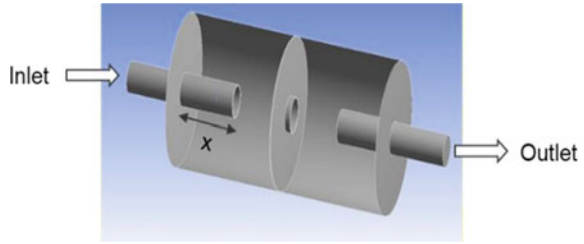
Fig. 3 Geometry of muffler with CATIA V5 software with changing inlet tube length. **a** $X = 100$ mm, **b** $X = 50$ mm

3.3 Meshing

ANSYS R19.2 was used in this study is to analyse the muffler whereas tetrahedron meshing was produced. After meshing geometry, fine meshing is utilized to obtain accurate results. The fluid domain contained the greatest number of elements feasible due to the usage of fine mesh, which also contributed to the highest possible accuracy of the flow (Fig. 4; Table 2).

Fig. 4 Meshing of geometry with 5 mm element size
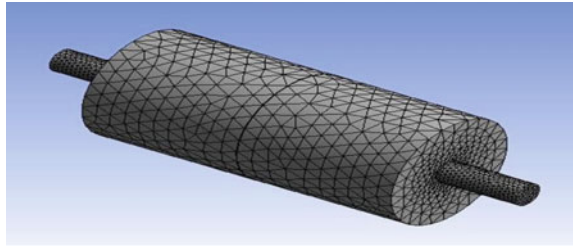
Table 2 Meshing parameters

Geometries with different Inlet tube positions	Domain	Nodes	Elements
Inlet tube length (X) at 150 mm	Shell	13,040	65,708
Inlet tube length (X) at 100 mm	Shell	11,850	59,526
Inlet tube length (X) at 50 mm	Shell	10,587	52,804

Table 3 Boundary conditions for the analysis

S. No	Parameters	Aluminium	Steel
1	Inlet velocity (m/s)	40	40
2	Temperature (K)	673	673
3	Heat transfer coefficient (W/m² k)	400	312
4	Turbulence intensity (%)	10	10

3.4 Boundary Conditions

The *k* epsilon model is the turbulence model employed in the current work. Exhaust gas having a density of 0.5508 (kg/m³) and a viscosity of 3.814e−5 (Pa) is employed as the working fluid. The inlet temperature is assumed to be 400 °C, with a mass flow rate of 180 kg/h. 10% turbulence intensity is also taken into account. Additional input and outlet boundary conditions for the study are shown in Table 3.

3.5 Governing Equations

The numerical simulation was carried out using steady state with pressure focused techniques. The partial differential equation is used to calculate overall values of mass and momentum under steady-state conditions.

The conservation of mass is described by the continuity equation and is given by

$$\frac{\partial p}{\partial t} + \frac{\partial pU_1}{\partial x_1} + \frac{\partial pU_2}{\partial x_2} + \frac{\partial pU_3}{\partial x_3} = 0 \tag{1}$$

$$\frac{\partial p}{\partial x} + \frac{\partial v}{\partial x_1} = 0 \tag{2}$$

For compressible flow

$$\frac{\partial p}{\partial t} = 0 \tag{3}$$

The momentum equation is given by CFD software

$$\rho\left(u\frac{\partial u}{\partial x} + v\frac{\partial v}{\partial x}\right) = -\rho g - \frac{\partial p}{\partial x} + u\frac{\partial^2 y}{\partial x^2} \tag{4}$$

The governing energy equation is given by,

$$\rho C_p\left(u\frac{\partial t}{\partial x} + v\frac{\partial T}{\partial x}\right) = k\left(\frac{\partial^2 T}{\partial y^2}\right) \tag{5}$$

4 Results and Discussion

In this study, we focused on the material aspect and adjusting the inlet tube length to optimize temperature distribution at the muffler outlet. Figure 5 shows that with the inlet tube set at $X = 150$ mm, high-temperature distribution was observed in aluminium material at 637.86 K.

Noise reduction is contingent on temperature and velocity, as exhaust gases in pulses can lead to discontinuous flow, generating various noises, including high-velocity-induced whistling. Our analysis and comparison of temperature and velocity plots for aluminium and steel mufflers revealed varying results in total pressure and flow velocity with changes in material. Velocity contours in Fig. 6a, b illustrate this difference.

- For Aluminium, the inlet velocity was 40 m/s, and the outlet velocity increased to 48.06 m/s, a rise of 8.06 m/s.
- For Steel, the inlet velocity was 40 m/s, and the outlet velocity increased to 47.86 m/s, a rise of 7.86 m/s.

Comparing the results, we observed a greater temperature drop in Aluminium compared to Steel, as depicted in Fig. 7, while maintaining the same inlet temperature in both cases.

Next, we varied the inlet tube of the muffler at $X = 100$ mm and $X = 50$ mm, respectively (using Aluminium material), conducting two iterations. Figure 8 illustrates the impact on temperature due to changes in the inlet tube length.
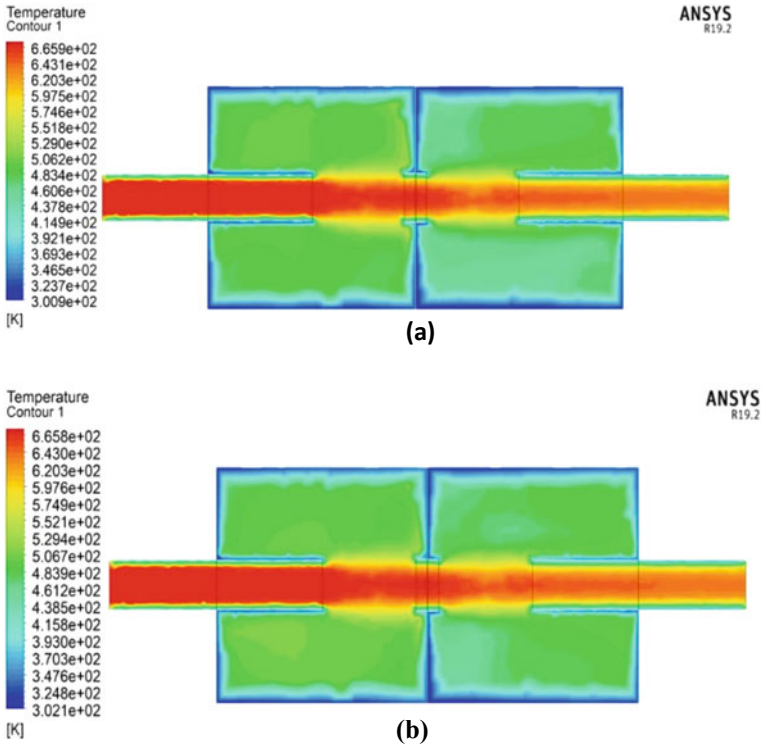
Fig. 5 Temperature variation for two different materials. **a** Aluminium, **b** Steel

Despite the distance change to $X = 100$ mm and $X = 50$ mm, the velocities remained 47.6 m/s and 47.72 m/s, respectively showed in Figs. 9 and 10, indicating a normal velocity change compared to temperature.

Upon comparison, from Table 4 the maximum temperature distribution in Aluminium occurred at an inlet tube distance of $X = 50$ mm, surpassing the Steel temperature distribution.

Our results indicate that the most effective reduction in temperature distribution is achieved at the inlet tube distance of $X = 50$ mm in ITR 3, contributing significantly to the reduction in muffler noise levels.
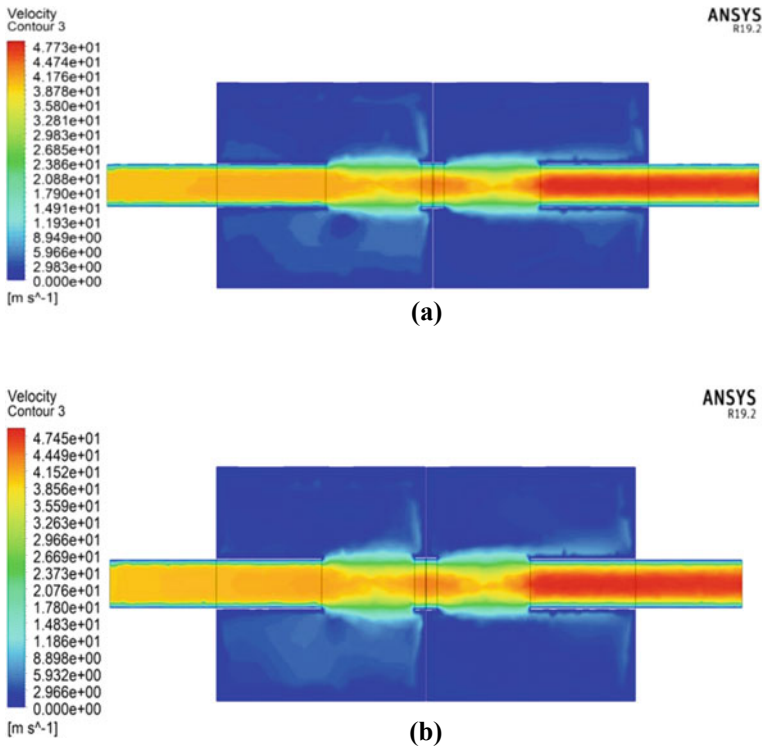
Fig. 6 Velocity contours shows the velocity distribution in muffler for two different materials. **a** Aluminium, **b** Steel

4.1 Validation of Present Study with Literature Results

Validation of results is essential in numerical study in order to make conclusions from the research. So, we have compared our result with research paper. To begin, geometry was prepared in CATIA V5 software and pre-processing and post-processing were completed in Ansys workbench software by providing proper boundary conditions as specified in the paper. After a several iterations (Fig. 11).

We obtained a proper temperature distribution in the muffler outlet that is relatively similar to the literature paper. Figure 12 illustrates the temperature variation at the muffler's outlet, which is discussed further below.

In the literature, the researcher has reduced the temperature from 800 to 786.8 K by providing taper at an inlet as well as outlet tube and analysing the temperature distribution of the muffler from inlet to outlet [14]. So, for validation, we used the same geometry with their dimensions and boundary conditions in our CFD analysis of the muffler and achieved a satisfactory temperature distribution result.
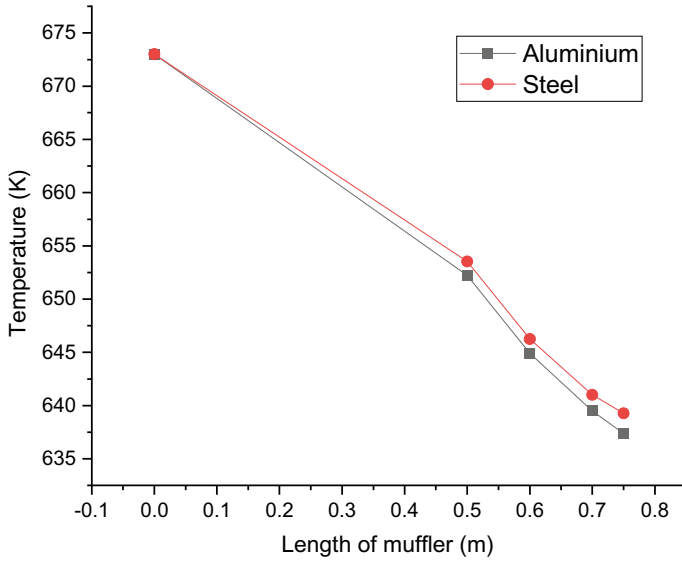
Fig. 7 Comparison of temperature variation between two different materials
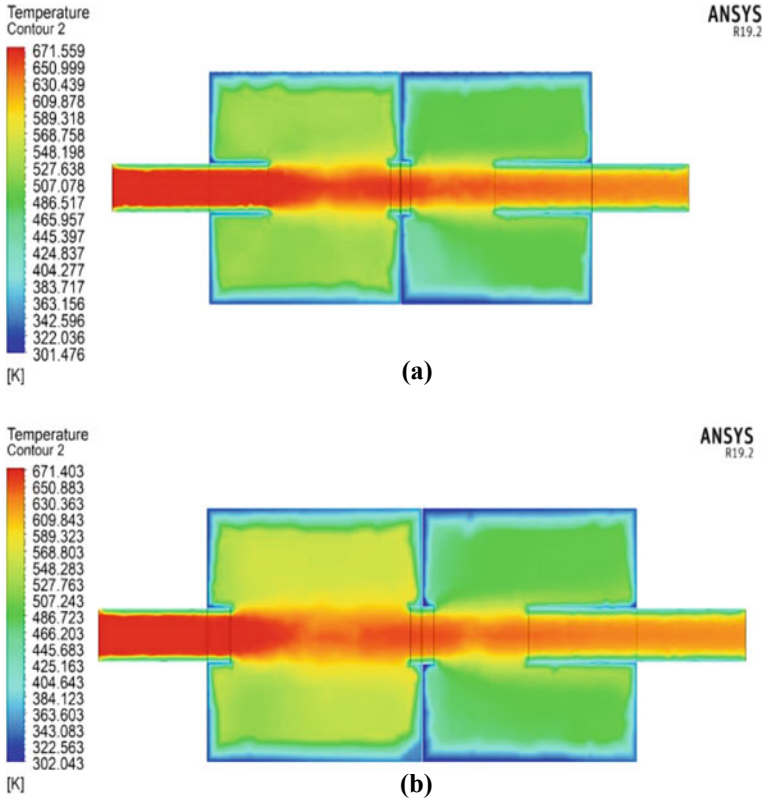
Fig. 8 a Temperature contours for iteration 2 by varying inlet tube ($X = 100$ mm). b Temperature contours for iteration 2 by varying inlet tube ($X = 50$ mm)
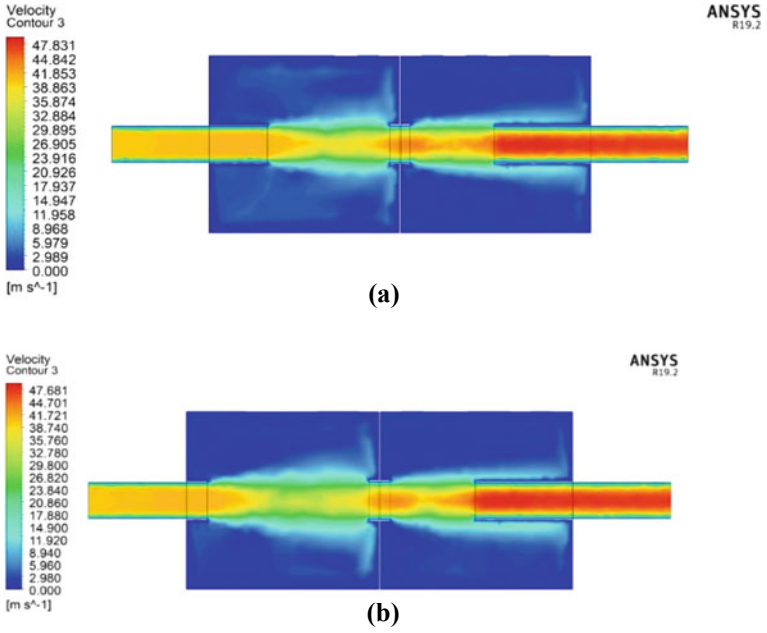
Fig. 9 Velocity contours shows the velocity distribution in muffler for inlet tube distance of **a** $X =$ 100 mm and **b** $X = 50$ mm
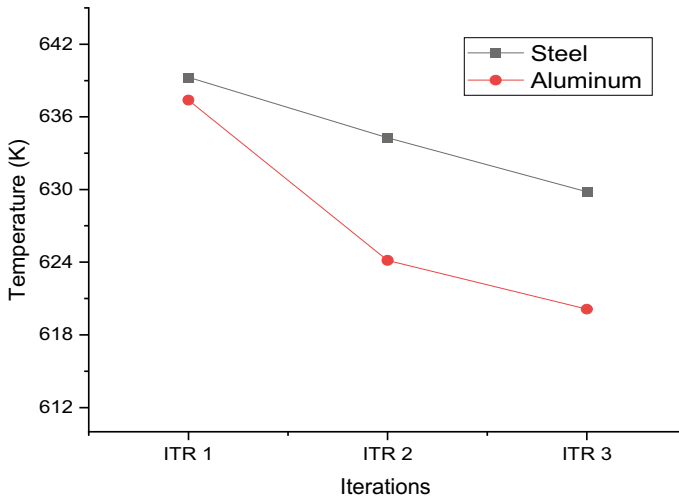

Fig. 10 Comparison between no of iterations and temperature of Steel and Aluminium

Table 4 Results of CFD analysis for ITR 1, ITR 2 and ITR 3

S. No	Iterations and inlet tube length	Temperature (K)
1	ITR 1 ($X = 150$ mm)	637.38
3	ITR 2 ($X = 100$ mm)	624.15
3	ITR 3 ($X = 50$ mm)	620.12
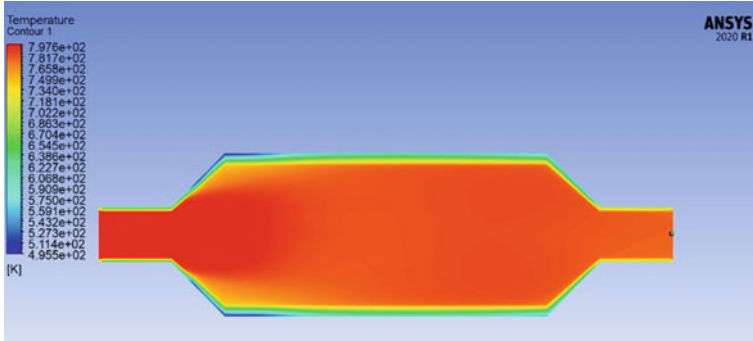
Fig. 11 Temperature contours represents the temperature variation from muffler inlet to outlet using literature aspects and boundary conditions
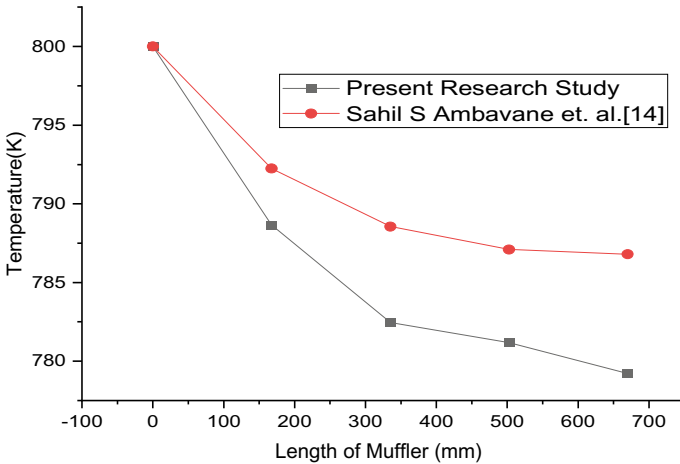
Fig. 12 Comparison of temperature variation between present research study and Sahil S Ambavane's research paper

5 Conclusion

The CFD analysis has been carried out for Aluminium and Steel mufflers, then these CFD results have been compared. For Aluminium, inlet temperature is 673 K and the outlet temperature is 637 K and temperature drop = 36 K, while for Steel, for same inlet temp the outlet temperature is 639 K, and temperature drop was of 34 K, which clearly indicates that the temperature reduction is more in Aluminium. The reduction in temperature also reduces the noise level from the muffler and improves sound attenuation [15]. Further study is carried out by changing the value of inlet pipe length, i.e. X, for $X = 100$ mm and $X = 50$ mm, it was observed that the temperature drop was maximum for $X = 50$ mm, which will eventually result in better sound attenuation. Similarly, analysis was carried out for velocity and pressure change. The inlet velocity was 40 m/s and the outlet velocity is 48.06 m/s which is increase of 8.06 m/s, while for Steel, with same inlet velocity, outlet velocity is 47.86 m/s which is increase of 7.86 m/s, however it was found that the velocity variation and pressure variation is not significant with changes in length and material. The reduce in temperature also reduces the noise level from the muffler and improves sound attenuation from results we can conclude that for the same parameters range, Aluminium material-based muffler is better in terms of heat dissipation and noise reduction for inlet pipe length of 50 mm.

References

1. Yasuda T, Wu C, Nakagawa N, Nagamura K (2013) Studies on an automobile muffler with the acoustic characteristic of low-pass filter and Helmholtz resonator. Appl Acoust 74(1):49–57. https://doi.org/10.1016/j.apacoust.2012.06.007
2. Munjal ML (1997) Plane wave analysis of side inlet/outlet chamber mufflers with mean flow. Appl Acoust 52(2):165–175. https://doi.org/10.1016/S0003-682X(96)00053-9
3. Singh NK, Rubini PA (2015) Large Eddy simulation of acoustic pulse propagation and turbulent flow interaction in expansion mufflers. Appl Acoust 98:6–19. https://doi.org/10.1016/j.apacoust.2015.04.015
4. Guhan CPOA, Arthanareeyswaran G, Varadarajan KN, Krishnan S (2018) Exhaust system muffler volume optimization of light commercial vehicle using CFD simulation. Mater Today Proc 5(2):8471–8479. https://doi.org/10.1016/j.matpr.2017.11.543
5. Mishra PC, Kar SK, Mishra H, Gupta A (2016) Modeling for combined effect of muffler geometry modification and blended fuel use on exhaust performance of a four-stroke engine: a computational fluid dynamics approach. Appl Therm Eng 108(x):1105–1118. https://doi.org/10.1016/j.applthermaleng.2016.08.009
6. Guhan CPOA, Arthanareeswaren G, Varadarajan KN (2015) CFD study on pressure drop and uniformity index of three cylinder LCV exhaust system. Procedia Eng 127:1211–1218. https://doi.org/10.1016/j.proeng.2015.11.466
7. Wu CJ, Wang XJ, Tang HB (2007) Transmission loss prediction on SIDO and DISO expansion-chamber mufflers with rectangular section by using the collocation approach. Int J Mech Sci 49(7):872–877. https://doi.org/10.1016/j.ijmecsci.2006.11.007
8. Guojiang W, Song T (2005) CFD simulation of the effect of upstream flow distribution on the light-off performance of a catalytic converter. Energ Convers Manag 46(13–14):2010–2031. https://doi.org/10.1016/j.enconman.2004.11.001

9. Jeong SJ, Kim WS (2003) A study on the optimal monolith combination for improving flow uniformity and warm-up performance of an auto-catalyst. Chem Eng Process Process Intensif 42(11):879–895. https://doi.org/10.1016/S0255-2701(02)00140-X
10. Kumar A, Mazumder S (2010) Toward simulation of full-scale monolithic catalytic converters with complex heterogeneous chemistry. Comput Chem Eng 34(2):135–145. https://doi.org/10.1016/j.compchemeng.2009.05.018
11. Hayes RE, Fadic A, Mmbaga J, Najafi A (2012) CFD modelling of the automotive catalytic converter. Catal Today 188(1):94–105. https://doi.org/10.1016/j.cattod.2012.03.015
12. Nazir MH, Khan ZA, Saeed A, Stokes K (2016) A predictive model for life assessment of automotive exhaust mufflers subject to internal corrosion failure due to exhaust gas condensation. Eng Fail Anal 63:43–60. https://doi.org/10.1016/j.engfailanal.2016.02.014
13. Inoue Y, Kikuchi M (2003) Present and future trends of stainless Steel for automotive exhaust system. Nippon Steel Tech Rep 88:62–69
14. Ambavane SS, Achari VC, Khandebharad MR, Kulkarni PA (2021) Design and thermal analysis of vehicle exhaust muffler. IRJET 8(12):19–25
15. Milani E, Paze C, Ambrosino M, Pagliano P (2012) Reduction of exhaust noise by means of thermal acoustics. SAE Int J Passeng Cars Mech Syst 5(2):956–961. https://doi.org/10.4271/2012-01-0804

CFD Analysis of Vortex Shedding Behaviour Over Different Geometries

V. Amirthavarshini, K. Manikandan, S. S. Kamalakcshy, T. Santra, R. Haribalaji, and S. Dhanisha

Nomenclature

Re   Reynolds number
C_d Drag coefficient
L Length (mm)
H Breadth (mm)
D_h Hydraulic diameter (mm)
U Velocity (mm s^{-1})
St   Strouhal number
f Frequency of vortex shedding (s^{-1})
A Area of object (mm^2)
P Perimeter of object (mm)

1 Introduction

Nowadays, one of the main focus areas of aerodynamicists is vortex shedding, as it is directly connected to noise generation. This phenomenon is associated with the flow over blunt bodies. It depends on the Reynolds number of the flow and is more clearly seen in the subcritical regime. Vortices form and shed from the top and then, the bottom surface periodically in the wake region of the body. This periodic shedding forms a repetitive pattern called the Kármán vortex street. The pattern of shedding depends on the velocity, Reynolds number, shape, surface roughness, turbulence levels, and the length-to-diameter ratio of the body. The alternate shedding

V. Amirthavarshini · K. Manikandan (✉) · S. S. Kamalakcshy · T. Santra · R. Haribalaji ·
S. Dhanisha
School of Mechanical Engineering, SASTRA Deemed to be University, Thanjavur 613401, India
e-mail: manikandan@mech.sastra.edu

produces alternate forces on the body. The shedding frequency depends on Reynolds number and directly affects the noise that is being generated by the flow. Hence, vortex shedding forms a major section of the aeroacoustics of flow in the subcritical region. The frequency of vortex shedding can also be represented in the form of a non-dimensional number called the Strouhal number (i.e. $St = \frac{f\,D_h}{U}$). The extensive literature review in the next chapter is versatile and explores the available methods to understand and predict the vortex shedding characteristics of different models.

2 Literature Review and Objective

Roshko et al. [1], experimentally studied the vortex shedding patterns for the Reynolds numbers (Re) 40–10,000. Later [2], he tried to prove empirically the dependence of Re on the base pressure and shedding frequency. He found the possibility of a similarity in trend for Re up to 10^5, that is, the critical Reynolds number.

King et al. [3], presented the effects of length-to-diameter ratio and surface roughness on the vortex shedding of cylinders that are placed perpendicular and at other different angles to the flow.

Sarpkaya et al. [4] investigated the oscillatory response in a 2-D circular cylinder caused by vortex shedding and recorded the variation in lift and drag. They have developed a discrete vortex model based on potential flow and boundary-layer interaction, discretization of shear layers and circulation dissipation to determine the characteristics of the flow around a cylinder. They have explained and listed papers explaining the trends in Strouhal numbers and their relation to Reynolds number.

Davis et al. [5], did a numerical study for a 2-D time-dependent flow over a rectangle for Reynolds numbers from 100 to 2800. The computations were carried out using 51×62 grid since the rate of increase of the coefficient of drag (C_d) was greater while 61×74 grid was adopted for only two Reynolds numbers because of limited computer resources. Also, the near wall regions of the geometry were treated with a fine mesh strategy to effectively account the viscous effects of the boundary layer. They concluded that the flow properties of vortices, lift, drag, and Strouhal numbers are all dependent on the Reynolds number.

Bearman et al. [6], studied the flow around a circular cylinder over Reynolds numbers from 10^5 to 7.5×10^5. He observed that narrow band vortex shedding forms up to the critical regime. The corresponding Strouhal number to this Re has been found to have a high value. Later in 1984, he presented a review on the progress in the study of vortex shedding of cylinders and pressed on the necessity for the study of cylinders of geometries other than a circle and over a larger range of Reynolds number.

Kelkar et al. [7], computed the steady two-dimensional flow around a square and a cylinder and determined the onset of unsteadiness by varying the Reynolds number. They utilised Neumann conditions at the outflow and no-slip boundary conditions

on the model. The flow is governed by the steady and unsteady forms of the Navier–Stokes equations. The domain was developed with $L/D = 14$ and $H/D = 7$. The critical Reynolds number for which steady flow turned to unsteady was determined.

Ali et al. [8], computed numerically the behaviour of sound due to Kármán Vortex Street for circular and square cross-sections for the Re 22,000. The Reynolds-Averaged equations of mass and momentum are used to numerically compute the fundamental variables of the flow fields. In the current study, turbulence transport was modelled using k-ε for the case of a circular cylinder and k-SST for the case of a square cylinder flow due to severe separation and wake structure. They also studied the sound pressure levels due to fluctuations in lift and drag.

Bosch et al. [9], presented a comparison of various turbulence models used to compute the vortex shedding past a free-standing square cylinder at Re 22,000. The comparison was done using the same computational domain and boundary conditions and it was concluded that using Kato-Launder modification gave the best results.

Fezai et al. [10], studied numerically the vortex shedding characteristics of rectangular cylinders of various configurations over a range of Reynolds numbers from 1 to 200. At the channel entrance, the horizontal velocity was fixed as one and the vertical velocity as zero. No-slip conditions were imposed on the object and the upper and lower walls were defined as a slip wall. They computed the solutions for steady and unsteady flow and also studied the frequency of vortex shedding for the above-mentioned Reynolds numbers using a staggered grid approach. To better estimate the flow field at these sites, particularly where large gradients were anticipated, mesh refinement was done close to the obstruction is whereas larger meshes were found at distance from the obstruction where the predicted gradients are modest. Time step study was done by ensuring the convergence of results for temporal evolution of lift coefficient, vertical, and horizontal velocity respectively for different time steps.

Based on the literature [1–10] studied, the current paper aims to apply 2-D simulations for both steady and unsteady analysis. Geometry effects on the range of subcritical Reynolds numbers can be simulated and analysed with reasonable accuracy as mentioned in the literature.

3 Design and Computational Methodology

3.1 Geometry

In the present study, flow over two different geometries namely circle and square are considered.

Fine mesh is adapted around the bluff body especially behind it to capture the shedding patterns. The velocity conditions were defined at the inlet boundary condition and the flow was simulated at atmospheric pressure. The domain specifics and mesh details are given in Figs. 1 and 2, respectively.
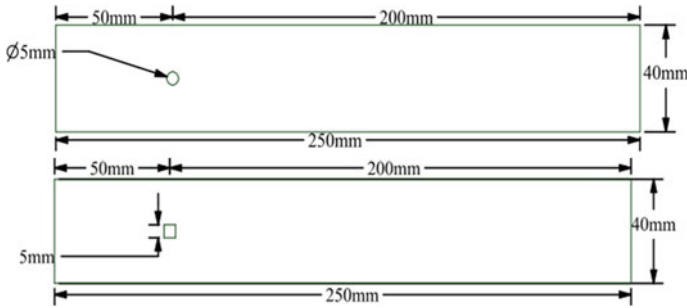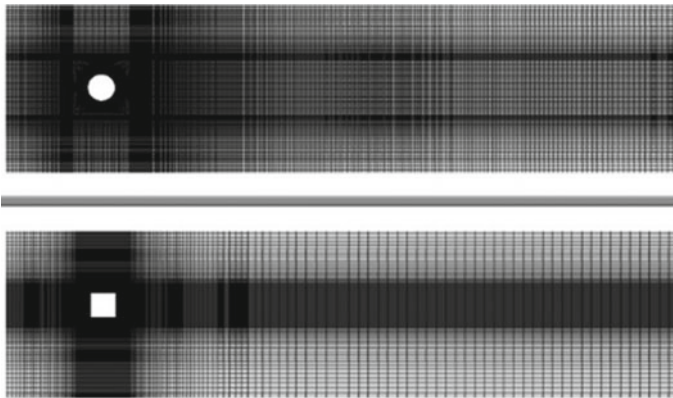
Fig. 1 Geometry and domain details

Fig. 2 Mesh details of the bluff bodies

3.2 Mesh Independence

A structured grid with quadrilateral mesh elements was generated using ANSYS FLUENT 19.2. To fine-tune the cell size surrounding the obstacle geometry and to better resolve the gradients along the solid surfaces and wake zones of the cylinder in advance, the grid is separated into multiple individual zones and meshed appropriately to improve the results and reduce the computational time. Each zone is biased so as to generate a higher number of elements near the object and a gradual decrease in the number of elements as distance from the body is increased. Numerical calculations were conducted to test for grid independence for various numbers of mesh elements to find the optimum grid. Optimization of mesh was achieved by calculating the C_d for a number of variations of mesh differing in their total number of elements. Meshes with 30–100 thousand elements were generated and their C_d was plotted against the said number of elements. The respective details are given in Figs. 3 and 4, respectively.
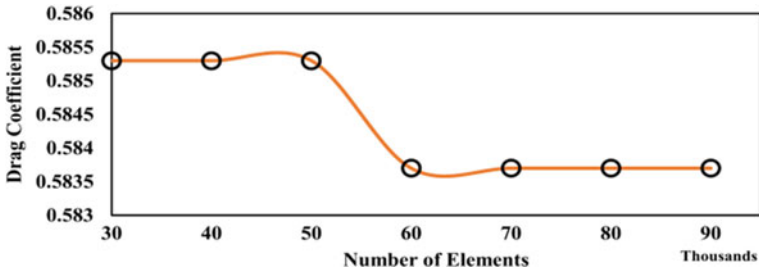
Fig. 3 Grid independence study for the circular model
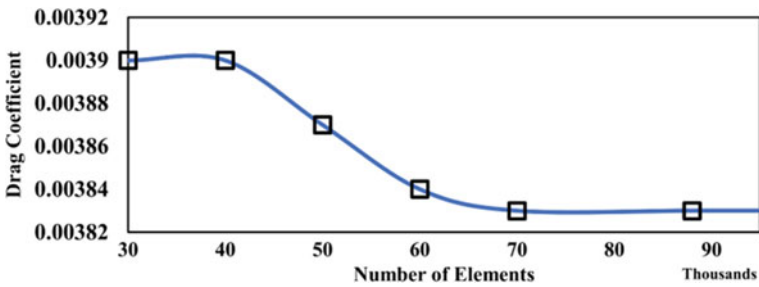
Fig. 4 Grid independence study for the square model

Figures 3 and 4 represents the C_d versus number of elements for geometries of both the square and circular. It is inferred that C_d begins to settle down around 70,000 elements and no further variation was observed after number of elements was increased to 80,000. Hence, 80,000 elements are fixed for the rest of the simulation.

3.3 Time Step Independence Study

The selection of the time step is critical since a time step value that is too high would generate inaccurate results, while a time step value that is too low would cause extra processing time. The four selected time increments are 0.0001, 0.0005, 0.001, and 0.0025 s. Figure 5 shows that as the time step is increased, the C_d continues to decrease. For smaller time steps, the C_d variation was almost nil (i.e. constant). As a result, 0.0005 s was selected as the time step for unsteady-state calculations.

Fig. 5 Time step independence study
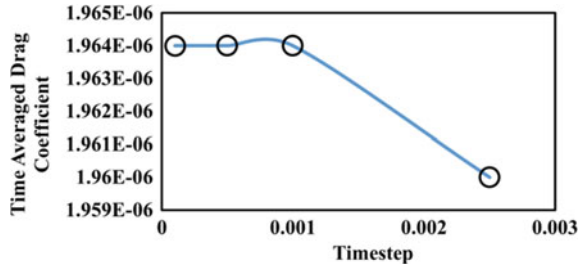
3.4 Validation

The validation of the study was done by comparing the results of Fezai et al. [10], with the results obtained from the current square model. At low Re, C_d is reduced in the laminar layer due to reduction of the friction coefficient. The C_d basically holds steady for high Re while it gradually decreases for lower Re ($45 < Re < 100$). We find the results nearly match with those observed in the aforementioned paper. The small differences seen can be attributed to the difference in mesh and the number of elements that was chosen. The same can be observed from Fig. 6.
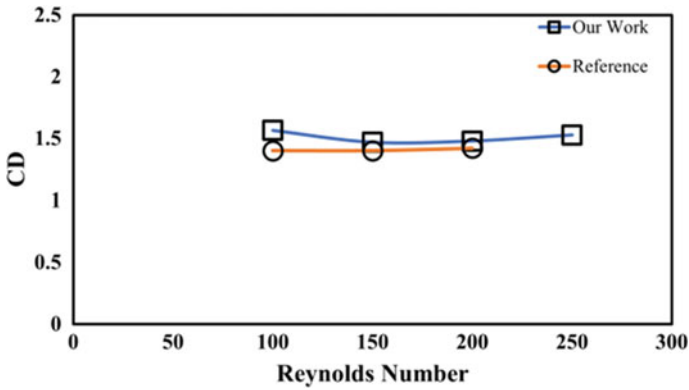
Fig. 6 C_d versus Re

4 Results and Discussion

4.1 Steady-State Results

Figure 7 shows the velocity contours of mentioned Re values over the cylindrical body. For the Reynolds number 45, flow separation causes the visible wake region behind the body and similarly for Re = 250 the intensity of flow separation increases significantly with wider and longer recirculation zones. As the Re value increases above 250 (i.e. 800 and 1435) the flow separation intensity gets reduced with significant reduction in the wake zone behind the circular model. Similarly, the square model is also observed to have the similar trend of flow separation, except that the square has the longest low-velocity trail when compared to the circular geometry for Re = 250. The velocity magnitude variation over the square model can be seen in Fig. 9. Similarly, Figs. 8 and 10 show the vorticity magnitude of the cylinder and square models, for the Re values of 45, 250, 800, and 1435. For a Re value of 250 in the circular model, the vorticity magnitude extends to larger length in the downstream, similar to the velocity magnitude for the same Re value. The same development can be seen from the square model as well, as observed from Fig. 10. However, for the higher Re values (i.e. 800 and 1435) vorticity magnitude decays at a faster rate for both the models. The same can be witnessed from Figs. 8 and 10, respectively. But, for the low value of Re (i.e. 45) the intensity of change in magnitude leads to a smaller trail length for both the geometry models.

The time-averaged value of drag coefficient for the two geometries was calculated and consolidated into a graph. Figure 11 represents the variation of C_d with respect to Re for the circular and square geometries. It can be inferred that both the geometries are following a similar trend of decrease on C_d value with the increase in Re. The C_d drops steeply with an increase in Reynolds numbers (i.e. 45–250) and becomes almost constant beyond the Re of 250. Comparing the C_d values alone, the circular cross-section has the lowest drag coefficient. The circular geometry shows the favourable drag characteristics (i.e. smaller drag) than the square geometry of same hydraulic diameter. Hence, it confirms that, streamlining the body favours improved aerodynamic characteristics for the same Reynolds numbers range.

4.2 Unsteady-State Results

Figures 12 and 13 show the unsteady characteristics of vortex shedding development over the cylinder for the Re values of 250 and 800, respectively. Figure 12 shows that up to 0.195 s, the vortex shedding is developing and nearly at 0.27 s, the flow exhibits periodic shedding from the cylindrical model. However, for the Re value of 800, flow exhibits periodic shedding at 0.04 s itself and the corresponding shedding patterns can be seen from Fig. 13. Similarly, from Figs. 14 and 15, shedding characteristics of the square model for the Re values of 250 and 800 can be observed. For the Re value
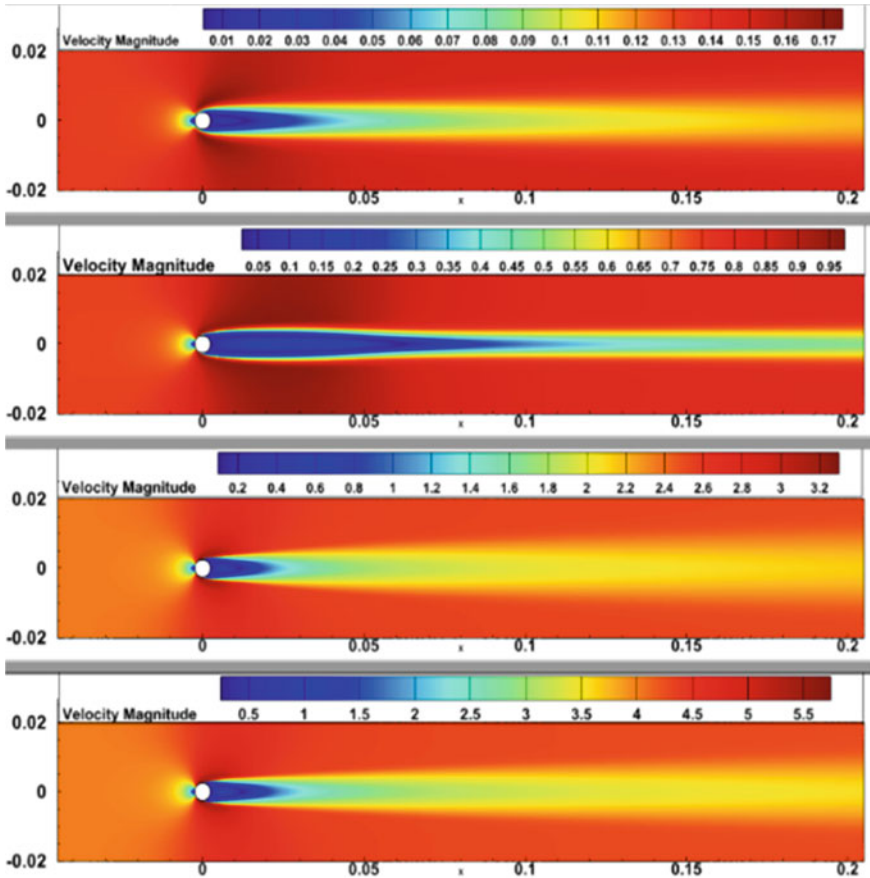
Fig. 7 Velocity magnitude of the circular model. **i** Re = 45, **ii** Re = 250, **iii** Re = 800, **iv** Re = 1435

of 800, both the models (i.e. cylinder and square) are showing additional disturbances from multiple local flow separations over them.

The impact of Reynolds number on the Strouhal number was tested and the same is depicted in Fig. 16. It should be noticed that the Strouhal number rises with low Reynolds numbers (45 < Re < 200) and that it reaches a maximum around Re = 200 and then decreases with the increase of Re. Both the models display the same trend but with a difference in magnitude, which can be inferred from Fig. 16.

The circle is discovered to have the lowest shedding frequency for larger Re (i.e. Re > 800) when compared to square.
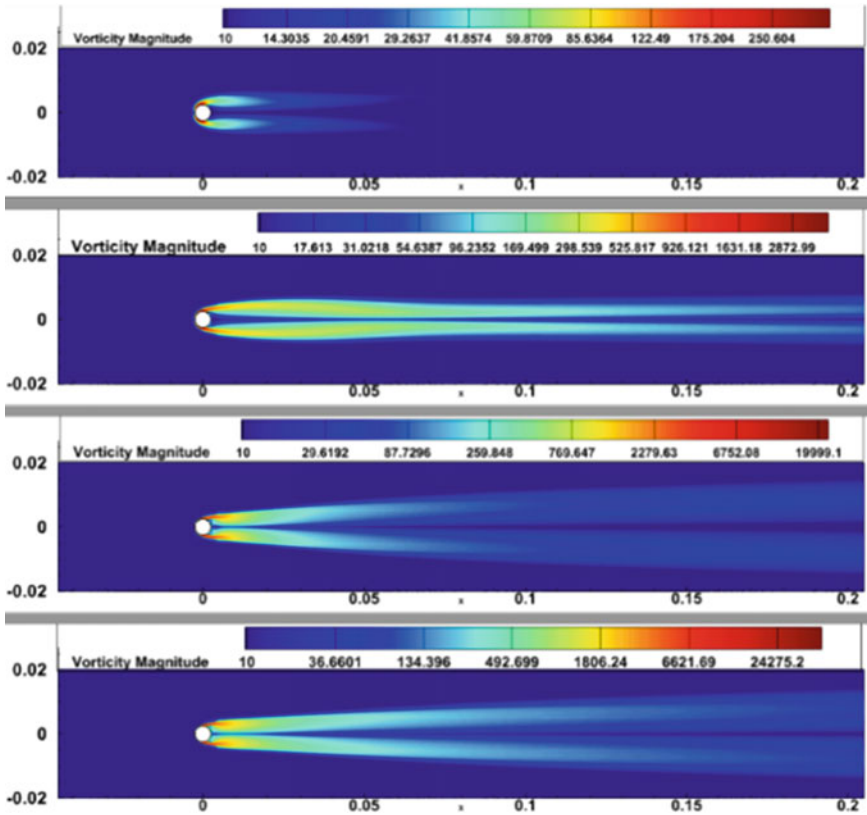
Fig. 8 Vorticity magnitude of the circular model. **i** Re = 45, **ii** Re = 250, **iii** Re = 800, **iv** Re = 1435

5 Conclusions

In the subcritical regime, the steady and unsteady flows for two different geometries are examined numerically over four different Reynolds number values. Two global parameters, St and C_d, have been measured to study the vortex shedding past various obstacle geometries. The observed conclusions are well-aligned with recent experimental findings. It is perceived that the Strouhal number of both the geometries increases with decreasing Re and reaches a maximum around Re = 200 before declining with higher Re. The square geometry reaches a St value of 0.14 at Re = 250 while the circular geometry reaches 0.21. Similarly, for Re = 1435 the square model attains a value of St = 0.00004 while the circular model attains a value of 0.015317. For both low and high Reynolds numbers, it has been observed that square geometry exhibits less intense vortex shedding behaviour and minimal noise generation.
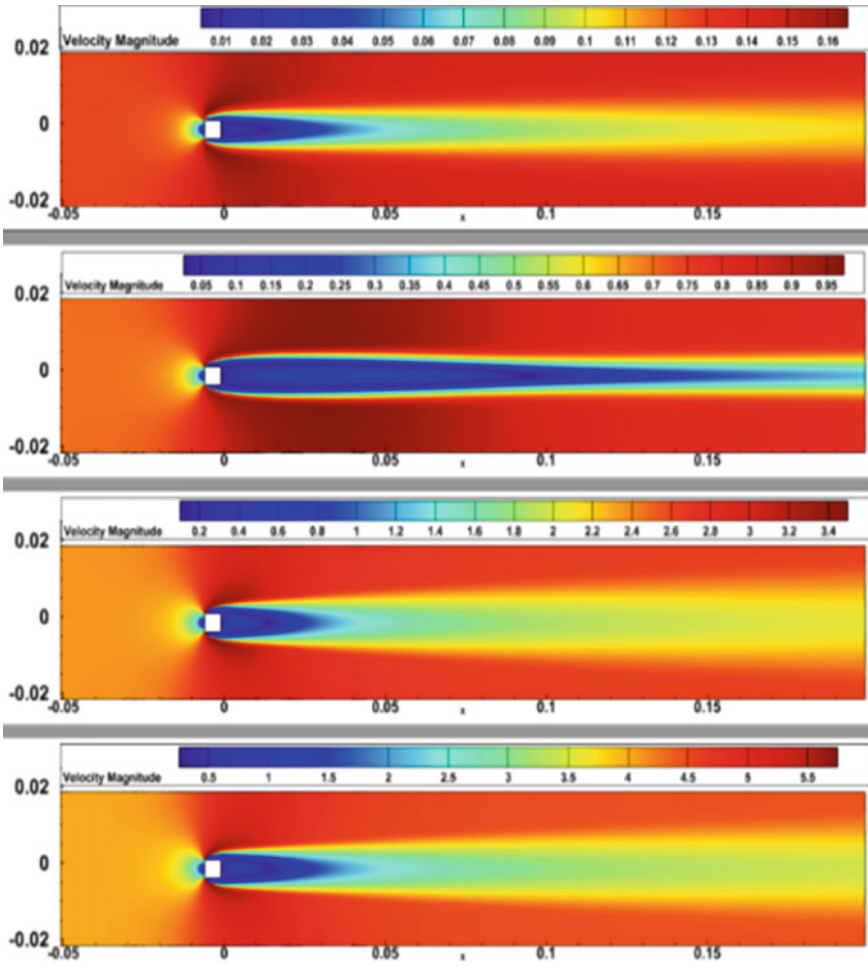
Fig. 9 Velocity contours of the square. **i** Re = 45, **ii** Re = 250, **iii** Re = 800, **iv** Re = 1435
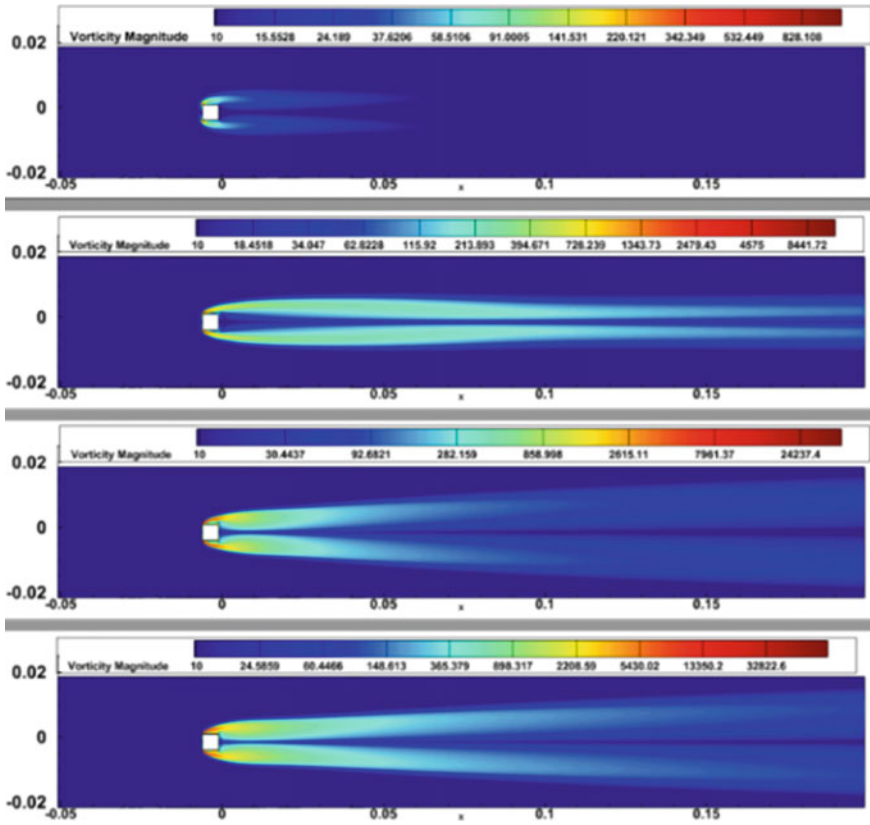
Fig. 10 Vorticity magnitude contours of the square. **i** Re = 45, **ii** Re = 250, **iii** Re = 800, **iv** Re = 1435
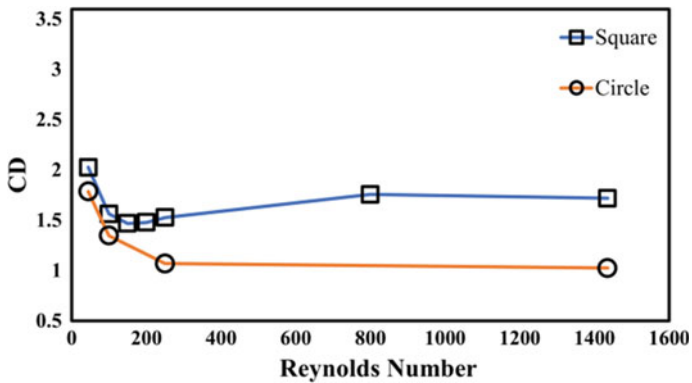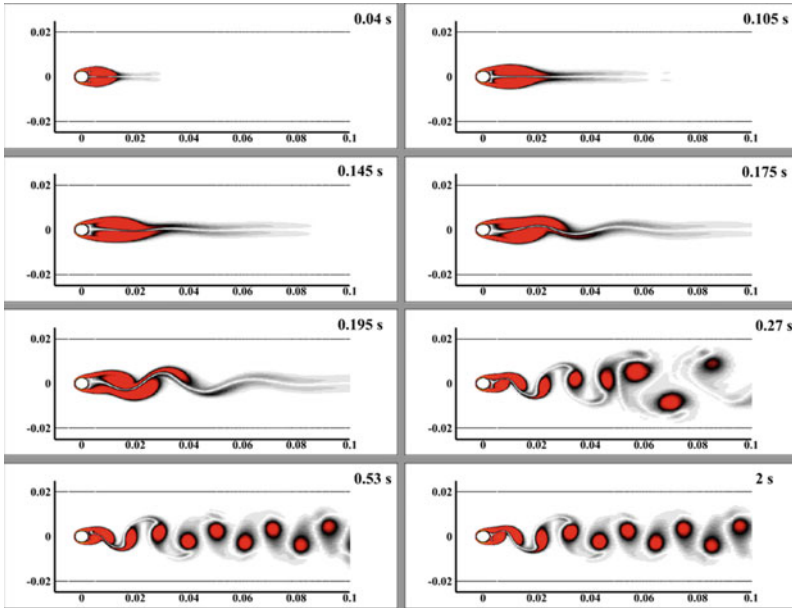

Fig. 11 C_d versus Re for all geometries

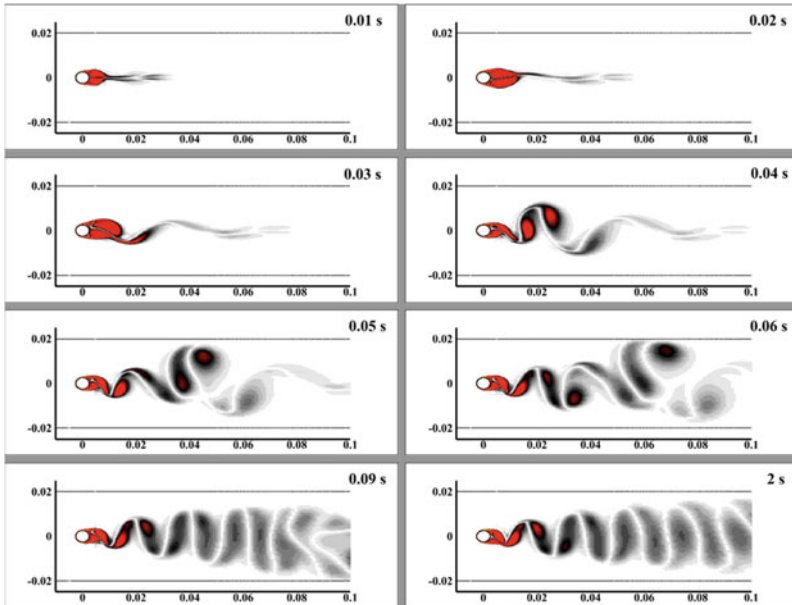**Fig. 12** Shedding pattern of cylinder for Re = 250 w.r.t to time

Fig. 13 Shedding pattern of cylinder for Re 800 w.r.t to time
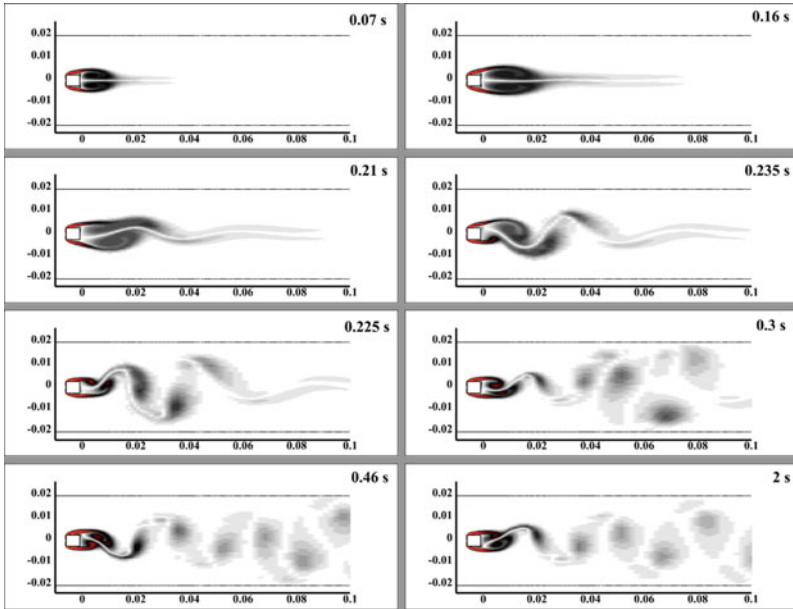
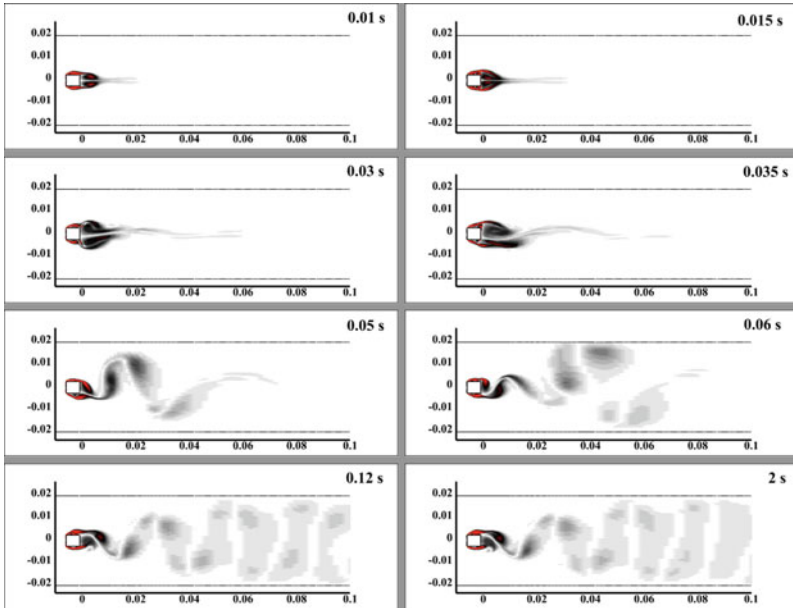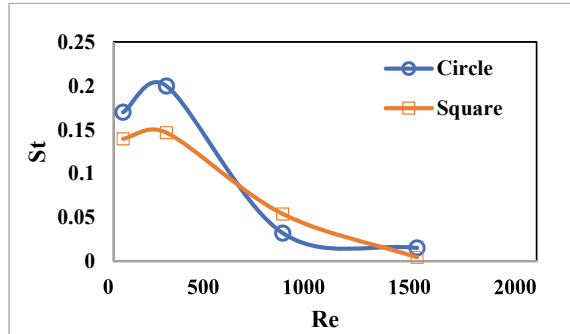**Fig. 14** Shedding pattern of square for the Re 250 w.r.t to time

Fig. 15 Shedding pattern of square for the Re 800 w.r.t to time

Fig. 16 Re versus St for all geometries

References

1. Roshko A (1954) On the development of turbulent wakes from vortex streets. No. NACA-TR-1191
2. Roshko A (1954) On the drag and shedding frequency of two-dimensional bluff bodies. No. NACA-TN-3169
3. King R (1977) A review of vortex shedding research and its application. Ocean Eng 4(3):141–171. ISSN 0029-8018
4. Sarpkaya T (June 1, 1979) Vortex-induced oscillations: a selective review. ASME J Appl Mech 46(2):241–258
5. Davis RW, Moore EF (1982) A numerical study of vortex shedding from rectangles. J Fluid Mech 116:475–506
6. Bearman PW (1969) On vortex shedding from a circular cylinder in the critical Reynolds number regime. J Fluid Mech 37(3):577–585
7. Kelkar KM, Patankar SV (1992) Numerical prediction of vortex shedding behind a square cylinder. Int J Numer Meth Fluids 14(3):327–341
8. Samion SRL, Mat Ali MS, Abu A (2015) Sound from high-Reynolds number flow over bluff bodies. Aircr Eng Aerosp Technol 87(6):551–556
9. Bosch G, Rodi W (1998) Simulation of vortex shedding past a square cylinder with different turbulence models. Int J Numer Methods Fluids 28(4):601–616
10. Fezai S, Ben-Cheikh N, Ben-Beya B, Lili T (2020) Numerical study of obstacle geometry effect on the vortex shedding suppression and aerodynamic characteristics. Int J Numer Meth Heat Fluid Flow 30(2):469–495

Numerical Simulation of 2D Tube Convection

M. G. Visakh, Chetan D. Bankar, and Jaywant H. Arakeri

Nomenclature

Ra	Rayleigh number
Ra_g	Gradient Rayleigh number
Re	Reynolds number
Nu	Nusselt number
Nu_g	Gradient Nusselt number
Pr	Prandtl number
Gr	Grashof number
Gr_g	Gradient Grashof number
g	Acceleration due to gravity (m/s^2)
H	Vertical extend of domain (m)
L	Horizontal extend of domain (m)
d	Diameter/width of tube (m)
Γ	Aspect ratio d/H or L/H
u_x, u_y	Horizontal and vertical velocities (m/s)
ν	Kinematic viscosity (m^2/s)
α	Thermal diffusivity (m^2/s)
β	Thermal expansion coefficient (K^{-1})
ρ	Density (kg/m^3)
k	Thermal conductivity (W/mK)
C_p	Specific heat at constant pressure (J/kgK)
ϵ	Dissipation rate (m^2/s^3)

M. G. Visakh (✉) · J. H. Arakeri
Department of Mechanical Engineering, Indian Institute of Science, Bangalore, Karnataka, India
e-mail: visakhmg@iisc.ac.in

C. D. Bankar
Centre for Atmospheric and Oceanic Sciences, Indian Institute of Science, Bangalore, Karnataka, India

1 Introduction

Rayleigh–Bénard Convection (RBC) is the convection setup in a fluid sandwiched between two horizontal plates maintained at an unstable temperature difference: a cold top plate and heated bottom plate. When the temperature difference is large enough, the density differences within the fluid cause hot fluid at the bottom to rise, and cold fluid at the top to sink—resulting in free convection. RBC is one of the most studied thermal convection systems, due to its simplicity and richness in flow phenomena. The buoyancy forcing in RBC systems is parametrized by the Rayleigh number given by $Ra = g\beta\Delta T H^3/\nu\alpha$, which is the ratio of buoyancy to viscous forces. The critical Rayleigh number for the onset of convection is $Ra_c \approx 1708$. For small Rayleigh numbers just above this critical value, one gets steady and laminar convection rolls. If one keeps increasing the Ra, the flow transitions into unsteady rolls followed by chaos and finally into turbulent convection. The Reynolds number $Re = UH/\nu$ and the non-dimensional flux transport given by $Nu = q''H/k\Delta T$ are usually expressed in terms of Ra and the Prandtl number $Pr = \nu/\alpha$ as power laws, with the aspect ratio $\Gamma = L/H$ sometimes playing a role. While people have proposed slight variations in the scaling exponent of $Nu \sim Ra^n$ with $n = 0.3$, $n = 2/7$ [4, 16], etc., they all are close to the classical scaling of $n = 1/3$ [9, 11], which essentially means that the fluxes are independent of the length scales involved. At very high Ra, it was proposed that the boundary layers would break down and a scaling exponent of $n = 1/2$ would persist [10], moving the system to an "ultimate regime" where the fluxes are independent of the diffusivities [17]. Although some groups have claimed evidence of transition to such a regime, ultimate regime remains elusive in classical RBC. For detailed review on developments in research related to RBC, see [1, 6].

An alternative thermal convection system is when one replaces the top and bottom walls with reservoirs of infinite heat capacity and connects a long vertical tube between them. This is the "Tube Convection" (TC) which was introduced by Jaywant et al. [2], where the authors used salt instead of heat to create the density difference. They classified the flow dynamics into four different regimes as a function of (gradient) Rayleigh number. At very low Rayleigh numbers, they observed half-and-half flow, where there were two straight and uniform streams of fluid going up and down, without mixing each other. At slightly higher Ra, they observed that these streams take a helical structure, but the flow was still steady, which they called the helical flow regime. At further higher Ra, they observed the unsteady laminar regime, where unsteady mixing of heavier and lighter fluids occurs, but the flow was still laminar. At high enough Ra, they observed fully turbulent exchange flow where the mixing was fully three-dimensional and random. Further experiments were performed by Authors [7, 8] who observed several interesting features of tube convection compared to the classical RBC. In tube convection, for sufficiently long tubes, one gets a linear temperature gradient along the length of the tube (in contrast to the isothermal core of RBC). Analogous to a pipe flow which is driven by a pressure gradient, tube convection is driven by a density gradient. The flow is axially

homogeneous away from the ends, with negligible mean velocities and Reynolds stresses, and the flow is dominated by fluctuating velocities. Due to this, the turbulence production is entirely due to buoyancy. The buoyancy forcing here is expressed by the gradient-based Rayleigh number $\mathrm{Ra}_g = g\beta\frac{\mathrm{d}T}{\mathrm{d}y}d^4/\nu\alpha$ and fluxes by gradient-based Nusselt number $\mathrm{Nu}_g = q''/k\frac{\mathrm{d}T}{\mathrm{d}y}$. In a later study, [13] classified the scaling of Nu_g versus Ra_g into two regimes. Below a critical Grashof number $\mathrm{Gr}_{gc} = 1.6 \times 10^5$, they observed $\mathrm{Nu}_g \sim \mathrm{Ra}_g^{0.3}$, whereas above this limit, they observed $\mathrm{Nu}_g \sim \mathrm{Ra}_g^{1/2}$, the ultimate regime. Thus, the ultimate regime was easily achievable in tube convection, compared to classical RBC systems. See [3] for a review on different thermal convection systems.

One way to study thermal convection systems, especially RBC at higher Rayleigh numbers, is by performing 2D numerical simulations, as they are computationally much more viable than full-scale 3D simulations. Although real flows are inherently 3D, there exist many similarities between 2 and 3D RBCs [18]. There have been numerous studies on 2D RBC [5, 20] due to these reasons. However, there have been no numerical studies of tube convection in the literature except [14], where the authors performed 3D DNS of RBC with top and bottom walls replaced by periodic boundaries and found results very similar to those of the tube convection experiments of [8]. However, there have been no studies of 2D tube convection (2DTC) in literature. We try to address this gap in literature by performing 2D simulations of an insulated vertical tube connecting two closed tanks whose walls are maintained at specified temperature difference. The questions we try to address are the following: What is the flow dynamics of free convection established in a 2D tube with an imposed unstable density stratification? How do the fluxes and velocities scale in 2D tube convection, and how different are they from 3D simulations and experiments?

2 Methodology

2.1 Numerical Method

The continuity, momentum, and energy balance equations for incompressible buoyancy driven flows are of the form:

$$\frac{\partial u_i}{\partial x_i} = 0, \tag{1}$$

$$\frac{\partial u_i}{\partial t} + \frac{\partial (u_i u_j)}{\partial x_j} = -\frac{1}{\rho_0}\frac{\partial p}{\partial x_i} + \nu\frac{\partial^2 u_i}{\partial x_j \partial x_j} + g\beta(T - T_0)\delta_{iy}, \tag{2}$$

$$\frac{\partial T}{\partial t} + \frac{\partial (u_j T)}{\partial x_j} = \alpha\frac{\partial^2 T}{\partial x_j \partial x_j}, \tag{3}$$

where the density dependence of temperature is assumed to be of the linear form under the Boussinesq approximations

$$\rho = \rho_0[1 - \beta(T - T_0)]. \tag{4}$$

Equations 1–3 are solved (without any turbulence modeling) using *buoyant-BoussinesqPimpleFoam*, a solver in the open-source package OpenFOAM based on Finite Volume methods [12]. For temporal derivative terms, a second-order backward scheme was used. For spatial derivatives, Gauss gradient scheme with linear interpolation was used for gradient terms, while for divergence terms, Gauss linear upwind scheme was used for velocity and Gauss limited linear scheme was used for temperature.

The (2D) computational domain is shown in Fig. 1. The hot and cold reservoirs are mimicked by two tanks at the bottom and top. The vertical tube has a "diameter" or width of d and height $H = 10d$, so that the aspect ratio $d/H = 0.1$ is maintained across all simulations. The top and bottom tanks have horizontal and vertical dimensions of $4d$ and $1.5d$, respectively. No-slip velocity boundary conditions are imposed on all the walls. For temperature, the tube walls have insulated (zero-gradient) boundary conditions, while fixed temperatures of $T_C = 295$ K and $T_H = 305$ K are imposed at the top and bottom tank walls, respectively. A hypothetical fluid with the following properties: $\nu = \alpha = 10^{-6}$ m^2/s (so that Pr = 1), $\rho = 1$ kg/m^3, $k = 10^{-3}$ W/mK, and $C_p = 1000$ J/kgK is used as the working fluid across all the simulations. For achieving different Rayleigh numbers, we vary the tank dimensions keeping the fluid properties, wall temperatures (T_H and T_C), aspect ratio of the tube, and relative sizes of the tanks constant.

For mesh requirements, we follow the suggestions by Shishkina et al. [15]. First, an estimate of the boundary layer thickness at the tank walls is made assuming maximum temperature drop at the (tank) walls, and no temperature drop in the tube. Similarly, an estimate of the Kolmogorov length scale is made by assuming maximum temperature drop in the tube and estimating the dissipation rate ϵ from [8]. A uniform mesh is used throughout the domain such that the atleast 8–10 grid points are present at the (estimated) boundary layers, and grid spacing is less than the Kolmogorov scale expected in the tube. This approach ensures that the grid is always over-resolved. The time step dt is selected such that the CFL number is less than 0.5.

Simulations are started with zero velocity initial conditions and fixed temperature of $T_0 = 300$ K. We sample data at fixed probe locations positioned in the tube and tanks (see Fig. 1). Data are also sampled along different probe lines (horizontal and vertical) in the domain. All the averagings are done only after inspecting the time-series data in all the probes such that a statistical stationary state is achieved.

Fig. 1 Computational domain
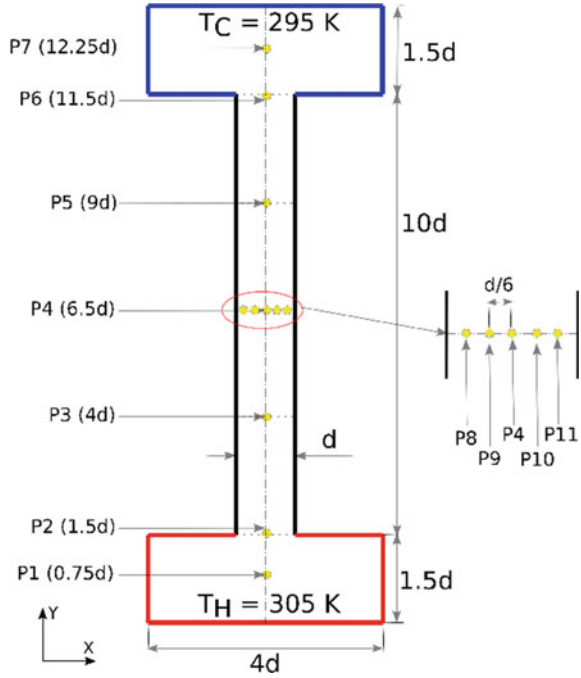
2.2 Validation

Validation studies are performed for 2D Rayleigh–Bénard systems with aspect ratio $L/H = 2$ with air as the working fluid. Rayleigh number is varied from Ra $= 10^6$ to 3×10^8, and the resulting Nusselt numbers are compared with results from some recent publications of 2D RBC [5, 19] (see Fig. 2). It can be seen that the Nusselt number results obtained in our simulations are very close to that in literature. A curve fit yields a scaling relation of Nu $\sim$ Ra$^{0.2658}$ for our data points.

3 Results and Discussion

As mentioned earlier, simulations for 2D tube convection were run for different gradient Rayleigh numbers Ra$_g$ by varying the dimensions, while keeping fluid properties, tank surface temperatures, aspect ratio, etc., constant. The exact Ra$_g$ was calculated after the simulations, because the average temperature gradient in the tube is unknown to begin with. We started at very low values of Ra$_g \sim 10^3$ where we expect the first critical Rayleigh number for the onset of convection and slowly increased Ra$_g$ such that almost all decades are covered till the highest case Ra$_g \sim 10^7$ which was limited by our computational requirements. All simulations
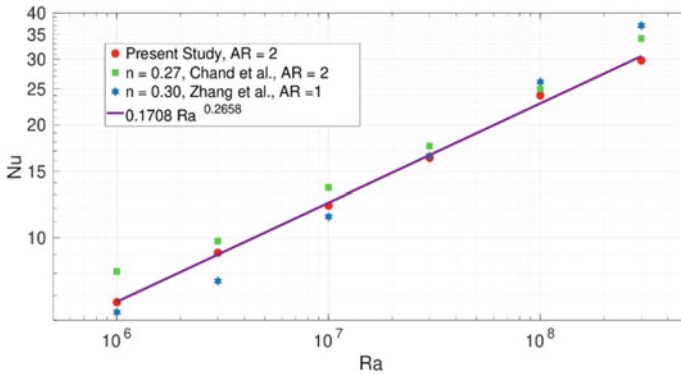
Fig. 2 Nu versus Ra for 2D RBC—current study and recent studies from literature

start from rest, till the instability kicks in to start the convection. In the following sections, we discuss the instantaneous flow structures observed, time-series data recorded by fixed probes, time-averaged fields, scaling of the fluxes, and variation of average quantities along the tube length and cross-section.

3.1 Instantaneous Flowfield

Figure 3 shows the instantaneous flowfields of temperature, horizontal and vertical components of velocities, and the vorticity at a randomly chosen time instant for a case at $Ra_g = 2.56 \times 10^6$. It can be seen that the inside of the tanks are nearly isothermal. The major temperature drop occurs across the length (height) of the tube. The most noticeable feature of the flowfield is the array of vertically stacked eddies or rolls along the height of the tube. These are counter-rotating in nature, as evident from the changing signs in the vertical velocity and vorticity plots. This feature seems to be the prominent one and appears for all the cases above $Ra_g \sim 10^4$. At the onset of convection ($Ra_g \sim 10^3$), the flow is very weak and resembles the half-and-half flow regime identified in the experiments of [2]. However, the streams were only long as half.

At small Rayleigh numbers in this vicinity ($10^3 < Ra_g < 10^4$), counter-rotating vortices start to appear but are elongated vertically, and only a few of them are present. With increase in Ra_g, the vertical extend of these rolls seem decreases, until they reach the dimension of the tube diameter at $Ra_g \sim 10^4$, after which these eddies scale roughly with the diameter of the tube. These structures look very similar to the Large-Scale Circulation (LSC) rolls in RBC, which scale with the height of the RBC system. These eddies or rolls have roughly the dimension of the tube width, as observed in the movies for different Rayleigh numbers.

Figure 4 compares the instantaneous temperature fields at different Rayleigh numbers. The increase in the scales of structures with Ra_g is evident from this
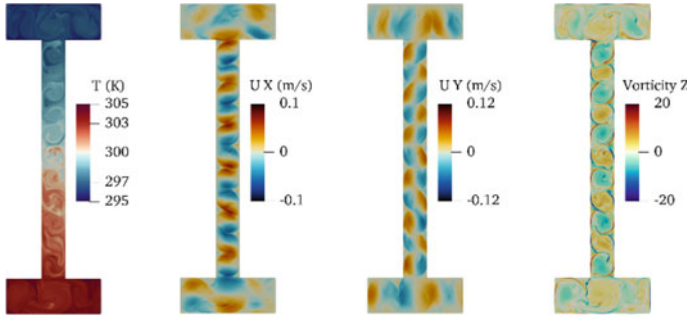
Fig. 3 Instantaneous flowfields of T, u_x, u_y, and ω_z for $\mathrm{Ra}_g = 2.56 \times 10^6$
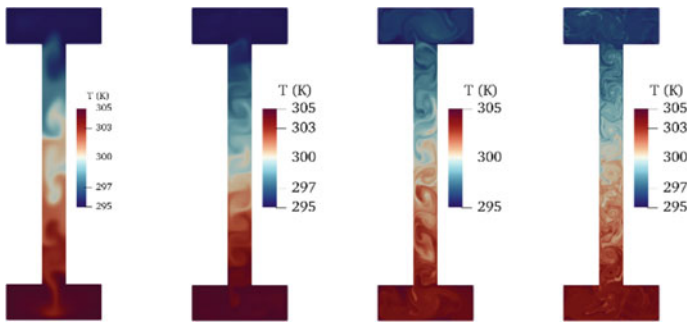
Fig. 4 Instantaneous temperature fields for (from the left) $\mathrm{Ra}_g = 3.47 \times 10^3, 9.15 \times 10^4, 6.23 \times 10^5$, and 2.19×10^7

sequence. It can be noticed that the eddies are elongated in the vertical direction for the lowest $\mathrm{Ra}_g = 3.47 \times 10^3$. For the other three cases shown, Ra_g is above 10^4, and the rolls appear to have largest scale of the width of the tube. Another important observation from the movies of these simulations is that location of these eddies appears to be roughly a constant. Although the flow is highly unsteady and chaotic, there appears to be some order associated with these rolls. These qualitative observations are later validated by the quantitative observations of the average flowfield.

3.2 Time-Series Data

Time-series data of temperature and components of velocity were recorded at various probe locations within the domain (see Fig. 1). These data are stored for every time step at 11 probe locations. Figure 5 shows this time-series data for temperature recorded by probes at the bottom (P2), mid-height (P4), and top (P6) of the tube at
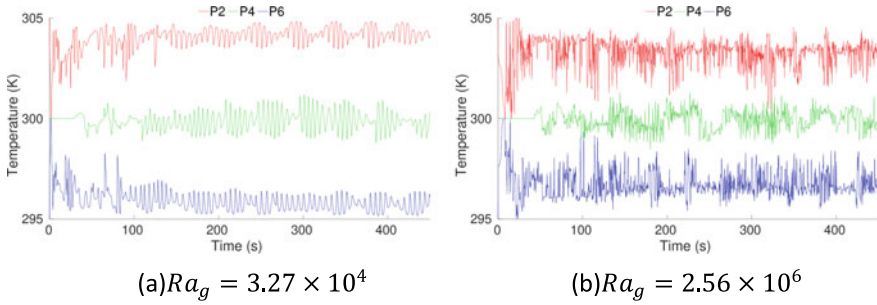
(a)$Ra_g = 3.27 \times 10^4$ (b)$Ra_g = 2.56 \times 10^6$

Fig. 5 Temperature versus time data from probes P2, P4, and P6 for two different cases

the centerline, for two different cases. It can be seen that after the initial transient phase of around 100 s or less, the data fluctuate around some mean value for each probe. We neglect this initial transient and consider only this statistical steady-state part for all the averaging processes. Hence, it is important to look into the probes data before starting the averaging process. It can also be seen that the data of the lower Rayleigh number case $Ra_g = 3.27 \times 10^4$ are much more smooth and periodic compared to the higher case of $Ra_g = 2.56 \times 10^6$ which appears much more chaotic and random. In addition to the regular fluctuations, there seem to be some low-frequency oscillations embedded in the signals of both cases, which require further investigation.

Figure 6 compares the temperature signals at the same probe location P4, i.e., mid-height of the tube for different Rayleigh numbers. It can be seen that convection is virtually absent for the lowest case of $Ra_g = 5.02 \times 10^2$. For $Ra_g = 2.31 \times 10^3$, a weak signal is observed. For higher cases of $Ra_g \sim 10^4$, 10^5, 10^6, the signal shows increasing frequency and disorder, showing that the flow transitions from smooth steady flow to unsteady chaotic and turbulent flows at extreme Rayleigh numbers. However, it is interesting to note that the low-frequency modulation signal of unknown origin mentioned earlier is present in some way in all these signals.

3.3 Average Flowfield

Based on the observations from time-series plots of the probe data, field variables are averaged in time for mean and RMS quantities once the system reaches a statistical steady state. Mean and RMS temperature and the components of velocity in the tube region are shown in Fig. 7 for the case with $Ra_g = 2.56 \times 10^6$. Several observations can be made from these contours. The mean temperature shows a predominant variation in the vertical direction, as expected. The total temperature drop in the tube part is around 8 K, very close to the total temperature difference of 10 K between the top and bottom tank walls. This is true for most of the cases and means that the major temperature drop is along the tube and is much more than the temperature
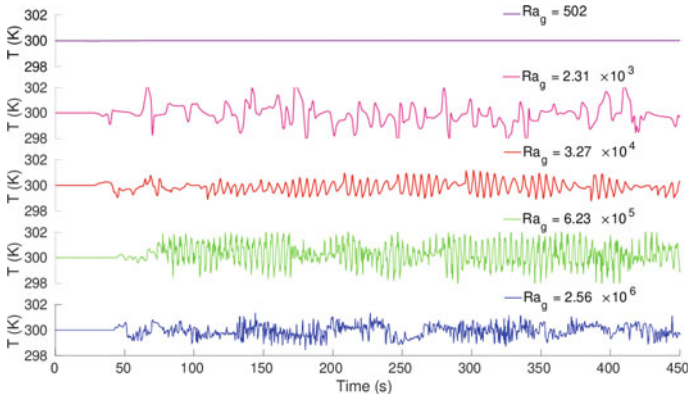
Fig. 6 Comparison of temperature versus time data at probe location P4 for different cases

drops at the tank walls. This is in sharp contrast with the RBC system, where the average temperature drops are almost entirely at the top and bottom boundary layers. In RBC, due to the presence of large convection rolls (LSC), the average flowfield in the core is almost isothermal.

Root Mean Square (RMS) of the temperature field shows signature of the vertically stacked rolls discussed earlier. In fact, this is more clear in the average fields of horizontal and vertical velocities. Existence of such sharp vortices in the average field means that the eddies are roughly stationary in space. Had the rolls been moving around, they would have appeared smeared in these contour plots. Around 11 rolls can be identified along the length of the tube, which is roughly the number of diameters present along the tube length ($H/d = 10$). This again means that the rolls have roughly the same dimension as the diameter of the tube. An estimate for the scale of vertical velocity fluctuations in tube convection was given by a mixing length model in [8] as $w_m = \sqrt{g\beta \frac{dT}{dy} d^2}$. For the above case of $Ra_g = 2.56 \times 10^6$, this gives an
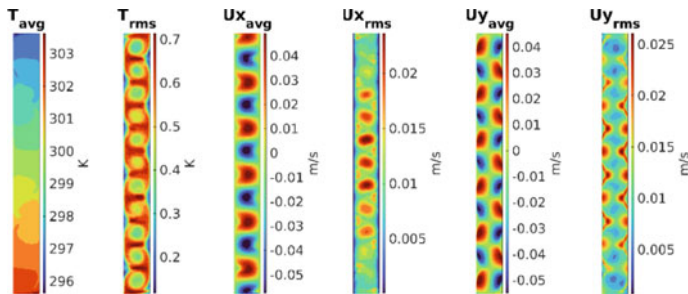

Fig. 7 Time-averaged flowfields for $Ra_g = 2.56 \times 10^6$. From the left: T_{avg}, T_{rms}, $u_{x,avg}$, $u_{x,rms}$, $u_{y,avg}$, $u_{y,rms}$

(a) $\langle T \rangle_{t,x}$ vs y (b) $\langle u_{x,rms} \rangle_y, \langle u_{y,rms} \rangle_y$ vs x
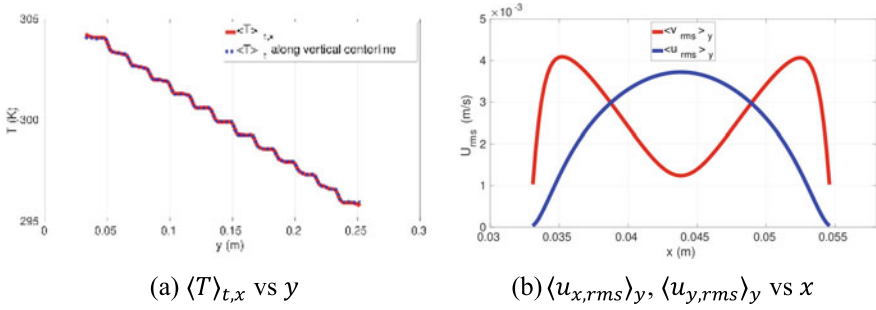
Fig. 8 Line plots of time average temperature and RMS velocities for $Ra_g = 9.15 \times 10^4$

estimate of $w_m = 0.021$ m/s, which is very close to the range observed in the average flowfield of $u_{y,rms}$.

Figure 8a shows the variation of temperature in the tube which is averaged in both time and tube width, i.e., $\langle T \rangle_{t,x}$ along the length of the tube y for $Ra_g = 9.15 \times 10^4$. Superimposed on that is the variation of temperature of the vertical centerline $\langle T \rangle_t$ averaged only in time. It can be seen that these plots are almost the same, which means that time average temperature of tube centerline is a good representative of the average tube temperature. It can be seen that the average temperature profile along the length of the tube is approximately linear. The bumpiness in the plot is again a representation of the stacked vertical rolls. These characteristics of the plot are very similar for different Rayleigh numbers $Ra_g \gtrsim 10^4$. For obtaining the average temperature gradient, a least square fit is done on this distribution. This temperature gradient is in turn used to calculate the gradient-based Rayleigh and Nusselt numbers.

Figure 8b shows the variation of RMS horizontal and vertical velocities averaged along the length of the tube $\langle u_{x,rms} \rangle_y$, $\langle u_{y,rms} \rangle_y$ along the width of the tube x for the same $Ra_g = 9.15 \times 10^4$. The horizontal velocity RMS shows a maxima at the center and symmetrically reduces to zero toward the walls of the tube. The vertical velocity RMS is also symmetric with maxima near the tube walls and minimum at the tube center. It should be noted that for both horizontal and vertical velocities, the value should go to zero at the walls. However, the plots do not show zero value as the line of extraction is just short of the tube width. The overall behavior of these plots looks very similar to those seen in the experiments of [8] and 3D DNS studies of [14], which indicates that the basic flow mechanisms associated with 2D and 3D tube convection flows are very similar.

3.4 Nusselt Number Scaling

The variation of heat flux as a function of temperature gradient in the tube is expressed in a non-dimensional manner as the $Nu_g - Ra_g$ relation. This scaling relation has central importance in any convection problem. For tube convection studies [13],

combined all the experimental and numerical data till then and classified into two regimes: For $Gr_g > Gr_{gc}$, $Nu_g/Pr \sim Gr_g^{1/2}$, and for $Gr_{g1} < Gr_g < Gr_{gc}$, $Nu_g/Pr \sim Gr_g^{0.3}$. Here, $Gr_g = Ra_g/Pr = g\beta \frac{dT}{dy} d^4/\nu^2$ is the gradient-based Grashof number, and $Gr_{gc} = 1.6 \times 10^5$ is the critical Grashof number for transition between 0.3 and 0.5 regimes. Gr_{g1} is an unknown lower limit till which the 0.3 regime scaling is valid and remains undetermined as there are no data at such low Rayleigh numbers.

The scaling regimes proposed by Pawar and Arakeri [13] are shown as green and blue lines in Fig. 9. Their intersection point is the critical Grashof number Gr_{gc}. The data of Nu_g obtained from current simulations are shown as red markers. It is seen that the Nu_g values predicted by the current 2D simulations are much less than those predicted by scaling relations of [13]. This should be expected, as restriction of motion in one direction (normal to the plane) in the 2D simulations restricts the mixing and thus the fluxes as well. It may be noticed that since $Pr = 1$ for the current simulations, $Gr_g = Ra_g$, and either of them can be used interchangeably. The entire spectrum of the current data may be divided into atleast three regimes. At the lowermost spectrum where $Ra_g \lesssim 10^4$, Nu_g increases sharply with Ra_g. From $Ra_g \sim 10^4$ to 10^5, the variation in Nu_g is very small. Above $Ra_g \sim 10^5$ (which is interestingly close to Gr_{gc}), there is a sudden jump in the values of Nu_g and the data points tend to follow the trend of the 1/2 power regime, although the values are lower. We do not attempt to do a curve fit on these data points and propose a scaling relation at this point of time, as some of these data need further analysis. There are not enough data points to fit trend lines in some of the regimes. More importantly, statistical independence of the results has to be established by varying the averaging window for all the cases. The stagnation of the Nu_g data between $10^4 < Ra_g < 10^5$ and the sudden jump in the trend, thereafter, needs a closer look. A few more simulations for more data points and detailed analysis of the existing results are under progress.
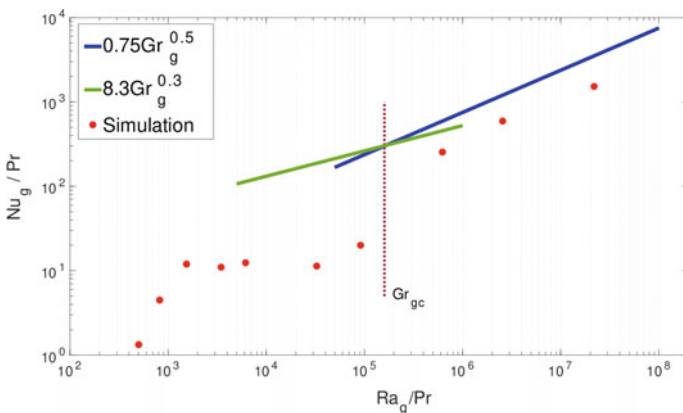

Fig. 9 Nu_g/Pr versus Gr_g plot with current simulation data compared with the two regimes of scaling proposed by Pawar and Arakeri [13]

4   Conclusions

We have presented preliminary results for numerical simulations of 2D tube convection for gradient Rayleigh numbers $Ra_g \sim 10^3 - 10^7$. The main dynamical feature of the flow was identified to be an array of vertically stacked counter-rotating eddies that roughly scale with the width of the tube. With increase in Ra_g, finer scales tend to appear, and the flow moves progressively from ordered periodic laminar flow to chaotic and random turbulent flow. This observation was also evident from the time-series data acquired using probes which also showed presence of low-frequency modulation which are yet to be understood. The rolls were also found to be stationary in space, as evident from the average flowfields of temperature and velocity components. Time-averaged temperature field was approximately linear, with bumpiness due to presence of rolls. Scaling of RMS velocities was close to the mixing length model predicted by Cholemari and Cholemari [8] and their distribution across the tube width was found to be similar to experiments and 3D simulations in literature. Scaling of Nusselt number showed evidences of different regimes and 1/2 power scaling in 2D tube convection. However, further analysis is required for better explanation and deeper understanding of the results.

References

1. Ahlers G, Grossmann S, Lohse D (2009) Heat transfer and large scale dynamics in turbulent Rayleigh-Bénard convection. Rev Mod Phys 81(2):503–537
2. Arakeri JH, Avila FE, Dada JM, Tovar RO (2000) Convection in a long vertical tube due to unstable stratification—a new type of turbulent flow? Curr Sci 79(6):859–866
3. Arakeri JH (2013) Convection. In: Fernando HJ (ed) Handbook of environmental fluid dynamics, vol 1, 1 ed. CRC Press, pp 489–503
4. Castaing B, Gunaratne G, Heslot F, Kadanoff L, Libchaber A, Thomae S, Wu X-Z, Zaleski S, Zanetti G (1989) Scaling of hard thermal turbulence in Rayleigh-Bénard convection. J Fluid Mech 204:1–30
5. Chand K, Sharma M, Vishnu VT, De AKr (2019) Statistics of coherent structures in two-dimensional turbulent Rayleigh-Bénard convection. Phys Fluids 31(11):1–15
6. Chilla F, Schumacher J (2012) New perspectives in turbulent Rayleigh-Bénard convection. Eur Phys J E 35(7):58
7. Cholemari MR, Arakeri JH (2005) Experiments and a model of turbulent exchange flow in a vertical pipe. Int J Heat Mass Transf 48(21–22):4467–4473
8. Cholemari MR, Arakeri JH (2009) Axially homogeneous, zero mean flow buoyancy-driven turbulence in a vertical pipe. J Fluid Mech 621:69
9. Globe S, Dropkin D (1959) Natural-convection heat transfer in liquids confined by two horizontal plates and heated from below. J Heat Transf 81(1):24–28
10. Kraichnan RH (1962) Turbulent thermal convection at arbitrary Prandtl number. Phys Fluids 5(11):1374

11. Malkus WVR, Chandrasekhar S (1954) The heat transport and spectrum of thermal turbulence. Proc Royal Soc London Ser A Math Phys Sci 225(1161):196–212
12. OpenFOAM (2018) The open source cfd toolbox, version 6.0
13. Pawar SS, Arakeri JH (2016) Two regimes of flux scaling in axially homogeneous turbulent convection in vertical tube. Phys Rev Fluids 1:042401
14. Schmidt LE, Calzavarini E, Lohse D, Toschi F, Verzicco R (2012) Axially homogeneous Rayleigh-Bénard convection in a cylindrical cell. J Fluid Mech 691(2012):52–68
15. Shishkina O, Stevens RJAM, Grossmann S, Lohse D (2010) Boundary layer structure in turbulent thermal convection and its consequences for the required numerical resolution. New J Phys 12(7):075022
16. Shraiman BI, Siggia ED (1990) Heat transport in high-Rayleigh-number convection. Phys Rev A 42(6):3650
17. Spiegel EA (1971) Convection in stars in basic Boussinesq convection. Ann Rev Astron Astrophys 9(1):323–352
18. Van Der Poel EP, Stevens RJAM, Lohse D (2013) Comparison between two-and three-dimensional Rayleigh-Bénard convection. J Fluid Mech 736:177–194
19. Zhang Y, Zhou Q, Sun C (2017) Statistics of kinetic and thermal energy dissipation rates in two-dimensional turbulent Rayleigh-Bénard convection. J Fluid Mech 814:165–184
20. Zhu X, Stevens RJAM, Shishkina O, Verzicco R, Lohse D (2019) $Nu - Ra^{1/2}$ scaling enabled by multiscale wall roughness in Rayleigh-Bénard turbulence. J Fluid Mech 869:R4

Study of the Impact of Flow Valve Design on the Temperature Separation in the Vortex Tube with Computational Approach

Ravi Kant Singh, Arunabha Mahato, Achintya Kumar Pramanick, and Subhas Chandra Rana

Nomenclature

VT	Vortex tube
ΔT_h	Hot temperature gradient, K
T_s	Static temperature, K
d_c	Diameter of cold exit, mm
ρ	fluid density, kg/m^3
ΔT_c	Cold temperature gradient, K
k	Thermal conductivity of intake fluid (W/mK)
D	Diameter of main tube, mm
Z	Distance between chambers
L	Length of vortex tube, mm
$\dot{m}_c$	Mass flow rate at cold exit, kg/s
μ_c	Cold mass fraction
$\dot{m}_{in}$	Mass flow rate at inlet, kg/s
γ	Specific heat ratio
C_p	Specific heat of fluid, J/kgK

R. K. Singh (✉) · A. Mahato · A. K. Pramanick · S. C. Rana
Department of Mechanical Engineering, NIT Durgapur, Durgapur 713209, India
e-mail: ravikantsingh941@gmail.com

1 Introduction

The Ranque–Hilsch Vortex Tube (VT) is mainly used to separate a compressed high-energy gaseous fluid into two low-energy gaseous fluids at high and low temperatures exiting from the hot and cold exits simultaneously. The VT is a mechanical device having high mechanical efficiency due to less wear and tear since it has no moving components. It drew the attention of many researchers due to its large practical applications, i.e. for gas liquefaction of compressed natural gas, refrigeration, inexpensive spot cooling, and it may also reasonably be used in the steam power generation units for quick start-up. The concept of vortex tube was originally explained by Ranque [1], which he discovered while studying the flow through cyclone separators. The improvement in the VT performance has been carried out ever since it was found due to its efficient cooling and easy maintainability. Skye et al. [2] investigated the VT performance for different μ_c and inlet pressure experimentally and numerically. They found that the cold temperature decreases with increased inlet pressure. Aljuwayhel et al. [3] studied the thermal separation phenomenon in VT two-dimensional model with the CFD approach and reported the parameters which affect the separation phenomenon in the VT. Ahlborn et al. [4] explained the importance of normalised pressure drop in VT thermal performance. Khazaei et al. [5] examined the use of various fluids on VT cooling behavior and found that energy separation is maximum when considering working fluid is helium. Farouk and Farouk [6] studied the VT using the LES method and showed that the least total temperature and swirl velocity lie in the same region. Pourmahmoud et al. [7] observed the effect of nozzles and shape on VT behaviour. They claim that high swirl velocity can be obtained with helical nozzles. The study of convergence ratio of intake nozzles and intake pressure was studied by Rafiee et al. [8]. They claimed that the cold exit temperature increases with increment in inlet pressure. Behera et al. [9] examined the cold exit area effect on the secondary flow in the VT. They concluded that secondary flow increases as the cold exit area decreases. Dincer et al. [10] experimentally investigated the effect of a hot mobile plug located at the hot exit of VT and investigated for the angle, position, and optimum diameter of a hot plug. The 5 mm diameter of mobile plug shows the maximum temperature difference between cold and hot fluids. Lewins et al. [11] observed that angular velocity is the reason for frictional coupling between the rotating fluid layers. Kumar et al. [12] examined the thermal separation for different types of VT with various intake pressure and mass fractions experimentally. They conclude that maximum relative humidity is 65 and 67% at 4 bar temperatures for insulated and non-insulated vortex tubes. Thakare et al. [13] studied the behaviour of VT for cooling when different tube materials are used. They observed that VT with PA6 material with high inlet pressure has the highest thermal efficiency than mild steel.

The objective achieved with the present study is as follows: The solid works software has been used to develop a 3D model for all the different types of control valve VT considered. The flow simulation has been carried out with the help of ANSYS FLUENT software. The effect of intake pressure, cold mass fraction, shape

of control valve, i.e. conical, square, and truncated at hot and cold exits and *Z/L* ratio on thermal performance of the VT are studied. The coefficient of performance (COP) of all the three models of VT is analysed.

2 Materials and Methods

The energy characteristics and flow inside the VT are determined by considering a similar model in terms of length and primary tube diameter as Thakare et al. [13]. However, there are changes in the control valve. The dimension and thermophysical of the model are presented in Tables 1 and 2, respectively. The schematic diagram of the vortex tube with three types of flow control (throttle) valve, namely conical shape, square shape, and truncated shape having a single intake section with five nozzles, is presented in Fig. 1a–c. The air enters the tube tangentially through nozzles in the vortex tube. The shape and opening of the throttle valve at the hot exit regulate the flow rate through the hot exit.

2.1 Governing Equations

The nonlinear partial differential equations of mass, momentum, energy balance, and ideal gas are governed by swirl flow inside the VT. The equations are presented below:

Continuity equation:

$$\frac{\partial}{\partial x_i}(\rho u_i) = 0. \tag{1}$$

Table 1 Dimensions of vortex tube

Specification	Dimension
Working length of vortex tube	106 mm
Shape of control/throttle valve	Conical, square, and truncated
Diameter of cold outlet, d_c	6.2 mm
Diameter (D) of VT	11.4 mm
Number of nozzles (N)	5

Table 2 Thermophysical properties of the air

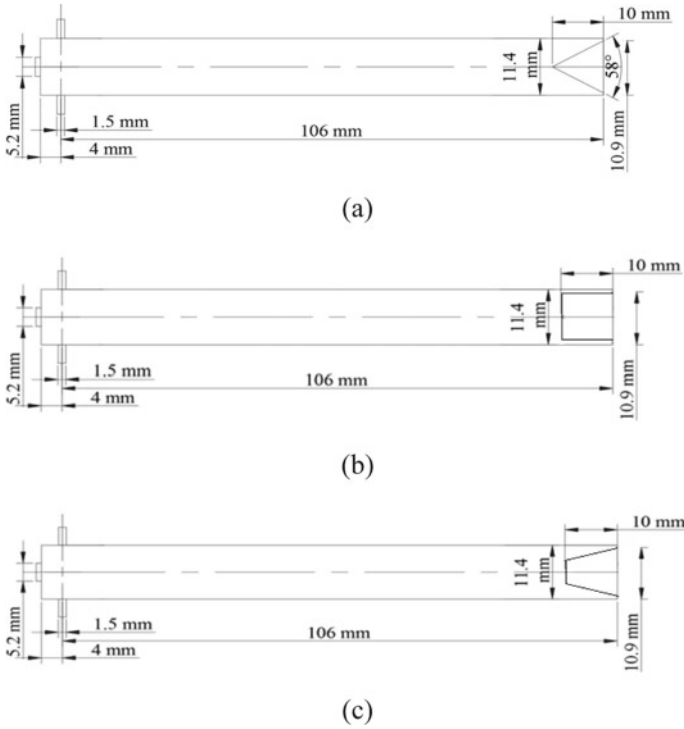| Density (ρ)	Ideal gas equation
Thermal conductivity of air (K)	0.0242 W/mK
Specific heat (C)	1.00643 kJ/kg-k

Fig. 1 Schematic view of the vortex tube having **a** conical shape, **b** square shape, and **c** truncated shape control valve used for numerical simulation

Momentum balance equation:

$$\frac{\partial}{\partial x_i}(\rho u_i u_j) = -\frac{\partial P}{\partial x_i} + \frac{\partial}{\partial x_j}\left[\mu\left(\frac{\partial u_i}{\partial x_i} + \frac{\partial u_j}{\partial x_j} - \frac{2}{3}\delta_{ij}\frac{\partial u_k}{\partial x_k}\right)\right] + \frac{\partial}{\partial x_i}\left(-\overline{\rho u_i' u_j'}\right).$$

$$(2)$$

Energy balance equation:

$$\frac{\partial}{\partial x_i}[u_i(\rho E + P)] = \frac{\partial}{\partial x_j}\left[\left(k_e + \frac{c_p \mu_t}{\mathrm{Pr}_t}\right)\frac{\partial T}{\partial x_j} + u_i(\tau_{ij})_{eff}\right] + S_h, \qquad (3)$$

$$(\tau_{ij})_{\mathrm{eff}} = \mu_{\mathrm{eff}}\left(\frac{\partial u_j}{\partial x_i} + \frac{\partial u_i}{\partial x_j}\right) - \frac{2}{3}\mu_{\mathrm{eff}}\frac{\partial u_k}{\partial x_k}\delta_{ij}. \qquad (4)$$

Ideal gas equation:

$$P = \rho R T_s. \qquad (5)$$

For the turbulence simulation of the flow field, a standard k-ε model along with standard wall function has been considered. The transport equations associated with turbulent Kinetic Energy (k) and dissipation (ε) for the standard k-ε model, together with the energy and Reynolds Average Navier–Stokes equations as

$$\frac{\partial}{\partial t}(\rho k) + \frac{\partial}{\partial x_i}(\rho k u_i) = \frac{\partial}{\partial x_j}\left[\left(\mu + \frac{\mu_t}{\sigma_k}\right)\frac{\partial k}{\partial x_j}\right] + G_k + G_b - \rho\varepsilon - Y_M, \quad (6)$$

$$\frac{\partial}{\partial t}(\rho\varepsilon) + \frac{\partial}{\partial x_i}(\rho\varepsilon u_i) = \frac{\partial}{\partial x_j}\left[\left(\mu + \frac{\mu_t}{\sigma_\varepsilon}\right)\frac{\partial\varepsilon}{\partial x_j}\right] - \rho C_2 \frac{\varepsilon^2}{k + \sqrt{\nu\varepsilon}}$$
$$+ C_{1\varepsilon}\frac{\varepsilon}{k}(G_k + C_{3\varepsilon}G_b). \quad (7)$$

The convergence criteria of 10^{-6} for energy and 10^{-3} for all other quantities have been considered. The constants for the above turbulence model are as follows:

$$\sigma_{1\varepsilon} = 1.44, \sigma_k = 1.0, \sigma_t = 0.9, \sigma_\varepsilon = 1.2, \text{ and } C_2 = 1.9.$$

2.2 Parameters Considered for the Study

Cold mass fraction (μ_c) is the ratio of cold mass flow rate to intake mass flow rate in the VT, given as

$$\mu_c = \frac{\dot{m}_c}{\dot{m}_{\text{in}}}. \quad (8)$$

Temperature gradient of cold exit (ΔT_c) is the difference between the fluid inlet temperature and the fluid at cold exit, that is,

$$\Delta T_c = T_{\text{in}} - T_c. \quad (9)$$

Temperature gradient at hot exit (ΔT_h) is the difference between the hot exit temperature and fluid inlet temperature of the VT, that is,

$$\Delta T_h = T_h - T_{\text{in}}. \quad (10)$$

3 Boundary Conditions

The energy separation patterns observed for both hot and cold fluids by applying different shapes of control valve, i.e. conical, square, and truncated at the hot outlet. For the pressure–velocity coupling, SIMPLE algorithm has been applied. Pressure inlet is considered at intake and the pressure outlet condition at both cold and hot exits. The adiabatic condition has been applied to the wall. Consequently, the effect of convection has been neglected. The no-slip boundary condition is applied between the rotational flow and wall of the VT. The pressure at the air intake for all slots has varied from 0.35 to 0.55 MPa. The temperature of air at the intake is taken as 294.15 K. Air is the working fluid inside the VT and is considered with the ideal gas properties. The boundary condition is similar for all the three different models of control valve, i.e. conical, square, and truncated in order to obtain the compared outcomes by a computational study using the FLUENT software package.

4 Model Solver, Computational Domain, and Meshing Grid Test

The numerical grid and calculation domain of 3D VT has been presented. ANSYS FLUENT software has been used to perform the flow simulation. The governing equation has been solved by an implicit solver (pressure based). For the convective terms in energy, the momentum equation second-order scheme has been applied. The displacement term has been neglected by using a QUICK scheme for turbulence equations. In the case of dependent variables, under relaxation has been used. Figure 2 depicts the unstructured grid of a truncated control valve three-dimensional VT with five inlet nozzles. The stability and convergence are strongly influenced by the grid density; therefore, the critical section of the model has high-density grid so that minute details of the region get simulated. The grid independence evaluation is performed to obtain the optimum number of grids suitable for the present problem for high accuracy, reducing the computational cost and time. The unstructured mesh has been used for the current three-dimensional structure of VT, as shown in Fig. 2. The trend followed by cold outlet temperature with the number of grid cells from the grid number 19,587–135,000 has been depicted in Fig. 3. The cold mass fraction $\mu_c = 0.35$ and $L/D = 9.298$ has been maintained throughout the study. As seen in Fig. 3, a very close value of cold outlet temperature is obtained at higher grid cells above 120,000. So, further simulation is carried out for 120,000 grid cells.
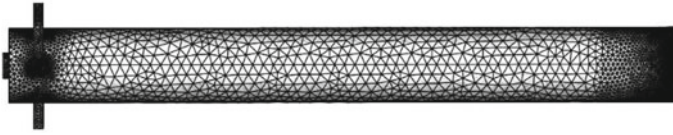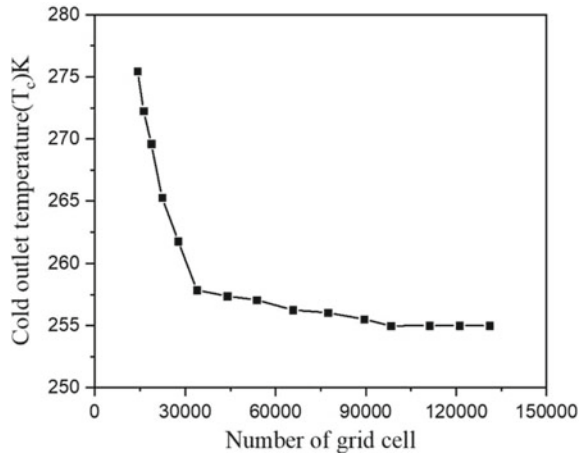
Fig. 2 Unstructured mesh of a truncated control valve vortex tube

Fig. 3 Grid independence evaluation

5   Validation

The derivative terms in energy, turbulence, and momentum equations are discretised by second-order upwind, and quick schemes are applied. The present computational results are validated with the experimental as well as computational study of Thakare et al. [13]. Figure 4 depicts the variation of cold temperature gradient with the cold mass fraction. It is seen from Fig. 4 that the increment in the μ_c leads to the rise in the value of cold temperature gradient initially, achieves maxima, and then decreases. The present result follows the same trend and is in close accordance with Thakare et al. [13], as seen in Fig. 4, which shows that a suitable methodology has been used in the computational study. This analysis follows the same general trend as Thakare et al. [13], and the average variance in present outcomes is 4.5%, which is reasonable.

6   Result and Discussion

The computational study with ANSYS FLUENT software is carried out to examine the thermal separation behaviour of the fluid, and velocity distribution inside the VT, considered as a cooling device in three different cases: the VT with a conical, square, and truncated control valve. The VT performance with various operating conditions
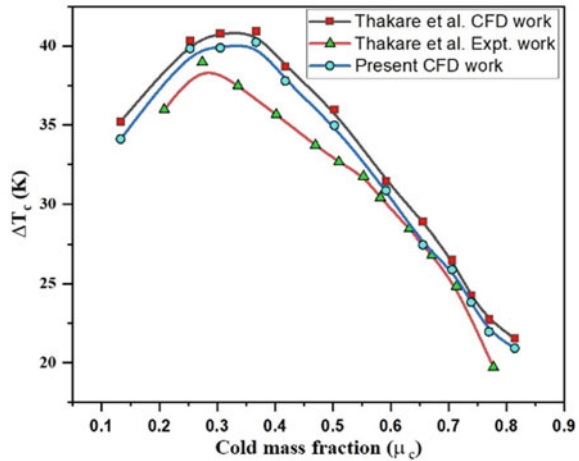
has been determined. The coefficient of performance (COP) and cold temperature difference (ΔT_c) for different models of VT have been presented in this section.

The total temperature contour of three types of flow control valves, namely conical, squared, and truncated shaped in VT, is presented in Fig. 5a–c. It is seen that core fluid temperature is less than the peripheral inner wall from Fig. 5. This temperature difference between other longitudinal regions and at the intake nozzle is apparent. The core fluid volume mainly depends on the type of control valve used at hot exit, as seen in Fig. 5. The fluid obtained at the cold outlet is coldest for truncated-shaped control valve and is least for the square-shaped control valve. The conical shape performance is less than truncated shape and more than square shape control valve, which is depicted in Fig. 5. The flow inside vortex tube is analysed for the intake pressure of 5.5 bar, and mass fraction equals 0.25 for all the three temperature contours as shown in Fig. 5, which corresponds to the optimum operating condition that provides the minimal cold exit temperature.

The structure of the streamlined form of fluid inside the VT is depicted in Fig. 6a–c. The streamline patterns in longitudinal cross-section are presented for all three models of vortex tube (having different control valves). It can be clearly observed from Fig. 6a–c that two vortex flows have formed inside the VT, one near the periphery and another at the core of the VT. The temperature separation between the peripheral and core fluid occur near control valve at hot outlet due to momentum transfer and diffusion activity between peripheral and core fluid, as per Thakare et al. [13]. Ramakrishna et al. [25] explained the reason for work transfer between the peripheral and core fluid for flow separation. This is the reason why the shape of the control valve is important to govern the temperature separation between hot and cold fluid.

Furthermore, it can be observed from Fig. 6b that the maximum velocity for the square-shaped control valve is less in comparison to conical and truncated valve. The maximum velocity has seen in case of a truncated control valve. Figure 6c indicates the maximum flow rate for the VT in terms of cold and hot fluid, which in turn
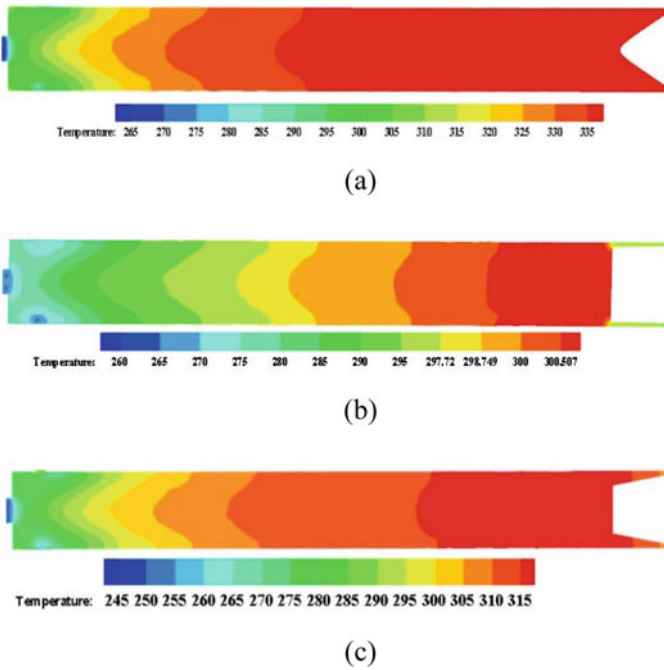
Fig. 5 Thermal contour of a conical, square, and truncated shape control valve VT

increases the utility of truncated-shaped VT. The formation of a recirculation zone in the form of vortices is observed near the cold outlet as intake pressure increases. As the vortices of different shapes and sizes increase near the cold outlet, the level of intermixing of core and peripheral fluid increases, which hinders flow separation potential of VT, thus decreasing the cooling capacity drastically.

The swirl velocity for the VT having a conical, square, and truncated control valve has been shown in Fig. 8. The variation of swirl velocity with radial distance from the axis for all three different models of control valve for $Z/L = 0.1$ and 0.7 in the longitudinal direction has been depicted in Fig. 8a, b. The rotational velocity varies considerably by replacing the shape of the throttle valve. The rotational velocity changes maximum with the stream-wise section and varies along the longitudinal direction of flow towards the hot exit with decreasing trends. Figure 8 depicts that the highest swirl velocity occurs near the entrance of the flow at $Z/L = 0.1$, and as the gas expands, it decreases to a lower value along the hot exit at $Z/L = 0.7$. A drag force is created between the flow field and cold core due to the pressure difference, which continuously affects the movement of the fluid particle towards the hot exit. The expansion occurs between core and peripheral fluid when fluid velocity reaches zero due to non-resistible drag force. The fluid temperature decreases strongly due to expansion and redirects to the central cold core because of restriction of the control valve at the hot exit. An accelerating movement is created due to pressure difference
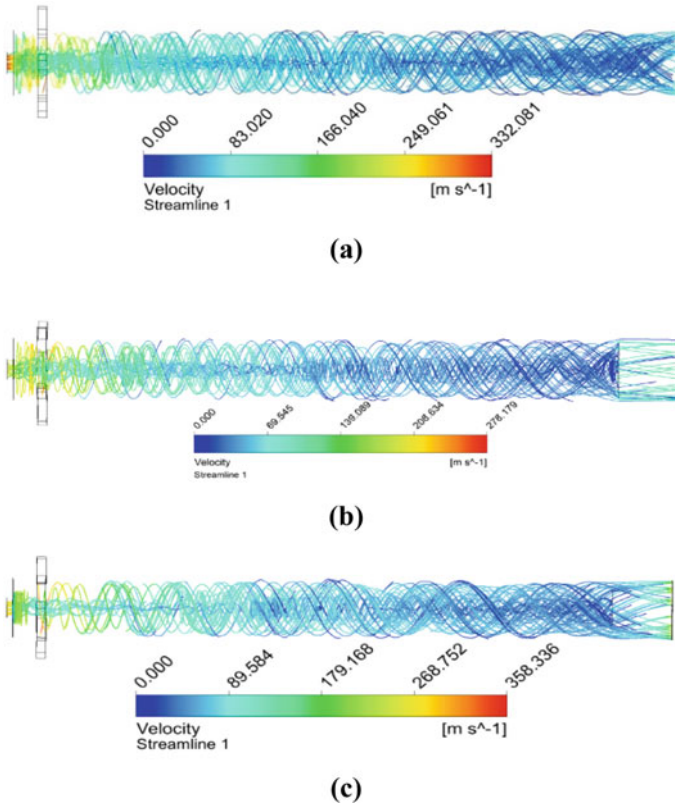
Fig. 6 Velocity streamlines of a VT with conical, square, and truncated shape control valve

which assists the particle flow towards the cold exit. It has been mentioned previously that the VT with a truncated control valve depicted the highest separation and cooling capability. The axial velocity decreases in the longitudinal direction along the hot exit because the pressure created due to restricted passage at the hot exit increases gradually, also observed by Rafiee and Rahimi et al. [8].

Figure 7a–c are presented the trends of temperature gradient for hot and cold outlets with μ_c at different inlet pressures as Pin = 0.35 MPa, 0.45 MPa, and 0.55 MPa, respectively. There are four observations drawn from Fig. 7. Firstly, it is seen that as the μ_c value increases, the ΔT_c increases initially, reaches a maximum at $\mu_c = 0.25$, and decreases thereafter. Secondly, the ΔT_h follows increasing trends for the entire μ_c in all four cases. Third, Fig. 7 depicts that cold temperature gradient increases, which means that low cold outlet temperature obtained as the intake pressure increases from 0.35 to 0.55 MPa. This trend is also seen in the study of Aljuwayhel et al. [4], Ahlborn et al. [3]. Fourth, the cold temperature gradient is obtained maximum for the truncated-shaped control valve VT and then conical shapes and last square shape. The square shape control valve cooling performance

is low in all cases of cold mass fraction because the vortices form at the hot exit are more as compared to conical and truncated shape due to which the flow separation phenomenon of peripheral and core fluid gets disturbed, and eventually, the temperature of the core fluid increases. As per Kumar et al. [12], the coefficient of performance (COP) is defined as the relation between work required and the refrigeration effect and is given as,

$$\text{COP} = \frac{Q_c}{W} = \frac{\mu C_p \Delta T_c}{\frac{\gamma}{\gamma-1} R T_{\text{in}} \left[\left(\frac{P_{\text{in}}}{P_{\text{atm}}} \right)^{(\gamma-1)/\gamma} - 1 \right]}. \tag{11}$$

R is the specific gas constant, C_p is the specific heat at constant pressure, Q_c is the refrigeration effect, and W is the required work. It is seen from Fig. 9 that as the value of μ_c increases, an increment in COP is up to $\mu = 0.65$ and then follows the decreasing trend. It is highest for the truncated shape control value VT and then follows the conical shapes, and least COP is obtained for the square shape control valve for entire cold mass fractions considered.

7 Conclusion

The computational study of a 3D vortex tube having three different flow control valves, i.e. conical, square, and truncated shaped, has been carried out with ANSYS Fluent software. The results of the CFD study mainly focus on energy separation variation for cold and hot fluids by changing the shape of the control (throttle) valve for constant working tube length. The following conclusion has been drawn from the study mentioned below:

(a) The cold outlet temperature of fluid with truncated throttle valve is lower in comparison with the square and conical shapes, respectively.
(b) The temperature gradient of fluid for both hot and cold outlets increases with intake pressure in all the three models of the vortex tube. The highest increase is noted in the case of a truncated throttle valve at all the intake pressures and the lowest for the square throttle valve model. The temperature gradient at the cold exit increases initially with μ_c and declines after $\mu = 0.25$. A steady increase in hot temperature gradient is observed in all three models with mass fraction and at all the intake pressures.
(c) The highest cooling efficiency can be attained with truncated throttle valve. Also, the VT with a truncated valve possesses highest magnitude of tangential and axial speeds in comparison to the conical and square control valve.
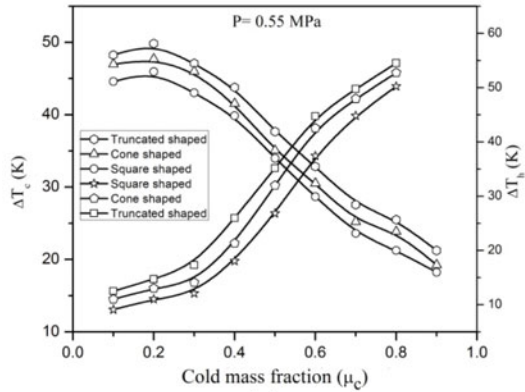
Fig. 7 Effect of mass fraction and intake pressure on cold and hot temperature gradients of different models of VT
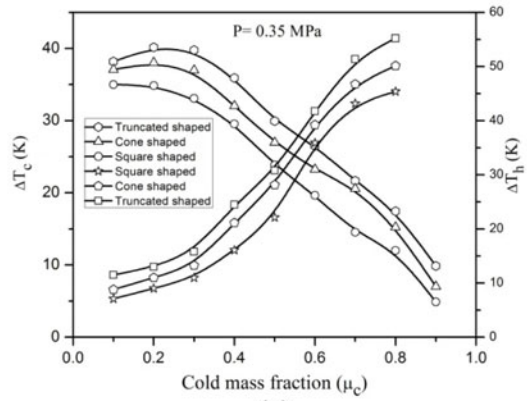
(a)
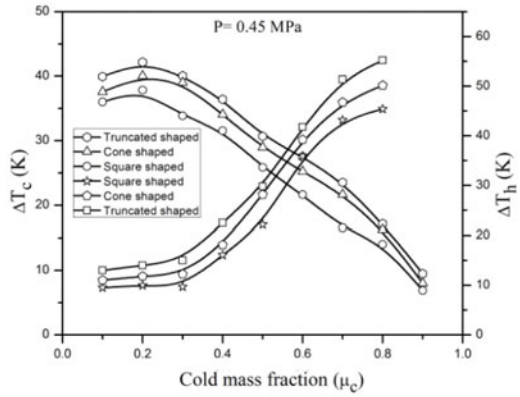
(b)

(c)

Fig. 8 Swirl velocity variation with radial distance for **a** $Z/L = 0.1$ and **b** $Z/L = 0.7$
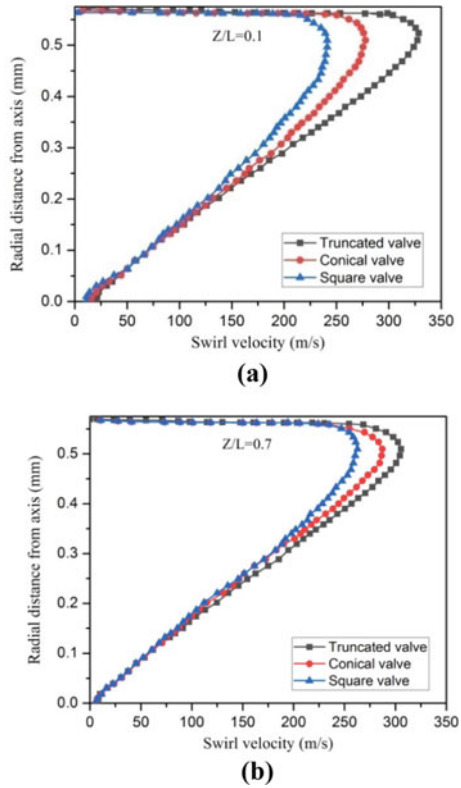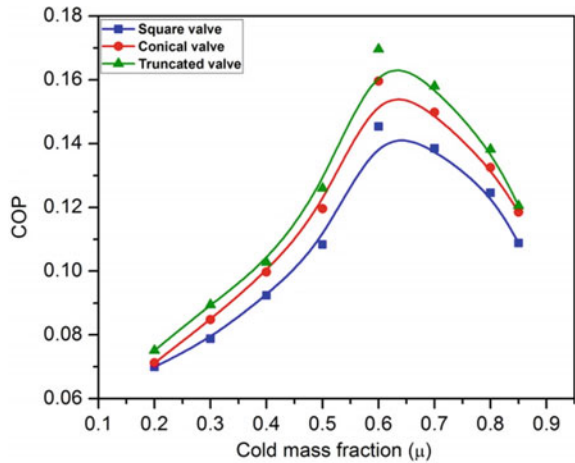

(a)

(b)

Fig. 9 Effect of mass fraction on coefficient of performance (COP) trend for square, conical, and truncated-shaped control valve VT

References

1. Joseph RG, GIRATION DES FLUIDES SARL (1934) Method and apparatus for obtaining from alpha fluid under pressure two currents of fluids at different temperatures. U.S. Patent 1,952,281
2. Skye HM, Nellis GF, Klein SA (2006) Comparison of CFD analysis to empirical data in a commercial vortex tube. Int J Refrig 29(1):71–80
3. Ahlborn B, Camire J, Keller JU (1996) Low-pressure vortex tubes. J Phys D Appl Phys 29(6):1469
4. Aljuwayhel NF, Nellis GF, Klein SA (2005) Parametric and internal study of the vortex tube using a CFD model. Int J Refrig 28(3):442–450
5. Khazaei H, Teymourtash AR, Malek-Jafarian M (2012) Effects of gas properties and geometrical parameters on performance of a vortex tube. Scientia Iranica 19(3):454–462
6. Farouk T, Farouk B (2007) Large eddy simulations of the flow field and temperature separation in the Ranque-Hilsch vortex tube. Int J Heat Mass Transf 50(23–24):4724–4735
7. Pourmahmoud N, Zadeh AH, Moutaby O, Bramo A (2012) Computational fluid dynamics analysis of helical nozzles effects on the energy separation in a vortex tube. Therm Sci 16(1):151–166
8. Rafiee SE, Rahimi M (2013) Experimental study and three-dimensional (3D) computational fluid dynamics (CFD) analysis on the effect of the convergence ratio, pressure inlet and number of nozzle intake on vortex tube performance—validation and CFD optimization. Energy 63:195–204
9. Behera U, Paul PJ, Kasthurirengan S, Karunanithi R, Ram SN, Dinesh K, Jacob S (2005) CFD analysis and experimental investigations towards optimizing the parameters of Ranque-Hilsch vortex tube. Int J Heat Mass Transf 48:1961–1973
10. Dincer K, Baskaya S, Uysal BZ, Ucgul I (2009) Experimental investigation of the performance of a Ranque-Hilsch vortex tube with regard to a plug located at the hot outlet. Int J Refrig 32(1):87–94
11. Lewins J, Bejan A (1999) Vortex tube optimization theory. Energy 24(11):931–943
12. Kumar A, Subudhi S (2017) Cooling and dehumidification using vortex tube. Appl Therm Eng 122:181–193
13. Thakare HR, Parekh AD (2020) Experimental investigation of Ranque-Hilsch vortex tube and techno–economical evaluation of its industrial utility. Appl Therm Eng 169:114934

CFD Analysis on Cooling of Conical Plug Aerospike Nozzle with Secondary Fluid Injection

S. Swathish and P. Rakesh

1 Introduction

Researchers have worked on improving the thrust performance of rocket nozzles in conditions other than those specified in the design since the era of jet and rocket propulsion. Advanced unconventional rocket nozzles including the dual-bell, plug, expansion-deflection, dual-expander, and extendible nozzles, which can be employed effectively in the future, have been the subject of investigations. Long interplanetary trips now require high-performance altitude compensating nozzles and reusable launch vehicles due to advancements in space technology. An aerospike engine maintains its aerodynamic effectiveness across a wide altitude range. The category of altitude compensating nozzles includes aerospike nozzles. Altitude adjustment is a technique for having a rocket nozzle produce the most thrust possible under non-design situations. Aerospike nozzles perform 90% better overall than traditional bell nozzles.

The main issue with an aerospike nozzle is that its central spike sees a far higher heat flow than a bell nozzle would. The secondary flow aids in central body cooling. The current study compares the flow phenomena with and without film cooling inside the Conical Plug Aerospike Nozzle. The nozzle's throat is where the film cooling is first applied.

S. Swathish (✉) · P. Rakesh
Department of Mechanical Engineering, College of Engineering Trivandrum, Kerala 695016, India
e-mail: swathishsreevishak@gmail.com

## 2   Literature Review and Objective

Since the middle of the 1950s, the aerospike nozzle's properties have drawn researchers' attention amid these numerous designs. The aerospike nozzle was the subject of numerous theoretical researches in the 1960s.

The aerospike nozzle is a choice for altitude compensation, which was first addressed by Griffith [1] and then was promoted by Rocketdyne [2]. Different techniques were suggested by Rao [3] and Angelino [4] for the contouring of the nozzle surface to improve the thrust.

Hagemann et al. [5] narrate the flow features in the Future European Space Transportation Investigations Programmed linear plug nozzle and the multidimensional flow outcomes in annular clustered plug nozzles. Ito et al. [6] carry out a computational analysis of 25^0 half-angle conical plug nozzles and an axisymmetric contoured plug nozzle. According to the study, the performance of the contoured plug nozzle was 5–6% better than the conical plug nozzle and the base thrust at higher altitudes compensated for any truncation-related thrust. Nair et al. [7] Conical aerospike nozzles with various amounts of truncation and flow conditions were researched for their flow properties. Asymmetric and full two-dimensional models in two dimensions are used to numerically simulate full-spike and truncated aerospike nozzles. Also mentioned was how much more heat is transferred through the middle spike than a bell nozzle. Verma [8] go through an experimental investigation to study the performance and base pressure characteristics of an annular conical aerospike nozzle with and without freestream flow. Nair et al. [9] In order to compare the performance when a base bleed is introduced, numerical simulations of the studied flow through the conical plug and truncated conical plug nozzles are first validated with experimental data. Herbert and Oliver [10] scrutinize if the addition of film cooling to the expansion ramp of the Aerospike nozzle put in place a thermal boundary layer near the body of the nozzle without detracting from the performance. Raju et al. [11] A two-dimensional axisymmetric model of a dual-bell nozzle with coolant injection at its inflection zone is subjected to a numerical examination with hot flow. Analysis is carried out using a supplementary gaseous hydrogen film injection into the gas mixture.

The novelty of this study is found in the hot flow experiments carried out in a Conical Plug Aerospike Nozzle with film cooling to comprehend different flow, heat transfer, and performance characteristics. It is necessary to compute the impact of coolant injection on the throat region and the effect of specific impulse.

Fig. 1 Schematic diagram of aerospike nozzle [7]
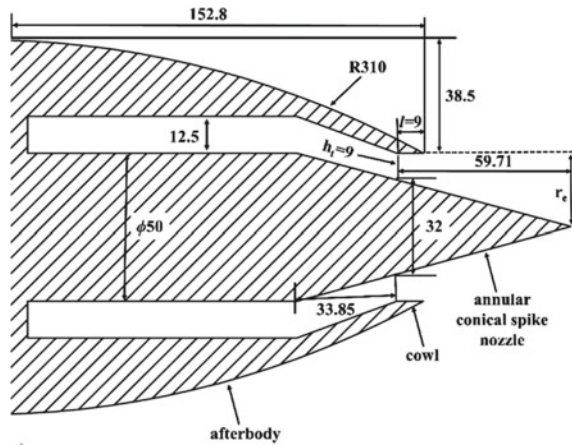
3 Experimental Details and Numerical Modeling

3.1 Experimental Details

The experimental study done by Verma [8] is taken into consideration to validate the numerical outcomes. In a unique motive blow down-type tunnel with a 0.5 m base flow facility, experiments were conducted. The findings of the experimental study suggested axisymmetric jet flow and eternal consistency in the tunnel. The experimental study made use of the 15^0 half-angle annular conical plug model. Radius of the exit nozzle (r_e) was set at 25 mm. According to Fig. 1 [7], the annular space at the throat (h_t) measures 9 mm. The cowl's length, l, which is measured from its throat portion to its tip, is set at 9.0 mm.

Assumptions considered are,

- Gas considered follows ideal gas law.
- There is no friction.
- Adiabatic flow.
- Steady-state condition.
- Particle collision is neglected.

3.2 Numerical Method

ANSYS Fluent software was used for the numerical modeling and flow analysis of the conical plug nozzle and truncated conical plug nozzle. The CFD analysis uses Reynolds-averaged Navier–Stokes (RANS) equations along with different turbulence models for validation. The turbulence model utilized was Menter's shear stress

transport (SST k-ω) model [12], and the ideal gas equation of state was used to finish the system of equations.

3.3 Governing Equations

Mass conservation equation:

For two-dimensional axisymmetric geometry, the mass conservation equation is as follows:

$$\frac{\partial}{\partial x}(\rho v_x) + \frac{\partial}{\partial r}(\rho v_r) + \frac{\rho v_r}{r} = 0. \tag{1}$$

Momentum conservation equation:

For two-dimensional axisymmetric geometries, the axial and radial momentum conservation equations are as follows:

$$\frac{1}{r}\frac{\partial}{\partial x}(r\rho v_x v_x) + \frac{1}{r}\frac{\partial}{\partial r}(r\rho v_r v_x) = -\frac{\partial p}{\partial x} + \frac{1}{r}\frac{\partial}{\partial x}\left[r\mu\left(2\frac{v_x}{\partial x} - \frac{2}{3}(\nabla \cdot v)\right)\right]$$
$$+ \frac{1}{r}\frac{\partial}{\partial r}\left[r\mu\left(\frac{\partial v_x}{\partial r} + \frac{\partial v_r}{\partial x}\right)\right], \tag{2}$$

$$\frac{1}{r}\frac{\partial}{\partial x}(r\rho v_x v_r) + \frac{1}{r}\frac{\partial}{\partial r}(r\rho v_r v_r) = -\frac{\partial p}{\partial r} + \frac{1}{r}\frac{\partial}{\partial r}\left[r\mu\left(2\frac{v_r}{\partial r} - \frac{2}{3}(\nabla \cdot v)\right)\right]$$
$$+ \frac{1}{r}\frac{\partial}{\partial x}\left[r\mu\left(\frac{\partial v_r}{\partial x} + \frac{\partial v_x}{\partial r}\right)\right] - 2\mu\frac{v_r}{r^2} + \frac{2}{3}\frac{\mu}{r}(\nabla \cdot v), \tag{3}$$

where

$$\nabla \cdot v = \frac{\partial v_x}{\partial x} + \frac{\partial v_r}{\partial r} + \frac{v_r}{r}. \tag{4}$$
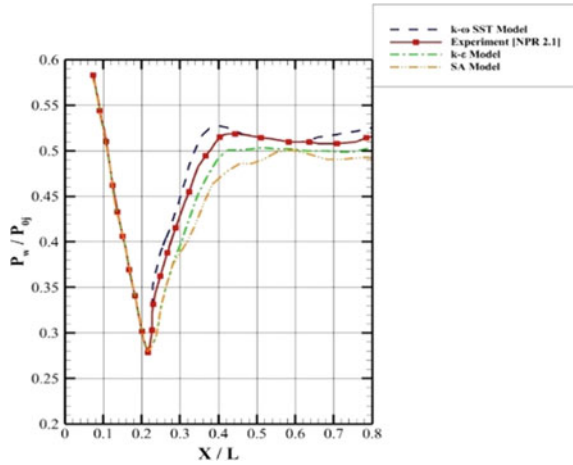
Energy equation:

Thus, the energy equation can be given by,

$$\frac{\partial}{\partial x_i}[u_i(\rho E + p)] = \frac{\partial}{x_j}\left[k_T + \frac{C_p\mu_t}{Pr_t}\frac{\partial T}{\partial x_j}\right] + u_i\left(\tau_{ij}\right)_{\text{eff}}. \tag{5}$$

$$\text{Equation of state, } p = \rho\text{RT}. \tag{6}$$

Fig. 2 Wall pressure versus position for NPR 2.1

3.4 Turbulence Model

The results of the turbulence investigation, which was carried out at NPR 2.1 using several turbulence models, are displayed in Fig. 2. From the study, k-ω SST model seems to have an appropriate match with the experimental results.

The equation for k-ω SST model is as follows:

$$\frac{\partial}{\partial x_i}(\rho k u_i) = \frac{\partial}{x_j}\left(\Gamma_k \frac{\partial k}{\partial x_j}\right) + G_k - Y_k, \tag{7}$$

$$\frac{\partial}{\partial x_i}(\rho \omega u_i) = \frac{\partial}{x_j}\left(\Gamma_\omega \frac{\partial \omega}{\partial x_j}\right) + G_\omega - Y_\omega + D_\omega. \tag{8}$$

In these equations, G_k denotes the generation of k due to mean velocity gradients, G_ω denotes the generation of ω, Γ_k denotes the effective diffusivity of k, and Γ_ω denotes the effective diffusivity of ω. Y_k and Y_ω stand for the dissipation of k and ω due to turbulence, and D_ω stands for the cross-diffusion term.

3.5 Injection of Secondary Fluid

In aerospike nozzle, the central spike experiences far greater heat flux. This problem can be approached by passing cold cryogenically cooled fuel through the spike [10]. In this study, the geometry of the conical plug nozzle is modified such that a coolant is injected at the throat region of the nozzle. During analysis, liquid oxygen or liquid hydrogen has been injected through secondary inlet into the combustion mixture entering the nozzle through primary inlet. Secondary inlet width is taken as 10 mm

[11]. Domain for secondary fluid injection at the throat region is shown in Fig. 3 and corresponding mesh generated with 274,781 cells is shown in Fig. 4.
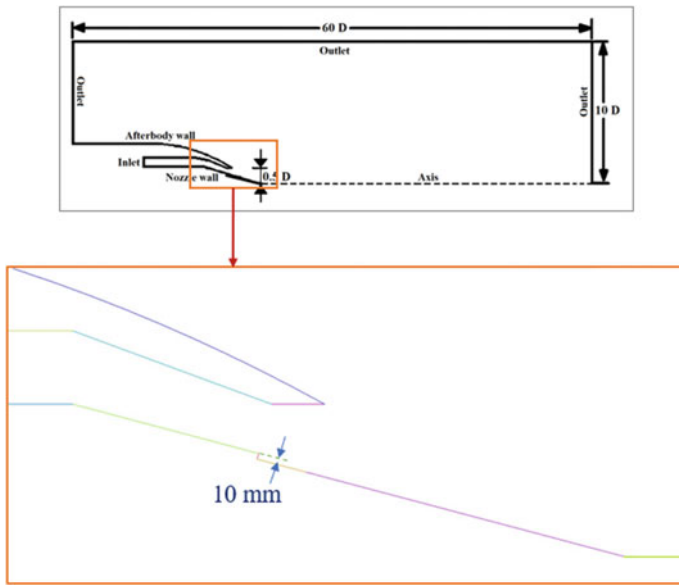

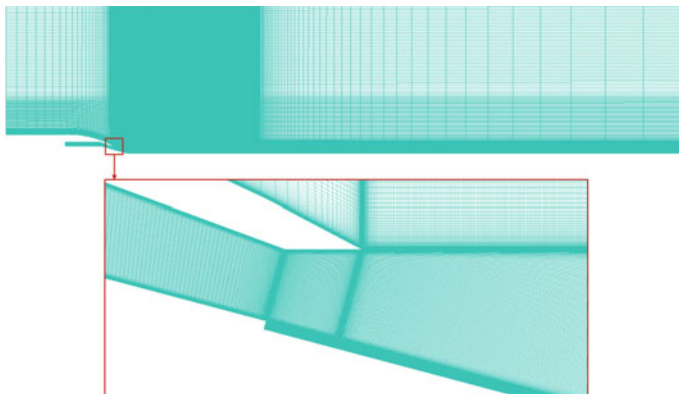**Fig. 3** Domain for secondary fluid injection at the throat region

Fig. 4 Mesh generated

3.6 Boundary Conditions and Flow Solver

The secondary inlet mass flow rate, which is introduced at the throat region as previously described and in the axial direction, was set to 2%, 3%, and 4% of the inlet mass flow rate. No slip stationary wall conditions were used, together with an inlet temperature of 3328 K and pressure of 3.8 MPa. About 101,325 Pa was used as the ambient pressure, and 300 K was used as the outlet temperature. Secondary fluids include liquid hydrogen and liquid oxygen. With different secondary fluid mass flow rates, it is possible to calculate the temperature distribution on the nozzle wall and the cooling efficiency of the coolant on the nozzle wall. The baseline solver was a pressure-based coupled double precision solver. The analysis is carried out in a steady-state environment. The solution is assumed to vary linearly and is discretized using least squares cells. The Courant number was initially maintained at 30, and as the solution developed, it steadily reduced until it reached a value of 20. The initialization method chosen is hybrid initialization.

4 Results and Discussion

4.1 Geometry Validation

With the help of Verma's experimental findings, the computed results of full-spike aerospike nozzles have been validated [8]. Figure 5 compares the experimental data [8] to the ratio of wall pressure P_w to jet stagnation pressure P_{0j} for NPRs 2.1, 2.6, 3.8, and 5.2.
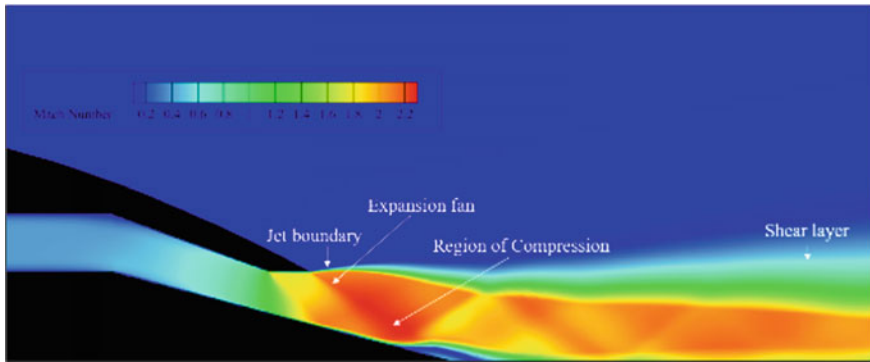
Fig. 5 Geometry validation
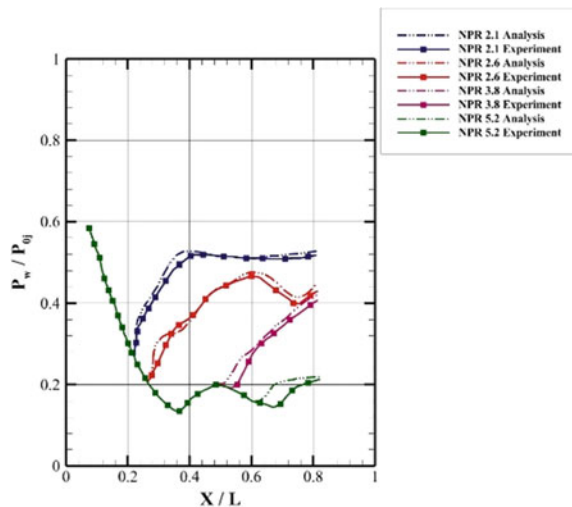
Fig. 6 Mach contour of flow without cooling at NPR 3.8

The flow on the nozzle surface is over expanded by expansion fans that rise from the cowl tip, creating an overexpansion shock that causes flow separation. A compression area is created on the nozzle surface as a result of the shock coming from the inner nozzle, as depicted in Fig. 6. The overexpansion shock from the jet boundary is reflected, creating an expansion fan, which, with further reflection, becomes a compression fan. The flow then reattaches to the nozzle surface. Free shock separation happens at the nozzle tip as the shock resulting from overexpansion interacts with the shock resulting from overexpansion at the cowl tip.

4.2 Effect of Secondary Injection

Film cooling is a reliable cooling technique that can also be used for next generation rocket engines because of its reusability and very easy system configuration [13]. The mixing layer or shear layer is where cooling and hot gas will mix. The wall heat fluxes in a region of pure coolant gas are presumed to be dominated by the coolant gas temperature. The mixing layer reaches the nozzle wall after leaving the injection point for a brief period of time. From this point on, the local coolant-hot gas mixture controls the wall heat fluxes. Liquid hydrogen and liquid oxygen are taken as secondary fluids. Flow structure has been obtained using each of the secondary fluid. Flow analysis was done at 3.8 NPR. Flow contours depicting the influence of injection at NPR 3.8 are shown in Figs. 7 and 8. T_f is specified as 90 K, and for liquid hydrogen, T_f is specified as 20 K.
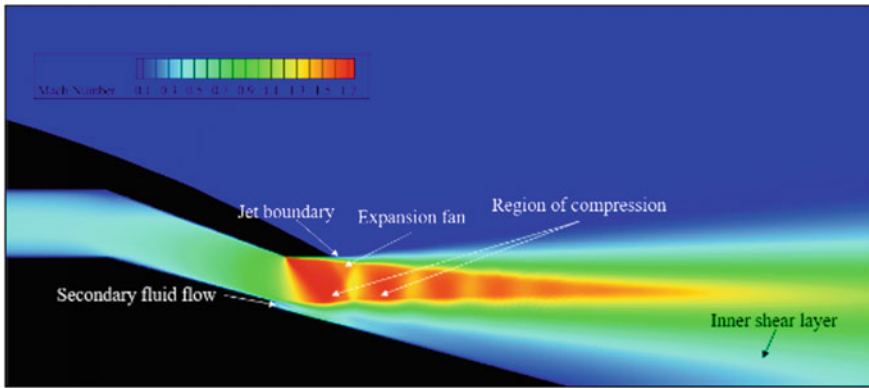
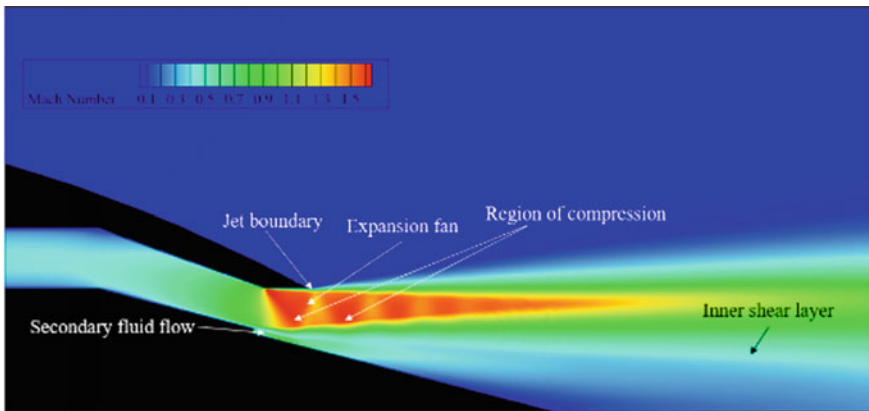**Fig. 7** Mach contour for flow with oxygen as secondary fluid at NPR 3.8

**Fig. 8** Mach contour for flow with hydrogen as secondary fluid at NPR 3.8

4.3 Cooling Effectiveness

The ratio of the highest theoretically feasible wall temperature drop to the wall temperature reduction in the event of coolant injection is known as the cooling efficiency.

$$\theta = \frac{T_w(x) - T_{w,f}(x)}{T_w(x) - T_f},$$ (9)

where Θ is the cooling effectiveness, $T_w(x)$ is the temperature of the wall at a point x before coolant injection, $T_{wf}(x)$ is the wall's temperature at a certain position x after coolant injection, and T_f is the temperature of injected coolant. The coolant

Fig. 9 Wall temperature distribution when oxygen is injected as coolant
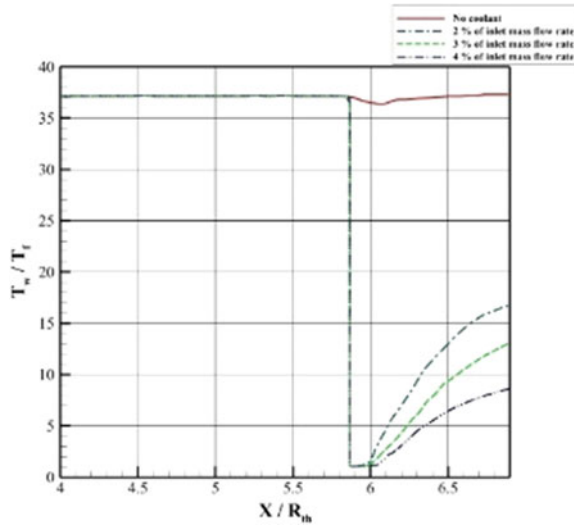
flow, however, cannot be increased above a certain point since it would negatively impact the specific impulse.

Comparison of coolant effectiveness was performed for LO_2/LH_2 engine with two types of secondary fluids: liquid hydrogen and liquid oxygen. Here, liquid hydrogen cooling is more efficient than liquid oxygen cooling in LO_2/LH_2 engines. For 2% secondary mass flow inlet, at $X/R_{th} = 6.9$, the cooling effectiveness value is 0.79 when LH_2 is used as coolant and is 0.57 when LO_2 is used as coolant. For 3% secondary mass flow inlet, at $X/R_{th} = 6.9$, the cooling effectiveness value is 0.83 when LH_2 is used as coolant and is 0.67 when LO_2 is used as coolant. For 4% secondary mass flow inlet, at $X/R_{th} = 6.9$, the cooling effectiveness value is 0.85 when LH_2 is used as coolant and is 0.79 when LO_2 is used as coolant. This demonstrated the significance and value of using LH_2 film cooling in an aerospike nozzle with a conical plug (Figs. 9, 10, 11 and 12).

4.4 Specific Impulse Loss Due to Secondary Coolant Injection

The thrust produced by a rocket engine per weight flow rate of fuel used is known as the specific impulse (I_{sp}). The excess fuel consumption utilized for cooling the nozzle walls is what causes the specific impulse loss caused by secondary coolant injection.

Specific impulse has been calculated using the equation given below:

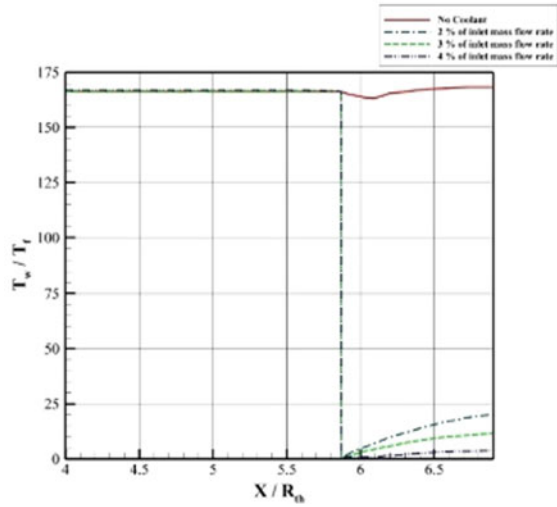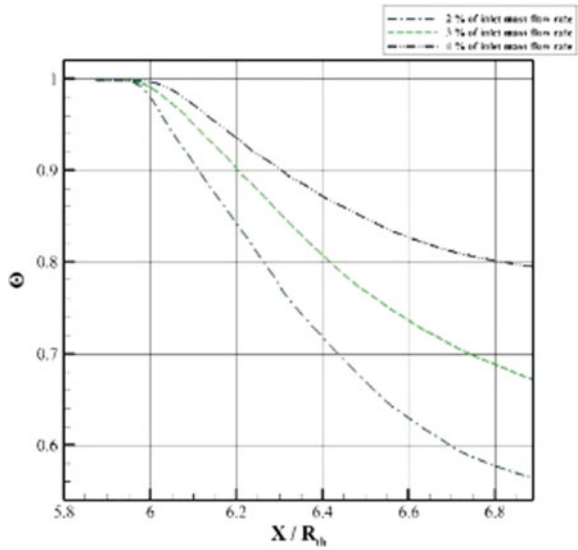**Fig. 10** Wall temperature distribution when hydrogen is injected as coolant

**Fig. 11** Cooling effectiveness of engine when oxygen is injected as coolant

$$I_{sp} = \frac{F}{\dot{m}g},\tag{10}$$

where g is the acceleration due to gravity, F is the thrust produced by the rocket engine, and $\dot{m}$ is the mass flow rate of propellant consumed, which consists of combustion mixture and coolant fuel flow.

The equation is used to determine thrust which is:

Fig. 12 Cooling
effectiveness of engine when
hydrogen is injected as
coolant
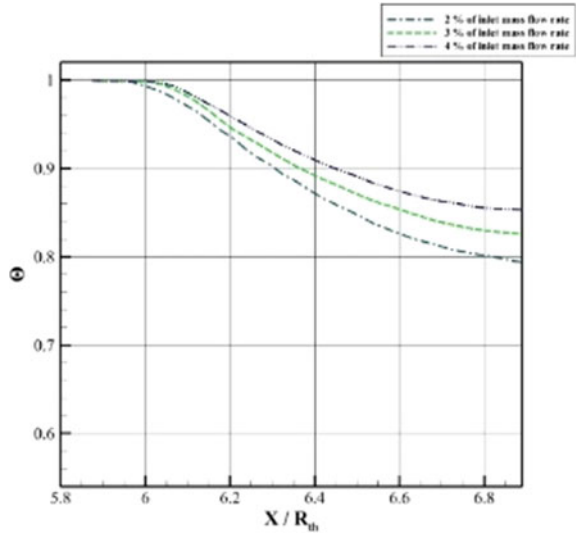
$$F = mV_e + (P_e - P_a)A_e \qquad (11)$$

Here, v_e denotes the speed of the exhaust jet, P_e the exit pressure, P_a the ambient
pressure, and A_e the exit area. The area-weighted average along the nozzle outlet is
used to calculate the velocity and pressure at the nozzle exit.

Specific impulse values and their percentage reduction from the beginning value
are shown in Tables 1 and 2 for LO_2 and LH_2 coolants at various mass ratios.
Figures 13 and 14 depict the pattern in a specific impulse's decline as the coolant
flow rate rises. Despite existing penalty in specific impulse for film cooling, there is
a key benefit of protecting the nozzle-spike wall from high-temperature combustion
gas.

Table 1 Specific impulse reduction when LO_2 is secondary fluid

Secondary inlet mass flow rate (%)	Specific impulse I_{sp}	% Reduction from initial value
0	231.176	0
2	216.731	6.24
3	209.628	9.32
4	206.329	10.74

Table 2 Specific impulse reduction when LH_2 is secondary fluid

Secondary inlet mass flow rate (%)	Specific impulse I_{sp}	% Reduction from initial value
0	231.176	0
2	211.384	8.56
3	206.824	10.53
4	202.894	12.23

Fig. 13 Specific impulse loss for oxygen as secondary fluid
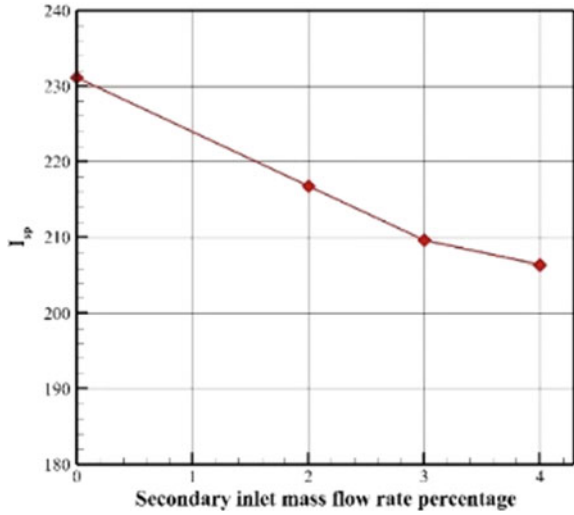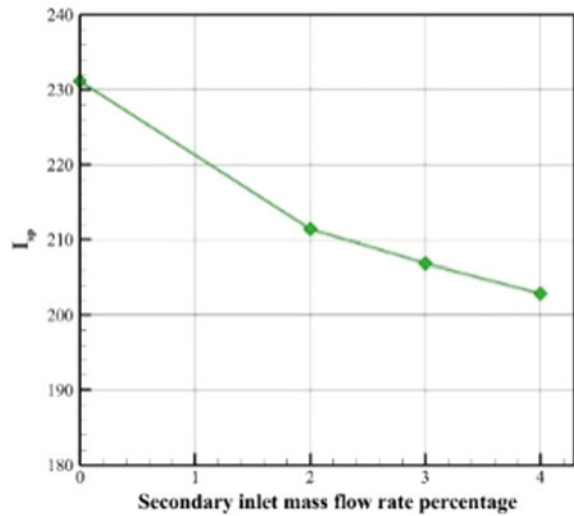

Fig. 14 Specific impulse loss for hydrogen as secondary fluid

5   Conclusions

A successful implementation of a numerical model for the analysis of the flow phenomena within a 2D axisymmetric Conical Plug Aerospike Nozzle with secondary coolant injection at the throat region. The distribution of wall temperatures with and without coolant flow at various mass flow rates was examined, and it was shown that a larger coolant concentration had a beneficial effect on lowering the extension wall temperature. It was examined and compared how effective LH_2 and LO_2 were as coolants. When using LH_2 as the coolant, the cooling effectiveness value for a 2% secondary mass flow input is 0.79, while when using LO_2, it is 0.57. This demonstrated the significance and value of using LH_2 film cooling in an aerospike nozzle with a conical plug. The rocket engine's performance was hindered in order to efficiently lower the high temperature of the nozzle walls, as seen by the reduction of specific impulse with rising coolant flow rate. For LH_2 coolant and LO_2 coolant, the drop in specific impulse at 2% of the main flow was 8.56% and 6.24%, respectively.

Nomenclature

D_w	Cross-diffusion term
G_ω	Generation of ω
k	Turbulence kinetic energy, J/kg
k_T	Thermal conductivity, W/(m · K)
P_a	Atmospheric pressure, Pa
P_b	Base pressure, Pa
P_{0j}	Jet stagnation pressure, Pa
P_{rt}	Turbulent Prandtl number
Y_k	Dissipation of k
Y_ω	Dissipation of ω
Γ_k	Effective diffusivity of k
Γ_ω	Effective diffusivity of ω
μ_t	Eddy viscosity, Pa s
ω	Specific rate of dissipation, s^{-1}
ε_i	Area ratio of inner nozzle

References

1. Griffith AA (1954) Jet propulsion nozzle for use at supersonic jet velocities. Docket No. 2683962 (filed 20 July 1954)
2. Sutton GP (2006) History of liquid propellant rocket engines, chap 7. AIAA, Reston, VA, pp 339–340
3. Rao GVR (1961) Spike nozzle contours for optimum thrust. In: Planetary and space science, vol 4, pp 92–101
4. Angelino G (1964) Approximate method for plug nozzle design. AIAA J 2(10):1834–1835
5. Hagemann G, Immich H, Terhardt M (1978) Flow phenomena in advanced rocket nozzles: the plug nozzle. AIAA Paper
6. Ito T, Fujii K, Hayashi AK (2002) Computations of axisymmetric plug-nozzle flowfields: flow structures and thrust performance. J Propul Power 18(2):254–260
7. Nair PP, Suryan A (2019) Study of conical aerospike nozzles with base-bleed and freestream effects. J Spacecr Rockets 56(4):990–1005
8. Verma SB (2014) Performance characteristics of an annular conical aerospike nozzle with freestream effect. J Propul Power 25(3)
9. Nair PP, Suryan A (2019) Computational study on flow through truncated conical plug nozzle with base bleed. Propul Power Res 8(2):108–120
10. Hombsch M, Oliver H (2013) Film cooling in laminar and turbulent supersonic flows. J Spacecr Rocket 50(4):742–753
11. Raju M, Suryan A, Simurda D (2021) Computational investigation of cooling effectiveness for film cooled dual-bell exhaust nozzle for LO2/LH2 liquid rocket engines. Energy Sour Part A Recov Util Environ Effects
12. Menter FR (1994) Two-equation eddy-viscosity turbulence models for engineering applications. AIAA J 32(8):1598–1605
13. Ludescher S, Olivier H (2021) Film cooling in rocket nozzles, vol 146, NNFM

Numerical Study on Drag Reduction for Flow Past a Circular Cylinder

Kevin Mathew, Isha Debashish Nandi, and Pankaj Kumar

1 Introduction

Drag forces acting on cylinders are an extensive problem as it is relevant to many engineering applications like power transmission towers, support columns of bridges, aircraft struts etc. It is critical to conduct research and find ideal methods to reduce drag on bluff bodies from an engineering design aspect. Some of the researched ways to reduce drag are surface roughness on the cylinder [1] and the use of splitter plates or rods placed downstream or upstream [2, 3].

Reducing the drag of a circular cylinder has been the subject of research as it fundamentally helps economically by lowering the maintenance cost, material cost, etc. When a circular cylinder is submerged in flowing fluid, a wake is developed behind a circular cylinder. Boundary layer separation and very strong flow oscillations are typical. In a particular Reynolds number range, a periodic flow motion will develop in the wake as a result of the shedding of boundary layer vortices alternately from both the sides of the circular cylinder. This pattern of vortices in the wake is referred to as a "Vortex sheet or von Karman Vortex Street" [4]. It produces an oscillating flow with a discrete frequency proportional to its Reynolds number. When the shedding frequency coincides with one of the structural resonant frequencies, the periodic nature of the vortex shedding phenomenon can cause unwanted structural vibrations. These vibrations are referred to as "vortex-induced vibrations." As a result, the cylinder experiences unfavourable lateral forces.

Here, the usage of a splitter plate as a method to reduce drag acting on the cylinder can be demonstrated. This technique can be used to suppress or weaken vortex shedding, typically by attaching additional devices in the flow field (such as Roshko's splitter plate) or by attempting to change the shape of the bluff body. Cylinders and

K. Mathew · I. D. Nandi · P. Kumar (✉)
Department of Mechanical Engineering, SRM Institute of Science and Technology
Kattankulathur, Chennai, Tamil Nadu 603203, India
e-mail: pankajkr@srmist.edu.in

small rods are two additional examples of passive control techniques. Roshko [5] was among the first to investigate the control of vortex shedding behind a circular cylinder by affixing a splitter plate downstream. It is observed that when a geometric modification is made through an attached/detached splitter plate or the placement of an in-line bluff body upstream, the flow approaching the bluff body experiences a loss in momentum. This reduces pressure significantly along the upstream face of the bluff body. Consequently, the drag experienced by the body is reduced. A bifurcated flow impinges on the cylinder in the presence of the upstream splitter plate, resulting in a lower forward stagnation pressure in front of the cylinder than in the absence of the plate.

The effect of splitter plates on drag reduction was also investigated numerically [6] for a variety of plate lengths and Reynolds numbers (Re) in the range of 80–160. They discovered that the frequency of vortex shedding due to a circular cylinder decreases as the length of the splitter plate increases. The maximum reduced percentages of drag and lift forces for the circular cylinder reach 12.04% and 82.35% [7]. It is observed that the research on controlling the wake created by a circular cylinder by introducing a splitter plate is relatively limited compared to its practical relevance in engineering applications.

In this paper, the control of vortex shedding and drag reduction by the usage of splitter plates attached upstream and downstream of a circular cylinder are examined. It is observed that there exists a research gap in this method of drag reduction. Splitter plates of varying lengths in different combinations are attached to both sides of a smooth circular cylinder parallel to the flow. It is numerically analysed to see how each combination splitter plates affect the drag acting on the cylinder and will ultimately help to find the most optimum setup of splitter plates to be used.

2   Literature Review and Objective

Keeping in mind that earlier studies of effect of splitter plate have been only observed under fluids with low Reynolds number ranging from as low as 100 to 35,000 [4, 7]. The current numerical study focuses on the effect of splitter plate at Reynolds number 100,000.

It was generally observed that to design splitter plates, the diameter of the circular cylinder was taken into consideration by means of an "*L/D*" ratio. The *L/D* ratios taken for the splitter plates are 0.5, 1, 1.5, 2, and 2.5, respectively, for both upstream and downstream where the diameter of the cylinder is 20 mm.

Cylindrical bluff bodies are used in many key components in engineering applications. There is a need to analyse and find the optimum method to minimise the drag force acting on them. This, in turn, will decrease any adversarial circumstances that can weaken the structure in the long run. It will also help to reduce maintenance costs.

There exists a research gap specifically pertaining to the reduction of drag with splitter plates, and it was also observed that there is no specific research pertaining

to the effect of multiple splitter plates placed both upstream and downstream to the flow past a circular cylinder and the reduction in drag induced by it.

3 Computational Method

For the purpose of this research, Finite Volume Methods are being utilised for numerical investigation. Commercially available software "ANSYS Fluent" is used for unsteady and incompressible simulation. As for meshing, the in-built meshing software available in the ANSYS suite has been utilised.

3.1 Problem Formulation

The present study aims to determine the variation of C_d with splitter plates of varying lengths placed at the front and rear stagnation point of the circular cylinder at a Reynolds number of 100,000. The characteristic length used is kept constant as diameter of cylinder.

An L/D ratio of 0.5, 1.0, 1.5, 2.0, and 2.5 has been used for the splitter plates. The thickness of the splitter plate has also been taken as 0.1D. A rectangular domain of size 20D × 8.5D was used to carry out the numerical simulations (Fig. 1). The time step taken for the transient simulations was 0.01 s and run up to 10 s.
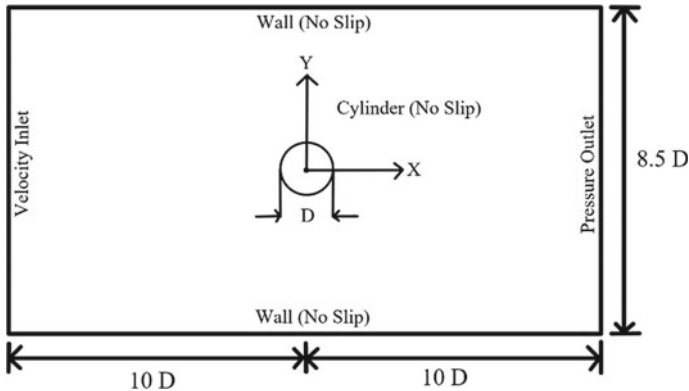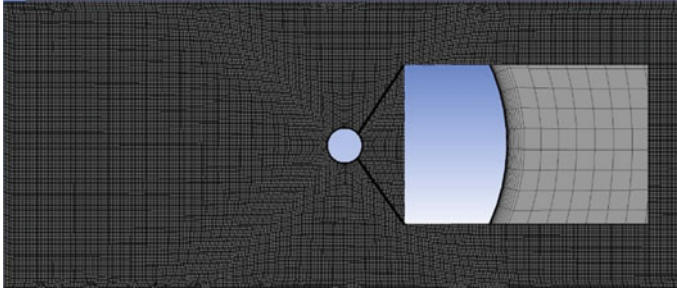

Fig. 1 Computational domain

Fig. 2 Structured mesh with zoom mesh near cylinder shown in inset

Table 1 Mesh quality parameters

Quality metric	Maximum	Minimum	Average
Skewness	0.63725	1.3057×10^{-10}	2.0122×10^{-2}
Orthogonal quality	1	0.63178	0.99832

Skewness mesh metrics spectrum

Excellent	Very good	Good	Acceptable	Bad	Unacceptable
0-0.25	0.25-0.50	0.50-0.80	0.80-0.94	0.95-0.97	0.98-1.00

Orthogonal Quality mesh metrics spectrum

Unacceptable	Bad	Acceptable	Good	Very good	Excellent
0-0.001	0.001-0.14	0.15-0.20	0.20-0.69	0.70-0.95	0.95-1.00
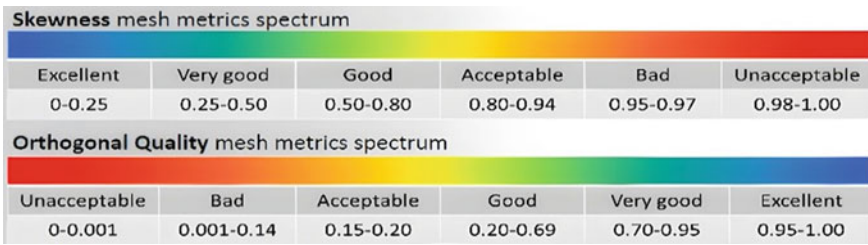
Fig. 3 Mesh quality spectrum [8]

3.2 Meshing

A quadrilateral mesh was used, having a size of 0.001 m. On the surface of the cylinder and splitter plates, an inflation layer of first height 0.000002 m with 25 layers was implemented to capture near wall flow more precisely (Fig. 2).

It was also observed that decreasing the mesh size further did not create any appreciable change in the readings. So as to ensure the quality of our mesh, we have extracted the orthogonal quality and skewness (Table 1; Fig. 3).

3.3 Mathematical Model

The turbulence model used for the numerical simulation is k–omega SST [9]. As the flow around the cylinder is turbulent after boundary layer separation, it is important

to capture the complex turbulent flow downstream of the cylinder (near wall). The turbulence model solves for continuity as well as two additional transport partial differential equations that account for convection and diffusion of turbulent energy. The equations governing this model are as follows [10]:

$$\nabla \overline{u} = 0, \tag{1}$$

$$\frac{\partial \alpha}{\partial t} + \nabla \cdot (\overline{u}\alpha) = 0, \tag{2}$$

$$\frac{\partial (\rho \overline{u})}{\partial t} + \nabla \cdot (\rho \overline{uu}) = -\nabla \overline{p} + \nabla \cdot \overline{\tau} + \rho \overline{f}, \tag{3}$$

$$\frac{\partial (\rho k)}{\partial t} + \nabla \cdot (\rho \overline{u}k) = \tilde{P}_k - \beta * \rho k\omega + \nabla \cdot ((\mu + \alpha_k \mu_t)\nabla k)$$

$$\frac{\partial (\rho \omega)}{\partial t} + \nabla \cdot (\rho \overline{u}\omega) = \gamma \rho \dot{s}^2 - \beta \rho \omega^2 + \nabla \cdot ((\mu + \alpha_\omega \mu_t)\nabla \omega) + 2(1-F_1)\rho \alpha_{\omega 2} \frac{1}{\omega} \nabla k \cdot \nabla \omega. \tag{4}$$

In the above equations, $\overline{u}$ is the speed of the fluid, α is the volume fraction of the fluid, ρ is the fluid density, $\overline{p}$ is pressure, $\overline{f}$ is the density of body forces, k represents the turbulent kinetic energy, ω is the specific turbulent kinetic energy dissipation rate, $\tilde{P}_k$ is the production rate of turbulent kinetic energy by Reynolds averaged flow, F_1 is the blending function, and α_k, α_ω, β, γ are the turbulent model coefficients.

3.4 Boundary Conditions

We have assumed D to be 20 mm and have taken water (25 °C) as our fluid material. A velocity inlet of 6.542 m/s is taken for a Re of 100,000. The outlet is set to pressure outlet with gauge pressure 0 Pa. The cylinder and domain walls have been given a stationary wall boundary condition with no-slip shear condition.

3.5 Validation

To ensure that the numerical scheme is providing us accurate results, we have validated our CFD against the experimental data obtained by Naresh [4]. The CFD was performed in air at a Re of 35,000. The obtained drag coefficient for our cylinder is 1.078, whereas the experimental data indicate a drag coefficient of 1.015. Therefore, the results are in good agreement and our setup has been validated.

4 Results and Discussion

A total of 25 computational simulations were run by varying the *L/D* of the splitter plates placed upstream and downstream. The results obtained are compared with a control cylinder of similar dimensions without splitter plates. The computed values are plotted and graphed.

4.1 Observations

From the data (Fig. 4; Table 2), we can see that the configuration of splitter plates with the least drag is 1.5D upstream and 2.5D downstream with a C_d of 0.502. Compared to the plain circular cylinder with a C_d of 0.620, a decrease in drag coefficient (0.118) is found for the case of splitter plate. The velocity and pressure contour plots have been generated and presented below.

From the pressure plots attached (Figs. 5 and 6), it is observed that the addition of the splitter plates greatly decreases the pressure difference between the windward and leeward side of the cylinder, thus decreasing pressure drag. It can also be seen that the area of pressure due to stagnation is significantly reduced.

The downstream splitter plates delay the interaction of the vortices shed by the cylinder post-boundary layer separation. This vortex interaction causes creates an

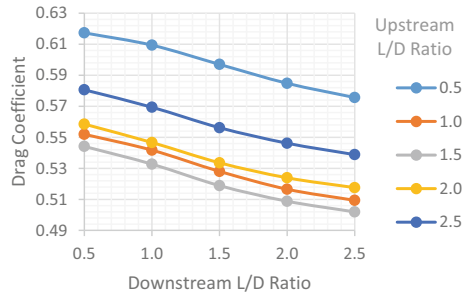**Fig. 4** Drag coefficients versus splitter plate configuration

Table 2 Obtained drag coefficient values

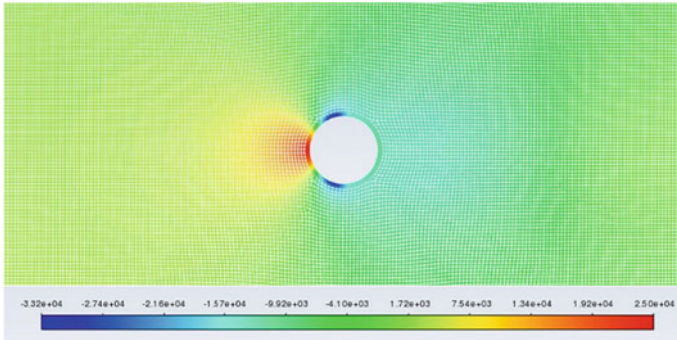| Length of splitter plate upstream	Length of splitter plate downstream				
		0.5D	1.0D	1.5D	2.0D	2.5D
	0.5D	0.617	0.609	0.597	0.585	0.576
	1.0D	0.552	0.542	0.528	0.517	0.509
	1.5D	0.544	0.533	0.519	0.509	0.502
	2.0D	0.559	0.547	0.534	0.524	0.518
	2.5D	0.581	0.569	0.556	0.546	0.539

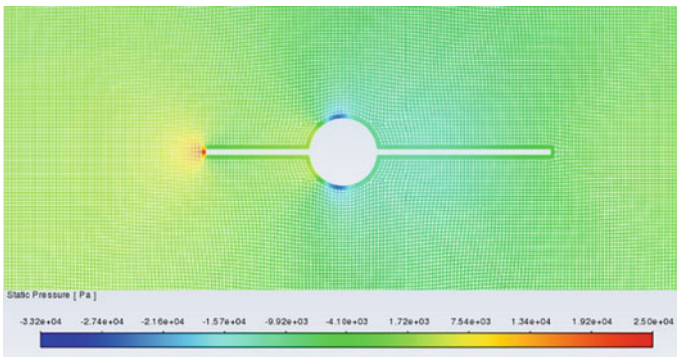**Fig. 5** Pressure contour plot of the control cylinder

Fig. 6 Pressure contour plot of 1.5D–2.5D cylinder

area of low pressure behind the cylinder that contributes to drag. The velocity contour plot (Figs. 7 and 8) of the optimum setup also indicates a loss of momentum of fluid approaching the cylinder. It can also be seen that an increase in upstream splitter plate length beyond 1.5D is detrimental to its drag reduction capability. Figure 9 shows the recirculation zone in wake. The recirculation length is estimated and listed in Table 3 (Figs. 10 and 11).

5 Conclusions

Numerical studies on the drag reduction around the cylinder were conducted for analysing the *drag coefficient* (C_d) at Reynolds number of 100,000. Splitter plates of lengths 0.5D, 1D, 1.5D, 2D, and 2.5D were attached on a cylinder at upstream and downstream together and were observed to see which combination of splitter plate
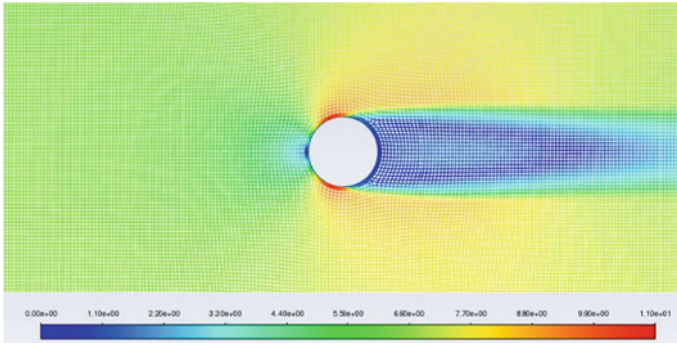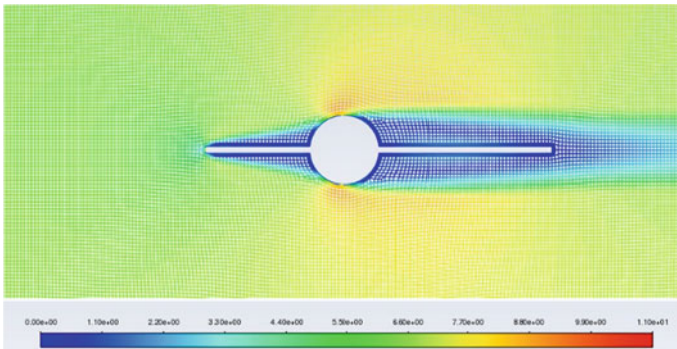
Fig. 7 Velocity contour plot of the control cylinder

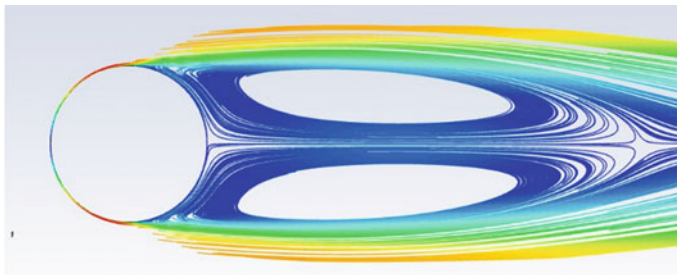**Fig. 8** Velocity contour plot of 1.5D–2.5D cylinder

Fig. 9 Streamline for plain cylinder

gives the optimum decrease in C_d. The following conclusions can be derived from the conducted research:

The introduction of splitter plates alters the flow of the fluid around the cylinder.

Table 3 Downstream vortex recirculation length

Length of splitter plate upstream	Length of splitter plate downstream				
		0.5D	1.0D	1.5D	2.0D	2.5D
	0.5D	52.26	54.71	56.89	59.64	60.52
	1.0D	46.19	48.09	51.02	53.06	51.95
	1.5D	42.28	45.15	48.51	49.36	50.08
	2.0D	41.97	44.48	48.38	49.03	50.04
	2.5D	43.38	46.26	49.61	50.95	50.37
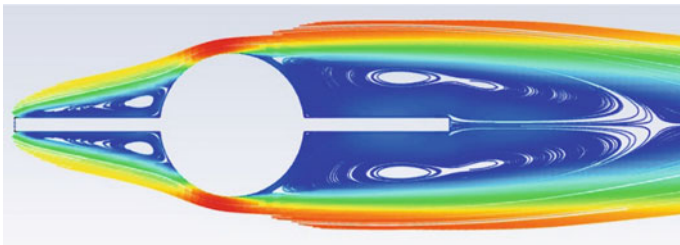
Fig. 10 Streamline for 1D–1D splitter plate attached to circular cylinder
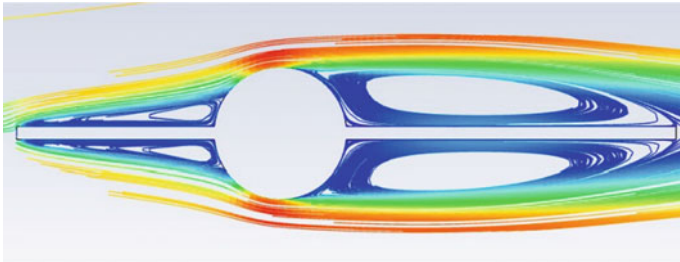

Fig. 11 Streamline for optimised splitter configuration (1.5D–1.5D) attached to circular cylinder

It is observed that the C_d decreases maximum with spillter plate configuration 1.5D.

There is a reduction in C_d of 19.03% overall.

The upstream splitter plate must be designed with precaution, as an excessively long splitter plate can decrease its effectiveness.

Nomenclature

D	Diameter of circular cylinder (m)
L	Length of splitter plate (m)
C_d	Drag coefficient (–)
Re	Reynolds number (−)

References

1. Chakroun WM, Abdel Rahman AA, Quadri MMA (1997) The effect of surface roughness on flow around a circular cylinder. Wind Eng 21(1):1–12
2. Hwang J-Y, Yang K-S (2007) Drag reduction on a circular cylinder using dual detached splitter plates. J Wind Eng Ind Aerodyn 95(7):551–564. ISSN 0167-6105
3. Wang J, Zhang P, Lu S, Wu K (2006) Drag reduction of a circular cylinder using an upstream rod. Flow Turbul Combust 76:83–101
4. Naresh E, Dileep Kumar P, Nagaraj Goud B, Anil Kumar N (2017) Drag reduction over a circular cylinder. Int J Civ Eng Technol 8(8):1334–1345
5. Roshko A (1961) Experiments on the flow past a circular cylinder at very high Reynolds number. J Fluid Mech 10:345–356
6. Kwon K, Choi H (1996) Control of laminar vortex shedding behind a circular cylinder using splitter plates. Phys Fluids 8(2):479–486
7. Zhu H, Tang T, Alam MdM, Song J, Zhou T (2022) Flow-induced rotation of a circular cylinder with a detached splitter plate and its bifurcation behavior. Appl Ocean Res
8. How to verify mesh quality in ANSYS workbench 2022. FEA Tips/Website. Accessed 30th Aug 2022. https://featips.com/2021/05/07/how-to-verify-mesh-quality-in-ansys-workbench/
9. Near-wall treatment for k-omega models 2021. CFD Online/Website. Accessed 30th Aug 2022. https://www.cfd-online.com/Wiki/Near-wall_treatment_for_k-omega_models
10. Romanova D, Ivanov O, Trifonov V, Ginzburg N, Korovina D, Ginzburg B, Koltunov N, Eglit M, Strijhak S (2022) Calibration of the k-ω SST turbulence model for free surface flows on mountain slopes using an experiment. Fluids 7:111

Computational Study of 2D Flow Past a Circular Cylinder Oscillating Transversely to Incoming Flow

Abhishek Goyal, Amulya Tiwari, and Raj Kumar Singh

1 Introduction

In structural, offshore, and thermal power engineering disciplines, the correlation within the movement of circular cylinder and the inconsistent wake of a round cylinder in a cross-flow is critical [1, 2]. In cross-flow oscillations, one important thing about the cylinder–wake interaction phenomenon is the position in the flow cycle (where vortices form and break apart) depends on the frequency of oscillation of the circular cylinder.

The duration of vortex formation (evaluated concerning circular cylinder vibration) needs to switch phase by about 180° for a significantly narrow spectrum of forced oscillation frequencies, according to observations by Ongoren and Rockwell [3]. The above sensitivity is demonstrated for flows in which the frequency of the circular cylinder in cross-flow oscillation (fo) is similar to the natural shedding frequency of the fixed cylinder (fv). The research suggests that, at least for low vibration amplitudes, the vortex-shedding behavior on both sides of a switch is identical to the normal Karman-street wake. The switch can also change the direction of mechanical energy transmission among the vibrating cylinder and the flow as well as the phase of strains caused by vortices on a cylinder.

A. Goyal (✉)
Department of Civil Engineering, Delhi Technological University, New Delhi 110042, India
e-mail: abhishekgoyal9868@gmail.com; abhishekgoyal_2k19ce003@dtu.ac.in

A. Tiwari · R. K. Singh
Department of Mechanical Engineering, Delhi Technological University, New Delhi 110042, India
e-mail: rajkumarsingh@dtu.ac.in

Koopman [1] studied flow visualization of forced transverse excitation at various amplitude ratio values and found that the lock-on range is adapted to greater DA. Up to DA 5, Williamson and Roshko [4] explored the impact of high amplitude ratio values on the wake. They identified a variety of unusual wakes and designated them with numbers and letters that reflected the mixture of duos of single vortices (S) shed and vortices (P) shed within one cycle of forced oscillation. Using the k-epsilon model, Hines and Thompson [5] investigated the turbulent flow over a square cylinder with specified motions. Moreover, the anticipated lock-on region is substantially greater than the findings of other researchers. In comparison to cross-flow-forced excitations, experimental investigations of inline forced cylinder oscillations are rather rare. This is because the cylinder is subjected to a smaller stream-wise fluctuating force F_x, which is just one-tenth the size of the transverse varying force F_y [6].

The current study focuses on a detailed computational analysis of the cylinder–wake interaction behavior for a single oscillation amplitude, but over a wide range of frequencies near the fixed cylinder's vortex shedding frequency. The Re was established large enough to observe the occurrence of switch behavior at the utilized amplitude of oscillation. The constraint to a single amplitude, Re, as well as 2D flow simulations, were done so as to keep the requirement on computational assets to a minimum meanwhile still producing invaluable information.

2   Literature Review and Objective

The purpose of this research is to see how changes in frequency ratio $F = f_e/f_{so}$ affect entrainment characteristics caused by forced cross-flow oscillation in the main synchronization scheme. Our estimates are only limited to 2D flows with a low Reynolds no. as well as Reynolds numbers of 500 and 1000 with a natural frequency of circular cylinder at $Re = 500$ and 1000 being 0.573 and 1.3, respectively. Furthermore, to lessen the strain on computational system, the analysis is limited to a single cross-flow oscillation at an amplitude ratio of $A/D = 0.02$.

The relevance of 2D solutions for this challenge requires some clarification. The wake of a stationary cylinder is 3D and chaotic at $Re = 500$. Past studies have shown that span-wise association of forces, wake velocities, and other variables increases with increasing amplitude of cylinder motion or oscillation [7–12]. It is fair to conclude that the harmonic motion of a long circular cylinder suppresses 3D nature and produces flows that are more 2D than fixed circular cylinder equivalents, at least in the near-wake zone.

This has been established that forcing a cylinder to oscillate at modest amplitudes can postpone the advent of 3D in its wake. For R_e up to 300–400, Koopman [1] and Griffin and Ramberg [13] established that the wake was virtually 2D at vibration amplitudes beyond 10% of the cylinder diameter. Berger [14] demonstrated that regulated oscillations could stable and extend a laminar vortex-shedding regime to $Re = 350$–300 in experimental research. The span-wise relation of the wake street is improved with $Re = 1000$ and $A/D = 0.05 < 0.125$; however, the vibration is not powerful enough to completely inhibit the 3D instability.

3 Materials and Methods

Quadrilateral cells were used throughout to achieve discretization. The no-slip wall boundary criteria were used to specify the cylinder's surface. To accomplish pressure–velocity coupling, the incompressible Navier–Stokes equations were resolved utilizing a second-order unsteady solver methodology using the software ANSYS FLUENT 2021, along with the combination of SIMPLE approach. The circular cylinder in Fig. 1 has a diameter of $D = 0.05$ m, which represents a standard domain employed in the investigation.

A user-defined function (UDF) was utilized to create cylinder's oscillating motion. Furthermore, oscillation orientation, frequency of excitation, and amplitude determine the cylinder's specified motion. Consider the motion of a circular cylinder driven to oscillate in response to an incoming flow field, as shown in Fig. 2. The amplitude is A and the cylinder's path at any time (t) is $\xi(t)$.

$$(t) = A \sin[2\pi f_e(t - t_0)], \tag{1}$$

where t_0 is the time delay in this investigation. As orientation in this study is transverse $(\alpha = 90°)$. For $\alpha = 90°$, $x(t) = 0$ and $y(t) = A \sin(2\pi f_e t)$, a UDF was utilized to create the cylinder's oscillating motion with whole cells of mesh being updated following each time step with the help of dynamic mesh model.

a. *Mesh independence*

For mesh refinement investigation, three meshes were created. The force coefficient along the x-axis (C_x), Strouhal number (St), and peak-to-peak readings of the
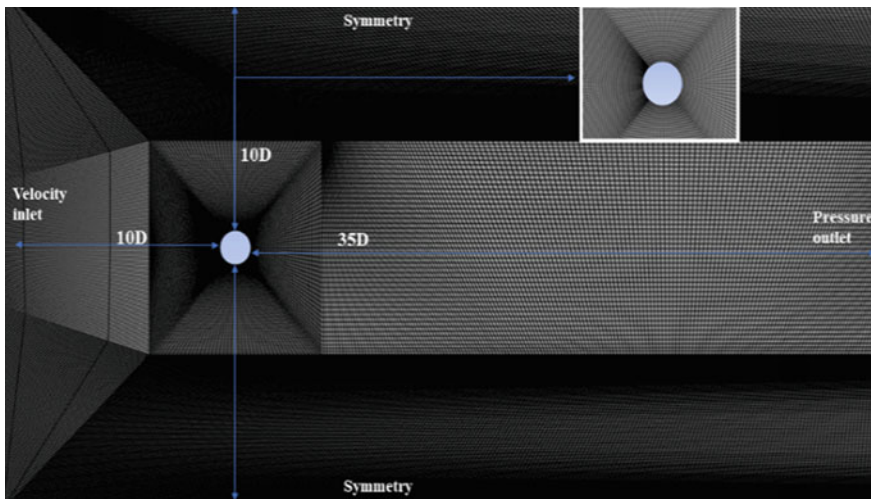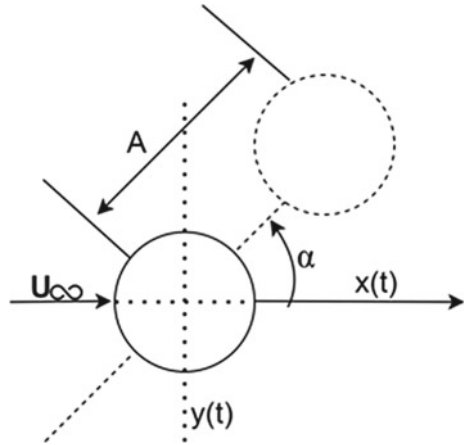

Fig. 1 Schematic of mesh distribution in a 2D computational domain

force coefficient along y-axis (C_y), along with the specifics of the meshes, are all
compared in Table 1. The given produced readings of fluid flow across an oscillating
circular cylinder were for $Re = 500$. With the improvement of meshes, the difference
between the solutions reduces, and grid independence is attained. Then, Mesh 2 was
selected for further calculations. The increase in the number of nodes for meshes is
considered to be ~ 20,000. The primary flow properties were compared and found
to be in excellent endorsement with published information.

b. *"P + S" vortex-shedding modes*

The confirmation was required in the provision of two "exotic" vortex-shedding
modes to achieve better assurance in the CFD analysis using Ansys. The first wake
mode to be verified was P + S, which denotes the vortex pair continued by a single
vortex shed in one oscillation period [4]. The oscillation of cylinder was transverse at
Reynolds no = 500, A/D = 0.02, and $F = f_e/f_{s0} = 0.875$ in this instance. Figure 3
depicts the comparison of P+S mode for cylinder as given in present study with Black-
burn and Henderson [15] which utilized the discrete-vortex approach with viscous
diffusion. The P + S configuration bears a strong resemblance to every one of the

Table 1 Comparison of drag and lift coefficient with published data, Blackburn et al. [15], $A = 0.25$, $F (f_e/f_{s0}) = 1.0$, $Re = 500$

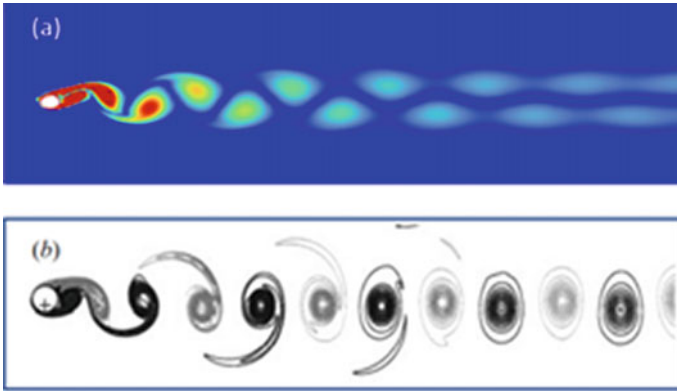| Mesh	Total nodes	Sf	Cl	Cd
Mesh 1	56,605	0.195	1.335	1.531
Mesh 2	71,965	0.223	1.735	1.429
Mesh 3	91,440	0.216	1.651	1.445
Blackburn et al. [15]	–	0.228	1.776	1.414
% Error (compared with Mesh 2)	–	2.19	2.3	1.06

Fig. 3 P + S mode comparison for circular cylinder at $Re = 500$, $A/D = 0.02$, $F = 0.875$: **a** present investigation: **b** Blackburn and Henderson [15]

two analyses. The present simulation also shows the vortex pairs rotating clockwise as they go downstream, which is consistent with Blackburn and Henderson's [15] simulation. They also discovered that the flow under this situation had some "memory," even though the vortex-shedding pair's part was dependent upon the circular cylinder's beginning orientation. Additionally, this outcome of memory is validated within the present investigation, though not displayed herein.

4 Results and Discussion

The examination of a circular cylinder's wake is significant when it oscillates due to to self-excitation. In addition, the physics of wake formations can be best defined. As a result, numerical simulations were performed for a diverse combination of excitation frequencies (f_e/f_{s0}) ranging from 0.76 to 1.02 and amplitude of vibration a/d fixed to 0.02 and for the low Re as well as $Re = 500$ and $Re = 1000$.

4.1 Lock-in Boundary at Re = 500 and Re = 1000 and A/D = 0.02 with A = 90° (Transverse Oscillation)

The "lock-in" boundary or the "synchronization regime" is developed by examining the types of reactions to a different excitation frequency. A phase plane graph is a plot that shows the relationship between each and every two domain state vectors across time. In this scenario, the velocities across the X-direction (U_x) and Y-direction (U_y) of the stream fulfill this objective. In short, Fig. 5 simply shows the effect of excitation frequency at a constant vibration amplitude (a/d) of 0.02.

For $Re = 500$

For $F < 0.8$ with $Re = 500$, the phase plane, C_d and C_l, can be observed in quasi-periodic regime. According to Fast Fourier transforms, the time series of lift exhibited substantially spiked spectral characteristics, including two major frequency responses. Meneghini et al. (as seen in Fig. 9a) [16] show identical trend at $Re = 200$ discrete-vortex numerical simulation outcomes at $F = 0.75$, $A = 0.25$. For $f_e/f_{s0} = 0.8$, though, the chaotic phase plane disappears and is replaced by a single, stable periodic orbit which is referred to as the "limit cycle."

For F in between 0.905 and 0.95, the existence of two fundamental, incommensurate frequencies characterized in accordance with the weakly chaotic zone has been reported: One is at the frequency of the cylinder oscillation, whereas the other results from a nearly periodic switching between waking phases. Throughout such regime, the cylinder oscillation frequency and its odd harmonics have steeply peaked spectra in the Fast Fourier transform of lift time series; however, the long-period switching frequency has no discernible spike. Figure 4a shows a time series of Cl for the outcomes calculated under the given domain at $F = 0.94$. The time necessary to switch approaches has been shortened as F has increased. Due to the extraordinarily long periods associated in accordance to the lowest frequency ratios, the precise specifics of the variations in switching periods with F have not been validated.

For $F > 1.016$, Fig. 4b demonstrates the time evolution of C_d (coefficient of drag) and C_l (coefficient of lift) considering flow regime in the chaotic zone (for $F = 1.02$). Moreover, the Fast Fourier transform (FFT) of time series of C_l (Coefficient of lift) shows a dominating, but not very sharp, spike at Strouhal frequency, as well as peaks at its odd harmonics. These characteristics, including the randomness of time series depicted in Fig. 4b, imply the nature of flow as chaotic.

Furthermore, the occurrence of these frequencies could be described using Fast Fourier transforms (FFTs) derived from the data of coefficient of lift, which are also shown in a similar figure. The occurrence of a single distinct spike signifies "lock-on," whereas the hegemony of both frequencies is referred to as "non-lock-on." In Koopman's early investigations [1], a Lissajous figure was seen to determine
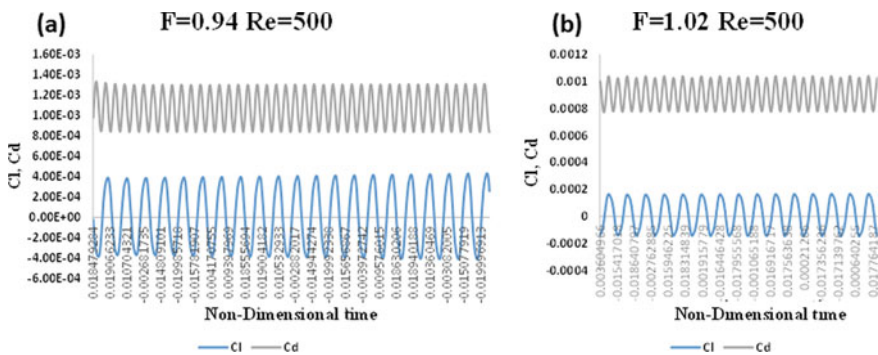

Fig. 4 Time series of C_d and C_l at **a** $F = 0.94$ and **b** $F = 1.02$
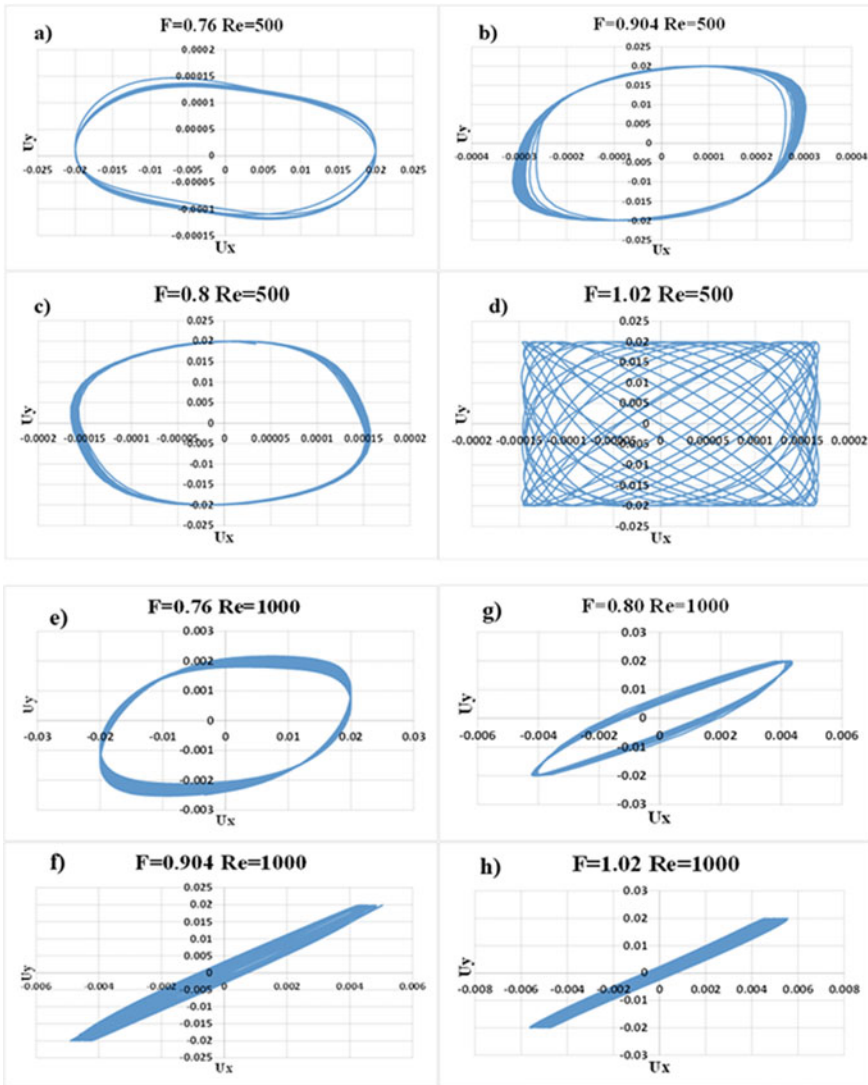
Fig. 5 FFTs and phase plane schematics for oscillating cylinder at $Re = 500$ and 1000

whether the driver oscillator and the hot-wire signal were of the same frequency. Furthermore, whereas the Lissajous figure was displayed as a "steady single loop," the vortex street was called "locked-in." The circular cylinder vibrated at a natural shedding frequency in his investigations. Since this work used a more reliable simulation approach associated with a robust numerical method, the current findings are consistent with the experimental data.
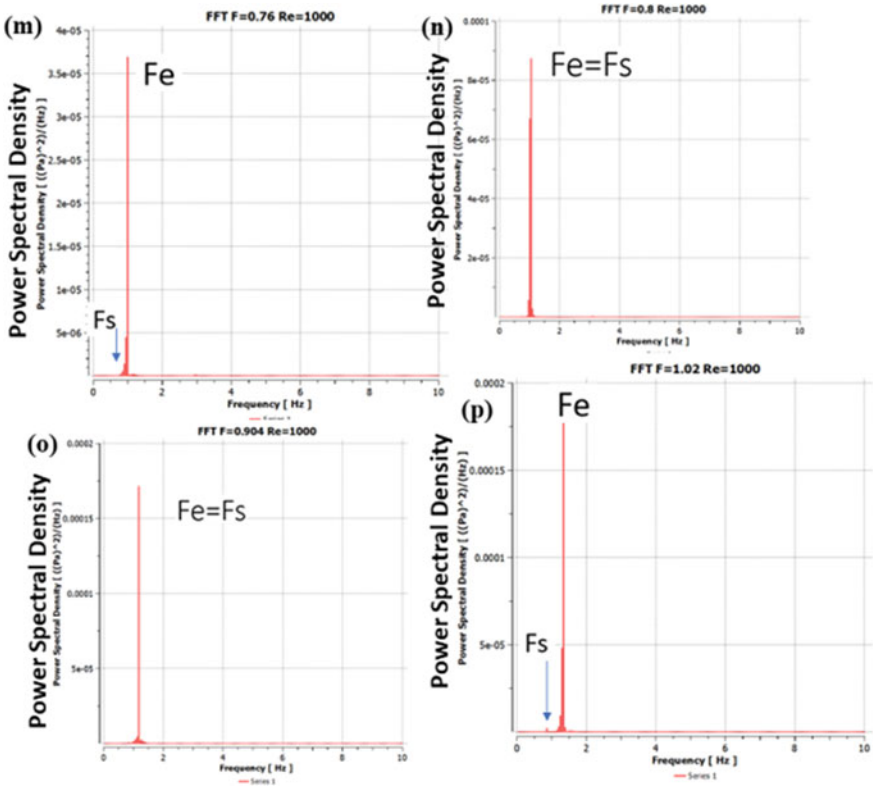
For $Re = 1000$
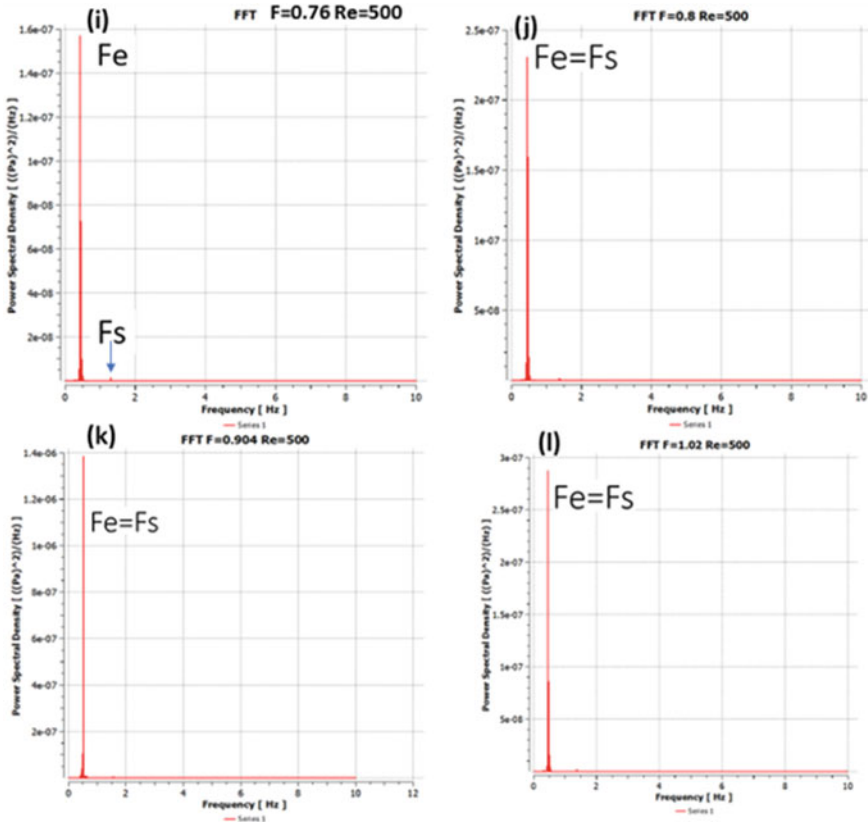
Fig. 5 (continued)

Fig. 5 (continued)

During the instances when $F < 0.8$, the phase plane is visible in unstable periodic courses, and hence, the presence of weakly chaotic zones can be seen. Even so, at $F = 0.8$, it is interesting to observe the weakly chaotic zones converging into a single, stable periodic course. The aforementioned is commonly referred to as a "limit cycle." There is, however, a band during which the frequency of excitation is capable to force the frequency of vortex shedding within its corresponding value, as shown in Fig. 5 where it sustains up to $F = 0.904$. The phase plane once more turns chaotic and aperiodic for $F \geq 1.02$. The Fast Fourier transforms (FFTs) derived from the lift coefficient histories, which are also shown in the very same image, could also be used to demonstrate the origins of these frequencies.

5 Conclusions

The dynamic mesh approach was used to model laminar incompressible flow across a cylinder with a user-defined function (UDF) utilized to create cylinder's transverse oscillating motion to the free-stream flow along with the combination of the SIMPLE approach. This function offers a potent method for modeling a flow past objects. Thorough verification of the simulation's outcomes using "physical" motion across the transverse axis has also produced outcomes that were in accordance with the findings of the existing numerical and experimental studies. The associated excitation and flow parameters also led to the observation of several near-wake vortex shedding phenomena that have been earlier found in several studies. Force amplifications and typical lock-on features, for like $F = 1$, were correctly anticipated.

Some of the findings of the present study are:

- The effect of "phase-lock-on" was extensively proven by plots of Fast Fourier transform, wake structure, phase-plane, temporal drag and lift coefficients, etc.
- A phase plane is uneven, non-periodic, and weakly chaotic in the non-lock-on condition.

Nomenclature

A Amplitude
St Strouhal frequency
C_d Drag coefficient
α The angle of oscillation of cylinder with respect to incoming flow field
C_l Lift coefficient
Re Reynolds no

References

1. Koopman GH (1967) The vortex wakes of vibrating cylinders at low Reynolds numbers. J Fluid Mech 28:501–512
2. Bishop RED, Hassan AY (1964b) The lift and drag forces on a circular cylinder oscillating in a flowing fluid. Proc Roy Soc A 277:51–75
3. Ongoren A, Rockwell D (1988) Flow structure from an oscillating cylinder. Part 1. Mechanisms of phase shift and recovery in the near wake. J Fluid Mech 191:197–223
4. Williamson CHK, Roshko A (1988) Vortex formation in the wake of an oscillating cylinder. J Fluids Struct 2:355–381
5. Hines J, Thompson GP, Lien FS (2009) A turbulent flow over a square cylinder with prescribed and autonomous motions. Eng Appl Comput Fluid Mech 3(4):573–586
6. Bishop RED, Hassan AY (1964) The lift and drag forces on a circular cylinder in a flowing fluid. Proc Roy Soc A 277:32–50

7. Toebes GH (1969) The unsteady flow and wake near an oscillating cylinder. Trans ASME J Basic Eng 91:493–505
8. Novak M, Tanaka H (1975) Pressure correlations on a vibrating cylinder. In: 4th international conference on wind effects building & structure. Heathrow. Cambridge University Press, pp 227–232
9. Tanida Y, Okajima A, Watanabe Y (1973) Stability of a circular cylinder oscillating in uniform flow or in a wake. J Fluid Mech 61:769–784
10. Patnaik BSV, Narayana PAA, Seetharamu KN (1999) Numerical simulation of laminar flow past a transversely vibrating circular cylinder. J Sound Vib 228:459–475
11. Al-Mdallal QM, Lawrence KP, Kocabiyik S (2007) Forced stream wise oscillations of a circular cylinder: locked-on modes and resulting fluid forces. J Fluids Struct 23:681–701
12. Öngören A, Rockwell D (1988) Flow structure from an oscillating cylinder Part 2. Mode competition in the near wake. J Fluids Mech 191:225–245
13. Griffin OM, Ramberg SE (1974) The vortex street wakes of vibrating cylinders. J Fluid Mech 66:553–576
14. Berger E (1967) Suppression of vortex shedding and turbulence behind oscillating cylinders. Phys Fluids 10:191–193
15. Blackburn HM, Henderson RD (1999) A study of two-dimensional flow past an oscillating cylinder. J Fluid Mech 385:225–286
16. Meneghini JR, Bearman PW (1995) Numerical simulation of high amplitude oscillatory flow about a circular cylinder. J Fluids Struct 9:435–455

General Pressure Equation-Based Incompressible Flow Solver

Raghunathan Dheeraj and Y. Sudhakar

1 Introduction

It is well known that the absence of a separate equation for pressure is primarily responsible for the numerical difficulties associated with solving the incompressible Navier–Stokes equations. Instead of a pressure evolution equation, we have the continuity equation which indicates that the velocity divergence is zero. This divergence-free constraint imposes an inevitable necessity to solve the elliptical pressure Poisson equation (PPE) [14], and researchers conventionally adopted such an approach. Methods like Marker and Cell [9], SIMPLE algorithm [3] and its derivatives, projection methods such as fractional step method [2], etc., are examples of such numerical techniques. Nevertheless, solving PPE is quite time-consuming and hence is numerically expensive.

The artificial compressibility method (ACM) [6] is one alternative approach that avoids solving the pressure Poisson equation. In this method, slight compressibility is introduced, and eventually, the well-developed algorithms used for solving compressible flow equations can now be applied to solve incompressible flow equations. This method is numerically less expensive than the conventional methods but has some limitations also. The classical ACM's major drawback is that it applies only to steady-state flows and a dual time-stepping [12] approach is necessary to extend their application to unsteady flow problems. Studies reveal that dual time-stepping algorithms are more time-consuming than the conventional methods [11] and hence are not suitable for solving computationally intensive problems like the direct numerical solution of turbulent flows.

Recent developments in the area of pseudo-compressible methods point towards a few single time-stepping ACM methods like kinetically reduced local Navier–Stokes (KRLNS) [1], entropically damped artificial compressibility (EDAC) [7],

R. Dheeraj (✉) · Y. Sudhakar
School of Mechanical Sciences, IIT Goa, Ponda 403401, India
e-mail: dheeraj183631001@iitgoa.ac.in

and general pressure equation (GPE) [17]. These approaches have the benefit that
neither time-consuming PPE nor dual time-stepping is necessary and hence is found
to be computationally efficient [18].

Unlike the classical ACM, which was directly proposed, GPE is derived from
compressible flow and energy conservation equations. Thus, it offers a physical
justification for artificial compressibility [17]. In vector form, GPE is written as
follows.

$$\frac{\partial p}{\partial t} + \beta \, \nabla \cdot \overrightarrow{V} = \frac{\gamma}{Re \, Pr} \nabla \cdot \nabla p. \tag{1}$$

Here, pressure and velocity vector are denoted by p and $\overrightarrow{V}$, respectively. The artificial
compressibility parameter, β, is expressed in terms of Mach number, Ma as $\beta = 1/$
Ma^2. Other parameters such as γ, Re, and Pr correspond to heat capacity ratio,
Reynolds number, and Prandtl number, respectively.

The continuity equation in the incompressible Navier–Stokes equations is substi-
tuted by GPE (Eq. (1)). Eventually, the need for a time-dependent equation for solving
pressure is satisfied, reducing the complexity of the solution algorithm. Thus, to simu-
late incompressible flow problems, the momentum equations and Eq. (1) are solved
numerically. The above-mentioned GPE-based approach is used in the current work
to create a finite volume solver that simulates unsteady incompressible flows. A few
unsteady and steady test cases are simulated successfully with the solver, and the
scheme is validated by comparing the results obtained with those reported in the
literature.

The well-known shortcoming of ACMs is the deviation of the velocity field from
the solenoidal condition. It is found that despite this, ACMs are widely used to
simulate incompressible fluid flow problems [10, 13, 15].

Following is how the rest of the report is organised. The methodology is explained
briefly in Sect. 2. The outcomes of numerical experiments are presented in Sect. 3.
In Sect. 4, the report is concluded.

2   Methodology

In two-dimensional Cartesian coordinates, GPE (Eq. 1) is written as,

$$\frac{\partial p}{\partial t} + \frac{1}{Ma^2} \left[\frac{\partial u}{\partial x} + \frac{\partial v}{\partial y} \right] = \frac{\gamma}{Re \, Pr} \left[\frac{\partial^2 p}{\partial x^2} + \frac{\partial^2 p}{\partial y^2} \right]. \tag{2}$$

The parameters γ and Pr mentioned in Eq. (1) are problem dependent [18] and
their values are taken as unity for the test cases that we discuss in Section III.
Moreover, we use the value $Ma = 0.02$ to evaluate β.

Additionally, to compute the velocity components, we numerically solve the
following momentum equations.

Table 1 Coefficients for three-stage third-order Runge Kutta scheme

i	α_i	β_i	γ_i
1	0	1/3	0
2	$-5/9$	15/16	1/3
3	$-153/128$	8/15	3/4

$$\frac{\partial u}{\partial t} + \frac{\partial (u^2)}{\partial x} + \frac{\partial (uv)}{\partial y} + \frac{\partial p}{\partial x} = \frac{1}{Re}\left[\frac{\partial^2 u}{\partial x^2} + \frac{\partial^2 u}{\partial y^2}\right],$$
$$\frac{\partial v}{\partial t} + \frac{\partial (uv)}{\partial x} + \frac{\partial (v^2)}{\partial y} + \frac{\partial p}{\partial y} = \frac{1}{Re}\left[\frac{\partial^2 v}{\partial x^2} + \frac{\partial^2 v}{\partial y^2}\right]. \tag{3}$$

We use a staggered grid to avoid odd–even decoupling, and all the spatial derivatives are discretised using central schemes. The time derivative is discretised using a three-stage, third-order Runge–Kutta method, proposed by Williamson [19], and is of the form,

$$\boldsymbol{u}^{(0)} = \boldsymbol{u}^{(n)}$$
$$\boldsymbol{k}^{(i)} = \alpha_i \boldsymbol{k}^{(i-1)} + \Delta t \, \boldsymbol{L}(\boldsymbol{u}^{(i-1)}, t^n + \gamma_i \Delta t)$$
$$\boldsymbol{u}^{(i)} = \boldsymbol{u}^{(i-1)} + \beta_i \boldsymbol{k}^{(i)} \quad \text{for} \quad i \in [1, 2, 3]$$
$$\boldsymbol{u}^{(n+1)} = \boldsymbol{u}^{(3)}. \tag{4}$$

Here, n and $n + 1$ represent the current and next time steps respectively. $\boldsymbol{L}(\boldsymbol{u}, t)$ is the spatial discretisation operator. The coefficients α, β, and γ for the three-stage, third-order scheme are listed in Table 1.

3   Results and Discussion

In this section, we present the results from unsteady and steady-state test cases, simulated using the GPE-based solver. Two-dimensional test cases of Taylor–Green vortex problem, laminar flow over flat plate, and backward facing step are considered for the same.

3.1   Laminar Taylor–Green Vortex

To test the performance of the present algorithm in unsteady flow simulations, we use the Taylor–Green vortices problem. We set the initial flow field and allow the flow to evolve with time. For this case, the analytical solution [18] is available and is given by,
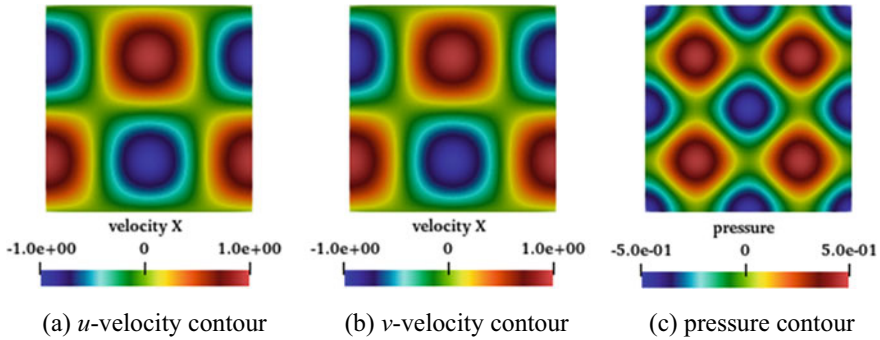
velocity X
-1.0e+00   0   1.0e+00

velocity X
-1.0e+00   0   1.0e+00

pressure
-5.0e-01   0   5.0e-01

(a) *u*-velocity contour   (b) *v*-velocity contour   (c) pressure contour

Fig. 1 Initial conditions of Taylor–Green vortex problem

$$u(x, y, t) = \cos(Ax)\sin(By)e^{-Ct}, \tag{5a}$$

$$v(x, y, t) = -\sin(Ax)\cos(By)e^{-Ct}, \tag{5b}$$

$$p(x, y, t) = -\frac{1}{4}(\cos(2Ax) + \cos(2By))e^{-2Ct}. \tag{5c}$$

Here, $A = 2\pi$, $B = 2\pi$, and $C = 8\pi^2/Re$. The initial conditions are obtained from the above equation by setting $t = 0$ (Fig. 1). The flow is confined to a unit square domain with periodic boundary conditions in both x and y directions. The Reynolds number, $Re = 100$, and the time-step used is 10^{-4}. The code is run till the actual time reaches 1.0 s and the computed results are compared with that of the analytical solution.

We observe that the computed values of velocity and pressure match well with the exact solution. The maximum value of error observed for velocity is of the order of 10^{-4} for a grid of 64 × 64. Error for pressure is also in the same range. To check the order of convergence, a graph between L_∞-norm of error and number of mesh points for velocity and pressure is plotted (Fig. 2) at time $t = 1.0$ s. Here, the error is plotted for different mesh points such as 8 × 8, 16 × 16, 32 × 32, 64 × 64, 128 × 128, and 256 × 256. It is observed that both velocity and pressure follow second-order convergence.

3.2 *Laminar Flow over Flat Plate*

Fluid flow over flat plate is a popular test case to study the boundary layer development in viscous flows. It is widely used in numerical studies to validate solution algorithms. The schematic diagram of the problem is presented in Fig. 3. Fluid flows with a uniform velocity of $U_0 = 1$ through the inlet. It then approaches the flat plate of unit length, L, through a symmetry region. The length of the symmetry region, L_s is

Fig. 2 Convergence plot for Taylor–Green vortex problem indicating second-order convergence
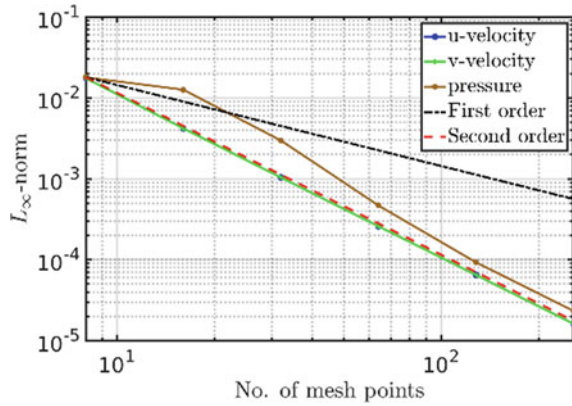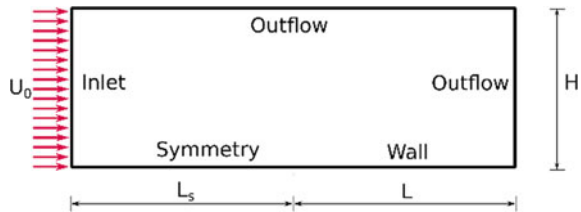

Fig. 3 Diagram showing the geometry and boundary condition details of flat-plate problem

equal to that of the length of the plate. The width of the flow field represented by H is related to the boundary layer thickness as $H = 5\delta$ [16]. Here, δ is the thickness of the boundary layer computed at the tip of the flat plate. The flow takes place at a Reynolds number of $Re = 10,000$ and the viscosity is calculated from the Reynolds number. Also, the fluid density, $\rho = 998.2$ kg/m^3. The flow evolves over time, and the results are taken at steady state.

With reference to Fig. 3, the boundary conditions necessary to solve the problem are specified as follows. The flat plate is represented as a wall region ($u = v = 0$). The symmetry boundary condition implies that, $\partial u/\partial y = 0$ and $v = 0$. As mentioned above, a uniform velocity is applied at the inlet, i.e. $u = U$ and $v = 0$. The rest of the boundaries have outflow conditions meaning that there is no velocity gradient normal to the boundary ($\nabla \boldsymbol{u} \cdot n = 0$). The boundary conditions are summarised in Table 2.

In order to validate the computational algorithm, the velocity plot can be compared with that of the Blasius solution. Through Blasius' solution, the boundary layer equations in the form of a partial differential equation (PDE) are converted to an ordinary differential equation. To do so, Blasius introduced a similarity variable, η, which is a non-dimensional independent variable that is obtained by combining the independent variables x and y.

$$\eta = y\sqrt{\frac{U}{\nu x}}. \tag{6}$$

Table 2 Boundary conditions for laminar flow over flat plate

Type	u-velocity	v-velocity	Pressure
Inlet	$u = U$	$v = 0$	$\frac{\partial p}{\partial x} = 0$
Symmetry	$\frac{\partial u}{\partial y} = 0$	$v = 0$	$\frac{\partial p}{\partial y} = 0$
Wall	$u = 0$	$v = 0$	$\frac{\partial p}{\partial y} = 0$
Outflow (right)	$\frac{\partial u}{\partial x} = 0$	$\frac{\partial v}{\partial x} = 0$	$\frac{\partial p}{\partial x} = 0$
Outflow (top)	$\frac{\partial u}{\partial y} = 0$	$\frac{\partial v}{\partial y} = 0$	$\frac{\partial p}{\partial y} = 0$

Fig. 4 Plot between similarity variable η and u/U, obtained from the simulation of flow over flat plate, compared with Blasius' solution
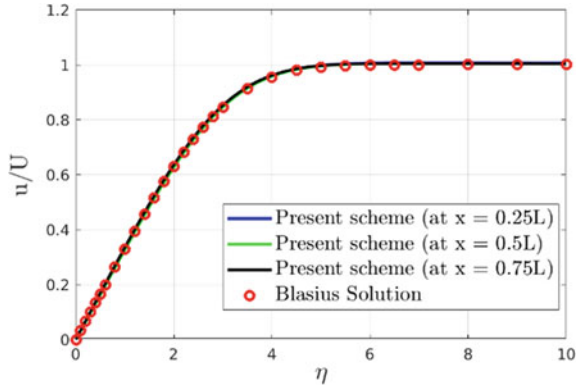
Blasius then solved for a non-dimensional speed $f'(\eta) = u/U$ as a function of the similarity variable, η [4]. We compare Blasius' solution with the values obtained from the present simulation in Fig. 4. It is evident that the computed solution and the one provided by Blasius have an excellent agreement, supporting the solution's self-similarity nature. The mesh used for the simulation is 256×256, and the time-step value is 10^{-5}.

3.3 Backward Facing Step

Flow over a backward facing step is a 2D laminar flow problem where in flow encounters a sudden expansion at a step as shown in Fig. 5. The channel width, $H = 1$, and the length is taken as $L = 20$. The step height, h, is half of that of the channel width. We use a uniform mesh of size 400×40 and a time-step of 10^{-4}. The flow is restricted to the laminar regime with $Re = 800$ and simulation is carried out till steady state is reached.

The boundary conditions are specified as follows:

- At top and bottom boundaries as well as on the step, $u = 0$ and $v = 0$.
- At the inlet $u = 24y(0.5 - y)$ with $0 \le y \le 0.5$ and $v = 0$.

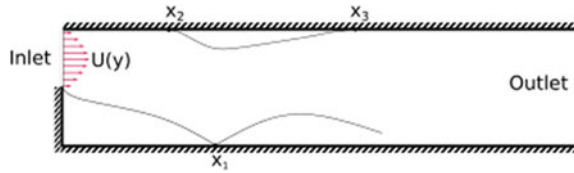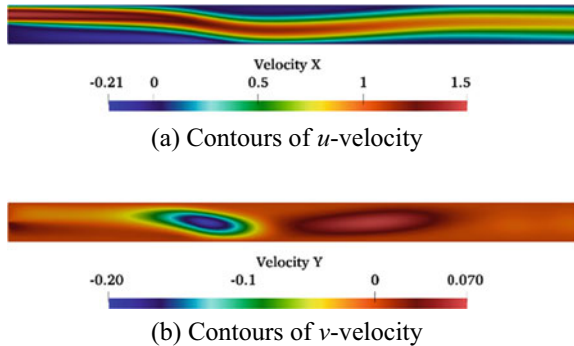**Fig. 5** Schematic of the backward facing step problem

Fig. 6 Velocity contours at steady state obtained from the simulation of flow over backward facing step

(a) Contours of u-velocity

(b) Contours of v-velocity

- At the outlet we have outflow condition, i.e. $\nabla U \cdot n = 0$. So, $\partial u/\partial x = 0$ and $\partial v/\partial x = 0$.
- At all the boundaries, the pressure gradient is zero (i.e. $\partial p/\partial n = 0$).

The velocity field from the simulation is presented in Fig. 6. Here, we see that the flow detaches initially from the walls at a few locations but later reattaches back. Eventually, re-circulation regions appear at a few locations in the flow field. To validate the scheme, we compare the location of a few detachment and reattachment points mentioned in Fig. 5. The obtained values are $x_1 = 5.58$, $x_2 = 4.6$, and $x_3 = 9.7$ and found to be in agreement with that reported by Chiu [5].

To further test the accuracy of the solution algorithm, we plot the velocity profile at a location, $x/H = 7$ and compare the results with that reported by Gartling [8]. It can be seen that there is an excellent agreement between the computed and the reference values. The negative values in the plot indicate the presence of a re-circulation region (Fig. 7).

4 Conclusions

In this work, we have developed an incompressible flow solver based on the general pressure equation, which belongs to the family of single time-stepping ACMs. The accuracy of the solver is tested using the standard test cases. The unsteady flow simulation of Taylor–Green vortex problem demonstrated second-order convergence for both velocity and pressure. Also, when compared with the analytical solution, the

Fig. 7 *u*-velocity plot along *y*-direction for the backward facing step problem at *x/H* = 7.
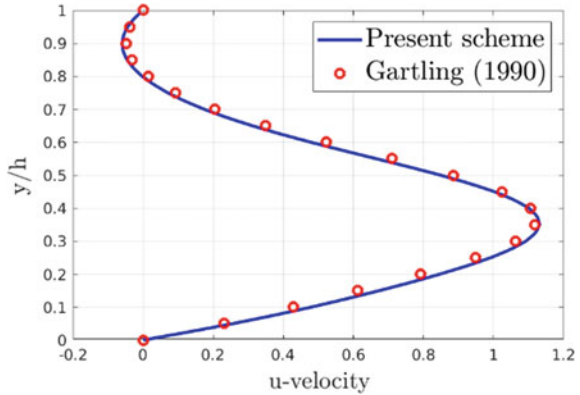
maximum error obtained is of the order of 10^{-4} for a grid of 64×64 at $t = 1.0$ s. Additionally, the GPE-based solver was tested with two steady test cases involving laminar flow over flat-plate and backward facing step. The results obtained from the laminar flow over flat-plate problem indicate an excellent match with Blasius' solution, and that from backward facing step is validated using results reported in the literature. Evidently, the solver demonstrates an excellent alternative to the conventional incompressible flow solvers.

Nomenclature

Re   Reynolds number
Pr   Prandtl number
Ma   Mach number
γ Heat capacity ratio
β Artificial compressibility parameter

References

1. Ansumali S, Karlin IV, Ottinger HC (2005) Thermodynamic theory of incompressible hydrodynamics. Phys Rev Lett 94(8):1–4
2. Brown DL, Minion ML (1995) Performance of under-resolved two-dimensional incompressible flow simulations. J Comput Phys 122(1):165–183
3. Caretto LS, Gosman AD, Patankar SV, Spalding DB (2007) Two calculation procedures for steady, three-dimensional flows with recirculation. Proc Third Int Conf Numer Methods Fluid Mech 19:60–68
4. Cengel YA, Cimbala JM (2006) Fluid mechanics: fundamentals and applications. McGraw-Hill series in mechanical engineering. McGraw-Hill Higher Education

5. Chiu PH (2018) An improved divergence-free-condition compensated method for solving incompressible flows on collocated grids. Comput Fluids 162:39–54
6. Chorin AJ (1968) Numerical solution of the Navier-Stokes equations. Math Comput 22(104):745
7. Clausen JR (2013) Entropically damped form of artificial compressibility for explicit simulation of incompressible flow. Phys Rev E 87(1):1–12
8. Gartling DK (1990) A test problem for outflow boundary conditions—flow over a backward-facing step. Int J Numer Methods Fluids 11(7):953–967
9. Harlow FH, Eddie Welch J (1965) Numerical calculation of time-dependent viscous incompressible flow of fluid with free surface. Phys Fluids 8(12):2182–2189
10. Kim WW, Menon S (1999) An unsteady incompressible Navier-Stokes solver for large eddy simulation of turbulent flows. Int J Numer Methods Fluids 31(6):983–1017
11. Kiris C, Kwak D (2002) Aspects of unsteady incompressible flow simulations. Comput Fluids 31(4–7):627–638
12. Merkle CL, Athavale M (1987) Time accurate unsteady incompressible flow algorithms based on artificial compressibility. In: 8th computational fluid dynamics conference, pp 397–407
13. Nithiarasu P, Liu CB (2006) An artificial compressibility based characteristic based split (CBS) scheme for steady and unsteady turbulent incompressible flows. Comput Methods Appl Mech Eng 195(23–24):2961–2982
14. Pan D (2022) A high-order finite volume method solving viscous incompressible flows using general pressure equation. Numer Heat Transf Part B Fundam 82(5):146–163
15. Rahman MM, Siikonen T (2001) An artificial compressibility method for incompressible flows. Numer Heat Transf Part B Fundam Int J Comput Methodol 40(5):391–409
16. Tirandazi P, Hidrovo CH (2020) Study of drag reduction using periodic spanwise grooves on incompressible viscous laminar flows. Phys Rev Fluids 5(6):64102
17. Toutant A (2017) General and exact pressure evolution equation. Phys Lett Sect A General Atomic Solid State Phys 381(44):3739–3742
18. Toutant A (2018) Numerical simulations of unsteady viscous incompressible flows using general pressure equation. J Comput Phys 374:822–842
19. Williamson JH (1980) Low-storage Runge-Kutta schemes. J Comput Phys 35(1):8–56

Modal Analysis of a Flow Past a Cylinder

Arvind Thirunavukkarasu, Rahul Sundar, and Sunetra Sarkar

1 Introduction

Unsteady flow situations are characterized by high complexity and a need for a huge amount of computational resources. For real-world problems, CFD simulations, even though highly accurate, may take weeks, sometimes even months, to complete for just a single parameter instance. In this setting, an optimization study across several parameters is computationally intractable. It is therefore motivating to research the construction of reduced-order models for unstable flows, that avoid this issue by approximating solutions to the problem in a significantly lesser amount of time with reasonable accuracy. Proper orthogonal decomposition (POD) and dynamic mode decomposition (DMD) are two common modal analysis methods through which a reduced basis can be generated to build a reduced-order model in a low dimensional subspace. There are several reviews in the literature which cover these methods in detail and their role in reduced-order modeling [1–3].

The most popular method, POD, uses the energy content of the flow field to identify coherent structures [4]. The POD modes' orthogonality is a desirable attribute for creating reduced-order models. Even though POD decomposition is optimal in the least squares sense [4], it does not give any information about the temporal scales of the various structures present in the flow. There can be dynamically important structures that might not be energetically important [5] and, thus, would not be captured in POD.

To overcome this impediment, DMD was introduced by Rowley et al. [6]. Contrary to POD, which orders the flow structures by energy, DMD results in dominant dynamic modes of the flow field, with each mode having a characteristic frequency. Since the introduction of DMD, many variations of DMD have been formulated with applications in the field of fluid mechanics. The exact DMD method [7] is used in this

A. Thirunavukkarasu (✉) · R. Sundar · S. Sarkar
Department of Aerospace Engineering, IIT Madras, Chennai 600036, India
e-mail: arvi3981@gmail.com

paper for further analysis and is referred to as just DMD for the sake of convenience. It is worth noting that DMD modes are not orthogonal, in contrast to POD modes. Also, even if the modes have a characteristic frequency that helps in identifying the different temporal scales in the flow, there is no particular order of importance for these modes. The popular methods to rank these modes have been proven to be inadequate [8, 9]. Hence, the focus has lately been shifting toward a variant of POD known as spectral POD (SPOD) [10]. SPOD produces a set of orthogonal basis at discrete frequencies, ranked by their energy. SPOD has been used in the analysis of various problems ranging from pipe flows [11], turbulent jets [12, 13], channel flows [14], and wakes behind bluff bodies [15, 16]. Towne et al. [10] established the theoretical relationship of SPOD with POD, DMD, and resolvent analysis.

In this work, SPOD analysis on a flow over a stationary circular cylinder is performed and compared with POD and DMD. The simple case of flow over a circular cylinder is an ideal entry point to test these modal analysis techniques. Even though the robustness of these modal analysis techniques can only be seen in the analysis of complex flows, a cylinder wake is a better model for learning these procedures since the results of these techniques applied to it are simpler to understand. Following brief introductions and implementation methodologies of POD, DMD, and SPOD in Sect. 2, the results for the case of cylinder flow are discussed in Sect. 3. The summary and conclusions are presented along with the scope for further work in Sect. 4.

2 Methodology

2.1 Proper Orthogonal Decomposition

POD is a common technique to extract coherent patterns from flow fields [4]. When using POD on a fluid flow problem, the variations in the flow field $q'(x, t)$ are obtained by subtracting the temporal mean from the data snapshot ($q'(x, t) = q(x, t) - \bar{q}(x)$). The snapshot matrix Q is then constructed by stacking variations of the flow field as column vectors.

$$
Q = \begin{bmatrix}
q'(x_1, t_1) & \cdots & q'(x_1, t_N) \\
q'(x_2, t_1) & \cdots & q'(x_2, t_N) \\
\vdots & \ddots & \vdots \\
q'(x_M, t_1) & \cdots & q'(x_M, t_N)
\end{bmatrix}
\tag{1}
$$

where the number of degrees of freedom is denoted by M (number of spatial points multiplied by number of flow field variables), and the number of snapshots is denoted by N [17]. The covariance matrix is then computed as,

$$
C = \frac{1}{N-1} Q Q^T.
\tag{2}
$$

Then, the covariance matrix's eigen-decomposition is used to calculate the POD modes, such that,

$$C\Phi = \Lambda\Phi. \tag{3}$$

The eigenvectors Φ are called the POD modes [17]. The eigenvalues λ_k are helpful in the truncation of modes to reconstruct the data since they can be used to assess how effectively each mode ϕ_k represents the original data in the least squares sense. If only r $(0 < r < \min(M, N))$ modes are retained, the flow field data can be reconstructed by the truncated series,

$$q(x, t) = \underline{q}(x) + \sum_{k=1}^{r} a_k(t)\phi_k(x) \tag{4}$$

in an optimal manner, effectively lowering the dimensionality of the data. The data are projected onto these modes to get the temporal coefficients $a(t)$ as,

$$a_k(t) = \left\langle \left(q(x, t) - \underline{q}(x)\right), \phi_k(x) \right\rangle. \tag{5}$$

In cases where the spatial size of the data is large $(M \gg N)$, computation of the spatial covariance matrix $(C = QQ^T)$ of size $M \times M$ becomes cumbersome, making it impossible to employ the traditional spatial POD approach in fluid simulations. Method of snapshots described in [18] overcomes this drawback by utilizing the fact that the temporal covariance matrix (QQ^T) of size $N \times N$ will still produce the same nonzero eigenvalues and similar eigenvectors, however, resulting in a computationally tractable problem. In snapshot POD, the following eigenvalue problem,

$$Q^T Q\varphi_k = \lambda_k\varphi_k \tag{6}$$

is solved and original POD modes are recovered through,

$$\phi_k = Q\varphi_k \frac{1}{\lambda_k}. \tag{7}$$

2.2 Dynamic Mode Decomposition

High-dimensional data can be broken down into dynamically relevant modes using DMD [7], which is a common alternative to POD. Each mode has a unique oscillation frequency and growth/decay rate. Similar to POD, the columns of matrices X and Y are designed to represent the snapshots of data collected at constant time intervals

Δt, such that,

$$X = [q_1, q_2, \ldots, q_{N-1}] \quad Y = [q_2, q_3, \ldots, q_N], \tag{8}$$

with $X, Y \in C_{M \times N}$. Here, locally, flow field dynamics is approximated in a linear manner [7] so that a linear mapping is used to model the relationship between a flow field snapshot q_i and the subsequent flow field snapshot q_{i+1}, such that,

$$q_{i+1} = A q_i \tag{9}$$

Since $M \gg N$, direct calculation of A is computationally intractable. Hence, the following minimization problem is solved instead (in the least square sense):

$$\min \|AX - Y\|_F^2, \tag{10}$$

solution of which is now provided by calculating the pseudo-inverse of X such that,

$$A = YX^\dagger. \tag{11}$$

The eigenvectors (V) and eigenvalues (Λ) of A are used to define the DMD modes and eigenvalues. These can be obtained without explicitly computing the matrix A by the algorithm given in Tu et al. [7]. Then, $A = V \Lambda V^{-1}$. From Assumption (9),

$$q_k = (V \Lambda V^{-1})^k q_0 = V \Lambda^k b. \tag{12}$$

Thus,

$$x_k = \sum_{j=1}^{n} \lambda_j^k b_j v_j \tag{13}$$

for $k = [0, N]$, where b denotes the coefficients of the weighted summation of the first snapshot x_0 in terms of the eigenvectors, i.e., $b = V^{-1} x_0$ [19].

2.3 Spectral Proper Orthogonal Decomposition

SPOD, being the frequency-domain counterpart of POD, decomposes the data into a set of ranked modes across distinct frequencies. The resulting modes exhibit coherent spatial and temporal evolution and are the best representations of the second-order space–time flow statistics [10]. Firstly, using Welch's approach, a single time series of N_t snapshots is divided into N_b blocks to create an ensemble of realizations of the data [20]. Then, the blocks are Fourier transformed and eigen-decomposed to get the
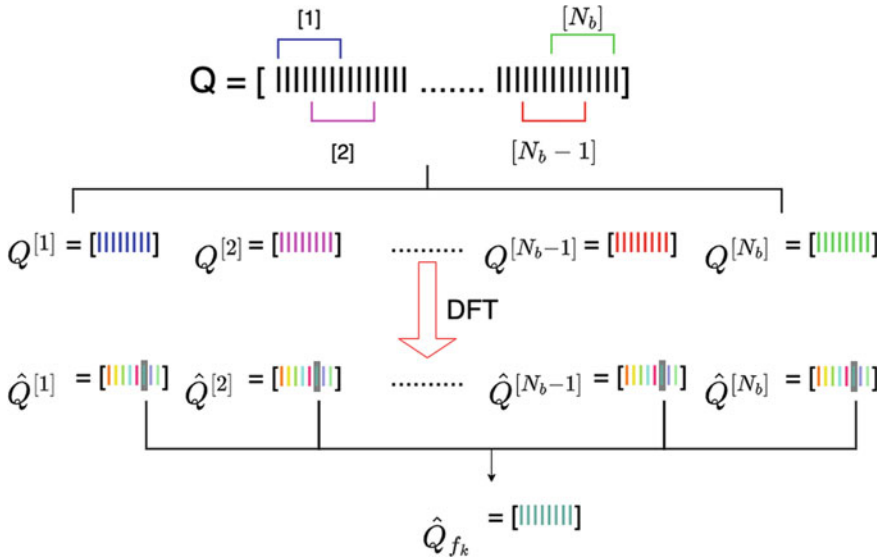
Fig. 1 Schematic depiction of Welch's method to obtain the CSD matrix (schematics adapted from [10])

SPOD modes and eigenvalues. An overview of the algorithm is explained in Fig. 1, which is adapted from [10].

Once the Fourier transformed blocks are rearranged, the cross-spectral density matrix at a particular frequency is computed as,

$$S_{f_k} = \hat{Q}_{f_k} \hat{Q}_{f_k}^*. \tag{14}$$

Now, the eigen-decomposition of S_{f_k} results in

$$S_{f_k} \Psi_{f_k} = \Psi_{f_k} \Lambda_{f_k}, \tag{15}$$

where the columns of Ψ_{f_k} represent the SPOD modes and are ranked according to their corresponding eigenvalues [10]. Similar to snapshot POD, the cross-spectral density is calculated as, $S_{f_k} = \hat{Q}_{f_k}^* \hat{Q}_{f_k}$, to reduce the computational complexity (as $N \gg N_b$) [20]. It can be shown that the eigenvalue problem

$$\hat{Q}_{f_k}^* \hat{Q}_{f_k} \Theta_{f_k} = \Theta_{f_k} \Lambda_{f_k} \tag{16}$$

gives the same nonzero eigenvalues as Eq. 15. The original eigenvectors can be retrieved as

$$\Psi_{f_k} = \hat{Q}_{f_k} \Theta_{f_k} \Lambda_{f_k}^{-1/2}. \tag{17}$$

The detailed algorithm is explained in [20]. Reconstruction of the data from the modes can be done in two ways: by exactly doing the inverse of all the steps in the frequency domain, or in the time domain based on oblique projection [21]. After truncating the modes, the frequency-domain method illustrated in [21] is followed, to obtain the reconstructed data. It should be noted that the modes obtained here are orthogonal like POD and have a characteristic frequency like DMD; however, they are arranged in a particular order based on energy, thus combining the advantages of both POD and DMD.

3   Results and Discussion

Unsteady flow across the cylinder is simulated using an in-house immersed boundary method (IBM)-based flow solver [22] by solving the 2D incompressible Navier–Stokes equation. The IBM solver has been extensively validated in [22]. In this study, the flow Reynolds number Re is kept constant at $Re = 100$ for all the modal decomposition methods. In the current case, the Strouhal number of the flow, $St = fD/U$, comes out to be 0.171, which matches with the existing literature [23–25]. Figure 2 displays a snapshot of the vorticity flow field for reference.

3.1   POD

POD analysis on the flow across a stationary circular cylinder at $Re = 100$ is performed first. After discarding the initial transients, 100 snapshots, corresponding to 5 cycles of vortex shedding, are considered. The distinct, coherent structures in the modes became more apparent with increasing snapshots. The sampling interval Δt between two consecutive snapshots is 0.252 s. The normalized eigenvalues as a function of modes are presented in Fig. 3. The POD modes can be seen to occur in pairs, indicating symmetry in the flow.
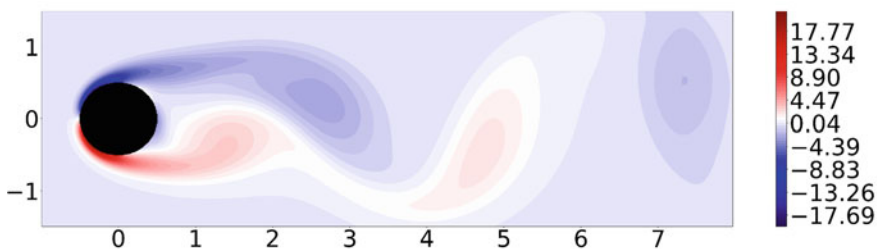

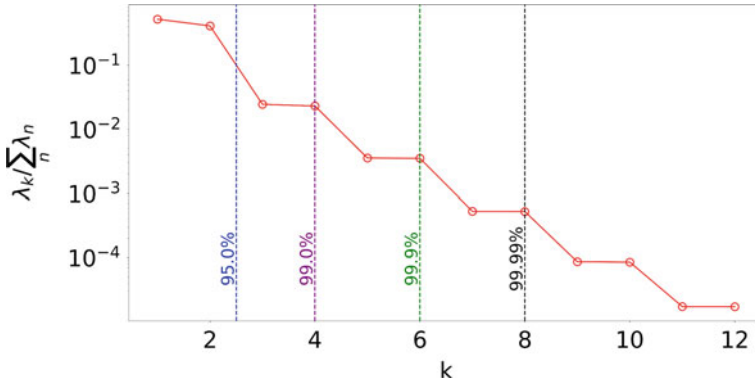**Fig. 2**   Vorticity flow field at $t = 25$ s

Fig. 3 Normalized eigenvalues of POD modes

The first two modes arranged as per descending energy content are shown in Fig. 4. As indicated by the eigenvalues, there is symmetry in the modes as well. Clearly, the modes predominantly have structures resembling vortices in the flow, bolstering the importance of the actual vortices in the flow.

The vertical lines in Fig. 3 correspond to the percentage of total energy captured by the modes before them. It is evident that just two modes account for 95% of the total energy, and with eight modes, 99.99% of the total energy can be captured. As a result, it is possible to accurately represent the flow field with just eight modes. As expected, the error in the reconstructed flow field resembles the higher-order

(a) POD Mode 1
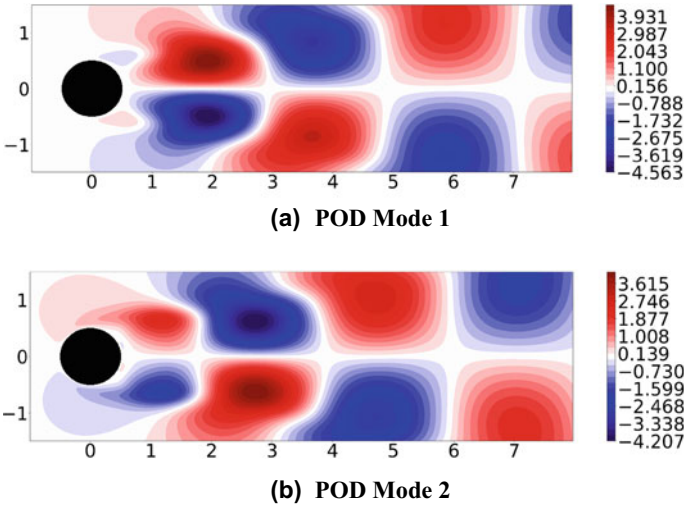
(b) POD Mode 2

Fig. 4 First two POD modes of U velocity

POD modes, which were neglected. Thus, the dimension of the original data can be reduced to just eight modes, with an error of $O(10^{-2})$.

3.2 DMD

Similar to POD, DMD is performed on 100 snapshots and the resulting eigenvalues were all found to be lying on a unit circle as demonstrated in Fig. 5. This indicates that the growth/decay rate of the modes is almost zero.

The magnitude of the amplitudes of the DMD modes is plotted against frequency in Fig. 6. The highest peak is at zero which corresponds to the time-averaged flow or the base flow (Mode 0) and the subsequent peaks were at the vortex shedding frequency (f_s) and its higher-order harmonics. This clearly indicates that the dynamically important modes are the ones that correspond to the vortex shedding.

Unlike POD modes, DMD modes are complex. The first dominant DMD mode (that corresponds to the vortex shedding frequency) is shown in Fig. 7. It can be seen that the first and second POD modes are identical to the real and imaginary components of the first DMD mode, indicating the fact that the POD modes, in this case, consist of structures oscillating at fs and its harmonics. Even though the POD algorithm does not have any constraints on the frequency of the modes, it can be observed that there is no mixing of frequencies in the modes. This is explained by the fact that the flow is periodic with only one dominant frequency (vortex shedding frequency). Thus, the POD modes correspond to the dominant frequency and its harmonics in the flow in this case. The real and imaginary components of the next important DMD mode ($2 f_s$) are similar to the third and fourth POD modes.
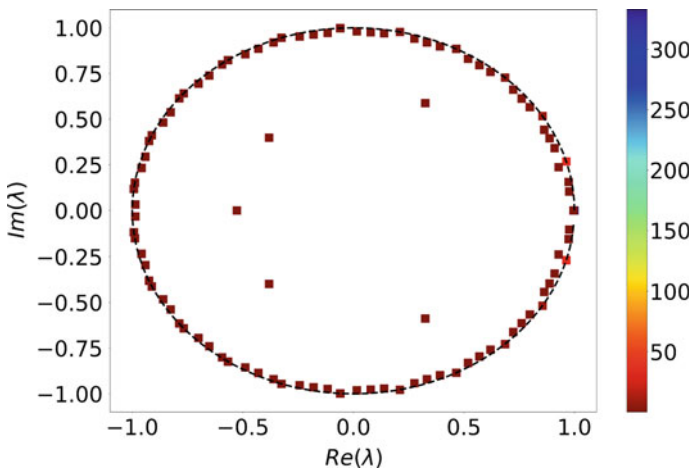

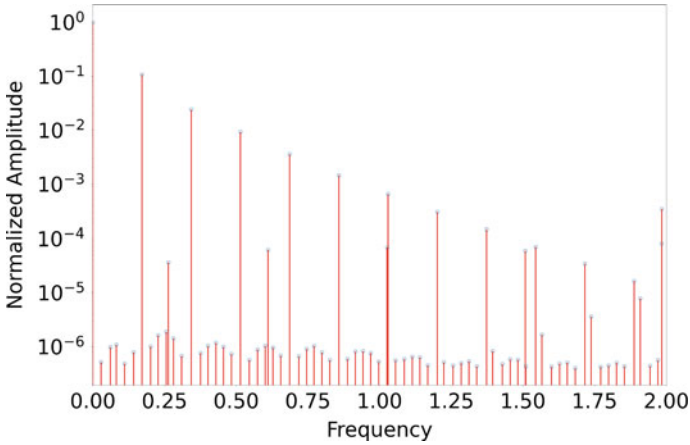**Fig. 5** DMD eigenvalues in the complex plane

Fig. 6 Normalized amplitudes of the DMD modes at their respective frequencies
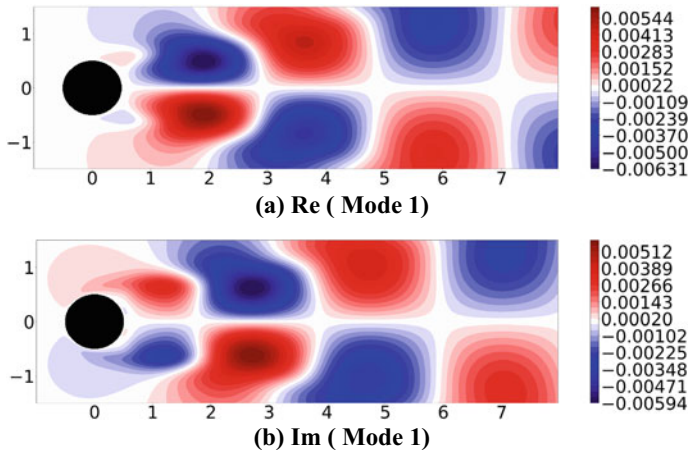

Fig. 7 First DMD mode of U velocity at the vortex shedding frequency

When the flow field data were reconstructed using the first eight dominant DMD modes, the error in the flow field, similar to POD, resembled the neglected higher-order modes.

3.3 SPOD

The SPOD is computed from 1080 snapshots to attain convergence in the reconstruction error. Following the guidelines established in [20], the number of snapshots per
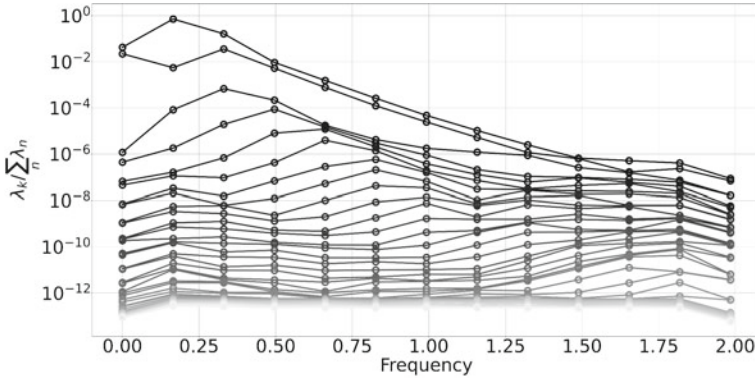
Fig. 8 SPOD eigenvalue spectrum

block, N_f, is set to 24 to make the lowest resolvable frequency correspond to the vortex shedding frequency. A hamming window is used, to compensate for the spectral leakage. The full eigenvalue spectrum for different frequencies is shown in Fig. 8. The eigenvalues were normalized with respect to the total energy in the flow. As the mode number increases, the color of the curves changes from black to white. The low-rank nature of the flow is evident from the figure, as the first two modes capture a significant amount of energy across the frequency range. As expected, the most significant mode happens to be the first mode at the vortex shedding frequency.

The first two SPOD modes of u-velocity at f_s are shown in Fig. 9. It can be observed that the first SPOD mode resembles the first POD and DMD modes. This can be explained by the low-rank characteristics of the flow (the first two modes are able to account for almost all of the energy in the flow). The second mode resembles the higher-order modes of POD (not shown) reinforcing the lesser significance of these structures in the flow.

The flow field can be reconstructed within $O(10^{-2})$ accuracy with just the first two modes of the first four dominant frequencies. As expected, the error in the reconstructed flow resembles the neglected modes.

The relative reconstruction error,

$$E = \frac{||u - u_{\text{rec}}||}{||u||}, \tag{18}$$

where u is the actual flow field, and u_{rec} is the reconstructed flow field, which is plotted across the number of modes used for reconstruction in Fig. 10. Since DMD modes are complex and have two components per mode (real and imaginary), there is a multiplicative factor $k = 2$ multiplied to the number of modes to represent the effective size of the latent space. Since the first 2 SPOD modes for each frequency were used in the reconstruction of the flow field, $k = 2$ for SPOD as well. It can be inferred that the flow field can be reconstructed with only 0.8% error using just four
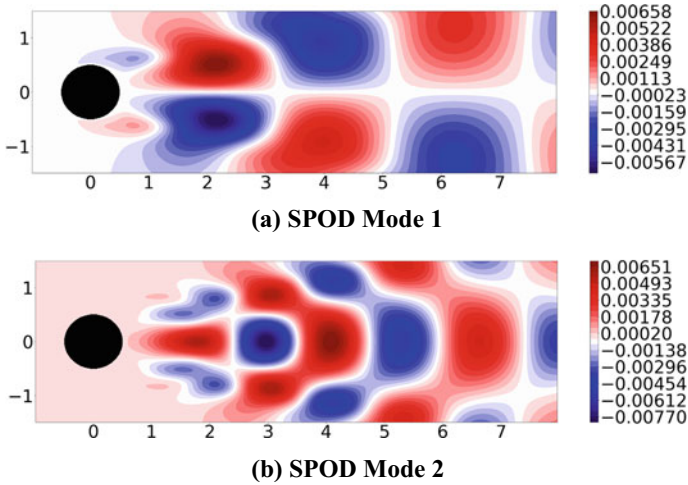
(a) SPOD Mode 1

(b) SPOD Mode 2

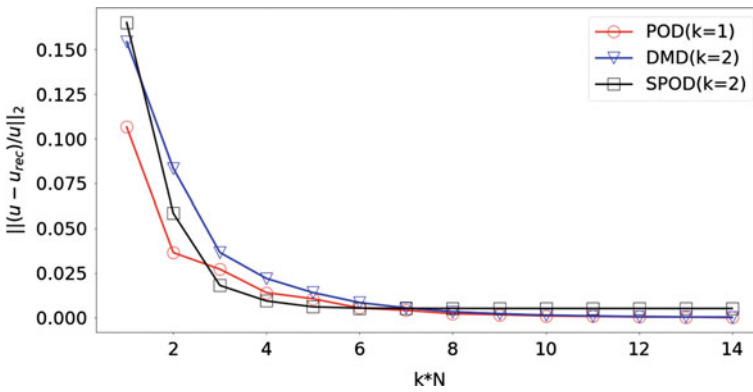**Fig. 9** First two SPOD modes of U velocity at vortex shedding frequency

Fig. 10 Relative reconstruction error as a function of the number of modes used for reconstruction for different methods

SPOD modes, whereas it requires six modes of POD and DMD to reconstruct the flow field with the same error margin.

4   Conclusions

In this study, SPOD is used to analyze the wake structures of the flow past a stationary circular cylinder and compared to popular existing methods like POD and DMD. As expected, the vortices in the flow field were the significant structures in the flow,

both energetically and dynamically. Overall, SPOD performed better than both POD and DMD in capturing dynamically important structures and produced an efficient reduced basis to reconstruct the flow field. The only disadvantage of SPOD was the requirement for a larger dataset to converge compared to the other methods. Even though the true potential of SPOD would be established in a flow with multiple temporal scales, this analysis serves as a good starting point. Building on this, future work can be directed toward analyzing complex flows with multiple dominant frequencies.

Nomenclature

Re Reynolds number
f_s Vortex shedding frequency (Hz)
$X^\dagger$ Moore–Penrose pseudoinverse
$\underline{q}$ Mean flow field

References

1. Taira K, Brunton SL, Dawson STM, Rowley CW, Colonius T, McKeon BJ, Schmidt OT, Gordeyev S, Theofilis V, Ukeiley LS (2017) Modal analysis of fluid flows: an overview. AIAA J 55(12):4013–4041
2. Rowley CW, Dawson STM (2017) Model reduction for flow analysis and control. Annu Rev Fluid Mech 49(1):387–417
3. Taira K, Hemati MS, Brunton SL, Sun Y, Duraisamy K, Bagheri S, Dawson STM, Yeh C-A (2020) Modal analysis of fluid flows: applications and outlook. AIAA J 58(3):998–1022
4. Lumley JL (1967) The structure of inhomogeneous turbulent flows. In: Atmospheric turbulence and radio wave propagation
5. Noack BR, Afanasiev K, Morzyński M, Tadmor G, Thiele F (2003) A hierarchy of low-dimensional models for the transient and post-transient cylinder wake. J Fluid Mech 497:335–363
6. Rowley CW, Mezić I, Bagheri S, Schlatter P, Henningson DS (2009) Spectral analysis of nonlinear flows. J Fluid Mech 641:115–127
7. Tu J, Rowley C, Luchtenburg D, Brunton S, Kutz J (2013) On dynamic mode decomposition: theory and applications. J Comput Dyn 1:11
8. Kou J, Zhang W (2017) An improved criterion to select dominant modes from dynamic mode decomposition. Eur J Mech B Fluids 62:109–129
9. Krake T, Reinhardt S, Hlawatsch M, Eberhardt B, Weiskopf D (2021) Visualization and selection of dynamic mode decomposition components for unsteady flow. Visual Inf 5(3):15–27
10. Towne A, Schmidt OT, Colonius T (2018) Spectral proper orthogonal decomposition and its relationship to dynamic mode decomposition and resolvent analysis. J Fluid Mech 847:821–867
11. Hellström LHO, Smits AJ (2017) Structure identification in pipe flow using proper orthogonal decomposition. Philos Trans Roy Soc A Math Phys Eng Sci 375(2089):20160086

12. Schmidt OT, Towne A, Rigas G, Colonius T, Brès GA (2018) Spectral analysis of jet turbulence. J Fluid Mech 855:953–982
13. Pickering E, Rigas G, Nogueira PAS, Cavalieri AVG, Schmidt OT, Colonius T (2020) Lift-up, Kelvin-Helmholtz and Orr mechanisms in turbulent jets. J Fluid Mech 896
14. Muralidhar SD, Podvin B, Mathelin L, Fraigneau Y (2019) Spatio-temporal proper orthogonal decomposition of turbulent channel flow. J Fluid Mech 864:614–639
15. Ghate AS, Towne A, Lele SK (2020) Broadband reconstruction of inhomogeneous turbulence using spectral proper orthogonal decomposition and Gabor modes. J Fluid Mech 888
16. Nidhan S, Chongsiripinyo K, Schmidt OT, Sarkar S (2020) Spectral proper orthogonal decomposition analysis of the turbulent wake of a disk at Re $=$ 50,000. Phys Rev Fluids 5(12):124606
17. Weiss J (2019) A tutorial on the proper orthogonal decomposition. In: AIAA aviation 2019 forum, p 3333
18. Sirovich L (1987) Turbulence and the dynamics of coherent structures. I. Coherent structures. Quart Appl Math 45(3):561–571
19. Krake T, Weiskopf D, Eberhardt B (2019) Dynamic mode decomposition: theory and data reconstruction. arXiv preprint arXiv:1909.10466
20. Schmidt OT, Colonius T (2020) Guide to spectral proper orthogonal decomposition. AIAA J 58(3):1023–1033
21. Nekkanti A, Schmidt OT (2021) Frequency-time analysis, low-rank reconstruction and denoising of turbulent flows using SPOD. J Fluid Mech 926
22. Majumdar D, Bose C, Sarkar S (2020) Capturing the dynamical transitions in the flow-field of a flapping foil using immersed boundary method. J Fluids Struct 95:102999
23. Xu S, Wang ZJ (2006) An immersed interface method for simulating the interaction of a fluid with moving boundaries. J Comput Phys 216(2):454–493
24. Zhang H-Q, Fey U, Noack BR, König M, Eckelmann H (1995) On the transition of the cylinder wake. Phys Fluids 7(4):779–794
25. Lai M-C, Peskin CS (2000) An immersed boundary method with formal second-order accuracy and reduced numerical viscosity. J Comput Phys 160(2):705–719

Computational Analysis of Serpentine Nozzles

Somrick Das Biswas, Keshav Anand Kabra, Shailesh R. Nikam, and Siddharth Anish

1 Introduction

Serpentine nozzles completely shield the high-temperature core flow and the tail cone inside the core wall, which indicates that the core walls and the high-temperature parts inside the core wall are invisible from all directions at the rear of the serpentine nozzle.

Recently, serpentine nozzles have attracted considerable attention, especially in military aviation. Serpentine nozzles suppress the thermal and acoustic signatures of the engine exhaust, making the aircraft difficult to track by radars and IR-homing missiles and seekers. In this paper, the main focus is on improving the expansion characteristics to reduce the performance penalty associated with serpentine nozzles. However, little research exists on predicting elementary flow characteristics like pressure and velocity gradients within the nozzle. Furthermore, the effects of inlet and outlet shapes on the flow parameters are not known. The paper aims to infer a relationship between geometry and flow behaviors. The literature survey has proved that serpentine nozzles have excellent stealth characteristics and avoid detection. As stealth becomes a primary consideration in future wars, the significant thrust penalties are the tradeoffs for operating in hostile airspace.

S. Das Biswas (✉) · K. A. Kabra · S. Anish
Department of Mechanical Engineering, K. J. Somaiya College of Engineering, University of Mumbai, Mumbai, India
e-mail: somrick.d@somaiya.edu

K. A. Kabra
e-mail: keshav.kabra@somaiya.edu

S. Anish
e-mail: siddharth.anish@somaiya.edu

S. R. Nikam
Department of Mechanical Engineering, K. J. Somaiya College of Engineering, Somaiya Vidyavihar University, Mumbai, India

2 Literature Review and Objective

Several research papers were consulted and studied during the literature study phase to gain a deeper understanding of the topic. The different research papers consulted for this paper are summarized below.

Hui et al. [1] investigated the serpentine nozzle experimentally and computationally. They studied flow characteristics of serpentine nozzles and axisymmetric nozzles with the employment of a schlieren system, PSI electronic pressure scanning valves, a six-component force balance system, and flowmeters. Their results show that the static pressure distributions on the upper and down walls of serpentine nozzles are different from those of axisymmetric nozzles, which are mainly affected by the flow tube near the walls. The flow velocity increases and the static pressure drops when the flow tube contracts. This paper serves as the primary basis of our validation.

Cheng et al. [2] found that the shielding ratio has a significant impact on the infrared signature of the serpentine nozzle. The analysis indicates that the serpentine nozzle with $\Delta Y = 1$ has a better stealth performance; additionally, the visible area ratio is suggested to be under 0.041. The swirl angle significantly affected the infrared signature level of the serpentine nozzle. Compared to the no-swirl case, the average reduction of the total infrared signature level increased from 2.29 to 13.84% in the horizontal plane for an increase in the swirl angle from $5°$ to $20°$. An increased reduction from 5.83 to 31.21% is seen in the vertical plane.

Shan et al. [3] had the following findings. The nozzle with an aspect ratio of 5 is recommended for achieving optimal aerodynamics. The increase in aspect and offset ratios could effectively suppress plume radiation, which was not sensitive to overall radiation. Compared with circular nozzles, the double S-shaped nozzles reduced infrared radiation by over 50%, proving significant stealth ability. A balance between aerodynamic performances and infrared radiation suppression could be reached for double S-shaped nozzles.

Nageswara Rao et al. [4] experimentally discussed the effect of the nozzle shape on the flow field and acoustic characteristics of a high Mach no. subsonic jet emanating from a serpentine nozzle at Mach number 0.84. Near-field OASPL mapping results indicate that the dominant noise is emanating at the end of the potential core breakdown.

Sun et al. [5] investigated and surmised that the centerlines with a rapid turning at the exit would result in a high Mach number, which brings on high friction loss and secondary loss at the turnings. For maximum efficiency of centerline distributions, it is recommended that curves with gentle turns at each serpentine passage exit should be chosen.

Da et al. [6] theorized that with a sectional PI control law, the RMS control error was reduced by more than 56% under arbitrary changing conditions. Works in this paper also showed that the dynamics of this non-dimensional system can be simplified as a stable second-order overdamped system.

3 Materials and Methods

In the present investigation, CFD simulations are undertaken using the Ansys Fluent 2021R2 version. The first step was to validate the CFD results from existing literature in [1]. Once an accurate enough model was established to give predictable results, new iterations were undertaken to study the control variables of a serpentine nozzle to derive the optimum geometry.

After a few iterations, the established CFD model could accurately and consistently deliver the expected values. Once the CFD models attained critical stability based on a grid independence study, literature data [1] were compared with our model predictions. This process is highlighted in Fig. 10.

The present results match well within 10% of the literature result with a similar trend and thus helped us gain reasonable confidence in our CFD model.

Post-validation, we decided to focus our attention on the different geometrical parameters of the serpentine nozzles. We have mainly focused on revamping the inlet and outlet geometries and tried multiple iterations such as elliptical, circular, rectangular, and cambered rectangular outlet geometries. These geometries and their CAD models and properties are discussed in the subsequent section.

Following this, pressure and velocity contours of the geometries were studied and investigated to arrive upon the most optimum geometry, which would meet our objectives of reducing thrust penalties, by modulating pressure and velocity flows.

The pressure and velocities contours have been plotted in the nozzle mid-plane. We have attempted to reduce the pressure perturbations to reduce abrupt pressure variations.

The secondary objective is to study the velocity flow lines to ensure maximal exhaust velocity and to produce the highest amount of thrust possible from the engine.

3.1 Nozzle Geometry

The basic profile of the serpentine nozzle is seen in Fig. 1. The serpentine nozzle is modeled using Bezier curves in SolidWorks 2021. Five guide points are used to model the profile.

Several variations in inlet and outlet geometries were simulated, and their characteristics are analyzed. Their specifications are listed as follows:

3.1.1 Cambered Rectangular Exit

See Figs. 2 and 3.

Inlet diameter: 250 mm.
Rectangular exit camber diameter: 100 mm.
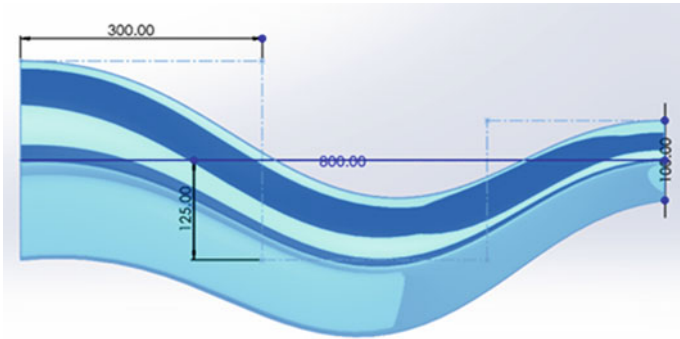Rectangular exit straight length: 150 mm.

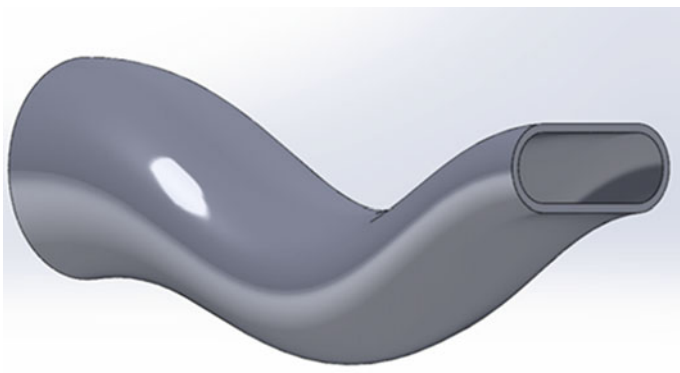**Fig. 1** Basic profile of the serpentine nozzle
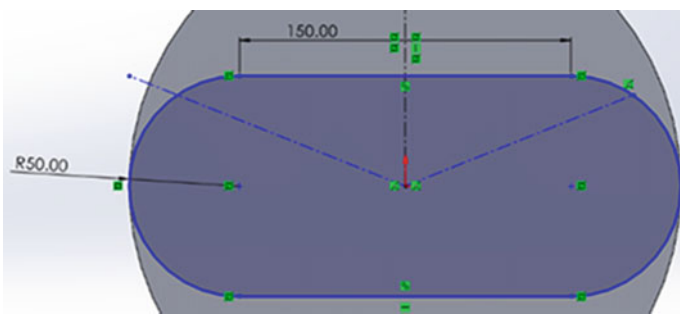

Fig. 2 Cambered rectangular exit

Fig. 3 Cambered rectangular exit cross-section
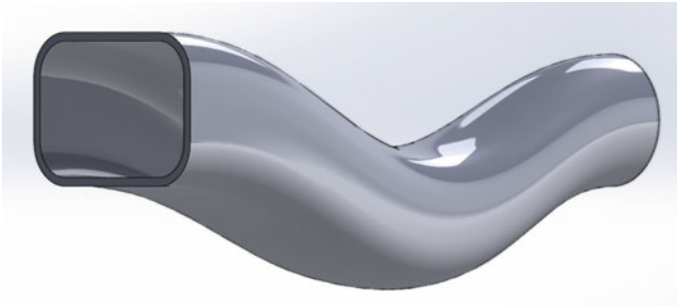
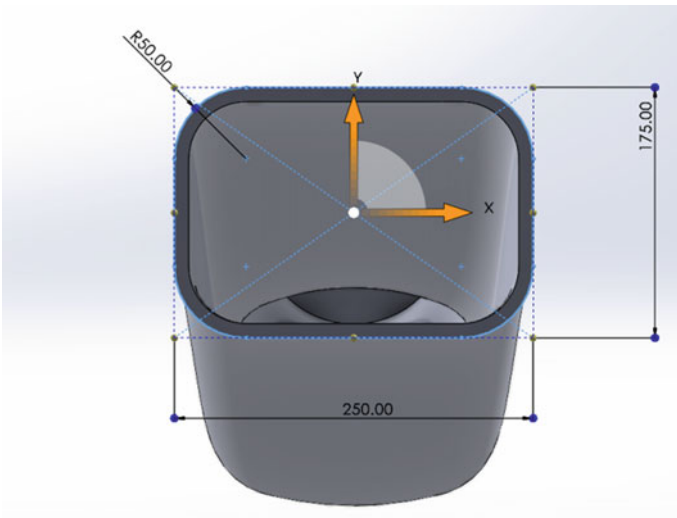**Fig. 4** Cambered rectangular exit

Fig. 5 Cambered rectangular exit cross-section

3.1.2 Cambered Rectangular Inlet

See Figs. 4 and 5

Length of inlet: 250 mm.
Breadth of inlet: 175 mm.
Corner radius: 50 mm.
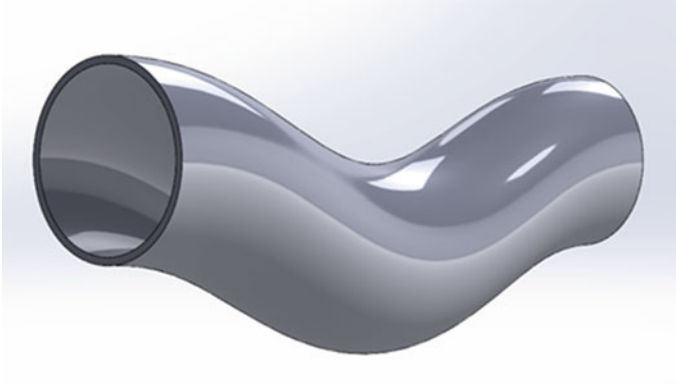Exit diameter: 150 mm.

3.1.3 Circular Inlet and Exit

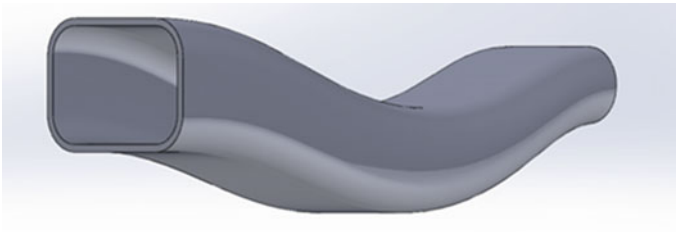See Fig. 6.

Fig. 6 Circular inlet and exit

Fig. 7 Rectangular inlet and outlet

Circular inlet and exit.
Inlet diameter: 250 mm.
Exit diameter: 200 mm.

3.1.4 Rectangular Inlet and Exit

See Figs. 7 and 8.

- Same inlet as iteration 3.1.2.
- Same outlet as iteration 3.1.1.

3.2 Modeling and Meshing

In the CFD procedure, Unsteady Reynolds-Averaged Navier–Stokes (URANS) equations are used to simulate the flow. Since the nozzle is intended for subsonic flows, with a converging nozzle, as per the Rankine–Hugoniot conditions, there will be no flow separation inside the nozzle. This indicates that URANS equations will deliver
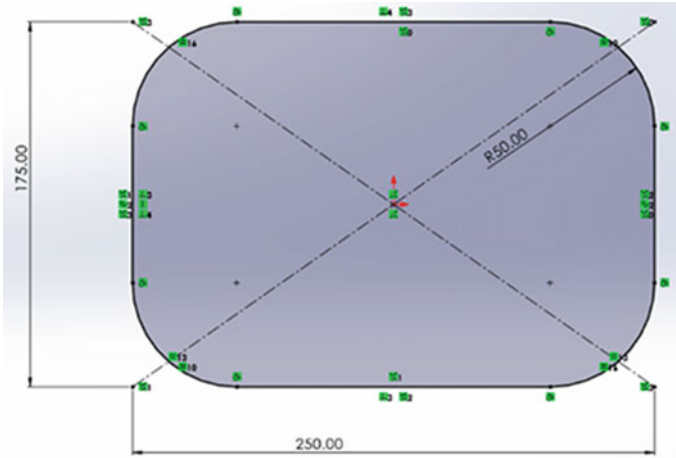
Fig. 8 Rectangular inlet cross-section

accurate results. For modeling the serpentine nozzle, the Realizable k-ε Turbulence Model is used. Due to high Reynolds numbers and high-pressure gradients, the standard k-ε Turbulence Model is not used as it cannot resolve boundary layer flow according to the law of the wall at higher pressure gradients. The equations governing the flow are as follows:

$$\frac{dk}{dt} = \frac{1}{\rho}\frac{\partial}{\partial x_j}\left(\frac{\mu_1 \partial k}{\sigma_k \partial x_j}\right) + \frac{\mu_t}{\rho}\left(\frac{\partial U_i}{\partial x_j} + \frac{\partial U_j}{\partial x_i}\right)\frac{\partial U_i}{\partial x_j} - \varepsilon,\tag{1}$$

$$\frac{d\varepsilon}{dt} = \frac{1}{\rho}\frac{\partial}{\partial x_j}\left[\frac{\mu_t}{\sigma_\varepsilon}\frac{\partial \varepsilon}{\partial x_j}\right] + \frac{c_{\varepsilon 1}\mu_t \varepsilon}{\rho K}\left(\frac{\partial U_i}{\partial x_j} + \frac{\partial U_i}{\partial x_i}\right)\frac{\partial U_i}{\partial x_j} - c_{\varepsilon 2}\frac{\varepsilon^2}{k}.\tag{2}$$

The flow conditions are to be simulated at about Mach 0.9 at an altitude of 2000 m above mean sea level. The engine outlet parameters at this altitude are used as the boundary conditions. These have been derived from literature [1]. The boundary conditions are as follows:

- Inlet pressure: 1.25 MPa
- Inlet velocity: 299 m/s
- Inlet temperature: 1200 K
- Outlet pressure: 0 (Gauge)
- Outlet temperature: 290 K

Due to the complexity of the domain, Tet-Dominant meshing was preferred. A mesh independence study was conducted to study the effects of cell size and number on the flow. The coefficient of pressure at the core at $x/L = 0.5$ was chosen to be the control variable. The edge length was varied until a significant difference in

Table 1 Mesh metrics

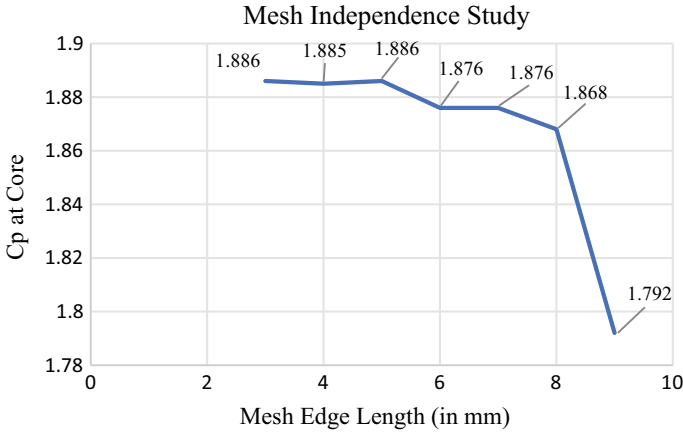| Iteration	No. of cells	No. of nodes
Cambered rectangular exit	79,486	83,433
Cambered rectangular inlet	78,225	82,680
Circular inlet and exit	79,942	89,235
Rectangular inlet and exit	79,774	86,534

Fig. 9 Mesh independence study

the control variable was detected. The results of this mesh independence study are summarized in Table 1 (Fig. 9).

As per the study, the mesh with an edge length of 8 mm was the last mesh-independent solution. Meshing details and boundary conditions are given in Table 1.

- Tetrahedral meshing.
- Patch conformational.
- Average edge length: 8 mm.
- Inflation factor: 1.25.
- No. of inflation layers: 5.
- Transition ratios: 0.3.

3.3 Validation

Pressure values against the dimensionless length of the serpentine nozzle were plotted and compared with the CFD and wind tunnel testing data from the literature [1] as shown in Fig. 10.

Our CFD model shows remarkable similarity with the literature data, especially after 35% of the length. The maximum deviation from literature data is about 30%

Fig. 10 Validation against literature data [1]

at x/L equals 0.25. This deviation at the beginning of the serpentine nozzle is inconsequential for this paper, as it focuses primarily on the effects near the exit of the nozzle, which is where the pressure distribution matters.

Furthermore, the CFD model accurately predicts the trend of the pressure changes throughout the serpentine nozzle, which is of primary importance for making qualitative decisions about optimal decisions.

4 Results and Discussion

Post-simulations, the obtained results for each of the four geometries have been summarized below:

4.1 Cambered Rectangular Exit

The pressure variation along the flow is observed in Fig. 11a. Static pressure drops after x/L 0.4 for the upper surface and x/L 0.6 for the lower surface. It can also be observed that the pressure drops from 2.36 to 0.4 bar at the exit.

Figure 11b exhibits that velocity starts picking up at 50% of the length. Velocity accelerates from about 300 m/s to almost 693 m/s, which is a significant increase in speed.

These two factors make this iteration a viable and preferred design for aircraft exhaust nozzles.
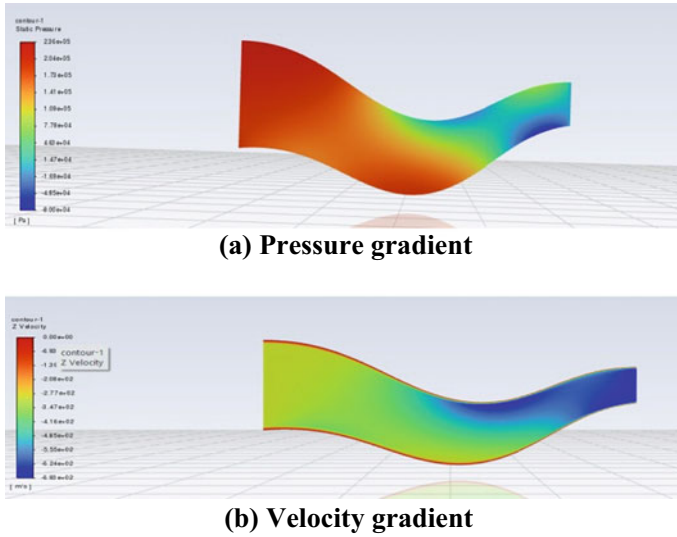
(a) Pressure gradient

(b) Velocity gradient

Fig. 11 a Pressure gradient. **b** Velocity gradient

4.2 Cambered Rectangular Inlet

Figure 12a shows the static pressure field distribution along the central plane for the iteration. The contour shows that the pressure drops later if compared to the previous iteration. At the upper surface, the pressure drops at around $x/L = 0.5$ and $x/L = 0.8$ for the lower surface. Thus, expansion takes place later.

From Fig. 12b, it can be inferred that the final velocity at the nozzle exit is 766 m/s which is a significant expansion. It indicates that even though the expansion happens near the nozzle exit at $x/L = 0.6$, it occurs quite rapidly.

4.3 Pure Circular Exit

From Fig. 13a, it is evident that the peak pressure drop is encountered earlier in this iteration. However, the static pressure at the exit is higher than in the previous iteration. Pressure drop along the upper surface starts at $x/L = 0.35$, but the pressure drop across the lower surface starts at the same time.

Figure 13b indicates that the final velocity is smaller compared to the rectangular iteration at around 561 m/s, indicating that the expanding gasses have not been able to expand fully in the nozzle. This iteration is not ideal.
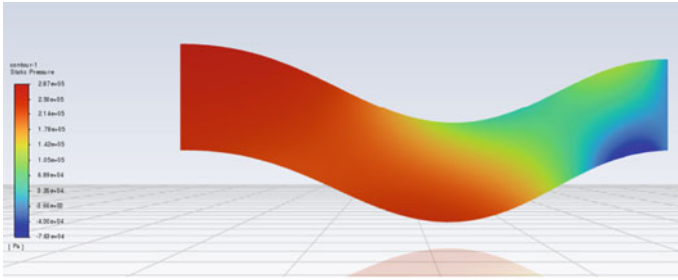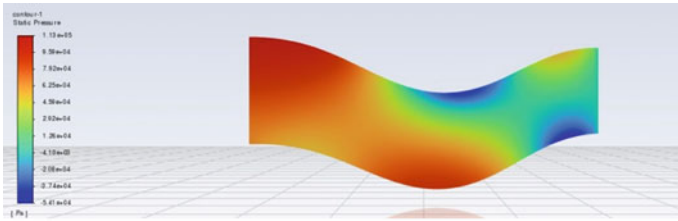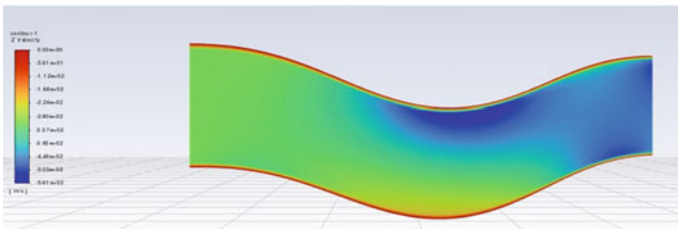
(a) Pressure gradient
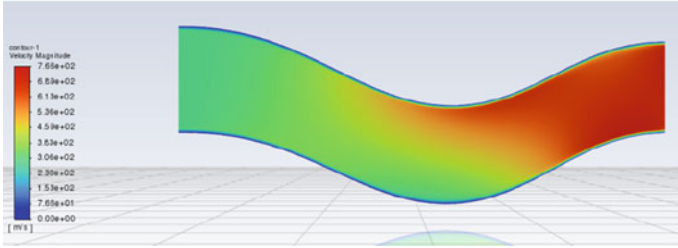
(b) Velocity gradient

Fig. 12 **a** Pressure gradient. **b** Velocity gradient

(a) Pressure gradient

(b) Velocity gradient

Fig. 13 **a** Pressure gradient. **b** Velocity gradient

(a) Pressure gradient
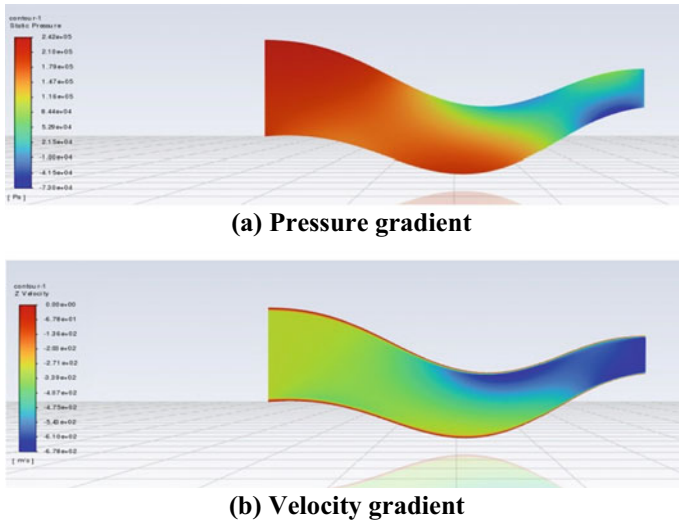

(b) Velocity gradient

Fig. 14 **a** Pressure gradient. **b** Velocity gradient

4.4   Pure Rectangular Exit

From Fig. 14a, inferences indicate that the magnitude of static pressure drop is the least in this iteration, from 2.4 bar to 0.2 bar. The pressure characteristics for both surfaces are similar to the cambered rectangular iteration.

Figure 14b indicates that freestream velocity picks up quite late, at around 80% of the cavity length. There is a significant flow acceleration, from 300 m/s to about 678 m/s, indicating good acceleration.

The results obtained from these simulations allow us to plot the velocity ratio as a function of the area ratio for serpentine nozzles, as seen in Fig. 15.

From Fig. 15, we find a quadratic relation between the area and velocity ratios. The graph further highlights that the increase in area ratio does not keep up with the increase in velocity ratio.

5   Conclusions

From the present computational investigation, the following conclusions are drawn:

- Rectangular inlets and circular outlets give the best flow characteristics.
- Significant velocity increase and the pressure penalty are also lower when compared to other inlet outlet conditions investigated.
- It follows that a smaller exit area leads to a velocity increase but results in unfavorable pressure characteristics.
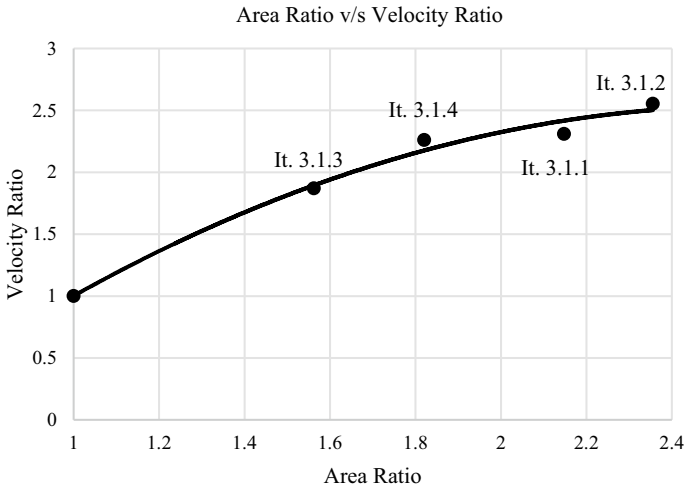
Fig. 15 Area ratio versus velocity ratio

- Increasing the area ratio from 1.56 to 1.82 (~16% increase) leads to an 18% increase in the velocity.
- Increasing the area ratio further does not lead to proportionate velocity gains. Increasing the area ratio from 1.82 to 2.15 (~18% increase) leads to only a 2% increase in the velocity ratio.
- Similarly, increasing the area ratio from 1.82 to 2.35 (~29% increase) leads to only a 13% increase in the velocity ratio.

Nomenclature

C_P	Pressure coefficient (–)
OASPL	Overall sound pressure level (dB)
x	Distance from the nozzle inlet (m)
L	Length of the serpentine nozzle (m)
M_∞	Free stream Mach No. (–)
P	Static pressure (Pa)
P_b	Back pressure (Pa)
AMSL	Above mean sea level (m)
σ	Wall stress (Pa)
K	Turbulent kinetic energy (m^2/s^2)
ε	Rate of dissipation of TKE (m^2/s^3)

μ Kinematic viscosity (cm/s^2)

u_i Relative velocity (in direction) (m/s)

$c_{\varepsilon 1}$, $c_{\varepsilon 2}$ Closure coefficients (–)

References

1. Hui Z, Shi J, Zhou L, Wang Z, Liu Y (2021) Experimental investigation of serpentine nozzles for turbofan. Shaanxi Key Laboratory of Internal Aerodynamics in Aero-Engine, School of Power and Energy, Northwestern Polytechnical University, 710072, Xi'an, People's Republic of China
2. Cheng W, Wang Z, Zhou L, Sun X, Shi J (2019) Investigation of infrared signature of serpentine nozzle for turbofan. J Thermophys Heat Transf 33(1):170–178
3. Shan Y, Zhou X, Tan X, Zhang J, Wu Y (2019) Parametric design method and performance analysis of double S-shaped nozzles. Int J Aerosp Eng 2019:24 Article ID 4694837. https://doi.org/10.1155/2019/4694837
4. Nageswara Rao A, Arora R, Kushari A High subsonic flow field from the serpentine nozzle. In: 8th international conference on fluid flow, heat and mass transfer (FFHMT'21). https://doi.org/10.11159/ffhmt21.144
5. Sun X, Wang Z, Zhou L, Shi J, Liu Z (2015) Experimental and computational investigation of double serpentine nozzle. Proc Inst Mech Eng Part G J Aerosp Eng. 229(11):2035–2050. https://doi.org/10.1177/0954410014564402
6. Da X, Fan J (2020) Closed-loop flow control of an ultra-compact serpentine inlet based on non-dimensional model. Chin J Aeronaut 33(10):2555–2562. ISSN 1000-9361

Direct Flux Reconstruction for Accurate Resolution of Complex Flow Structures

Raagvendra Singh, Abhishek M. Kalluri, V. K. Suman, and Rakesh Kumar

1 Introduction

There have been continual efforts in simulating compressible flows using high-order accurate schemes. The goal is to preserve and capture flow structures with high resolution. This work has led to the development of high-order methods, including Discontinuous Galerkin (DG), Weighted Essentially Non-Oscillatory (WENO), and Flux Reconstruction (FR) schemes.

Direct Flux Reconstruction [1] is one such high-order scheme that belongs to the class of Flux Reconstruction schemes and is simple compared to FR laid by Hyunh [2] since it does not use correction functions. With the reasonable choice of solution points, other high-order schemes can be recovered, such as the nodal DG method [1]. DFR is a nascent and promising candidate for simulating compressible, turbulent flows. The reader is encouraged to consult [1] to understand the mathematical formulation of the DFR approach.

The robustness and accuracy of a code are often analyzed using flows containing shocks and instabilities. In the present work, we have solved three problems using the in-house CFD solver based on DFR to evaluate the performance of this high-order scheme in simulating flows involving complex structures. These include shock–vortex interaction, Rayleigh–Taylor instability, and Kelvin–Helmholtz instability problems. We also validate our code using Sod's shock tube problem.

R. Singh (✉) · V. K. Suman · R. Kumar
Department of Aerospace Engineering, IIT Kanpur, Kanpur 208016, India
e-mail: rsingh20@itk.ac.in

R. Kumar
e-mail: rkm@iitk.ac.in

A. M. Kalluri · V. K. Suman
Computational and Theoretical Fluid Dynamics Division, NAL, Bengaluru 560017, India

© The Author(s), under exclusive license to Springer Nature Singapore Pte Ltd. 2024
K. M. Singh et al. (eds.), *Fluid Mechanics and Fluid Power, Volume 3*, Lecture Notes in Mechanical Engineering, https://doi.org/10.1007/978-981-99-6343-0_57

Shock–vortex interaction is paramount in understanding noise generation mechanisms in high-speed flows. Practically, such an interaction occurs during the flow of a supersonic jet.

Rayleigh–Taylor (RT) instability happens at the interface of two fluids having different densities when an acceleration is being directed from the denser fluid to the lighter one. The instability results in the bubbles of lighter fluid rising in the denser fluid and spikes of denser fluid falling in the lighter fluid.

Kelvin–Helmholtz (KH) instability occurs when there is a velocity discontinuity at the interface of two superposed fluids, one above the other.

2 Governing Equations

The governing equation for the shock–vortex interaction, RT instability, and KH instability is the Euler equation, which in 2D is represented by

$$\frac{\partial U}{\partial t} + \frac{\partial F}{\partial x} + \frac{\partial G}{\partial y} = S, \tag{1}$$

$$U = \begin{bmatrix} \rho \\ \rho u \\ \rho v \\ E \end{bmatrix}, \ F = \begin{bmatrix} \rho u \\ \rho u^2 + P \\ \rho u v \\ u(E + P) \end{bmatrix}, \ G = \begin{bmatrix} \rho v \\ \rho u v \\ \rho v^2 + P \\ v(E + P) \end{bmatrix}, \tag{2}$$

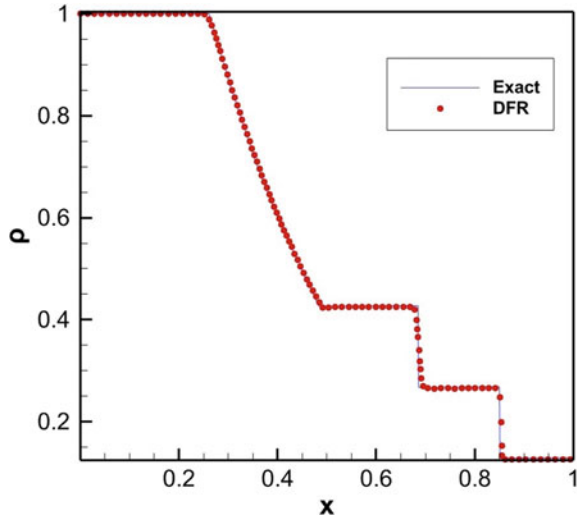$$E = \rho \left[\frac{1}{2} (u^2 + v^2) + e \right], \tag{3}$$

and the expression for e is the caloric equation of state. For the Sod's shock tube problem, shock–vortex interaction and KH instability

$$S = \begin{bmatrix} 0 \\ 0 \\ 0 \\ 0 \end{bmatrix} \tag{4}$$

and for the RT instability

$$S = \begin{bmatrix} 0 \\ 0 \\ \rho \\ \rho v \end{bmatrix}. \tag{5}$$

Fig. 1 Density variation with x as obtained analytically and using DFR with LLAV at $t = 0.2$

3 Code Validation

The Sod's shock tube problem consists of the one-dimensional Riemann problem with the conditions, as $(\rho, u, p) = (1, 0, 1)$ for $x \leq 0.5$, $(\rho, u, p) = (0.125, 0, 0.1)$ for $x > 0.5$.

The domain is $[0, 1] \times [0, 0.125]$. Shock capturing is implemented using the artificial viscosity method by Persson and Perraire [3]. The results are plotted for $t = 0.2$. From Figs. 1 and 2, we can see that the results obtained using DFR are in agreement with the exact results.

4 Shock–Vortex Interaction

We numerically simulate the interaction of a vortex with a shock using DFR with shock capturing. The computational domain is $[0, 2] \times [0, 1]$. For the present case, we choose a Mach 1.1 shock, which is stationary and a vortex positioned at $(x_c, y_c) = (0.25, 0.5)$. The conditions left to the stationary shock are defined as $(\rho, u, v, p) = (1, 1.1\sqrt{\gamma}, 0, 1)$, and the conditions on the right are obtained using Rankine–Hugoniot conditions. Temperature is given by P/ρ. The vortex is defined using perturbation to quantities of mean flow

$$u' = \epsilon \tau e^{\alpha(1-\tau^2)} \sin \theta,$$

$$v' = \epsilon \tau e^{\alpha(1-\tau^2)} \cos \theta,$$

Fig. 2 Pressure variation with *x* as obtained analytically and using DFR with LLAV at $t = 0.2$
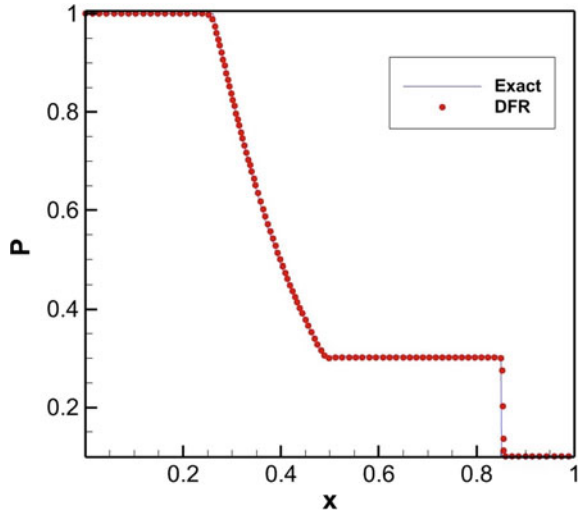
$$T' = -\frac{(\gamma - 1)\epsilon^2 e^{2\alpha(1-\tau^2)}}{4\alpha\gamma},$$

$$S' = 0.$$

$\tau = r/r_c$, $r = \sqrt{(x - x_c)^2 + (y - y_c)^2}$, $\varepsilon = 0.3$, $r_c = 0.05$, and $\alpha = 0.204$. It is important to note that ε, α, and r_c are the vortex's strength, decay rate, and radius. The reader is encouraged to go through [4] for more details.

Reflective boundary conditions are imposed for the bottom and top boundaries, and on the left and right boundaries, we have used Dirichlet boundary conditions. Pressure contours for $t = 0.05, 0.2$, and 0.35 are obtained. From a qualitative comparison of Fig. 3, which represents the pressure contours for $t = 0.05, 0.2$, and 0.3 with [4], we can see that DFR captures the shock and vortex quite accurately.

5 Rayleigh–Taylor Instability

For this case, we have the computational domain as $[0, 0.25] \times [0, 1]$. At $t = 0$, the interface is at $y = 1/2$, the denser fluid is below the interface with density $\rho = 2$, and the lighter fluid with density $\rho = 1$ is above the interface. The acceleration is directed in the positive y-direction.

In the same direction, a small perturbation is given to the fluid speed. The initial conditions are as mentioned in [5], for $0 < y < \frac{1}{2}$, $(\rho, u, v, p) = (2, 0, -0.025c \cdot \cos(8\pi x), 2y + 1)$ and for $\frac{1}{2} \leq y < 1$ $(\rho, u, v, p) = (2, 0, -0.025c \cdot \cos(8\pi x), y + 3/2)$. Here, *c* is the speed of sound $c = (\gamma P/\rho)^{1/2}$ and $\gamma = 5/3$. The boundary conditions

(a) t = 0.05
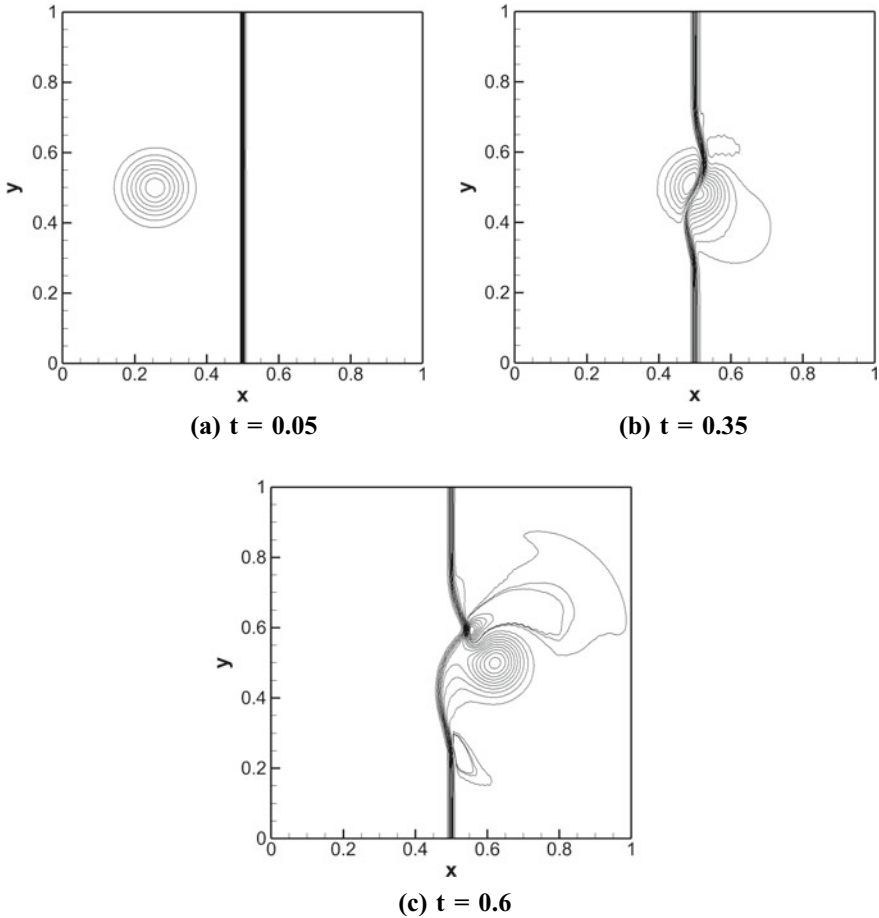
(b) t = 0.35

(c) t = 0.6

Fig. 3 Pressure contours for shock–vortex interaction using $\Delta x = \Delta y = 0.02$ and third-order solution polynomial

consist of reflective type for left and right boundaries, while for the top and bottom, the values are set as $\rho = 1$, $p = 2.5$, $u = 0$, $v = 0$ and $\rho = 2$, $p = 1$, $u = 0$, $v = 0$, respectively.

The density contours obtained in Fig. 4 are for $\Delta x = \Delta y = 1/400$ and third-order solution polynomial at $t = 1.75$, 2, 2.25, 2.5. For $t = 1.75$, $t = 2$, $t = 2.25$, and $t = 2.5$, there are 15 equally spaced contour lines from $\rho = 0.966967$ to $\rho = 2.10314$, $\rho = 0.942342$ to $\rho = 2.16773$, $\rho = 0.911713$ to $\rho = 2.24208$, and $\rho = 0.864408$ to $\rho = 2.33799$, respectively. As a part of the grid study, we increase the order of the solution polynomial to the fifth order and decrease the grid size to $\Delta x = \Delta y = 1/200$.

The density contours obtained in Fig. 5 are for $\Delta x = \Delta y = 1/200$ and fifth-order solution polynomial, and the time intervals are taken as previously stated that is $t =$
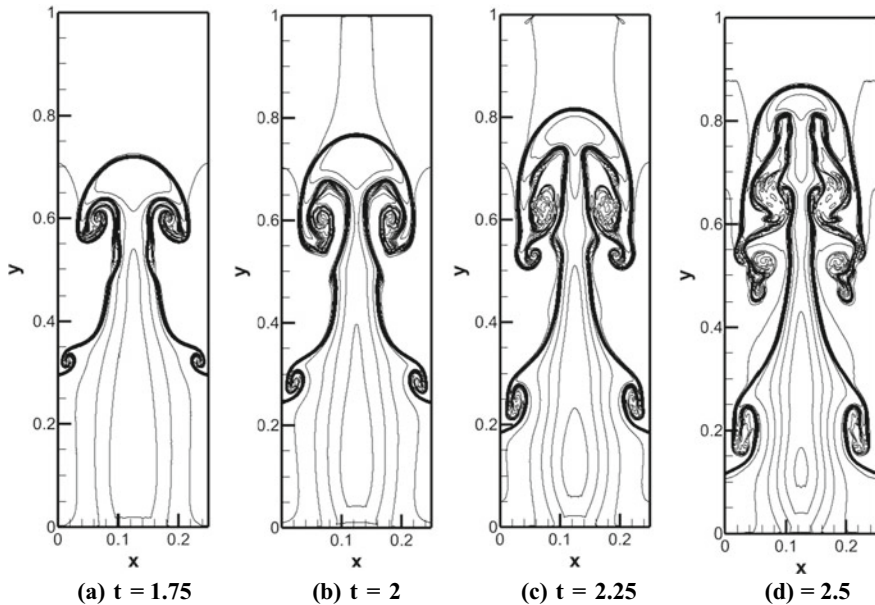
(a) t = 1.75   (b) t = 2   (c) t = 2.25   (d) = 2.5

Fig. 4 Density contours for $\Delta x = \Delta y = 1/400$ and third-order solution polynomial

1.75, 2, 2.25, and 2.5. Again, there are 15 equally spaced contours having minimum and maximum values the same as mentioned previously.

Comparing the contours for the two grids for the same times, we observe that the resolution obtained using the higher-order polynomial is better than the first grid. A key takeaway is that the number of degrees of freedom for the first grid is 640,000, while for the second grid, it is 360,000. Therefore, a higher-order solution polynomial can obtain better resolution even though the grid is coarser.

6 Kelvin–Helmholtz Instability

For numerically simulating the Kelvin–Helmholtz instability, the domain is taken as $[-0.5, 0.5] \times [-0.5, 0.5]$. The initial conditions [6] are, for $-0.25 \le y \le 0.25$, $(\rho, u, v, p) = [2, -0.5, 0.01 \sin(2\pi x), 2.5]$, and everywhere else $(\rho, u, v, p) = [1, 0.5, 0.01 \sin(2\pi x), 2.5]$. For all the boundaries, periodic boundary conditions are used.

The perturbation is given to the vertical velocity using the sine function, and the amplitude is 0.01. Figure 6 represents the density contours for the Kelvin–Helmholtz instability problem for a fifth-order solution polynomial and 200^2 elements at $t = 1, 2,$ and 3. The same figure shows that the vortical structures are well resolved, and the instability grows as time progresses. There are spurious oscillations near the
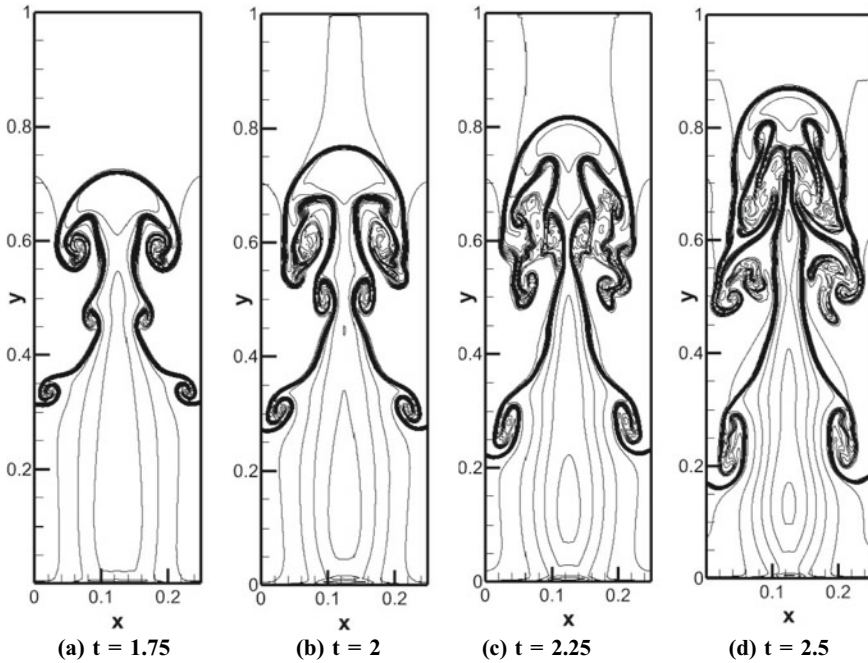
(a) t = 1.75   (b) t = 2   (c) t = 2.25   (d) t = 2.5

Fig. 5 Density contours for $\Delta x = \Delta y = 1/200$ and fifth-order solution polynomial

discontinuity; we have tried suppressing these oscillations using artificial viscosity. DFR can capture small-scale flow features and the roll-ups at the interface caused due to instability.
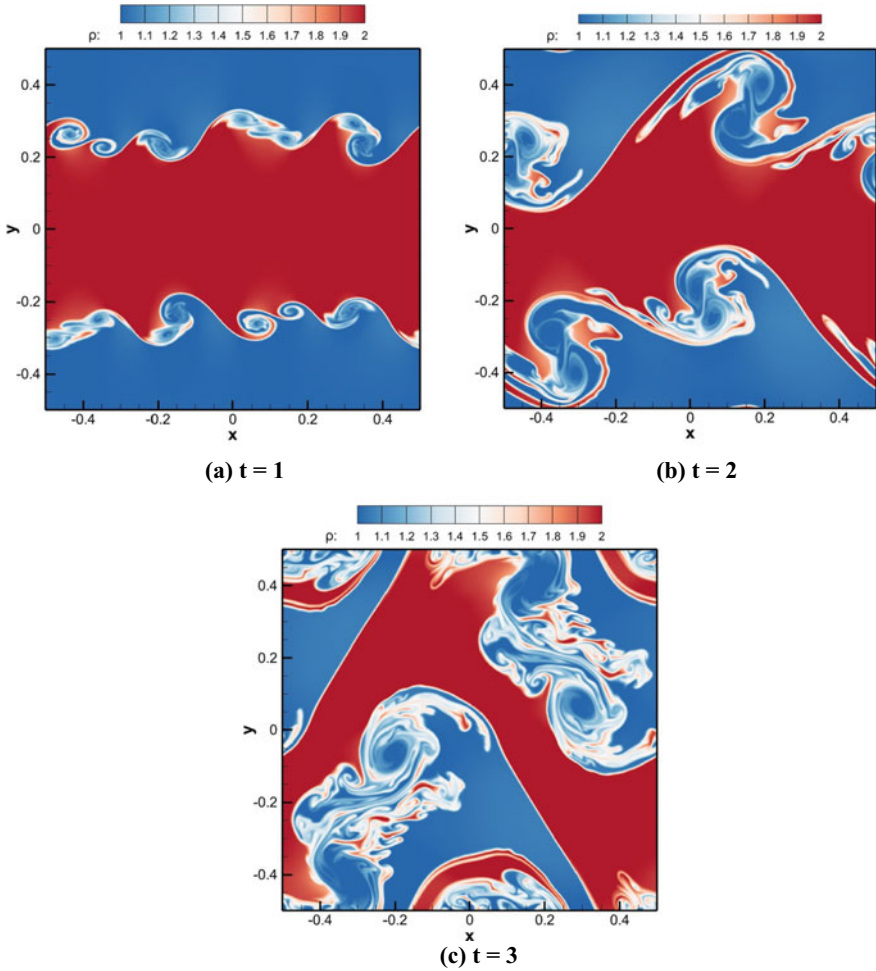
(a) t = 1

(b) t = 2

(c) t = 3

Fig. 6 Density contours for Kelvin–Helmholtz in-stability using 200^2 elements and fifth-order solution polynomial

7 Conclusion

A numerical study is performed to investigate the potential of DFR in resolving shocks and instabilities. We use the in-house DFR code with shock capturing in the inviscid framework. For the present paper, we performed simulations for three problems: Shock–vortex interaction, Rayleigh–Taylor instability, and Kelvin–Helmholtz instability problem. We have also validated the code using the Sod's shock tube problem.

For shock–vortex interaction, we note that the shock and vortex structure is very well preserved both before and after the interaction, and the results are qualitatively comparable to [4].

We see that the complex flow structures are captured for the RT instability problem. We also demonstrate the method's capability in resolving flow structures wherein a coarse grid with a higher-order polynomial shows better resolution than the finer grid.

For KH instability, DFR can capture complex and small- scale flow features. We have suppressed oscillations near the discontinuity using artificial viscosity because such oscillations often introduce errors in the flow.

Nomenclature

P	Pressure
ρ	Density
u	X-Velocity
v	Y-Velocity
E	Total energy
T	Temperature
e	Internal energy
γ	Specific heat ratio
S	Entropy
t	Time
c	Speed of sound
u'	u-Velocity perturbation
v'	v-Velocity perturbation
T'	Temperature perturbation
S'	Entropy perturbation

References

1. Romero JD (2017) On the development of the direct flux reconstruction scheme for high-order fluid flow simulations. Ph.D. thesis, Stanford University, Stanford, CA
2. Hyunh (2007) A flux reconstruction approach to high-order schemes including discontinuous Galerkin methods. In: 18th AIAA computational fluid dynamics conference
3. Persson PO, Peraire J (2006) Sub-cell shock capturing for discontinuous Galerkin methods. In: 44th AIAA aerospace sciences meeting and exhibit

4. Shu CW (1998) Essentially non-oscillatory and weighted essentially non-oscillatory schemes for hyperbolic conservation laws. In: Advanced numerical approximation of nonlinear hyperbolic equations. Springer, Berlin Heidelberg, pp 325–432
5. Shi Y-T, Shu C-W (2003) Resolution of high order WENO schemes for complicated flow structures. J Comput Phys 186:690–696
6. San O, Kara K (2015) Evaluation of Riemann flux solvers for WENO reconstruction schemes: Kelvin–Helmholtz instability. Comput Fluids 117:24–41